(1)

AGARD-AR-265

AGARD

ADVISORY GROUP FOR AEROSPACE RESEARCH & DEVELOPMENT

7 RUE ANCELLE 92200 NEUILLY SUR SEINE FRANCE

AGARD ADVISORY REPORT No.265

Report of the Fluid Dynamics Panel Working Group 11

Rotary-Balance Testing for Aircraft Dynamics

(Les Essais sur Balance Rotative pour l'Etude de la Dynamique du Vol de l'Avion)

NORTH ATLANTIC TREATY ORGANIZATION

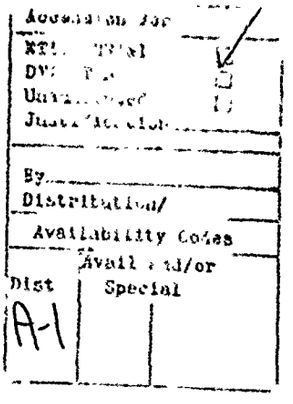
Accession For
NTIS GRA&I
DTIC TAB
Unannounced
Justification
By
Distribution/
Availability Codes
Dist
Avail and/or
Special
A-1

AGARD-AR-265

NORTH ATLANTIC TREATY ORGANIZATION

ADVISORY GROUP FOR AEROSPACE RESEARCH AND DEVELOPMENT

(ORGANISATION DU TRAITE DE L'ATLANTIQUE NORD)

AGARD Advisory Report No.265

Report of the Fluid Dynamics Panel

Working Group 11

Rotary-Balance Testing for Aircraft Dynamics

(Les Essais sur Balance Rotative pour l'Etude de la Dynamique du Vol de l'Avion)

This Advisory Report was prepared at the request of the Fluid Dynamics Panel of AGARD.

The Mission of AGARD

According to its Charter, the mission of AGARD is to bring together the leading personalities of the NATO nations in the fields of science and technology relating to aerospace for the following purposes:

- Recommending effective ways for the member nations to use their research and development capabilities for the common benefit of the NATO community;
- Providing scientific and technical advice and assistance to the Military Committee in the field of aerospace research and development (with particular regard to its military application);
- Continuously stimulating advances in the aerospace sciences relevant to strengthening the common defence posture;
- Improving the co-operation among member nations in aerospace research and development;
- Exchange of scientific and technical information;
- Providing assistance to member nations for the purpose of increasing their scientific and technical potential;
- Rendering scientific and technical assistance, as requested, to other NATO bodies and to member nations in connection with research and development problems in the aerospace field.

The highest authority within AGARD is the National Delegates Board consisting of officially appointed senior representatives from each member nation. The mission of AGARD is carried out through the Panels which are composed of experts appointed by the National Delegates, the Consultant and Exchange Programme and the Aerospace Applications Studies Programme. The results of AGARD work are reported to the member nations and the NATO Authorities through the AGARD series of publications of which this is one.

Participation in AGARD activities is by invitation only and is normally limited to citizens of the NATO nations.

Published December 1990

ISBN 92-835-0597-2

Printed by Specialised Printing Services Limited
40 Chigwell Lane, Loughton, Essex IG10 3TZ

Recent Publications of the Fluid Dynamics Panel

AGARDOGRAPHS (AG)

Techniques Expérimentales Liées à l'Aérodynamique à Basse Densité
AGARD AG-318 (FR), April 1990

A Survey of Measurements and Measuring Techniques in Rapidly Distorted Compressible Turbulent Boundary Layers
AGARD AG-315, May 1989

Reynolds Number Effects in Transonic Flows
AGARD AG-303, December 1988

Three Dimensional Grid Generation for Complex Configurations – Recent Progress
AGARD AG-309, March 1988

Computational Fluid Dynamics: Algorithms & Supercomputers
AGARD AG-311, March 1988

REPORTS (R)

Inverse Methods in Airfoil Design for Aeronautical and Turbomachinery Applications
AGARD R-780, Special Course Notes, November 1990

Aerodynamics of Rotorcraft
AGARD R-781, Special Course Notes, November 1990

Three-Dimensional Supersonic/Hypersonic Flows Including Separation
AGARD R-764, Special Course Notes, January 1990

Advances in Cryogenic Wind Tunnel Technology
AGARD R-774, Special Course Notes, November 1989

Aerothermodynamics of Hypersonic Vehicles
AGARD R-761, Special Course Notes, June 1989

ADVISORY REPORTS (AR)

Calculation of 3D Separated Turbulent Flows in Boundary Layer Limit
AGARD AR-255, Report of WG10, May 1990

Adaptive Wind Tunnel Walls: Technology and Applications
AGARD AR-269, Report of WG12, April 1990

Drag Prediction and Analysis from Computational Fluid Dynamics: State of the Art
AGARD AR-256, Technical Status Review, June 1989

Boundary Layer Simulation and Control in Wind Tunnels
AGARD AR-224, Report of WG09, April 1988

CONFERENCE PROCEEDINGS (CP)

Vortex Flow Aerodynamics
AGARD CP-494, October 1990

Missile Aerodynamics
AGARD CP-493, April 1990

Aerodynamics of Combat Aircraft Controls and of Ground Effects
AGARD CP-465, October 1989

Computational Methods for Aerodynamic Design (Inverse) and Optimization
AGARD CP-463, April 1989

Applications of Mesh Generation to Complex 3-D Configurations
AGARD CP-464, April 1989

Fluid Dynamics of Three-Dimensional Turbulent Shear Flows and Transition
AGARD CP-438, October 1988

Validation of Computational Fluid Dynamics
AGARD CP-437, May 1988

Aerodynamic Data Accuracy and Quality: Requirements and Capabilities in Wind Tunnel Testing
AGARD CP-429, October 1987

Aerodynamics of Hypersonic Lifting Vehicles
AGARD CP-428, April 1987

Aerodynamic and Related Hydrodynamic Studies Using Water Facilities
AGARD CP-413, October 1986

Applications of Computational Fluid Dynamics in Aeronautics
AGARD CP-412, April 1986

Store Airframe Aerodynamics
AGARD CP-389, October 1985

Unsteady Aerodynamics — Fundamentals and Applications to Aircraft Dynamics
AGARD CP-386, May 1985

Aerodynamics and Acoustics of Propellers
AGARD CP-366, October 1984

Improvement of Aerodynamic Performance through Boundary Layer Control and High Lift Systems
AGARD CP-365, May 1984

Wind Tunnels and Testing Techniques
AGARD CP-348, September 1983

Aerodynamics of Vortical Type Flows in Three Dimensions
AGARD CP-342, April 1983

Missile Aerodynamics
AGARD CP-336, September 1982

Prediction of Aerodynamic Loads on Rotorcraft
AGARD CP-334, May 1982

Wall Interference in Wind Tunnels
AGARD CP-335, May 1982

Fluid Dynamics of Jets with Applications to V/STOL
AGARD CP-308, November 1981

Aerodynamics of Power Plant Installation
AGARD CP-301, May 1981

Computation of Viscous-Inviscid Interactions
AGARD CP-291, October 1980

Subsonic/Transonic Configuration Aerodynamics
AGARD CP-285, May 1980

Turbulent Boundary Layers Experiments, Theory and Modelling
AGARD CP-271, September 1979

Aerodynamic Characteristics of Controls
AGARD CP-262, May 1979

High Angle of Attack Aerodynamics
AGARD CP-247, October 1978

Dynamic Stability Parameters
AGARD CP-235, May 1978

Unsteady Aerodynamics
AGARD CP-227, September 1977

Laminar-Turbulent Transition
AGARD CP-224, May 1977

Preface

Rotary flows and rotary-balance testing have in the past been of interest mainly for the study and prediction of the spinning and spin-recovery behavior of aircraft. However, the relative interest in this technology has been stimulated recently by the introduction of highly agile military aircraft which possess a substantially expanded flight envelope compared to previous aircraft. These advanced aircraft maneuver at high angles of attack, performing rapid, large-amplitude motions which are characterized by rotary, nonlinear, and unsteady flows. Hence, an increased knowledge of rotary flows and of aerodynamic characteristics in the presence of rotation at high angles of attack is now necessary for the successful design of future fighter aircraft. Consequently, the AGARD Fluid Dynamics Panel formed a Working Group to review the state of the art for rotary-balance technology and the application of rotary data to aircraft flight dynamics, and this report summarizes the findings of that Group. Six NATO nations, namely France, Canada, Germany, Italy, the United Kingdom and the United States, participated in the preparation of the report.

Préface

L'Aérodynamique des ecoulements helicoidaux et l'expérimentation en soufflerie sur balance rotative ont connu dans le passé quelques développements liés principalement à l'etude et à la prevision des comportements en vrilles des avions ainsi qu'à la récupération du vol contrôlé Aujourd'hui l'intérêt porté à ces sujets s'est considérablement accru avec l'avénement des avions de combat hautement manoeuvrables qui disposent d'un domaine de vol contrôlé, largement etendu compare aux formules antérieures Ces avions de technologie avancée évoluent à des incidences élevées et réalisent des manoeuvres amples et rapides qui impliquent des phénomènes aérodynamiques hélicoidaux, non linéaires et instationnaires Ainsi, une connaissance approfondie des caractéristiques aerodynamiques de l'avion en presence de mouvements de rotation à haute incidence est désormais necessaire pour optimiser les futurs avions de combat.

Dans ce contexte, l'AGARD (Panel de Dynamique des Fluides) a constitue un groupe de travail pour analyser l'état de l'art en ce qui concerne les techniques relatives aux Balances Rotatives et l'exploitation des données expérimentales utilisees pour l'etude de la dynamique du vol de l'avion Ce rapport résume les conclusions de ce groupe. Six pays de l'OTAN. France, Canada, Allemagne, Italie, Royaume Uni et Etats-Unis ont participé à l'élaboration du présent rapport.

Dr K.J.Orlik-Ruckemann
Chairman
FDP WG 11

Mr J.R.Chambers
Deputy Chairman
FDP WG 11

Contents*

* Chapter and section editors are indicated in parentheses.

Page

PART II: TEST RESULTS AND APPLICATIONS

CHAPTER 1

INTRODUCTION

At the joint FDP/FMP Symposium on *Unsteady Aerodynamics - Fundamentals And Applications To Aircraft Dynamics*, held in Göttingen in May, 1985, the meeting Technical Evaluators suggested that the time was appropriate for a critical examination of the rotary-balance techniques used in the AGARD community for the analysis of high-angle-of-attack dynamic behavior of aircraft. It has now been generally recognized that modern, highly agile fighter aircraft have flight envelopes that encompass rapid maneuvers at high angles of attack, which in turn cause the flow over the aircraft to become rotary, unsteady and highly nonlinear. There is, therefore, a great need to obtain the aerodynamic characteristics required for flight dynamics predictions of fighter aircraft in the proper aerodynamic scenario—that is, in the presence of rotation at high angles of attack. In the past, this scenario was only required for analysis of the spin and spin-recovery characteristics of aircraft.

It was felt that such a critical examination should encompass both the experimental techniques used to obtain rotary-flow aerodynamic data and the procedures involved in using this type of data in the mathematical modeling of the dynamic behavior of a maneuvering fighter aircraft. The experimental techniques are based mainly on the use of the so-called "rotary balances" which permit measurements of aerodynamic data during rotary motions. A surprisingly large number of such balances exist in several countries of NATO (and in some countries outside of NATO as well), and, in general, the use of these balances is definitely on the increase. In addition to a review of the technical approach used in each country, specific hardware and problems encountered in this type of experiment were addressed and advanced applications noted. These considerations included methods to establish tare loads, descriptions of the test apparatus and data-reduction procedures, flow visualization techniques, discussion of errors introduced by support and wind-tunnel interference and possible new concepts for rotary-testing techniques. On the applications side, typical rotary-flow data for various types of aircraft were reviewed and the mathematical models and procedures employed by several organizations in the prediction of flight dynamic behavior were examined and compared. Special effort was made to summarize experience involving correlation of dynamic behavior predictions with the observed motions of free-flight models and aircraft in flight. Finally, possibilities for undertaking joint international studies of some of the remaining problem areas were discussed and appropriate recommendations were formulated.

The Working Group was proposed by the Fluid Dynamics Panel in the Fall of 1985 and approved by the AGARD National Delegates Board in March of 1986 as FDP Working Group 11 on Rotary Balances. In addition to performing the tasks envisioned, the Working Group visited several wind-tunnel establishments for demonstrations of rotary-balance test procedures and data reduction, and established, for the first time, a working relationship and contacts among the various rotary-balance operators.

The Working Group members were:

CANADA

Dr. Martin E. Beyers
National Aeronautical Establishment, Ottawa

Dr. Kazimierz J. Orlik-Rückemann
(Chairman and FDP Member)
National Aeronautical Establishment, Ottawa

GERMANY

Mr. Bernd Schulze
MBB - Helicopter and Aircraft, Munich

UNITED KINGDOM

Mr. Charles O. O'Leary
Royal Aircraft Establishment, Bedford

Mr. Alan Vint (FDP Member, Meetings 1, 2, 3)
British Aerospace Warton, Preston

FRANCE

Mr. Dominique Tristrant
ONERA-IMFL, Lille

Mr. Robert A. Verbrugge
ONERA-IMFL, Lille

ITALY

Mr. Ernesto Valtorta
AerMacchi SpA, Varese

Mr. Livio Visintini
AerMacchi SpA, Varese

UNITED STATES

Mr. William Bihrle
Bihrle Applied Research Incorporated, Jericho, NY

Mr. Joseph R. Chambers (Deputy Chairman)
NASA Langley Research Center, Hampton, VA

Dr. Robert A. Kilgore (Meetings 1, 3, 4, 5)
NASA Langley Research Center, Hampton, VA

Mr. Gerald N. Malcolm
Eidetics International, Torrance, CA

CONSULTANTS

Dr. Robert A. Kilgore (Meeting 2)
NASA Langley Research Center
Hampton, VA

Dr. Lars E. Ericsson (Meetings 2, 3, 4)
Lockheed Missiles and Space Company, Incorporated
Sunnyvale, CA

OBSERVERS

Dr. Lars E. Ericsson (Meetings 1, 5, and 6)
Lockheed Missiles and Space Company Incorporated
Sunnyvale, CA
USA

Dr. Horst Otto (Meeting 3)
DFVLR
Braunschweig, FRG

In the period from 1986 to 1989 the Working Group held six meetings

1. Stanford University
   October 16-17, 1986
2. BAe, Warton and RAE, Bedford
   April 1-3, 1987
3. DFVLR, Braunschweig and AerMacchi, Varese
   September 23-25, 1987
4. ONERA-IMFL, Lille and AGARD, Paris
   April 20-22, 1988
5. NASA-Langley
   November 15-18, 1988
6. AGARD, Paris
   May 2-4, 1989

Considerable assistance and information, as well as most congenial hospitality, were provided to the Group by the various host organizations, for which the Group expresses its sincere appreciation

This final report was jointly prepared by the Working Group members The names of the individual section authors and chapter editors are given in the Contents, but the entire report was discussed and reviewed in detail by all the members of the Working Group and the two consultants Dr Martin Bevers, NAE, was the overall technical editor. In addition to ensuring technical correctness and clarity, he was concerned with achieving a measure of consistency amongst the different contributions an important consideration in a report prepared by 14 authors from 6 countries

The appreciation of the Working Group is extended to those who prepared the material, and to the staff of the NASA-Langley Research Center, who collated the inputs from the group and prepared the report in a consistent and uniform manner In this regard, the enthusiastic support and untiring efforts of the WG Deputy Chairman, Mr Joseph Chambers, and other members of the NASA-Langley staff deserve special acknowledgement. The efforts of theNAE Graphics and Illustrative Services in preparing the final layout of the figure pages are also recognized with thanks. The contributions of Dr. Jean Ross of RAE to Section 9.4 and Dr. Juri Kalviste of the Northrop Aircraft Corporation to Section 9.5 are greatly appreciated, as is the assistance of the Lockheed Missiles and Space Company in providing support for Dr. Lars Ericsson's attendance at Meetings 1, 5 and 6.

Dr K J Orlik-Ruckemann
Chairman
FDP WG 11

CHAPTER 2

ROTARY-BALANCE TECHNIQUES

2.0 INTRODUCTION

The rotary-balance test technique was developed to provide information on the effects of angular rates on the overall aerodynamic forces and moments acting on aircraft in flight. Certain motions, such as the developed spin, generate large differences in local flow angles for various airframe components, and the separated airflow characteristics experienced in spins are extremely difficult to predict or analyze using other techniques.

This chapter provides information regarding the history and development of the test technique in several AGARD nations, general characteristics of the test equipment, data reduction process and other techniques used to provide additional information for the analysis of rotary-balance test results.

2.1 HISTORICAL BACKGROUND

1915-1945

The need for steady-state rotational-flow aerodynamics for spin analysis was recognized relatively early in the history of aeronautical research. For example, Glauert[1] attempted in 1919 to calculate such data using strip theory. By the early 1920's, a rolling balance was used in England to obtain rotary data experimentally.[2,3] Gates and Bryant[4] remarked in 1926, however, that this simple rolling balance should be replaced with an apparatus that actually reproduces, in a wind tunnel, the conditions of a relatively fast spin. NACA investigators also reasoned that subjecting all components of an airplane to a constant velocity vector during static force tests was unsatisfactory for simulating flow conditions in a spin. This hypothesis was supported by Irving and Batson,[5] who noted in 1928 that the use of static force test data resulted in erroneous conclusions when applied to the spin.

Consequently, in 1933 Allwork,[6] as well as Bamber and Zimmerman,[7] reported on rotary balances installed in the NPL 7-Ft Wind Tunnel in England and the NACA 5-Ft Vertical Wind Tunnel in the U.S., respectively. The NACA apparatus was capable of measuring the six components of aerodynamic forces and moments as functions of angle of attack, angle of sideslip and rotation rate. A large number of wing designs and complete airplane configurations were tested with this apparatus, and the results are documented in the NACA publications cited in Reference 8.

During the early thirties, aircraft rolling or spinning conditions were investigated at the Deutsche Versuchsanstalt fur Luftfahrt (DVL) in Germany by introducing rotating flow in the test section. Although this technique presented some obvious advantages, such as obtaining rotary data on a less-complex non-rotating model, it was discarded because of problems encountered in generating the desired rotational flow. Apparently, force measurements were also obtained on a simple type of rotary-balance apparatus, since it was observed that "force measurements yield only integral values and show little concerning the nature of the flow phenomena." Subsequently, pressure measurements on a rotating model[9] were performed in Gottingen in 1935 to understand the flow phenomena at the tail surfaces in the spin. By 1940, DVL was using a rotary balance which could rotate at up to 300 rpm to measure rolling and yawing moments on models in a 10-ft low-speed wind tunnel.

The first French rotary balance,[10,11] developed in 1937, was used in efforts to determine the six force and moment components for a model by measuring pressures inside pneumatic jacks that maintained the equilibrium of the model about all axes. Since this technique could not produce precise measurements, it was subsequently abandoned. By 1937, Bamber, House, and Zimmerman[12,13] presented a method for solving the three moment equations for steady-state equilibrium spin conditions using rotary balance data as inputs. This analytical technique was developed through necessity since obtaining simultaneous solutions to the six equations of motion and other associated mathematical expressions before the existence of analog and digital computers was a formidable task, requiring step-by-step integration procedures laboriously performed by hand.

1945-1975

The effectiveness of the first NACA rotary balance was limited by the relatively large ratio of model size to wind-tunnel cross-sectional area. Also, the six-component balance was mounted external to the model, was large relative to the size of the model, and was of dubious accuracy. These shortcomings were eliminated when a new rotary balance was installed in the Langley Spin Tunnel in 1945. Because of the limited instrumentation then available, an undesirable amount of time and effort was needed to obtain a small amount of data, which in many instances were not repeatable. Understandably, the rotary balance fell into disuse after obtaining data for only one airplane configuration. These data were applied during subsequent analytical studies.[8,14,15]

In the early fifties, AerMacchi in Italy began spin analysis.[16] In support of this effort, it constructed a simple windmilling rig, followed by a forced-rotation two-component rig in 1956, and finally a six-component setup.

By the mid 1950's, the mass distribution of high-performance fighters had become concentrated in the fuselage, which led to a concern over vertical tail loads resulting from inertial coupling during uncoordinated rolling pull-out maneuvers. Fortunately, analog computers were in wide use by this time and many engineers became familiar with large angle, six-degree-of-freedom calculations. Eventually, these studies of inertial coupling were extended to include spins by simply extending

the aerodynamic model, consisting of static data and dynamic derivatives, to higher α values. The need for rotary-balance data was virtually overlooked by the aerospace industry in the United States from the mid-1950's to the mid-1970's.

Although the NACA updated its rotary balance in the late 1950's, it was used for only one analytical airplane study by NASA in 1964.[17] The NASA study properly employed rotary-balance data and, therefore, significantly contributed to the computational methods available for spin analysis. Nevertheless, the erroneous practice of using conventional static data and dynamic derivatives to calculate spinning motions continued. These calculations always required arbitrary adjustments in the magnitude of some dynamic derivatives in order to obtain correlation with a small amount of time history records obtained from flight tests.

NASA also installed a rotary-balance apparatus in the Langley 30- by 60-Foot Wind Tunnel[18] and conducted large-angle, six-degree-of-freedom computer studies in the early 1970's to establish rigorously the aerodynamic models required for spin calculations. Several studies[19,20] simulated the motions of a fighter airplane, using both a conventional aerodynamic model and one which included the effect of spin rotation rate. The computed time histories were compared with those obtained with an unpowered, radio-controlled, dynamically-scaled model. It was shown that the developed spin exhibited by the model could not be duplicated using a conventional aerodynamic model, but the use of rotary data resulted in good agreement with the experimental results.

1975-Present

In the mid-1970's, NASA modernized the spin tunnel rotary balance by incorporating the latest state-of-the-art instrumentation and computer technology. Valid data are now obtained rapidly and economically, and over 60 configurations representative of general aviation, fighter and trainer aircraft, have been tested in the NASA facility. New rotary balances in France,[21] Italy[22] and Germany[23] were also installed during this period. More recently, rotary balances were installed in Great Britain at British Aerospace (Warton Aerodrome) and RAE (Bedford) in both low- and high-speed wind-tunnel facilities.

Tests conducted in all AGARD countries with a rotary-balance capability have consistently demonstrated the pronounced nonlinear, complex dependency of aerodynamic moments on rotational rate at high angles of attack; and the test results continue to emphasize the futility of computing spin equilibrium conditions or time histories without rotary-balance data.

2.2 GENERAL PHYSICAL ARRANGEMENTS

2.2.1 Introduction

Rotary-balance apparatuses have been developed in several of the countries participating in AGARD. Most countries have at least one apparatus which is actively being used and some have more than one. There are also some apparatuses that have been deactivated, either because of lack of research or because they have been replaced by improved equipment. A historical overview of rotary balances in general was provided in the previous section, and more detailed accounts of the histories of rotary balances in each country are provided in Chapter 3. The purpose of this section is to describe in general terms some typical physical characteristics of rotary-balance apparatuses. The specific designs of many apparatuses are shown in Chapter 3 and some of these will be referred to in this introductory section.

The primary purpose of a rotary-balance apparatus is to produce a "coning motion"—that is, a continuous rolling motion of the vehicle about the free-stream velocity vector as shown in Figure 2-1. The angle of attack and sideslip are constant during the rotational cycle.

An examination of the flow field experienced by an aircraft in terms of the local values of velocity and flow angularity in a rotational regime will be helpful in understanding the importance of acquiring rotary-balance data. Shown in Figure 2-2 is an illustrative sketch of an airplane in a flat spin ($\alpha = 90°$). In this situation, the free-stream velocity vector is perpendicular to the X-Y plane of the aircraft, and the aircraft is spinning about its Z axis (which is colinear with the velocity vector). The local flow angle at any point on the airplane is dependent on both the local velocity due to rotation and the free-stream velocity (or sink rate in the case of a vertical spin axis). In fact, the local flow angle is proportional to the ratio of the local velocity due to rotation and the free-stream velocity. It is common practice to use a reference nondimensional rotation rate expressed in terms of the angular velocity Ω, the free-stream velocity V and a reference length which is usually taken to be half the wing span, $b/2$. With this convention, the ratio of the velocity at the wing tip to the free-stream velocity is $(\Omega b/2)/V$ or $\Omega b/2V$. This ratio is also equal to the arctangent of the helix angle at the wing tip when an airplane is in an equilibrium steady spin. In applications of rotary-balance technology, the AGARD nations frequently interchange the symbols Ω and ω for angular velocity. The reader should note that both symbols have been used in this report.

Since airplanes do not necessarily spin about an axis coincidental with the center of mass, a spin radius may exist, as shown in Figure 2-3. Efforts have been made in the development of some rotary-balance rigs to provide a capability for simulating the spin radius. This capability is necessary for certain types of motions such as steep spins, and for certain test techniques designed for the extraction of dynamic stability parameters.

2.2.2 Coning Motion in the Wind Tunnel

To generate a coning motion in the wind tunnel, a model is fixed to a support system that can be rotated at constant rate about an axis that is usually parallel to the free-stream velocity vector of the wind tunnel. Thus, the attitude of the model remains constant with respect to the airstream (resulting in constant values of α and β) throughout a rotational cycle. The primary purpose of the experiment is to determine the overall forces and moments on the model as a function of the rotation

rate. These forces and moments are typically determined from a six-component strain-gauge balance mounted internally in the model and fastened to a sting, either through the rear or tail of the model or, for high angles of attack, through the top of the fuselage. A typical example of model-mounting procedure is shown in Figure 2-4.

2.2.3 General Description of a Rotary-Balance Apparatus

The need for rotary-balance experiments and the nature of the rotational motion required for experiments in the wind tunnel have been described. The designs for apparatuses to produce the required motions in specific wind tunnels vary significantly. Many factors have influenced the specific physical characteristics of the apparatuses now in operation. However, the fundamental design criteria influencing all the apparatuses are very similar. The apparatuses must rotate in either direction and have the capability to vary the rotational speed from zero to a value that will provide nondimensional rotation rates, $\Omega b/2V$, consistent with those experienced by full-scale aircraft. Generally, values up to 0.3 are adequate for most fighter aircraft; and values as high as 0.8 may be required for some light aircraft. Obviously, the value of the nondimensional rotation rate can be controlled by varying either the free-stream velocity V or the rotational velocity Ω. Generally, however, one desires to set the free-stream velocity at a level consistent with the flight regime of interest. The other important parameter is Reynolds number. It has been shown, as will be discussed in Chapter 5, that the aerodynamic forces and moments on many fuselage shapes and some wing configurations undergoing rotary motions can be strongly influenced by Reynolds number. See also detailed discussion of scaling considerations in Section 8.3.

It is important to maintain the selected rotation rate at a constant value for the duration of the data acquisition cycle. To accomplish this goal, most apparatuses are driven by servo-controlled hydraulic or electric motors. For most fighter aircraft, it is also necessary to be able to vary the angle of attack from approximately $-10°$ to $90°$ and to vary the angle of sideslip from $-20°$ to $20°$. These requirements will vary somewhat depending on the specific application. These angles can be set manually or remotely, and the choice of manual or remote capability is a significant factor in the resulting design complexity and operational productivity of the apparatus.

The loads on the model are typically measured with an internal five- or six-component strain-gage balance. The electrical signals to and from the balance are transmitted through slip rings.

When the model is rotated in the wind tunnel, there are contributions to the forces and moments measured by the balance from three sources. The first source is the inertial forces and moments of the model itself, which vary with model attitude and rotation speed; the second source is the cyclical variation of model weight, which can either be compensated for or filtered out with low-pass filters; and the third source of loads measured by the balance is that of the aerodynamic loads. In order to isolate the desired aerodynamic loads it is necessary to measure the inertial loads in a wind-off condition and to subtract these tare loads from the combined loading with the wind on. The typical procedures for data reduction are described in Sections 2.3 and 2.4.

To minimize the inertial loads and the periodic gravitational force input to the balance, it is important to design the model for minimum weight and moments of inertia. The relationship between the inertial loads and the model moments of inertia is discussed in more detail in Section 2.3.

The physical characteristics of the individual apparatuses currently in operation vary significantly. Most of the apparatuses have been constructed to operate in closed-circuit continuous-flow wind tunnels with horizontal test sections. Two of the apparatuses in active use are mounted on the side walls of vertical spin tunnels. Brief descriptions of some of these apparatuses follow, and more detailed discussions are given in Chapter 3 of this report. Table 2-1 provides a summary of the characteristics of the subject apparatuses.

2.2.4 United States

The rotary-balance testing capability in the United States has been concentrated in recent years at the NASA Langley Research Center and the NASA Ames Research Center.

2.2.4.1 NASA Langley Research Center

Rotary-balance testing at NASA-Langley was first introduced in the 1930's with an apparatus that could be operated in a small vertical tunnel. Over the last 50 years, rotary balances have been developed for the 7- by 10-Foot High-Speed Tunnel the 8-Foot Transonic Tunnel and the 30- by 60-Foot Wind Tunnel. The only rotary-balance apparatus now in active use is a rig developed for the Langley Spin Tunnel. Figure 2-5 shows a sketch of the apparatus, and Figure 2-6 shows a typical model installation. This apparatus is electrically driven and provides rotation rates up to 90 rpm. Nondimensional spin rates ($\Omega b/2V$) as high as 1.0 can be achieved by operating the tunnel at an airspeed as low as 20 ft/sec. Reynolds numbers up to 0.3×10^6 based on reference chord can be achieved at the maximum tunnel speed of 60 ft/sec. The angle of attack can be varied from $-90°$ to $90°$ and sideslip angles up to $\pm 30°$ can be used.

2.2.4.2 NASA Ames Research Center

Two apparatuses have been in use at NASA Ames Research Center in recent years. One is a relatively complex apparatus designed specifically for tests at high Reynolds numbers in the Ames 12-Foot Pressure Wind Tunnel. Figures 2-7 and 2-8 show a sketch and a photograph of this apparatus. Since this apparatus was developed for operation in a pressure tunnel, the angle of attack and sideslip are changed remotely. This is accomplished by rotating about the ϕ_1 and ϕ_2 axes shown in Figure 2-7. With the use of two top-mount and one base-mount sting arrangements, angle of attack can be varied from $-30°$ to $100°$ and sideslip can be varied between $\pm 30°$. The maximum rotation rate is $\Omega = 350$ rpm. The 12-Foot Wind Tunnel

is typically run at $M = 0.25$ for rotary-balance tests. This Mach number coincides with the maximum Reynolds number obtainable in this tunnel, approximately 8.0×10^6/ft.

The second apparatus, shown in Figure 2-9, was developed for the Ames 6- by 6-Foot Supersonic Wind Tunnel. A hydraulic motor is used to turn a shaft aligned with the wind-tunnel airstream. A series of interchangeable bent stings can be attached to the rotating shaft to vary the angle of incidence with respect to the airstream. The stings are designed to support a model on a strain-gauge balance at pitch angles ranging from 0° to 30° while maintaining the same axial model station.

The angles of attack and sideslip can be selected from various combinations of the discrete pitch angles available with the bent stings and adjusting the roll angle of the model on the balance. The rotation rate can be varied up to ±600 rpm. This apparatus is used primarily for higher Mach number tests, typically from $M = 0.6$ to 0.8.

2.2.5 Italy

Rotary-balance apparatuses have been in use at AerMacchi in Italy since the early 1950's. An evolution of design has resulted in the apparatus shown in Figure 2-10. This apparatus is operated in the AerMacchi Low Speed Wind Tunnel at speeds up to 60 m/s. The open test section is 2.0 m in diameter and 2.6 m in length. The maximum rotational speed is 300 rpm. The angles of attack and sideslip, which are set manually, can be varied from −180° to 180° with various model mounting arrangements. The apparatus provides for a spin radius of up to 8 inches.

2.2.6 United Kingdom

2.2.6.1 British Aerospace

British Aerospace currently operates two rotary-balance apparatuses. One rig is for use at low values of Mach and Reynolds numbers in the British Aerospace (BAe) 5.5-m LSWT (Low Speed Wind Tunnel) and the other rig, sponsored by the RAE, is primarily for testing in the BAe 1.2-m HSWT (High Speed Wind Tunnel) at Warton. The latter apparatus can also be accommodated in a number of other U.K. facilities.

The low-speed rig, which is shown in Figure 2-11, is designed for manual model attitude changes. The angle-of-attack range is achieved by mounting the model through the base or the top and moving the sting around an arc centered at the model reference center. Sideslip is achieved by rotating the model about its longitudinal body axis. The rig is driven by an electric motor and can achieve rotational speeds up to 60 rpm. The capabilities of the rig are as follow:

$$-45° \leq \alpha \leq 90°$$
$$-45° \leq \beta \leq 90°$$
$$\Omega b/2V \leq 0.2$$

The high-speed rig, shown in Figure 2-12, was designed primarily for operation in the 1.2-m HSWT (a blowdown tunnel) at BAe, Warton Division , but it was also required to function in three other U.K. tunnels: the 2.7- by 2.1-m LSWT at BAe, Warton Division; the 9- by 8-Foot Transonic Tunnel at A.R.A., Bedford; and the 8- by 8-Foot HSWT at RAE, Bedford. The design specifications included a maximum Mach number of 0.95, a maximum Reynolds number of 46×10^6/m, angle of attack to 40° (0° − 90° in the 2.7- by 2.1-m LSWT), sideslip angles to 10° (up to $\alpha = 20°$) and roll rates to 600 rpm. These design choices produced a reduced spin rate, $\Omega b/2V$, of 0.14 for $M = 0.4$, using a 1/20-scale model of a typical combat fighter. An additional requirement for this rig, because of the desired operation in a blowdown tunnel (with run time ranging from 25 sec at $M = 0.4$ to 9 sec at $M = 0.95$) is the capability of rapidly changing from one rotational speed to another and acquiring data at each stabilized rotation rate.

2.2.6.2 RAE Bedford

A rotary-balance apparatus has been developed recently at RAE Bedford for operation in both low-speed and high-speed tunnels. Figure 2-13 shows a photograph of the apparatus, which is driven by a servo-controlled hydraulic motor and can be rotated up to 350 rpm. The angle of attack can be varied from −12° to 60° using two different sting mounts. The apparatus has been tested in the atmospheric 4-m × 2.7-m Low Speed Wind Tunnel, and in the high-speed pressurized 2.4-m × 1.8-m tunnel at Mach numbers up to 0.8.

2.2.7 Federal Republic of Germany

A rotary-balance apparatus is in operation in the 3-m Low Speed Wind Tunnel of the DFVLR Research Center in Braunschweig. Figure 2-14 shows a sketch of the apparatus, and Figure 2-15 is a photograph of the apparatus installed in the 3.25-m by 2.8-m LSWT with an open test section. The apparatus is driven by a servo-controlled hydraulic motor and the rotation rate can be varied up to 300 rpm. The angle of attack can be varied by remote control over a range of 30° even while rotating the apparatus. Using three different stings, the angle of attack can be varied from −30° to 90°. The angle of sideslip can be changed between ±90° by manually rotating the front portion of the sting about its axis.

2.2.8 France

A rotary balance is in continuous use in the vertical spin tunnel at the Institute of Fluid Mechanics of Lille (ONERA-IMFL). The earliest development of a rotary balance for the spin tunnel occurred in 1937–1938. Sketches of the spin tunnel

and the present-day apparatus are shown in Figures 2-16 and 2-17. A photograph of the apparatus in the vertical wind tunnel, SV4, is shown in Figure 2-18. The open test section of the tunnel is 4 m in diameter with a maximum flow speed of 40 m/s. A typical model wing span is 1.0 m. The maximum rotation rate of the apparatus is approximately 100 rpm. With the available ranges for the angle parameters shown in Figure 2-17, the angle of attack can be varied up to 135° and angle of sideslip to 45°. A reduced spin rate of 0.2 to 0.6 can be achieved within the usable velocity range of the tunnel. The Reynolds number obtained in a test is typically 2.0×10^6/m.

2.2.9 Sweden

There are two rotary-balance apparatuses operated by the Aeronautical Research Institute of Sweden (FFA) in their low-speed tunnels. The first rig, shown in Figure 2-19, was developed in the early 1960's for operation in the low-speed wind tunnel L2. The facility has an octagonal closed test section of 2 m × 2 m and a maximum speed of 65 m/s. The maximum rotation rate is 300 rpm. The angles of attack and sideslip are obtained by rolling the sting about its longitudinal axis and pitching the sting on the C-strut shown in Figure 2-19. The maximum pitch angle of the sting is 40°. The sting can be rolled from 0° to 360°. A second apparatus has recently been built to operate in the low-speed tunnel LT1, an atmospheric tunnel, 3.6 m in diameter, with a maximum speed of 80 m/s. The new apparatus, shown in Figure 2-20, has a maximum rotation rate of 360 rpm. The angle of attack can be varied from 0° to 100° with three different sting arrangements. In addition, there is a rotary balance available for high-speed tests in the 1-m by 1-m trisonic wind tunnel S4 (Figure 2-21).

2.3 TEST PROCEDURES

The test procedures for a typical rotary-balance wind-tunnel test are relatively straightforward. The specific procedures for operating each of the apparatuses introduced in the previous section are described in detail in Chapter 3. There are, however, certain operational aspects which are common to most of the individual rigs.

As mentioned in the previous section, the primary difference between the test procedures used in a rotary-balance test and a conventional fixed-model or "static" test is the need to account for rotational inertial loads and balance load variations due to gravity. For an apparatus mounted in a vertical wind tunnel, where the spin axis is parallel to the gravity vector, the effect of gravity is constant.

Since the model attitude relative to the sting assembly is constant during the continuous rotating motion, the aerodynamic force input to the balance is constant (except for natural aerodynamic unsteadiness in the flow over the model). The inertial contribution is also constant, and the gravitational contribution is periodic. In order to separate the contributions so that the effects of the aerodynamics can be assessed, the inertial and gravitational contributions must be accurately subtracted. Typically, the gravitational component can be eliminated either by averaging over a number of test cycles, by using an analog low-pass filter at the time the balance signals are being received for processing, or by digitizing the signal for filtering in the data reduction system. It should be noted that if there are vibratory inputs to the model which have higher harmonics than the forced oscillatory frequency due to gravity, there can be some error in the mean values of the forces as determined by the filter system. In most cases, this error is small enough to ignore. Removing the inertial load effect from the balance signal requires special consideration.

In theory, the magnitude of the inertial contribution can be calculated if the moments of inertia about the principal axes of the model and the location of the model center of mass with respect to the rotational axis are known. The moments, assuming the center of mass of the model is on the spin axis, are the following:

$$\text{Pitching moment:} \quad M = \Omega^2 \sin\alpha \cos\beta \cos\alpha (I_Z - I_X)$$

$$\text{Yawing moment:} \quad N = \Omega^2 \sin\beta \cos\alpha \cos\beta (I_X - I_Y)$$

$$\text{Rolling moment:} \quad L = \Omega^2 \sin\beta \sin\alpha \cos\beta (I_Y - I_Z)$$

where α = angle of attack, β = angle of sideslip and Ω = rotation rate
I_X, I_Y, I_Z = moments of inertia about X, Y, Z body axes

The resulting equations for the three moments illustrate several important points. First, the magnitude of the inertial moments is a function of Ω^2 and depends on differences in body moments of inertia. Second, if the moments of inertia of the model are known, then the rotary-moment tares can be calculated. To minimize the magnitude of the inertial tare loads, one must minimize the moments of inertia of the model, or at least minimize the moment of inertia differences. Minimizing the moments of inertia can be achieved by constructing models of low-density material and concentrating the mass near the center of rotation. However, requirements for adequate material strength to withstand the aerodynamic loads tend to result in model designs of higher density material, i.e., model design criteria are conflicting, and a compromise between these demands must usually be arrived at.

Despite the relatively straightforward equations for calculating the inertial tares, there are numerous problems in relying on computed values to subtract from the wind-on measured loads. An important consideration is that the model/sting combination will experience some deflection during rotation, and the mass center of the model will not be at exactly the same location relative to the rotary axis at all rotation speeds (even if the center of mass of the model is on the rotary axis to begin with at low speeds, as was assumed in the above derivation of the moment tare formulas). Any changes during the rotational motions that affect either the moments of inertia about the rotation center of the model or the model attitude will cause the tare load to vary from the analytically determined value. Therefore, it has been found necessary to measure wind-off tare loads at the model attitude and rotation rate conditions planned for wind-on tests. These measurements are

stored in the data acquisition system and later subtracted from the wind-on measurements. It should also be pointed out that the model and sting will deflect due to the aerodynamic loads with the wind on, which will introduce additional error into the measured tare values since the model is not located exactly in the same position with respect to the spin axis. This error is usually ignored because it is extremely difficult to determine.

To be absolutely correct, tare loads should be measured with the model either in a vacuum or surrounded by an enclosure that rotates with the model in order to prevent any interaction between the surrounding still air and the rotating model. In some cases, depending on such factors as model size, rotation rates and expected wind-on aerodynamic loads, the effect is negligible and can be ignored. In cases where it cannot, enclosures such as thin-shelled rigid spheres, fastened to the sting and surrounding the model have been used, which allows the enclosed air to rotate with the model; or, in some cases, if the tunnel cannot be pumped to a near vacuum, tare measurements at several tunnel pressure levels can be determined and the results extrapolated to the absolute vacuum condition. Another technique is to take tares in both directions and average the readings. This has the effect of cancelling the effect of any damping in the rolling and yawing moment but not in the pitching moment. This technique is described further in Section 2.4. In most cases, the tare measurements can be made while the tunnel is occupied for the actual wind-on tests, but in cases where tunnel occupancy time is at a premium, these tares must be determined in a separate test area outside the tunnel prior to tunnel entry. Tare tables can be produced, with values determined at conditions (i.e., model attitude and rotation rate combinations) to be run in the tunnel or, alternatively, a sufficient number of measurements can be made over a wide enough range of variable combinations to allow accurate interpolation of table values for any combination chosen for tests in the tunnel. Procedures for handling the tares and reducing the data are discussed further in Section 2.4.

The actual procedure for acquiring the tare data differs from one apparatus to another. However, in almost all experiments, the tares are taken either at the time of the test or shortly before. Experience has shown that unless the tares can be taken ahead of time on a model support system identical to the system to be used for the wind-on tests, there will likely be errors introduced into the tares that are measured and stored for later use. The ideal approach is to acquire the tare data immediately prior to the wind-on run, with the physical setup of the entire rotating system and model identical to that in the test.

The following sequence of operations is common to nearly every rotary-balance wind-tunnel test:

1) Set the model at the desired attitude (either manually or remotely)

2) Acquire wind-off tares (using a variety of methods to account for wind-off aerodynamic damping or choosing to neglect it). Tares are usually taken in both rotational directions and at small enough increments of rotational speed to allow a least-squares fit of a curve through the balance loads vs. rotational speed.

3) Acquire wind-on data

4) Subtract tare loads from wind-on loads and process data to compute aerodynamic coefficients

In most cases, it is essential to acquire the wind-on data in both rotational directions. When there is some evidence of hysteresis in the forces and moments with rotation rate, it is recommended that data be recorded not only in both directions but also while increasing and decreasing the rotation rate, perhaps over several repeat cycles.

In those tunnels where the model attitude can be changed remotely, it is much more efficient to obtain the rotary tares for several angle settings with the wind off and then acquire wind-on data over the same range of angles. This procedure eliminates the need to start and stop the tunnel for each run. If the tunnel needs to be entered after each run for a manual model attitude change, this procedure, of course, will not help. For a test matrix where either Reynolds number or Mach number will be changed for the same model attitude settings, the model tares would typically be taken at the beginning of the test sequence, followed by all the desired runs at various tunnel conditions.

It has been found to be particularly desirable to be able to reduce the data on-line so that within a few seconds of acquiring the wind-on data the tares have been properly accounted for and final aerodynamic coefficients can be plotted or printed for the matrix of rotation rates. This capability is particularly useful if one is attempting to define a hysteresis effect. Having the results from the previous data point is of great benefit when choosing the test conditions for the next data point.

In addition to acquiring data from a strain-gauge balance, for almost all apparatuses which have the capability for high rotation rates ($\Omega > 100$ rpm), there is usually an array of sensors such as accelerometers and additional strain gauges to monitor the vibrational and critical structural characteristics of the apparatus and tunnel support system. Many of these systems are integrated directly into warning systems to alert the operator if safety limits are about to be exceeded.

2.4 BASIC DATA REDUCTION

2.4.0 Introduction

In this section it is assumed that the axis of rotation of the model is aligned along the wind axis. The reader should refer to Chapter 4 for the special techniques used when the axis of rotation is inclined relative to the wind axis.

2.4.1 Forces Acting on a Rotating Model

Assuming that the model is mounted on a strain-gauge balance and is rotating at a constant speed about a horizontal axis, the balance will measure forces due to gravity, inertia and aerodynamics as shown in Figure 2-22. Effects due to gravity are sinusoidal in this case, but if the rotational axis is vertical, as in a vertical spin tunnel, gravity effects are constant and may be included with the inertial effects. Inertial effects depend on the moments of inertia of the model, the position of the center of mass relative to the balance center and rotational axes, the angle of attack and the square of the rotational speed. At the steady rotational speed in rotary tests, inertial effects are of course constant. The contribution from aerodynamic forces on the model should also be constant at constant rotation rate and wind speed.

2.4.2 Elimination of Gravity Components

Although it is possible to account for the gravitational components analytically, it is easier and more precise to use direct signal processing. Various techniques are available for this task. The two most commonly used are low-pass filtering and an averaging process using a computer.

If a low-pass filter is used, care must be taken to ensure that the filter design is consistent with the measurement accuracy required. Cut-off frequency, steepness of cut-off and the measurement time for each data point are factors which must be given careful consideration.

Another technique is to use a computer to average the digitized analog signal from the strain-gauge balance. If K signal samples are taken over one revolution, then the computer algorithm to obtain the mean value of the signal is:

$$\frac{1}{K}\sum_{k=1}^{K} F(k)C$$

$F(k)$ represents any of the measured signals and C is a scaling constant. Measurements are made over a number of cycles for each data point.

2.4.3 Inertial Loads

If an inertial component constitutes a large proportion of the balance signal, then the aerodynamic component will probably be determined with poor accuracy. Therefore, models are made as light as possible and balanced to keep the center of mass close to the balance center. It is possible to determine the inertial contributions analytically, but since the sting, model and balance will deflect under load, inertial components are determined from wind-off tests and subtracted from wind-on measurements at identical rotational rates. This procedure is not strictly accurate since the model position relative to the rotational axis is affected by aerodynamic loads. Therefore, the inertial components wind-off and wind-on will not be identical. However, in most cases, the error is estimated to be small and no attempt is made to correct for it.

2.4.4 Processing of Balance Signals and Data Presentation

Rotary-balance tests are subject to many sources of noise which can contaminate the measurements. Structural noise and other mechanical effects can severely limit the operational performance and accuracy of these tests. Noise can completely mask the unsteady aerodynamic effects which may be of interest at high angles of attack. In most cases the situation is aggravated by coupling effects between aerodynamic loads and the structural modes of the balance/model/sting combination. A discussion of structural effects is presented in Chapter 4, including some specific techniques to improve the performance of the rotary apparatus.

In most instrumentation systems some arrangements are made to eliminate noise and interaction effects before the balance signals are processed in the computer. Signal noise is generally of high frequency and can be eliminated by filtering. Since only the mean level of the signal is of interest in rotary tests, accuracy of measurement is unlikely to suffer. However, it is advantageous, if the level of electrical noise is excessive, to install pre-amplifiers near the balance if space is available. Thus, a higher level signal is passed through the slip rings and cable from the working section of the wind tunnel and the amplification of noise is reduced.

Strain-gauge balance interactions are removed either in the computer by multiplication of the signals by the inverse interaction matrix or, for linear first-order interactions, in an analog computing network prior to computer processing.

High-quality data amplifiers are used to amplify the signals to a convenient level, usually in the range ± 10 V, and the voltages are multiplied by previously determined calibration factors to define forces and moments which are non-dimensionalized in the usual way to obtain coefficients. Since the model is rotated about a wind axis and, as measured, the coefficients relate to a system of body axes, the engineer may convert the coefficients to a wind axes system. For each angle-of-attack and wind-tunnel condition, the data are plotted against the reduced rotational rate, as in Figure 2-23. In the case of the lateral coefficients C_l, C_n and C_y when in wind axes, the slopes of the forces and moments vs. rotation rate, when linear, may be measured to give the derivatives C_{l_p}, C_{n_p} and C_{y_p} in terms of wind axes.

2.4.5 Sources of Error

In common with other types of wind-tunnel testing, errors in rotary testing emanate from various sources which can be broadly classified into the areas of instrumentation, mechanical sources and aerodynamics. It is felt that the average

accuracy of rotary data is far from that obtained in conventional precision tests for performance, for example. It should also be recognized that standards of accuracy have not yet been established for these tests.

Instrumentation accuracy plays a key role in the overall test effectiveness, including considerations of balance resolution, slip rings, amplifiers, filters, analog-to-digital converters and other components in the signal processing equipment. Six-component strain-gauge balances designed for static tests are used for rotary testing with good success. However, a rotary balance is often required to be very sensitive in the roll and yaw components, while being subjected to large normal forces and pitching moments arising from a combination of aerodynamic and inertial loads. Axial force is usually less significant than in low-angle-of-attack performance testing, and a five-component balance may be satisfactory for most testing. In this situation, it may be possible to design a balance which is more suitable for rotary testing. Slip rings may incur errors in transmission of signals due to wiper lift or thermal emf generation. In the case of the former, there is a "drop-out" due to momentary loss of contact, but the risk can be minimized by connecting contacts in parallel for each line. Spurious voltages may be generated because the slip ring materials are manufactured from different metals which, when in contact and subject to temperature changes, will exhibit a change in resistance. Careful design of the slip ring unit usually reduces this source of error to less than 1% of a typical signal. Typical strain-gauge amplifiers and filters used in static wind-tunnel testing are adequate for rotary testing, and have less than 1% error, provided filter cut-off frequencies and amplifier gains are set at appropriate values and enough time is allowed for recording of the data. After amplification and filtering, balance signals are normally converted to digital form suitable for input to a computer. Current A-D converters are generally of such accuracy that any errors introduced during this process are likely to be insignificant.

Errors arising from mechanical features include the deflection of the model support, vibration, and rotational speed control. Of these, the first is likely to be the most significant. The balance and sting will deflect under normal force loading, and as stated in Section 2.4.3, model position will vary between wind-on and wind-off conditions. However, rotary rigs are designed to maximize the structural stiffness/weight ratio to avoid low natural frequencies of the various structural modes, resulting in deflections that are likely to be small compared to sting rigs for conventional static tests. For installations where a rear or bottom sting entry is used, a significant deflection under load may occur. Corrections would then be made in the data reduction process. Vibration will occur to various degrees depending on the stiffness of the support structure, loading of the model, unsteadiness of the airflow and proximity of the rotational speed to a modal natural frequency. Any vibration will invariably be reflected in the balance output signals. Unless the vibration results in exceeding the maximum allowable balance signal, or is of low frequency, it should be possible to filter out vibration components from the balance signals. Since wind-off data are subtracted from wind-on data at the same rotation rate, it is necessary to ensure that the speed setting is constant. It is generally possible to set and hold speed to within 1 rpm, which keeps the errors down to insignificant levels

A further source of reduced accuracy is the relatively high value of inertial loads compared to the aerodynamic loads. A simple dimensional analysis shows that the ratio of aerodynamic to inertia forces and moments is only dependent on the model density and reduced rotation rate, and not on model size or dynamic pressure. Inertia and aerodynamic moments may be represented as:

$$M_i = J_m\omega^2 = k_i\rho_m l^5\omega^2 \qquad \text{and}$$

$$M_a = k_a\rho_a l^3 V^2$$

so that:

$$\frac{M_a}{M_i} = k\frac{\rho_a}{\rho_m}\left[\frac{\omega l}{2V}\right]^{-2}$$

This relationship shows that measurements of the aerodynamic loads will become more difficult as the nondimensional rate of rotation increases.

The aerodynamic sources of error of most concern are those related to interference effects caused by the relatively bulky rotary apparatus, and the potential effects of the tunnel walls. In the case of conventional static tests, the aerodynamic interference problem has been studied extensively, and guidelines have been established for the selection of support geometry and model size to minimize aerodynamic support interference. In dynamic tests, however, it is often not possible to reduce the interference to the level of insignificance. The problem of aerodynamic interference increases dramatically at high angles of attack, where wing/fuselage vortices can be influenced by the support structure.

To date, unsteady wall effects have been overlooked as a factor in rotary testing. Unsteady wall interference arises when disturbances generated by the rotating model and support hardware are reflected back to the model as periodic flow disturbances. The severity of such effects is expected to depend on several factors, including the geometry of the test installation, wall porosity, coning rate and Mach number.

Little is known about the foregoing aerodynamic concerns at the present time; however, the relative successes obtained for specific designs have seemingly indicated a lack of important problems for existing rigs. The topic of aerodynamic interference effects will be discussed in more detail in Chapter 5.

Rotary-balance tests for high-angle-of-attack conditions require special considerations of flow unsteadiness associated with separated flows. Although the magnitude of flow fluctuations may be no larger than those observed in static testing, their levels may result in measurements which represent a large percentage of the relatively low aerodynamic damping of interest. Flow unsteadiness is of two basic types; one is motion independent, generating the aerodynamic forcing function usually connected with the buffet type of vehicle response; the other type of flow unsteadiness is highly motion dependent, generating aerodynamic damping that often is negative, as in the case of stall flutter, for example. In a static high-alpha test the motion independent unsteadiness of the slender forebody vortices will generate a time-average (static) side force that is of lesser magnitude than the instantaneous (maximum) side force. In a high-alpha flight maneuver, on the other hand, the

motion-dependent unsteadiness can cause the separation-induced side force to stay at its maximum value for an extended period of time. This presents a real problem for the vehicle designer in regard to the use of wind-tunnel test results.

A final issue relating to the accuracy of rotary testing involves model accuracy requirements. A traditional school of thought states that models intended for high-angle-of-attack testing and spinning do not require manufacturing precision and that configuration layout effects are more important than details. Recently, however, several investigations have indicated that the character of separated flow phenomena can depend greatly on configuration details, asymmetries and fidelity. It is apparent that, as more information becomes available on high-angle-of-attack aerodynamics, there will be a greater need to define requirements for model construction for rotary testing, and that the major effort in current tests of specific configurations will need to be augmented by generic and more fundamental research.

2.5 NEED FOR SUPPLEMENTARY INFORMATION

2.5.1 Flow Visualization

Currently, the major applications of rotary-balance test technology typically involve measurements of the various aerodynamic forces and moments acting on vehicles during rotary motions, particularly at high angles of attack and during spins. Unfortunately, data which are limited to the overall forces and moments do not provide the aerodynamicist with sufficient insight and information for the analysis of important physical phenomena which produce the trends noted in the force and moment data. In addition, the lack of such fundamental understanding of rotary flow aerodynamics severely limits any advances in fluid dynamic methods for the prediction of such phenomena. As a result of this limitation, several organizations have implemented auxiliary systems to provide flow visualization during rotary testing. These organizations include AerMacchi, RAE Bedford and NASA Langley.

Typical installations for flow visualization studies consist of motion-picture or video cameras which are mounted on the rotating model-sting assembly, usually at a point above and behind the model. Visualization of flow fields is accomplished by the conventional practice of using wool tufts or fluorescent "mini-tufts" of extremely fine thread which illuminate under fluorescent light. Continuous records of the flow patterns are obtained simultaneously with the force and moment measurements, providing time-correlated results for in-depth analysis.

A method used at NASA-Ames for flow visualization of forebody vortices at high-subsonic to low-supersonic speeds is the vapor-screen technique. Water is injected into the wind-tunnel airstream to produce a fine fog or vapor. A thin light sheet or light screen, usually using a laser as a light source, is passed through the flow field normal to the model longitudinal axis. The light sheet illuminates the fine water particles in the vortex and provides a cross-sectional view of the vortex structure and location. The positions of the vortex cores with changing rotation rates are recorded with a movie camera mounted on the rotating sting. At very low airspeeds this technique can also be applied, using smoke rather than water vapor.

The use of flow visualization techniques has proven to be particularly informative for studies of relatively high aspect-ratio, unswept wings during autorotation. By utilizing the technique, the aerodynamicist is able to correlate the onset and severity of autorotative tendencies with flow separation and stalling of the inner- and outer-wing panels during rotary motions near stall and during post-stall gyrations. Another potential application of these techniques is for studies of local flow conditions which exist on the long, pointed forebodies of high performance aircraft during post-stall motions. With rising interest in flight at angles of attack beyond maximum lift, future fighters may operate at unprecedented high-angle-of-attack conditions, which are known to be conducive to extensive forebody flow separation, the effects of which dominate the aerodynamic stability of such vehicles.

2.5.2 Pressure Measurements

In addition to a visual indication of the flow state on and near the model, the aerodynamicist may require aerodynamic pressures to be measured over selected surfaces for analysis of component contributions to the overall forces and moments. Pressure measurements were first made under the difficult dynamic conditions of rotary testing many years ago; this included a major effort[24] at NASA-Ames in 1947 which determined full-span pressure distributions for a series of full-scale wings tested on a large-scale rotary apparatus in the Ames 40- by 80-Foot Wind Tunnel.

More recently, rotary tests involving pressure measurements have been conducted at NASA-Langley by Bihrle Applied Research. In this study, over 200 pressure ports were utilized on the empennage and aft fuselage of a model of a propeller-driven trainer configuration to determine the effects of component interactions on aerodynamics of the spin. The results of the tests, which will be discussed in Section 8.1 of this report, were successful in identifying unexpected interference effects and the development of a test technique that uses state-of-the-art electronically-scanning pressure instrumentation and slip-ring assemblies.

2.5 3 Spin Radius

The potential impact of spin radius on rotary aerodynamics is greatly dependent on the angle-of-attack range of interest. As the angle of attack approaches 90° in a developed spin, the spin axis becomes more aligned with the center of gravity of the aircraft, resulting in a near-zero spin radius. Experience with many configurations (particularly military types) has shown that the aerodynamic effects of small, non-zero spin radii at such elevated angles of attack are negligible. In view of these considerations, most of the rotary testing for low-aspect-ratio high-performance configurations is conducted with zero spin radius.

In contrast to the foregoing situation, configurations which employ high-aspect-ratio unswept wings usually require an evaluation of the effects of spin radius for valid analysis of rotary data. Such configurations usually exhibit relatively steep spin modes, with partial flow separation on the outer (upgoing) wing panel. The geometry of the steep spin is such that a relatively large spin radius may exist, to the extent that the spin axis is near the nose of the airplane. The effects of the induced flow conditions with non-zero spin radius for this class of airplanes could conceivably be large, and data should be obtained to account for such effects.

Recently, researchers at IMFL have explored the use of spin radius (also referred to as "turning radius") to decouple the linear kinematic relationships which exist between p, r and β during rotary motions at a constant angle of attack. Using this technique, IMFL was able to identify the dynamic stability parameters and correlate the results with those obtained from other test techniques. However, it was found that the spin radius required for sufficient excitation of the aerodynamic model was necessarily large, resulting in greater mechanical complexity.

2.5.4 Derivatives in Rotary Flow

Aerodynamic data obtained in steady rotary testing may be regarded as analogous to conventional static wind-tunnel data, since they are used to identify potential "trim" conditions which may exist during spinning motions. However, as is the case for conventional dynamic stability analyses, the aerodynamic variations caused by dynamic perturbations from the trimmed condition are also required for analysis of the stability of a potential spin. Dynamic data are also needed for the analysis and prediction of oscillatory spins and for an accurate prediction of spin recovery characteristics. In lieu of such data, investigators sometimes use questionable estimates of dynamic derivatives for flight dynamics studies of the spin. The estimation procedure is, of course, very difficult in view of the nonlinear aerodynamics.

Two approaches to obtaining dynamic derivatives about steady rotary conditions have been proposed. The first approach would utilize a combined rotary- and forced-oscillation test apparatus with associated electronic instrumentation and data reduction methods commonly used for conventional forced-oscillation tests. While the data reduction for such an approach would be relatively straightforward, the complexity of the mechanical and data acquisition systems and the operational constraints of the system would appear to be a major challenge.

The second approach to obtaining dynamic derivatives would make use of a conventional forced-oscillation apparatus mounted in a wind-tunnel facility which approximates the nature of rotary motion by imparting rotary, or rolling motion to the free-stream flow. In this manner, the mechanical complexity of combined model motions is avoided, and the experiment appears to be somewhat more feasible. In the United States, the subsonic wind tunnel (previously the Langley Stability Tunnel) located at the Virginia Polytechnic Institute can provide the rolling flow feature. At this time, however, the concept of combining rotary and forced oscillations has not been implemented.

Recently, the concept of an inclined spin axis has been used by the staff of IMF-Lille to assess the unsteady dynamic phenomena at high angles of attack and to identify dynamic stability parameters at low angles of attack. This research will be discussed in Chapter 4.

Additional possible approaches to obtaining derivatives under rotary-flow conditions are discussed in Sections 6.1 and 6.2.

2.6 REFERENCES

1. Glauert, H.: The Investigation of the Spin of an Aeroplane. R and M 618, British A.R.C., 1919.

2. Relf, E. F.; and Lavender, T.: A Continuous Rotation Balance for the Measurement of L_p at Small Rates of Roll. R and M 828, Aug. 1922.

3. Lavender, T.: A Continuous Rotation Balance for the Measurement of Pitching and Yawing Moments due to Angular Velocity of Roll. R and M 936, Feb. 1925.

4. Gates, S. B.; and Bryant, L. W.: The Spinning of Aeroplanes, R and M 1001, British A.R.C., 1926.

5. Irving, H. B.; and Batson, A. S.: Experiments on a Model of a Single-Seater Fighter Airplane in Connection with Spinning. R and M 1184, British A.R.C., 1928.

6. Allwork, P. H.: A Continuous Rotation Balance for the Measurement of Yawing and Rolling Moments in a Completely Represented Spin. R and M 1579, British A.R.C., 1933.

7. Bamber, M. J.; and Zimmerman, C. H.: The Aerodynamic Forces and Moments Exerted on a Spinning Model of the NY-1 Airplane as Measured by the Spinning Balance. NACA TR 456, 1933.

8. Stone, R. W., Jr.; Burk, S M., Jr.; and Bihrle, W., Jr.: The Aerodynamic Forces and Moments on a 1/10-Scale Model of a Fighter Airplane in Spinning Attitudes as Measured on a Rotary Balance in the Langley 20-Foot Free Spinning Tunnel. NACA TN 2181, 1950.

9. Kohler, M.; and Mautz, W.: Pressure-Distribution Measurements on the Tail Surfaces of a Rotating Model of the Design BFW-M31. (Gottingen, Sept. 30, 1936), NACA TM 1220.

10. Commission de l'Aéronautique de la Chambre des Députes, Report of 11 March 1937.

11. Journal of Aeronautics No. 230, July 1938.

12. Bamber, M. J.; and Zimmerman, C. H.: Spinning Characteristics of Wings, I-Rectangular Clark Y Monoplane Wing. NACA TR 519, 1935.

13. Bamber, M. J.; and House, R. O.: Spinning Characteristics of the XN2Y-1 Airplane. NACA TR 607, 1937.

14. Scher, S. H.: An Analytical Investigation of Airplane Spin Recovery Motion by Use of Rotary Balance Aerodynamic Data. NACA TN 3188, 1954.

15. Burk, S. M., Jr.: Analytical Determination of the Mechanism of an Airplane Spin Recovery with Different Applied Yawing Moments by Use of Rotary Balance Data. NACA TN 3321, 1954.

16. Bazzocchi, E.: Un Metodo per la Determinazione alla Galleria del Vento dell'indice di Efficacia degli alettoni - L'AEROTECNICA - No. 5/1952 Vol. XXXII.

17. Anglin, E. L.; and Scher, S. H.: Analytical Study of Aircraft Developed Spins and Determination of Moments Required for Satisfactory Spin Recovery. NASA TN D-2181, 1964.

18. Grafton, S. B.; and Anglin, E. L.: Static and Dynamic Aerodynamic Characteristics of a 0.15-Scale Model of the YF-17 Airplane at Spin Angles of Attack-Coord. No. AF-AM-407 (U), NASA TM SX-3217, 1975.

19. Bihrle, W., Jr.; and Barnhart, B.: Effects of Several Factors on Theoretical Predictions of Airplane Spin Characteristics. NASA CR 132521, 1974.

20. Bihrle, W., Jr.: Correlation Study of Theoretical and Experimental Results for Spin Tests of a 1/10-Scale Radio Control Model. NASA CR 144995, 1976.

21. Verbrugge, R.: Balance Rotative de l' IMF. Lille et Techniques Experimentales Associées. IMF Lille No. 79/63, 1979.

22. Bazzocchi, E.: Stall Behavior and Spin Estimation Method by Use of Rotary Balance Measurements. AGARD-CP 199, 1975.

23. Schulze, B.: Development and Trial of a Rotary Balance for the 3m Low Speed Wind Tunnel of West Germany. ICIASF 81, Dayton, U.S.A. (1981).

24. Hunton, L. W.; and Dew, J. K.: Measurements of the Damping in Roll of Large-Scale Swept-Forward and Swept-Back Wings. NACA RM No. A7D11, July 1947.

Table 2.1 Rotary Balance Apparatuses
(Representative Values Indicated)

Country	Apparatus Name	Facility	Facility Size	Max Velocity or Mach	Max RN $\times 10^{-6}$/m	Max Model Span, m	Max Ω rpm	Typical max $\frac{\Omega b}{2V}$	α Range, degrees	β Range, degrees	Model Mass, kg	Inclined Axis Capability	Spin Radius	Operational Status
USA	NASA-Langley Spin Tunnel Rotary Balance	Langley Spin Tunnel	6 7 m	30 m/sec	1.8	2.0	90	1 0	-90 to 90	-30 to 30	5	No	Yes	Active
USA	NASA-Langley Steady Rolling Rig	Langley 7 ft × 10 ft Tunnel	2.1 m × 3 m	M = 0 to 0 4	8.3	0.8	600	0.3	0 to 90	0	10	No	No	Inactive
USA	NASA-Langley 30 × 60 Tunnel Rotary Balance	Langley 30 ft × 60 ft Tunnel	9 m × 18 m	M = 0 to 0 1	2 7	1.3	200	0 3	30 to 90	-90 to 90	65	No	Yes	Inactive
USA	NASA-Ames Large-Scale Rotary Balance	Ames 12 ft Pressure Tunnel	3 6 m	M = 0 to 0 6	23.0	0.6	350	0 3	-30 to 100	-30 to 30	15	No	No	Inactive
USA	NASA-Ames Small-Scale Rotary Balance	Ames 6 ft × 6 ft Supersonic Tunnel	1 8 m × 1 8 m	M = 0 25 to 2 2	13 0	0.3	600	0 3	0 to 30	-5 to 5	5	No	No	Inactive
ITALY	AerMacchi 6CR	AerMacchi Low-Speed Wind Tunnel	2 m	60 m/sec	3 3	1 3	300	0 3	-180 to 180	-30 to 30	20	No	Yes	Active
ENGLAND	British Aerospace Low-Speed Rolling Rig	Warton 5 5 m Low-Speed Wind Tunnel	5 5 m	22 m/sec	1.5	2 0	60	0.2	0 to 90	-90 to 90	60	No	No	Active
ENGLAND	British Aerospace Multifacility Derivative Rig	Warton 1 2 m High-Speed Blowdown	1 2 m	M = 0 4 to 0 86	30-65	0 6	300	0.3	0 to 90	-90 to 90	30	No	No	Active
ENGLAND	RAE-Bedford Rotary Balance	RAE-Bedford Low-Speed Tunnel	4 m × 2 7 m	90 m/sec	6.0	0 7	400	0 2	-20 to 60	-60 to 60	15	No	No	Active
ENGLAND	RAE-Bedford Rotary Balance	RAE-Bedford Transonic Tunnel	2 4 m × 1 8 m	M = 0 1 to 1 2	25 0	0 7	400	0 2	-20 to 60	-60 to 60	15	No	No	Active
WEST GERMANY	DFVLR Rotary Balance	DFVLR 3 m Low-Speed Tunnel	3 25 m × 2 8 m	80 m/sec	5.5	1 0	300	0 3	-30 to 90	-90 to 90	20	No	No	Active
FRANCE	IMF Lille Toumebroche	SV4 Vertical Wind Tunnel	4 m	40 m/sec	2.0	1.0	120	0 6	-135 to 135	-90 to 90	10	Yes (20 deg)	Yes	Active
SWEDEN	FFA L2 Rotary Rig	FFA Low-Speed Tunnel L2	2 m × 2 m	65 m/sec	3 5	0 5	300	0 2	-40 to 40	-40 to 40			No	Active
SWEDEN	FFA LT1 Rotary Rig	FFA Low-Speed Tunnel LT1	3 6 m	80 m/sec	6 0	1 0	360	0.3	0 to 100					
SWEDEN	FFA S4 Rotary Rig	FFA Transonic-Supersonic Tunnel S4	1 m × 1 m	M = 0 5 to 2 0	14.0	0 4	700		0 to 25		5	No	No	Active

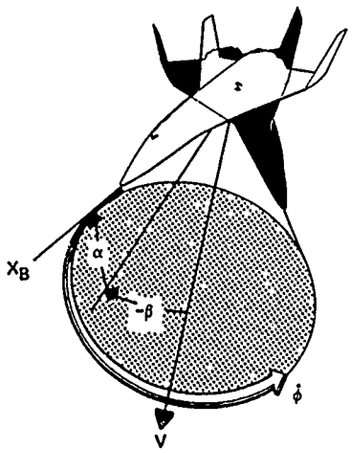

Figure 2-1. Coning motion.

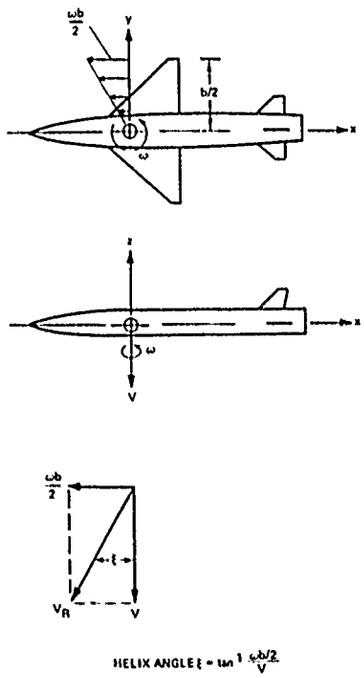

Figure 2-2 Rotational flow field, helix angle for flat-spin case

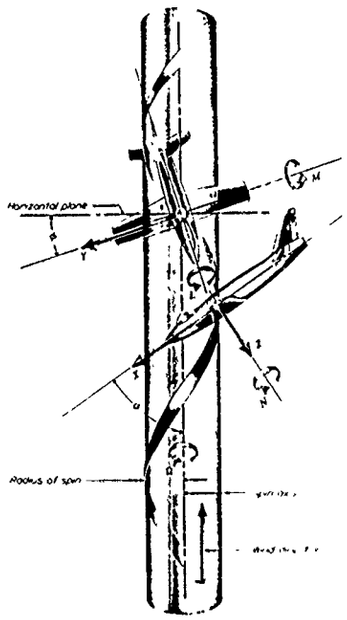

Figure 2-3 Steady spin with spin radius.

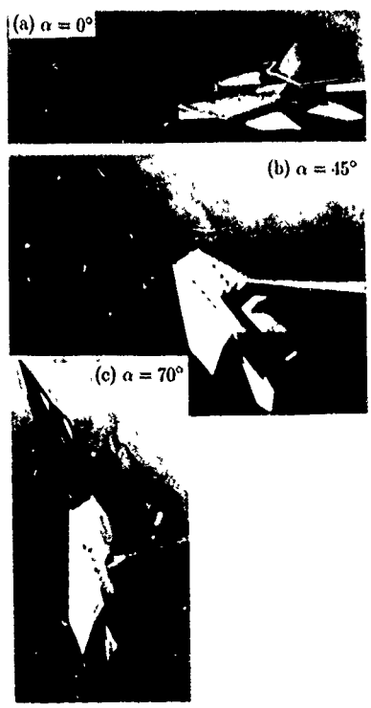

Figure 2-4. Typical model/sting mounting arrangements

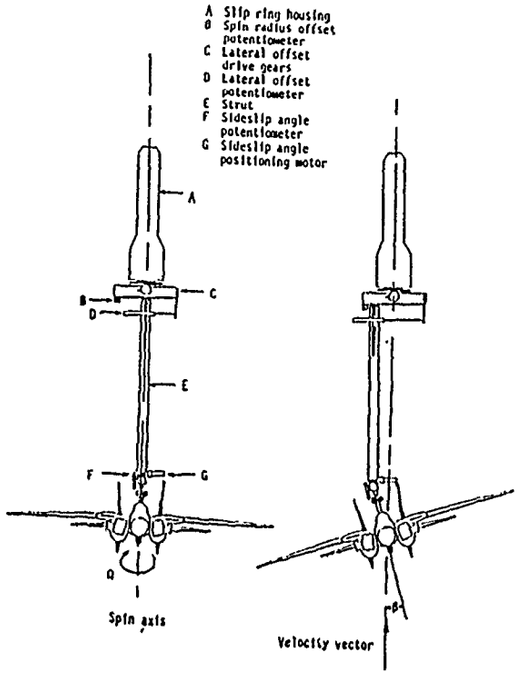

(a) Front view

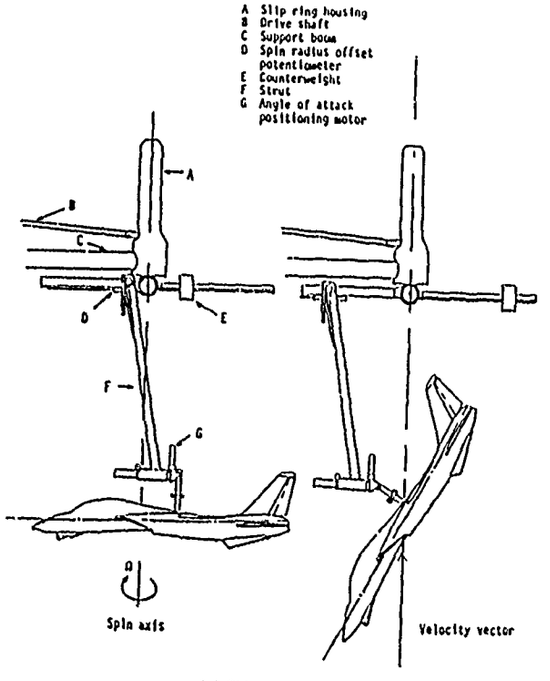

(b) Side view

Figure 2-5. Drawing of Langley Research Center's spin-tunnel rotary-balance rig.

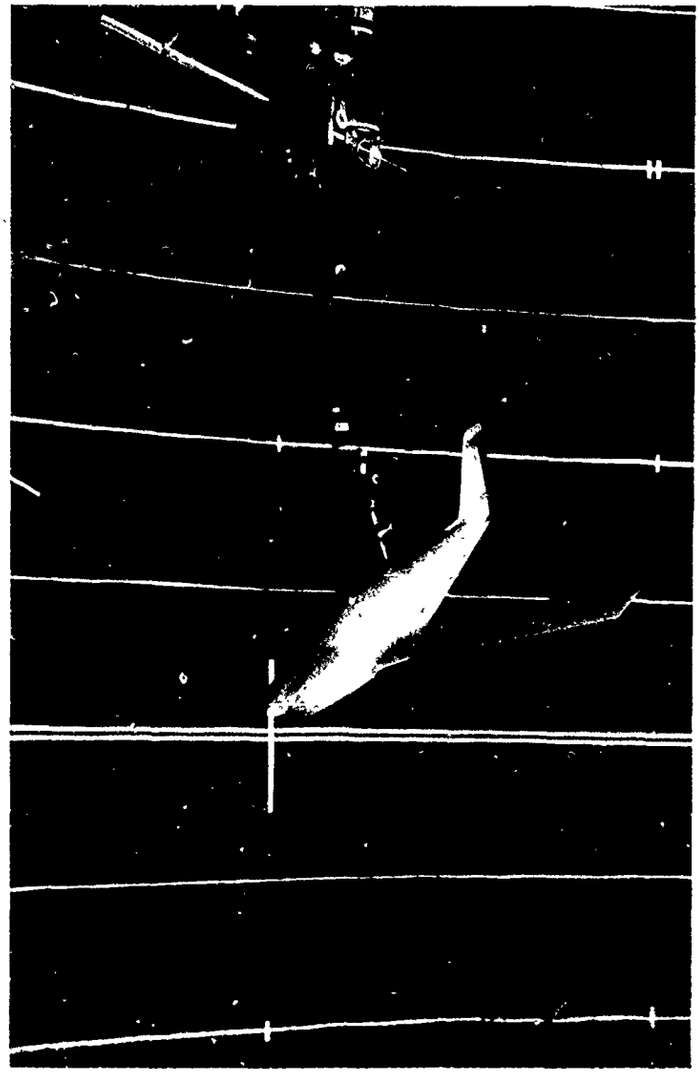

Figure 2-6. Langley Research Center's rotary-balance rig.

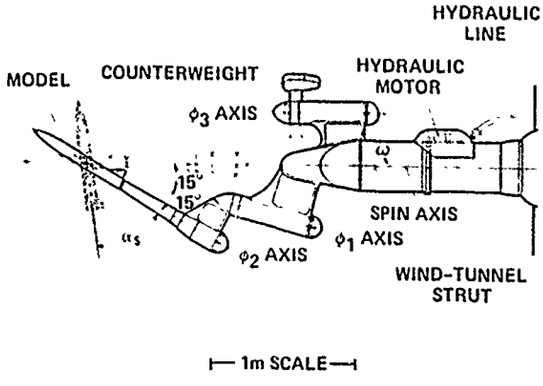

Figure 2-7 Drawing of Ames Research Center's large-scale rotary-balance rig

Figure 2-8. Ames Research Center's large-scale rotary-balance rig.

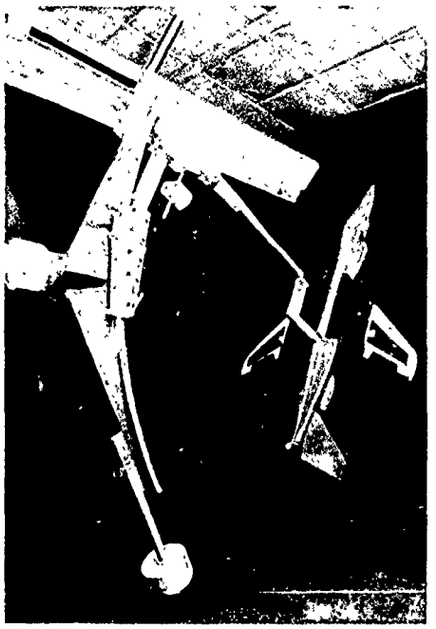

Figure 2-11. British Aerospace LSWT rotary rig.

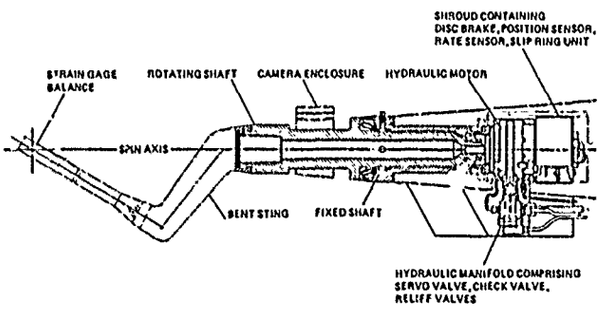

Figure 2-9 Ames Research Center's small-scale rotary-balance rig

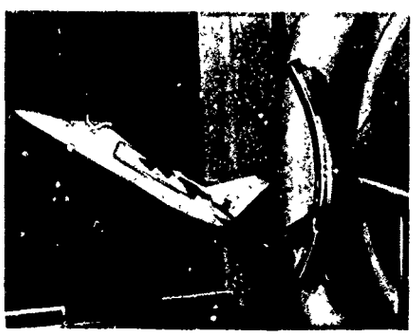

Figure 2-10. AerMacchi's rotary-balance apparatus.

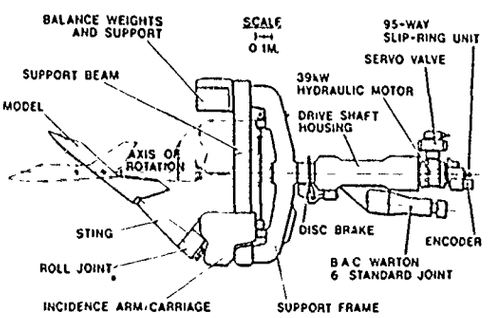

Figure 2-12 British Aerospace multi-facility rotary rig

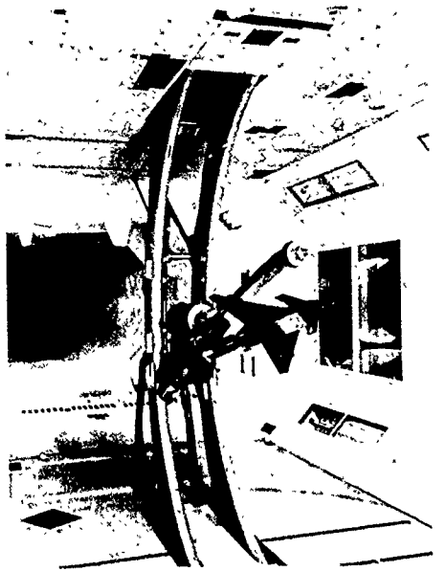

Figure 2-13. RAE rotary balance in 4m × 2.7m wind tunnel.

Figure 2-15. Rotary balance of DFVLR in the open test section of 3.25m × 2.80m LSWT in Braunschweig.

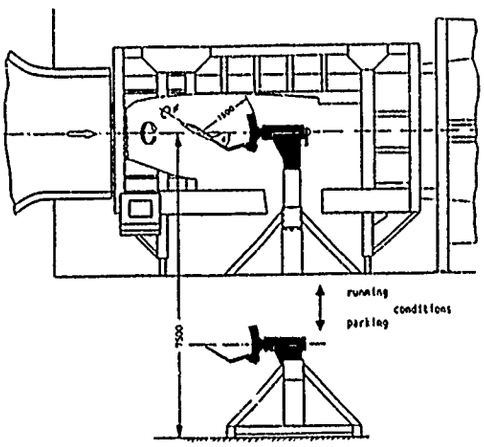

Figure 2-14. Rotary balance of DFVLR in the closed test section of 3.25m × 2.80m LSWT in Braunschweig.

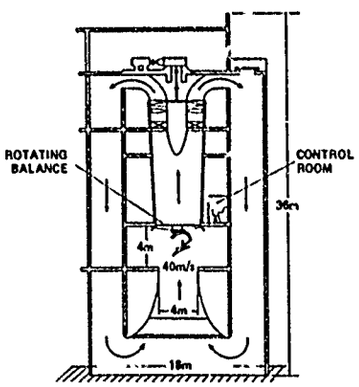

Figure 2-16. IMF Lille rotary apparatus mounted in the SV4 tunnel.

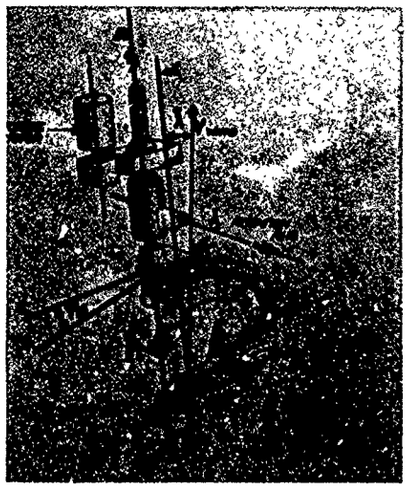

Figure 2-17. Degrees of freedom of IMF-Lille rotary apparatus.

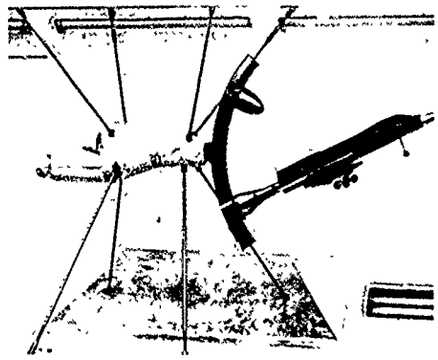

Figure 2-19. FFA rotary-balance apparatus for the low-speed wind tunnel LT2.

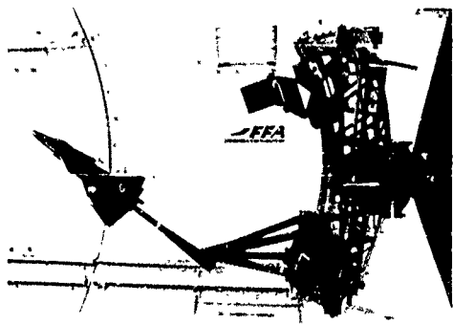

Figure 2-20. FFA rotary rig for the low-speed wind tunnel LT1.

Figure 2-18. Rotary rig in the vertical wind tunnel SV4.

Figure 2-21. FFA rotary rig for the 1m × 1m transonic wind tunnel.

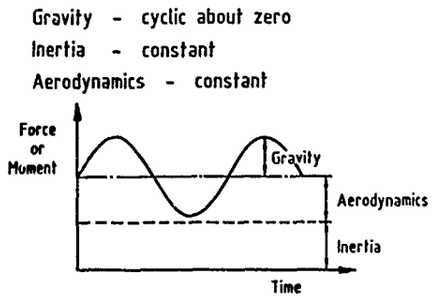

Figure 2-22. Forces measured by a balance supporting a model rolling at constant rate about a horizontal axis.

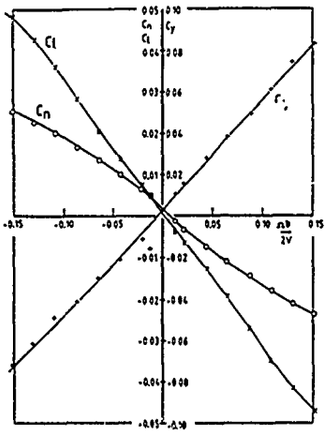

Figure 2-23. Typical variation of lateral coefficients with rate of roll.

CHAPTER 3

ROTARY-BALANCE APPARATUSES

3.0 INTRODUCTION

The previous chapter discussed rotary-balance testing techniques and provided an introduction to the rotary-balance facilities operated by the AGARD participants. This chapter presents a detailed discussion of all AGARD rotary apparatuses that are, or have been, active in the various nations. For completeness, the rotary-balance capabilities of other nations, including Sweden and Japan, are included. The chapter utilizes a common format for presenting information on each apparatus, including the historical background, description of the apparatus, data acquisition system, test procedures, operational limits and future plans.

3.1 NASA-LANGLEY RESEARCH CENTER

3.1.1 Background

The NASA Langley Research Center has traditionally directed a research effort toward the development of technology required for the prediction and analysis of the flight behavior of aircraft. The program has emphasized the area of flight dynamics and, in recent years, the more specific area of stall/spin technology. As part of the overall approach used in these studies, several rotary-balance apparatuses have been developed and operated in various wind-tunnel facilities. As previously discussed, a rotary balance was put into operation in the first spin tunnel at Langley in the early 1930's to study spinning, and NACA experience with the test technique and analysis of the associated data had a direct influence on the subsequent development of updated equipment at Langley. The effectiveness of the first rotary balance was limited by the relatively large ratio of model size to wind tunnel cross-sectional area. Also, the six-component balance was mounted external to the model, was large relative to the model, and was of dubious accuracy. In an effort to eliminate these shortcomings, a new rotary rig was installed in the new Langley 20-Foot Spin Tunnel in 1945. Unfortunately, the limitations of the instrumentation and data acquisition systems at the time resulted in an unacceptable expenditure of resources and tunnel time for a relatively small amount of data. The system was used for only one test of an airplane configuration, after which it fell into disuse.

Interest in the area of dynamic stability analysis at transonic speeds and, in particular, the effects of Mach number on aerodynamic damping in roll resulted in the construction of a steady-rolling apparatus for transonic testing in the early 1950's. This rig was designed to be used in both the Langley 7- by 10-Foot High-Speed Tunnel and the Langley 8-Foot High-Speed Tunnel (predecessor of the current 8-Foot Transonic Pressure Tunnel), and it was used in these facilities during several studies of the effects of various parameters on roll damping at relatively low angles of attack.

The need for rotary-balance data for the analysis of stall/spin phenomena was virtually forgotten in the United States during the 1950's to early 1970's. This situation was caused by a combination of design philosophy and facility demands for higher-priority work. The military philosophy of the day emphasized stand-off missile launch tactics, with little need for maneuvers at high angles of attack. As a result, the interest in high-angle-of-attack aerodynamic phenomena and stall/spin technology declined to an insignificant level. In addition, the extensive time required for rotary tests was judged to be unacceptable in view of higher-priority research being conducted in the spin tunnel by the NACA and NASA. Ironically, numerous computer-based studies of the spin were conducted in the 1960's using crude mathematical representations of the aerodynamic data at extreme angles of attack, with dubious results. These studies were characterized by arbitrary and questionable adjustments to aerodynamic data in order to obtain better correlation with flight.

In the early 1970's, the rising interest in highly maneuverable fighters stimulated a re-examination of the rotary-balance test technique, and this impetus resulted in the construction of a large-scale test rig for the Langley 30- by 60-Foot Wind Tunnel and a refurbishment and updating of the existing smaller apparatus in the Langley Spin Tunnel. These rigs, together with the steady rolling apparatus, represent the rotary-balance apparatuses of interest at Langley. The steady-rolling apparatus and the 30- by 60-foot tunnel apparatus have not been used in almost 15 years and are inactive at the present time; however, the apparatus in the spin tunnel is extremely active in the area of spin research, conducting virtually all of the rotary testing in the U. S. for government agencies and industry. A detailed description of the spin-tunnel apparatus is presented herein, and brief descriptions of the other two inactive rigs are included for completeness.

3.1.2 Descriptions of Apparatuses

3.1.2.1 Spin-Tunnel Apparatus

Sketches of the rotary-balance apparatus installed in the Langley Spin Tunnel are shown in Figure 3-1 and photographs of typical model installations are presented in Figure 3-2. The spin tunnel test section is oriented vertically, with the rotary sting assembly being supported by a horizontal boom and driven by an electric motor mounted external to the test section. Auxiliary guy wires are used for additional bracing. Rotation of the model-strut arrangement occurs about the vertically-rising velocity vector. A six-component internally-mounted strain-gauge balance is used to measure the aerodynamic forces and moments acting on the model. Individual electric motors are used to position the model at the desired attitudes in pitch and bank, and spin radius offsets may be adjusted, together with a corresponding adjustment in counterbalance weight. Potentiometers are used for readouts proportional to the model attitude. The angle-of-attack range of the rig is 0° to 90°, and the sideslip range is ±30°. The system is capable of rotating up to 90 rpm in either direction. Typical velocities employed in the tests result in values of Reynolds number of about 0.3×10^6. Models used on the apparatus are of lightweight construction,

and balsa/composite construction has proven to be adequate for models at the low values of dynamic pressure experienced in these tests.

3.1.2.2 7- by 10-Foot Wind-Tunnel Apparatus

A photograph of a delta-wing research model mounted on the steady rolling apparatus installed in the Langley 7- by 10-Foot Tunnel is shown in Figure 3-3, and a sketch of a typical model installation is shown in Figure 3-4. The apparatus is operated in a horizontal attitude, with the model mounted on a conventional six-component strain-gauge balance commonly used for static testing. The model/sting combination is driven by a constant-displacement, reversible hydraulic motor located inside the main sting body. The hydraulic motor is actuated by a variable-displacement hydraulic pump driven by a constant speed electric motor, and the rig utilizes external bracing struts to the tunnel walls for additional rigidity. A counterweight mounting beam is provided for statically balancing models, although no provision is made for spin radius offsets. The speed of rotation is measured by a system based on the signals generated by a magnetic pickup which measures the frequency of rotary motion. The operational range of angle of attack for the apparatus is from $\alpha = 0°$ to $\alpha = 35°$ for conventional tail-mounted sting installations, and alternate mounting arrangements through the top of the model have been used to permit testing for angles of attack near 90°. In the 7- by 10-foot tunnel, typical test conditions result in a unit Reynolds number of about 2.5×10^6 at a Mach number of 0.40.

3.1.2.3 30- by 60-Foot Wind-Tunnel Apparatus

A photograph of the rotary apparatus installed in the 30- by 60-foot tunnel is shown in Figure 3-5, and a sketch showing some of the more important features of the rig is shown in Figure 3-6. This particular rig was designed to permit testing of the relatively large-scale drop models (up to 6 ft wingspans) normally used in studies of stall/spin motions at Langley. Using this approach, aerodynamic data obtained in the wind tunnel can be used as inputs in computer predictions of the spinning behavior of the models at values of Reynolds number identical to those obtained in the model flight tests. The sting is driven by a hydraulically-operated motor which is mounted to the truss structure of the rig, and a jackscrew located in the pitch motor housing is used to vary the angle of attack. The apparatus was initially designed to employ a bent sting arrangement with a capability for simulating a spin radius and offset, however, structural vibrations and problems with dynamic balancing prevented the operational use of this feature. The pitch attitude can be varied from $\alpha = 30°$ to $\alpha = 90°$. The rig is capable of rotational speeds of up to 200 rpm in either direction. Tests with the rig typically result in a value of Reynolds number of about 0.8×10^6 based on wing chord.

3.1.3 Data Acquisition Systems

3.1.3.1 Spin-Tunnel Apparatus

Electrical signals from the elements of the strain-gauge balance, spin-radius-offset motor and model-positioning motors are conducted through slip rings with 42 channels. As shown in Figure 3-7, the data acquisition, reduction and presentation systems are composed of a 12-channel scanner/voltmeter, a minicomputer with internal printer, a plotter and a CRT display. This equipment permits data to be presented via real-time digital printouts or graphical plots. Real-time observations of the model during tests are permitted by the clear viewing walls of the spin tunnel. The relatively low tunnel speeds used in the tests permit the use of simple internally mounted strain-gauge balances which are extremely linear in output with negligible cross-talk and interactions between channels. Thus, the data reduction equations and process are straightforward and rapid. The real-time capability for aerodynamic data collection is combined with an on-line vehicle motion analysis program to permit rapid evaluations of airplane spin characteristics.

3.1.3.2 7- by 10-Foot Wind-Tunnel Apparatus

The data acquisition system employs slip rings for transmission of balance readout information and conventional computer-based data reduction concepts. Filtering is used to eliminate the periodic inputs of gravitational effects. When last used (1972) the rig was used with a contemporary data acquisition system. Today, the 7- by 10-foot tunnel is equipped with an updated data system and an effort would be required to update the data reduction system for the steady rolling apparatus.

3.1.3.3 30- by 60-Foot Wind-Tunnel Apparatus

The data reduction process utilized for this apparatus included the use of a sine-cosine resolver system to null out the sinusoidal variations caused by the gravity effects experienced in the horizontal test setup. The balance signals are transmitted through slip rings to the gravity nulling system where they are manually nulled by the operator and then to a conventional multi-channel magnetic tape storage device. Reduction and analysis of the data are performed off-line with a standard data reduction program. As was the case for the spin-tunnel apparatus, the low speeds involved in the testing permit the use of simple non-interacting balance gauges which greatly simplifies the data reduction process.

3.1.4 Test Procedures

3.1.4.1 Spin-Tunnel Apparatus

The inertial tares acting on the model should ideally be obtained by rotating the model in a vacuum, thus eliminating all still-air damping. The magnitude of still-air damping at the low dynamic pressures involved in these tests can be relatively large compared to wind-on levels, and the still-air damping effects must therefore be minimized. In lieu of a vacuum sphere

and its associated operational complications, a more practical approach has been adopted, in which the model is enclosed in a spherical lightweight structure (see Figure 3-7) which rotates with the model. The air immediately surrounding the model rotates with it, and a very low still-air damping tare reading is obtained. As the rig and enclosure are rotated to determine wind-off tares, the balance readout information is recorded on magnetic tape for later use in data reduction. To determine the aerodynamic data for rotary motions these tares are subtracted from readings obtained with the enclosure removed and the tunnel on.

3.1.4.2 7- by 10-Foot Wind-Tunnel Apparatus

The high dynamic pressures involved in transonic testing result in relatively large wind-on readings and high loads; therefore, no attempt was made to enclose the model to reduce still-air damping. The high pressures also resulted in deflections of the support system. The angle of attack was corrected on the basis of sting deflections under steady load. The effects of model product of inertia and displacement of the model center of mass from the axis of rotation resulted in centrifugal loads which were accounted for by obtaining data with the model rotating in equal and opposite directions. Corrections for sting-support interference were not applied to the data.

3.1.4.3 30- by 60-Foot Wind-Tunnel Apparatus

The level of still-air damping in tests with this apparatus was comparable to the wind-on levels for studies of aerodynamics at spin attitudes; therefore,a spherical enclosure was used to contain the model and enable tare readings which minimize these effects to be taken. During the wind-off tare runs, the gravity-nulling system readings were set to minimize gravitational effects, and the test proceeded in a manner similar to that employed in the spin-tunnel rotary-balance tests.

3.1.5 Operational Limitations

3.1.5.1 Spin-Tunnel Apparatus

The spin-tunnel rotary apparatus has proven to be a very versatile research tool. The horizontal support arm is pivoted at the tunnel wall, thereby permitting the rig to be rotated out of the area of interest when free-spinning tests are performed in the facility In this manner, it is possible to conduct rotary tests on alternate daily shifts, if necessary. The models used in the tests must be constrained to about 20 pounds. With its unique orientation, the rig experiences only minor gravitational effects, and, as a result, the vibration level of the apparatus is relatively low over the entire range of reduced frequencies. Thus, tests can routinely be conducted at values of reduced frequency of up to about 1.0, which corresponds to extremely fast, flat spins With regard to aerodynamic interference effects, some effects have been noted for a few configurations at relatively low angles of attack approaching maximum lift.

3.1.5.2 7- by 10-Foot Wind-Tunnel Apparatus

This apparatus was limited to a rotational speed of about 10 revolutions per second. Information is not available concerning experiences with aerodynamic interference effects.

3.1.5.3 30- by 60-Foot Wind-Tunnel Apparatus

The massive apparatus utilized for these tests represented a challenging problem in the area of structural vibration. The system was inherently flexible with low natural frequencies, particularly with regard to the model/balance-beam combination, and the support-structure/tunnel-turntable combination. Severe vibrations were encountered near 200 rpm, resulting in a constrained operational envelope which required reduced tunnel speeds to obtain the values of reduced frequency of interest. The reduction in tunnel speed virtually eliminated the potential for obtaining aerodynamic data at the same values of Reynolds number as those obtained in drop model tests. Perhaps the most severe operational constraint on the system involved aerodynamic interference effects caused by the presence of the massive truss structure behind the model. These effects were negligible for angles of attack greater than about 50°, but large differences from static data measured with the same model on other support systems were noted near $\alpha = 30°$, where many fighter designs exhibit strong vortical flows This phenomena was caused by premature vortex breakdown forced by the adverse pressure gradients associated with the large structure.

3.1.6 Applications

3.1.6.1 Spin-Tunnel Apparatus

Following the refurbishment and updating of the test rig and instrumentation in the early 1970's, the spin-tunnel rotary rig has been continually used in tests of over 30 military designs and over 15 civil configurations. An arrangement has been made wherein industry can conduct proprietary studies in the facility on a fee-paying basis, and this capability has been utilized extensively by U. S. and foreign industry teams. The arrangement has greatly stimulated the interest and appreciation of the industry, and as the accuracy and validity of the test technique became more well known numerous applications have arisen The objectives of typical test programs include the effects of configuration components, control surface deflections and analysis of spin characteristics based on the aerodynamic data. Recently, relatively sophisticated tests have been conducted, including power-on tests (see Figure 3-2) and pressure tests during rotary motions. Some specific configurations tested include the F-14, F-15, F-16, X-29, X-31, EA-6B, F-5, AV-8B, A-6 and numerous military trainer designs. Civil designs tested have

ranged from single- and twin-engine general aviation designs to business jets. Data for some of the configurations tested have been published in NASA reports.[1–20]

3.1.6.2 7- by 10-Foot Wind-Tunnel Apparatus

The steady rolling apparatus at Langley has been used for studies of aerodynamic damping in roll, and for limited evaluation of aerodynamics associated with flat spins at extremely high angles of attack. It was used extensively for tests of generic models during the development of the variable-sweep concept due to concern over the lateral characteristics of highly swept configurations. Specific configurations tested include the F-104, F-105, F-111 and F-14 aircraft. In addition to steady rolling tests, the rig was used by Polhamus in the evaluation of fuselage cross-sectional shapes on yaw damping for flat-spin motions. In 1972, tests were conducted to evaluate the effects of leading-edge flap deflection on roll damping at angles of attack near stall, and the results were used to analyze and explain abrupt wing-dropping motions encountered during a flight evaluation of tracking accuracy at NASA-Dryden. This study was the last operational use of the rig.

3.1.6.3 30- by 60-Foot Wind-Tunnel Apparatus

The large-scale rotary rig in the 30- by 60-foot tunnel was utilized for several studies of the aerodynamics of the spin in the 1970's. Specific configurations tested include the F-4, B-1, YF-16, YF-17 and F-14. The major emphasis in these studies was the definition of aerodynamic data and the use of such data in computations of spinning motions which were then correlated with flight motions observed for spin-tunnel models and drop models. More fundamental aerodynamic studies were also conducted with the configurations. For example, the effects of horizontal tail dihedral angle on aerodynamics of the flat spin were studied for the F-4, and correlation between rotary- and forced-oscillation lateral-directional data for the YF-17 was documented.

3.1.7 Future Plans

The apparatus in operation in the spin tunnel is utilized on a daily basis for studies in the area of stall/spin behavior. When conducted in conjunction with spin-tunnel tests of free-spinning models, the rotary-balance test technique provides considerable insight as to the spin characteristics of aircraft designs. The effectiveness of this approach has become widely known, and it is expected that the spin-tunnel rotary test technique will continue to be used in the future.

At the present time, the steady rolling rig at Langley has been placed in storage with no current plans for future applications. The facility normally used for steady-rolling tests has been affected by operational difficulties. More specifically, the 7- by 10-foot tunnel experienced an accident in 1986 which resulted in loss of its drive fan blades and an extensive down time for repairs. This facility situation has resulted in an extended backlog of potential projects, and it is unlikely that the steady rolling rig will see use at Langley in the foreseeable future.

The rotary apparatus for the 30- by 60-foot tunnel has not been used since the mid-1970's, when NASA interest in stall/spin research changed emphasis from studies of phenomena affecting the developed spin to studies of departure and spin prevention. The 30- by 60-foot wind-tunnel facility is still a major contributor to stability and control research, and the rig may be utilized in the future, particularly if the current interest in "Supermaneuverability" and flight at angles of attack beyond stall is maintained.

3.2 NASA-AMES RESEARCH CENTER

3.2.1 Background

NASA-Ames has had an active research program in high-angle-of-attack aerodynamics since the early 1970's, particularly oriented towards fighter aircraft. One of the important tasks in this program has been the development and use of rotary-balance apparatuses to study the stall/spin aerodynamic characteristics of both generic and specific aircraft configurations.

The first rotary-balance apparatus[21] developed at Ames Research Center (ARC) was run in 1968 in the ARC 6- by 6-Foot Supersonic Wind Tunnel. The model was a simple ogive cylinder, fixed rigidly to a rotating sting with strain gauges to measure pitching and yawing moments. The sting was rotated up to 600 rpm. Shortly after these exploratory experiments, a new apparatus[22] was developed for the same tunnel to test a 10° semi-angle cone model undergoing simultaneous coning about the wind vector and spinning about its own axis of symmetry. The model attitude could be varied through a set of manually changed bent stings up to 30°. The coning and spinning rates varied at up to 600 rpm. A photograph of the rig is shown in Figure 3-8 and a sketch of the apparatus is shown in Figure 3-9.

With an increased emphasis on research in fighter aircraft aerodynamics at Ames Research Center, the rig was modified (in 1974) to accommodate a small airplane-like configuration for testing in the ARC 12-Foot Pressure Wind Tunnel. The first experiments are reported in Reference 23; subsequently, more refined experiments were conducted.[24,25] A photograph of the model mounted in the wind tunnel for those experiments is shown in Figure 3-10. These were exploratory experiments undertaken to evaluate separately the contributions of the nose, tail and of the complete configuration, including the wing, during a steady spin motion over a wide variation in Reynolds number. Some of the flow mechanisms that can contribute to pro-spin moments are shown in Figure 3-11, including asymmetric vortices on an ogive nose, asymmetric flow on a square-type cross section and vortex flow on a simple tail configuration. An example of the aerodynamic side force acting on a nose with a square cross section in a flat-spin motion ($\alpha = 90°$) is shown in Figure 3-12.

This result clearly demonstrates the strong dependence of the side-force coefficient on Reynolds number and rotation rate for the nose tested. One interesting feature of the results is the hysteresis loop with rotation rate that occurs in the mid-Reynolds number range. This phenomenon occurs as a result of the flow separation characteristics, as the rotational speed (and consequently the local angle of the flow on the nose) is increased and decreased.[24]

3.2.2.1 12-Foot Pressure Wind-Tunnel Apparatus

Although the modified rotary-balance apparatus was very useful in exploratory investigations of simple airplane-like configurations, the need was recognized for an improved apparatus for efficient test operation and for providing the load capability required for large models at high Reynolds numbers. A large-scale rotary apparatus was developed for use in the ARC 12-Foot Pressure Wind Tunnel.[25,26] The rotary apparatus was designed to simulate full-scale, steady-spin motions by use of the proper combination of rotation speed and model size. Figure 3-13, a plot of reduced spin rate versus free-stream velocity, indicates the region for most full-scale airplane spins of the military fighter class. A rotary apparatus with a rotational speed capability of 42 rad/sec (400 rpm), and a load capability for a model with a wing span of 61 cm (2 ft), provides a test envelope that encompasses most full-scale spin cases.

Avoiding unnecessary startups and shutdowns for model attitude changes is essential for efficient operation of a pressure tunnel. To accomplish this, the angles of attack and sideslip are capable of being changed remotely from outside the tunnel. The rotary apparatus was also designed to accommodate models of a size chosen to maximize the model Reynolds number but to minimize blockage effects or interference with the model. Figures 3-14 and 3-15 show the new apparatus. The angle of incidence of the model on a straight base-mounted sting can be varied up to 30°. With the use of bent stings and top-mounted models, the angle of attack and sideslip changes are accomplished through rotation about two axes (ϕ_1 and ϕ_2, Figure 3-14), which intersect the spin axis at the designated longitudinal location on the model representing the center of gravity of a full-scale, free-spinning vehicle.

Changes in model orientation, made remotely with small electric motors mounted in the apparatus, are done before spinning the whole assembly in the tunnel. The counterweight assembly is driven to a predetermined position that statically balances the mass distribution of the system about the spin axis. No attempt is made to balance the system dynamically. The entire apparatus is then rotated in the wind-tunnel airstream, using a servo-controlled hydraulic drive system that can be varied in speed between 0 and 37 rad/sec (350 rpm) in either a clockwise or counterclockwise direction. The magnitude of the centrifugally induced dynamic moment was, in the worst case, as much as 42,500 Nm (400,000 in-lb). Because of the large dynamic loads experienced by the fixed part of the rotary rig and tunnel support system, special provisions were made to secure the system as rigidly as possible. The center body of the support system is normally traversed and pitched on the vertical blade strut to vary the model attitude. For this test, the center body was rigidly fastened to the strut with threaded pins to prevent any motion between the rig/centerbody and the tunnel strut. To eliminate possible resonance of the rotary-apparatus/tunnel-support system, it was designed to have a natural frequency at least three times the maximum rotational frequency of 350 rpm.

Figure 3-16 shows the attitude envelope obtainable with the stings selected for the first series of tests, including a base-mounted straight sting ($\alpha_s = 0°$) and two top-mounted bent stings ($\alpha_s = 45°$ and 70°).

Electrical power leads to the positioning drive systems and the power and signal paths from the balance are provided by a slip-ring assembly mounted in the circular housing near the strut mount. This is a low-level signal slip-ring unit that contains 84 channels; it provides adequate signal paths to run two six-component, strain-gauge balances simultaneously, in addition to providing for remote changes in model control deflections. An angle encoder to determine position information about the spin axis, if needed, is mounted on the rear of the slip-ring unit. A tachometer to determine spin rate is mounted on the hydraulic drive motor shaft.

The first model tested on this rig was the 0.05-scale F-15 fighter model shown in Figure 3-17 with the model mounted on each of the stings, one through the base and two through the top of the model. Figure 3-18 is an assembly sketch of the model, balance and the 70° top-mounted sting. A special, solid, six-component strain-gauge balance was built for this model to optimize the load capacity of the various gauges. The model was constructed of aluminum, steel and fiberglass to make it as light as possible, but strong enough to withstand dynamic pressures up to 500 lb/ft^2 with the required safety factors for safe tunnel operation. Construction with modern composite materials would enable the model to be constructed with lighter weight. Figure 3-19 shows a photograph of the model and the rotary apparatus mounted in a test enclosure for check-out operations and in the Ames 12-Foot Pressure Wind Tunnel.[27,28]

3.2.2.2 6- by 6-Foot Supersonic Wind-Tunnel Apparatus

The most recent apparatus developed for rotary-balance tests at Ames is a rig for performing tests in the Ames 6- by 6-Foot Supersonic Wind Tunnel. The basic apparatus was a redesigned and modernized version of the rotary-balance apparatus used originally for tests on a 10° semi-angle cone.[22] The apparatus was designed to use the same bent stings as the previous apparatus.

Figure 3-20 is a diagram of the small-scale rotary-balance apparatus. A hydraulic motor is used to turn a shaft aligned nominally parallel to the wind-tunnel airstream. A series of interchangeable bent stings can be attached to the rotating shaft to vary the angle of incidence with respect to the airstream. The stings are designed to support a model on a strain-gauge balance at pitch angles ranging from 0° to 30°, while keeping the same axial model station on the axis of rotation.

The balance used was a standard six-component 3.81 cm (1.5 in) diameter balance, with all power and signal lines routed through the bent sting and the shaft of the hydraulic motor. A set of gold slip rings and brushes was used to transfer the signals to the nonrotating portion of the rig. Model attitude was set by adjustment of the pitch and roll angles of the model. Pitch angles were determined by the choice of bent sting, and roll angles by choice of a fixture located between the balance and the model which maintained a set roll angle. A set of such roll fixtures was available, including one for use with all bent stings giving zero sideslip angle, and one for each of the bent stings to obtain sideslip angles of $\pm 5^{\circ}$.

The rig is capable of being driven at rotation rates from 0 to 600 rpm (63 rad/sec) in either direction. Since the rotating parts are neither statically nor dynamically balanced, the centrifugally induced oscillatory loads generated on the nonrotating structures at maximum rotation rate are quite large. The rig is designed to withstand these loads, but some additional measures were necessary to prevent excessive deflection of the rig support structure in the tunnel. The center body of revolution, which is vertically supported by lead screws and laterally restrained by rollers, was clamped rigidly to the vertical strut in this case. Brass pads were installed between the body of revolution and the vertical strut to distribute the load and prevent damage to the strut surface. In addition, a pair of diagonal braces, extending from the leading edge of the vertical strut to the tunnel floor, was installed to restrain lateral movement of the rig support. Vibration amplitudes in both vertical and lateral planes were monitored by accelerometers mounted on the body of revolution, and these confirmed that no excessive vibration levels occurred while the rig was running.

An additional feature of the rotary rig is the camera enclosure shown in Figure 3-20. This is capable of holding a miniature video or movie camera, with power and signal lines routed through the previously mentioned slip ring set. The camera views the upper surface of the model, and since the camera and model rotate together the model image remains steady regardless of the motion of the rig. This feature was included to enable vapor-screen investigations of the behavior of the vortex wake of the model in response to the coning motion.

Figure 3-21 is a photograph of a model (designated the Standard Dynamics Model, SDM) tested recently.[27,29] The basic planform is that of a current high-performance aircraft configuration. The model was designed for manufacture by simple machining techniques to encourage its widespread use as a standard model for testing in different wind tunnels and on different dynamic test rigs. The model was designed and manufactured by the National Acronautical Establishment (NAE), Canada. A more complete description of its geometry and characteristics is contained in References 30 and 31.

3.2.3 Data Acquisition and Reduction System

The data for rotary-balance apparatuses were acquired and reduced with a common stand-alone microcomputer system. Conventional analog signal-conditioning equipment was used to process and filter the balance and tachometer signals. Low-pass filtering of the balance signals eliminated the oscillatory signals due to model weight. A special data-acquisition unit processed the signals from the balance, shaft tachometer, rig angular position encoder and (in the case of the 12-ft tunnel apparatus) the arm-position potentiometers. Tunnel conditions, including tunnel temperature and pressures, were routed to the system by paralleling the conventional tunnel sensors.

In addition to the data-acquisition unit and the main central processing unit, the data system included a dual floppy disk drive, external printer and multicolor on-line plotter. The data system provided complete on-line listings and plots of the six force and moment coefficients as a function of the apparatus spin rate.

3.2.4 Rotary and Stationary Tare Measurements

There are three types of forces and moments acting on the balance when the apparatus and model are rotated in the wind tunnel. The first are the inertial forces and moments due to the moments of inertia of the rotating model. These vary with model attitude and rotation speed, and may be compensated for by measuring wind-off rotating tares and subtracting them from the wind-on data. The second are oscillatory forces caused by the change in orientation of the gravitational vector relative to the balance frame of reference. Although it is possible to account for these forces analytically, they were eliminated in a more straightforward manner by low-pass filtering the balance signals. The remaining forces and moments are the aerodynamic loads of interest. The magnitude of the inertial loads can be calculated in a straightforward manner if the moments of inertia about the principal axes of the model and the location of the model center of mass with respect to the rotation axis are known and do not vary with rotation rate. However, the model/sting combination deflects during rotation and will cause the actual inertial loads to vary from the analytically determined values. Therefore, it is necessary to measure wind-off tare loads at the model attitude and rotation rates planned for the wind-on tests. These measurements are stored in the data-acquisition system and later subtracted from wind-on measurements.

For accuracy, the inertial tare loads should be measured with the model either in a complete vacuum or surrounded by an enclosure that rotates with it. This will prevent any interaction of the surrounding still air with the model as it rotates. However, in some cases, depending on such factors as model size, rotation rates and expected wind-on loads, the contribution from this effect can be ignored. In these tests, the tare values measured in the clockwise and counterclockwise directions were averaged. For the case where the sideslip angle is set to zero, the respective effects of the surrounding air on side force, yawing moment and rolling moment should be equal and opposite in sign. In this case, averaging the measured values is nearly the same as measuring the tares in a vacuum. However, even though the effects on normal force, pitching moment and axial force are not eliminated by averaging the measurements from both rotational directions, it is felt that the still-air loads are small enough to ignore, particularly for these experiments where the inertial loads and the air loads are very large in comparison.

Typically, wind-off forces and moments are determined at several fixed rotation rates from zero to the maximum for each rotary rig. The respective forces and moments are fit with a five-term polynomial of the form:

$$F = A_0 + A_1\omega + A_2\omega^2 + A_3\omega^3 + A_4\omega^4$$

where F is the force or moment and ω is the rotation rate. The coefficients A_0 through A_4 are then stored. The same procedure is used for rotation in the opposite direction. The two sets of coefficients are then averaged to create a combined tare file of one set of coefficients that is applicable to all rotation rates for that particular angle of attack and sideslip.

Prior to the first test of the large rotary apparatus in the 12-foot tunnel, the intent was to measure all the rotating tare loads in the laboratory prior to installing the apparatus in the tunnel and store them for later use during the tunnel test. The purpose was to eliminate the expenditure of valuable tunnel occupancy time to perform the tare measurements. Tares were, in fact, measured prior to tunnel installation, but it was soon recognized, after repeating some tare measurements in the tunnel, that there was enough variation in the measurements (when compared to those previously acquired in the laboratory) that new tares would have to be measured in the tunnel. The discrepancy was caused by a small difference between the stiffness of the support systems in the tunnel and the laboratory which resulted in a difference in the deflections of the model center of mass relative to the rotation axis for the two support systems.

An additional effect of deflection is the change in position of the model with respect to the rotation axis caused by the wind-on load as compared to the wind-off condition. This effect cannot easily be accounted for and, since it was felt to be small, no attempt was made to correct the wind-on data.

When data are taken with the model stationary ($\omega = 0$) in the wind tunnel with the wind on, the weight of the model must be accounted for. (For the case where the model is rotating, the weight is averaged to zero over a cycle by using low-pass analog filters.) Model weight is accounted for by performing a series of wind-off static tare measurements at various known angular positions around the rotation axis and determining the weight effect on the balance. The weight component on the balance with the wind on is then calculated, using the angular position of the rig with respect to the tunnel and the attitude of the model with respect to the rig.

3.2.5 Future Plans

Both of these rotary-balance apparatuses have been placed in temporary and, perhaps, permanent storage. Perhaps equally as significant for the large-scale apparatus, the 12-Foot Pressure Wind Tunnel, for which the large rig was developed to study Reynolds number effects, can no longer operate as a pressure facility due to recently discovered cracks in the pressure shell. NASA has plans to construct a new 12-foot tunnel, but there are no plans to reactivate the rotary rigs at this time.

3.3 AERMACCHI

3.3.1 Background

Interest in rotary-balance tests arose at AerMacchi in the early fifties, in connection with the theoretical analyses of Dr Bazzocchi[32,33] and the emphasis on "good" spin behavior which is required of trainer aircraft. The first attempts were a simple free-rotation rig (Figure 3-22) which was followed by a two-component forced-rotation rig (Figure 3-23). The first true rotary balance, shown in Figure 3-24, started operation in 1969.[34] The arrangement and basic testing techniques developed at that time have been carried through the present balance which actually is an update of the previous one, featuring improved capabilities in terms of model attitudes and supports, rotation speeds and data acquisition.[35] The testing which has been performed over the years with these rigs has always dealt with aircraft configurations, including actual aircraft (AerMacchi's family of trainers MB 326 and MB 339, and light aircraft AL 60 and AM 3, Aeritalia G 222, Panavia Tornado, Piaggio P-180, Aeritalia/AerMacchi/Embraer AMX) and a number of designs, both from AerMacchi and other customers.

3.3.2 Physical Arrangement

The general arrangement of the balance is shown in Figure 3-25. The body of the balance is supported on the tunnel axis by three swept struts attached to the tunnel diffuser. This body contains the bearings for the rotating arm which is driven by an asynchronous motor via a variable-speed drive, two cardanic joints and a bevel gear pair. A clutch is also available. The body also contains a slip ring assembly which carries in power supplies and carries out signals from the balance or other transducers.

The general specifications of the balance are:

- Rotation rate from 0 to ±300 rpm
- Model supports by rear sting or dorsal/ventral strut
- Spin radius (up to 200 mm) possible with model mounts 3 and 4
- The entire angle of attack and sideslip ranges of ±180° can be covered with the different model mounts (See Figure 3-26)
- Model attitude is set manually between runs

- Rotation speed is actuated remotely but manually
- Forces are measured by an internal six-component strain-gauge balance
- Model weight should not exceed 20 kg; for larger weights maximum rpm must be reduced.

The general characteristics of the AerMacchi low speed wind tunnel are:

- Closed return circuit operated by a 300 hp DC motor
- Open test section, 2 m diameter, 2.6 m length
- Speed continuously variable from 0 to 60 m/sec

3.3.3 Test Procedures

The present test technique aims at measuring time-averaged values of aerodynamic forces on the model. Each run consists of the following sequence:

- Set-up of model configuration and attitude
- Wind-off tare readings (balance offsets and inertia values)
- A sequence of wind-on measurements, usually taken from maximum negative rpm to maximum positive rpm at a constant step. Different sequences or hysteresis loops are executed when considered of interest.

Real time display, printout and plotting of results are available.

3.3.4 Data Acquisition

Figure 3-27 shows the general arrangement of the data acquisition system in the tunnel. For rotary-balance measurements the following quantities are measured:

- Wind-tunnel data (i.e., dynamic pressure, temperature and ambient pressure)
- Balance data
- Rotation rate

Rotation rate is obtained by measuring the time for a complete turn as indicated by two subsequent pulses of a proximity switch connected to the balance axis.

Time averages of balance data are obtained by the following procedure: balance signals are filtered by low-pass (1 Hz) filters and digitized by a 14-bit A-D converter. About 150 measurement samples are taken over a number of complete turns spanning a total time of at least 1 second (each sample includes one measurement per each channel at a rate of about 2 kHz; this requires about 3.5 msec). The procedure of averaging over a complete number of turns automatically compensates for any periodic effect of model weight.

3.3.5 Data Reduction

The data reduction equations are based on the following assumptions:

(1) The model and balance arm assembly is a rigid body rotating around a fixed axis. This implies that the inertia forces transmitted by the model to the balance can be written as:

$$(F_I) = (I)\omega^2$$

The actual form of the inertia vector (I) depends on the actual reference axes and contains effects of model unbalance and products of inertia.

(2) When rolling the model with wind off a small amount of damping is present, which is assumed to be proportional to rotation speed:

$$(F_D) = (D)\omega$$

(3) The balance calibration matrix is linear:

$$(s) = [C]^{-1}(F) + (s_0)$$

where (s) are the balance signals, $[C]^{-1}$ the inverse calibration matrix and (s_0) the balance offsets

From these assumptions, the wind-off measurements can be expressed as:

$$(s) = [C]^{-1}(F) + (s_0) = [C]^{-1}\left((I)\omega^2 + (D)\omega\right) + (s_0) \\ = (s_I)\omega^2 + (s_D)\omega + (s_0) \tag{1}$$

while the wind-on measurements are:

$$(s) = [C]^{-1}(F) + (s_0) = [C]^{-1}\left((F_A) + (I)\omega^2\right) + (s_0) \\ = [C]^{-1}(F_A) + (s_I)\omega^2 + (s_0) \tag{2}$$

Inertia tares (vector (s_I)) and balance offsets (vector (s_0)) are measured by taking a total of six wind-off measurements, three speeds in both clockwise and counterclockwise directions. A least-squares fit to the data gives the coefficients of equation (1). Aerodynamic forces acting on the model with wind on are then obtained from equation (2).

$$(F_A) = [C]\left((s) - (s_I)\omega^2 - (s_0)\right)$$

The effects of the small deflections of the balance are compensated for by the procedure of fitting equation (1) to measurements which include deformations due to inertia forces. Also, the model attitude is corrected for deformations due to total (inertia + aerodynamic) forces by a deformation matrix. No model balancing is required by the foregoing procedure. The rotating system (model plus balance sector) is statically balanced by a counterweight in order to avoid periodic changes to rotation speed. Of course, a large unbalance reduces precision and light models are desirable.

3.3.6 Support Interference

Both static effects (i.e., effects on the forces at zero rotation) and dynamic effects (i.e., changes in these forces due to rotation) are present in rotary-balance measurements. Both effects may be split into effects due to the main balance structure, and to the model support arm. The following policy is used:

- For static effects, the procedure is the same as for ordinary measurements. A wind-tunnel calibration is used which takes into account the presence of the balance rig, while support interference can be measured with the usual technique of dummy struts on the static balance.

- For dynamic effects, the test may be repeated with a different model support. Also, whenever the complete angle-of-attack range for a test requires different model supports, tests are repeated at the common angle-of-attack with the two model supports involved.

3.3.7 Wall Interference

The conventional corrections (lift interference) used for static tests are also used in rotary-balance measurements.

3.3.8 Flow Visualization Techniques

The following techniques have been successfully used:

- Tufts recorded by a television camera mounted on the balance sector and rolling with the model. Camera signals are transmitted to a television receiver.

- Oil flows which are photographed after stopping the wind and rotation. It has been shown that the effects of centrifugal forces acting on the oil are negligible.

- Both tufts and oil flows may be recorded by taking pictures with a still camera and synchronized flash.

3.3.9 Derivation of Pitch Damping Data

A technique of data analysis has been developed that can give some useful information about effects due to pitching around the body axis in addition to the direct information about the effects due to rolling around the wind axis. Under the hypotheses of independence of longitudinal and lateral-directional characteristics due to pitching and rolling (which is strictly valid only for the linear flow regime), and insensitivity of the dynamic moments to the angle of sideslip, it can be shown that the difference in lift and pitching moment between tests at zero and non-zero sideslip is due to the pitching velocity component $q = \Omega \sin\beta$. It can be shown that:

$$C_{m_q} = \frac{b}{c}\frac{\partial\left(C_{m_{(\beta\neq 0)}} - C_{m_{(\beta=0)}}\right)}{\partial(\Omega b/2V)}\frac{1}{\sin\beta}$$

with a similar expression for C_{L_q}.

This technique is related to the oscillatory coning technique described in Chapter 4.0. With careful experimentation, the technique has also been extended to angles of attack beyond the linear range.

3.3.10 Future Developments

The following developments are planned in order to both increase the accuracy of measurements and the productivity of tests:

- Develop data reduction methods which take full account of the effects of support deformation. There have been a few cases in the past when the present technique has been unable to cope with heavily unbalanced models.
- Develop a procedure for identification of inertial characteristics of model configurations, in order to reduce the time required for wind-off measurements.
- Add an incidence actuator in order to permit a range of angles of attack during the same wind-tunnel run.
- Reduce the pressure gradient induced upstream by the balance sector. This gradient cannot be fully corrected and may have effects on sensitive flows.

3.4. BRITISH AEROSPACE-WARTON

3.4.1 Background

The design of supersonic combat aircraft (Lightning, Jaguar, Tornado, Eurofighter) produced a vital need to understand flying behavior beyond the stall, to forecast derivatives, and to develop satisfactory configurations prior to first flight. Damping in roll and the phenomenon of autorotation were soon recognized, leading to extensive pressure plotting of the Lightning wing, and spanwise integrations using strip theory. A direct measurement of roll damping $(-l_p)$ was made in 1952 using a free-rolling model driven by the allerons. Reduced damping was measured at incidences near wing stall, but this model did not reach autorotation.

Spinning models were tested in vertical wind tunnels, and in free flight, from which matched sets of derivatives were derived that were consistent with flight behavior. These techniques were used to achieve flight clearance for Lightning, Jaguar, Jet Provost Mark 5 and Strikemaster, for conditions which included some large-amplitude motions and appreciable effects caused by variations of mass distribution across the wing span due to stores and tanks.

A more direct approach to design was sought, whereby each derivative could be forecast independently, and hence flight behavior could be derived. Presentation by flight simulator allowed assessment of the sensitivity to each derivative, and hence whether the exact value was important, and what levels were desirable and acceptable. Various sources of derivatives were available, including direct calculations, data sheets and wind-tunnel measurements. The adequacy of each source was compared with the needs of accuracy for each derivative, remembering that large-amplitude motions will be accompanied by nonlinear characteristics, separated flows, vortex interferences, rotations and fluctuating motions.

The Tornado and EAP aircraft, and other contemporary advanced projects have been designed based on roll damping values measured on rotary-balance rigs. Two rigs are operational at the Warton Aerodrome site of British Aerospace, at the 5.5-meter Low-Speed Wind Tunnel, and at the 1.2-meter Transonic and Supersonic Blowdown Wind Tunnel.

3.4.2 Warton 5.5-Meter Low-Speed Wind Tunnel

Design of this rotary-balance rig started in 1975, and commissioning runs were carried out during 1976. Practical operating procedures were developed, and data handling techniques were established that gave good quality derivatives even when the model was buffeted by flow separations. The rig, shown in Figure 3-28, has produced design data for several aircraft and advanced projects, and is maintained in fully operational condition.

3.4.2.1 Rig Design Parameters

The wind tunnel has a width of 5.5 meters, which gives low blockage even when a large model is set at an incidence of 90°. Model span is normally limited to 2 meters.

Rig rotation rates up to 60 rpm are provided, which gives wing-tip helix angles up to $\Omega b/2V = 0.2$, with a wind speed of 22 meters/second. The wind tunnel was designed and built for jet interference measurements on vertical takeoff aircraft, and the combination of large size and low speed has been found to be well suited for stability and control testing at large incidence angles.

Model mass is kept within 70 kilograms because of rig and balance stress limits and to avoid severe vibrations. This is a convenient limit, which allows ample scope for a variety of models, without requiring special lightweight model construction.

The rig quadrant is symmetrically positioned about the roll axis, giving a range of 45°. Alternate stings then allow a choice of incidence range:

0° to 45° is given by an aft-entry sting,

45° to 90° is given by a top-entry sting,

15° to 60° could be provided by a cranked sting.

The model sting is carried in a roll joint, which gives sideslip capability. A roll angle of 26° gives 20° of sideslip, but reduces the incidence limit to 40° from 45°. The roll joint is suspended below a sliding carriage on the incidence quadrant. Incidence is set by manual operation of a screwjack, and all joints are securely clamped to avoid backlash.

In the interests of stiffness the quadrant radius was set at 1.8 meters, which allows for a rather short sting. The model strain-gauge balance center is positioned at the quadrant center on the rig axis; thus the model motion represents rolling or spinning about the aircraft center of gravity.

The main bearing block is suspended from the sting-mounting rig of the tunnel, fixed in the horizontal position such that the rig rotation is aligned with the wind direction. Drive was originally provided by an air-driven motor, through a step-down gearbox. This was replaced by a direct-drive hydraulic motor.

Balance signals are passed through a commercial slip-ring unit, which has given satisfactory service. Six-component balances were already available from static stability and control work, and were put into service on the rolling rig without alteration. (Combat aircraft configurations led to the adoption of sting mountings and reliance on strain-gauge balances many years previously, giving negligible mounting interference.)

Balances with load ranges fully suited to rotary operation were subsequently made. Data readout is handled by the standard tunnel system, which already had an adequate digital performance. Analog filters are fitted to damp out high-frequency excursions, especially when the model is experiencing buffet in the most interesting region of wing stall. However, the output signals fluctuate due to the gravity effect, so must not be filtered too heavily, or undue lag will occur. Digital averaging is then applied, with the eventual production of derivatives that are repeatable, and with little scatter. Signals are recorded 120 times per cycle of rotation, triggered at every 3° of roll angle by the pulses from the tacho-generator that monitors rotational speed. Output signals are integrated over several complete cycles to reduce data scatter. Five cycles are preferable at attitudes and speeds where the model is buffeting, or derivative values are changing. However, at low rotational speeds this takes a long time, so three or even two cycles are accepted.

3.4.2.2 Operating Procedures

During a wind-tunnel run the only variables are wind rate and rig rotation rate. Incidence and sideslip angles are preset between runs, and the mechanisms are then clamped at every joint and screwed tight to avoid backlash. The rig plus model is then mass balanced statically so that the drive torque requirement is constant, and steady rotation is achieved.

Dynamic balancing would require large masses, in positions that would produce aerodynamic interference, and was therefore not attempted. It is not believed that this approach produced any serious effect on the results. Action to reduce inertia effects was taken, by lightening the model construction, both to reduce mass and to position the mass center at the center of the balance. This procedure can be difficult and costly; eventually it was also found to be nonessential. Inertia effects can be measured accurately and though it is worthwhile to take simple measures to reduce them, it is not necessary to go to extremes.

When inertia effects are measured in the wind-off condition, there is a small effect from still-air aerodynamic damping, and although this is much smaller than the wind-on damping, it is in fact easy to extract. It was realized that any inertial effects due to model asymmetry would not change sign when the model rotation was reversed, but the wind-off damping would reverse sign. Mean values between positive and negative rotation thus subtract the wind-off damping effect. This technique is very simple and convenient, and avoids the requirement to enclose the model in a sphere.

3.4.2.3 Operating Experience

Vibration was a problem initially, with the rig shaking the entire tunnel shell. Mating surfaces of the rig joints suffered deterioration due to stress corrosion, where straining under load caused surface pick-up. The sting joint is a tapered plug in a barrel type socket, and this had to be renovated. The stiffness of the vertical beams across the tunnel was increased in order to reduce the lateral motion of the sting support, and bracing struts were inserted between the main bearing block and the tunnel walls. By these means, the vibration levels were significantly reduced, and this was beneficial to the scatter level of the roll damping values.

The original drive motor was pneumatic, and was not able to hold constant rotational speed under varying gravitational moments, especially under slow rotation conditions. A more powerful hydraulic motor was fitted, giving a peak torque of 150 Nm.

The natural inclination to use as large a model as possible to avoid scale effects leads to a heavier model, and a greater need to mass balance carefully. However, for models of configurations that are not expected to be sensitive to scale effect, at least in the regions where autorotation (or nonlinear derivatives) are of interest, the use of small models has been found to be successful. Inertial and gravity terms are thus reduced, and it has been found that the aerodynamic loads can be extracted successfully, even though these loads are themselves reduced. Fortunately, combat aircraft come into this useful category.

The rig has been used to gather data on several aircraft and advanced projects, notably EAP. At certain rates of roll, and in certain attitudes, the models experience significant changes in aerodynamic derivatives. These effects depend on aircraft configuration, and often need to be developed; direct test results are therefore very valuable.

3.4.3 1.2-Meter Blowdown Wind Tunnel

This rig originated in 1975, when the low-speed tunnel rig design was started, for it was realized that roll damping would depend on compressibility. All of the loads would be appreciably higher, and the achievement of realistic wing-tip helix angles would require fast rotation; 600 rpm was required. These ideas were presented to the Ministry of Defence, who awarded a research contract. This explains the family resemblance between the Multi-Facility Rolling Rig, and that subsequently made by R.A.E. Bedford. The tunnels to be used were:

1. Warton 1.2-meter blowdown tunnel; this set the requirement, being the smallest tunnel, but giving the highest loads due to its operating pressures.

2. ARA Bedford 2.7 × 2.4-meter transonic tunnel; this tunnel is large enough to avoid blockage effects due to the rig.

3. RAE Bedford 2.4-meter tunnel; for supersonic tests, and subsonic tests within the range of solid walls.

4. Warton 2.7 × 2.1-meter low-speed tunnel; for initial operating experience in order to gain confidence prior to installation in the Bedford tunnels, and for comparison with tests of the 5.5-meter tunnel rig.

The rig was commissioned during 1978, has been regularly operated, and is kept in full commission as a successful and useful test facility for aircraft design purposes.

3.4.3.1 Rig Design Parameters

A photograph of the Multi-Facility Rotary Rig is presented in Figure 3-29 (see also, Figure 2-12). Dimensions were set by the 1.2-meter working section. Choking precludes testing near to Mach 1 and the rig chokes at Mach 0.86, which is more restrictive than was intended. (Transfer to the ARA tunnel eases this problem, but the rig wake survives the return circuit and is felt as increased turbulence, and tunnel drive power requirements are increased.) The rig is a self-contained unit, with hydraulic power supplies and computer (for rig control and data acquisition), ready to travel to each facility. Between tests the unit is stored in a laboratory and regularly operated in order to maintain it in good condition.

Model attitude is fixed at pre-set values by insertion of tapered pins into mating holes. This system avoids backlash and produces a stiff mounting system. Pitch attitude is set in increments of 2° and roll attitude in increments of 4°, which gives a set table of incidence and sideslip values, providing adequate coverage over a restricted total range. Special stings would give increased incidence range, if required.

The roll-rate requirement was set at 600 rpm, such that a 1/20-scale model would experience the helix angle of an aircraft rolling 360° in 2 seconds. Drive is by a 39 kw hydraulic motor, on closed-loop servo control from the dedicated minicomputer. Disc brakes are provided, which stop the rig in 2.3 seconds in the absence of aerodynamic damping from the model and rig.

3.4.3.2 Operating Experience

The drive motor ran out of torque during tunnel runs, resulting in much slower rotation than in wind-off conditions. This condition was caused by aerodynamic damping from the rig itself, and a simple fix was to fit "ailerons" which were very effective.

The vibration characteristics of the rig while rotating have caused much concern, for the rig vibrates alarmingly at about 300 rpm. This was initially thought to be the shaft whirling phenomenon, whereby centrifugal loads due to off-center mass causes lateral displacement of the support shaft. However, even the most pessimistic assumptions about rig mass and stiffness suggest that whirling would not occur until rotation is speeded up sixfold.

The vibrations occur in the first fundamental mode, at the lowest natural frequency of about 10 Hz. Exactly why this mode is excited by rotation at 5 cycles/second was not satisfactorily explained, although the lack of dynamic balance may have played a key role. Extra bracing was added to the main rig support, and stiffening of the sting carriage was added. These modifications both served to delay the onset of vibration, but only by small amounts. Model mass has a detrimental effect, but practical models have to be robust to withstand the heavy airloads, so their mass cannot be helpfully reduced.

The balance mass can be as large as 32 kg, and its radial position is used as the fine adjustment to give static balance to the rig. Each change of model configuration and attitude has to be individually balanced. The longitudinal position of the balance mass was chosen to minimize dynamic out-of-balance, and this could be zeroed if the mass balance could be moved longitudinally. However, it was concluded that this adjustment would have to be made while the rig was rotating, and be dependent on rig deflections that would vary with rotational speed. At the time when this need was rejected for the rig specification, it was thought that dynamic balance would not be essential. Subsequently, it was seen to be at least desirable, or even vital if the faster rotation speeds were to be achieved.

A useful result occurred when a model was tested without applying the usual requirement for static balance of the model around the strain-gauge balance center. Normally, the solid metal nose is replaced by a glass fiber and resin component, such

that inertial (centrifugal) loads will be minimized. In this case, timescale and cost demands led to rolling tests on a model with a heavy nose. The inertia loads were indeed larger than usual, but were regular and sustainable. This model could be rolled more rapidly before the onset of rig vibration. Apparently, the dynamic out-of-balance situation had been fortuitously improved. Unfortunately, these variations in behavior have not led to a complete understanding of the phenomena

Accelerometers are fitted to record the onset of vibration, and the computer is set to switch off the drive when the signals reach a modest level. Typically, the rig is operated up to 300 rpm, and this limit has been found to be adequate for tests on combat aircraft. Several programs have been carried out, producing interesting and useful results.

3.5 RAE BEDFORD

3.5.1 Background

During the last 10 years, the RAE has been engaged in a program of work to widen the understanding of flight dynamics phenomena associated with advanced combat aircraft at high angles of attack. Mathematical modelling techniques have been developed to predict such phenomena at or near departure at low speeds and free-flight models are used for validation. Complementary to these activities are extensive static and dynamic wind-tunnel tests on the same configurations where the basic aerodynamics are established and, where necessary, improved to provide input data for the mathematical model. Dynamic characteristics have been measured, until recently, exclusively with the Small-Amplitude Oscillatory Rig. Within the last 3 years, however, a rotary balance has been built to investigate forces and moments due to continuous rate of roll; such experiments being more appropriate to the modelling of high-amplitude lateral motions and spinning of combat aircraft. The apparatus has been used in a low-speed atmospheric wind tunnel and in a high-speed pressurized tunnel at speeds up to $M = 0.8$. The maximum test angle of attack is 60° and the rotation rate is usually limited to 350 rpm. Two generic combat aircraft configurations have been tested to date. Models are typically of 0.6-m span and weigh about 15 kg.

3.5.2 Description of Apparatus

A diagram of the apparatus in the 4-m × 2.7-m Low-Speed Wind Tunnel is shown in Figure 3-30 and details of the rotating assembly are shown in Figure 3-31. A five-component strain gauge balance (axial force is excluded) is machined on the end of the sting, which can be axially rotated by means of a worm-and-wheel mechanism in the sting carrier. The root end of the sting fits into a socket in the carrier and is clamped with pinch bolts. Facilities for axial adjustment and fixing of the sting are provided. The carrier is traversed along the machined steel rotor to vary angle of attack in increments of 1°. The angle of attack can be varied between −12° and 40° or, with the alternative sting carrier, between 8° and 60°. When the angle of attack is set, the carrier is secured to the rotor with clamping bolts normal to the plane of the rotor and screwed wedges in the plane of the rotor. Weight carriers are bolted to the ends of the rotor and a selection of weights can be fixed to either carrier to maintain static balance. At the higher angles of attack the weight carrier nearer the sting carrier is removed so that a smaller balance weight is required at the other end of the rotor. A covered channel in the rotor accommodates the cable from the strain gauge balance. The rotor is bolted to the rotor holder which is fixed to the drive shaft with a tapered joint. The shaft runs in bearings in a cast-steel housing and is driven, through a 2:1 reduction gearbox, by a hydraulic rolling-vane motor. A variable-displacement pump supplies the motor with fluid at 1500 psi. Rotational speed is controlled by a servo valve with feedback from a tacho-generator geared to the drive shaft. Strain-gauge balance signals are brought out by a cable through a bore hole in the drive shaft and a slip-ring unit at the motor end of the shaft. Vibration level on the rig is continuously monitored using an accelerometer on the forward shaft bearing housing. A visual and audible alarm is triggered if vibration increases beyond a preset level. The rotor can be brought to rest from maximum rotation speed in 8 seconds.

3.5.3 Test Procedure

Prior to installation of the apparatus in the wind tunnel it is necessary to statically balance the model about the balance axis and the complete rotating assembly. Model balancing is desirable to minimize centrifugal tare loads on the balance, which enhances accuracy of measurement of the aerodynamic loads. Models are designed with a weight compartment in the fuselage for longitudinal CG adjustment and heavy compensating weights can be fitted in the fuselage when control surfaces are removed for particular tests. Weights are also fitted to correct for CG displacement along the Z axis due to wings, fin, etc., which may be above or below the centerline. Since the balance of the model about all three axes is checked using knife edges at the CG, the strain-gauge balance must be removed and due allowance must be made for the mass of the active part of the balance when fore and aft adjustments are made.

Balancing of the rotating assembly (the rotor, sting carrier, sting and model) is carried out in the laboratory on a special shaft mounted in needle roller bearings. With the sting carrier set at each angle of attack to be used in the tests, weights are added to the weight carriers to balance the assembly about the axis of rotation. When possible, one of the weight carriers is removed to minimize the total rotating mass. Balance weights used for each angle of attack are carefully noted for use during the tunnel tests.

When the apparatus has been assembled in the working section of the wind tunnel the sting is set at zero incidence and the strain-gauge balance is calibrated in the usual way by static loading of a calibrating frame. However, for the first calibration of a new balance an iterative procedure is required to remove first-order balance interactions from the final signals to the data processing equipment. The amplified balance signals are passed through an "interaction matrix" with variable potentiometers to cancel outputs on channels other than the loaded one. The calibration procedure is repeated until all interactions are eliminated.

When the calibrations are complete, the model is assembled on the balance and checks are made on vibration characteristics wind-off and wind-on. Throughout the tests the apparatus is carefully monitored using a video display and accelerometer indications.

The test procedure is as follows:

1. Model configuration and angle of attack are set as required and the appropriate balance weights fitted.

2. With wind-off, the model is rotated and readings are taken over a range of positive and negative speeds.

3. Then, at identical rotation speeds to those set wind-off, readings are taken for each wind speed and tunnel pressure required.

A set of readings, covering the rotational speed range, takes about 15 minutes to acquire and a change of angle of attack takes about 1 hour.

3.5.4 Signal Processing and Data Reduction

3.5.4.1 Physical System

A block diagram of the system is shown in Figure 3-32. Signals from the five-component strain-gauge balance are processed in a unit containing signal-conditioning amplifiers and an analog computing network which eliminates first-order interactions of the balance. The corrected signals are then fed to the computer input system consisting of an analog-to-digital converter and direct memory interface.

A digital encoder segment provides a square wave at the model rotational frequency 'f' which, together with the number of samples/rev 'K' from the computer, are fed to a pulse multiplier to generate 'Kf' pulse/second which determine the sampling times. When a 'Kf' pulse arrives at the analog-to-digital-converter external scan control, the signals are sampled in parallel, serially digitized with a resolution of 15 bits and passed via a direct memory access controller into one of two computer memory buffers. When a buffer is full, the processor is interrupted and the other buffer used. The buffers are used alternatively until 'K' samples of all channels have been taken. At the same time, an interlocking program accesses the buffers and performs an averaging process on each signal. As this is a real-time process these signals may be averaged over as many cycles as required.

The pulse multiplier is a prerequisite for correct results and hence an additional board is attached, permitting a computer-controlled diagnostic check to be performed automatically before each measurement.

The rate of revolution of the model is obtained from the digital encoder segment and recorded for each run.

3.5.4.2 Computer Operations

The strain-gauge signals consist of a steady component due to inertia and aerodynamics, and a sinusoidal component due to gravity, oscillating at a frequency equal to the rate of revolution of the model. This gravity component is eliminated by averaging over one complete cycle.

The computer algorithm is:

$$\frac{1}{K}\sum_{k=1}^{K} F(k)\cdot C$$

where:

K is the number of samples per revolution,

C is a scaling constant, and

$F(k)$ represents any of the measured signals.

Other signal components which might give rise to errors are harmonics of the gravitational components and noise generated by either electrical interference or mechanical imperfections in the system. Aliasing errors, which could arise from the correspondence of harmonic frequencies with the sampling frequency, are constant for each measurement and may be eliminated by selectively changing, under computer control, the number of samples/cycle 'K' and hence the sampling frequency. Aliasing errors due to noise (i.e., oscillatory signals not phase-locked to the rotational frequency) vary with each measurement and are eliminated by averaging over more cycles of revolution.

3.5.4.3 Off-Line Processing

When the model is rotating at constant speed, each channel of the strain-gauge balance measures components due to gravity, inertia and aerodynamics. The component due to gravitational force is a cyclic, equal and opposite variation about zero whereas the inertial force is a function of model mass distribution and proportional to the square of the rotational speed. The aerodynamic damping force is proportional to wind speed, air density and also to rotational speed. As stated

in Section 3.5.4.2, the gravity component is eliminated from both wind-on and wind-off data by integrating and averaging the signal. The inertial component is assumed to be constant wind-on and wind-off, so the aerodynamic component is the difference between wind-on and wind-off measurements at the same rotational speed, provided wind-off measurements are made in a vacuum. However, if wind-off tests are made at atmospheric pressure, as is usually the case, the wind-off damping is also subtracted from the wind-on measurement. To reduce the wind-off measurement to the inertial component alone, it is necessary to take the mean of the balance output for positive and negative rotations at the same speed, where wind-off damping should be equal and opposite, but inertial forces will be constant. This mean is then subtracted from the wind-on reading at the same rotational speed to give the total aerodynamic damping. Since the model is displaced by aerodynamic loads, the assumption that the inertial component is constant wind-on and wind-off introduces a small error, but the effect is estimated to be negligible.

The strain-gauge balance measures forces and moments about the geometric body axis. Since the rolling motion is about the stability axis, the aerodynamic coefficients are converted to stability axes before plotting against reduced roll rate $\Omega b/2V$. It is not possible to convert for rolling about a geometric body axis without corresponding data on parameters due to yaw. When appropriate, the rate of change of coefficients C_n, C_y and C_l with $\Omega b/2V$ is measured for comparison with data from oscillatory tests.

3.5.5 Vibration and Other Limiting Factors

Rotation speed is limited by one of three factors:

1. Vibration.

2. Torque available from the hydraulic motor.

3. Fluid flow available from the hydraulic pump.

With wind-off, vibration reaches an unacceptable level at about 420 rpm. Vibration is considered to be unacceptable when lateral movement of the assembly is visible on the video display. Static vibration tests on the apparatus revealed that the lowest natural frequency was a lateral mode at 14 Hz, so it would appear that the limiting vibration occurs at a rotational speed corresponding to half the lowest natural frequency. During development testing, the frequency spectrum revealed several small peaks which, it was assumed, corresponded to submultiples of frequencies of the various modes. With wind-on, vibration level is affected by normal force on the model which may further limit rotation speed, depending on dynamic pressure and angle of attack.

When testing at high air speeds and/or high air density, rotation speed may be limited by damping loads on the rotating assembly which reach the limit of torque available from the hydraulic motor. This limit may be reached before vibration becomes a problem. During tests with direct drive from the motor, rotation speed was limited to less than 250 rpm when testing at $M = 0.7$, 1/3 bar and at low speed, 3 bar. A 2:1 reduction gearbox was then installed between the motor and drive shaft, effectively doubling the torque applied to the shaft. However, a consequence of this modification was that the motor had to be driven at double the speed of the shaft and flow rate from the hydraulic pump proved to be inadequate. A second pump, operating in parallel with the first, was added to provide the flow rate required to drive the shaft at 350 rpm.

A further problem with pump performance was encountered when testing in a variable-density wind tunnel. To avoid running hydraulic pipes through the pressure shell, the pump was positioned in the plenum chamber, so that when the air density was reduced for the higher Mach number tests, the ambient air pressure on the pump and oil reservoir was about 1/3 bar. The rotational speed under these conditions was limited to about 220 rpm because of inadequate oil flow rate. This speed limitation applied with wind-off. It was therefore concluded that reduced air pressure on the pump reservoir had reduced pump performance. For future tests the pump will be positioned outside the pressure shell.

3.5.6 Future Plans

Testing of HIRM 1 and HIRM 2 models is continuing and it is hoped to begin design of another combat aircraft model in the near future.

Major rig development is not planned, but it is hoped to extend the test angle-of-attack range to 90° by the addition of another balance, probably with a top-entry support. Tests are being made with a dummy top-entry support to investigate aerodynamic interference effects using an existing balance at angles of attack up to 60°

3.6 DFVLR-BRAUNSCHWEIG

3.6.1 Background

For evaluation of the spin behavior of aircraft, a pressurized spin tunnel was operated at Deutsche Versuchsantalt fur Luftfahrt (DVL) in Germany in 1936. In order to obtain a better understanding of the spin by quantitative data, before 1940, pressure plotting tests were performed with rotating wing or aircraft models in the horizontal wind tunnel. German publications about direct measurements of aerodynamic forces and moments of a rolling model during this time are not known.

During the thirties DVL investigated the feasibility of simulating aircraft rolling or spinning conditions by application of rotating flow in the test section. Although the advantages of the simple measuring technique using a non-rotating model were obvious, this test method was given up because of inaccurate simulation conditions caused by the radial pressure gradient in the rotating flow and by the increased non-homogeneous turbulence level, resulting in an unfavorable impact on aircraft stalling results.

In 1940 a simple roll apparatus was available at Aerodynamische Versuchs-Anstalt (AVA)-Göttingen for measuring the rolling moment due to rolling. In a research program initiated in 1940, a rotary balance was constructed at DVL in Berlin-Adlershof to be used in studies to improve lateral stability and spin behavior of aircraft.[36] The main features of this balance are shown in Figure 3-33.

The apparatus was built for a 3-m low speed wind tunnel and included the capability to measure rolling moment and yawing moment. The maximum rate of rotation was 300 rpm, and the maximum flow speed achieved was 70 m/sec. The angle of attack of the model could be adjusted remotely by means of the mechanism shown in Figure 3-34. This capability was needed to simulate flow conditions due to hysteresis effects around a rotating and stalling wing correctly.

In 1964 a small rotary rig was constructed by Entwicklungsring-Süd (EWR) for a 1-m low speed wind tunnel to measure aerodynamic damping coefficients due to rolling for the VJ 101 aircraft project, which was of importance at that time.[37] The details of this rig are to be seen in Figure 3-35.

Although simple equipment for damping measurements due to rolling existed at research institutions or technical universities in the 1960's, such equipment was inadequate for the development of aircraft projects which were planned by industry.

In 1974 a national working group[38,39] on "Dynamic Wind Tunnel Balances" was founded by the Ministry of Research and Technology (BMFT) in the Federal Republic of Germany with the aim to improve and extend dynamic testing capabilities for research and industry in West Germany. This working group, which was headed by Prof. X. Hafer of the Technical University of Darmstadt consisted of scientists and engineers of DFVLR, Technical Universities and the aircraft industry.

As the third of four different dynamic balances studied, a rotary balance was developed and built between 1975-1979 with Messerschmitt-Bölkow-Blohm (MBB) as prime contractor; it was sponsored by the BMFT and commissioned in the 3-m Low-Speed Wind Tunnel (LSWT) of the DFVLR-Research Center (RC) in Köln.[40,41] The measuring system was developed with DFVLR as a subcontractor.

In 1980, this wind tunnel of DFVLR-RC/Köln was chosen to be modified for cryogenic temperatures and the rotary balance was transferred to the DFVLR-RC in Braunschweig. The balance was installed on a new, very stiff and vertically movable support system, which provides the capabilities to park and prepare the rotary rig below the test-section floor and to introduce the rig into the open or closed test section from beneath, thus beginning operations within 2 to 4 hours. Today, the rotary balance is an integral part of the 3-m LSWT of DFVLR-RC/Braunschweig (Figures 3-36 and 3-37).

After the transfer to Braunschweig, the measuring system was modified in such a way that signal integration is no longer done by electronic counters, but performed by using a fast A-D converter to store the time-variant signals in a computer and to evaluate the time-averaged signals numerically. Since its installation in Braunschweig, the rotary balance has been operated by customer request for 5 weeks only. This reduced use of the test facility was caused mainly by worksharing agreements of the German aircraft manufacturers in international aircraft programs.

3.6.2 Physical Arrangement

The required capabilities and the range of simulation which have been established for the development of the rotary balance are shown in Figure 3-38. The present test arrangement allows dynamic derivatives to be determined in the horizontal wind tunnel by means of a measuring system similar to that used for steady force and moment measurements.

Tests with the rotary balance can be conducted up to a unit Reynolds number of 5.5×10^6 per meter in the closed, variable slotted and open test sections of the 3-m LSWT of DFVLR-RC in Braunschweig. The rate of rotation may be varied up to 300 rpm in either clockwise or counterclockwise direction. The relationship between Reynolds number and reduced frequency is shown in Figure 3-39.

The specified total range of angle of pitch between $-30°$ and $+90°$ is covered by using three different interchangeable stings (Figure 3-40). The angle of sideslip is manually adjusted by rotating the front part of the sting about its axis, which is the longitudinal or vertical body axis of the model, depending on the sting being used.

The critical rate of rotation due to sting bending (first resonance frequency) of the sting mounting leads to a restriction of the model mass as a function of the maximum permissible rate of rotation as shown in Figure 3-41.

The rotary rig includes the capability of changing the angle of pitch remotely within a range of 30° (Figure 3-42), even during rotation and wind-on conditions. This capability allows the engineer to set the angle of pitch continuously, to increase the test efficiency and to better investigate hysteresis effects in the stall and post-stall regimes of rolling or spinning aircraft at Ω = constant and α variable

3.6.2.1 Mechanical Setup

The rotary-balance apparatus (Figure 3-43) was designed as an attachment to an existing model support rig in the 3-m LSWT of DFVLR-RC in Köln. After its transfer to Braunschweig, a new, very stiff support was built to bear the apparatus. The support together with the rotary balance is parked in a room under the tunnel and can be lifted up into the test section by motorized spindles. The rig consists of (1) a heavy bearing box with spindle, (2) a hydraulic drive system with tooth belt transmission, (3) a device for remote setting of the angle of pitch, (4) three interchangeable stings and (5) an internal 6-component strain-gauge balance.

The drive mechanism supplies a torque to counter the forces acting on the model and its support. These forces are composed of steady aerodynamic and inertial forces as well as of a periodically varying gravitational force The drive mechanism is a complete unit consisting of the hydraulic motor, a servo-valve and the hydraulic pump. The entire system is constructed as a closed hydraulic circuit. A smaller quantity of oil is thus required and the need for a large oil tank is avoided. The hydraulic pump, which is installed near the test section, produces a continuously variable supply of up to 120 l/min at a constant pressure of 80 bar.

The motor data referred to the drive shaft are:

- nominal power: 4 kW
- nominal torque: 93 Nm
- rate of rotation: 1 to 300 rpm
- constancy of rate of revolution: 1% of value
- direction of rotation: clockwise and counterclockwise

The rate of rotation of the drive mechanism is controlled with the aid of a tacho-alternator and a proportional/integral controller.

In the event of a power failure at the control devices or the hydraulic system in the wind tunnel, the rotation of the drive mechanism may not be decelerated suddenly, as this would cause the model and the entire installation to be damaged. The maximum permissible deceleration is, therefore, restricted to:

$$\left[\frac{d\omega}{dt}\right] = 2\pi \left[s^{-2}\right]$$

If the servo-valve closes as the result of power failure, the hydraulic circuit is short-circuited behind the servo-valve with the aid of a specially dimensioned 2/1-way-valve. The kinetic energy of the rotating mass is then slowly reduced by frictional losses in the shortened hydraulic circuit.

The present sting guideway design (Figure 3-44) was selected as the result of different investigations of the feasibility of such a rotating system. Its large mass of about 350 kg and the corresponding large moment of inertia provides for a sufficient constancy in the rate of revolution of the rotating system and the installed model. The mass distribution of the rotating system is statically balanced; it was not possible to balance the masses dynamically.

The sting guideway has been constructed as a box girder with high torsional strength. To obtain sufficient length of guideway the counterweight, which compensates for the static mass of the external carriage and the model sting, runs in its interior. The sting is traversed along the guideway with the aid of a DC motor (rate of rotation = 750 rpm; torque = 4.48 Nm) which is attached to the reverse side of the sting guideway. Electric power for the motor is supplied by means of a slip-ring unit.

The motor drives via a universal joint a set of four-stage cylindrical gears (gear ratio = 30.3:1), which are positioned at one end of the sting guideway. The central output shaft of the gears is connected to a threaded spindle on which a nut, attached to the counterweight, is able to move The nut is guided by a sliding-block system in such a way that it can only move longitudinally and does not exert any shearing forces on the spindle. The outside output shaft is also connected to a threaded spindle. Both spindles are guided radially in sleeves. The outside spindle is connected mechanically to the central spindle with a gear ratio of -1. Similarly, a guided nut moves on the outside shaft, this nut is connected to the external carriage. The external carriage is able to move free from play on a backing bearing system on the sting guideway. This system is constructed such that all loads produced by aerodynamic or inertial forces are distributed evenly on the backing bearings.

At the other end of the sting guideway, a block contains a bearing system (Figure 3-44) which absorbs all tensile and pressure forces exerted on the spindles. The position of the sting on the guideway is controlled by a rotary potentiometer which is connected to the drive mechanism via a small gear box.

There are two rear stings available at the moment:

- Rear sting no. 1	- Rear sting no. 2
$-30° \leq \theta \leq 30°$	$30° \leq \theta \leq 60°$

Angles α and β are determined by the angle of the front part of the rear sting about its longitudinal axis (ϕ), set manually with the aid of Hirth-type serrations, and the inclination of the longitudinal axis to the flow (θ), set by remote control:

$$\tan\alpha = \tan\theta\cos\phi$$
$$\sin\beta = \sin\theta\sin\phi$$

This relationship applies for both rear stings.

3.6.2.2 Measuring and Control System

In general, the measuring technique applied to the rotary balance corresponds to the conventional technique that is used to measure steady forces and moments acting on a model in the wind tunnel. The rate of rotation of the balance is kept constant by an electro-hydraulic control system; the angle of pitch can be set remotely. The measuring system as shown in Figure 3-45 is organized as follows:

- measurement of the mean values of tunnel parameters by integrating digital voltmeters
- measurement of the mean values of the angle of pitch by an integrating digital voltmeter via a slip-ring unit
- measurement of forces and moments using a six-component strain-gauge balance
- measurement of the rate of rotation using trigger impulses by a fast ADC via a slip-ring unit
- storing of the signal history and integration of the signals numerically in the computer
- data output (listing, diagrams)

While the signals of relevant data representing the test conditions are fed over integrating digital voltmeters into the computer, all analog signals from the rotating system are converted by a fast ADC and transferred to an HP 1000 computer. During the performance of forced-roll tests the model is subject to periodic weight components superimposed on the steady aerodynamic and inertial loads. The fast digitizing of the balance signals allows the investigator to study the time history of each individual signal of the balance and to check for distortions.

The following measuring procedure is adapted to obtain damping derivatives as accurately as possible (Figure 3-46):

- determination of rotational speed of the balance by trigger impulses from an incremental rotary sensor
- calculation of the starting phase and the number of data points for one rotation in advance
- measurement during a desired number of revolutions
- data evaluation between first and last trigger impulse by using:
  - Arithmetic averaging
  - Fourier analysis
  - Regression analysis

3 6.3 Test Procedures

It is possible to prepare a test sequence by first gathering the rotary data for wind-off conditions in the parking/calibration room of the rig for all configurations to be tested. However, in order to prevent any error in the final results wind-off data normally are measured in the tunnel. A test sequence, consisting of test runs with and without airflow, is usually carried out in a way that all parameters such as the angle of attack and sideslip and the dynamic pressure are kept constant while the rate of rotation is altered in steps.

Damping derivatives due to rolling at si .eslip conditions are obtained by manually setting the angle of roll at the sting and remotely setting the angle of pitch.

For all these test sequences, a complete set of data, consisting of:

- rate of rotation
- angle of pitch/attack
- angle of roll
- angle of yaw
- dynamic head (q_∞)
- six aerodynamic coefficients
- static pressure (p_∞)
- static temperature (T_∞)
- reduced frequency ($\Omega b/2V$)

is obtained for every individual rate of rotation.

The zero point of the balance is read at the beginning and end of a test run for a slowly rotating model (4 rpm). The inertial forces resulting from the slow rate of rotation are negligibly small. However, the resistance of the slip rings can be better accounted for when the model is in motion. The second reading of the zero point at the end of a test run is used to correct for the zero point drift of the balance signals during the course of the test sequence.

3.6.4 Data Reduction

The following data reduction procedures are applied:

- Determination of inertial and total forces and moments acting on the model using the calibration matrix of the balance
- Verification of inertial data variation and curve fitting with respect to rate of rotation
- Correction of the angle of attack for sting deflection
- Calculation of the aerodynamic forces and moments by subtracting inertial reactions from total forces and moments
- Correction of the tunnel dynamic pressure for model and support blockage
- Calculation of aerodynamic coefficients and their dynamic derivatives as required (e.g., Figure 3-47)

As a simple method of compensating for damping in stationary air during determination of the inertial forces and moments, the following procedure is applied:

- Forces (F_x, F_y, F_z) and moments (L, M, N) are measured without airflow for $+n_1$ and $-n_1$
- The arithmetic mean is then calculated as:

$$\overline{F}_{y_1} = \frac{F_y(-n_1) + F_y(+n_1)}{2}$$

- The inertial forces and moments can be calculated as a function of n^2

$$\overline{F}_y = \frac{\overline{F}_{y_1}}{n_1^2}\, n^2$$

3.6.5 Aerodynamic Support Interference

During the design stage of the remote setting device for the angle of pitch, the flow field was studied in front of the sting guideway with the aid of a dummy guideway of rectangular cross section and a hot wire anemometer in order to ascertain the effect of the relatively bulky geometry of the model support system on tunnel blockage. Considering the test results achieved with this dummy guideway (Figure 3-48) a new guideway having a more aerodynamic shape was built. The results confirm that the guideway configuration chosen has the least influence on blockage of all the configurations investigated in the design phase. The correction of the dynamic pressure for blockage due to the sting guideway and model can be performed by using a semiempirical formula:

$$q_{corr} = q_\infty \left[1 + \lambda\tau \left(\frac{s}{A_T}\right)^{3/2}\right]^2$$

where

s = displacement area of model and support
A_T = area of test section
λ = corresponds to type of displacement and
τ = corresponds to wind-tunnel test-section shape

3.6.6 Supplementary Information

It is planned to extend the capabilities of the facility (stings, flow visualization) according to the requests from future customers.

To date, two aircraft configurations and two basic wing models have been tested, resulting in a total test time of 8 weeks.

Future research is planned on the aerodynamic interference of the rotating strut/sting system in order to quantify its influence on the flow field at the model location. The possibility exists to investigate wall interference effects on derivatives with the rotary balance since the present test section is capable of many configurations (open/variable slots/closed). No definite plans regarding this subject have been made to date.

3.7 ONERA-IMFL

3.7.1 Background

The activities at IMFL (Institute of Fluid Mechanics of Lille, France) devoted to the study of the high-angle-of-attack behavior of aircraft started about 50 years ago. A preliminary investigation was carried out to design and build a specific facility in order to provide an experimental capability in this field and to predict aircraft spin behavior under representative similarity conditions. The first vertical wind tunnel was built at IMFL during 1937-38.[42] The diameter of the open test section was 2 m, its height was 1.25 m and the maximum flow speed was 35 m/sec. A drawing of the tunnel is shown in Figure 3-49.

Two basic test techniques were developed for use in the tunnel. The first one was based on the motion analysis of Froude-scaled free-flight models (overall length of 0.6 m) during tests in the test section of the vertical wind tunnel. At this time, the main purpose of the tests was to identify the specific characteristics of the various developed spins and recovery capability for each model aircraft. Emphasis was placed on the development of a satisfactory recovery procedure for the various aircraft configurations.

The second test technique developed during 1937-38 involved the analysis of results obtained using the first French rotary balance.[42,43] This apparatus was created in order to simulate continuous spin rotation of the model and to measure the six aerodynamic components using an external balance. At that time, strain-gauge balances were unknown and the forces were measured by means of pressure measurements inside the pneumatic jacks which assured the equilibrium of the model for the different degrees of freedom. The technical difficulties associated with attempts to obtain precise measurements using this technique were unacceptable, and this shortcoming resulted in abandoning the use of the facility many years later.

Since 1960, the evolution in aircraft design (especially for military aircraft) has resulted in extremely complex high-angle-of-attack phenomena (e.g., oscillatory motions, autorolls, slightly divergent phenomena). A requirement therefore existed for more quantitative studies and associated test techniques. In addition, an enlarged tunnel test section for free spinning studies had become necessary.

In 1962, the current vertical wind tunnel was constructed at Lille (SV4). A sketch of the facility is presented in Figure 3-50. The open test section has a diameter of 4 m, and free-spinning motions can be observed over a height of 6 m. The maximum flow speed is 40 m/sec. Specific devices were introduced in order to allow auto-stabilization of the free-spinning model in the test section for continuous motion observation; rapid adjustment of the flow speed increases the test duration when divergent motion occurs. In addition, the free-spinning test technique was improved and updated. Although the model size is about the same as that used before (up to 0.8 m), radio-control on-board instrumentation and optical trajectory recordings are currently used. The free-spinning model tests conducted to date involved about 120 different types of aircraft (light, transport or military designs) from numerous countries.

In response to the increasing requirements for analytical studies and the necessary development of prediction tools in the field of high-angle-of-attack phenomena (especially for advanced combat aircraft), the vertical wind tunnel was equipped with a rotary balance. This setup was designed and manufactured entirely at IMFL in close cooperation with AMD-BA, and the first tests were carried out in 1978 (Figure 3-51).

The different application areas for the rotary balance at IMFL concern the following activities

- Measurement of static aerodynamic characteristics up to high angles of attack and sideslip, including control surface effects

- Identification of dynamic stability parameters at low angles of attack[48] and sideslip

- Measurement of steady and unsteady aerodynamic components up to high angles of attack and sideslip in continuous rotation

- Simulation of representative developed spin motions.

Additionally, the apparatus is used to investigate special problems like forebody effects or local flow analysis by use of complementary instrumentation like additional internal balances or pressure transducers.

Many light transport or military aircraft configurations have been tested to date (Mirage 2000, Rafale, Alpha-Jet, ATR 42, for example) for various customers, and general evaluation and synthesis studies are carried out for the understanding of phenomena of interest, for analytical purposes or for future developments of dynamic simulation test techniques in wind tunnels.

3.7.2 Description and Specifications

3.7.2.1 General Aspects

The installation of the rotary balance in the vertical wind tunnel offers the specific conditions for direct simulation of developed steady spins. An important advantage of this approach is the elimination of the mechanical load variations produced by the gravitational forces which would occur in a horizontal-type tunnel.

The installation of the apparatus in the test section is easily accomplished. Mounted on a vertical pivot, the setup is maneuvered by a hydraulic jack and fastened to the wind-tunnel structure by four beams This arrangement allows installation of the apparatus in the test section in about 6 hours. That figure is the time required to convert from the free-spinning configuration to the rotary-balance configuration. Once the mechanical installation has been completed and before a test program is carried out, different procedures are undertaken in order to calibrate and qualify the setup. These operations include the calibrations of the six-component balance, the mounting of the model, the calibrations of the encoders for the different degrees of freedom, the identification of the structural modes, the preliminary "wind-off" tests to identify mass and inertia effects, etc. These operations are usually completed in 2 days.

The current model size is about 1.0 m and the maximum mass is about 50 kg (usually 10 kg). The models are usually mounted on an internal six-component balance. Different types of model support used include. rear-sting, curved-sting and through-the-top mounting (see Figure 3-52), appropriate to the aircraft configuration and the test domain to be considered in order to minimize the aerodynamic interference. The rotation is provided by a slaved electric torque motor giving high torque for a small size. The rotation speed is maintained within 1 per thousand when the resisting torque suddenly changes by 50 percent.

3.7.2.2 Description of Degrees of Freedom

A schematic view of the apparatus is presented in Figure 3-53. The different motion and adjustment degrees of freedom provided by the rig are the following:

ϕ: Rotation around the axis of the sting, through 360°. In most tests (rear sting) this motion corresponds to a rotation about the longitudinal reference axis of the model. This motion is motorized and must be accomplished without wind or rotation. A hydraulic locking device is engaged during the tests.

θ. This rotation around the moment center of the balance is obtained by the displacement of the curved arm, introducing an angle between the axis of the sting (longitudinal reference axis) and the direction parallel to Ω in the symmetry plane of the curved arm. The amplitude of the rotation is 45°. This motion is motorized and is accomplished without wind or rotation. A hydraulic locking device is engaged during the tests. The motions in ϕ and θ do not move the center of gravity of the model in the test section.

Ψ_R: The curved arm is fastened to a pivot connected to a slide. The rotation around the pivot introduces the relative heading of the model Ψ_R. This parameter is specific to the spin. The adjustment is manual over a range of $\pm 180°$

R. The slide connected to the main shaft of the apparatus introduces the spin radius The actual maximum amplitude is 0.2 m. This function is motorized and hydraulic locking is engaged during the tests Ψ_R and R are specific parameters for spin simulations. Nevertheless, they can be used to implement some kinematic relations between flight state variables (see Chapter 4).

Ω Continuous rotation of the apparatus Ω is generally constant during a test, but specific laws of variation can be introduced. The maximum angular speed is 11 rad/sec (reduced frequency of 0.6)

λ. This degree of freedom is unique to the ONERA/IMFL apparatus. λ is the angle between the Ω vector and the V vector. This motion is provided by an electric actuator. Without rotation and with the wind on, it is used to obtain static polars in a slow sweeping motion With Ω and wind on, an oscillatory coning motion is obtained The details of this specific capability and the associated applications will be given in Chapter 4

The main specifications of the rotary balance apparatus are summarized as follows:

Degrees of Freedom:

ϕ	$\pm 180°$
θ	$0° - 45°/45° - 90°$
Ψ_R	$360°$
R	0.2 m
λ	$20°$ with Ω, $30°$ without Ω
Ω	± 11 rad/sec

State Variables:

V	up to 40 m/sec
α	$135°$
β	$\pm 45°$
p	± 11 rad/sec
q	± 5 rad/sec
r	± 11 rad/sec

Other Characteristics:

$\Omega b/2V$	up to 0.6
RN	usually 2.1×10^6/m

Model mass usually 10 kg, max 50 kg
Model average size of 1 m

3.7.3 Test Procedure

Typical experimental measurements are obtained with a six-component strain-gauge balance. The forces and moments acting on the balance are due to gravity, inertia and the aerodynamic flow.

A rotary test in steady coning motion is carried out at constant values of attitudes and rotation rate. The inertial forces and moments are then constant during a test. Due to the fact that the rotation vector is vertical, the gravity forces and moments are also constant during such a test. The straightforward test procedure consists of two data acquisitions at equivalent model attitudes and rotation speed: the first "wind off" and the second "wind on". The "wind-off" measurements are tare loads which are subtracted from the "wind-on" data to obtain the aerodynamic loads.

The aerodynamic loads acting on the model during a "wind-off" rotation are neglected. In some cases it is necessary to take them into account. This depends on the model's geometrical dimensions, and more precisely on its wing span, on the wind-tunnel velocity and on the test program planned. A preliminary test program is carried out specifically to identify the inertial characteristics of the weighted system assembly (model + weighted part of the balance system). These tests are "wind-off" coning motions where the spin radius is zero. The basic assumption made in order to identify these quantities is that the aerodynamic moments acting on the model during "wind-off" tests are damping torques. The "wind-off" aerodynamic forces are relatively small and can be neglected, whereas the torques are estimated by performing "wind-off" rotations in both directions. As these torques are damping effects, their values are opposite with respect to the direction of the rotation. These tests are performed for several attitudes and rotation speeds. It is possible to identify the inertial quantities, (B-C), (C-A), (A-B) and E, of the weighted assembly in the balance axis system. (A,B,C,E are terms of the inertial matrix). The mass and the location of the center of gravity are also identified with static "wind-off" tests. With these quantities known, it is possible to extract analytically the aerodynamic loads from the wind-on data acquisitions. A simple static "wind-off" calibration is required to determine the references of the strain-gauge balance. The operator in the wind tunnel can then modify these electric references to adjust the measurement range to the experimental loads encountered, in this manner improving the accuracy of the results. In all cases, the sting deflections are assumed to be small and of the same value for the "wind-off" and "wind-on" tests, all other parameters being equal at identical attitudes and rotation speed. Another way of proceeding is to place the model in a surrounding box that could rotate with it, in this manner avoiding the unwanted aerodynamic effects However, the increase in weight of the rotating system, the vibrations generated and the loss of time during a test program were such that this procedure was abandoned.

3.7.4 Data Reduction

The data obtained with the rotary-balance apparatus are recorded on a magnetic tape.[44] The different signals stored are the six components measured by the balance, the time base, the encoded angular position $(\theta, \phi, \lambda, \Psi_R)$, the rotation speed and the dynamic pressure in the wind tunnel. Electrical-, encoder- and model-positioning activator signals are transmitted through a gold slip-ring assembly mounted on the strut. The frequency of acquisition is 330 Hz for each parameter except for the balance signal acquisition frequency, which is 660 Hz.

Two special balances have been constructed and optimized at IMFL to obtain the best possible compromise between sensitivity and rigidity for the load range encountered with this apparatus.[45] Low-pass filtering of the analog signals at 100 Hz eliminates high frequency noise and spectral folding. The processing of these data is completed off line, and therefore different kinds of signal treatment may be chosen and applied.

For coning motion tests the more usual and practical method is to average the signals, but in some cases, especially at high angles of attack, the signals are treated in another way. If the phenomena are assumed to be periodic, then the different signals are assigned to an angular window according to the Ψ encoder (Ψ is the coning angle). In each angular window the average values and deviations are calculated. The forces and moment coefficients can then be plotted and analyzed as functions of the values of the angle Ψ. A spectral analysis of these new signals can detect aerodynamic phenomena at low frequencies and low-pass filtering eliminates the structure-induced frequencies. The same procedure can also be used with respect to time instead of the angle Ψ.

3.7.5 Limitations

The rotary balance was initially designed to support models weighing up to 50 kg. The progress in new material technology has resulted in a decrease of the model's weight in the past few years. For this reason, the apparatus can be regarded as being rigid, and the deflections of the mounting are very small for the nominal cases. The lowest structural frequencies are about 20 Hz, which is six times the maximum value of the rotation rate.

The rotating system is neither statically nor dynamically balanced, but for the high values of θ and Ω it is necessary to install a counterweight on the apparatus. The problems of noise and vibration are particularly important for certain dynamic tests conducted with this apparatus like oscillatory coning motion. This point will be treated in detail in the next chapter, and specific devices able to reduce the structural modes will be illustrated (Timoschenko clapper-mass technique).[46]

With regard to aerodynamic interference, some effects have been noted at high angles of attack in the post-stall region. In particular, some discrepancies between lift and pitching-moment measurements appeared in comparing the rear- and top-mounting results obtained with the same model. Some empirical wind-tunnel correction rules are currently applied for these tests.[47]

3.7.6 Future Plans

Timewise, the utilization of the vertical wind tunnel is divided between rotary-balance and free-spinning tests. The rotary-balance apparatus has been used for several applications like: identification of dynamic derivatives, spin prediction and dynamic-stall analysis. Recently, pressure measurements at high angles of attack were performed on a cone to investigate the flow structure and to analyze the effects of the flow generated by the forebody on the spin characteristics of an aircraft.

The industrial applications developed up to now and generally integrated into the aircraft development programs contribute to a great extent to enriching knowledge in this area. They also suggest some basic studies and future needs in the field of appropriate facilities and general experimental methods.

Among the recent developments accomplished and the future adaptations being studied are:

- Minimization of the aerodynamic interference of the apparatus.
- Reduction of the structural effects on the measurements.
- An increase of the amplitude of the spin radius parameter in order to provide, for low angles of attack, better performance in dynamic stability parameter identification (See Chapter 4 and reference 48).
- Integration of flow analysis techniques and flow-visualization methods.

3.8 AERONAUTICAL RESEARCH INSTITUTE OF SWEDEN (FFA)

3.8.1 Background

There are presently three rotary-balance apparatuses in use at the FFA. Two have been used since the 1960's for low-speed tests in the 2-m × 2-m tunnel L2 and high-speed tests in the 1-m × 1-m tunnel S4. A new apparatus was recently introduced for operation in the 3.6-m diameter low-speed wind tunnel LT1.

3.8.2 Apparatus Descriptions

3.8.2.1 Rotary Rig for Tunnel L2

The low-speed tunnel, L2, has an octagonal closed test section of 2 m × 2 m and a maximum speed of 65 m/sec. The rotary rig is shown installed in the tunnel in Figure 3-54. The rig is mounted in the tunnel with tension rods, with the rotating shaft aligned with the tunnel centerline. An electric servomotor is installed in the rear part of the rig. The highest rotation rate is about 300 rpm. A set of gold-plated slip rings conducts the rotary-balance signals from the moving part of the rig to its static part. The rotating balance is a six-component strain-gauge balance mounted on a sting. The sting can be rolled in increments of 1° about its axis. A combination of the body roll angle and the angle between the body and rotation axes can be transferred to a set of α and β angles. The sting is designed in such a way that the center of the balance is situated on the axis of rotation, where the model reference point is also located. The angle between the tunnel centerline and the sting can vary from 0° to ±40°. During tare runs, the model is enclosed in a container to let the surrounding air close to the model rotate together with the model and thus not interfere with the inertia measurements.

3.8.2.2 Rotary Rig for Tunnel LT1

The low-speed tunnel, LT1, is an atmospheric, continuous, closed-circuit tunnel 3.6 m in diameter with a maximum speed of 90 m/sec. It has two interchangeable test sections. A new rotary-balance apparatus, shown in Figure 3-55, has recently been developed for this tunnel. The maximum design rotational rate is 360 rpm and the angle of attack can be varied from 0° to 100° by using three different sting-strut arrangements. The angle of attack can be continuously varied during tunnel testing within the limitation imposed by the sting support quadrant (maximum 40°). The apparatus will accommodate models typically in the 1/10- to 1/15-scale range for fighters.

3.8.2.3 Rotary Rig for Tunnel S4

Tunnel S4 is an intermittent suction wind tunnel with a rectangular test section of 1 m^2 cross-sectional area and a stagnation pressure slightly less than the ambient pressure. The Mach number range is 0.5 to 2.0. The transonic test section has slotted top and bottom walls and solid side walls. The rotary rig is shown installed in the tunnel in Figure 3-56. In order to maintain a good velocity distribution within the test section, the wall slots are shortened when the tunnel is used for rotary tests.

The rig is mounted on the tunnel strut with its axis along the tunnel centerline. In the lower part of the rig a hydraulic motor is installed. It is fed from outside the tunnel by an electrically driven hydraulic pump. A tachometer is mounted on an extension of the hydraulic motor drive shaft. The highest rotation rate available is 700 rpm, but 600 rpm is the commonly used value. The driving torque is transmitted from the hydraulic motor to the main drive by a set of gears. The drive shaft is also connected to a set of gold-plated slip rings where the signals from the rotating balance are fed to the static part of the rig. Different cranked stings can be attached, with each sting providing a given range of angle of attack. The stings are designed such that the center of the balance remains on the axis of rotation. The model is mounted with its center of gravity as close to the moment center as possible.

3.8.3 Data Acquisition and Data Reduction

The evaluation of the rotary derivatives is carried out as if it were a static test. Because of the rotation around the wind vector the rotary damping forces and moments are evaluated in a wind-fixed coordinate system. The forces and moments from the six-component balance are converted from the body-fixed coordinate system to the wind system.

To evaluate the forces and moments, a mean value calculation is performed by integration over a single revolution of the model. For each revolution, data are stored and the mean value and standard deviation of all the revolutions are calculated. The moments and forces depending on rotary damping are evaluated in several steps:

(1) Measurements of inertia forces and moments during a tare run, at the same rotational speed as the wind-on run. The model is enclosed in the container.

(2) The model is slowly rotated (10 rpm) during a tare run to record the gravitational forces and moments at the wind-off condition.

(3) Measurement of forces and moments at a slow rotational speed (10 rpm) with wind on.

(4) Measurements of forces and moment at the desired high rpm with the wind tunnel running.

Calculation of static forces and moments is done by subtracting (2) from (3) and the rotary damping forces by subtracting the tare forces and static forces from the wind-on high rpm data. The computation of the rotary roll derivatives for a fixed angle of attack is then carried out by dividing the rotary damping force and moment coefficients by the reduced rotational frequency. This procedure is valid as long as the derivatives are independent of roll rate.

3.9 TECHNICAL RESEARCH AND DEVELOPMENT INSTITUTE (TRDI) OF JAPAN

The Third Research Center of the Japanese TRDI utilizes a rotary-balance apparatus in conjunction with free-spinning tests and other forms of analysis of high-angle-of-attack behavior in support of the airplane development activities of the Japanese Defense Agency The Center, which is located at Tachikawa near Tokyo, uses an innovative dual-test section tunnel for this purpose

3.9.1 Description of Tunnel and Apparatus

The convertible wind tunnel shown in Figure 3-57 is used for both horizontal and vertical testing For vertical testing, the tunnel nozzle is replaced with a second tunnel configuration having turning vanes to direct the flow into a vertically-oriented nozzle The tunnel was built at the Third Research Center in 1971 for free-spinning and rotary testing. The figure shows details of the convertible tunnel and the vertical wind-tunnel configuration A rotary balance was installed in the wind tunnel in 1975.

The vertical wind-tunnel test section has an octagonal open test section of 4 m width and 4 3 m length and its maximum speed capability is about 35 m/sec. The rotary balance was installed in the spin test room and is shown in Figure 3-58 during a typical test When not in use, the apparatus is pivoted out of the test section and stored against a wall of the facility. A sketch of the rotary apparatus is shown in Figure 3-59. The apparatus is driven by a hydraulic motor with a maximum

rotational rate of 200 rpm. The angle of attack can be varied from 0° to 180°, and the angle of sideslip can be varied from +90° to −90°. The angles are set manually. In recent rotary tests of the Japanese T-4 trainer, the model span was about 0.8 m and the model weight was about 6.5 kg. The models are mounted on an internal six-component balance for testing.

In the TRDI tests, the model is enclosed in a vacuum chamber for measurement of tare readings as shown in Figure 3-60. The model and detachable drive and model support systems are all placed in the vacuum chamber.

3.9.2 Test Procedure

The testing procedure consists of calibrating the balance, measuring the inertial tares in the vacuum chamber and performing the wind-on measurements. Measurements of the inertial tares are carried out at the same rotation speeds and model attitudes as used in the wind-on tests. The pressure in the vacuum chamber is about 1/20 of the ambient pressure.

The wind-on data obtained by the rotary-balance apparatus include the aerodynamic and inertial loads. In order to extract the pure aerodynamic loads, the inertial loads obtained in the vacuum chamber tests are subtracted from the wind-on data. The balance signals are filtered by a low-pass (1 Hz) filter. The data processing approach is shown in Figure 3-61.

3.10 REFERENCES

1. Ralston, J. M.: Rotary Balance Data and Analysis for the X-29A Airplane for an Angle of Attack Range of 0° to 90°. NASA CR-3747, August 1984.

2. Hultberg, R.: Low-Speed Rotary Aerodynamics of the F-18 Configuration for 0° to 90° Angle of Attack-Test Results and Analysis. NASA CR-3608, August 1984.

3 Ralston, J. N.; and Barnhart, B. P.: Rotary Balance Data for a Typical Single-Engine General Aviation Design for an Angle of Attack Range of 8° to 90° III-Influence of Control Deflection on Predicted Model D Spin Modes. NASA CR-3248, June 1984.

4. Ralston, J.: Rotary Balance Data for a Typical Single-Engine General Aviation Design for an Angle of Attack Range of 8° to 90°, I.-Influence of Airplane Components for Model D. NASA CR-3246, March 1983

5. Barnhart, B.: Rotary Balance Data for a Typical Single-Engine General Aviation Design for an Angle of Attack Range of 8° to 90°, II.-Influence of Horizontal Tail Location for Model D. NASA CR-3247, November 1982.

6. Barnhart, B.: Rotary Balance Data for an F-15 Model with Conformal Fuel Tanks for an Angle of Attack Range of 8° to 90°. NASA CR-3516, May 1982.

7. Barnhart, B.: F-15 Rotary Balance Data for an Angle of Attack Range of 8° to 90°. NASA CR-3478, May 1982.

8. Barnhart, B.: Analysis of Rotary Balance Data for the F-15 Airplane Including the Effect of Conformal Fuel Tanks NASA CR-3479, April 1982.

9. Mulcay, W.; and Chu, J.: Rotary Balance Data for a Single-Engine Agricultural Airplane Configuration for an Angle of Attack Range of 8° to 90°. NASA CR-3311, December 1980.

10. Mulcay, W.; and Rose, R.: Rotary Balance Data for a Typical Single-Engine General Aviation Design Having a High-Aspect-Ratio Canard for an Angle of Attack Range of 30° to 90°. NASA CR-3170, December 1980.

11. Hultberg, R.; Chu, J., and Dickens, W.: Rotary Balance Data for a Typical Single-Engine General Aviation Design for an Angle of Attack Range of 8° to 90° II.-High-Wing Model C. NASA CR-3201, October 1980

12. Mulcay, W.; and Rose, R.: Rotary Balance Data for a Typical Single-Engine General Aviation Design for an Angle of Attack Range of 8° to 90° I.-Low-Wing Model C. NASA CR-3200, October 1980.

13. Hultberg, R.; and Mulcay, W.: Rotary Balance Data for a Typical Single-Engine General Aviation Design for an Angle of Attack Range of 8° to 90° I.-Low-Wing Model A. NASA CR-3100, February 1980

14. Bihrle, W., Jr., and Mulcay, W.: Rotary Balance Data for a Typical Single-Engine General Aviation Design for an Angle of Attack Range of 8° to 35° III.-Effect of Wing Leading-Edge Modifications Model A. NASA CR-3102, November 1979

15. Mulcay, W.; and Rose, R.: Rotary Balance Data for a Typical Single-Engine General Aviation Design for an Angle of Attack Range of 8° to 35° II.-High-Wing Model A NASA CR-3101, September 1979

16 Bihrle, W., Jr , and Hultberg, R. Rotary Balance Data for a Typical Single-Engine General Aviation Design for an Angle of Attack Range of 8° to 90° I -High-Wing Model B NASA CR-3098, September 1979.

17. Bihrle, W , Jr ; and Hultberg, R.: Rotary Balance Data for a Typical Single-Engine General Aviation Design for an Angle of Attack Range of 8° to 90° I -High-Wing Model B. NASA CR-3097, September 1979

18. Pantason, P.; and Dickens, W.: Rotary Balance Data for a Single-Engine Trainer Design for an Angle of Attack Range of 8° to 90°. NASA CR-3099, August 1979.

19. Bihrle, W., Jr.; Hultberg, R.; and Mulcay, W.: Rotary Balance Data for a Typical Single-Engine Low-Wing General Aviation Design for an Angle of Attack Range of 30° to 35° I.-High-Wing Model B. NASA CR-2972, July 1978.

20. Bihrle, W., Jr., Barnhart, B.; and Pantason, P.: Static Aerodynamic Characteristics of a Typical Single-Engine Low-Wing General Aviation Design for an Angle of Attack Range of 8° to 35°. NASA CR-2971, July 1978.

21. Tobak, M.; Schiff, L. B.; and Peterson, V. L.: Aerodynamics of Bodies of Revolution in Conmg Motion, AIAA Journal, Vol. 7, No. 1, Jan. 1969, pp. 95-99.

22. Schiff, L. B.; and Tobak, M.· Results from a New Wind Tunnel Apparatus for Studying Coning and Spinning Motions of Bodies of Revolution, AIAA Journal, Vol. 8, No. 11, Nov. 1970, pp. 1953-1957.

23. Clarkson, M. H.; Malcolm, G. N.; and Chapman, G.: Experimental Poststall Rotary Aerodynamic Coefficients for Airplane-Like Configurations, J. Aircraft, Vol. 13, No. 8, Aug 1976, pp. 565-570.

24. Malcolm, G. N.; and Clarkson, M. H.: Wind Tunnel Testing with a Rotary-Balance Apparatus to Simulate Aircraft Spin Motions, Proceedings of AIAA 9th Aerodynamic Testing Conference, June 1976, pp. 143-146.

25. Malcolm, G. N.: New Rotation-Balance Apparatus for Measuring Airplane Spin Aerodynamics in the Wind Tunnel, J. of Aircraft, Vol. 16, No. 4, Apr. 1979, pp. 264-268.

26. Malcolm, G. N.: New Rotation-Balance Apparatus for Measuring Airplane Spin and Two-Dimensional Unsteady Aerodynamics, Paper No. 3, AGARD CP 235, Dynamic Stability Parameters, 1978.

27. Malcolm, G. N.; and Schiff, L. B.· Recent Developments in Rotary-Balance Testing of Fighter Aircraft Configurations at NASA Ames Research Center, Paper No. 18, AGARD CP-386, Unsteady Aerodynamics-Fundamentals and Applications to Aircraft Dynamics, 1985.

28. Malcolm, G : Rotary-Balance Experiments on a Modern Fighter Aircraft Configuration at High Reynolds Numbers, AIAA Paper 85-1829-CP, AIAA 12th Atmospheric Flight Mechanics Conference, August 19-21, 1985.

29. Jermey, C.; and Schiff, L. B.: Aerodynamic Characteristics of the Standard Dynamics Model in Conmg Motion at Mach 0.6, NASA TM 86717, July 1985.

30. Beyers, M. E., and Moulton, B. E . Stability Derivatives Due to Oscillations in Roll for the Standard Dynamics Model at M h 0.6, Report LTR-UA-64, National Aeronautical Establishment, NRC, Canada, January 1983.

31. Beyers, M. E.; Kapoor, K. B.; and Moulton, B. E.. Pitch- and Yaw-Oscillation Experiments on the Standard Dynamics Model at Mach 0.6, Report LTR-UA-76, National Aeronautical Establishment, NRC, Canada, June 1984.

32. Bazzocchi, E.. Un metodo per la determinazione alla galleria del vento dell'indice di efficacia degli alettoni, L'AEROTECNICA, No. 5/1952 Vol. XXXII.

33. Bazzocchi, E.. Studio analitico della vite utilizzando esperienze eseguite alla galleria del vento orizzontale e metodo di prova di modelli in aria libera, L'AEROTECNICA, No. 4/1957 Vol. XXXVII

34. Bazzocchi, E.· Stall Behaviour and Spin Estimation Method by use of Rotating Balance Measurements, AGARD CP 199, Nov. 1975.

35 Marazzi, R, Malara, D , Lucchesini, M.; Comoretto, S , Pacori, F. Use of a Small Scale Wind Tunnel and Model Shop at Aeronautica Macchi as an Industrial Tool, AGARD CP-348, Sept 1983.

36 Thiel, G. Messungen an der Rollwaage/1 Teilbericht Die DVL-Rollwaage/Forschungsbericht Nr 1808/1 Deutsche Luftfahrtforschung.

37. Klinke, E . 4-Komponenten-Rollmessung am Rollmodell Typ 320/EWR-Bericht Nr 152-61/1964

38 Hafer, X Wind Tunnel Testing of Dynamic Derivatives in West Germany AGARD Fluid Dynamics Panel Meeting, Athens, 1978, AGARD CP 235

39 Hafer, X . Windkanalwaagen zur Messung Dynamischer Derivativa, 2 BMFT-Status-Seminar "Luftfahrtforschung/ Luftfahrttechologie"/Garmisch-Partenkirchen 1980.

40. Schulze, B.: Entwicklung und Erprobung einer Roll- und Trudelderivativawaage fur die 3m-Niedergeschwindigkeitswindkanale der Bundesrepublik Deutschland. BMFT-FB-W81-022/1981.

41 Schulze, B Development and Trial of a Rotary Balance for the 3m-Low Speed Wind Tunnels of West-Germany ICIASF 81, Dayton-USA (1981)

42. Commission de l'Aéronautique de la Chambre des Députés, Rapport du 11 mars, 1937.

43. Journal de l'Aéronautique No. 230 - juillet 1938.

44. Tristrant, D.: Synthèse sur les procédures utilisées pour les essais en rotation à la SV 4, Rapport No 81.63 du 22.12.81.

45. Deschamps, M.: Balances dynamiques pour tourne-broche, Rapport No 84.01 du 8.02.84.

46. Deschamps, M.: Atténuateur de modes propres pour balances dynamiques de soufflerie, Rapport 84.56 du 29.11.84.

47. Verbrugge, R. A.: Balance rotative de l'IMFL et techniques expérimentales associées, Rapport AAAF 16eme Colloque, Lille 13-15 Novembre, 1979.

48. Tristrant, D.; and Renier, O.: Récents développements des techniques de simulation dynamique appliquées à l'identification des paramètres de stabilité, AGARD CP 386.

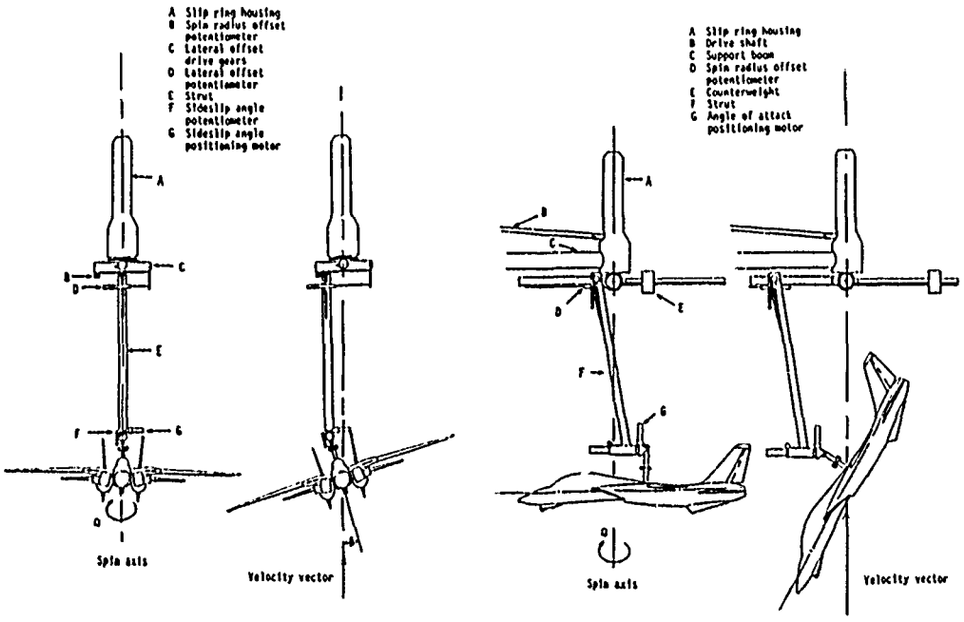

(a) Front view.

(b) Side view.

Figure 3-1. Sketch of the rotary-balance apparatus in the Langley Spin Tunnel.

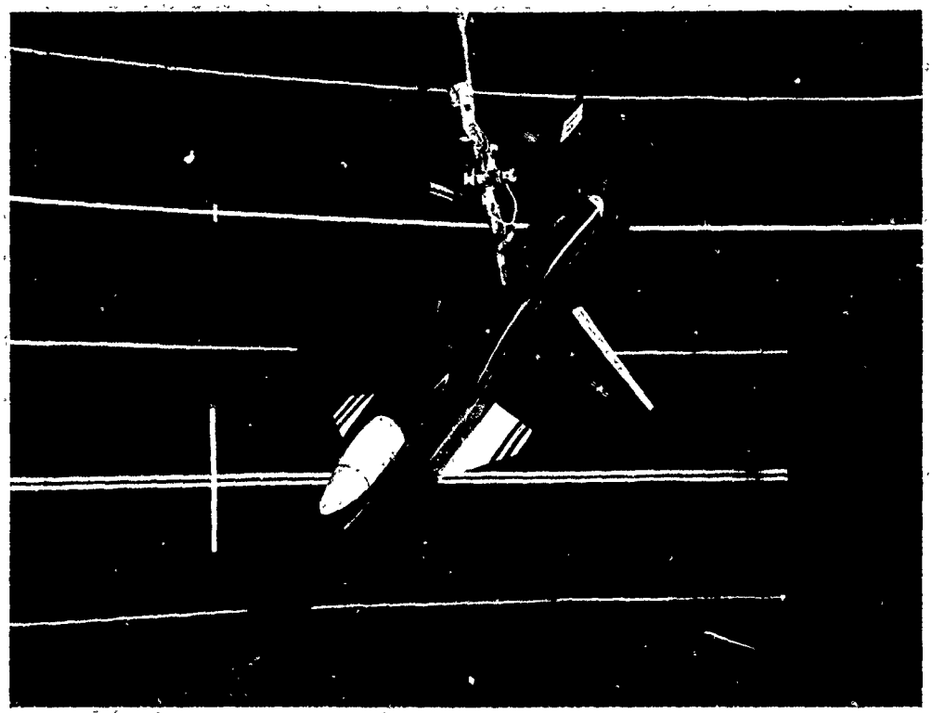

(a) X-29 research model.

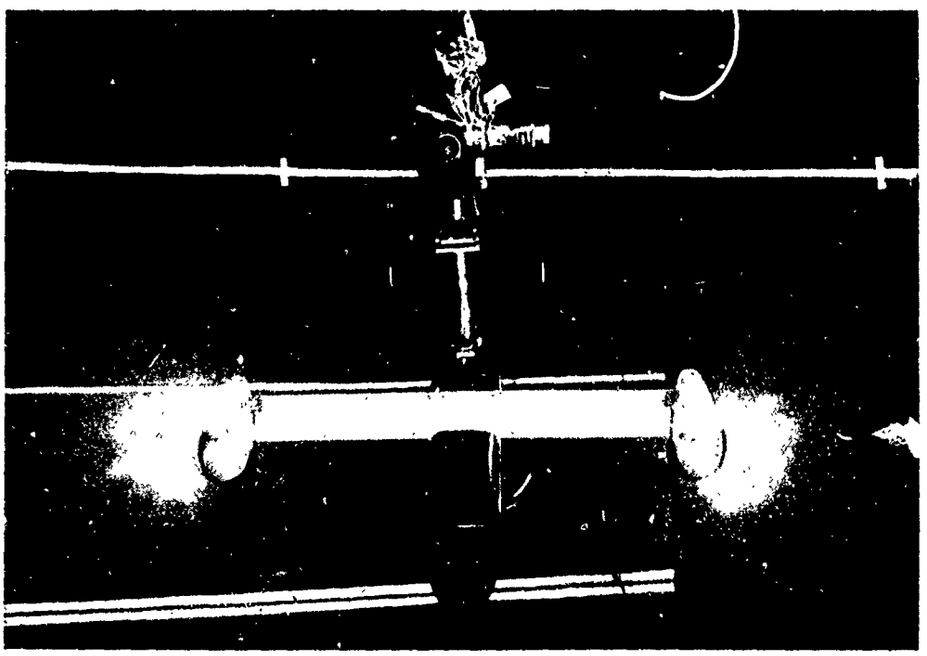

(b) Powered model.

Figure 3-2. Typical model installations.

Figure 3-3. Delta-wing research model mounted on the steady-rolling apparatus in the Langley 7- by 10-foot tunnel.

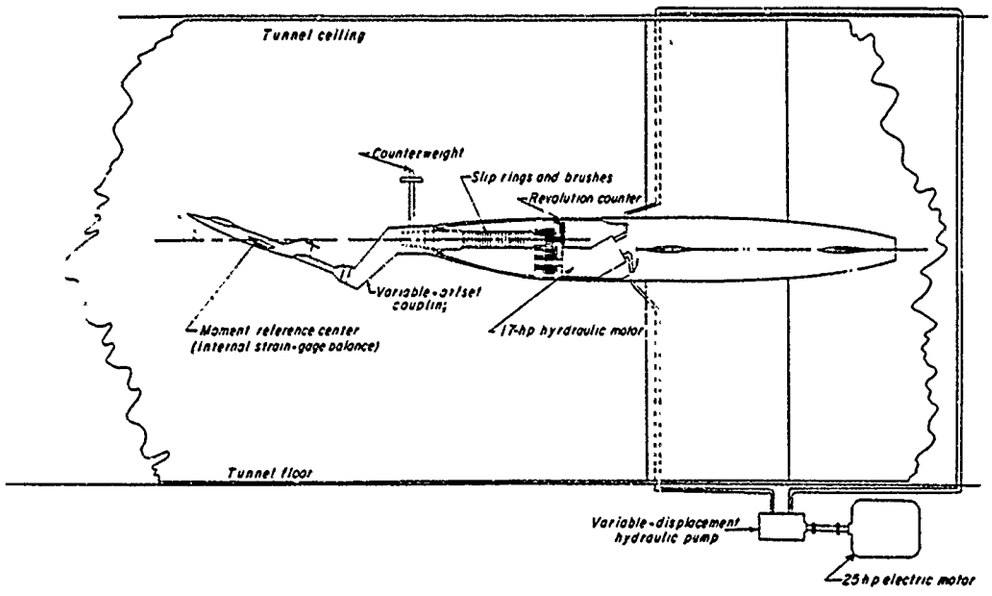

Figure 3-4. Sketch of the major components of the Langley 7 × 10-foot steady-rolling apparatus.

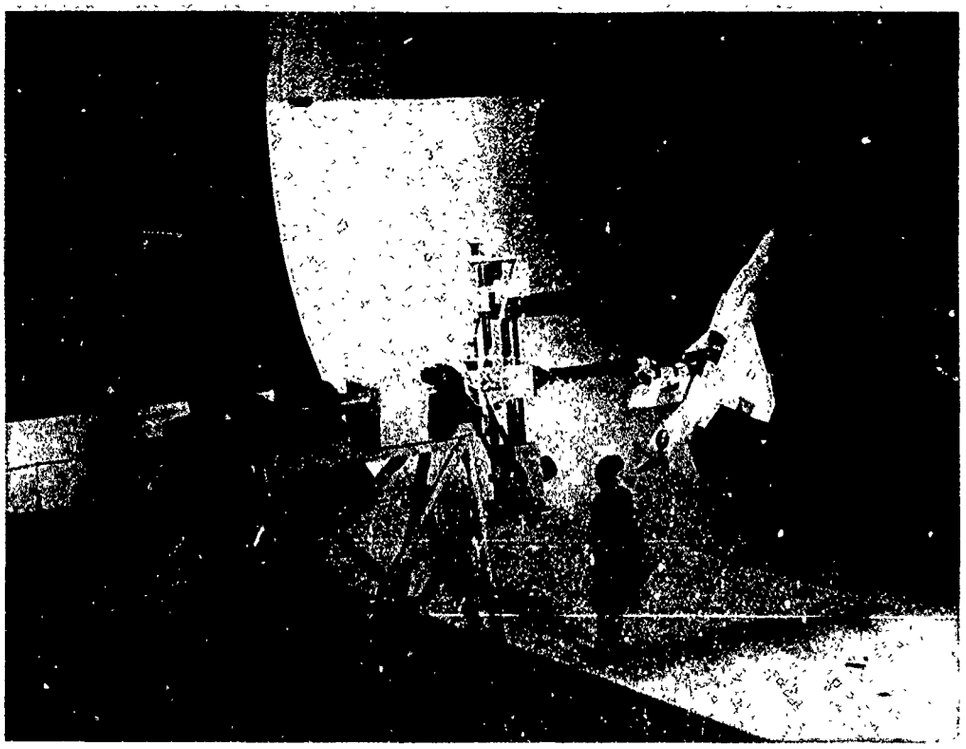

Figure 3-5. The rotary-balance apparatus used for large-scale models in the Langley 30- by 60-foot tunnel.

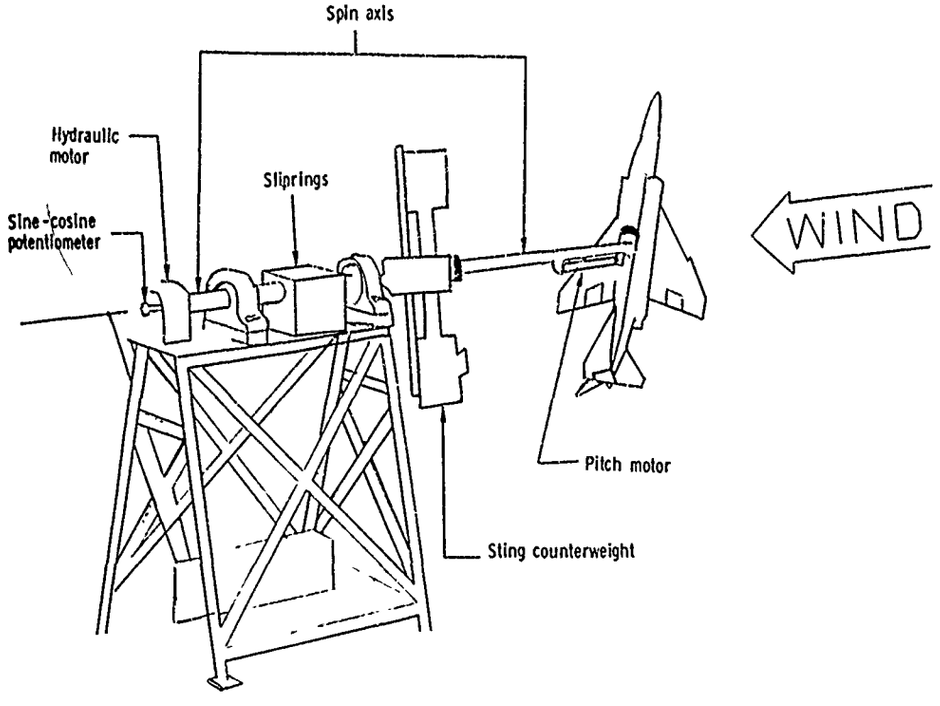

Figure 3-6. Major components of the rig used in the 30- by 60-foot tunnel

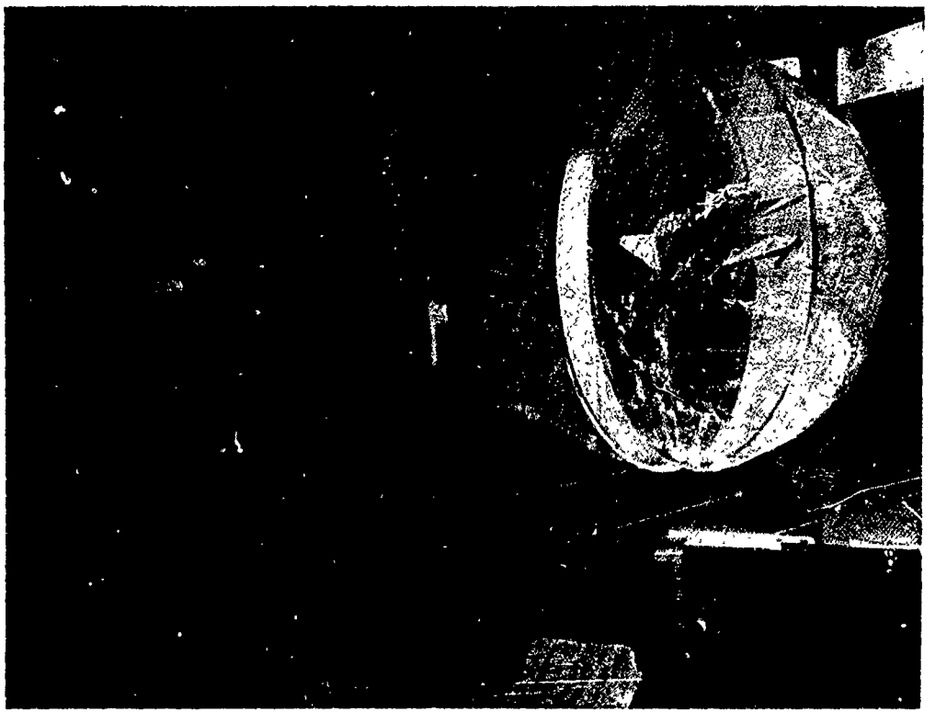

Figure 3-7. Data acquisition and reduction setup in the Langley spin tunnel showing model enclosed in tare sphere.

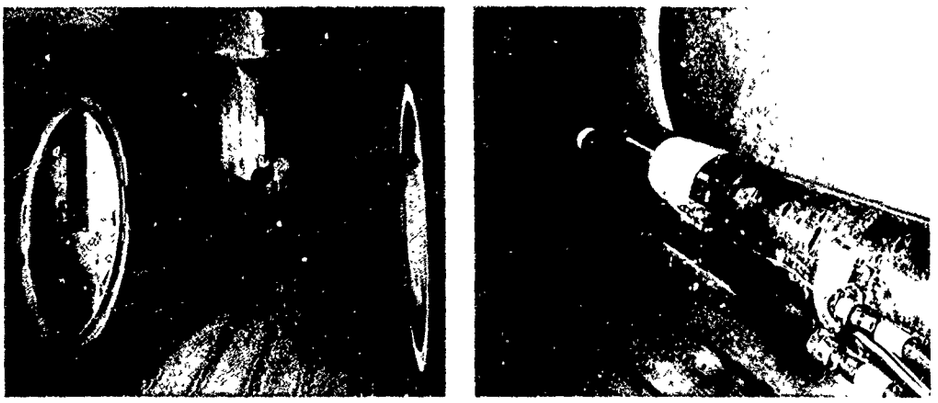

Figure 3-8. Early Ames Research Center rotary-balance rig with cone model.

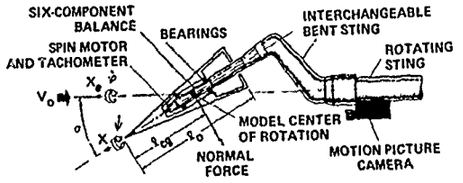

Figure 3-9. Early Ames Research Center rotary-balance rig.

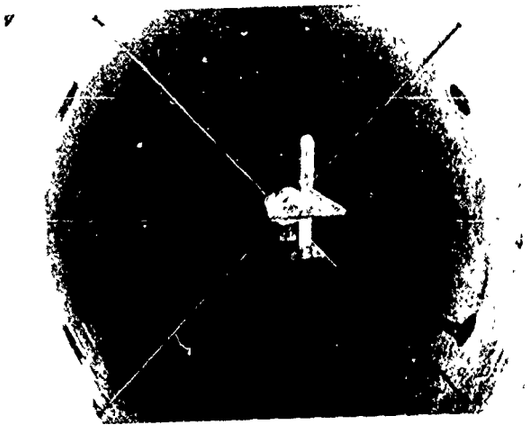

Figure 3-10 Early Ames Research Center rotary-balance rig modified for airplane model

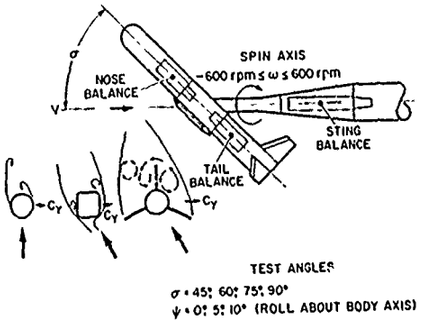

Figure 3-11 Pro-spin mechanisms

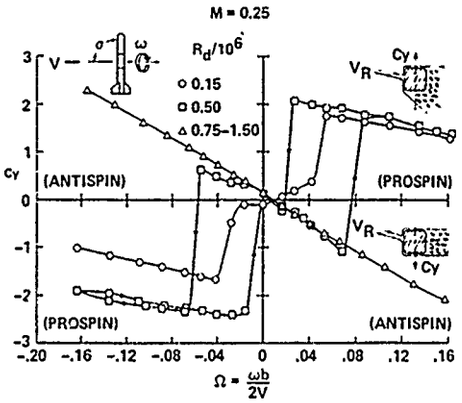

Figure 3-12 Effect of Reynolds number and rotation rate on nose side-force coefficient at $\alpha = 90°$.

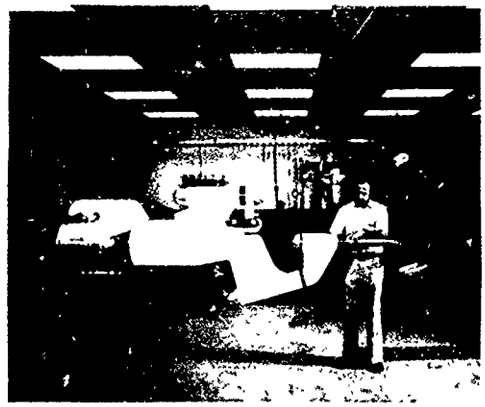

Figure 3-15. Ames Research Center's large-scale rotary-balance rig.

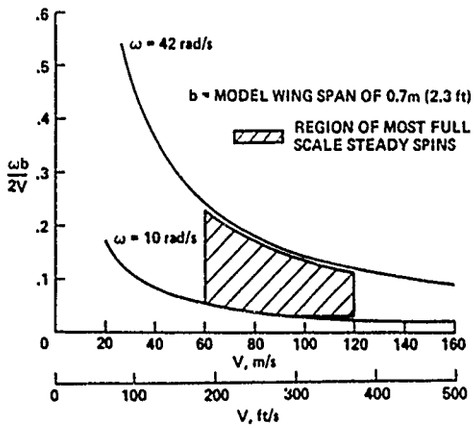

Figure 3-13 Reduced spin rate vs free-stream velocity for most full-scale spins of fighter-type aircraft.

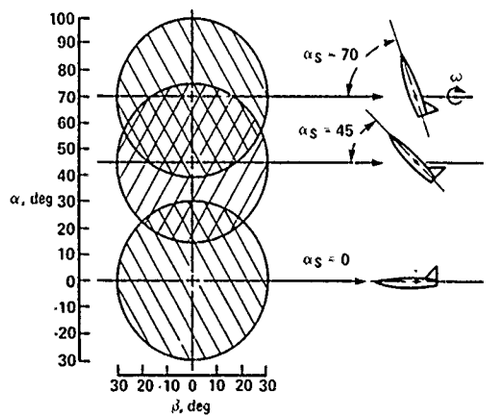

Figure 3-16. Attitude envelope for Ames rotary rig.

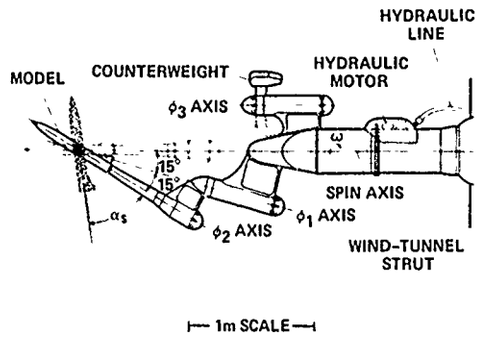

Figure 3-14 Large-scale rotary rig at Ames Research Center.

Figure 3-17. F-15 model mounted on various stings.

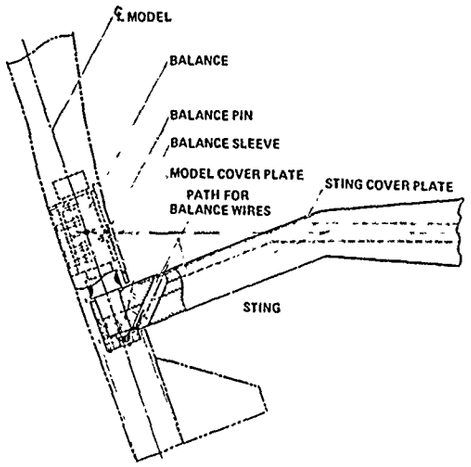

Figure 3-18 Assembly of model, balance and top-mounted sting.

(a) In 12-Foot Pressure Tunnel.

(b) On laboratory test stand.

Figure 3-19. Model mounted on rotary rig

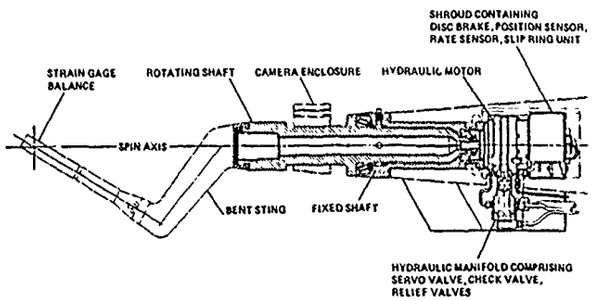

Figure 3-20. Small-scale rotary-balance apparatus

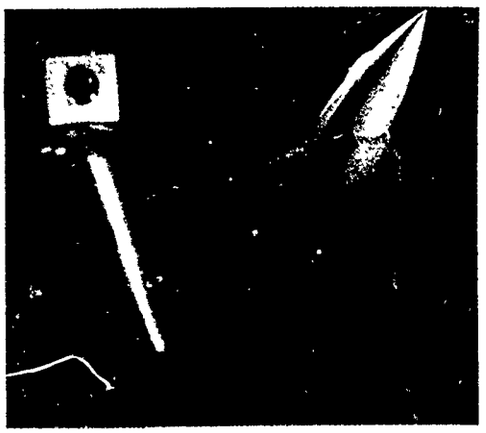

Figure 3-21. Standard Dynamics Model.

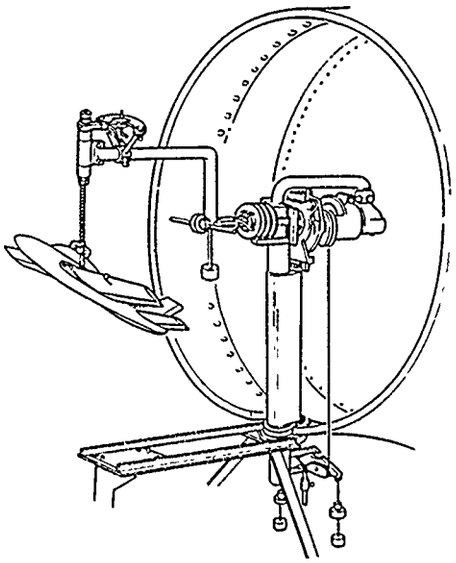

Figure 3-23 Two-component rotary balance (AerMacchi 1956)

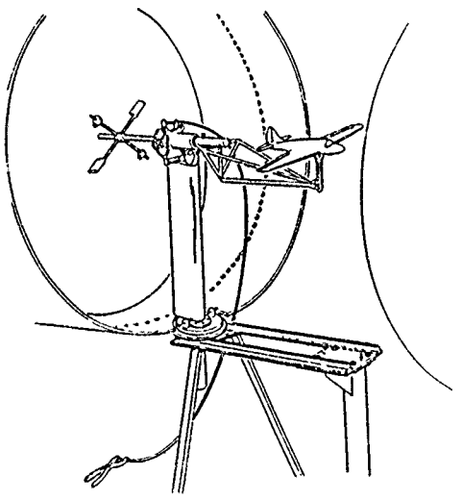

Figure 3-22 Early AerMacchi free-rolling rig (1950)

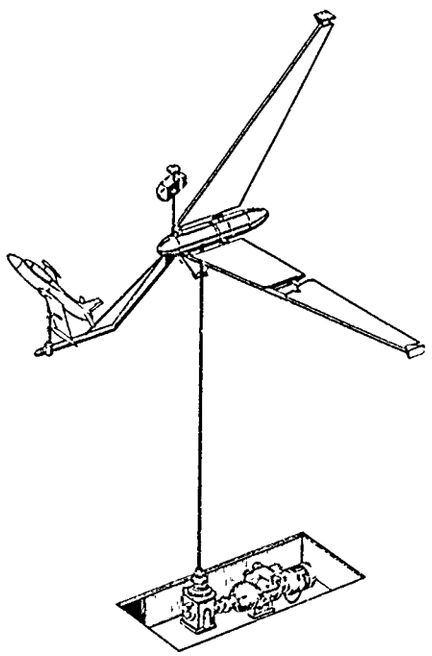

Figure 3-24 The AerMacchi rotary balance as first developed (1969)

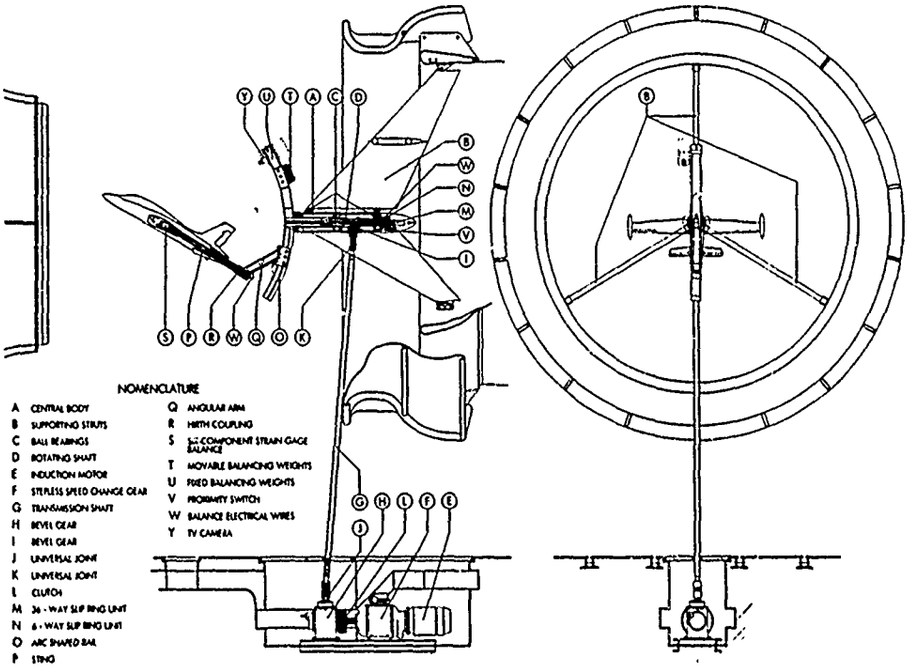

Figure 3-25. The present AerMacchi rotary balance 6CR (1983).

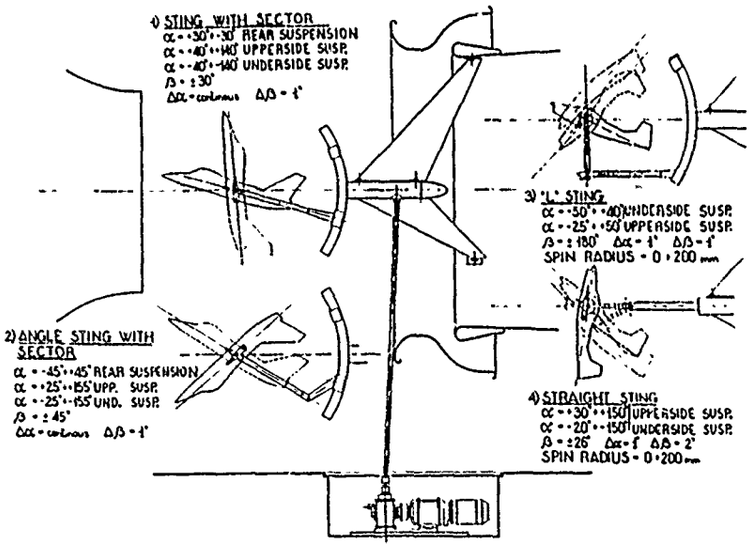

Figure 3-26 Range of model mounts and attitudes available on AerMacchi rotary balance

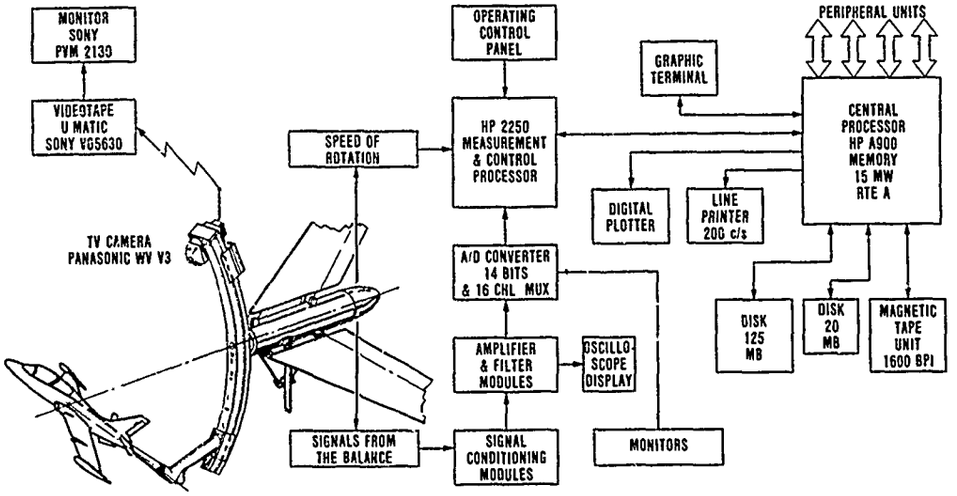

Figure 3-27. AerMacchi rotary balance data acquisition and processing.

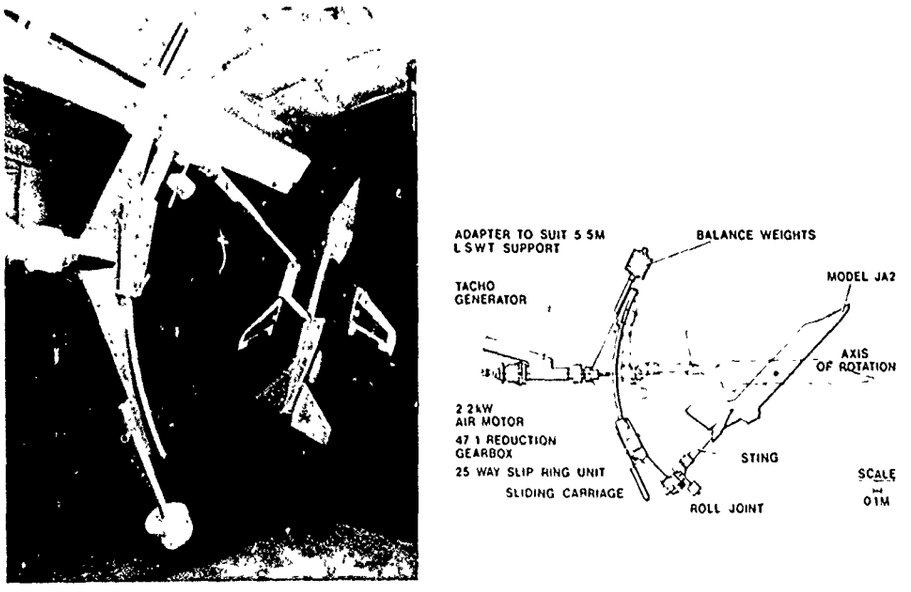

Figure 3-28 Rotary rig for 5.5 m LSWT

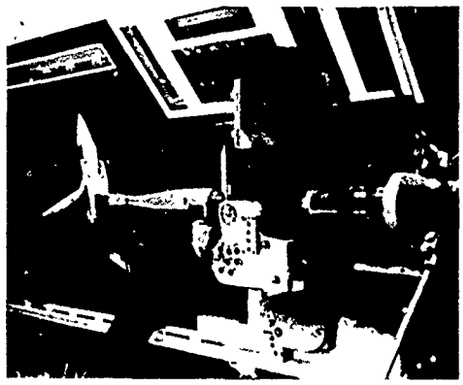

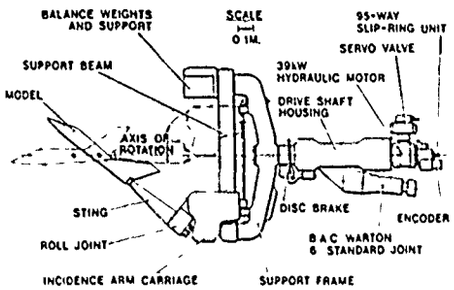

Figure 3-29. Multi-facility rotary derivative rig.

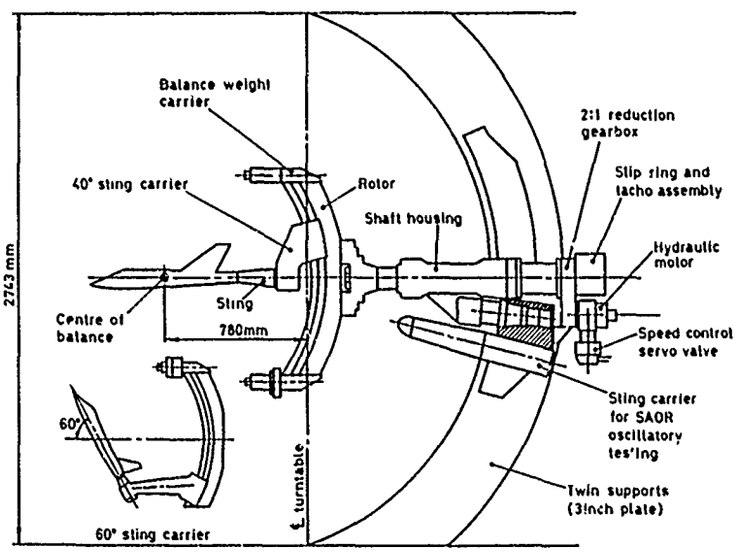

Figure 3-30 RAE rotary balance in 4m × 2.7m wind tunnel

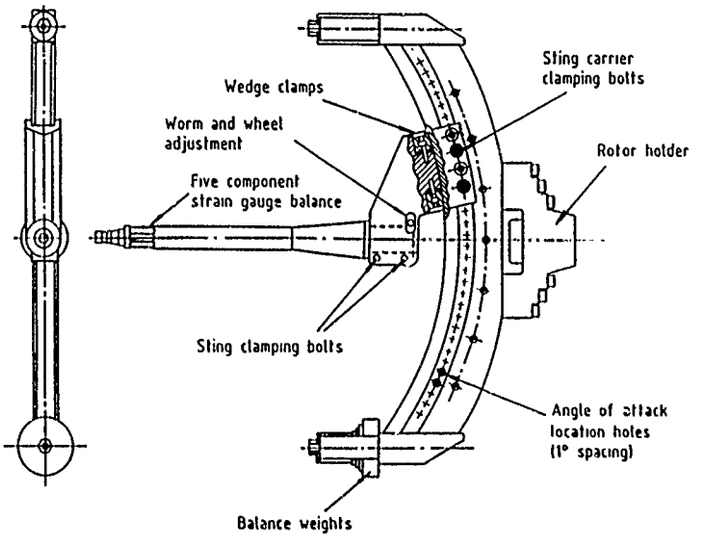

Figure 3-31. Rotor and sting.

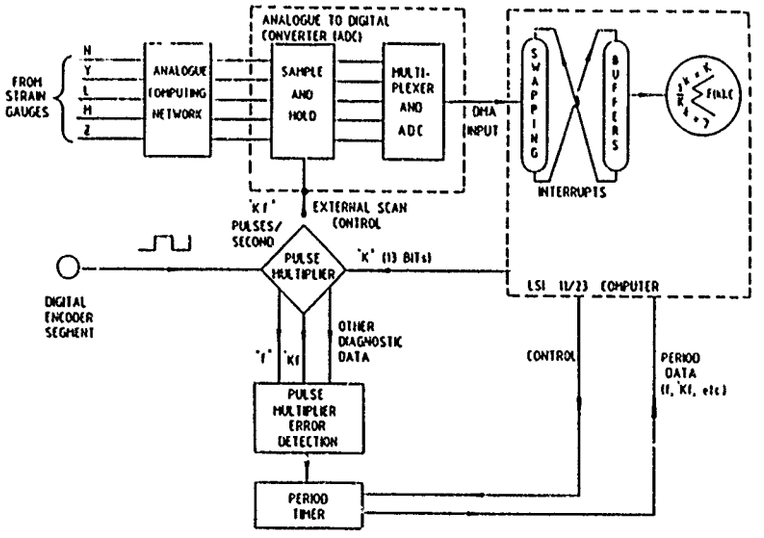

Figure 3-32. Schematic of signal processing

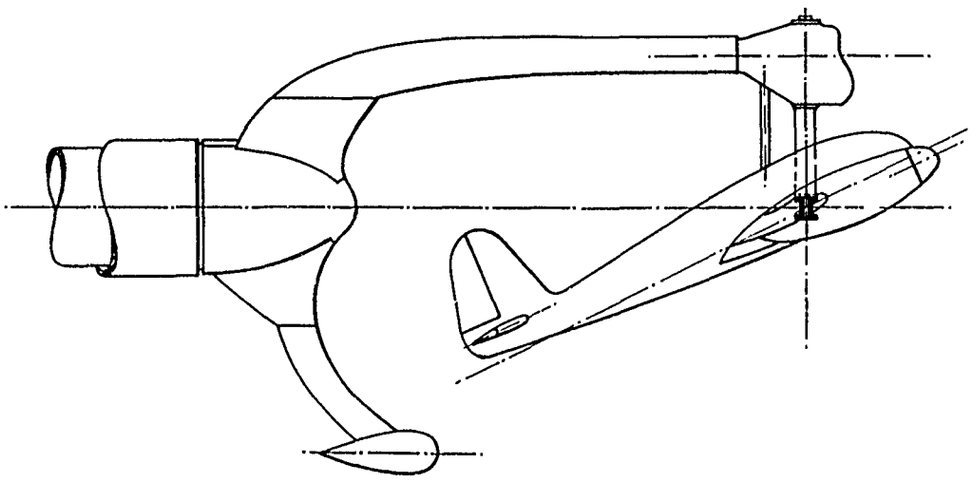

Figure 3-33. Rotary rig of DVL/Berlin-Adlershof.

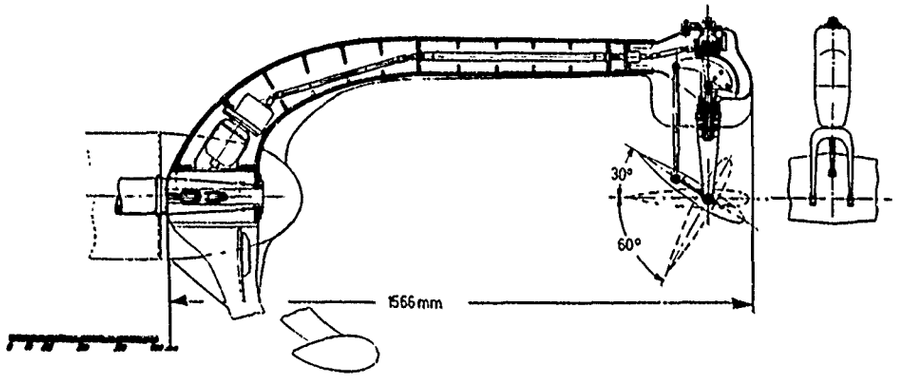

Figure 3-34. Design details of the DVL rotary rig for remote adjustment of incidence.

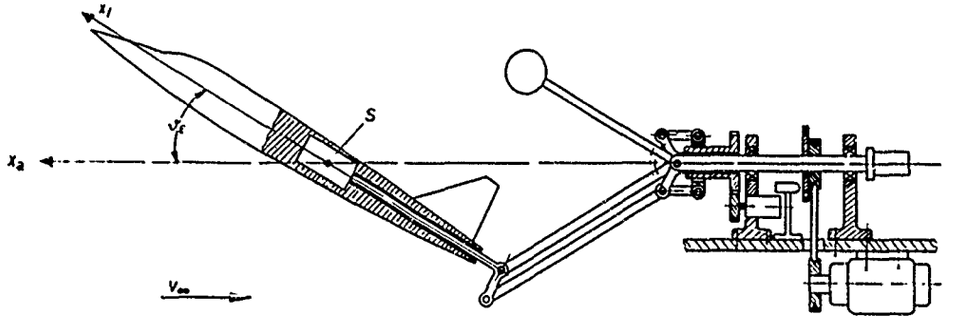

Figure 3-35. Early rotary rig of EWR (4 comp.-balance).

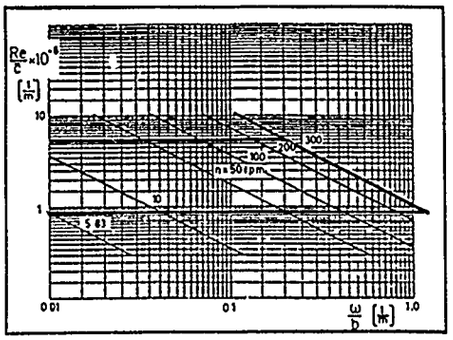

Figure 3-39. Reynolds-number range as a function of the reduced frequency.

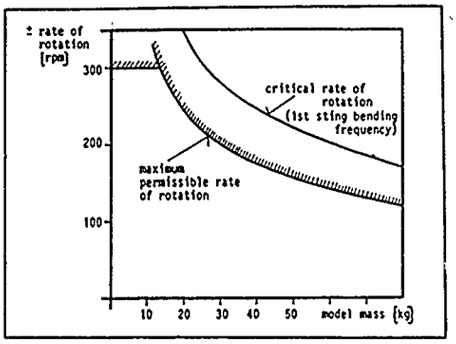

Figure 3-41. Critical rate of rotation, DFVLR apparatus.

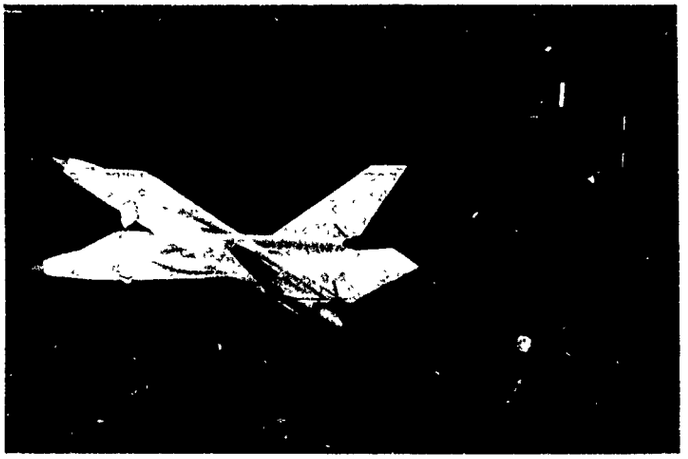

Figure 3-42. Model at two different angles of pitch, DFVLR apparatus.

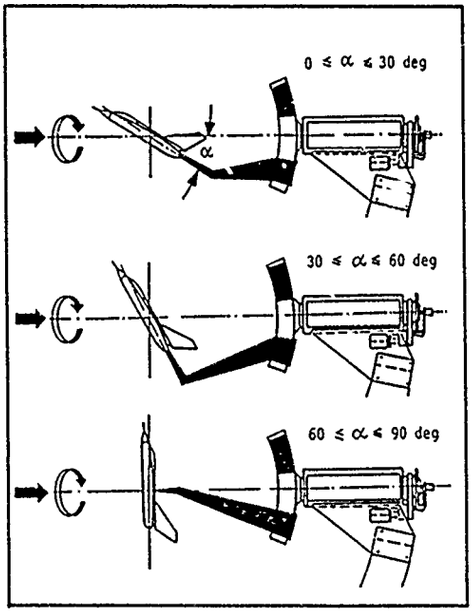

Figure 3-40. System of stings, DFVLR apparatus.

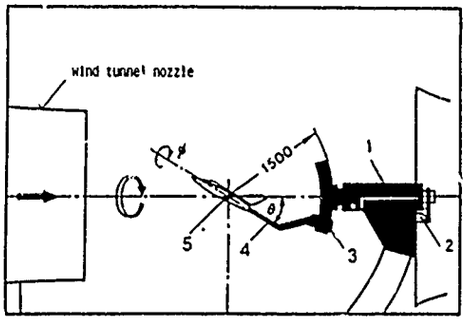

Figure 3-43. Mechanical setup, DFVLR apparatus.

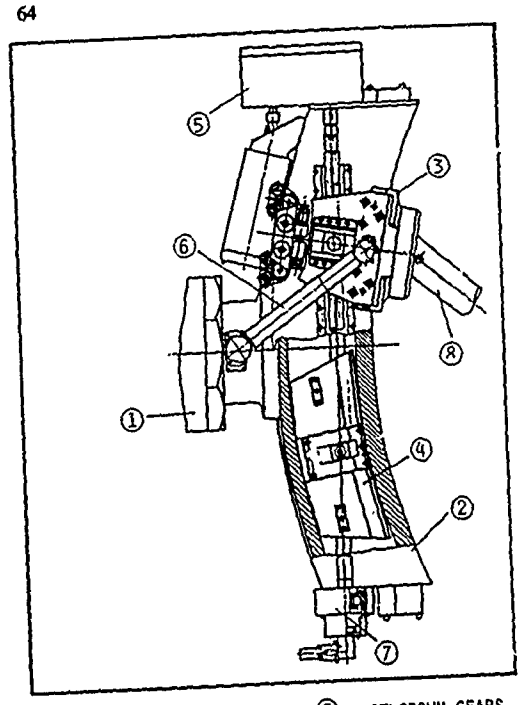

① BEARING HOUSING
② STING GUIDEWAY
③ EXTERNAL CARRIAGE
④ INTERNAL CARRIAGE
⑤ STEPDOWN GEARS
⑥ ELECTRICAL LEADS
⑦ FORCE ABSORBER
⑧ REAR STING

Figure 3-44. Guideway for remote setting of angle of attack, DFVLR apparatus.

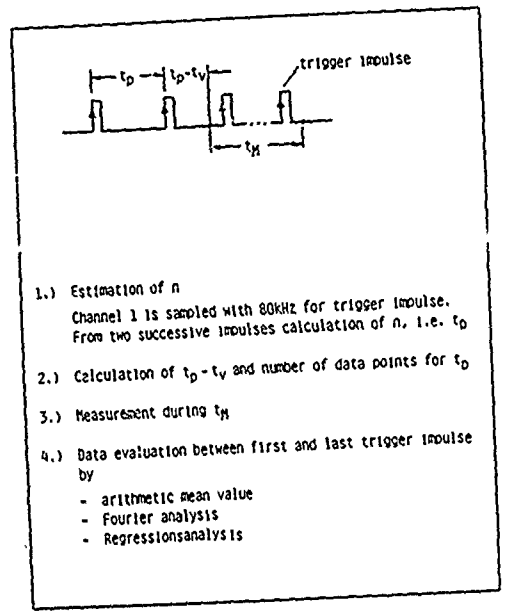

Figure 3-46. Measuring procedure, DFVLR apparatus.

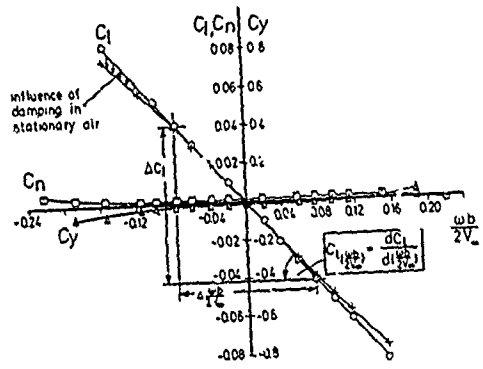

Figure 3-47. Example of aerodynamic forces and moments vs dimensionless roll rate, DFVLR.

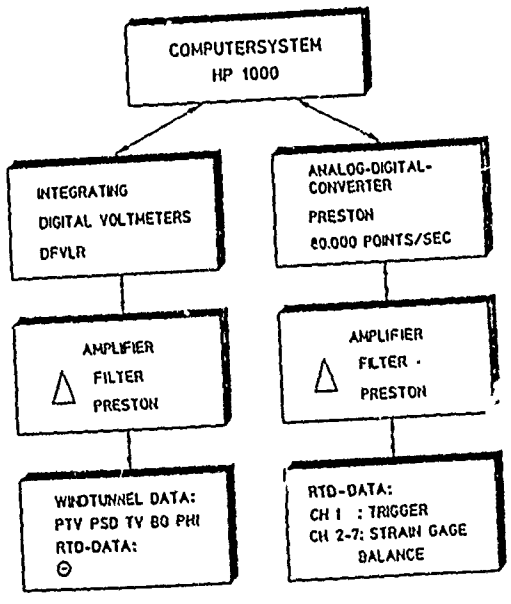

Figure 3-45. Block diagram of the measuring system, DFVLR apparatus.

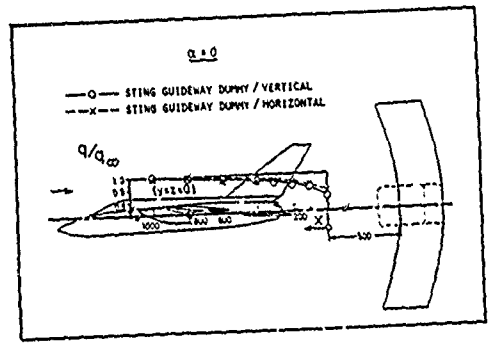

Figure 3-48 Dynamic pressure distribution on tunnel centerline in presence of an early guideway dummy, DFVLR apparatus.

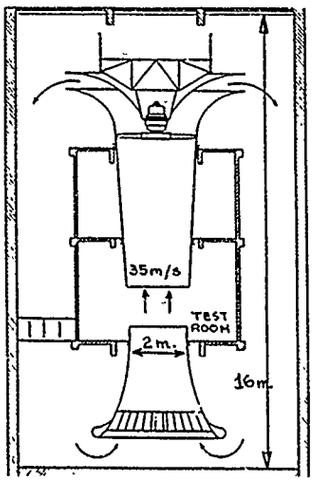

Figure 3-49. The first vertical wind tunnel of IMFL.

Figure 3-51. Photograph of IMFL rotary balance apparatus.

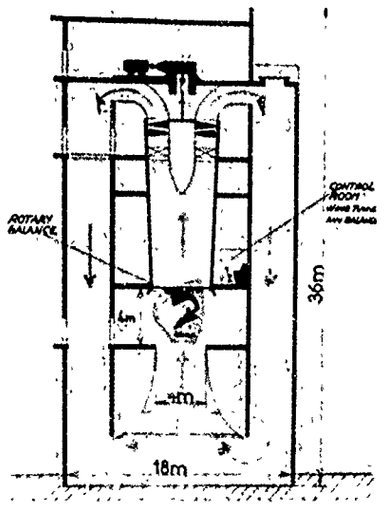

Figure 3-50. The current vertical spin tunnel (SV4).

(a) Trainer model top mount.

Figure 3-52. Examples of model mounting configurations.

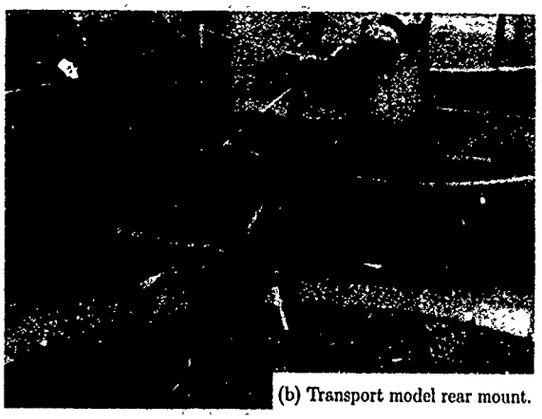

(b) Transport model rear mount.

Figure 3-52. Concluded.

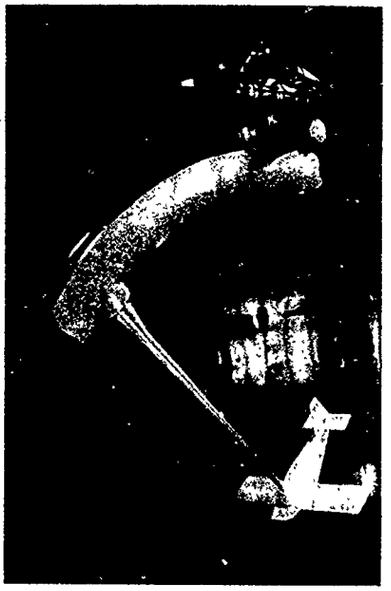

(c) General aviation model top mount.

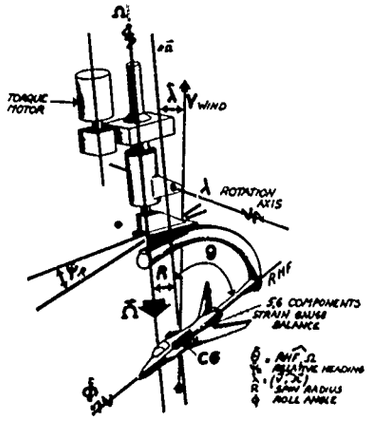

Figure 3-53. Rotary balance degrees of freedom.

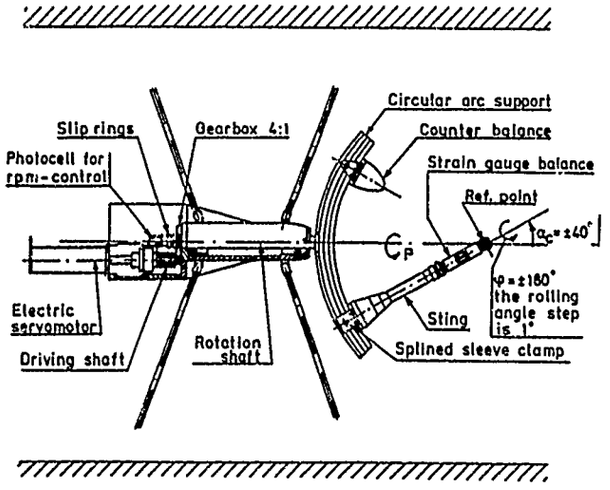

Figure 3-54. Rotary apparatus, FFA tunnel L2 (see also Fig. 2-19)

Figure 3-55. Rotary apparatus, FFA tunnel LT1 (see also Fig. 2-20).

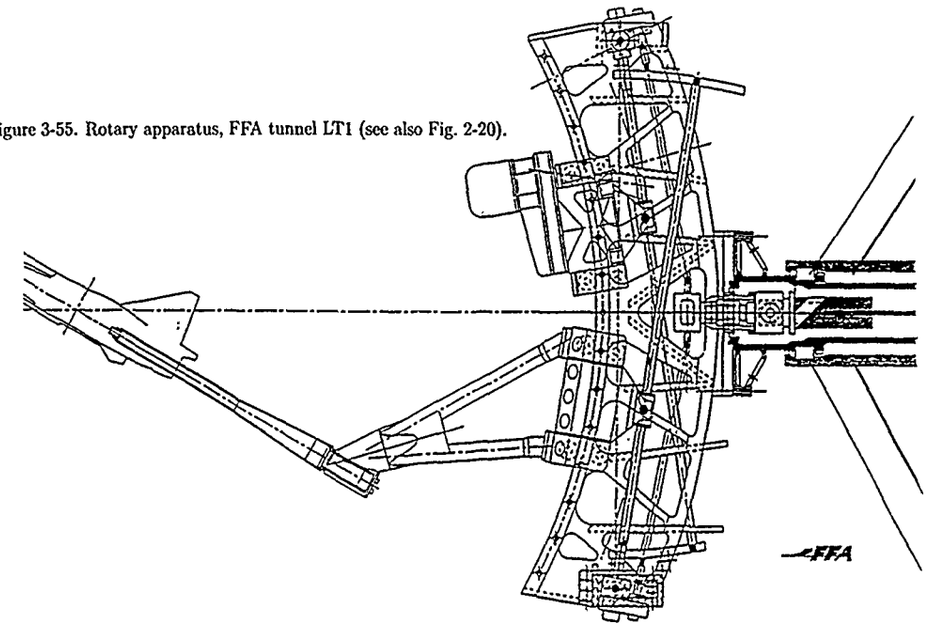

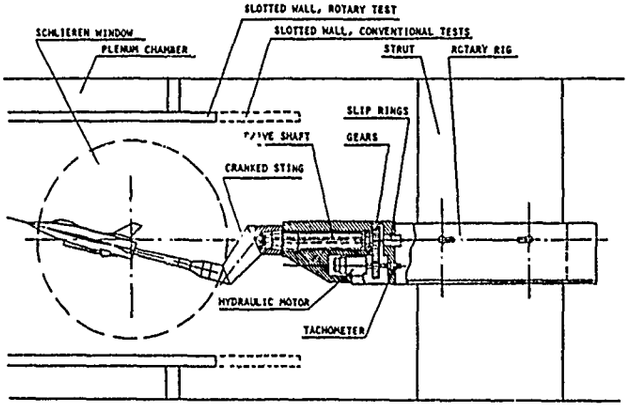

Figure 3-56 FFA rotary rig in the S4 wind tunnel (see also Fig 2-21)

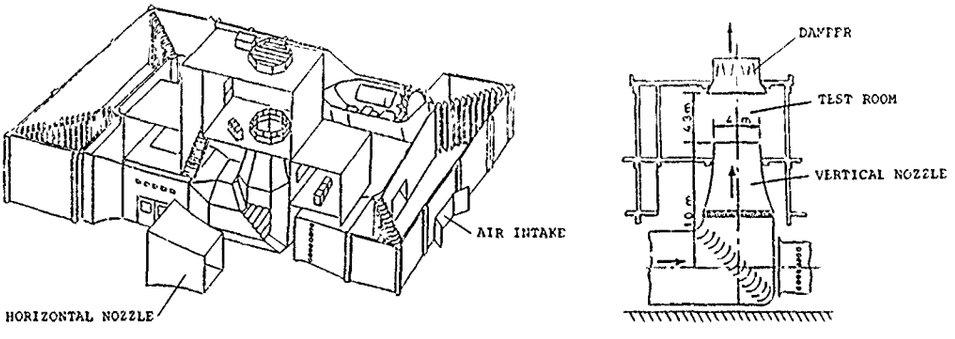

A Schematic View of the TRC Convertible Wind Tunnel

A Sectional View of the Vertical Wind Tunnel

Figure 3-57. The TRC Convertible Wind Tunnel.

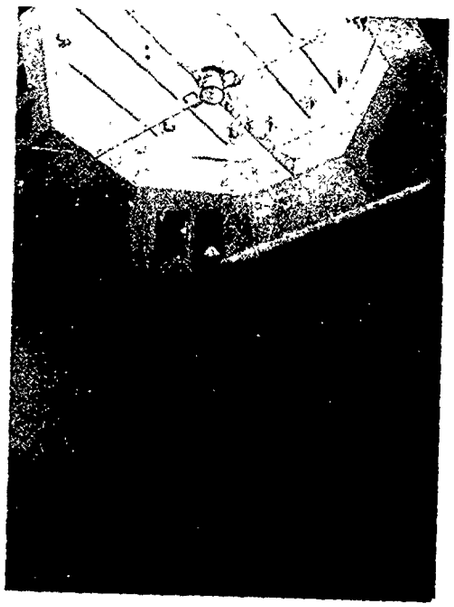

Figure 3-58. Rotary test setup at TRC.

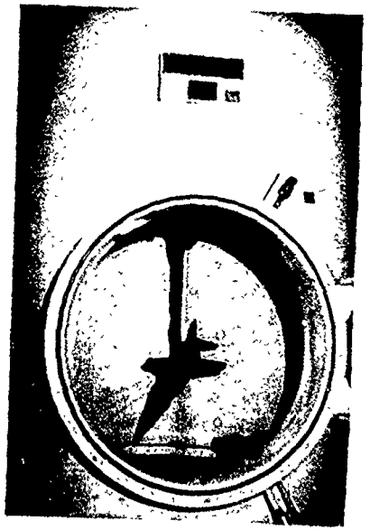

Figure 3-60. Vacuum chamber for rotary balance tests.

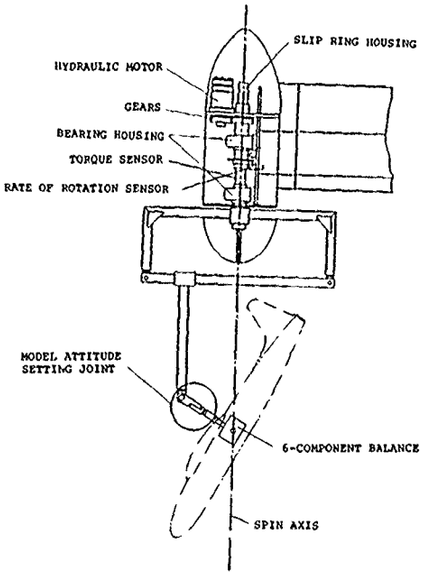

Figure 3-59. TRC rotary balance apparatus

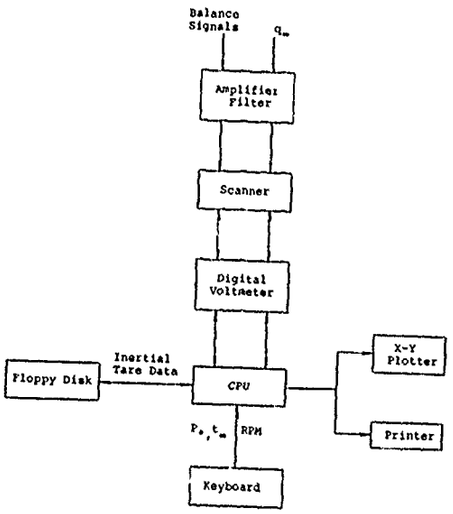

Figure 3-61 Data processing diagram

CHAPTER 4

OSCILLATORY CONING

4.0 INTRODUCTION

The traditional approach used in rotary-balance testing involves aligning the angular velocity vector $\vec{\Omega}$ of the model with the wind-tunnel free-stream velocity vector $\vec{V}$. This type of motion is referred to as "coning." Since the linear and angular velocity vectors are colinear in this arrangement, the angles of attack and sideslip are constant during the motion. For specified angles of attack and sideslip, the six components of forces and moments are determined for motions characterized by the nondimensional spin rate $\Omega b/2V$. The angular velocities p, q, and r are not independent for such motions, but are related by kinematic equations. Thus, there is only one dynamic degree of freedom, namely the coning motion.

If the axis of rotation is intentionally given an angle of inclination relative to the free stream, the possibility exists for obtaining certain types of dynamic aerodynamic data which may prove to be of great value in the analysis of large-amplitude, high-rate motions at moderate and high angles of attack.

Compared with other rotary rigs, the rotary balance at ONERA-IMFL is unique in that the axis of rotation can be tilted through an angle λ relative to the free-stream direction. In this technique, oscillations of angle of attack and angle of sideslip occur during the model motion, which is referred to as "oscillatory coning." The staff of ONERA-IMFL have gained experience with the operation and analysis of data obtained in this type of testing. This chapter will describe the apparatus and the governing kinematic equations, and present typical data measured using the technique.

4.1 APPARATUS DESCRIPTION

The IMFL rotary balance, which is located in a 4-m vertical spin tunnel, has been described in Chapters 2 and 3. In this chapter the use of the unique tilted-axis capability, which is indicated in Figure 4-1, is discussed.

As shown in Figure 4-1, the rig is capable of conventional coning tests with $\lambda = 0°$. The entire rig, model, and rotation axis can be tilted about a pivot axis in the horizontal plane. The tilting is achieved with an electric servo-control mechanism which is remotely actuated at a rate of about one degree per second. Without rotation ($\Omega = 0$) this degree of freedom can be used to perform a continuous sweep of angle of attack or sideslip (up to 30°). For rotary tests, λ must be constant and cannot exceed 20° for the present rig. Four hydraulic jacks are used to lock the λ adjustment. During rotation, the longitudinal axis of the model describes a coning motion of semi-angle θ about an axis tilted from the velocity vector by the angle λ (see Figure 4-2).

4.2 KINEMATIC RELATIONSHIPS

The kinematic relationships between the motion variables (ψ, Ω) and position parameters of the apparatus (θ, ϕ, λ), and the variables used in a flight mechanics analysis (α, β, p, q, r, $\dot{\alpha}$, $\dot{\beta}$), are now discussed.

4.2.1 Angular Velocities

Since the model and the Ω rotation axis are tilted together, the expressions for the angular velocities p, q, and r are independent of λ. The components of the vector $\vec{\Omega}$ in the body axes are:

$$\begin{aligned} p &= \Omega \cos\theta \\ q &= \Omega \sin\theta \sin\phi \\ r &= \Omega \sin\theta \cos\phi \end{aligned} \tag{1}$$

These relationships apply to both conventional coning and oscillatory coning tests.

4.2.2 Angle of Attack and Sideslip

For the case of the rear sting-mounted model, the equations for angle of attack and sideslip are:

$$\text{Coning motion}: \quad \begin{aligned} \alpha &= tan^{-1}(\cos\phi \tan\theta) \\ \beta &= \sin^{-1}(\sin\phi \sin\theta) \end{aligned} \tag{2(a)}$$

$$\text{Oscillatory coning motion}: \quad \begin{aligned} \alpha &= \tan^{-1}\left(\frac{\sin\lambda(\cos\psi\ \cos\theta\ \cos\phi - \sin\psi\ \sin\phi) + \cos\lambda\ \cos\phi\ \sin\theta}{\cos\theta\ \cos\lambda - \cos\psi\ \sin\theta\ \sin\lambda}\right) \\ \beta &= \sin^{-1}\left((\cos\psi\ \sin\phi\ \cos\theta + \sin\psi\ \cos\phi)\ \sin\lambda + \cos\lambda\ \sin\theta\ \sin\phi\right) \end{aligned} \tag{2(b)}$$

In steady coning motion, $\lambda = 0°$ and Equations 2(b) reduce to Equations 2(a), then the angle of attack and sideslip do not vary. In the case of oscillatory coning ($\lambda \neq 0°$), the values of α and β vary sinusoidally with ψ at frequencies equal to the rotational frequency. Since the model motion is smooth and continuous, the model structure is not subjected to large angular and linear accelerations, as might occur in forced-oscillation tests in pitch or yaw. Figure 4-3 shows a geometrical approximation of the α and β excursions during a complete revolution.

4.2.3 Intrinsic Relationships

The foregoing equations relate the aerodynamic variables (α, β, p, q, ...) to the parameters and motion variables of the apparatus. However, intrinsic relationships also exist which relate the aerodynamic variables to themselves These relations express the constraints of the model on the test apparatus. In the case of the steady coning motion, the relations are:

$$p = \Omega \cos\alpha \cos\beta$$
$$q = \Omega \sin\beta$$
$$r = \Omega \sin\alpha \cos\beta$$

By eliminating Ω, the following relationships are found for steady coning:

$$r = p \tan\alpha \tag{3(a)}$$

$$q \cos\alpha = p \tan\beta \tag{3(b)}$$

and

$$\alpha = \dot{\beta} = 0 \tag{3(c)}$$

For the case of oscillatory coning, the standard equations for rate of change of α and β due to arbitrary rotation are applicable.

$$\dot{\alpha} = q - \tan\beta(r \sin\alpha + p \cos\alpha) \tag{4(a)}$$

$$\dot{\beta} = p \sin\alpha - r \cos\alpha \tag{4(b)}$$

Equations (4) reduce to Equations (3) when $\dot{\alpha} = \dot{\beta} = 0$. Thus, in coning there are four intrinsic equations, and in oscillatory coning, only two by virtue of the λ parameter. These relationships are used to identify several important aerodynamic parameters.

4.3 SIGNAL PROCESSING AND DATA REDUCTION

The unsteady aerodynamic phenomena associated with the oscillatory motion can have different characteristics as seen from the points of view of frequency or amplitude, and it is necessary to perform some preliminary analyses of the strain-gauge balance signals before calculating the aerodynamic coefficients. A predetermined treatment could be unsuitable as the aerodynamic data included in the balance signals could be filtered out. Furthermore, the complexity of the unsteady behavior, the nonlinearity of aerodynamic responses, and the potentially large number of relevant variables at high angles of attack prove unwieldy to analyze in a direct on-line process. For these reasons, the signal processing and data reduction procedure are completed off-line. The signals are sampled at a frequency of 330 Hz and stored on magnetic tape.

Subsequently, it is possible to carry out supplementary signal processing (for example, spectral analyses). Data stored for analysis include the angular positions (ψ, θ, ϕ, and λ), the rotation speed (Ω or $\dot{\psi}$), the dynamic pressure of the free stream, time, and the six components of the strain-gauge balance signals.

During a test the only varying degree of freedom is the angle ψ, and aerodynamic data are measured for an angular sector corresponding to the value of ψ given by the angular encoder. A complete cycle is usually divided into 180 data windows, each having an angular width of 2°. Average values and standard deviations are calculated within each window. This eliminates high frequency noise. Each window has discrete values of angle of attack, sideslip, and balance output signals, corresponding to the average ψ value. The contributions of electrical reference signals and inertial and gravitational forces and moments are then extracted from the balance measurements in each angular window The global aerodynamic coefficients are then calculated.

The data reduction procedure yields 180 sampling points per test. A low pass filter with a fast Fourier transform eliminates the structural noise at frequencies higher than those within the spectral width considered. For each test, 180 measurement points of the aerodynamic forces and moments are obtained, corresponding to different combinations of p, q, r, α, β, $\dot{\alpha}$ and $\dot{\beta}$ A suitable division of windows and the cutoff frequency can be selected after a test when considering the physical characteristics of the phenomena.

4.4 IDENTIFICATION OF DYNAMIC STABILITY PARAMETERS (LINEAR DOMAIN)

The problem consists of determining the values of parameters included in a mathematical model of the aerodynamic behavior of an aircraft as applied to dynamic tests in a wind tunnel. In this section the data reduction technique used in oscillatory coning tests on the IMFL rotary rig[1] will be examined.

When the linearity assumptions are satisfied and the longitudinal and lateral effects can be separated, the frequently used mathematical model of the aerodynamic coefficients is expressed in the following way:

$$\text{Longitudinal.} \quad C_i = C_i(\alpha,\beta) + C_{i_q}(\alpha)\frac{ql}{V} + C_{i_{\dot{\alpha}}}(\alpha)\frac{\dot{\alpha}l}{V}$$
$$i = X, Z, \text{ or } m$$
$$\text{Lateral-directional:} \quad C_i = C_i(\alpha,\beta) + C_{i_p}(\alpha)\frac{pl}{V} + C_{i_r}(\alpha)\frac{rl}{V} + C_{i_{\dot{\beta}}}(\alpha)\frac{\dot{\beta}l}{V} \tag{5}$$
$$i = Y, l, \text{ or } n$$

It is assumed that longitudinal and lateral effects can be separated. The coefficients C_i are defined with respect to the body axes. The aim is to identify the values of the parameters $C_{i_q}(\alpha)$, $C_{i_{\dot\alpha}}(\alpha)$, $C_{i_p}(\alpha)$, $C_{i_r}(\alpha)$, and $C_{i_{\dot\beta}}(\alpha)$ for several discrete values of the angle of attack. The dynamic parameters have been assumed to be independent of sideslip in order to simplify the problem.

Figure 4-4 shows the part of the (α, β) plane in which the parameters are identified for a fixed angle of attack, α_o. The parameters are assumed to be constant within this rectangular area. In practice, the α width of the area is one or two degrees, while the β width could be somewhat larger, depending on the aerodynamic characteristics of the aircraft considered. Also, the procedure is assumed to be valid up to the maximum sideslip angle, β_{max}. This is investigated prior to the test. First, the static terms $C_i(\alpha_o, \beta)$ are evaluated over the sampling area. Subsequently, the tests required to identify the stability parameters are performed as described below.

4.4.1 Longitudinal Parameters

The following tests are performed (see Figure 4-4):

- Test No.1. A coning motion at $\alpha = \alpha_o$ with $\phi \neq 0$. Thus, the pitching velocity is nonzero and $\dot\alpha = \dot\beta = 0$.
- Test No.2. An oscillatory coning motion where the pitch velocity effects and the α variation effects are estimated together. Here the angles of attack and sideslip describe a quasi-circular trajectory in the (α, β) plane, but only the measurements in the part crossing the rectangular area are considered (i.e., when α is near α_o).

With these two basic tests, the parameters C_{i_q} and $C_{i_{\dot\alpha}}$ are identified separately at $\alpha = \alpha_o$. Generally, the two tests are performed at several values of the rotation rate. Then the variation of the parameters with $\Omega b/2V$ can be estimated, and if this dependence is linear, the accuracy may be improved by using the most significant values of $\Omega b/2V$ in the parameter identification.

4.4.2 Lateral-Directional Parameters

There are three lateral-directional derivatives for each coefficient, C_{i_p}, C_{i_r}, and $C_{i_{\dot\beta}}$. However, the three aerodynamic variables p, r, and $\dot\beta$ are related by the intrinsic relation $\dot\beta = p \sin\alpha - r\cos\alpha$. For a fixed angle of attack ($\alpha = \alpha_o$), this relation is a linear one between p, r, and $\dot\beta$. Consequently, only two combinations of these three variables can be identified. Substituting Equation (4) into (5), the following expressions are obtained:

$$C_{i_p} + C_{i_{\dot\beta}} \sin\alpha_o \qquad i = Y,\ l \text{ or } n$$

and

$$C_{i_r} - C_{i_{\dot\beta}} \cos\alpha_o$$

The two basic tests required to identify the parameters are (Figure 4-4).

- Test No.3. A coning motion ($\beta = 0,\ r = p\tan\alpha_o$).
- Test No.4. An oscillatory coning motion, where the r and β effects are investigated. The same remarks can be made as in Test No.2.

4.4.3 Comments and Results

When the tests are restricted to coning motions only the rotation rate effect can be estimated. Because of the relation $r = p\tan\alpha_o$, it is not possible to uncouple the roll and yaw effects. With the mathematical modeling postulated, the parameters identified from the oscillatory coning tests are $C_{i_q}(\alpha)$, $C_{i_{\dot\alpha}}(\alpha)$, $C_{i_p}(\alpha) + C_{i_{\dot\beta}}(\alpha)\sin\alpha_o$, and $C_{i_r}(\alpha) - C_{i_{\dot\beta}}(\alpha)\cos\alpha_o$.

This identification method has been tested at IMFL and comparisons with forced-oscillation results have been made. The comparisons were most satisfactory for combat aircraft configurations. However, certain examples of high-aspect-ratio models showed that the results could be configuration dependent, leading to some discrepancies. The effect of the large angle-of-attack variation at the wing tip due to rotation rate, the type of airfoil section tested, its sensitivity to Reynolds number variations and the linearity assumptions of the mathematical model were the main reasons for the disagreement.

When the span is large, the vortical nature of the flow is strong and the parameters identified in the rotary tests cannot be compared with those determined from forced oscillation. The parameters characterize the effects of high roll velocities rather than small disturbances of a rectilinear flight path.

4.4.4 Effect of Spin Radius

To separately identify the derivatives (direct or cross-coupling) an additional kinematic parameter of the apparatus is required in order that the intrinsic, linear kinematical relations existing during steady rotations (Eqs. (3)) or dynamic

rotations (Eqs. (4)), for each angle of attack, may be decoupled. Introducing a "spin radius" or, more exactly, a "turning-radius" provides this capability. The new kinematic relations are obtained by expressing the velocity of the model c.g. as:

$$\overrightarrow{V_G} = \overrightarrow{V_o} + \overrightarrow{\Omega} \times \overrightarrow{OG} \tag{6}$$

where $\overrightarrow{V_c}$ is the free-stream velocity, $\overrightarrow{OG}$ the gyration vector and the components of $\overrightarrow{\Omega}$ are given by Equations (1). The y-axis equation is:

$$\dot{V} \sin\beta + V \cos\beta[\dot{\beta} + r\cos\alpha - p\sin\alpha] = q(pa + rc) - b(p^2 + r^2) \tag{7}$$

where a, b, c are the components of $\overrightarrow{OG}$ in body axes.

If the gyration radius R is zero and V is constant, the relation (4(b)) is obtained. Conducting an optimal test program with $R \neq 0$, it is possible to obtain different values of the second term in Eq. (7) and an appropriate distribution of the $\dot{\beta}$, p, and r variables. Hence, it becomes practical to identify each derivative separately.

The specific contribution of the "turning radius" is illustrated in Figure 4-5. To increase the radius, the sting is curved, introducing the angle θ_3. In the (α, β) plane, M_o can be reached by adjusting θ and ϕ. If $R = 0$ and $\lambda = 0$, a steady rotation is obtained with p, q, and r constant, defined by Eq. (1) and α, β constant. If $R \neq 0$ and $\lambda = 0$ the test point (M) moves along the line tangent to the θ circle at M_o. The amplitude M_oM is equal to $\Omega R/V$. In this case, it is possible to obtain different values of α and β that are independent of p, q, and r. For example, it is possible to generate a steady rotation at $\alpha = 0$ with yaw rate $r \neq 0$. When $R \neq 0$ and $\lambda \neq 0$, the trajectory in the (α, β) plane is a pseudo-circle centered at M and with a radius equivalent to λ. This configuration is particularly interesting, being relevant to identification of $\dot{\beta}$ effects separately from those due to p and r.

Evaluation tests performed with the nonzero turning radius demonstrated the capability of identifying the derivatives C_{l_p}, C_{l_r}, and C_{l_β} in good agreement with the classical combined terms $C_{l_p} + C_{l_\beta} \sin\alpha$ and $C_{l_r} - C_{l_\beta} \cos\alpha$ obtained with $R = 0$.

4.4 5 Limitations

There are two main limitations of this method of identification of the dynamic stability parameters First, there is the assumption of linearity. Linear behavior about an equilibrium flight state is implicit in the definition of the dynamic stability parameters. Moreover, in the individual estimation of these parameters the additivity of the effects is assumed, and it is necessary to verify this. The associated requirement of insensitivity to β of the dynamic parameters, within the specified limits, should also be verified.

A second restriction concerns the applicability of the rotary-balance results and, more precisely, restricts the extrapolation of these results to other flight conditions The stability parameters are determined for a vortical flow with a high spin angular velocity. Extrapolation of such results to the stability parameters for a planar flight condition could be hazardous, particularly with configurations of high aspect ratio as mentioned previously.

Finally, due to the maximum speed limitation of the low-speed wind tunnel (maximum speed 40 m/s at IMFL), the aerodynamic measurements are restricted to low Reynolds numbers (2×10^6/m).

4.5 LARGE-AMPLITUDE UNSTEADY PHENOMENA (NONLINEAR DOMAIN)

The discussion will now be focussed on large-amplitude unsteady phenomena. For combat aircraft, these aerodynamic phenomena are associated with dynamic behavior such as dynamic stall, spin entry, pure rolling at high angles of attack, autoroll spin, or recovery from stall. During these motions, the angle λ between the rotational vector and the wind vector can be large. The rotation induces rapid variations in angle of attack and/or sideslip of possibly large amplitude

Some of these phenomena and, in particular, dynamic stall have been described by many authors. Numerous studies have been carried out on this subject. The conclusion that the phenomenon is characterized by a stall angle-of-attack increase and a hysteresis effect comes from experimental research on airfoils submitted to forced oscillations in pitching,[2] plunging or fore-and-aft motions.[3,4]

Oscillatory coning tests performed at IMFL on combat aircraft models have demonstrated analogous unsteady aerodynamic effects. In spite of the fact that these test motions are rotational and thus very different from those performed on airfoils, the characteristics of the observed phenomena were similar.

The oscillatory coning results for a delta wing[1] are shown in Figures 4-6(a), (b), and (c) and compared with the steady results (coning motion). The drag and lift coefficients are presented as functions of angle of attack. When λ is nonzero, the angle of attack varies cyclically (with amplitude λ), and so the aerodynamic coefficient variation describes a closed loop in the (α, C_{X_A}) or (α, C_{Z_A}) plane.

Figure 4-6(a) shows the tests results obtained at a large λ amplitude, for different values of the rotation rate Ω^*. In this case, the oscillatory coning motion occurred in the linear domain as the angle of attack did not exceed the stall angle, hence linear modelling which includes instantaneous $\dot{\alpha}$ effects can be used.

In Figure 4-6(b), the absolute value of the rotation rate was the same, but the angle-of-attack variations exceeded the stall angle for several different amplitudes. In this case, the following characteristics of the dynamic stall phenomenon may be observed:

- unsteady behavior with large amplitude effects
- dynamic stall incidence much greater than static stall incidence
- hysteresis effects corresponding to strongly time-dependent behavior

Since the aerodynamic responses are fairly similar whatever the direction of the rotation ($\Omega > 0$ or $\Omega < 0$), it may be concluded that the sideslip direction has no significant effect on the longitudinal coefficients during the dynamic phenomenon. Above the static stall angle, the longitudinal coefficients depend on the angle-of-attack history $\alpha(t)$. Also, in the dynamic situation, contrary to the steady case, the lift increases when α increases beyond the static stall angle of attack.

Figure 4-6(c) shows results obtained under conditions similar to those of Figure 4-6(b), but at a larger mean angle of attack (45°). The oscillatory coning motion is entirely in the post-stall domain, where the flow is completely separated and the unsteady large-amplitude effects are still present. The unsteady contributions to the lunar coning motions ($\lambda = 0$) are very small for the data shown, even though the separated flow is very sensitive to angle-of-attack variations (Fig. 4-6(c)).

The purpose of this section was not to explain or predict these aerodynamic phenomena, which are very complex Instead, it was intended to demonstrate the value of the technique by illustrating unsteady aerodynamic effects similar to dynamic stall that occur during oscillatory coning.

4.6 REMARKS ON STRUCTURAL NOISE AND VIBRATION

Since a rotary-balance apparatus is a dynamic simulation device operating at up to high angles of attack, its performance is strongly affected by mechanical vibration and noise. The different sources of noise which can affect the measurements are numerous: mechanical effects generated by the operation of the wind tunnel (propagation of vibrations due to the motor and fan assembly), by the rig (effect of $\vec{g}$ pulsation and $\vec{\Omega}$) and, particularly, by the flow characteristics (instabilities or unsteadiness). All of these could excite the proper vibration modes of the support, the balance and the model, resulting in parasitic motions and noise on the balance-signals. The most important source of vibrations comes from the aerodynamic effects on the model. They exist as well during "quasi-static" testing at high angles of attack, but are more serious in unsteady tests.

One of the most important criteria in the discussion of this question is the frequency pass-bandwidth necessary to restore the transient high-α aerodynamic effects satisfactorily. For example, for the IMFL apparatus the objective was to conduct analysis at up to about ten times the maximum frequency of rotation, i.e., about 15 to 20 Hz. This result was arrived at after a detailed study of the structure of the apparatus was conducted, defining the deformation under static loads and the dynamic proper modes of the entire setup, including the six-component dynamic balance.

Initially, however, attention must be focussed on mechanical noise reduction instead of filtering techniques, which present many disadvantages. In fact, the parasitic motions persist and are not without effects on the measurements themselves, due to coupling effects between the aerodynamics and structure.

The following are examples of techniques which can be applied to reduce noise and improve the dynamic performance of such apparatuses

Special dynamic models can be used for rotary balance testing. A carbon-fiber model combines stiffness and lightness: a 1-m span model weighs approximately 3 kg and the first structural proper mode is higher than 80 Hz

- The dynamic strain-gauge balance can be adapted to these specific tests; the choice of material and geometrical definition are designed to optimize sensitivity and stiffness.
- Vibration absorbers based on the pendulated mass technique, can be used This technique, under development at IMFL, has demonstrated interesting results. The basic technique is well-known, but the performance can actually be largely improved by the use of visco-elastic material having a very high damping ratio. A schematic representation of the system is shown in Figure 4-7. As an example, results are shown in Figure 4-8 for a one-degree-of-freedom system (pitch vibrations) The model frequency in the balance pitch mode is 23.1 Hz, and it may be seen that, when combined with the adapted absorber, the noise reduction is particularly significant

Complementary to these basic efforts of structural noise reduction, the use of special data reduction techniques can contribute to an effective dynamic analysis (FFT filtering techniques are particularly effective in such applications).

4.7 REFERENCES

1. Tristrant, D., and Remer, O. Récents développements des techniques de simulation dynamique appliquées à l'identification des paramètres de stabilité AGARD CP 386 No 22, Gottingen, Nov 1985.

2 McCroskey, W J The Phenomena of Dynamic Stall. VKI LS 1981-4, 1981

3. Ericsson, L. E.; and Reding, J. P.: Unsteady Flow Concepts for Dynamic Stall Analysis. Journal of Aircraft, August 1984, p. 601.

4. Favier, D.; Maresca, L.; and Rebout, J.: Dynamic Stall Due to Fluctuations of Velocity and Incidence. AIAA Journal, July 1982.

4.8 NOMENCLATURE

b	wingspan
C_i	body-axis aerodynamic coefficient, $i = X, Y, Z, l, m, n$
p, q, r	body-axes angular rates
R	spin radius or gyration radius
V	free-stream velocity
$\vec{V_c}$	free-stream velocity vector
$\vec{V_G}$	velocity vector of c.g. of model
α, β	angles of attack and sideslip
ψ	rotation angle
ψ_R	relative heading angle
$\theta, \phi, \lambda, \psi_R$	adjustment degrees of freedom (see Figure 4-1)
λ	tilt angle of rotation vector
$\vec{\Omega}$	rotation vector
Ω	rotation rate
Ω^*	reduced rotation rate $= \Omega b/2V$

Superscript

$(\cdot)$	derivative with respect to time

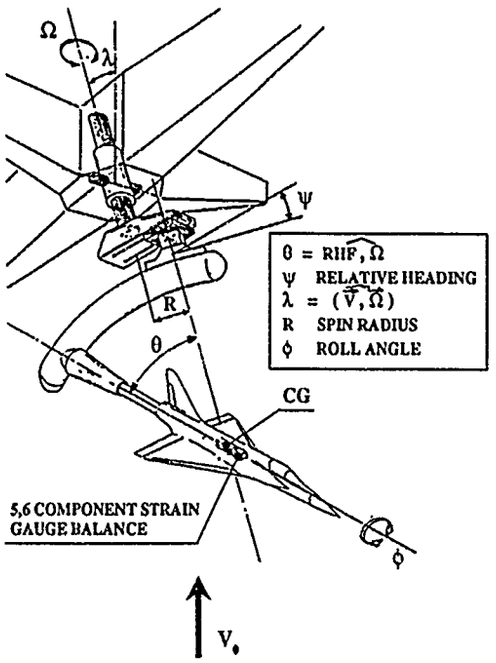

Figure 4-1 Schematic layout

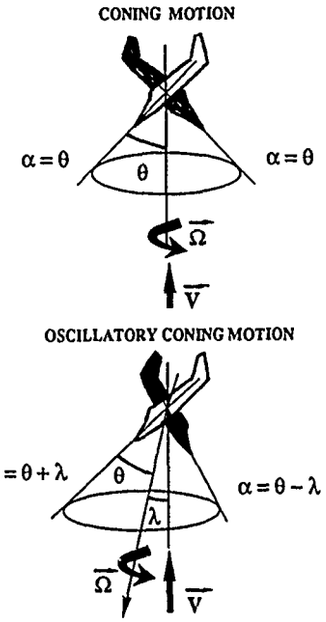

Figure 4-2. Geometric parameters.

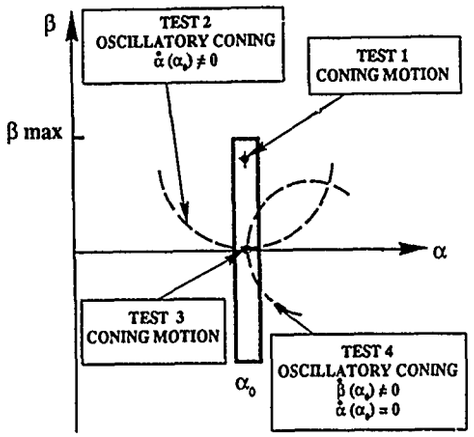

Only the measurements in the rectangular area are considered

TEST	TYPE	$\dot{\alpha}(\alpha_0)$	$\dot{\beta}(\alpha_0)$	p	q	r
1	CONING	O	O	X	X	X
2	OSCILLATORY	X	O	X	X	X
3	CONING	O	O	X	O	X
4	OSCILLATORY	O	X	X	O	X

Figure 4-4. Scheme for identification of stability derivatives.

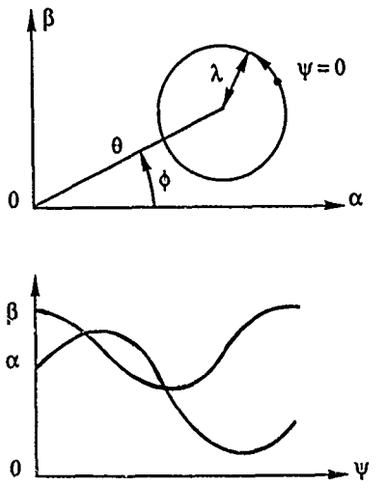

Figure 4-3. Geometrical approximation of α and β in oscillatory coning.

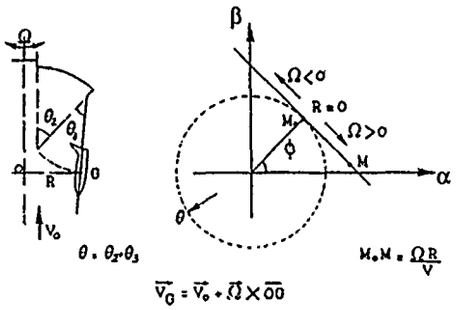

Figure 4-5. Representation of kinematic variables for non-zero turning radius.

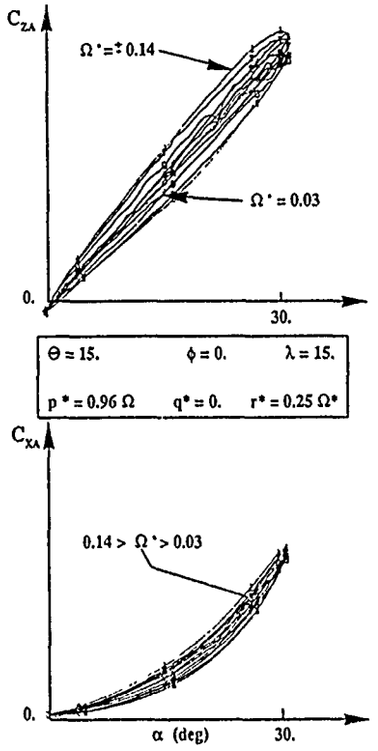

(a) α below stall.

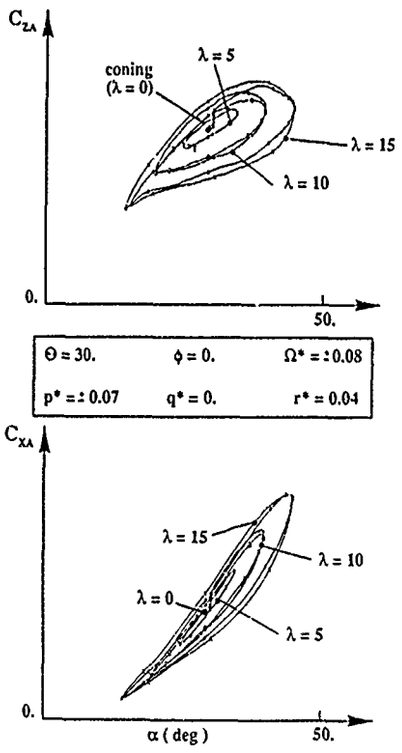

(b) α passing through stall.

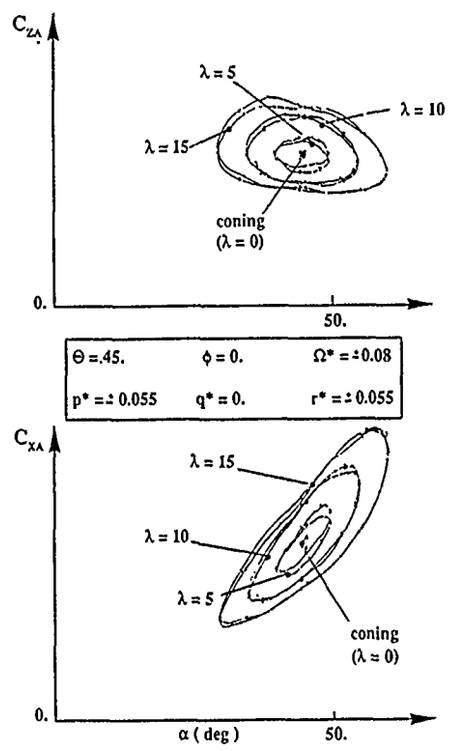

(c) Post-stall angles.

Figure 4-6 Oscillatory coning results for a delta wing.

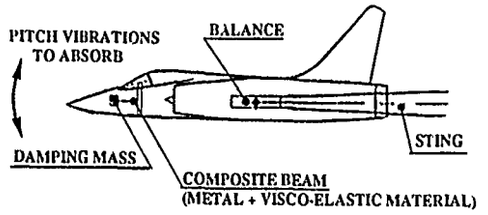

Figure 4-7 Schematic representation of absorber system.

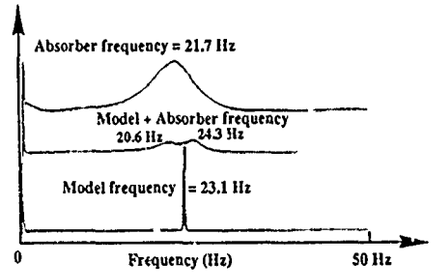

Figure 4-8 Spectral analysis of one-degree-of-freedom system

CHAPTER 5

SPECIAL AERODYNAMIC CONSIDERATIONS

5.0 INTRODUCTION

Unlike the case of static tests, where it is common practice to conduct extensive calibration of the effects of wall and support interference on the aerodynamic measurements, there is little evidence of similar diligence in previous unsteady testing. As will be shown, in the latter case the interference effects can be expected to be more severe. Support interference has been demonstrated to be significant over much of the testing envelope of interest. The effects are, however, very dependent upon configuration geometry, angle of attack, Reynolds number, etc. Examples are given in this chapter to illustrate diverse situations, all of which have significant interference effects. In the case of unsteady wall interference, logical arguments point to the existence of flow mechanisms capable of producing a significant interference contribution. In Chapter 12 a cooperative test program is described that could give quantitative answers in regard to the seriousness of these interference effects and provide the means to correct the measurements for such effects.

5.1 AERODYNAMIC SUPPORT INTERFERENCE

5.1.1 Background

In the case of static tests the aerodynamic support interference problem has been studied extensively,[1-3] and guidelines have been established for the selection of the support geometry and model size which ensure that the aerodynamic interference remains insignificant. In dynamic tests, however, it is often not possible to reduce the interference to the level of insignificance. For a forced oscillation test, for example, the support structure is of necessity much bulkier than in a static test, aggravating the problem of aerodynamic interference.[4,5] Even in the case of free oscillations, the support structure becomes rather large in order to provide the stiffness needed to ensure one-degree-of-freedom oscillations in pitch or yaw. In some cases a second degree of freedom in the form of sting plunging has to be accepted[4] in order to minimize the aerodynamic interference, in which case the measurements have to be corrected for the extra degree of freedom.[6,7]

The problem of aerodynamic interference increases both in severity and complexity when performing tests at high angles of attack, where body and wing vortices can interact with the support structure. The support becomes massive in the case of the rotary rig because of the high stiffness needed in order to keep deflections and vibrations, caused by large, unbalanced, centrifugal forces, within acceptable limits. Thus, the rotary rig support structure usually causes significant flow deflections.[8,9] The particular problem encountered in high incidence testing had just begun to receive attention[10-12] when the present effort was started. Available experimental results are analyzed to explore the possibility of correcting for the high-alpha dynamic support interference, similarly to what has been done at low angles of attack.[5]

5.1.2 Rotary-Rig Support Interference

Because of its bulkiness the rotary rig often causes a significant change of the flowfield in the test section, even in the absence of the model to be tested, as has been observed for the rotary rigs both at DFVLR[13] and ONERA-IMFL[14] (Figure 5-1). The longitudinal dynamic pressure gradient can by itself have a significant effect, not only on fin effectiveness, but more importantly, on boundary-layer transition, flow separation, and vortex breakdown. In one case, by using a slight area contraction over the length of the open test section, the blockage effect of the rotary rig could be compensated for, practically eliminating the adverse longitudinal dynamic pressure gradient with its potentially large effect on the development of separated flow at high angles of attack[14] (Figure 5-1). A similar blockage effect may have contributed to the poor agreement of the $C_m(\alpha)$-measurements using a rotary rig with those obtained in static tests with less bulky support structures[15] (Figure 5-2). Also contributing to the difference between the experimental results was, in all likelihood, interaction between the vortices from the aircraft model and the bulky rotary-rig support structure, a problem that will be fully discussed later The balance sector accounts for approximately half of the support blockage effect on the flow in the empty test section. The effect of the upwash generated by the rotating balance arm (at the location of a model to be tested) has, however, so far been found to be negligible.[16] It is important to eliminate the support blockage effect on the basic flow field in the empty test section before considering the more difficult problem of the interference effect of the rotary rig on the flow field generated by the model.[12]

Figure 5-3 shows the lateral static stability characteristics measured at $\alpha = 35°$ using two different support systems.[17] Both support systems can cause significant interference.[4] However, only the support with a downstream balance sector is likely to cause early breakdown of vortices generated by a slender forebody at high angles of attack, or of the leading-edge vortices from a slender wing for a certain range of sideslip angles. This is the conclusion to be drawn from the results of a reproduction by Johnson et al.[17] of Hummel's classical experiment[18] (Figure 5-4) using an arrow wing.

The vortices generated by a slender nose[19-21] can interact with a downstream support, especially at very high angles of attack when the vortices become asymmetric. In this case one vortex is left close to the fuselage[22] (Figure 5-5) Its interaction with downstream tail surfaces can be distorted severely by the support.

The rotary rig used for tests of a large model of an advanced aircraft[10] is shown in Figure 5-6. The sting angle α_s was zero for the aft-mounted model and had the values 45° and 70° for the top-mounted model, in order to cover the complete angle-of-attack range $-20° \leq \alpha \leq 90°$ for small sideslip angles, $|\beta| \leq 10°$. The model was tested with and without a nose boom.

One realizes that the support interference on an asymmetric vortex pair, of the type shown in Figure 5-5, will be large for the top-mounted model, as the lower vortex moves inboard close to the symmetry plane[23] (Figure 5-7). Figure 5-8 shows the support interference to be very different for $\alpha_t = 45°$ and $\alpha_s = 70°$, causing interference effects of opposite signs in the region of steady asymmetric vortex shedding. Although the region of steady asymmetric vortex shedding can be extended beyond the usual limit, $\alpha \approx 60°$, as has been discussed,[24,25] at $\alpha = 90°$ the vortex shedding should be of the unsteady type, giving a time average value $C_n = 0$. The non-zero values in Figure 5-8 are likely to have been caused by support interference of the type found by Dietz and Altstatt[26] (Figure 5-9). The loss of normal force is thought to be caused by the splitter-plate-like interaction of the strut with the unsteady Karman vortex shedding.[27] A similar interaction could have prevented the realization of the $C_n = 0$ time-average in Figure 5-8.

In the case of coning test data, the angle α_s affects the C_n characteristics at all angles where asymmetric vortex shedding occurs.[10] In the example in Figure 5-10, the results at $\alpha = 70°$ obtained with nose boom on are apparently of the critical type.[28] Thus, the asymmetric vortex geometry is affected strongly by "moving wall" effects,[28,29] causing the vortex asymmetry to flip between its two extreme positions in the presence of support interference, with associated reversals of the yawing moment (Figure 5-10). The presence of the support is likely to have contributed to the observed Ω hysteresis.

Recent tests of the HIRM 2 model[30] (Figure 5-11) show that when using a top-mounted dummy sting in addition to the aft sting support, the dummy sting added significantly to the support interference at $\alpha = 40°$ and at $\alpha = 60°$, whereas at $\alpha = 50°$ the effect was insignificant. Furthermore, at $\alpha = 40°$ the rolling moment is affected substantially, whereas at $\alpha = 60°$ only the yawing moment shows any appreciable influence.

Similar tests have been performed at AerMacchi[31] (Figure 5-12). An aircraft model tested at $\alpha = 45°$ should have asymmetric forebody vortex shedding (Figure 5-12a). The nose apex half angle is rather small, $\theta_A = 15°$, suggesting that asymmetric vortex shedding started at $\alpha = 30°$.[19-21] In this case there was no apparent effect of using forward or aft sting supports. One obvious interpretation of these test results is that the support interference was so large for the rear sting arrangement, caused more by the rotor arm than by the rear strut, that placing the strut support forward of the fin had no additional effect. Judging by Hummel's test results[18] (Figure 5-4), the balance arm could easily have caused vortex burst to occur forward of the fin, in which case the forward strut would only have the effect of moving the vortex burst further upstream. As the vortex-induced fin loads were already lost for the aft burst location, the forward strut would not have a very significant effect on the aerodynamic characteristics. In contrast, when the sideslip was increased from $\beta = 0°$ (Figure 5-12a) to $\beta = 10°$ (Figure 5-12b), the difference between the interference from the two support systems became more significant. Of particular interest is the change of interference effects occurring at $\Omega = 0.1$. The reason for this is considered next.

In Reference 12 it is described how the various support interference results obtained by Malcolm in his coning experiments[10] can be explained when considering how the support amplifies the coning-induced bias of the forebody vortices. Another way of inducing such a bias is by setting the model at an angle of sideslip. Even without the occurrence of vortex burst, the support will amplify the displacement of the vortex induced by sideslip and/or coning.

In their coning test of an ogive-cylinder Tobak et al.[32] found that the symmetric vortex geometry was tilted at an angle $\Delta\varphi_A$ along the full length of the body, where $\Delta\varphi_A$ is determined by the coning-induced lateral velocity at the apex.

$$\Delta\varphi_A = \tan^{-1}(V_A/U_\infty)$$
$$\frac{V_A}{U_\infty} = \frac{(x_{cg} - x_A)\sin\alpha}{b}\frac{\dot{\phi}b}{U_\infty} \tag{1}$$

Borrowing the coning sketch from Reference 33 (Figure 5-13), one can see that the vortex will be displaced in the same sense for $\dot{\phi} > 0$ as for $\beta > 0$. The tilt angle corresponding to $\Delta\varphi_A$ in Equation (1) is

$$\Delta\varphi(\beta) = \tan^{-1}(\sin\beta\cot\alpha) \tag{2}$$

For $x_{cg}/b = 1$ and $\alpha = 45°$, Equation (1) gives $\Delta\varphi_A = \Omega\sqrt{2}$, which for $\Omega = 0.1$ yields $\Delta\varphi_A = 8°$. For $\alpha = 45°$, Equation (2) gives $\Delta\varphi(\beta) = \tan^{-1}(\sin\beta) \cong \beta$. That is, $\Delta\varphi(\beta) = 10°$ for $\beta = 10°$. When considering the fact that the tilting of the vortex system will be amplified by moving wall effects, one can expect $\Delta\varphi_A$ and $\Delta\varphi(\beta)$ to be of roughly the same magnitude for $\Omega = 0.1$ and $\beta = 10°$, respectively. Following the analysis in Reference 12, one can interpret the data for $\beta = 10°$ in Figure 5-12b to show that when $\Delta\varphi_A$ is added to $\Delta\varphi(\beta)$ at $\beta = 10°$, the lower, inboard forebody vortex misses the rear strut.

Thus, using the rear sting makes it possible to measure the effect of the interaction between the (lower) forebody vortex and the tail at $\beta = 10°$ and $\Omega > 0.1$. On the other hand, the dorsal sting, because of its closeness to the vortex-generating forebody, bursts the vortex and makes such a measurement impossible. It is, in fact, suggested in Reference 16 that the dorsal sting made it impossible to measure the true nonlinear coning characteristics. It needs to be emphasized, however, that the important observation to be made is not that the true nonlinear coning characteristics could be measured at $\beta \geq 10°$, $\Omega > 0.1$ if the rear sting support was used, but rather, that at $\beta < 10°$ and $\Omega < 0.1$, both supports prevented the measurement of the true nonlinear coning characteristics. It is discussed in Reference 12 how coning tests performed for various sideslip angles gave similar results for the combined effects of β and Ω on the coning characteristics of an advanced aircraft.[10]

Support interference results, such as those shown in Figures 5-2, 5-3, 5-11 and 5-12, are easy to misinterpret. Without additional experiments and careful analysis, the results tell next to nothing about the total support interference of either one of the two support systems used. They only show the difference between the interference caused by the two supports. In the case of the very different support systems in Figure 5-3, it can be shown that both supports produce significant interference.[4] For the cases illustrated in Figures 5-11 and 5-12 the interference from the rear support and, in particular, the rotor arm is

large to start with. Consequently, it should not be surprising that the addition of or change to an upstream strut support has little effect. It is more unusual that a significant effect sometimes is observed for certain α-β-Ω combinations.

The test results in Figures 5-8 and 5-10 through 5-12 demonstrate that the support interference in rotary-rig tests can be of significant magnitude. As in the case of tests at low to moderate angles of attack,[4,5] one has to learn how to cope with this often unavoidable problem.[34,35]

5.1.3 Coping with Support Interference

As has been amply illustrated, the rotary apparatuses in use today are all likely to produce significant support interference over much of the testing envelope. In order to cope with this problem, the following steps should be taken: (1) identify the flow mechanism(s) through which the support interference acts, (2) design the support such that interference effects are minimized, and (3) if possible, derive the means through which the experimental results can be corrected for support interference. It appears that use of the orbital-platform concept,[36] which can provide close to interference-free test results, would be of great help in developing correction techniques.

In regard to (1), aside from the blockage effect discussed earlier (Figure 5-1), the main flow interactions causing high-alpha support interference are due to the obstructions presented by the support sting and rotor arm to the vortical flow field from a slender forebody and/or low-aspect-ratio lifting surfaces, as was illustrated by various examples in Section 5.1.2.

In regard to (2), some guidelines can be drawn from existing experimental results. As shown in Section 5.1.2, top-mounted supports should be avoided, particularly when steady, asymmetric vortical flow exists. The results[37] in Figure 5-14 demonstrate that an aft sting support will not by itself affect the vortical flow field generated by a slender forebody. As discussed in Section 5.1.2, the problem is presented by the downstream rotor arm and strut to which the sting is connected, as it can often present enough of a flow obstruction to cause vortex burst.

In regard to (3), correction for support interference will only be possible after systematic tests have been performed to provide the information needed for a meaningful analysis.

In Reference 5 it is shown how, by performing tests with a deflected sting, one could obtain static test data from which the support interference effect on the dynamic stability derivative $C_{m_q} + C_{m_{\dot{\alpha}}}$ could be determined. This low-alpha support interference is highly nonlinear, diminishing as the angle of attack is increased from $\alpha = 0°$. At $\alpha > 10°$, it is practically non-existent. As the angle of attack is increased further, however, at some point the support interference on forebody and/or swept wing vortices starts to have a significant influence on the measured aerodynamic characteristics. Although the support geometry is more complex in the case of coning experiments than for one-degree-of-freedom oscillations in pitch or yaw, the fluid mechanics of support interference is simplified considerably. The coning motion is stationary in nature, obviating the need to determine the time lag connected with the effect of the downstream support on the model. This is strictly true only if the wall interference, to be discussed later, is negligible. Thus, one only has to determine the static equivalent of the coning-induced displacement of the vortical wake or, at high angles of attack, of the free vortices generated by a slender forebody and/or by low-aspect-ratio lifting surfaces.

In the test programme outlined in Section 12.2 systematic tests are proposed using a model such as the widely tested Standard Dynamics Model (SDM), first by itself and then with lifting surfaces removed. These tests could supply the information needed for a determination of the support interference generated by vortical flow from a slender forebody at high angles of attack. This should not only provide the means for prediction of support interference for the SDM, but should also provide the basic framework for determining the support interference for other geometries.

5.2 WIND-TUNNEL WALL INTERFERENCE

5.2.1 Background

The steady nature of the flow in conventional rotary-balance tests breaks down in the presence of unsteady wall interference. The possibility of associated effects on the measurements has been explored,[38] but there is still a notable lack of supporting data on the subject. In a recent survey[39] it was concluded that, while the interference on two-dimensional oscillating airfoils[40–42] and specific examples of three-dimensional wings[43,44] have been treated theoretically, and boundary corrections have been derived for steadily rotating models in circular test sections,[40,45] the analysis of the general three-dimensional case of a model rotating at high-α in a noncircular test section was still beyond reach. Panel methods used to compute rotary aerodynamic data,[46] extended to include the walls, would not be applicable when large regions of flow separation are involved.

The situation with regard to experimental results is quite similar. Pitch damping data obtained on a variety of test configurations[47–50] have demonstrated large effects of the open-area-ratio and/or frequency. Tunnel resonance has been observed in large facilities[50] and theoretical predictions for two-dimensional airfoils have been verified,[51] demonstrating dramatic frequency effects.

It would appear that no experimental data have been published on unsteady wall interference in rotary-balance tests. However, some data are available on related high-α oscillatory experiments involving the Standard Dynamics Model (SDM)[52,53] and a secant-ogive-cylinder body (SOC).[54] The results suggest[38] that unsteady measurements, such as are

obtained in oscillatory coning,[55] could be significantly influenced and that even effects on the steady measurements cannot be ruled out. In certain circumstances, the effects on both steady and unsteady measurements may be less pronounced for an open-jet test section.[55]

The analysis of this problem is complicated by the fact that the unsteady wall and support interference effects are coupled. In this section the mechanisms of unsteady wall interference and the relevance of the high-α oscillatory test data are discussed.[38] Subsequently, the assessment of the unsteady aerodynamic interference contributions by means of the OPLEC[56] technique is considered.[38]

5.2.2 Sources of Unsteady Wall Interference

Consider an aircraft model at an angle of attack in steady rotation around the velocity vector. The rotation of the model and support, and of the associated separated wake, generate disturbances sweeping transversely along the boundaries of the working section. For a circular cross section, this reduces to a steady flow deflection which can be corrected for, but the introduction of any asymmetry will result in unsteady interference. Two interference mechanisms are identified here, namely transverse acoustic interference and vortex-wake/wall interference. A related effect is that of interference waves generated by wall vibrations due to the shaking of the rig or flow unsteadiness.

5.2.2.1 Transverse Acoustic Interference

In steady coning within noncircular walls, or asymmetrical coning* within circular or noncircular walls, the boundary disturbances are non-tangential and interact with the surfaces of the wall to generate acoustic waves which travel towards the model. For oscillatory coning within either circular or noncircular walls, acoustic disturbances are propagated from the model to the walls and reflected back to the model, as illustrated in Figure 5-15. This transverse acoustic interference is characterized by a time lag Δt_t associated with communication between the model and the wall. In oscillatory coning more than one time lag may be present, associated with disturbances due to oscillation of the model relative to the wind vector in the plane of the tilt angle and due to reflection from surfaces not rotating with the model.

Transverse acoustic resonance will occur in a rectangular section when

$$\omega = \omega_r = \pi\tilde{\beta}c\sqrt{\left[\frac{m}{w}\right]^2 + \left[\frac{n}{h}\right]^2} \tag{1}$$

Partial resonance may occur in slotted-wall test sections below Mach 0.62,[41] at a frequency given by

$$\frac{\omega_r h}{V_\infty} = \frac{(2n-1)\pi\tilde{\beta}}{M_\infty} \tag{2}$$

which reduces to Equation (1) when $n = 1$ and $m = 0$.

A phenomenon similar to the resonant condition for an oscillating airfoil could occur in coning. A disturbance emanating from a surface on the model reflects from the walls and impinges on another surface as shown in Figure 5-15, causing cyclical variations in the wing loading. This interference could be severe when the phase lag is 180°. For this condition a pressure node could form in the plane of the tilt angle in the case of asymmetrical coning.

Equation (2) shows that the lowest critical frequency for a vertical standing wave is about 55 Hz in a working section 3 m high. Moreover, since the resonance frequency is higher when the walls are slotted,[40] transverse tunnel resonance is not of much direct concern for steady measurements in rotary tests, where frequencies are typically lower than 7 rev/s. On the other hand, for unsteady measurements in closed as well as slotted-wall facilities, transverse wall interference may be expected to be appreciable even at frequencies below resonance, particularly at higher Mach numbers.[48]

5.2.2.2 Vortex-Wake/Wall Interference

When body and/or wing vortices are present, they are convected downstream as coaxial helical structures of common pitch, which sweep around in a circular path. The close proximity of wind-tunnel boundaries could distort these vortex formations cyclically as the distance from the walls varies.[38] (See Figure 5-16.) The nature of this interference is determined by configuration aerodynamics, angle of attack, and rotation rate.

Wake/wall interference could also be generated by the trailing tip vortices shed by the rotating support arm or rotor. This could be the prime source of interference when the rotor span b_s is large. As the vortex trails move towards or away from a point on the wall, boundary-layer separation will occur on the wall as illustrated in Figure 5-17. Thus, the separation line on the wall will oscillate longitudinally. Concomitantly, the wake blockage and upstream pressure gradient will fluctuate with the velocity-deficient region. Perhaps of greater significance, the interference of the rotor tip vortices with the model wake, either directly or via the separation regions on the walls, could contribute to the vortex-wake/wall interference. The flow-field disturbances associated with model-support and model-strut-wall interactions are coupled. Hence, the support interference, which is basically steady in lunar coning motion (see Section 5.1), will become unsteady if the vortex-wake/wall interaction is significant.

---

* "asymmetrical coning" refers to coning about an axis either offset or tilted with respect to the tunnel symmetry axis X_T (the latter case is known as oscillatory coning (see Chapter 4)).

Vortex interference could occur on slender bodies or configurations having pointed forebodies, in the regions of incipient vortex asymmetry and steady asymmetrical vortex shedding. The vortex closest to the body will pass nearer the walls, while the vortex which has lifted off will track a tighter helix around the spin axis (see Figure 5-16). Interaction with the vortex wake occurs primarily at the first spiral loop of the vortex core and fluctuates with a peak reached at its closest approach to one of the flat wall surfaces. The "reflected" disturbance travels back to the model as a perturbation of the core trajectory and/or burst location. The associated convective time lag is

$$\Delta t_V = \bar{s}\left(\frac{1}{\bar{U}_d} + \frac{1}{\bar{U}_u}\right) \tag{3}$$

where $\bar{U}_d \simeq U_\infty, \bar{U}_u \leq c$, and $\bar{s}$ is the effective distance travelled along the vortex trail. This time lag could become significant when the interaction takes place several model lengths downstream. As the angular deflection is proportional to the coning rate, $\bar{s}$, and thereby Δt_V, increases with increasing coning rate ω. A detailed analysis has shown[38] that Δt_V will also increase with increasing U_∞. Thus a resonance condition could occur in small as well as in large facilities. Vortex interference is, therefore, expected to become a problem more readily than transverse interference.

A similar mechanism could be present in circular open-jet test sections, where the vortex wake deflection takes place at the shear surface through the action of surface waves generated by the proximity of the rotating system. The effect would be steady for coning about the test-section symmetry axis but unsteady for any oscillatory motion (such as oscillatory coning; see Chapter 4).

5.2.3 Related Experimental Results

Within the linear domain there is a theoretical basis for comparing the instantaneous conditions in yaw oscillation with those in coning motion.[39] The geometrical relationship between the two characteristic motions is illustrated in Figure 5-18 Extending the comparison to the case of vortex interference, it is noted that the similarity exists only when the vorticity is low, thus ruling out aircraft configurations at realistic rotation rates. Nevertheless, for lack of any alternative unsteady data, it could be instructive to review aspects of the SDM and SOC data in the context of aerodynamic interference in rotary testing. Both experiments were conducted in the NAE 0.75 m × 0.40 m Dynamics Wind Tunnel (DWT), which has a most unusual asymmetrical test section; consequently, the unsteady interference effects are somewhat exaggerated.

5.2.3.1 Standard Dynamics Model

In the pitch oscillation experiment[53] conducted on the SDM, a generic fighter aircraft configuration[52] (see Figure 3-21), the degree of dynamic asymmetry at low α was investigated by varying the angle between the symmetry planes of the model and tunnel while maintaining a fixed mean α and constant magnitude of β. Figure 5-19 shows the cyclical ϕ'-dependence of the dynamic reactions. The absence of direct opposition between the dynamic and static reactions is indicative of the presence of more than one convective time lag and, therefore, of the combined effects of dynamic wall interference and support interference, both of significant magnitude.[38] At higher α, $\alpha > 15°$, the latter effect disappeared.[11] The overall interference was large; the variations in the derivatives with ϕ' were of the order of magnitude of that produced by a 5° sideslip increment.[11]

Although these are the yawing-moment derivatives due to pitch rather than yaw oscillation, the qualitative comparison with a rotary test can still be made as α is small and the rotation rate is low. The test conditions at $\alpha = 10°$ and $\beta = \pm 5°$ correspond to $\phi = \phi' = n(180°) \pm 26.7°$ in a coning test. This example is, therefore, analogous to the situation in rotary testing where both support and wall effects are significant, such as could occur when the region of vortex-wake/wall interaction coincides with the strut location.

5.2.3.2 Secant-Ogive-Cylinder Body

The effects of unsteady wall interference on the aerodynamics of the sharp-nosed 6-caliber SOC body were studied in high-α yaw-oscillation experiments[54] at different locations relative to the slotted wall $T = (Y_o - Y_T)/w$, where $Y_o \simeq w/2$ ($T \approx 0.5$ on the tunnel centerline). Figure 5-20 shows that proximity effects on the side-force and yawing-moment coefficients are large in the range of incipient asymmetrical vortex shedding, $\alpha_{av} = 25°$ to 30°, while Figure 5-21 demonstrates that the dynamic and static yaw derivatives are strongly influenced by wall interference at $\alpha \geq \alpha_{av}$. The undamping diminishes drastically as the wall is approached, showing that the true dynamic characteristics cannot be measured in the presence of unsteady wall interference. Support interference is not significant at these angles of attack for the side-mounted strut used.[11]

The yaw damping derivative $C^*_{n_r}$ is the direct counterpart of the coning derivative C_{n_ϕ} for a body of revolution within the mathematical model due to Tobak and Schiff.[57] Thus, if a coning test could be performed on the SOC in the same test section, the instantaneous effects on C_{n_ϕ} would be similar to those determined here, provided that the dependence on the angular rates is linear over the range covered in the two tests.

As noted before, the asymmetrical configuration of the DWT is not representative of facilities in which rotary tests are performed. On the other hand, in actual coning tests in a ventilated test section the aircraft forebody is naturally off-center at angle of attack, approaching the slotted walls in much the same way. The asymmetry effects will, therefore, still be present, albeit less pronounced, for a forebody-dominated configuration on the same type of support. On a rotating support arm, this effect would probably be washed out by the interference produced by interactions with the tip vortex wake from the support arm.

5.2.4 Effects on Aerodynamic Measurements

Steady Measurements. The time average of fluctuations in the static measurements, caused by disturbances at the walls, may be near zero if the rig is symmetrically mounted in the test section. On the other hand, as suggested by Figure 5-20, any large test section asymmetry, or a nonlinear dependence on rotation rate of the effects communicated upstream, could conceivably show up in the steady measurements as an apparent rate dependence, unless eliminated by low-pass filtering. In addition, any deflections of the vortex system will result in bias of the static signals.

Unsteady Measurements. Any unsteady wall disturbances, generating significant fluctuations at the model, will be reflected in the balance signals unless filtered out.

As an example, consider asymmetrical coning in various types of working sections. Measurements in closed or ventilated test sections could be affected by a pressure node forming on the wings as a result of transverse acoustic interference, even at off-resonance frequencies. In noncircular sections, in particular, acoustic disturbances as well as vortex wake deflection could be present due to surfaces not rotating with the model, resulting in more than one time lag effect. Finally, in a circular open-jet section there is a possibility of vortex-wake/surface-wave interaction, again with a large convective time lag.

From the results in Figure 5-21 it would appear that appreciable vortex-wake/wall interference could be present in rotary-balance measurements of unsteady flow phenomena. Under high-α separated flow conditions the fluctuating interference loads could excite one of the frequency components of the nonlinear loads.[38]

The effects of turbulence could also have a marked effect on the unsteady measurements. The use of sound-absorbing linings on the walls[58] would minimize transverse acoustic interference but would have a negligible effect on vortex-wake/wall interference.

5.2.5 Experimental Assessment of Unsteady Wall Interference

There could be some merit in applying quasi-steady techniques to the problem, following Ericsson's and Reding's[4,5] approach to analysis of support interference. Applied to unsteady wall interference in a rotary-balance test the incremental interference loads at a given time will depend on the coning angle at an earlier time. Such an approach requires that there is only one convective time lag effect present, i.e., that support interference is negligible, as in certain high-α aircraft testing situations,[11] and is, therefore, expected to be useful only in rather special circumstances.

Since the time lag effects of wall and support interference on the flow about the rotating model are coupled, any displacement of the wake through interaction with the support will inevitably change the wall effects and vice versa. Even if the data were recorded in a narrow angular window[55] to obtain the aerodynamic loads at discrete values of ϕ, between any stationary struts, the time lag effects of interactions with the struts would still be included. Thus, it is clear that the individual wall and support interference effects cannot be separated on a conventional rotary balance.

5.2.5.1 Interfacility Comparisons

One approach to the assessment of unsteady wall interference would be to perform tests on a particular model/rotary-rig combination installed in two wind tunnels of different size. Such a comparison of results from tests of the HIRM 2 model, performed in the 2.4 m × 1.8 m Pressurized Wind Tunnel at RAE Farnborough and in the 4 m × 2.7 m Wind Tunnel at RAE Bedford, revealed dramatic discrepancies between the yawing moments measured in the two facilities (see Chapter 7, Figure 7-67). While there were measurable Reynolds number effects, so that dissimilar turbulence levels in the two facilities could have had some influence, the trends in the coning rate data indicate that the main discrepancies were caused by differences in the unsteady wall interference. In the smaller test section the vortex-wake/wall interference appears to have smoothed out the nonlinearities in the yawing moment measured in the larger test section.

If the minimum test section dimension h is large enough in relation to the rotor span b_s, but not large enough for transverse acoustic interference to become a factor, the unsteady wall interference could possibly be reduced to the level of insignificance, although the steady support interference will remain present. The optimum ratio b_s/h could be deduced from comprehensive interfacility comparisons, provided that due consideration is given to all of the unsteady interference mechanisms present.

It should be emphasized that care will have to be exercised in interpreting the results of such comparisons, as the measurements reflect all effects present, including the strong coupling between support and wall interference. Moverover, although acceptable total interference levels could be determined, the individual effects of wall and support interference cannot be isolated by means of interfacility comparisons alone.

5.2.5.2 The Orbital-Platform Concept

In order to assess the individual contributions of various sources of aerodynamic interference, a more sophisticated approach is required. A technique offering the necessary flexibility was recently proposed.[56] The so-called OPLEC apparatus makes it possible, in principle, to simulate separately or in combination the effects of the walls and of the rotating arm and fixed struts. Thus, the individual interference contributions can be determined in isolation or in the presence of coupling with the other flow mechanisms present. A discussion of this concept appears in Section 6.2.

5.2.6 Summary

Two possible mechanisms of unsteady wall interference in rotary-balance tests have been identified, namely, transverse acoustic interference and vortex-wake/wall interference. The latter effect could occur either directly or through interaction with the vorticity shed behind the rotor arm, if present. Aerodynamic support interference becomes unsteady in the presence of wall interference, due to the coupling between the flow mechanisms present. It is this coupling with the support interference flow mechanism that is likely to cause the greatest difficulty.

Related oscillatory test results on two widely different configurations (an aircraft model and a pointed body of revolution), suggest that vortex-wake/wall interference can be large at high α when asymmetries are present. Although these data cannot be applied directly to diagnose the rotary-balance interference problem, there are similarities between the two types of experiments, as the vortex flow in any rotary test is asymmetrical during rotation at angle of attack, and the ratio b_s/w is often not much smaller than the ratio b/w in this study. As the RAE results in Figure 7-67 show, vortex-wake/wall interference can be serious even in large facilities.

Unsteady wall effects on the steady measurements may be small in many cases but can clearly be significant, as demonstrated by Figure 7-67, and should be considered in tests involving large asymmetries or highly nonlinear behavior, even at lower angles of attack. On the other hand, it is expected that the unsteady effects would be a factor in dynamic tests such as oscillatory coning, conducted in solid-walled or ventilated test sections of any cross-section. There is also a distinct possibility of similar influence on unsteady measurements in open-jet facilities.

Assessment of unsteady interference in conventional rotary-balance tests is complicated by the coupling between support and wall interference mechanisms. Nevertheless, a method based on the orbital platform concept would be capable of yielding the individual interference contributions.

5.3 VISCOUS FLOW EFFECTS

5.3.1 Background

The problem of applying subscale test results to full-scale flight is especially difficult in the case of rotary-rig tests. As these tests usually are performed at high angles of attack, the aerodynamics are dominated by separated flow effects. They are as a rule very sensitive to Reynolds number changes, a problem aggravated by the support interference effects discussed earlier, in Section 5.1. This is demonstrated by the static experimental results for an advanced aircraft model[10] (Figure 5-22). For the nose-boom-off configuration, which at $\alpha = 70°$ will not have any significant steady, time-average effects of asymmetric flow separation and associated vortices,[21] the Reynolds number effect dominates, the change from $\alpha_s = 45°$ to $\alpha_s = 70°$ having very little effect on the results. In contrast, the results for the nose-boom-on configuration, with its steady asymmetric forebody separation and vortices,[25] show a strong coupling between support interference and Reynolds number effects. Thus, for $\alpha_s = 70°$ a change from $Re = 2.4 \times 10^6$ to $Re = 4.0 \times 10^6$ has a dramatic impact on the C_n-characteristics in the range $45° < \alpha < 80°$.

The rotary (coning) test data obtained at $\alpha = 70°$ for the same model[10] (Figure 5-23) show a combined effect of Reynolds number and support interference that is similar to that for the static data (Figure 5-22). Thus, the Re-effect dominates for nose-boom-off, whereas the nose-boom-on configuration shows a strong coupling between Reynolds number and support interference effects (see also, Section 5.2.1). Changing the Reynolds number from $Re = 1.5 \times 10^6$ to $Re = 4.0 \times 10^6$ completely eliminates the discontinuity and the hysteresis from the $C_n(\Omega)$ characteristics.

A logical explanation for the observed presence or absence of the coupling between Reynolds number and support interference effects is the difference in forebody cross-flow characteristics at the different Reynolds numbers. At $Re = 1.5 \times 10^6$ (based upon mean aerodynamic chord) the forebody cross flow is probably subcritical (laminar), whereas at $Re = 4.0 \times 10^6$ it could be of the supercritical type. Thus, the vortex close to the body will be much farther inboard at $Re = 4 \times 10^6$ than at $Re = 1.5 \times 10^6$, resulting in dramatically different support interference effects.

5.3.2 Moving Wall Effects

In view of the always-present competition between the effects of Reynolds number, free-stream turbulence and surface roughness one should not be surprised by the large effect that body or nose-tip roll angle has on the high-alpha aerodynamics of an l/d = 3.5 pointed ogive[59] (Figure 5-24). The question of whether the roll angle effect was a manifestation of some interaction between wind-tunnel turbulence and the generation of forebody vortices,[60] or was caused by nose-microasymmetries,[21] was settled by tests in a low-turbulence-level wind tunnel.[61] The tests showed the roll angle effect to persist even when the turbulence level was reduced from 0.7% to 0.01%. That is, the effect of nose-microasymmetries dominated. In view of this, the experimental results for a cone-cylinder body[62] (Figure 5-25) give food for thought. The authors describe how only a slight push in one direction or the other would establish the coning motion in that direction regardless of the fact that the measured static yawing moment was biased in one direction, determined by the roll angle due to nose-microasymmetries.[21] Thus, whereas the static aerodynamic characteristics are dominated by microasymmetries, the dynamic (coning) characteristics are clearly dominated by body motion effects on the asymmetric forebody flow separation; i.e., by the so-called moving wall effects.

The classic Magnus lift of a rotating circular cylinder represents a well established example of moving wall effects on flow separation.[65] The wall-jet-like effect of the moving wall is illustrated in Figure 5-26. On the top side, favorable, downstream moving wall effects delay flow separation, whereas on the bottom half adverse, upstream moving wall effects

promote separation. This produces a positive Magnus lift. The so-called Magnus lift reversal occurs when a critical velocity ratio U_w/U_∞ is exceeded, the critical value being determined by the Reynolds number. In the subcritical case (Figure 5-26), when the rotation rate exceeds p_{crit} the upstream moving wall effect on the bottom side causes transition to occur upstream of the separation (changing it from the subcritical toward the supercritical type), creating a sudden suction peak that generates a negative Magnus lift.

Returning to Figure 5-25, and noticing that the moving wall effects are concentrated into the region near the flow stagnation point[64] where the boundary layer is thin, the moving wall effects for the translating circular cross section of the coning body are as shown in Figure 5-27. The lateral motion of the cross section causes the flow separation to be delayed on the advancing side and promoted on the retreating side. Thus, the motion produces a force that drives it until an equilibrium coning rate is reached, where the separation-induced driving moment is balanced by the drag-generated damping moment.[65]

The results[63] in Figure 5-25, and similar data for other configurations,[29] demonstrate that the moving wall effect can overpower the effect of nose microasymmetries, which in turn dominate over free-stream turbulence effects. This suggests that if the subscale tests are performed at a Reynolds number that is (high enough to be) on the same side of the critical value as the full-scale Re, it may be possible to extrapolate, e.g., through analytic means,[66,67] to obtain the full-scale dynamic characteristics. This will be discussed in Section 8.3.

Moving wall effects on boundary-layer transition can explain the anomalous subscale test results for the NACA-0012 airfoil obtained by Carta.[68] Like Rainey[69] earlier, Carta failed to measure the negative damping in plunge that Liiva[70] observed in his tests, performed at an order of magnitude higher Reynolds number. Figure 5-28 illustrates how plunging and pitching airfoils will have opposite moving wall effects for increasing effective angles of attack, $\dot{z}/U_\infty$ and α, respectively. Carta's hot film response data[68] (Figure 5-29)[†] show how the adverse, upstream moving wall effect $\dot{z}(t)$ promotes transition and causes the plunging airfoil to have a longer run of attached turbulent flow prior to stall. As a result, the flow stays attached past 7.5% chord, whereas flow separation occurs forward of 5% chord on the pitching airfoil, which has a shorter run of turbulent flow before stall due to the opposite, transition-delaying, moving wall effect. In addition to showing the opposite moving wall effects for pitching and plunging oscillations, Figure 5-29 also demonstrates that the moving wall effect completely dominates over the favorable flow-acceleration effect on the adverse pressure gradient upstream of flow separation (due to time history effects), as this effect is the same for pitching and plunging oscillations. This dominance of the moving wall effect is found in numerous flow situations, both in two-dimensional and three-dimensional flow.[29]

Similar plunging-induced moving wall effects on boundary-layer transition can generate negative damping, explaining[71] the transition-induced wing bending oscillations observed by Mabey et al.[72] It is pointed out in Reference 73 that advanced airfoils with flat-top pressure distribution would be especially susceptible to transition-induced negative damping, and that use of boundary-layer tripping devices can sometimes aggravate this effect. The effect of this coupling between body motion and boundary-layer transition is discussed at length in Reference 73 in regard to the problem of applying subscale test data to full-scale flight.

Free-to-roll tests of a generic aircraft configuration[74] produced a wing-rock motion (Figure 5-30) that was more violent than that observed earlier[75] for an 80° delta wing (Figure 5-31). In both cases asymmetric vortex shedding was observed. However, instead of the direct effect of the lifted-off leading-edge vortex on the slender delta wing,[76,77] the wing surfaces on the generic configuration are not directly involved in the asymmetry-switching process but only respond to the flow-field changes generated by the forebody vortices.[78]

In order to understand the asymmetry-switching process it is instructive to study the experimental results obtained for a coning flat-faced circular cylinder[62] (Figure 5-32). Initially, flow asymmetry or minute surface irregularities set the laminar flow separation asymmetry. The resulting coning motion reinforces the effects of the initial asymmetry, as the laminar flow separation is delayed on the advancing side by a favorable, downstream moving-wall effect, resulting in positive coning velocity and acceleration ($\dot{\psi}$ and $\ddot{\psi} > 0$). However, when $\dot{\psi}$ has increased beyond the critical value, the adverse, upstream moving-wall effect on the retreating side will cause boundary-layer transition to occur forward of the flow separation, reversing the separation asymmetry (as in the case of the Magnus lift reversal in Figure 5-26) and the coning motion starts to decelerate ($\dot{\psi} > 0$, but $\ddot{\psi} < 0$). Eventually, this results in accelerated coning in the opposite direction ($\dot{\psi}$ and $\ddot{\psi} < 0$) The rotation reversal moves transition back into the wake on the new advancing side, and asymmetric laminar separation is re-established. Finally, transition occurs on the retreating side, causing critical/subcritical flow separation, reversing the asymmetry and decelerating the coning motion ($\dot{\psi} < 0$, $\ddot{\psi} > 0$). The process continually repeats itself, resulting in a self-reversing coning motion with characteristics similar to those shown in Figure 5-25.

A similar moving wall effect, generated by body spin, is responsible for the wing rock of the generic fighter configuration[74] (Figure 5-30). The cross flow over the pointed circular cylinder body was in the critical Re region,[78] providing the following scenario (Figure 5-33). At $t = t_1$ the wing-body (removing the tail surfaces had little impact on the wing rock motion) is rolling in response to some disturbance. The upstream moving-wall effect generated on the starboard side causes transition to occur in the forebody cross flow ahead of separation, changing it from the subcritical towards the supercritical type in the manner discussed earlier in connection with Figure 5-26. On the opposite side, the favorable downstream moving-wall effect delays transition, reinforcing the subcritical nature of the separation. This description is somewhat over-simplified, as it neglects the presence of the laminar separation bubble (see Section 8.2 for a more detailed description of the moving wall effect at the critical flow condition). However, it accounts for the essential feature of the motion-induced effect on the flow separation asymmetry.

† Note that $|\dot{z}|/U_\infty = |\alpha|$.

Neglecting time lag effects, the vortex asymmetry sketched at $t = t_1$ in Figure 5-33 would result. Due to time lag effects, similar to those discussed in References 76 and 77 for slender wing rock, this vortex geometry (only the lower vortex is shown as only it will induce significant loads) is not realized until $t = t_2 = t_1 + \Delta t$. At $t \rightarrow t_3$, when the roll rate approaches its maximum in the opposite direction, another forebody switch in separation asymmetry occurs. Because of the time lag effect,[76,77] the vortex geometry at the (now nearly horizontal) wing has not changed, but is the same as at $t = t_2 = t_1 + \Delta t$, in agreement with the observed flow-visualization results.[74] It is during this time lag Δt that the vortex-induced rolling moment drives the rolling motion, generating the observed wing rock.[78]

The much-faster amplitude build-up for the wing-body (Figure 5-30), as compared with that for the slender delta wing, (Figure 5-31) can be explained as follows. In the case of the slender delta wing the driving rolling moment remains unchanged, as it is determined by the loss of the lift due to the lifting off of the leading-edge vortex.[77] However, in the case of the wing-body, the separation extent, and thereby the vortex-induced lift and associated rolling moment, will increase from half-cycle to half-cycle as the roll rate builds up.[78] That is, as the wing rock amplitude grows the driving rolling moment grows for the wing-body, whereas it remains constant for the slender delta wing.

If the cross-flow conditions were laminar everywhere on the forebody, it may be deduced from Figure 5-26 that self-induced wing rock would no longer be possible. That is, a certain roll rate is required, which is higher the lower the cross-flow Reynolds number becomes, before a motion-induced switch of separation asymmetry can occur. If the Reynolds number is increased, on the other hand, the critical cross-flow condition will occur somewhere on the slender nose, and self-induced wing rock will still materialize. This presents a difficult problem for dynamic simulation in subscale tests. That this type of wing rock can present a real problem was demonstrated recently for the X-29 aircraft.[79] It was shown how an installed wing rock damper could eliminate the wing rock observed at $20° < \alpha < 30°$, caused by the negative damping in plunge,[80] but could not suppress the high-alpha wing rock just discussed, because the ailerons used to control the wing rock were ineffective at these high angles of attack, $\alpha > 40°$ (Figure 5-34).

5.3.4 Summary

Support and wall interference will often have a significant influence on rotary-rig test results, as was demonstrated by the results in Figures 5-12 and 7-67, respectively. The correction for such interference effects is complicated by their mutual coupling and coupling with Reynolds number and moving wall effects. Until systematic tests can be performed which could make such correction possible, the prudent action is to minimize the interference to the greatest extent possible and use flow visualization or other complementary test techniques to obtain a thorough understanding of the viscous flow phenomena involved. This would, in many cases, make it possible to extrapolate from subscale test data to predict full-scale vehicle dynamics, as will be discussed in Section 8.3.

5 4 REFERENCES

1. Perkins, E. W.: Experimental Investigations of the Effects of Support Interference on the Drag of Bodies of Revolution at a Mach Number of 1.5. NACA TN 2292, Feb 1971.

2. Whitfield, J. P.: Support Interference at Supersonic Speeds. AGARD Report 300, March 1959.

3. Kavanau, L. L.: Base Pressure Studies in Rarefied Supersonic Flow. Journal of Aerospace Sciences, Vol. 23, March 1956, pp. 193-207.

4. Ericsson, L. E.; and Reding, J. P.: Review of Support Interference in Dynamic Tests AIAA Journal, Vol. 21, No. 12, Dec. 1983, pp. 1652-1666.

5. Reding, J. P.; and Ericsson, L. E.: Dynamic Support Interference. Journal of Spacecraft and Rockets, Vol. 9, No. 7, July 1972, pp. 547-553.3.

6. Ericsson, L. E.: Effect of Sting Plunging on Measured Nonlinear Pitch Damping. AIAA Paper 78-832, April 1978.

7. Beyers, M. E.: Direct Derivative Measurements in the Presence of Sting Plunging. J. Aircraft, Vol. 23, No. 3, March 1986, pp. 179-185.

8. Orlik-Rückemann, K. J.: Techniques for Dynamic Stability Testing in Wind Tunnels. Paper 1, AGARD CP-235, Nov 1978.

9. Ericsson, L. E.. A Summary of AGARD FDP Meeting on Dynamic Stability Parameters Paper 2, AGARD CP-260, May 1979.

10. Malcolm, G. N.: Rotary-Balance Experiments on a Modern Fighter Aircraft Configuration at High Reynolds Numbers. AIAA Paper 85-1829, Aug. 1985.

11. Beyers, M. E.: Some Recent NAE Experiences of Support Interference in Dynamic Tests. NRC NAE LTR-UA-83, Ottawa, Nov. 1983

12 Ericsson, L. E.; and Reding, J. P. Dynamic Support Interference in High Alpha-Testing. Journal of Aircraft, Vol. 23, No. 12, Dec. 1986, pp. 889-896

13. Entwicklung und Erprobung einer Roll- und Trudelderivativ-Waage für die 3m-Niedergeschwindigkeitswindkanale ler Bundesrepublik Deutschland. Report: BMFT-FB-W81-022/1981.

14. Verbrugge, R. A.: Balance Rotative de l'I.M.F.L. et Techniques Expérimentales Associées. Sept. 1979.

15. Chambers, J. R.: Private Communication. Sept. 28, 1988.

16. Visintini, L.: Short Summary of Information about Interference Effects Due to the Rotary Balance Rig. Memo. PRA/0 05/86, AerMacchi, May 30, 1986.

17. Johnson, J. L., Jr.; Grafton, S. B.; and Yip, L. P.: Exploratory Investigation of Vortex Bursting on the High-Angle-of-Attack Lateral Directional Stability Characteristics of Highly Swept Wings. AIAA Paper 80-0463, March 1980.

18. Hummel, D.: Untersuchungen über das Aufplatzen der Wirbel an schlanken Delta Flügeln. Z. f. Flugwissenschaften, Vol. 3, Heft. 5, 1965, pp. 158-168.

19. Ericsson, L. E.; and Reding, J. P.: Review of Vortex-Induced Asymmetric Loads-Part I. Z. Flugwiss. Weltraumforsch., 5 (1981), Heft 3, pp. 162-174.

20. Ericsson, L. E.; and Reding, J. P.: Review of Vortex-Induced Asymmetric Loads-Part II. Z Flugwiss. Weltraumforsch., 5 (1981), Heft 6, pp. 349-366.

21. Ericsson, L. E.; and Reding, J. P.: Asymmetric Vortex Shedding from Bodies of Revolution. *Tactical Missile Aerodynamics*, Vol. 104, Progress Astro. and Aero. Series, M. J. Hemsch and J. N. Nielsen, editors, 1986, pp. 243-296.

22. Skow, A. M.; Moore, W. A.; and Lorincz, D. J.: Forebody Vortex Blowing—A N[illegible]l Control Concept to Enhance Departure/Spin Recovery Characteristics of Fighter and Trainer Aircraft. Paper 24, AGARD CP-262, Sept. 1979.

23. Wardlaw, A. B. J.; and Yanta, W. J.: Multistable Vortex Patterns on Slender, Circular Bodies at High Incidence. AIAA Journal, Vol. 20, No. 4, April 1982, pp. 509-515.

24. Ericsson, L. E.: Reflections Regarding Recent Rotary Rig Results. Journal of Aircraft, Vol. 24, No. 1, Jan. 1987, pp. 25-30.

25. Ericsson, L. E.; and Reding, J. P.: Alleviation of Vortex-Induced Asymmetric Loads. Journal of Spacecraft and Rockets, Vol. 17, No. 6, Nov.-Dec. 1980, pp. 548-553.

26. Dietz, W. E.; and Altstatt, M. C.: Experimental Investigation of Support Interference on an Ogive-Cylinder at High Incidence. Journal of Spacecraft and Rockets, Vol. 16, Jan.-Feb. 1979, pp. 67-68. See also AIAA Paper 78-1675, Jan. 1978.

27. Nelson, R. C.; and Mouch, T. N.: Cylinder-Splitter-[illegible]late Data Illustrating High-α Support Interference. J. Spacecraft and Rockets, Vol. 16, March-April 1979, pp. 126-128.

28. Ericsson, L. E.; and Reding, J. P.: Dynamics of Forebody Flow Separation and Associated Vortices. J. Aircraft, Vol. 22, No. 4, April 1985, pp. 329-335.

29. Ericsson, L. E.: Moving Wall Effects in Unsteady Flow. J. Aircraft, Vol. 25, No. 11, Nov. 1988, pp. 977-990.

30. O'Leary, C. O.: Sting Interference Effects on HIRM 2 Results. Private communication of unpublished experimental results, Sept. 1987.

31. Visintini, L.: Private communication of unpublished experimental results, April 1988.

32. Tobak, M.; Schiff, L. B.; and Peterson, V. L.: Aerodynamics of Bodies of Revolution in Coning Motion. AIAA Journal, Vol. 7, No. 1, Jan. 1969, pp. 95-99.

33. Jermey, C.; and Schiff, L. B.: Wind-Tunnel Investigation of the Aerodynamic Characteristics of the Standard Dynamics Model in Coning Motion at Mach 0.6. AIAA Paper No. 85-1828, Aug. 1985.

34. Ericsson, L. E.; and Reding, J. P.: Practical Solutions to Simulation Difficulties in Subscale Wind-Tunnel Tests. AGARD-CP-348, Paper No. 16, Feb. 1984.

35. Ericsson, L. E.; and Reding, J. P.: How to Cope with the Problem of Scaling and Support Interference in Dynamic Subscale Tests. AIAA Paper 84-0382, Jan. 1984.

36. Beyers, M. E.; and Huang, X. Z.: The Orbital Platform Concept for Nonplanar Dynamic Testing. Aeronautical Note NAE-AN-52, NRC No. 29133, NAE, Ottawa, Canada, May 1988.

37. Keener, E. R.; Chapman, G. T.; and Kruse, R. L.: Effects of Mach Number and Afterbody Length on Onset of Asymmetric Forces on Bodies at Zero Sideslip and High Angles of Attack. AIAA Paper 76-66, Jan. 1976.

38. Beyers, M. E.: Unsteady Wall Interference in Rotary Tests. AIAA Paper 89-0046, Jan. 1989.

39. Beyers, M. E.: Wind-Tunnel Wall Interference in Rotary Balance Testing. NRC NAE-LTR-UA-90, Ottawa, Nov. 1987.

40. Acum, W. E. A.: Interference Effects in Unsteady Experiments. AGARDograph 109, Ch. 4, October 1966, pp. 219–278.

41. Mokry, M.: Prediction of Resonance Frequencies for Ventilated Wall Wind Tunnels. AGARD-CP-348, Paper No. 15, Feb. 1984.

42. Sawada, H.: A New Method of Estimating Wind Tunnel Wall Interference in the Unsteady Two-Dimensional Flow. NRC NAE-AN-9, Ottawa, Jan. 1983.

43. Acum, W. E. A.: Wall Corrections for Wings Oscillating in Wind Tunnels of Closed Rectangular Section, Parts I and II, ARC R&M 3312, Jan. 1958.

44. Drake, D. G.: Wind-Tunnel Interference for Oscillating Wings at Transonic Speed. ARC 21, 489-0.1515, Dec. 1959.

45. Mandl, P.; and Pounder, J. R.: Wind Tunnel Interference on Rolling Moment of a Rotating Wing. NRC AR-10, Ottawa, 1951.

46. Katz, J.: Numerical Simulation of Aircraft Rotary Aerodynamics. AIAA Paper 88-0399, January 1988.

47. Wight, K. C.: A Review of Slotted-Wall Wind Tunnel Interference Effects on Oscillating Models in Subsonic and Transonic Flows. J. Royal Aero. Soc., Vol. 68, Oct. 1964, pp. 670-674.

48. Bratt, J. B.; and Wight, K. C.: Measurements of Pitching Oscillation Derivatives at Subsonic and Transonic Speeds for an M-Wing (Interim Report), ARC 21 661-0.1534-LA 236, Feb. 1960.

49. Miles, C. J. W.; and Bridgman, K. B.: Measurements of the Direct Pitching Oscillation Derivatives for Three Cropped Delta and Three Arrowhead Planforms at Subsonic and Transonic Speeds. NPL Aero. Report 1033, August 1962.

50. Widmayer, E.; Clevenson, S. A.; and Leadbetter, S. A.: Some Measurements of Aerodynamic Forces and Moments at Subsonic Speeds on a Rectangular Wing of Aspect Ratio 2 Oscillating About the Midchord. NACA TN 4240, May 1958.

51. Runyan, H. L.; Woolston, D. S.; and Rainey, A. G.: Theoretical and Experimental Investigation of the Effect of Tunnel Walls on the Forces on an Oscillating Airfoil in Two-Dimensional Subsonic Compressible Flow. NACA Rep. 1262, Jan. 1956.

52. Beyers, M. E.: Subsonic Roll Oscillation Experiments on the Standard Dynamics Model. AIAA Paper 83-2134, Aug. 1983.

53. Beyers, M. E.; and Szyszkowicz, M.: Stability Derivatives of the Standard Dynamics Model at Mach 0.6, to appear as NRC publication.

54. Beyers, M. E.; Huang, X. Z.; Kapoor, K. B.; and Peter, E.: Dynamic Stability Derivatives of a Secant-Ogive-Cylinder Configuration at High Angles of Attack. NRC NAE-LTR-UA-89, Oct. 1987.

55. Tristrant, D.; and Renier, O.: Récents développements des techniques de simulation dynamique appliquées à l'identification des paramètres de stabilité. AGARD CP-386, No. 22, Nov. 1985.

56. Beyers, M. E.; and Huang, X. Z.: The Orbital-Platform Concept for Nonplanar Dynamic Testing, NRC NAE-AN-52, Ottawa, May 1988.

57. Tobak, M.; and Schiff, L.B.: On the Formulation of the Aerodynamic Characteristics in Aircraft Dynamics. NASA TR R-456, Jan. 1976.

58. Mabey, D. G.: The Reduction of Dynamic Interference by Sound-Absorbing Walls in the RAE 3-ft Wind Tunnel ARC R&M No. 3837, Aug. 1977.

59. Keener, E. R.; Chapman, G. T., Cohen, L., and Taleghani, J.: Side Forces on a Tangent-Ogive Forebody With a Fineness Ratio of 3.5 at High Angles of Attack and Mach Numbers from 0.1 to 0.7. NASA TMX-3437, Feb. 1977.

60. Lamont, P. J., and Hunt, B. L.. Pressures and Force Distributions on a Sharp-Nosed Circular Cylinder at Large Angles of Inclination to a Uniform Stream. J. Fluid Mech., Vol. 76, Part 3, 1976, pp. 519-559.

61. Hunt, B. L.; and Dexter, P. C.: Pressures on a Slender Body at High Angle of Attack in a Very Low Turbulence Level Air Stream. Paper 17, AGARD CP-247, Jan. 1979.

62. Yoshinaga, T.; Tate, A.; and Inoue, K.. Coning Motion of Slender Bodies at High Angles of Attack in Low-Speed Flow. AIAA Paper 81-1899, Aug 1981.

63. Swanson, W. M.: The Magnus Effect: A Summary of Investigations to Date. J. Basic Eng., Vol. 83, Sept. 1961, pp. 461–470.

64. Ericsson, L. E.: Circular Cylinder Response to Karman Vortex Shedding. J. Aircraft, Vol. 25, No. 9, Sept. 1988, pp. 769–775.

65. Ericsson, L. E.: Prediction of Slender Body Coning Characteristics. AIAA Paper 89-2223, Aug. 1989.

66. Ericsson, L. E.; and Reding, J. P.: Dynamic Simulation Through Analytic Extrapolation. J. Spacecraft and Rockets, Vol. 19, No. 2, March-April 1982, pp. 160–166.

67. Ericsson, L. E.; and Reding, J. P.: Analytic Extrapolation to Full Scale Aircraft Dynamics. J. Aircraft, Vol. 21, No. 3, March 1984, pp. 222–224.

68. Carta, F. O.: A Comparison of the Pitching and Plunging Response of an Oscillating Airfoil. NASA CR-3172, Oct. 1979.

69. Rainey, A. G.: Measurements of Aerodynamic Forces for Various Mean Angles of Attack, on an Airfoil, Oscillating in Bending with Emphasis on Damping in Stall. NACA Report 1305, 1957.

70. Liiva, J.: Unsteady Aerodynamic and Stall Effects on Helicopter Rotor Blade Airfoil Sections. J. Aircraft, Vol. 6, No. 1, Jan.-Feb. 1969, pp. 46–51.

71. Ericsson, L. E.: Transition Effects on Airfoil Dynamics and the Implication for Subscale Tests. J. Aircraft, Vol. 26, Dec. 1989, pp. 1051–1058.

72. Mabey, D. G.; Ashill, P. R.; and Welsh, B. L.: Aeroelastic Oscillation Caused by Transitional Boundary Layers and Their Attenuation. J. Aircraft, Vol. 24, No. 7, July 1987, pp. 463–469.

73. Ericsson, L. E.: Review of Transition Effects on the Problem of Dynamic Simulation. AIAA Paper 88-2004, May 1988.

74. Brandon, J. M.; and Nguyen, L. T.: Experimental Study of Effects of Forebody Geometry on High Angle of Attack Stability. J. Aircraft, Vol. 25, July 1988, pp. 591–597.

75. Nguyen, L. T., Yip, L.; and Chambers, J. R.: Self-Induced Wing Rock of Slender Delta Wings. AIAA Paper 81-1883, Aug. 1981.

76. Ericsson, L. E.: The Fluid Mechanics of Slender Wing Rock. J. Aircraft, Vol. 21, No. 5, May 1984, pp. 322–328.

77. Ericsson, L. E.: Analytic Prediction of the Maximum Amplitude of Slender Wing Rock. J. Aircraft, Vol. 26, No. 1, Jan. 1989, pp. 35–39.

78. Ericsson, L. E.: Wing Rock Generated by Forebody Vortices. J. Aircraft, Vol. 26 No. 2, Feb. 1989, pp. 110–116.

79. Fratello, D. J.; Croom, M. A.; and Nguyen, L. T.: Use of the Updated NASA Langley Radio-Controlled Drop-Model Technique for High-Alpha Studies of the X-29A Configuration. AIAA Paper 87-2559-CP, Aug. 1987.

80. Ericsson, L. E.: The Various Sources of Wing Rock. AIAA Paper 88-4370, Aug. 1988.

5.5 NOMENCLATURE

b	wing span
b_s	span of support arm, or rotor
c	speed of sound
$\bar{c}$	mean aerodynamic chord
C_{ij}	dynamic derivative with respect to reduced-rate parameter, $\frac{\partial C_i}{\partial\left(\frac{jl}{2V_\infty}\right)}$, $i = \ell, m, n$; $j = q, \alpha, \sigma$ ($\ell = \bar{c}$ or d) $j = p, \dot{\beta}, \dot{\phi}, \dot{\psi}$ ($\ell = b$ or d)
C_{ik}	static derivative with respect to k, $\frac{\partial C_i}{\partial k}$, $i = \ell, m, n$; $k = \alpha, \beta, \sigma$
C_ℓ	rolling-moment coefficient, $L/(\bar{q}_\infty S\ell)$, $\ell = b$ or d
C_L	lift coefficient, $L/(\bar{q}_\infty S)$
C_m	pitching-moment coefficient, $M/(\bar{q}_\infty S\ell)$, $\ell = \bar{c}$ or d
C_n	yawing-moment coefficient, $N/(\bar{q}_\infty S\ell)$, $\ell = b$ or d
C_N	normal-force coefficient, $N/(\bar{q}_\infty S)$
C_p	pressure coefficient, $(p - p_\infty)/\bar{q}_\infty$
C_Y	side-force coefficient, $Y/(\bar{q}_\infty S)$

d	maximum body diameter
h	height of test section
ℓ	generalized reference length
m, n	integers defining the order of the acoustic mode
M_c	corrected Mach number
M_∞	free-stream Mach number
p, q, r	body-axes angular velocities
$\bar{q}$	dynamic pressure
Re, Re_d	Reynolds number, $\mathrm{Re} = U_\infty \bar{c}/\nu_\infty$; $\mathrm{Re}_d = U_\infty d/\nu_\infty$
$\bar{s}$	distance along vortex trail
S	reference area, effective wing area or $\pi d^2/4$ for body alone
t	time
U_∞, V_∞	free-stream velocity
$\bar{U}_d, \bar{U}_u$	downstream and upstream mean convection velocities
V	lateral velocity
w	width of test section
x	axial distance
z	vertical deflection, positive downwards
X_T, Y_T, Z_T	tunnel-fixed reference system
α, β	angles of attack and sideslip
α_{av}	angle for onset of asymmetrical vortex shedding
$\check{\beta}$	$(1 - M_\infty^2)^{1/2}$
Δ	increment or amplitude
θ	pitch angle
λ	rotation about body z axis
ν	kinematic viscosity
σ	total angle of attack
Υ	nondimensional distance from slotted wall
φ	body azimuth
ϕ	coning angle
ϕ', φ'	bank angle
ω	coning rate or circular frequency, where appropriate
$\bar{\omega}$	reduced rate parameter, $\omega\ell/(2U_\infty)$
ω_r	resonance frequency
Ω	dimensionless coning rate, $\dot{\phi}b/(2U_\infty)$
Subscripts:	
A	apex
cg	center of gravity or rotation center
s	sting
V	vortex
∞	free-stream conditions
Superscripts:	
$(\cdot)$	differentiation with respect to time
$(')$	aerodynamic axes system
$(*)$	composite fixed-axis derivative
$(\sim)$	tilda, indicating time average value for oscillatory condition

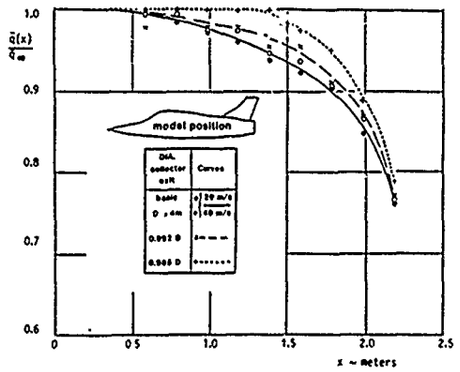

Figure 5-1. Elimination of support-induced dynamic pressure deficit by control of the exit diameter at $x = 0$.

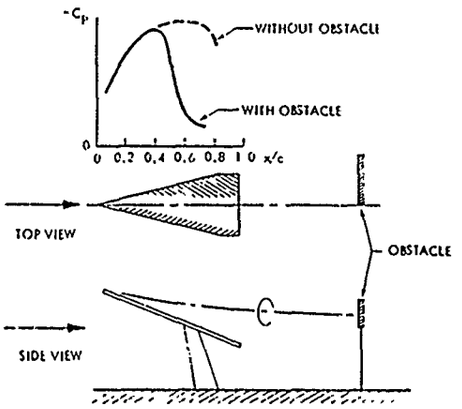

Figure 5-4. Vortex burst on a 75° delta wing caused by downstream obstacle.

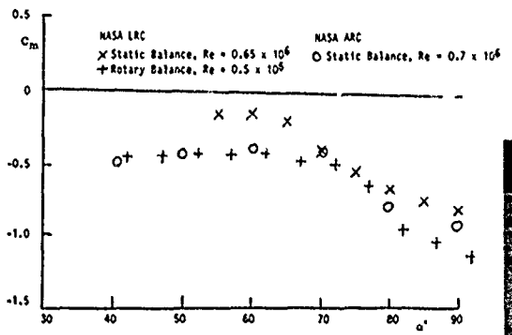

Figure 5-2. Effect of model support on the pitching moment of an advanced aircraft.

Figure 5-5. Asymmetric vortex shedding from the slender nose of an advanced aircraft model at $\alpha = 40°$ and $\beta = 0$.

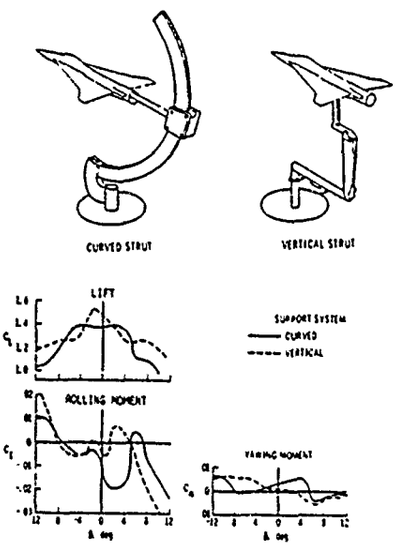

Figure 5-3. Effect of model support on lateral characteristics of an arrow wing at $\alpha = 35°$.

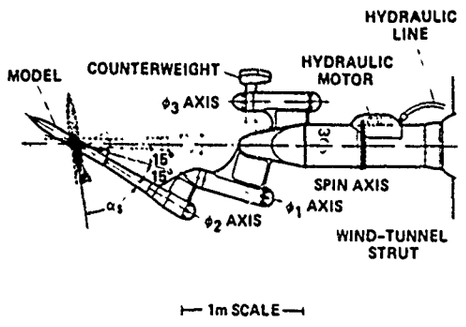

Figure 5-6. Rotary rig for coning tests of large aircraft models.

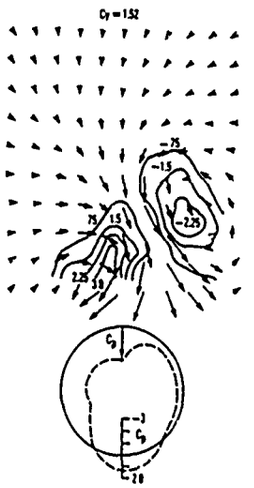

Figure 5-7. Flow-field survey above an ogive-cylinder body at $\alpha = 45°$.

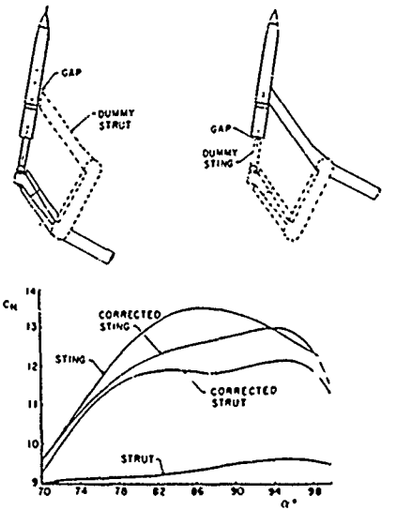

Figure 5-9. Effect of leeside support on $C_N(\alpha)$ of an ogive-cylinder model at $M_\infty = 0.6$ and $\mathrm{Re} = 3 \times 10^6$.

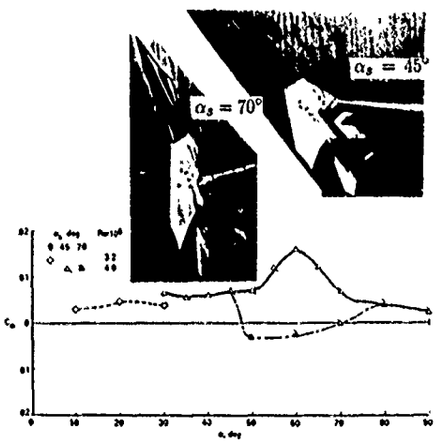

Figure 5-8. Effect of support inclination α_s and Reynolds number on $C_n(\alpha)$ at $\beta = 0$ of an advanced aircraft model with nose boom on.

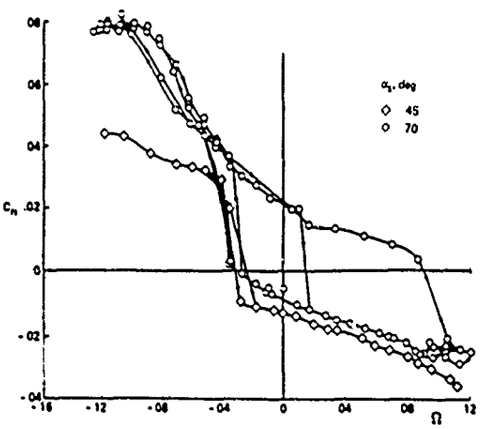

Figure 5-10. Effect of support inclination α_s on $C_n(\Omega)$ of an advanced aircraft model with nose boom on at $\beta = 0$ and $\mathrm{Re} = 1.5 \times 10^6$.

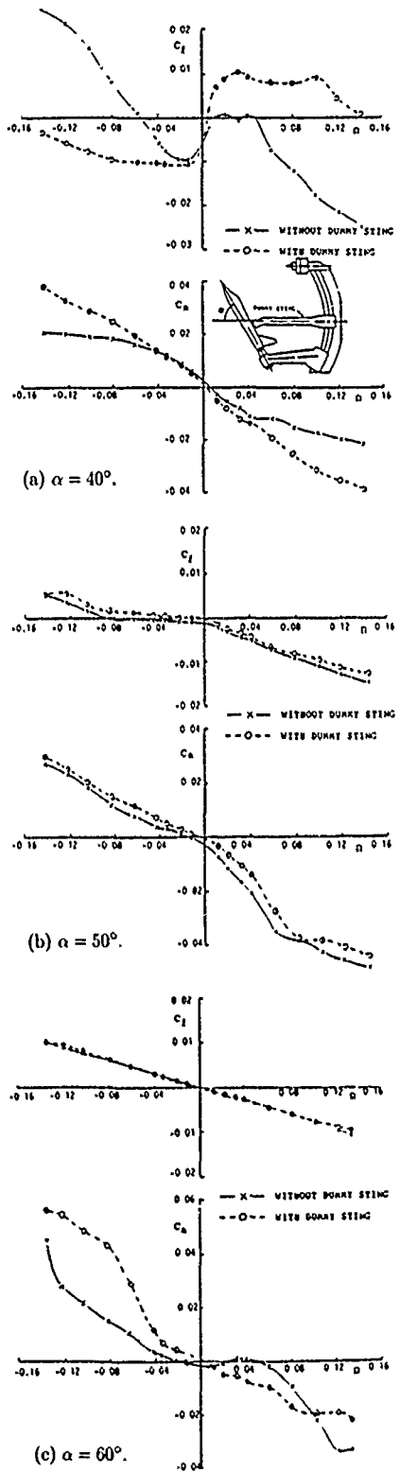

Figure 5-11. Effect of dummy sting on coning characteristics $C_\ell(\Omega)$ and $C_n(\Omega)$ of the HIRM 2 model at $M_\infty = 0.2$ and $\mathrm{Re} = 0.9 \times 10^6$.

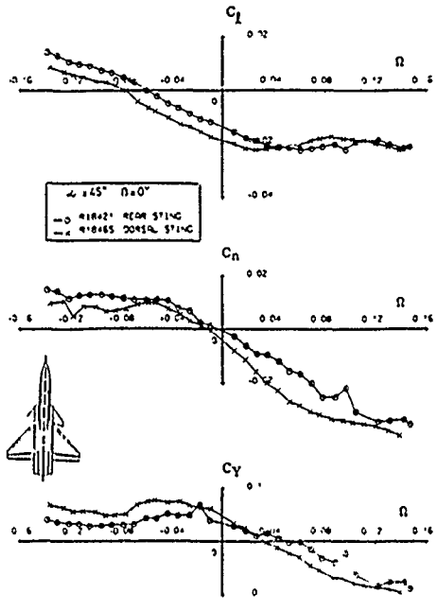

(a) Delta canard research configuration at $\beta = 0$.

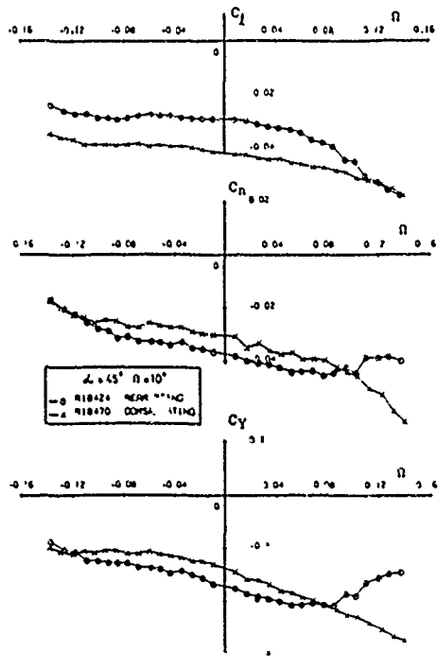

(b) Delta canard research configuration at $\beta = 10°$

Figure 5-12. Effect of model support change on the coning characteristics $C_Y(\Omega)$, $C_\ell(\Omega)$ and $C_n(\Omega)$

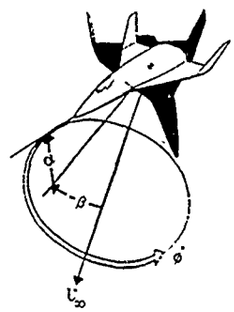

Figure 5-13. Definition of variables for coning motion.

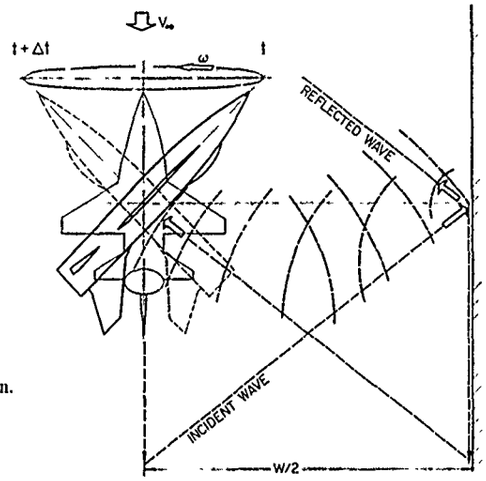

Figure 5-15. Transverse acoustic interference on coning model.

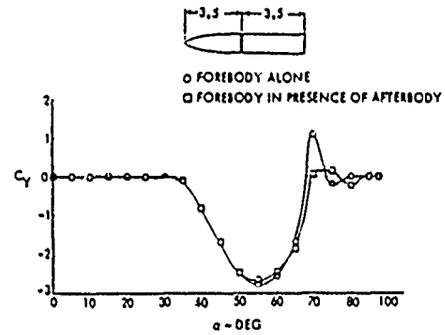

Figure 5-14. Effect of cylindrical aftbody on the measured side force of a pointed ogive.

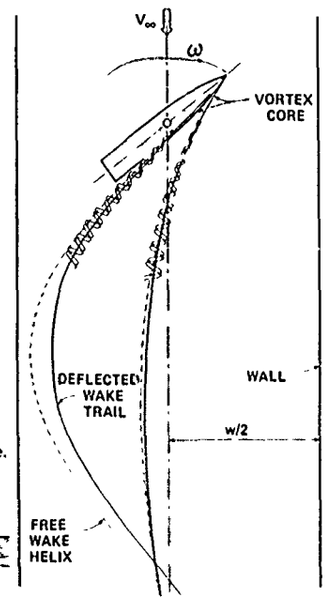

Figure 5-16. Vortex-wake/wall interference.

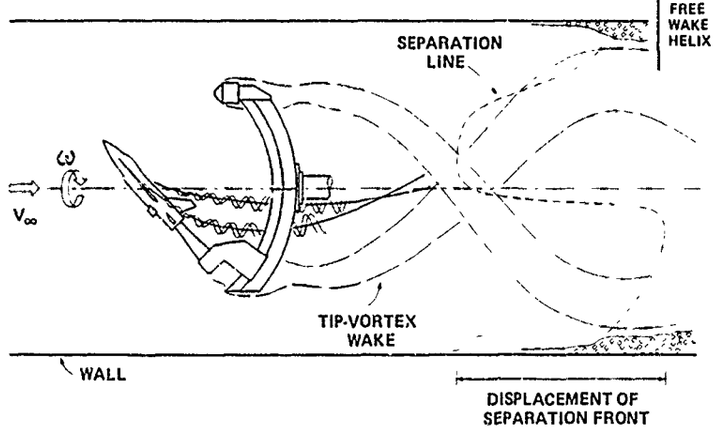

Figure 5-17. Aerodynamic interference with unsteady separation on walls.

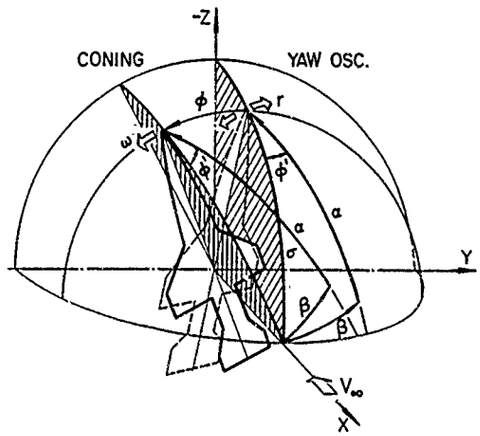

Figure 5-18. Relationship between characteristic motions.

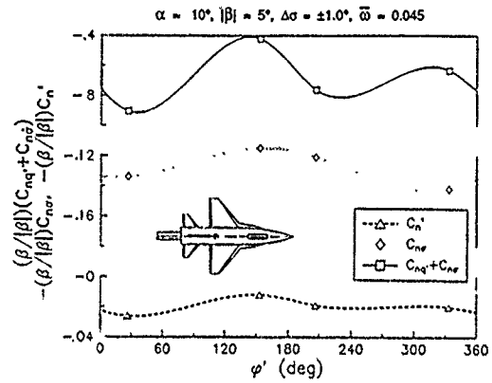

Figure 5-19. Effect of sting roll orientation on SDM yawing-moment derivatives ($M_c = 0.6$)

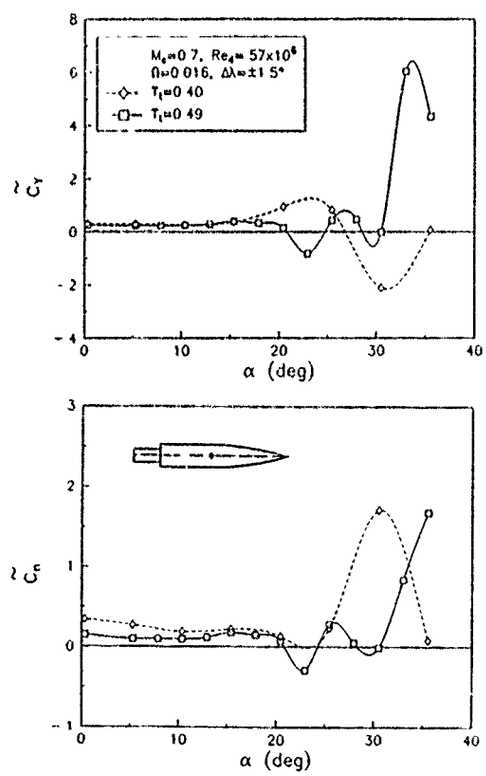

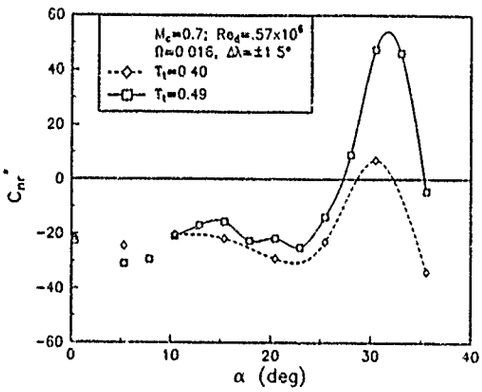

Figure 5-20 Effect of slotted-wall proximity on SOC lateral aerodynamic coefficients.

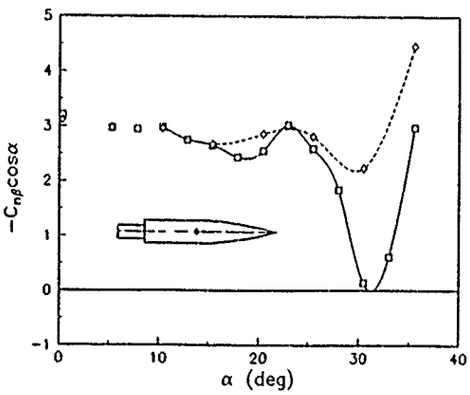

Figure 5-21 Effect of slotted-wall proximity on SOC direct yawing-moment derivatives

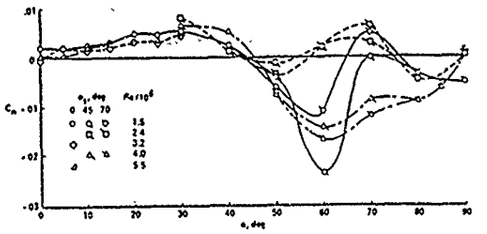

a. Nose Boom Off

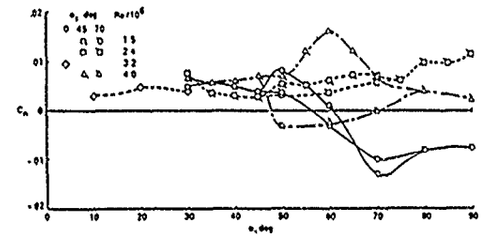

b. Nose Boom On

Figure 5-22. Effect of sting incidence α_s on static C_n characteristics of an advanced aircraft model.

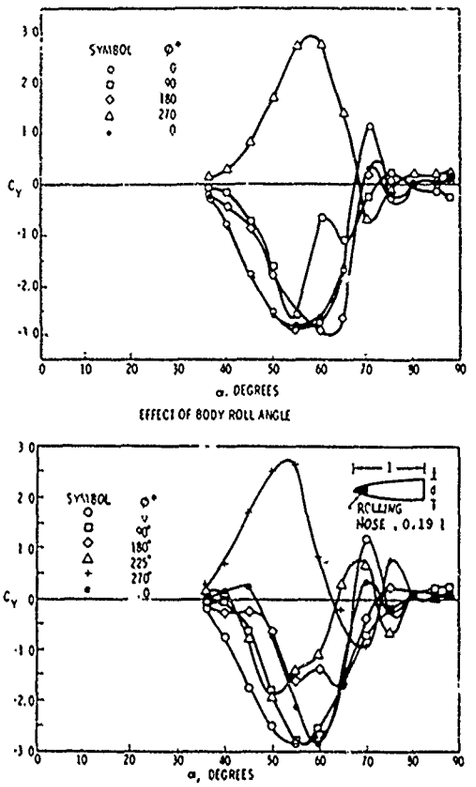

Figure 5-24. Effect of roll angle on the side force of a 3.5 caliber pointed ogive at $M_\infty = 0.25$ and Re $= 0.8 \times 10^6$.

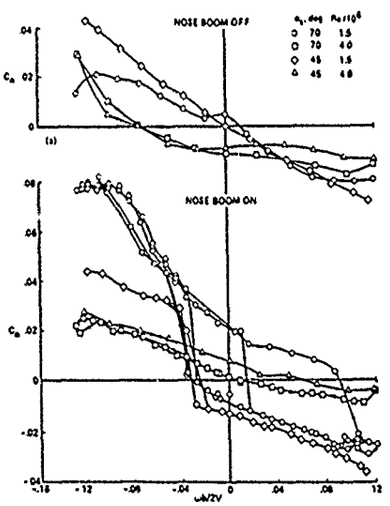

Figure 5-23. Effect of sting incidence α_s on dynamic C_n characteristics of an advanced aircraft model at $\alpha = 70°$.

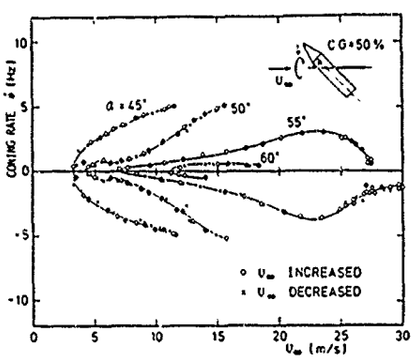

Figure 5-25. Coning characteristics of a cone-cylinder.

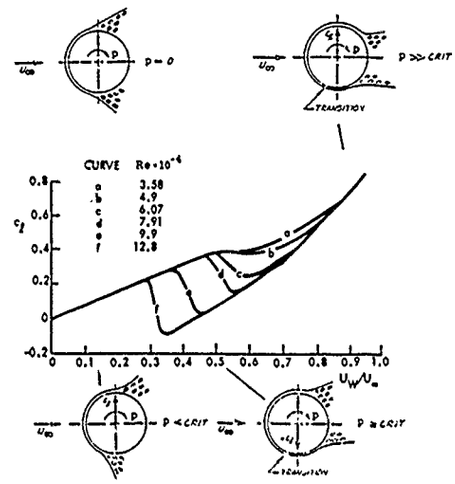

Figure 5-26. Magnus lift characteristics for initially subcritical flow conditions.

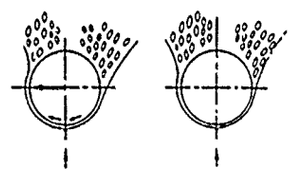

Figure 5-27. Coning-induced translational moving wall effect.

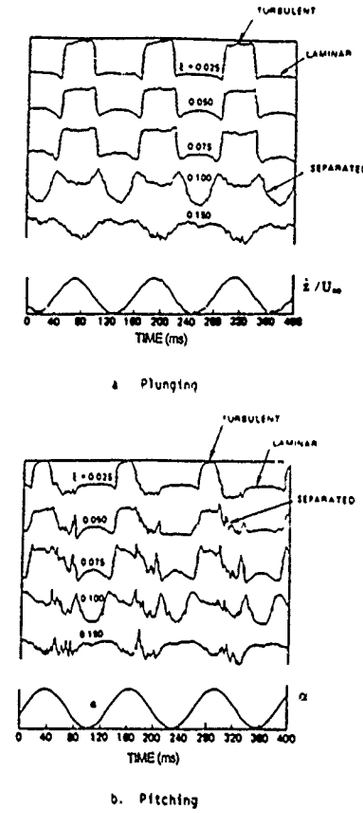

Figure 5-29. Hot film response for plunging and pitching oscillations of a NACA-0012 airfoil.

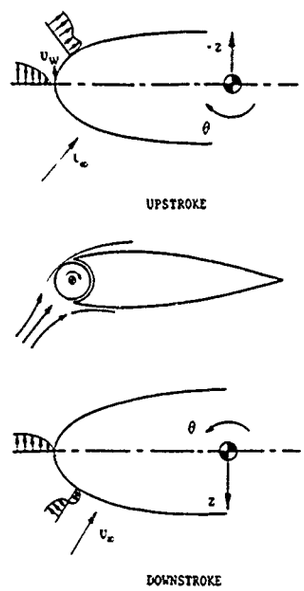

Figure 5-28. Moving-wall-induced leading-edge jet effect.

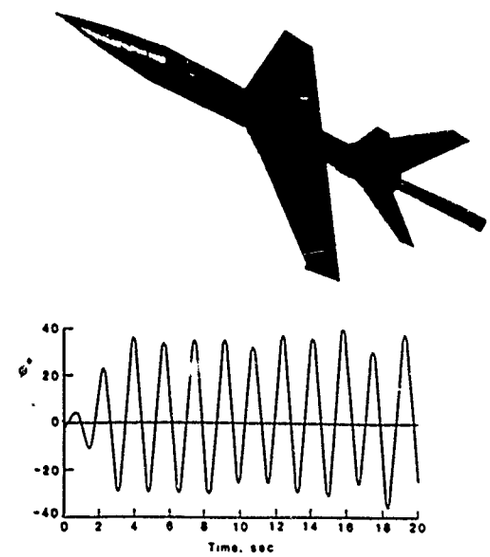

Figure 5-30. Wing rock build-up at $\alpha = 30°$.

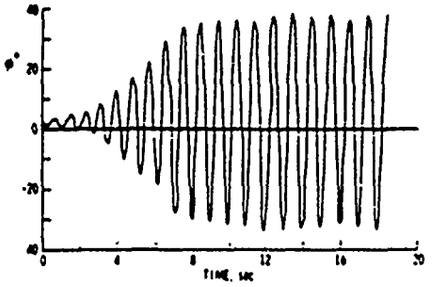

Figure 5-31. Slender-wing rock of an 80° delta wing at $\alpha = 27°$.

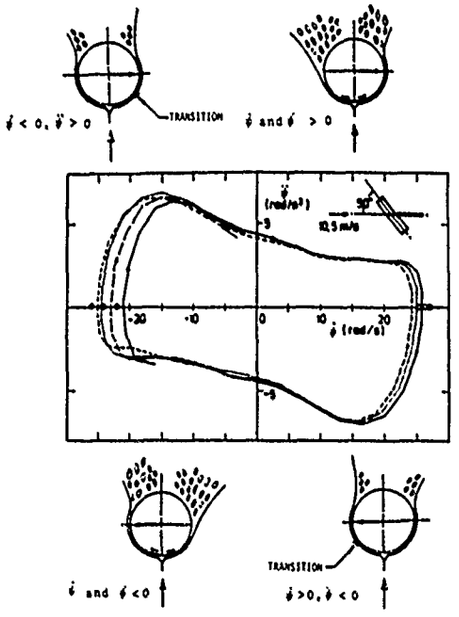

Figure 5-32. Angular acceleration and rate-time histories for a flat-faced circular cylinder coning at $\alpha = 50°$.

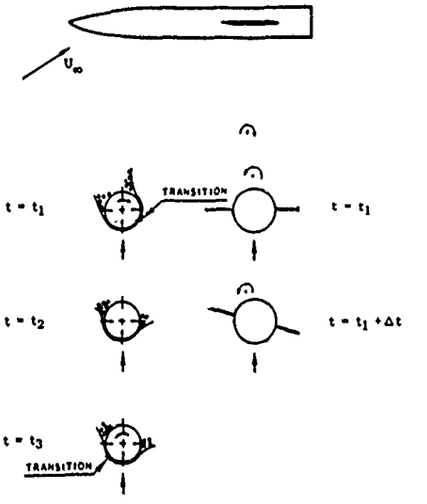

Figure 5-33. Conceptual flow mechanism for forebody-induced wing rock.

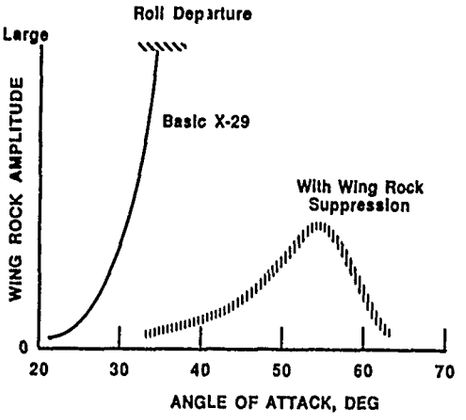

Figure 5-34. Wing rock characteristics of the X-29A configuration.

CHAPTER 6

FUTURE CONCEPTS

6.0 INTRODUCTION

This chapter describes three unconventional wind-tunnel techniques that might be used to obtain dynamic data. None of the techniques has yet been demonstrated, but deserve to be mentioned because of the increased testing capability they offer compared to conventional rotary-balance techniques.

6.1 ORBITAL MOTION

6.1.1 Background

The increasing recognition of the importance of nonplanar motion in vehicle dynamics under separated flow conditions[1-3] recently led to the conception of the principle of orbital characteristic motions.[4-6] The concept can be implemented in an apparatus for captive-model dynamic testing in wind tunnels.[4] The system would be capable of simulating a wide range of oscillatory motion conditions[6] while making possible the determination of dynamic stability parameters.[5]

In the initial design the emphasis was on the measurement of a complete set of dynamic derivatives such as specified in the basic aerodynamic formulation due to Tobak and Schiff,[7] using the set of "fixed-plane" motions,[5] and on the validation of that mathematical model. It was considered a major advantage if this could be achieved by means of a single apparatus. Mechanical details of the apparatus were presented in Reference 4. Subsequently, however, with the emergence of advanced data reduction systems for the extraction of locally-linear[8] or nonlinear aerodynamic characteristics,[9] it was considered more appropriate that the orbital apparatus be designed and optimized to generate arbitrary, two-degree-of-freedom (DOF) motions, of either large or small amplitudes. This change in design philosophy, resulting from the greatly expanded range of possible functions of the device, brought about a postponement of the implementation phase, at least until a clearer picture could be formed of the simulation requirements of nonplanar, post-stall maneuver studies.

Notwithstanding the question of optimization, the basic features of the apparatus have been established, two independent DOFs, harmonic motions of different frequencies or phase relationships, arbitrary angles of attack and large amplitudes and, possibly, minimal aerodynamic interference. This section summarizes the underlying kinematical relationships and data acquisition approaches, while the design optimization of kinematical requirements and for interference alleviation will be discussed in Section 6.2.

6.1.2 Geometrical Arrangement

The basic geometrical arrangement of an orbital apparatus appears in Figure 6-1. There are two nonintersecting axes providing continuous rotations Φ and Ψ, which may be mutually inclined through a tilt angle Λ, and two additional, pivotal axes. The latter provide for the inclination Θ of the complete motion relative to the free-stream flow direction and of the model relative to the Ψ axis, through the angle Γ. The Φ and Ψ axes are respectively referred to as the orbital and sting axes. In the layout proposed earlier, the model and balance are mounted on a shaft, denoted the countershaft, rotating within the sting, which in turn rotates about the orbital axis. When the objective is the determination of stability derivatives the model center of mass should lie on the sting axis. Linear adjustments of the tilt axis and the radius of the orbital motion, r_0, are made in the plane of a rotating platform shown in Figure 6-1.

Two families of motions are obtained, depending on whether the orbital axis is horizontal ($\Theta = 0$) or inclined ($\Theta > 0$), and the number of DOFs depends on the relationship between the two rotations. The angular adjustments required to generate some of the basic orbital characteristic motions are summarized in Table 6-1.

6.1.3 1-DOF Motion Relationships

In its simplest form, obtained when one of the axes is locked, $\dot{\Psi} = 0$, or $\dot{\Phi} = 0$, the orbital concept yields lunar coning ($\Theta = 0$, $\Lambda \neq 0$ or $\Gamma >> 0$), continuous rolling ($\Lambda = \Gamma = r_0 = 0$) or oscillatory coning ($\Theta > 0$ and $\Gamma >> 0$ or $\Lambda \neq 0$). Expressions for the angular velocities and rates in these three modes are well known[4,8] and will not be repeated here. Figure 6-2 illustrates the orbital motion parameters corresponding to an aircraft spin at nonzero spin radius ($\Theta \rightarrow 0$).

In the next level of complexity of characteristic motions, oscillatory motions are forced in two coupled DOFs (i.e., one independent DOF) to yield fixed-plane orbital motions. The term "fixed-plane" denotes motions such that a transverse axis of the model is constrained to move in a plane at fixed orientation with respect to inertial space. For constant model attitude, a pure translational motion is obtained as in Figure 6-3(a) and if the model axis is tilted into the relative wind vector, a pure rotational motion results since $\alpha = \dot{\beta} = 0$ (Figure 6-3(b)). In terms of the orbital parameters, the fixed-plane constraint is $\dot{\Psi} = -\dot{\Phi}$, with translational and rotational motions attained when $\Lambda = 0$ and $\Lambda = -\sigma$, respectively, where σ is the helix angle of the motion

$$\sigma = \omega r_0 / (V_\infty \cos\Theta) \tag{1}$$

Table 6-1 Basic Modes of Operation

Objective	Mode	Orbital axis	Typical α or β range, deg	Typical amplitude, deg	Non-zero adjustments	Continuous rotations
Dynamic derivative measurement	Fixed-plane translation	Horizontal	0–120	±2.5	r_0, Γ, ϕ_0	$\Psi = -\Phi$
		Inclined	0–40		r_0, Θ, ϕ_0	
	Fixed-plane rotation	Horizontal	0–120	±2.5	$r_0, \Lambda, \Gamma, \phi_0$	
		Inclined	0–40		$r_0, \Theta, \Lambda, \phi_0$	
	Lunar coning	Horizontal	0–120	...	Λ, Γ, ϕ_0	
	Rolling	Inclined	0–40		Θ	
Vehicle motion simulation	Oscillatory coning			40	$\Theta, \Lambda, \Gamma, \phi_0$	Φ (Ψ = const)
	Spinning	Inclined	0–120	25	$r_0, \Theta, \Lambda, \Gamma, \phi_0$	
	Fixed-plane coning/ precession	Horizontal or inclined		±4	θ or Γ, Λ, ϕ_0	$\Psi = -\Phi$

The reference systems are depicted in Figure 6-4, with sequences of rotations for (a) inclined and (b) horizontal orbital axes. The parametric relationships between the motion variables are presented in Table 6-2. The aerodynamic angles of attack and sideslip are obtained from expressions derived[5] for their fixed-plane counterparts. Then

$$\begin{aligned} \beta &= \sin^{-1}(\sin\bar{\alpha}\sin\phi) \\ \alpha &= \tan^{-1}(\tan\bar{\alpha}\cos\phi) \end{aligned} \tag{2}$$

In the fixed-plane modes, $\phi = \phi_0$. Explicit relationships therefore exist for the motion variables in terms of the orbital angle Φ, demonstrating that all of the oscillations are either pure or effectively-pure sinusoids (i.e., the impurities are small[5]). The dynamic derivatives identified in Table 6-2 constitute a complete set as prescribed by a mathematical model analogous to the Tobak-Schiff formulation applicable when the dependence on the motion rates is linear and the swerving is small.[7] Note that the derivatives determined are not composites as in fixed-axis oscillatory experiments (e.g., $C_{m_q} + C_{m_{\dot{\alpha}}}$) but pure derivatives such as C_{m_q} or $C_{m_{\dot{\alpha}}}$.

Table 6-2 Dynamic Stability Derivative Matrix

Mode	Parameter[a] $\dot{\alpha}$	$\dot{\beta}$	p	q	r	Derivative, $i = Y, Z, l, m, n$
Translation						
Horizontal	A	B	0	0	0	
Inclined	$\frac{A\cos\Theta}{\Delta}$	$\frac{B}{\Delta^{1/2}}$	0	0	0	$C_{i_\beta}, C_{i_{\dot{\alpha}}}$
Rotation						
Horizontal	0	0	$-B\sin\Gamma$	$-A$	$B\cos\Gamma$	
Inclined	$\frac{-A\sin^2\Theta}{\Delta\cos\Theta}$	0	0	$\frac{-A}{\cos\Theta}$	$\frac{B}{\cos\Theta}$	C_{i_q}, C_{i_r}
Coning	0	0	Π	$P\sin\phi_0$	$P\cos\phi_0$	C_{i_λ}

[a] $A = -\omega\Omega\sin\Phi$, $B = \omega\Omega\cos\Phi$; $\Delta = 1 + 2\,\Omega\cos\Phi\sin\Theta$; $\Pi = \omega\cos\Gamma$, $P = \omega\sin\Gamma$

6.1.4 2-DOF Motion Relationships

An intrinsic property of the orbital motion geometry defined in Figure 6-1 is its two independent DOFs: When the sting axis is driven at a rate Ψ independently of the orbital rate $\dot{\Phi}$ the resulting motions comprise two superimposed components which may have different frequencies and amplitudes. Such motions are epicyclic and may, therefore, be described by two fixed-amplitude vectors rotating in the $i\bar{\alpha}$, $\bar{\beta}$ plane as shown in Figure 6-5

$$\bar{\beta} + i\bar{\alpha} = K_1\epsilon^{i\phi_1 t} + K_2\epsilon^{i\phi_2 t} \tag{3}$$

K_1 and K_2 are the complex vector amplitudes and $\dot{\phi}_1, \dot{\phi}_2$ the angular rates. The complex plane is analogous to that used to describe the free-flight motion of missiles[10] and the angles $\bar{\beta}$ $\bar{\alpha}$ describe the orientation of the aircraft longitudinal axis in

the nonrolling frame of reference. To extend the analogy to high angles of attack, this is interpreted as the projection of the motion on the two-dimensional surface of a unit sphere.

Since the motion is symmetrical with respect to the orbital axis and $\dot{\psi}_m$ is small, it may be assumed that the phase angle between the nonrolling and fixed-plane systems is effectively zero so that the motion can be expressed in the latter system.[11] Then $\tilde{\beta} = \bar{\beta}$, $\tilde{\alpha} = \bar{\alpha}$ and, writing $K_1 = B_1 + iA_1$ and $K_2 = B_2 + iA_2$, Equation (3) yields

$$\begin{aligned} \bar{\alpha} &= A_1 \cos \dot{\phi}_1 t + B_1 \sin \dot{\phi}_1 t + A_2 \cos \dot{\phi}_2 t + B_2 \sin \dot{\phi}_2 t \\ \bar{\beta} &= B_1 \cos \dot{\phi}_1 t - A_1 \sin \dot{\phi}_1 t + B_2 \cos \dot{\phi}_2 t - A_2 \sin \dot{\phi}_2 t \end{aligned} \tag{4}$$

The modified Euler angle of roll, ϕ_m, is a function of the rotations Φ and Ψ and the aerodynamic angles of attack and sideslip α and β are related to their fixed-plane counterparts through Equation (2). Therefore, as before, it is possible to derive explicit relationships for the motion parameters in terms of the rotations $\Theta, \Phi, \Lambda, \Psi, \Gamma, \phi_0$ and rates $\dot{\Phi}, \dot{\Psi}$.

In general, the nutational vector K_1 will describe pitching and yawing oscillation and the precessional vector K_2, a coning motion, depending on the roll rate. When $r_0 = 0$ and $p = -\dot{\phi}_1$ the motion obtained is the fixed-plane coning mode, which is a combination of a pitching and yawing oscillation with steady coning at the same frequency,[5] and when $K_1 = 0$ and $p = \dot{\phi}_2$, lunar coning is obtained. For oscillatory coning, $\dot{\phi}_1 = 0$ and K_1 describes the angle of repose (Figure 6-5). When $r_0 \neq 0$ the motion becomes tricyclic.

$$\bar{\beta} + i\bar{\alpha} = K_1 e^{i\dot{\phi}_1 t} + K_2 e^{i\dot{\phi}_2 t} + K_3 e^{ipt} \tag{5}$$

The notion of measuring aerodynamic reactions in captive epicyclic motions opens up a whole new field of possibilities. Characteristic motions similar to those specified in the Tobak-Schiff model applicable when the dependence on coning rate is nonlinear[7] are depicted in Figure 6-6. The orbital mode, comprising a coning motion superimposed on circular pitching and yawing at a different angular rate yields small-amplitude α and β perturbations about large fixed mean values of α and β in rotary flow.

In the general case, this 2-DOF composite motion could be made representative of an oscillatory spin condition, i.e., spinning about an oscillating velocity vector. Here all of the parameters $\Theta, \Lambda, \Gamma, \phi_0, r_0$, and $\dot{\Phi}, \dot{\Psi}$ are nonzero and $|\dot{\Phi}| \neq |\dot{\Psi}|$. The number of characteristic motions/flight modes which may be generated is extensive; the various categories of motions are summarized in Figure 6-7. The captive epicyclic modes are all pure and not subject to any frequency or amplitude restrictions. The effects of deflections of the support system under inertial and aerodynamic loads can be eliminated for practical purposes, as will be shown in Section 6.2.

The capability of generating composite motions which can be decomposed into basic characteristic motions provides opportunities for validating mathematical models that utilize the superposition principle.[5]

6.1.5 Data Acquisition and Reduction

6.1.5.1 Linear Analysis

In the degenerate 1-DOF modes, coning and rolling, standard techniques applicable to rotary-balance testing are used.

In the fixed-plane rotation modes, α and β are constant and the only variables are q and r (see Table 6-2); hence, the measured balance signals are due to dynamic reactions superimposed on the inertial and gravitational contributions. When the objective is the determination of the corresponding derivatives, the following tare procedure may be used: The model is orbited at the prescribed frequency, but in the absence of flow. Therefore, the measured reactions are purely inertial and gravitational and equal to their counterparts in the dynamic test. A vectorial subtraction of the quantities obtained in the two cases yields the dynamic deflection vectors, which may be separated as they are in phase quadrature, to yield the dynamic derivatives C_{m_q} and C_{n_r}.

It is necessary to know the functional nature of the motions in the secondary DOFs *a priori* if the effects submerged in the corresponding signals are to be extracted. The primary motions are effectively sinusoidal at all amplitudes considered so that the responses in the secondary DOFs must also be sinusoidal. This does not involve any assumption of linearity since the form of the signals is given by their relationships to the reference signal, which may be generated by means of a position encoder.

6.1.5.2 Quasi-Linear Analysis

With the exception of the pure rotation mode discussed above, and lunar coning, all orbital modes are subject to the complication of a primary motion forced in two DOFs instead of one. Hence, the static deflection vectors due to the α and β slopes are overlayed with the $\dot{\beta}$ and $\dot{\alpha}$ reactions, respectively, and, therefore, indistinguishable in a single test using cross-correlation techniques. This is also true of the simpler, oscillatory coning mode.

In principle, these static components can be extracted in a rather complicated tare procedure and the dynamic components subsequently separated as they are in phase quadrature. However, any procedure involving a number of vector operations is not likely to yield accurate results in the presence of significant noise levels. A more reliable approach is the data reduction method presented in Reference 8 for the analysis of oscillatory-coning test data.

Using narrow angular windows at the parametric nodes, the effects due to the parameters in quadrature can be separated. For instance, in the pure translational mode (see Table 6-2), data are recorded when $\dot{\alpha} = \dot{\alpha}_{max}$ with $\dot{\beta} = 0$, $\beta = \beta_0$ and

$\alpha = \alpha_0$ (and similarly for $\dot{\beta}_{max}$). Since the dynamic reactions are in quadrature, the derivatives are obtained from a single test.

For more complex motions such as fixed-plane coning and epicyclic motions more than one motion parameter experiences a node within a given window. Hence, an additional test is required to uncouple the dynamic reactions if two parameters are involved, where the relationship between the parameters differs in the two tests. Naturally, this follows when the one test is a subset of the other, as in the example of lunar vs asymmetrical coning,[8] and in all orbital modes that are composites of simpler motions.

6.1.5.3 Nonlinear Analysis

Since nonplanar aerodynamic characteristics are intrinsically nonlinear, it is more correct to obtain these data by nonlinear analysis, even at angles of attack below stall. A nonlinear data reduction technique under development[9] utilizes the fact that nonlinear aerodynamic loads contain many frequencies harmonically related to the causative motion to reconstruct those loads. The only requirement is that the motion must be periodic. Instantaneous values of the aerodynamic reactions are measured throughout the motion cycle at the corresponding values of the position, velocity and rate and are displayed in an $n + 1$ dimensional load-position-velocity-rate space, where n is the number of such motion parameters and their derivatives.

For the oscillatory flight modes simulated on the orbital apparatus, the nonlinear analysis will, therefore, yield the history of the nonlinear loads recorded along the orbital path after periodic flow behavior has developed.

Specific motion conditions occurring in a 6-DOF maneuvering flight simulation could be reproduced on the orbital apparatus. The required combinations of attitudes, rates and accelerations would be achieved at particular points on the motion cycle and would be known (Equations (2), (4) and (5), and Table 6-2). Of course, this neglects any distant-past time-history dependence. To satisfy the requirement of periodicity, the nutational rate must be an exact multiple of the precessional rate. Thus, although the testing technique allows for completely arbitrary, independent frequencies, the data reduction requirement of periodicity does introduce a constraint. However, this is not restrictive when the difference between the rates is large.

The potential capability for obtaining the dynamic loading histories for complex 2-DOF motions and their components could facilitate the validation of aerodynamic force models and unsteady numerical flow computations.

6.1.6 Synopsis

1. A summary of the kinematical relationships following from the orbital motion concept was given and the approaches to the determination of aerodynamic parameters from the different characteristic motions were outlined.

2. Using a single apparatus, it is possible, in principle, to determine a complete set of dynamic stability derivatives, or alternatively, to extract the nonlinear load variations for periodic, 2-DOF motions.

3. The orbital motion concept is well-suited to the validation of aircraft mathematical models and unsteady CFD codes.

4. Several families of epicyclic motions and simpler modes, including the fixed-plane modes and various coning modes can be generated. The application of the orbital motion principle to the simulation of specific flight dynamic instabilities such as an oscillatory spin is feasible.

6.2 ORBITAL-PLATFORM CONCEPT

6.2.1 Background

A radically different approach to rotary-balance testing has been proposed [12] The orbital platform concept was spawned by the desire to fulfill the needs for reduced aerodynamic interference and vibration and for a nonplanar testing capability Aerodynamic interference generated by a rotating support strut has to be accounted for in conventional rotary tests (see Section 5.1), particularly in high-speed wind-tunnel facilities where the interference may include unsteady wall effects (see Section 5.2). The conceptual orbital apparatus described in Section 6.1 lends itself to the simulation of nonplanar motions which can be described by a coning vector superimposed on a nutational vector. It was desirable to extend the concept to the inverse situation as described by various authors, where an oscillatory[7,1,3] or nutational[6] motion is superimposed on the coning mode.

The dynamic testing apparatus concept that resulted is characterized by an annular orbital platform on which the model support sting and secondary drive systems are mounted and is, therefore, referred to as the "orbital-platform epicyclic coning" (OPLEC) system. Although offering possibilities for two-degree-of-freedom (DOF) testing, the system is primarily a coning device with unusually low interference levels and high rigidity.

6.2.2 The Annular Orbital Platform

A clue to the way in which the rotary experiment can be restructured is offered by the orbital motion scheme depicted in Figure 6-8. This is a simplification of the general arrangement (Figure 6-1) obtained when the orbital axis is horizontal. If the orbital platform is taken to be a cylindrical surface aligned with the axis, the sting may be directed inwards with the

model located on the axis of rotation at a finite pitch angle. An arrangement is obtained where the annular platform could be flush with the walls as in a vertical open-jet tunnel, as illustrated in Figure 6-9. Since most of the support hardware is outside the flow, the aerodynamic interference should be very low.

Circular test sections are something of a rarity and it was considered desirable to initially adapt the concept to test sections of arbitrary shape and, in particular, to a modified rectangular section. This requirement of universality resulted in the notion of a cylindrical installation housing the annular platform assembly, that would be mounted inside the working section.

6.2.3 Mechanical Design

The OPLEC mechanical layout is illustrated schematically in Figures 6-10 and 6-11. A variation of the concept appears in Figure 6-12. The test facility comprises a cylindrical test-section insert of circular cross section, carrying a rotating annular platform and support system. The unit is mounted on a vertical support strut between the floor and roof of the wind-tunnel working section (Figure 6-10). The tubular section is also anchored to the rectangular walls by means of a number of tension cables. The main drive system consists of a stepping motor mounted on the roof of the tunnel working section and a drive shaft within the strut. The drive pinion engages a webless bevel gear at the downstream end of the annular platform as shown in Figure 6-11. The downstream portion of this rotating section is covered by a stationary tubular section which makes up the aft circular test-section wall. The exposed portion of the rotating cylinder is denoted the "orbital platform," upon which the model support and secondary drive mechanism are mounted. The leading edge and forward test-section wall of the device is a stationary splitter-plate/fairing designed to provide parallel flow within the test section. The rotating cylinder runs on a set of three ball bearings mounted in an outer cylindrical casing which is integral with the main strut. Gas bearings have several advantages, including higher speeds and lower noise, but are not strictly necessary here.

The model is sting-mounted and a flange at the end of the sting is bolted directly to the orbital platform. Additional lateral location is provided by two lateral telescopic struts attached to stub shafts that are integral with the sting. An angle-of-attack change is accomplished by using one of a set of sting support struts, each corresponding to a particular pitch angle and a fixed reference center, while the lateral telescopic struts are extended and clamped at the appropriate attitudes and lengths required to complete the triangulation.

Complex, 2-DOF motions may be generated by means of a secondary-drive, stepping motor located within a housing integral with the sting end connected to the balance by a countershaft rotating within the sting (Figure 6-11). Thus, epicyclic motions are obtained by rotating the model around the sting axis, while coning with oscillatory perturbations can be produced by a conventional, inexorably-driven oscillatory mechanism bolted to the orbital platform.

The loads on the model are sensed by a five-component dynamic balance. The balance signals are transmitted by FM telemetry over the gaps between the rotating and stationary components. An external pulse source and control unit are located outside the tunnel working section. Further details of the electrical system are given in Reference 12.

When the orbital platform and annular support housing are inverted, the interior becomes a stationary circular duct and the orbital platform rides on its external surface, as in Figure 6-12, again using air or ball bearings. This is similar to the concept for a vertical tunnel (Figure 6-9). Externally-mounted struts are required, while the model is mounted forward of the leading edge of the splitter-fairing. Flow disturbances inside the duct are effectively eliminated if the orbital platform is located a short distance downstream of the leading edge and the struts are swept forward as shown. The model scale may be larger in relation to the orbital platform but the latter might have to be reduced in diameter to keep the blockage area within acceptable limits. There is some increase in mechanical complexity associated with the bent lateral telescopic struts, and the external configuration becomes impracticable at pitch angles below about 30° when a secondary drive motor is to be used (Figure 6-12).

6.2.4 Analysis of the Design

6.2.4.1 Vibration

Perhaps the most obvious advantage of the OPLEC device is the high rigidity of the model support. The conventional rotary-balance support may be thought of as a cantilever beam comprising three elements and the OPLEC support as a truss with a short cantilever extension. Since the effective length of the OPLEC cantilever is no more than 1/3 of its counterpart in the conventional system, the model support will be an order of magnitude stiffer in the former case. The external orbital platform configuration will be somewhat less stiff, but, nevertheless, far more rigid than the conventional system.

The OPLEC system provides for dynamic balance masses to be mounted in an annular enclosure adjacent to the orbital platform (see Figure 6-11). As illustrated schematically in Figure 6-13, the correct placement of a static counterweight and three dynamic balance masses would eliminate the cross products of inertia. In principle, a perfect dynamic balance can be achieved, but even approximate balancing of the secondary moments would be valuable as this is impossible in the conventional rotary-balance configuration.

6.2.4.2 Aerodynamic Interference

Support interference due to the curved strut and its wake is absent in the OPLEC configurations. The model burst-vortex wake is completely separate from that shed behind the sting and lateral struts at high α, particularly in the external orbital-platform configuration (Figure 6-12), while even at low incidence the cross section of the support structure is smaller

than in the conventional setup (Figure 6-11). Sting interference is steady in relation to the model, except in the oscillatory perturbation mode, where the model moves relative to the sting.

The moving wall effect produced by the rotating platform in the internal orbital-platform apparatus can be reduced by the use of a stationary cover over the aft portion and is not expected to be significant. The interaction of the vortex wake of the sting and model with the circular wall and the moving internal orbital platform, if present, results in a constant deflection of the wake trail (Figure 6-14). Moreover, unlike the conventional apparatus (see Figure 5-17) flow separation on the circular walls will be steady in relation to the rotating model. Both sources of unsteady wall interference, therefore, reduce to a fixed angle-of-attack change near the walls, which may be corrected for following the procedure used in propeller tests.[13]

The internal orbital-platform apparatus is well-suited to the investigation of support interference in conventional rotary-balance tests. Since there are both rotating and stationary sections of the circular test section, replicas of the rotating arm and the support strut can be respectively mounted on the orbital platform and on the aft circular section as shown in Figure 6-15, to simulate the effect of the support in a rotary-balance test. The incremental aerodynamic loads due to the presence of the rotating curved strut can then be determined directly. Since the test section is circular no unsteady wall interference will be present, and given the low base interference of the OPLEC strut system, the interference due to the dummy struts will be approximately equivalent to the difference between the loads measured with and without the dummy struts.

6.2.5 Characteristic Motions

The various characteristic motions which can be generated by the OPLEC system fall into two main categories, epicyclic and nonplanar oscillatory motions. The degenerate epicyclic modes include lunar coning, oscillatory coning and continuous rolling. The 2-DOF epicyclic motions and 1-DOF oscillatory modes, or fixed-plane orbital motions, were analyzed in Section [illegible] and elsewhere,[5,6] while the 2-DOF composite modes have been discussed in Reference 12.

6.2.5.1 Epicyclic Motion

In analyzing the epicyclic modes it is convenient to use Euler angles with the coning axis aligned with the wind as shown in Figure 6-16. The rotations about the coning and sting axes are, in general, independent. Then the aerodynamic angles α and β are obtained directly from the body-axes velocity components and, when the model longitudinal axis is along the sting axis, the angular rates are

$$\begin{bmatrix} q \\ r \\ p \end{bmatrix} = \begin{bmatrix} \sin\theta\sin\phi & 0 & \cos\phi \\ \sin\theta\cos\phi & 0 & -\sin\phi \\ \cos\theta & 1 & 0 \end{bmatrix} \begin{bmatrix} \dot{\psi} \\ \dot{\phi} \\ \dot{\theta} \end{bmatrix} \tag{1}$$

The kinematical relationships were analyzed in Reference 12.

Epicyclic motion may be described by rotating vectors in the complex plane (Figure 6-5)

$$\tilde{\beta} + i\tilde{\alpha} = K_1 e^{i\dot{\phi}_1 t} + K_2 e^{i\dot{\phi}_2 t} \tag{2}$$

As with the conceptual orbital apparatus, the complex vectors K_1 and K_2 describe arbitrary epicyclic motion but, in this case, their order is reversed. In the geometry of Figure 6-16 the nutational vector is superimposed on the steady coning motion. A suitable choice of the amplitudes and frequencies could yield a motion representative of an oscillatory spin of a fighter aircraft. However, it is possible that the geometry of Figure 6-8 would provide the closest analogue of this flight mode. Of course, when $K_2 = 0$, pure coning is obtained.

6.2.5.2 Nonplanar Oscillatory Motion

The fixed-plane motions have been analyzed in detail (see Section 6.1) and the kinematical relationships are summarized in Table 6-2. These modes have two coupled DOFs and may be thought of as degenerate modes of epicyclic motion.

The determination of dynamic derivatives under conditions of rotational motion becomes feasible by virtue of the high rigidity of the OPLEC system. Arbitrary small-amplitude planar oscillatory perturbations of the coning motion are possible but it should be noted that the requirement of periodicity has to be satisfied if aerodynamic parameters are to be extracted directly. Data reduction requirements were discussed in Section 6.1.5.

Characteristic motions specified in the Tobak-Schiff[7] mathematical model applicable when the dependence on coning rate is nonlinear and the swerving is small can be generated exactly. For harmonic motion the angular velocity in the pitch-oscillation-coning mode (Figure 9-32), as obtained from Equation (1), is

$$\begin{bmatrix} q \\ r \\ p \end{bmatrix} = \begin{bmatrix} \sin\theta\sin\phi & 0 & \cos\phi \\ \sin\theta\cos\phi & 0 & -\sin\phi \\ \cos\theta & 1 & 0 \end{bmatrix} \begin{bmatrix} \dot{\psi} \\ 0 \\ \dot{\theta}_0 \sin\nu_2 t \end{bmatrix} \tag{3}$$

and, in roll-oscillation coning,

$$\begin{bmatrix} q \\ r \\ p \end{bmatrix} = \begin{bmatrix} \sin\theta\sin\phi & 0 & \cos\phi \\ \sin\theta\cos\phi & 0 & -\sin\phi \\ \cos\theta & 1 & 0 \end{bmatrix} \begin{bmatrix} \dot{\psi} \\ \dot{\theta}_0 \sin\nu_2 t \\ 0 \end{bmatrix} \tag{4}$$

The angular velocities in the yaw-oscillation-coning mode (Figure 9-33) are obtained in a similar fashion.

The rate of change of α and β due to the rotational motion are given by

$$\begin{aligned}\dot{\alpha} &= q - (p\cos\alpha + r\sin\alpha)\tan\beta \\ \dot{\beta} &= p\sin\alpha - r\cos\alpha\end{aligned} \tag{5}$$

The combination of the basic coning mode with the two oscillatory modes given by Equations (3) and (4) represent a complete set of characteristic motions in the aerodynamic axes system (Figure 9-32) and similarly for the body axes system (Figure 9-33). When $\dot{\psi} = 0$, the conventional, planar oscillatory motions are, of course, obtained.

6.2.5.3 Characteristic Motion Vectors

It was recently suggested that the applicability of the nonplanar mathematical model due to Tobak and Schiff[7] may be extended at post-stall conditions if the oscillatory derivatives are replaced by directional, rate-dependent derivatives.[14]

Since the aerodynamic characteristics are directional, they should be represented in vectorial form. In Figure 6-17 the motion vectors, $\Delta\vec{\lambda}, \Delta\vec{\theta}, \Delta\vec{\sigma}$ and $\Delta\vec{\phi}$ are displayed on the two-dimensional surface of a unit sphere using spherical mapping.[15] The directional rate-dependent parameters are then defined as

$$\begin{aligned}\vec{C}_{ik} &= \vec{C}_{ik}\left[\alpha(t), \beta(t), \vec{k}\right]_{\alpha=\alpha_1, \beta=\beta_1}, \quad k = \dot{\vec{\lambda}}, \dot{\vec{\theta}}, \dot{\vec{\phi}} \\ \vec{C}'_{ik} &= \vec{C}_{ik}\left[\sigma(t), \psi'(t), \vec{k}'\right]_{\sigma=\sigma_1, \psi'=\psi_1}, \quad k' = \dot{\vec{\sigma}}, \dot{\vec{\psi}}, \dot{\vec{\phi}} \\ \vec{C}_{i\dot{\phi}} &= \vec{C}_{i\dot{\phi}}\left[\sigma_1, \psi'_1, \vec{\omega}\right]\end{aligned} \tag{6}$$

where $i = X, Y, Z, \ell, m, n$. $\dot{\vec{\lambda}}$ and $\dot{\vec{\theta}}$ are the vector yaw and pitch rates in body axes, $\dot{\vec{\sigma}}$ and $\dot{\vec{\psi}}$ the vector pitch and roll rates in aerodynamic axes and $\dot{\vec{\phi}}$ is the vector coning rate. The OPLEC concept lends itself to the measurement of directional, rate-dependent reactions. The required continuous characteristic motions can be generated as outlined in Section 6.2.5.1, while data reduction could be accomplished by means of the locally-linear extraction technique described in Section 6.1.5.2. The aerodynamic reactions associated with Equations (6) may be combined vectorially in a 6-DOF flight simulation.

6.2.6 Synopsis

1. The orbital platform, or OPLEC, system is a radically different rotary-balance design which eliminates the need for bulky rotating support hardware. The apparatus, which can be configured with either internal or external orbital-platform layouts, is inherently most rigid and vibration levels can be kept very low through dynamic balancing.

2. Aerodynamic support interference is very low in both OPLEC configurations. Unsteady wall interference is absent in the internal-platform configuration and could be negligible in the external arrangement.

3. The levels of support interference in conventional rotary-balance tests may be assessed in experiments involving representative "dummy" installations in the OPLEC test section.

4. The OPLEC system could be used to generate 2-DOF characteristic motions required in nonlinear mathematical models of aircraft dynamics, and is well-suited to the validation of these models.

5. A wide range of periodic motions associated with flight instabilities can be simulated, including arbitrary epicyclic and oscillatory coning perturbations.

6. Directional, rate-dependent parameters required in 6-DOF simulations of maneuvering flight could be extracted from the appropriate OPLEC characteristic motions

6.3 MAGNETIC SUSPENSION

The application of magnetic suspension technology to rotary-balance testing is discussed in this section. The practical problems associated with generating continuous rotary motions while measuring the forces and moments acting on the model are discussed. In addition, the possibility of generating more complex motions is considered.

Magnetically supporting the model in the wind tunnel can overcome some of the problems with mechanical rotary-balance techniques. The major advantage of the magnetic suspension and balance system (MSBS) for rotary-balance testing is the total absence of support interference and related mechanical problems.

Researchers at ONERA were the first to use magnetic suspension and balance systems for aerodynamic testing. Tournier and Laurenceau reported their initial test results in 1957.[16] There have been at least 17 MSBSs built since the mid 1950s. They range in size from about 5 × 5 cm to 40 × 60 cm and have been used for aerodynamic experiments at speeds from near zero to hypersonic speeds. The uses of these systems range from very simple drag measurements and wake studies to dynamic stability and Magnus studies. The papers cited in Reference 17 give details of these systems and their development

Whether used for rotary-balance testing or for more conventional testing, an MSBS solves the problem of support interference and offers other advantages. However, existing MSBSs have some severe limitations and problems of their own; both the promise and problems of the MSBS for rotary-balance testing are examined in this section.

6.3.1 Basic Principles

6.3.1.1 Open-Loop System

Figure 6-18 illustrates the principle of magnetic suspension. The sketch shows a single-degree-of-freedom open-loop system. The two basic elements of the system are the electromagnetic coil and a magnetic body. A third element, not shown, is the power supply for the coil.

The magnetic body can be a permanent magnet, a piece of soft iron magnetized by the coil, or a superconducting electromagnet. In practice, the magnetic body can be anything with a sufficiently strong magnetic moment. The sketch on the left shows the axis of the coil and the magnetic body both in the vertical plane with gravity acting downward. The coil carries constant current in this open-loop magnetic suspension system.

The sketch on the right shows the magnetic force on the body as a function of its distance from the coil. At $x = x_0$ the magnetic force of attraction exactly equals the weight of the body. When the body is moved away from the coil the magnetic force decreases; toward the coil the force increases. Thus, x_0 is a position of unstable equilibrium and no stable suspension is possible.

6.3.1.2 Closed-Loop System

Figure 6-19 shows a single-degree-of-freedom closed-loop system comprising the same two basic elements; the electromagnetic coil and the magnetic body. However, additional elements in the system are required to close the control loop. These are the model position sensor and a feedback controller. Also, the simple constant-current power supply is replaced with a power amplifier.

The model position information is fed to the controller. The controller estimates the velocity from the position data. Position and velocity, with suitable gain adjustments, provide command signals for the power amplifier. When adjusted properly, the power amplifier sends just the right current to the coil for stable equilibrium.

As before, the sketch on the right shows the magnetic force acting on the body as a function of distance. One obvious difference between this and the open-loop system is in the slope of the force-distance curve. Again, at $x = x_0$, the magnetic force of attraction exactly equals the weight of the magnetic body. A small movement of the magnetic body away from the coil causes the magnetic force to increase, returning the body to the equilibrium position. Moving the body nearer the coil causes the magnetic force to decrease. Now x_0 is a position of stable equilibrium and stable suspension is possible.

When adjusted properly, the current in the coil has a steady dc level with a small control ripple superimposed. Holmes developed the first such stable closed-loop system over 50 years ago at the University of Virginia.[18]

This single-degree-of-freedom closed-loop magnetic suspension system forms the basis for an MSBS for a wind tunnel. In practice, the number of degrees of freedom (actually, degrees of control) can range from one to six. Electromagnets, usually acting in pairs, apply magnetic forces or moments to the model.

6.3.2 Generating the Model Motion

The two main requirements of an MSBS for rotary-balance testing are:

Generating the Model Motion
Extracting the Aerodynamic Data

Figure 6-20 shows a schematic of the required model motion for rotary testing. The model has a spin radius R, an angle of attack α and a roll rate Ω. A mechanical rotary-balance rig typically rolls the model at about 5 revolutions per second and the MSBS has to duplicate the corresponding reduced rate.

A robust scheme of roll control is essential if the MSBS is to be used for rotary-balance testing. Unfortunately, one difficulty with MSBSs has been achieving active roll control. Researchers at both MIT and the University of Southampton have developed roll control schemes. For example, Goodyer and his colleagues at Southampton have achieved active roll control by using spanwise magnets.[19] These schemes have a limited roll angle range with singularities at 45°. Goodyer has proposed, but not demonstrated, a magnet design for full 360° roll angle control.

There is an important secondary advantage to using the MSBS for rotary-balance testing, namely, the possibility of independent control over all the degrees of freedom of the model. Because of this, it should be possible to superimpose arbitrary small-amplitude oscillations on the spinning model. This could make it possible to evaluate dynamic derivatives for

small disturbances under spinning conditions. To generate complex motions such as pitch/heave oscillations superimposed on the rotary motion, a 5 to 10 Hz bandwidth is required in the pitch/heave degree of freedom. However, the immediate problem is to generate the continuous single-degree-of-freedom rotary motion.

6.3.3 Design Studies for Large MSBS

To be of practical value, any MSBS used for rotary-balance testing must be used with a large wind tunnel. A minimum desirable size is perhaps a 2.4-m test section. This size is somewhat arbitrary. However, model details become hard to scale properly in tunnels much smaller.

Existing MSBSs are small. The largest is a 40 × 60 cm system in the USSR used with a subsonic tunnel. The next largest is the 0.33 m (13") system built by AEDC in the mid 1960s and now used at NASA-Langley. Increasing the size of the MSBS to work with a large tunnel has been difficult. In the mid 1960s Parker showed that the weight and power of a system using normal copper coils quickly get too large to be practical.[20] The practical upper limit for a normal copper coil MSBS is about 2 feet in diameter.

Building a large MSBS is now easier because of recent advances in several areas of technology. These advances include developing ac superconductors, better magnetic materials and better power supplies. They also include developing improved position and motion sensors and digital computers. Taken together, these advances in technology improve the chances for building a large MSBS capable of aerodynamic testing free of support interference.

NASA-Langley has funded two studies aimed at designing an MSBS to use with a large transonic tunnel. (A *large* tunnel in this context means a test section larger than 2 meters.)

In 1981 the General Electric Company (GE) studied the feasibility of building an MSBS for a large wind tunnel. One of the options considered was a 2.4 m transonic wind tunnel. A requirement of the GE study was to use superconducting coils and off-the-shelf components.[21] The model size and model loads used in the study were based on a highly-maneuverable fighter design. This class of aircraft presented a difficult design problem for an MSBS because of restricted internal volume and high aerodynamic load. The model angular displacements and loads for the design study were

±30° in pitch,	9790 N (2200 lb) lift,
±10° in yaw and	4180 N (940 lb) drag and
±20° in roll.	1380 N (310 lb) side force.

In 1984-85 NASA funded a follow-on design study by Madison Magnetics Incorporated (MM) using the same displacements and loads used for the GE study. However, MM were able to use recently developed technology in their design.[22,23]

One recommendation from the GE study was to use a superconducting core in the model. Working under a NASA grant, researchers at Southampton had developed the superconducting model core in 1982.[24] This became one of the main new features of the MM design. For large models, using a superconducting core increases the magnetic moment of the model over that available from iron or permanent magnet cores. This allows the external coils to be proportionally smaller for a given system performance.

Both the GE and the MM studies confirm the feasibility of building a large MSBS using existing technology. However, both studies limited the range of roll angles to ±120°. This is an important limitation when considering the use of an MSBS for rotary-balance testing.

Both studies also concluded that it would take very high power levels to force continuous 5-10 Hz model motion simultaneously in multiple degrees of freedom. Losses in the superconducting coils would cause rapid and perhaps unacceptable boil-off of liquid helium.

One possible way around this problem is to avoid continuous dynamic operation of the MSBS. For example, 1 or 2 seconds of rotary testing at each test condition should be enough to get accurate aerodynamic data. This intermittent mode of dynamic operation would reduce the total boil-off of liquid helium. However, it would not reduce the high instantaneous power requirement during the 1 or 2 seconds of dynamic testing. Here again, suitable operating procedures might overcome the problem. For example, the liquid helium could be sub-cooled before the dynamic testing. This would give the liquid added heat capacity and eliminate any instantaneous boil-off.

The success of any large MSBS is absolutely dependent on the use of superconducting coils. This is an area where the development of liquid-nitrogen-temperature or room-temperature superconductors would obviously provide welcome relief.

6.3.4 Model Position Sensing

Closely tied to model attitude control is the requirement to sense the model attitude. Until now, model attitude sensing has been accomplished by using optical or electromagnetic techniques. Typically, the optical techniques are limited to 10° of rotation. Extension of the optical techniques to work with the continuous motions required for rotary-balance testing may be a difficult problem.

The electromagnetic position system (EPS) developed at MIT offers more promise for extension to larger scale. The system built at MIT has a range of about ±40°. However, no one has yet built and demonstrated a large EPS.

Work is under way in the Instrument Research Division at NASA-Langley to develop a reliable infrared telemetry link from the model. If successful, this link will permit the use of strap-down inertial sensors, like the laser rate gyro, and accelerometers in the model. Such a combination would give the model attitude accurately (aircraft and missile attitude sensing systems now use these techniques extensively).

Position information from on-board sensors can also be used for model attitude control. Such information could very well become an essential requirement of rotary-balance testing. The bandwidth requirements of any telemetry link needs to be very high. Using inertial and rate sensors provides important data for mathematical modeling of the model motion and extraction of the aerodynamic and magnetic parameters.

6.3.5 Control and Calibration

In view of the pronounced nonlinearities in magnetic fields and the possibly complex aerodynamic forces, the control dynamics is complex. It is essential to relate the currents in the coils to the model inertial, magnetic and aerodynamic forces. Separation of these three forces is a nontrivial problem. For combined motions the attitude control becomes even more complex and requires closed-loop control.

The balance part of the MSBS gives the forces and moments acting on the model. The typical MSBS is difficult to calibrate. Calibration involves relating the currents in the coils to the forces and moments acting on the model. The best calibrations are naturally obtained for the single-degree-of-freedom MSBS. When an MSBS has several degrees of freedom, the calibration must include interaction terms. These terms are similar to the interaction terms for a multiple-component strain-gauge balance.

With existing MSBS systems, most researchers use a loading rig to apply static loads for force and moment calibration. A more recent approach uses a technique of dynamic calibration.[25] The dynamic calibration method consists of oscillating the model and relating the currents and displacement using the least-squares cubic spline approach. According to Reference 25 there are still some effects to be explained but dynamic lift calibration results were obtained agreeing to within 2 percent of the static calibration values. Dynamic calibrations are much faster than conventional calibrations. A major advantage of dynamic calibration is the absence of loading fixtures.

Another approach is to use an Identification and Parameter Estimation Procedure. This technique consists of describing the dynamics of motion of the model in a state space formulation. In postulating the state space model, Lagrangian methods are used to represent all the physical relations governing the motions and the energy storage and dissipation terms.

The state variables can be chosen to be compatible with either the body-axes or wind-axes systems. Using the experimental responses of the system, which are the observations, equations of observation based on the state space model can be developed. The output error method of parameter estimation finds the difference between the actual observations and the mathematical model estimations for the same input. A cost function based on the error is minimized by adjusting the parameters of the postulated model. This approach has been well researched and has matured into a reliable method of obtaining certain stability derivatives from aircraft flight tests,[26] and has also been used in wind-tunnel based derivative estimation.[27]

Figure 6-21 shows a block diagram of closed-loop control for an MSBS conceptualized for rotary-balance testing. Such a system is likely to be a multivariable nonlinear system because of the nonlinear relations between the coil currents and the magnetic forces acting on the model. The control problem relates to the stable control of the model attitude under sinusoidal and/or ramp inputs. The calibration problem relates to estimation of the parameters of the model, which describes the inertial, magnetic and aerodynamic coefficients relating the coil currents and model displacement.

Direct use of parameter estimation techniques to input-output data from a closed-loop system often creates identifiability problems [26] Such problems arise from linear dependence and correlation caused by feedback. The problems can be overcome with an appropriate choice of input disturbances and loop gain adjustments.

An example of the application of parameter estimation procedures to magnetic balance testing follows

6.3.6 Two-Degree-of-Freedom Longitudinal Model for the NASA-Langley 13" MSBS

As an example of the control and modeling problem, pitch/heave modeling of closed-loop system responses of an aerodynamic model in the NASA-Langley 13" MSBS is considered. Figure 6-22 shows a schematic diagram of the longitudinal control and measurement scheme For this wind-off study the control loop was disturbed with doublet inputs and the coil currents and model displacements were recorded for analysis.

A state space model is postulated to describe the motion of the aerodynamic test model. The Lagrangian approach is used to represent mathematically the energy functions involved in the magnetic and inertial systems. In the model for two degrees of freedom, the control and bias coils in the yy plane are merged into a pair of equivalent fore and aft currents, i_1 and i_2. These are the input to the system. The resulting model displacements are the output of the system.

State equations:

$$\begin{bmatrix} \dot{z}_1 \\ \dot{z}_2 \\ \dot{\theta}_1 \\ \dot{\theta}_2 \end{bmatrix} = \begin{bmatrix} 0 & 1 & 0 & 0 \\ \beta_1 & \beta_2 & 0 & 0 \\ 0 & 0 & 0 & 0 \\ 0 & 0 & \beta_3 & \beta_4 \end{bmatrix} \begin{bmatrix} z_1 \\ z_2 \\ \theta_1 \\ \theta_2 \end{bmatrix} + \begin{bmatrix} 0 & 0 \\ \beta_5 & \beta_6 \\ 0 & 0 \\ \beta_7 & \beta_8 \end{bmatrix} \begin{bmatrix} i_1 \\ i_2 \end{bmatrix}$$

Observation equations:

$$\begin{bmatrix} y_1 \\ y_2 \end{bmatrix} = \begin{bmatrix} 1 & 0 & 0 & 0 \\ 0 & 0 & 1 & 0 \end{bmatrix} \begin{bmatrix} z_1 \\ z_2 \\ \theta_1 \\ \theta_2 \end{bmatrix}$$

The Maximum Likelihood Estimation (MLE) Procedure is an output error method. Using the MLE method the parameters of the state equations can be estimated by minimizing the cost function,

$$L = \frac{1}{2} \sum (z - y)^T R^{-1} (z - y) + \frac{N}{2} ln|R| + \text{constant}$$

where

ζ is the estimated system response

y is the measured system response

R is the noise covariance

N is the number of samples used

Under wind-off conditions the state space model parameters have the following physical significance:

β_1 magnetic stiffness in heave

β_2 magnetic damping in heave

β_3 magnetic stiffness in pitch

β_4 magnetic damping in pitch

β_5, β_6, β_7, and β_8 provide current sensitivity to pitch and heave from each coil set.

For the same tests made under wind-on conditions, the model parameters correspond to the following:

β_2 magnetic damping in heave and the translational acceleration derivative $C_{m_{\dot{\alpha}}}$

β_3 magnetic stiffness in pitch and the static stability C_{m_α}

β_4 magnetic damping in pitch and rotary pitch damping term C_{m_q}

To date, the two-degree-of-freedom pitch/heave modeling has provided the following results for wind-off conditions: The vertical heave mode is unstable and the damping in heave is near zero. In terms of the pitching, the rotary damping results in a second-order dynamic system with low damping. The validity of the MLE modeling results was assessed by comparing the responses of the real system to those predicted by the mathematical model. The actual and estimated time trajectories for the same input disturbance showed good agreement.

The wind-off modeling of the model motion to extract the magnetic coefficients has been completed. Additional tests have to be made under wind-on conditions. After validation, this technique should be able to provide dynamic stability derivatives analogous to those obtained from the small-amplitude forced-oscillation technique. A major advantage of the MSBS in this context is the ease with which the center of rotation can be varied. This could make it practical to estimate separately the rotary and translational effects.

6.3 7 Remaining Problems Specific to MSBS Rotary Balance Testing

1. The problem of generating a continuous roll rate of 5 revolutions per second at a sufficiently large test scale must be addressed.

2. Combined rotary/oscillatory motions would require closed-loop control and introduce problems of alternating power and possibly large losses in the superconducting coils. Also, complex control algorithms would be required to achieve tight control of such complex model motions.

3 Nonintrusive model attitude sensing must be demonstrated under conditions of continuous rolling Inertial strap-down systems with telemetry are an alternative to existing techniques.

4. The ability of analysis techniques (like Identification/Parameter Estimation, or regression techniques) to evaluate and separate dynamic derivatives and coefficients must be demonstrated. Strong loop closures could pose problems in this type of analysis. These techniques should first be validated by making dynamic derivative measurements on an MSBS using forced-oscillation techniques

6.3.8 Summary

Especially at transonic speeds, model support interference can create difficulties. These problems can be of particular concern for the bulky mechanical rigs used for rotary-balance testing. The use of magnetic suspension and balance systems

offers the possibility of a unique solution to problems of support interference. Application of magnetic suspension techniques to rotary-balance testing appears feasible at small scale, but requires further development.

In recent years there have been major advances in ac superconductors, magnetic materials, power supplies, position and motion sensors, digital computers and analysis techniques. All of these advances improve the chances for building a large MSBS capable of support-interference-free aerodynamic testing. Demonstrations are needed of MSBS techniques at subsonic/transonic speeds for static and dynamic derivative estimation, possibly with additional degrees of freedom. Many activities are now in progress toward this end.

6.4 REFERENCES

1. Orlik-Rückemann, K. J.: Dynamic Stability Testing in Wind Tunnels. NRC, NAE LTR-UA-41, Ottawa, March 1977.

2. Beyers, M. E.: Investigation of High-Maneuverability Flight Vehicle Dynamics. ICAS-80-7.2, Oct. 1980, pp. 278-292.

3. Bihrle, W., Jr.; and Barnhart, B.: Spin Prediction Techniques. J. Aircraft, Vol. 20, Feb. 1983, pp. 97–101.

4. Beyers, M. E.: A New Concept for Dynamic Stability Testing. NRC, NAE LTR-UA-53, Ottawa, Sept. 1980.

5. Beyers, M. E.: A New Concept for Aircraft Dynamic Stability Testing. J. Aircraft, Vol. 20, Jan. 1983, pp. 5–14.

6. Beyers, M. E.. Characteristic Motions for Simulation of Post-Stall Manoeuvres and Flight Instabilities. AeSSA/SAIAeE J., Vol. 5, No. 1, 1984, pp. 20-34.

7. Tobak, M.; and Schiff, L. B.: On the Formulation of the Aerodynamic Characteristics in Aircraft Dynamics. NASA TR R-456, Jan. 1976.

8. Tristrant, D.; and Renier, O.: Récents developpements des techniques de simulation dynamique appliquées à l'identification des paramètres de stabilité. AGARD-CP-386, No. 22, Nov. 1985.

9. Hanff, E. S.. Determination of Non-Linear Loads on Oscillating Models in Wind Tunnels. Proc. 10th ICIASF, St. Louis, Sept. 1983.

10. Murphy, C. H.: Free-Flight Motion of Symmetric Missiles. BRL Report 1216, Aberdeen Proving Ground, July 1963.

11. Beyers, M. E.. Rolling Motion of Canard Missiles in Wind Tunnel Free-Flight Tests. CSIR Report ME 1561, Pretoria, March 1978.

12. Beyers, M. E.; and Huang, X. Z.. The Orbital Platform Concept for Nonplanar Dynamic Testing. NRC, NAE-AN-52, Ottawa, May 1988.

13. Mandl, P., and Pounder, J. R.. Wind Tunnel Interference on Rolling Moment of a Rotating Wing. NRC AR-10, Ottawa, 1951.

14. Beyers, M. E.: A New Look at the Tobak-Schiff Model of Nonplanar Aircraft Dynamics. NRC, NAE LTR-UA-101, Ottawa, December 1989.

15. Kalviste, J.: Spherical Mapping and Analysis of Aircraft Angles for Maneuvering Flight. AIAA-86-2283, Aug. 1986

16. Tournier, Marcel, and Laurenceau, P.. Suspension Magnétique d'une Maquette en Soufflerie. (Magnetic Suspension of a Model in a Wind Tunnel.) La Recherche Aeronautique No. 59, July-August 1957, pp. 21–27.

17. Tuttle, Marie H., Kilgore, Robert A., and Boyden, Richmond P. Magnetic Suspension and Balance Systems- A Selected, Annotated Bibliography. NASA TM-84661, July 1983.

18. Holmes, F. T.: Axial Magnetic Suspensions, Review of Scientific Instruments, Vol. 8, November 1937, pp 444–447

19. Goodyer, Michael J.. The Generation of Rolling Moments with the Superconducting Solenoid Model. NASA CR-172520, January 1985, 24 p.

20. Parker, H. M.: Principles, Typical Configurations and Characteristics of the University of Virginia Balance Presented at the ARL Symposium on Magnetic Wind Tunnel Model Suspension and Balance Systems, April 1966.

21. Bloom, H. L.: Design Concepts and Cost Studies for Magnetic Suspension and Balance Systems, Final Rept. November 1980—March 1981. NASA CR-165917, July 1982, 346 pp.

22. Boom, R. W.; Eyssa, Y. M., McIntosh, G. E.; and Abdelsalam, M. K.. Magnetic Suspension and Balance Study. NASA CR-3802, July 1984.

23. Boom, R. W.; Eyssa, Y. M.; McIntosh, G. E., and Abdelsalam, M. K.. Magnetic Balance System Advanced Study NASA CR 3937, October 1985.

24. Wu, Yu Yuan: Design of a Horizontal Liquid Cryostat for Refrigerating a Flying Superconducting Magnetic in a Wind Tunnel. NASA CR-165980, Progress Report June 1981–April 1982, August 1982, 65 pp.

25. Eskins, J: Further Investigation into Calibration Techniques for a Magnetic Suspension and Balance System. NASA CR 178056, February 1986, 44 pp.

26. Maine, R. E.; and Iliff, K. W.: AGARD Flight Test Techniques Series, Vol 3 on Identification of Dynamic Systems-Applications to Aircraft Part I: Output Error Approach.

27. Balakrishna, S.; and Niranjana, T.: Wind Tunnel Dynamic Flying Study of the Pitching Moment Derivatives of Standard Dynamics Model in Active Control. AIAA Paper 87-2626, Atmospheric Flight Mechanics Conference, Monterey, August 1987.

6.5 NOMENCLATURE

b	wing span
$\bar{c}$	mean aerodynamic chord
C_{ik}	dynamic derivative with respect to reduced-rate parameter $\frac{\partial C_i}{\partial\left[\frac{k\ell}{2V_\infty}\right]}$, $i = X, Y, Z, \ell, m, n$; $k = q, \dot{\alpha}, \dot{\sigma}, \dot{\theta}$ ($\ell = \bar{c}$ or d) $k = p, r, \dot{\beta}, \dot{\phi}, \dot{\psi}, \dot{\lambda}$ ($\ell = b$ or d)
C_ℓ	rolling-moment coefficient, $L/(q_\infty S\ell)$, $\ell = b$ or d
C_m	pitching-moment coefficient, $M/(q_\infty S\ell)$, $\ell = \bar{c}$ or d
C_n	yawing-moment coefficient, $N/(q_\infty S\ell)$, $\ell = b$ or d
C_X, C_Y, C_Z	body-axes force coefficients
$\bar{k}$	generalized reduced-rate parameter
K_1, K_2, K_3	tricyclic vectors
ℓ	generalized reference length
p, q, r	body-axes angular velocities
r_0	orbital radius or spin radius
u, v, w	body-axes or fixed-plane velocity components, where appropriate
V	velocity
V_∞	free-stream velocity
x, y, z	body-axes system
X, Y, Z	inertial frame of reference
x_c	center of mass coordinate
α	angle of attack $= \tan^{-1}(w/u)$
β	angle of sideslip $= \sin^{-1}(v/V)$
Γ	balance angle of pitch
Θ	strut pitch angle
Λ	tangential tilt angle
$\dot{\lambda}, \dot{\phi}$	coning rate
ν_2	secondary oscillation frequency
ξ, η, ζ	platform frame of reference
σ	orbital helix angle
σ, ϕ'	aerodynamic angles of attack and bank
ϕ_0	model roll angle relative to sting
$\dot{\phi}_1, \dot{\phi}_2$	epicyclic vector rates
Φ	orbital roll angle
ψ, θ, ϕ	Euler angles
ψ_m, θ_m, ϕ_m	modified Euler angles
Ψ	sting-shaft roll angle
ω	orbital angular velocity
$\bar{\omega}$	reduced coning rate $= \dot{\lambda}\ell/(2V_\infty)$
Ω	reduced orbital frequency $= \omega r_0/V_\infty$; also, coning rate

Superscripts

$(\dot{})$	differentiation with respect to time
$(\bar{})$	fixed-plane system
$(\sim)$	nonrolling angles
$(')$	aerodynamic axes system
$(\rightarrow)$	vector

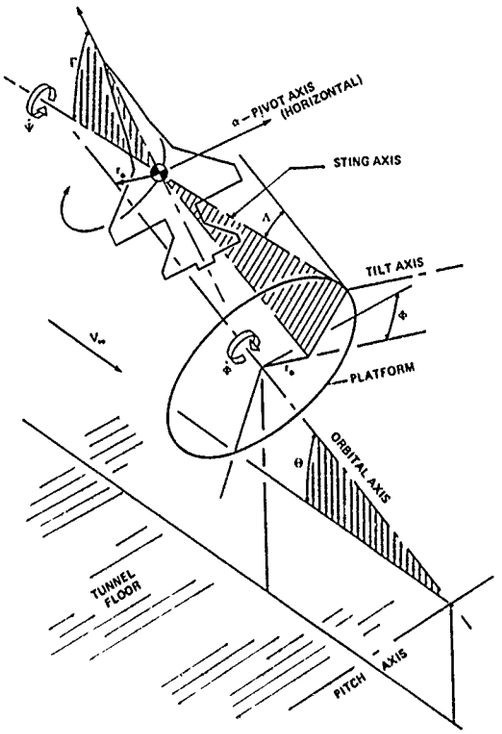

Figure 6-1. Geometrical arrangement.

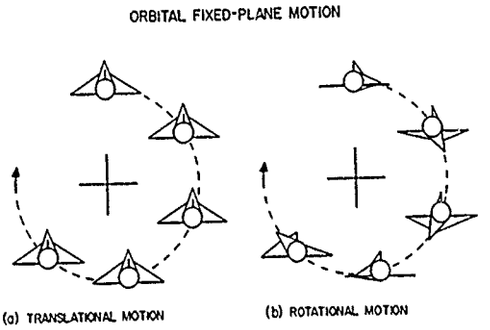

Figure 6-3. Orbital fixed-plane motion.

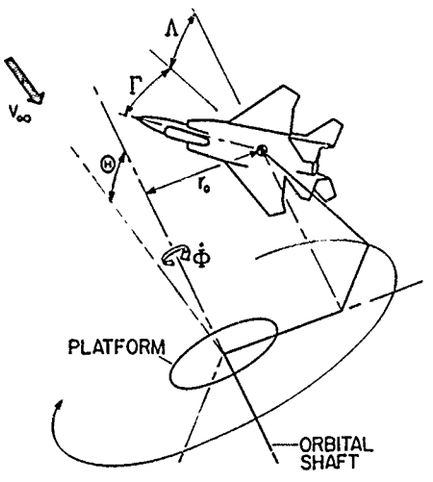

Figure 6-2. Simulation of aircraft spin.

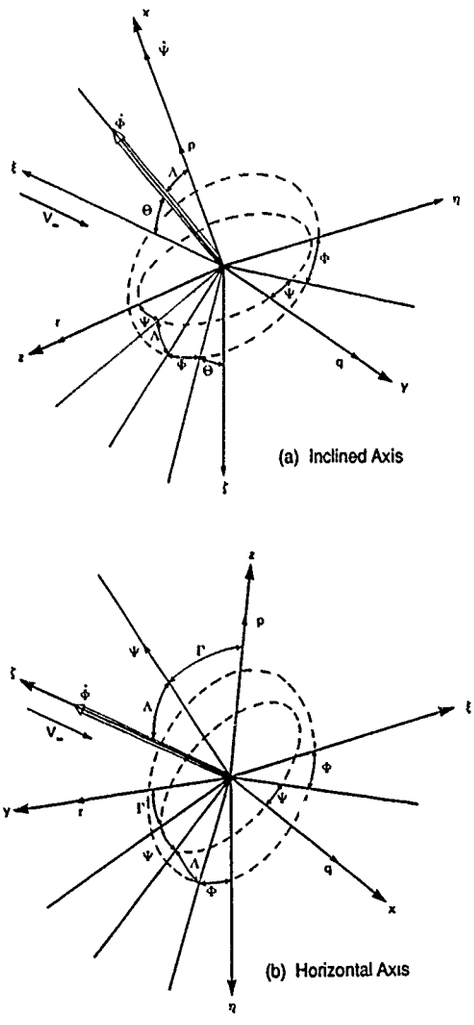

Figure 6-4. Sequences of rotations.

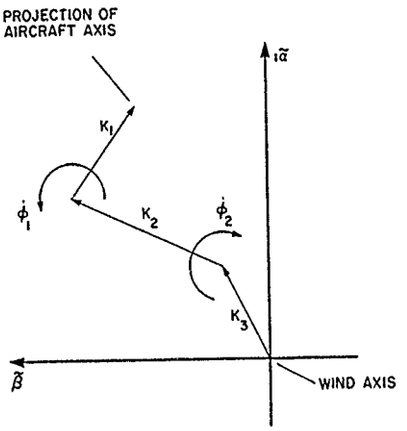

Figure 6-5. Epicyclic motion.

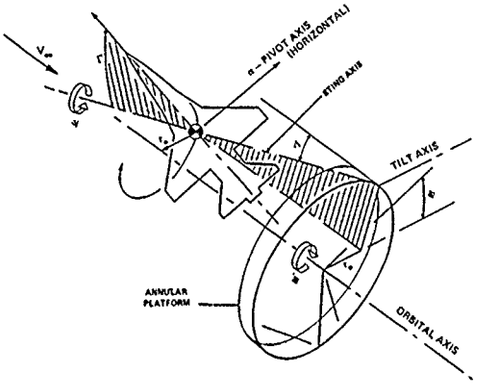

Figure 6-8. Orbital motion geometry (horizontal axis).

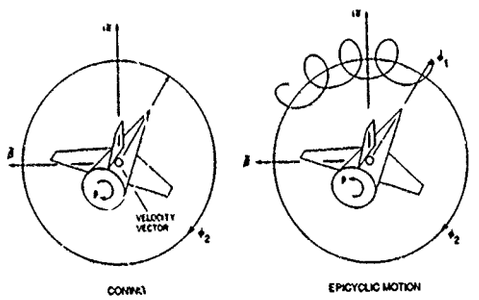

Figure 6-6. Nonplanar characteristic motions

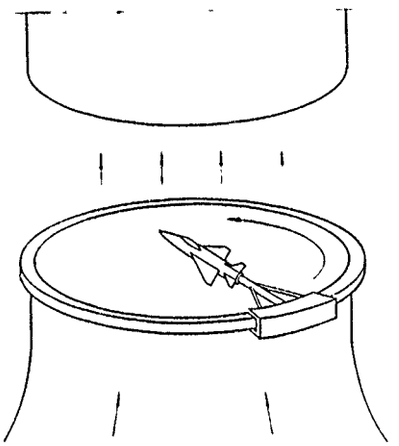

Figure 6-9 Orbital-platform concept for vertical tunnel

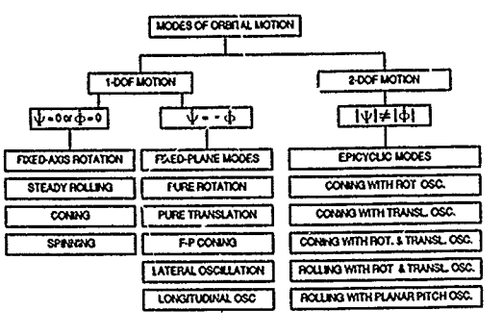

Figure 6-7. Categories of orbital characteristic motions

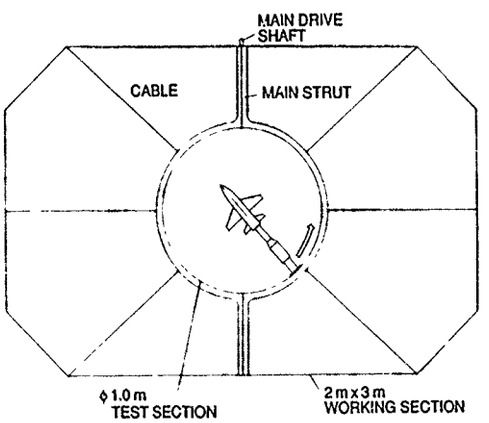

Figure 6-10 Layout in 2m × 3m Low Speed Wind Tunnel.

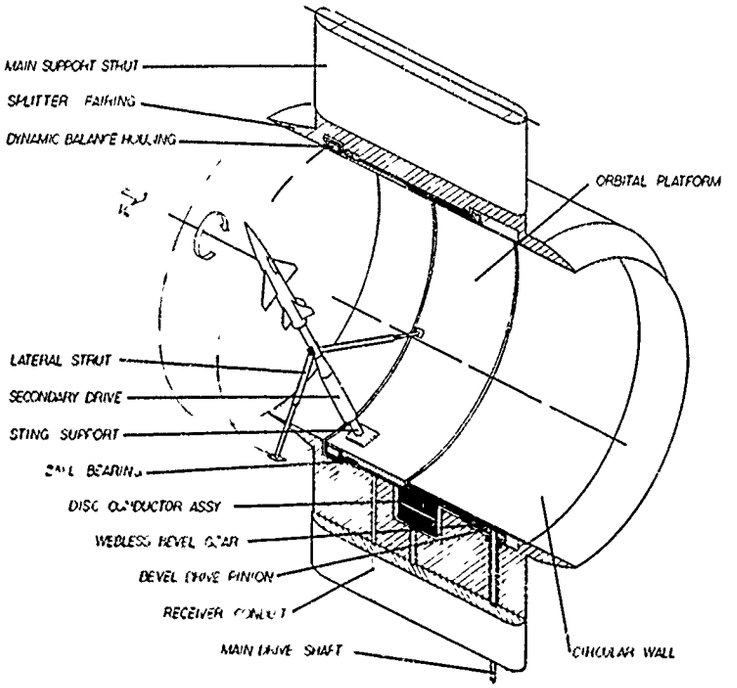

Figure 6-11. Layout of OPLEC apparatus.

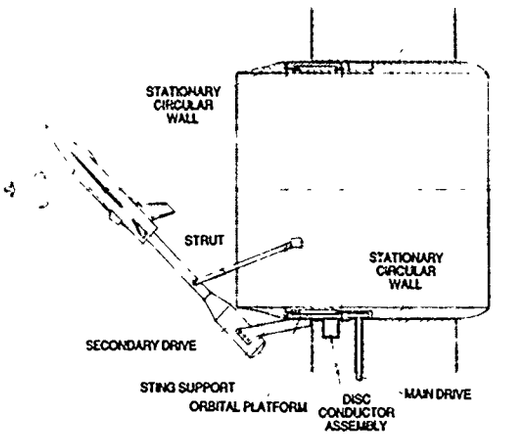

Figure 6-12. External orbital-platform concept.

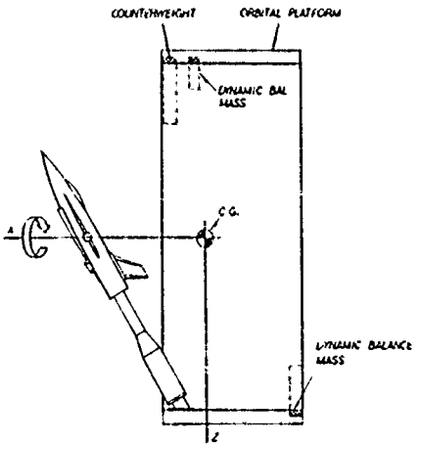

Figure 6-13 Dynamic balancing scheme.

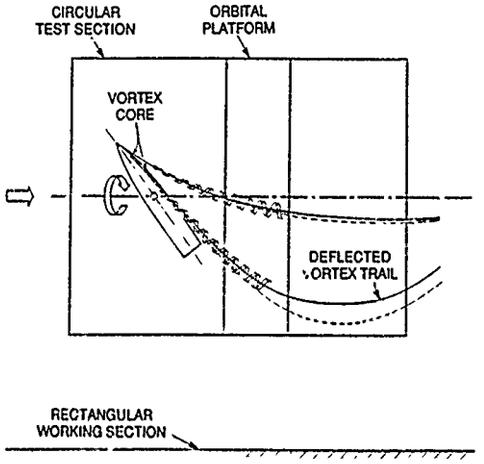

Figure 6-14. Vortex-wake/wall interaction.

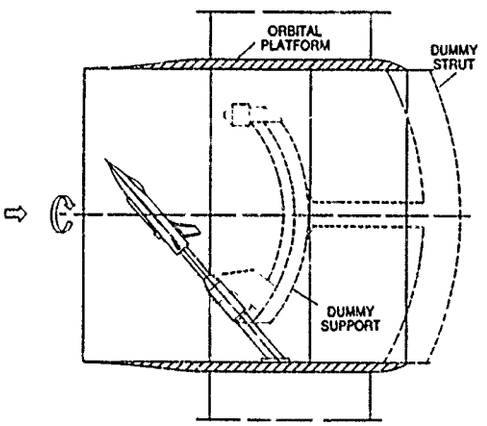

Figure 6-15. Investigation of support interference

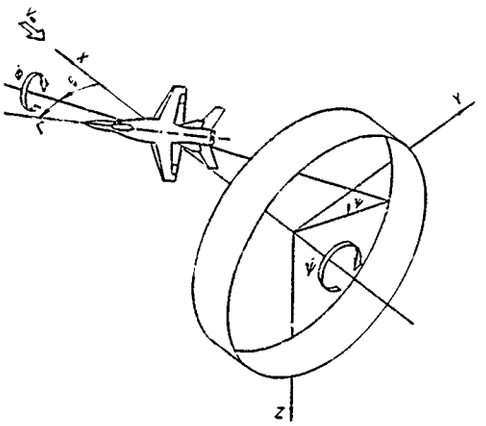

Figure 6-16. Epicyclic motion geometry.

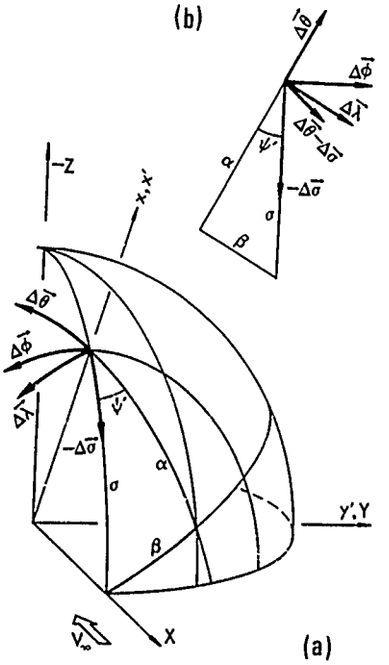

Figure 6-17. Characteristic motion vectors.

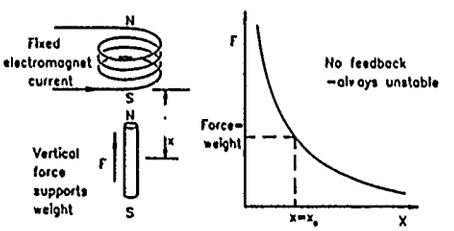

Open-Loop System - Not practical. Always unstable in at least one degree of freedom (Earnshaw's theorem).

Figure 6-18. Open-loop system.

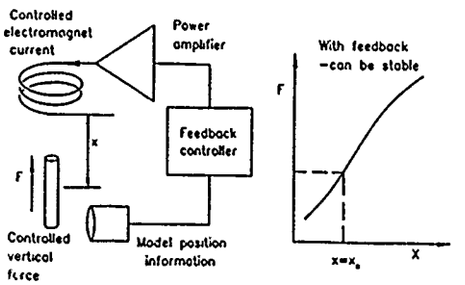

Closed-Loop System - Practical, relies on artificial stiffness and damping Position and velocity feedback required.

Figure 6-19. Closed-loop system

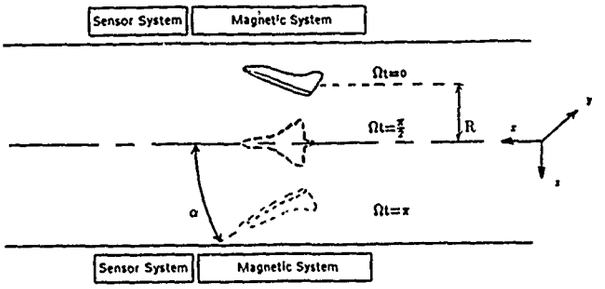

Figure 6-20. Idealized coning motion in MSBS.

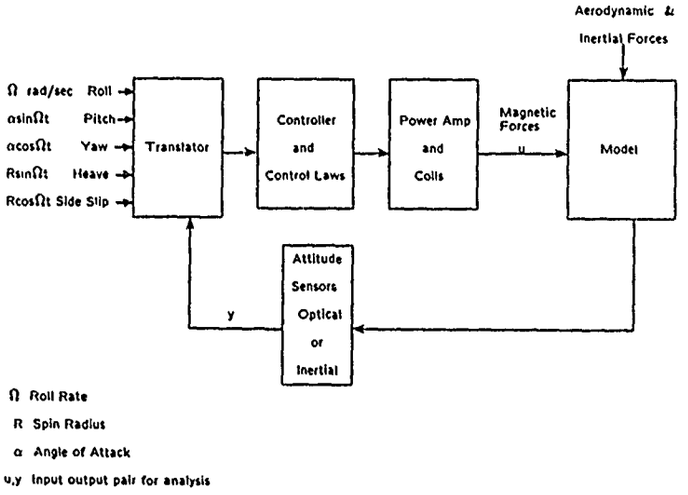

Figure 6-21. Idealized MSBS closed-loop system for rotary-balance testing.

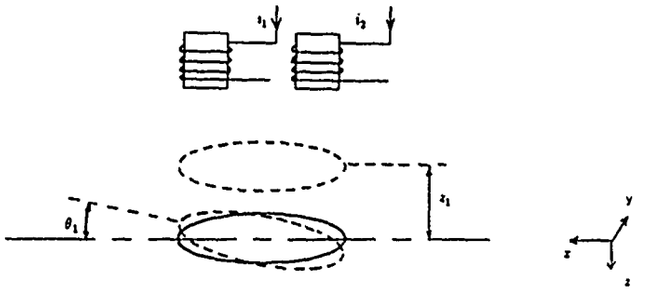

Figure 6-22. Two-degree-of-freedom longitudinal motion in 13 inch MSBS.

CHAPTER 7

ROTARY-BALANCE DATA FOR TYPICAL CONFIGURATIONS

7.0 INTRODUCTION

The experimentalist engaged in rotary-balance testing attempts to provide the most accurate prediction possible of extremely complex aerodynamic phenomena. In this endeavor, he must be cognizant of numerous flow mechanisms and the potential impact of rotary aerodynamics on aircraft performance and safety. In addition to the complexity of separated, unsteady flows, the configuration-dependent nature of many important parameters complicates the analysis and application of the data. Finally, the fact that seemingly minor configuration changes can result in marked changes in aerodynamic behavior demands a careful, deliberate test procedure and an awareness of typical rotary aerodynamic data.

The data presented in this chapter illustrate many significant trends and results which have been obtained during rotary-balance testing by the participating AGARD organizations. The examples selected and the discussion which follows are oriented toward providing a broad perspective of rotary data, with particular emphasis on the large effects of configuration variables and test conditions which may not be commonly experienced by personnel engaged in the more common, conventional static wind-tunnel testing techniques. For the reader's convenience, Table 7-1 lists the figures which illustrate the various effects discussed.

It should also be noted that the method of presenting rotary-balance data varies considerably from one country to another, perhaps due to the independent development of these techniques in the different countries of AGARD. For example, the nondimensional rate parameter $\Omega b/2V$ is also denoted by $\omega b/2V$ or Ω.

7.1 NASA-LANGLEY

From the more than 60 airplane configurations tested on the rotary balance at Langley to date, several results have been selected to illustrate some of the more important effects noted. These data include the effects of rotation rate and sideslip, as well as airplane configuration effects and are presented in body axes.

7.1.1 Effect of Rotation Rate

The variations of the aerodynamic moments with rotation rate can be highly nonlinear, as illustrated in Figures 7-1 through 7-3. Also, as shown, the type of variation realized can be either desirable or undesirable, and is highly dependent on the configuration. For example, model A has autorotative rolling and yawing moments over a significant range of $\Omega b/2V$ In addition, the model exhibits increasing nose-up pitching moments with increasing rotation rate and yawing and rolling moments in symmetrical conditions at zero rotation rate. All of these aerodynamic characteristics are undesirable. In comparison, model C exhibits desirable nose-down pitching moments with increasing rotation rate, and it is also highly damped in yaw (it does, however, have an undesirable yawing moment at zero rotation rate). Other configurations exhibit different combinations of desirable and undesirable behavior.

7.1.2 Effect of Sideslip

The variation of pitching moment with sideslip angle and rotation rate is presented in Figure 7-4 for a typical configuration. As is the case for many airplanes, sideslip has only a small effect on the static pitching moment. However, sideslip can appreciably influence the rotational pitching moment by skewing the pitching-moment variation with rotation rate, as shown here. Consequently, additional nose-down pitching moments are produced when the signs of the sideslip angle and rotation are the same and, conversely, nose-up pitching moments are realized when the rotation and sideslip angle are of opposite signs. Similar effects of sideslip can be exhibited in yaw.

7.1.3 Effect of Components

The data of Figure 7-5 show the complete model to be autorotative in yaw at low rotation rates, which is responsible for the configuration's spin mode. This configuration was selected to illustrate the adverse interactions which can occur between airplane components. As shown, the isolated fuselage is damped Adding the wing to the fuselage increases the damping, which is not significantly affected by the addition of the horizontal tail However, the damping of the wing-fuselage combination is significantly increased by the addition of the vertical tail. This situation is greatly altered when the vertical tail is in the presence of the horizontal tail. The damping contribution of the vertical tail is not only negated by the presence of the horizontal tail, but the vertical tail is now a highly propelling component, and is responsible for the model's autorotative behavior.

7.1.4 Influence of Forebody Strakes

The rotational moment characteristics and the existence of static rolling and yawing moments in symmetrical flight (Figure 7-6) are all highly indicative of a susceptibility to departure from controlled flight Since these undesirable characteristics were attributed to the model's forebody, the judicious location of strakes on the forebody can, as shown in Figure 7-6, alter the aerodynamic behavior to a large degree.

7.1.5 Effect of Control Deflection

Control deflections can significantly alter the aerodynamics in rotary flow. This effect is illustrated in Figure 7-7, which presents the rotational yawing-moment characteristics for a symmetrical canard deflection of 0° and −60° (trailing edge up). As shown, deflecting the canard −60° results in an autorotative configuration, whereas with an undeflected canard the yawing moment is damped. Since the −60° deflected canard yawing moment characteristics are equivalent to those with the canard off, the presence of the undeflected canard obviously alters the autorotative behavior of the basic configuration.

7.2 NASA-AMES

A research model was investigated[1,2] in the NASA Ames Research Center 12-Foot Pressure Wind Tunnel to study fundamental flow mechanisms (see Figure 7-8) that could produce autorotation on a simplified airplane configuration. The principal objective was to determine the sensitivity of the rotational flow fields to Reynolds number variations. Several nose and tail configurations were tested over a Reynolds number range of 0.15×10^6 to 1.5×10^6 based on the body diameter. Figure 7-9 shows the model and balance arrangement, including a sting balance and separate balances in the nose and tail. Figure 7-10 shows the various model components that were tested. Most of the experiments were at $M \approx 0.25$, and the angle of attack was varied from 45° to 90°. The rotation rate ranged from 0 to ±600 rpm, resulting in nondimensional spin rates up to 0.17. All data are presented in body axes, except where otherwise indicated.

It has been shown by many investigators that a slender aircraft forebody at high angles of attack can produce large side forces, even at zero sideslip, due to asymmetric separation and vortices on the leeward side of the body. It has also been shown by several investigators that rolling the forebody about its own longitudinal axis to a different position can cause the orientation of the forebody flow asymmetry and vortices to switch to a mirror image as viewed in the cross-flow plane. One objective of this test was to determine the behavior of these vortices and the resulting side force and moments with rotation rate about the model spin axis and with changes in Reynolds number. Figure 7-11 shows the variation in the spin moment coefficient (rolling moment about the airplane spin axis, i.e., the axis of rotation of the rotary-balance apparatus) with the nondimensional spin rate Ω or $\omega b/2V$ for the configuration N_1T_1 at an angle of attack of 60°. The figure shows that at $R_d = 0.3 \times 10^6$ the direction of the spin moment can be reversed (even at $\Omega = 0$) by rolling the nose 90° about its own axis. It also shows that the variation with Ω is similar regardless of the direction of the moment at $\Omega = 0$. The effect of changing Reynolds number is also apparent for both nose orientations. The variation with Ω is nearly linear, and the slightly negative slope indicates spin damping or an antispin, rather than pro-spin moment.

A more interesting experimental result was found when the nose section with the square cross section and rounded corners (N_2) was tested (see Figure 7-10). An example of the aerodynamic characteristics of this nose shape in a flat spin are shown in Figure 7-12. This figure shows the nose side-force variation with rotation rate for increasing Reynolds numbers. Particularly interesting is the observed hysteresis in the middle Reynolds number range. As shown in the sketch in Figure 7-12(a), at low Reynolds numbers the flow separates on the leeward corner producing a force in the direction of the spin. At higher Reynolds numbers the flow remains attached on the leeward corners resulting in an antispin side-force contribution to the total spin moment. At Reynolds numbers in between, for example, $R_d = 0.5 \times 10^6$, the flow stays attached with increasing rotation rate until approximately $\Omega b/2V = 0.08$. At this point the local flow angle is too great for the flow to remain attached, and it separates, resulting in a sudden change in the side force to the positive or pro-spin direction. With decreasing rotation rate, the flow remains separated until $\Omega = 0.03$ where the flow reattaches on the leeward corner. Separation and reattachment as shown produce a hysteresis not unlike that seen on airfoils when the lift shows hysteresis with increasing and decreasing angle of attack. If the Reynolds number is high enough, the flow never separates from the leeward corner and the variation of the side force can be quite linear with Ω. Figure 7-13 shows the nose side force for an angle of attack of 45°. No hysteresis effects were observed, but substantial effects of Reynolds number are observed. The wide variation with Reynolds number, particularly as shown in Figure 7-12, shows the importance of having high enough test Reynolds numbers to be representative of full-scale flight.

Various approaches have been used when the Reynolds number cannot be simulated. The use of laminar results can be expected to yield useful results as long as transition effects are not important or stall characteristics are not significantly different at the turbulent flow conditions (see Section 8.3). The question of accounting for Reynolds number discrepancies is discussed in Section 8.4.

A set of experiments[3,4] were conducted on a model now known as the Standard Dynamics Model (SDM), shown in Figure 7-14. The tests were conducted in the NASA-Ames Research Center 6- by 6-Ft Supersonic Wind Tunnel on the apparatus described earlier in Section 3.2.

The tests were conducted at Mach 0.6 and a Reynolds number of 0.88 million based on the wing mean aerodynamic chord. These test conditions were chosen to match those of complementary forced-oscillation tests performed at the NAE[5,6] The aerodynamic coefficients measured in the 6- by 6-ft tunnel included normal force, pitching moment, side force, yawing moment, rolling moment and axial force. The model center of rotation was located at 0 35 of the wing mean aerodynamic chord. This point was also chosen as the moment reference center.

Figure 7-15 shows the force and moment coefficients measured at $\alpha = 30°$ for $\beta = 0°$ and $\beta = \pm 5°$ At zero angle of sideslip, symmetry conditions dictate that the lateral aerodynamic coefficients (C_l, C_n and C_Y) should be odd functions of the spin rate. This is demonstrated by the data presented in Figure 7-15(a). For all angles of attack tested, the lateral aerodynamic coefficients were observed to be nearly linear with respect to the spin-rate parameter over the range of spin rates achieved in the test. The longitudinal aerodynamic coefficients were seen to be even functions of the spin-rate parameter The axial-force and pitching-moment coefficients show a parabolic variation with the spin-rate parameter. Some of this parabolic variation is undoubtedly real, and is probably caused by increased tail lift. However, limitations of data resolution

at these low levels of C_A and C_m, and, in particular, the choice of the moment center position, may also be responsible for exaggerating the scale of the variation.

The effects of variation of sideslip angle are shown in Figure 7-15(b), which presents data obtained at $\beta = -5°$ and $\beta = +5°$. Once again, the linear variation of the lateral aerodynamic coefficients with spin-rate parameter is apparent. The nonlinear variation of the pitching-moment and axial-force coefficients with spin rate is also apparent. The longitudinal aerodynamics also show an effect due to sideslip, which, as expected, introduces a reasonably symmetric and linear component with spin-rate parameter. In general, the results show a reasonable symmetry with direction of sideslip, but with some offsets possibly introduced by small asymmetries in the model and/or the effects of combined centrifugal and aerodynamic loading.

An F-15 model was tested[7,8] in the NASA-Ames Research Center 12-Foot Pressure Wind Tunnel using the Large-Scale Rotary Balance described in Section 3.2. Photographs of the model installed in the 12-foot tunnel and a testing enclosure are shown in Figures 7-16 and 7-17. The angle-of-attack range from 0° to 90° is covered through model/sting combinations as shown earlier in Figures 3-14 and 3-16. The model is a 0.05-scale version of an F-15 fighter configuration with two nose configurations available, one with a nose boom and one without (see Figures 7-16 and 7-17). The center of moments is at 0.26 of the mean aerodynamic chord of the wing. This location is also the center of rotation of the model about the spin axis.

The effects on the aerodynamics of a number of variables were examined during this experiment. Included were variations in Reynolds number, angles of attack and sideslip, sting angle and the presence of a nose boom. The Mach number selected for the majority of the tests was 0.28, since this maximized the Reynolds number capability of the tunnel. The following discussion will introduce some examples of data obtained during this test.

The results in Figures 7-18 and 7-19 show the yawing-moment coefficient for angles attack of 30° and 70°, respectively, for the model with and without the nose boom. The different curves compare results obtained at high and low Reynolds numbers for a given sting angle, and for results obtained with different sting angles at the same Reynolds number. Figure 7-18 shows a linear behavior of the moment with the spin-rate parameter at $\alpha = 30°$ for both the boom-off and boom-on configurations. Some differences caused by Reynolds number variation can be observed at the higher rotation rates, especially for the case with the boom on. There is a slight effect of sting angle on the data, as well, which is observed primarily at the higher rotation rates.

The most interesting of the cases is shown in Figure 7-19 for $\alpha = 70°$. Looking first at the configuration without the nose boom in Figure 7-19(a), there is very little effect of the sting angle at the higher Reynolds number, but at the lower Reynolds number a significant effect of the sting angle is observed at the higher rotation rates. There is also a considerable difference between the results obtained for the two Reynolds numbers using the same sting.

The effects caused by adding the nose boom at this angle of attack are rather dramatic, as can be seen by examining Figure 7-19(b). The first characteristic to note is that the data obtained on the 70° sting at $R = 1.5 \times 10^6$ show a yawing-moment coefficient that is multivalued over a wide range of values of the spin-rate parameter. This multivalued variation and the accompanying hysteresis loop indicate that two flow field states can exist around the model for a given spin rate. Which of the two possible values observed experimentally depends on the past history of the flow, that is, whether that spin rate is approached from a rate that is higher or lower. The hysteresis effect is quite sensitive to model support interference. Although two flow states are also evident for the results obtained using the 45° sting at $R = 1.5 \times 10^6$, the hysteresis is almost negligible. This difference in hysteresis effect and the large difference between yawing-moment coefficient values at negative spin rates demonstrate the sensitivity of the aerodynamics to sting angle differences and resulting support interference effects (see Section 5.1). It is apparent from these results that there is a sizeable influence of the two stings on the leeward flow field which, in turn, affects the yawing moment. At the higher Reynolds number, 4.0×10^6, no hysteresis was observed in the measurements made with either sting, and the results obtained with both stings are in reasonably close agreement.

For the case at $R = 1.5 \times 10^6$, with $\alpha_s = 70°$ and the nose boom on, the initial value of the yawing-moment coefficient was negative. The initial rotation direction was in the negative direction, and the yawing-moment coefficient remained negative until $\Omega b/2V = -0.036$; then it jumped to a positive value. The moment remained positive as rotation rate slowly increased in the negative direction to $\Omega b/2V = -0.12$. The rotation rate was then slowly decreased to zero and increased in the opposite or positive direction. The corresponding yawing-moment coefficient response remained positive until the model reached a value of spin-rate parameter of 0.09 and then jumped to a negative value. As the spin-rate parameter was slowly increased to its maximum value and then decreased through zero, the yawing-moment coefficient again jumped to a positive value as $\Omega b/2V$ decreased through -0.03. However, as the spin-rate parameter was decreased to its maximum negative value and then increased through zero for the second time, the jump in the yawing-moment coefficient to a negative value occurred at $\Omega b/2V = 0.01$ rather than at $\Omega b/2V = 0.09$ as before. It is apparent, following this path as shown, that there is hysteresis in the value of the yawing-moment coefficient with variation of the spin-rate parameter. This type of variation indicates the dependency of the flow-field asymmetry not only on the direction of rotation but also on the history of the rotation direction. It is interesting that this characteristic of a multivalued yawing-moment coefficient was observed only at this angle of attack and a small range of Reynolds numbers on the configuration with the nose boom. Repeated runs at these same conditions produced nearly identical results with only a small variation in the value of $\Omega b/2V$ where the jumps occurred. The repeatability of the jump condition is very sensitive to the Reynolds number.

The effect of variation of sideslip angle on the hysteresis is illustrated in Figure 7-20. Data are shown for $R = 1.5 \times 10^6$ at $\alpha = 70°$ for the boom-on configuration, with β ranging from $-5°$ to $+10°$. At $\beta = 5°$ and $-5°$, the jumps in the yawing-moment coefficient occur at values of spin-rate parameter on either side of the value at which the jump was observed at $\beta = 0°$. For $\beta = 10°$, the flow angularity on the model resulting from the combination of sideslip and rotation angles is apparently not sufficient to cause a jump in the flow orientation as seen in the other cases. For comparison, the data are

shown for the model without a nose boom at $\beta = 0°$ at the same conditions. As seen earlier in Figure 7-19(a), there is little indication of asymmetry, which is a significant contrast to the data obtained with nose boom on.

7.3 AERMACCHI

7.3.1 Introduction

The rotary balance was introduced at AerMacchi with the purpose of providing the necessary aerodynamic data for spin prediction by the equilibrium spin method: the application of such a method requires the availability of the three aerodynamic moment coefficients in a wind axes reference system as a function of rotation speed, angles of attack and sideslip and control deflections. All data in this section are presented in wind axes.

Even though the application of rotary-balance results has now widened to become a source of information for high-angle-of-attack flight simulation, the main parameter of interest in a quick look of results remains the rolling-moment coefficient in wind axes. Most of the following results will concentrate on C_l and, to a lesser extent, on C_n. Pitching moment C_m is normally very little dependent on rotation rate, but the variation shown in tests with sideslip can be used to extract information on pitch damping (Section 7.3.5).

The experience available at AerMacchi mainly covers moderate to high aspect-ratio configurations (transports, executive jets, military trainers) tested at low to moderate angles-of-attack, and combat configurations (both subsonic and high performance) tested in the full angle-of-attack range from 0° to 90°. No fundamental research programs on generic configurations have been undertaken. The main geometric characteristics of a few aircraft models which will be used to illustrate typical effects are listed in Table 7-2.

Phenomena involved in the generation of roll damping can be discussed on the basis of Figure 7-21, which shows derivatives C_{l_w} and C_{n_w} of model A. The angle-of-attack range from 0° to 90° can be divided in three zones:

1. Linear range ($0° < \alpha < \alpha_{st}$), where attached flow conditions exist; prediction is relatively easy by linear theories; and the main contribution to the roll damping derivative is from the wing and, to a lesser extent, from tail surfaces.

2. Stall range ($\alpha_{st} < \alpha \leq 35°$), where the wing behavior dominates; roll damping is heavily influenced by the stall pattern on the wing, and any change affecting wing stall also influences the rotary-balance results.

3. High angle-of-attack range ($35° \leq \alpha < 90°$), where the forebody flow is the main feature and the presence of other components may be effective through their indirect effect on, or direct interaction with, the forebody flow.

The actual boundaries between the three regimes are, of course, heavily dependent on configurational features. The wing stall angle of attack depends on aspect ratio, wing thickness, presence of high-lift devices, presence of vortex-flow effects, etc. On the other hand, the angle of attack where forebody flow starts to be predominant depends mainly on the forebody fineness ratio and cross-section shape. An overlap region may exist for configurations having a high α_{st} (low AR, vortex lift) and high fineness-ratio forebodies, typical of modern high-performance aircraft.

The foregoing classification is well suited to transport aircraft (in which case angles of attack higher than the stall range are not normally of interest) and combat aircraft. Different phenomena may occur at very high angles of attack—for example, on general aviation aircraft which do not feature long forebodies, but no data are presently available at AerMacchi for this class of airplanes.

7.3.2 Linear Range Phenomena

Very little needs to be said about the linear flow regime, which is, of course, the simplest case. However, a few remarks seem appropriate:

1. A linear behavior can be expected only in a fully attached flow situation. This fact has a number of consequences:

   - The range of $\Omega b/2V$ for linear behavior shrinks as angle of attack is increased towards the limit of attached flow at zero rotation (Figure 7-22).

   - The presence of separated flow due to a deployed spoiler, for example, may, in principle, destroy the possibility of linear behavior at any angle of attack.

   - Control deflections and/or sideslip can also introduce asymmetries due to locally higher lift coefficients (Figure 7-23).

2. Measurements in the linear flow regime are always very steady and repeatable.

3. For simple configurations, roll and yaw derivatives agree well with predictions by lifting surface or surface panel programs.

4. Effects of small changes to the configuration can be easily obtained. Effects of control deflections (Figure 7-23) and external stores can be measured (Figure 7-24). Underwing stores usually show very little effect on roll damping, while tip stores have a significant one.

7.3.3 Stall Range Phenomena

In the angle-of-attack range above wing stall, the flow is highly nonlinear and the roll damping behavior of a configuration can be very well correlated with the onset, structure and development of separated flow on the wing. For this reason, the knowledge of the steady $C_L(\alpha)$ curve from static tests and of the flow breakdown pattern from oil flows are essential for the planning and interpretation of rotary-balance tests. Of course, in this regime rotary-balance results will be affected as much as static data by scale effects in cases where the Reynolds number influences the character and development of the flow breakdown. Care must be exercised in the testing procedure (boundary layer tripping) and interpretation of results. Typical results are, of course, heavily dependent on the wing planform parameters, presence of high-lift devices, etc., that influence the character of the stall. A few examples are given in the following discussion.

A typical high aspect-ratio, clean-wing stall is shown by models F (Figure 7-25(a)) and G (Figure 7-25(b)). A progressive reduction in damping is shown with tip stall appearing on the downgoing wing at $\alpha = 8°$ (Figure 7-25(a)). Autorotation is present at stall, with the unstable damping then going progressively to zero when a fully separated flow is obtained (flat plate regime).

Effects of double-slotted flaps (approach configuration) for model F are shown in Figure 7-26. Reductions in damping occur at lower angle of attack compared to the cruise configuration, due to the higher local lift coefficients. Damping is maintained up to stall because flow breakdown is initiated at the wing root. The presence of "stall cells" on the wing is the cause of the discontinuous behavior of the damping at the higher angles of attack. This behavior is typical of high aspect-ratio wings which may be segmented by the presence of nacelles, pylons, fences, struts, etc. A different behavior is shown by model G, in which case the stall starts outboard of the nacelles and significant autorotative moments appear (Figure 7-27).

The behavior of a moderate aspect-ratio thick wing (model B1) with slow propagation of the stall from the root is shown in Figure 7-28. Roll damping reduces progressively to zero without any significant autorotative tendency. Zero damping is present when complete separation has been reached.

Effects of a wing change on the same model, to an airfoil having a higher $C_{L\max}$ followed by an abrupt lift loss, are shown in Figure 7-29 (Model B2). Two flow states are possible for $11° < \alpha < 17°$, with attached or separated flow on each wing depending on the past history of the flow itself. The same behavior is also shown by the rotary-balance data. The damping is linear up to $\alpha = 10°$, while at $\alpha = 13°$ a hysteretical behavior is shown. The branch passing through zero corresponds to attached flow on both wings, while, after the downgoing wing has stalled at $\Omega b/2V \simeq 0.11$, the second branch of the curve corresponds to attached flow on one wing and separated flow on the other. At higher angle of attack, the damping goes to zero (fully separated flow on both wings).

The effect of aerodynamic fixes (a fence plus vortex generators on the same wing) shows that, at the same angle of attack, the value of $\Omega b/2V$ for flow breakdown on the downgoing wing is increased to about 0.13. The difference in lift between the two wings is also reduced, thus leading to a smaller hysteresis loop (Figure 7-30).

Effects of a positive sideslip angle of 10° on model C are shown in Figure 7-31. In this case, a nonlinearity is introduced by the fact that the flow is relieved on the retreating wing and worsened on the advancing one. The values of $\Omega b/2V$ for the breaks in C_l and C_n are correspondingly displaced asymmetrically.

Effects of control deflections are also shown for model C (Figure 7-32). Aileron and aileron plus spoiler effects show that an apparent damping is produced by the fact that the rolling moment generated by the spoiler (on the right wing) is progressively reduced by wing stall when the wing is downgoing, and increased when the wing is upgoing.

The behavior of a configuration characterized by the presence of extensive vortex flow (model E) is shown in Figure 7-33. The well-organized structure of the vortex flow produces a reasonably linear behavior up to the angle of attack for maximum lift, which is relatively high (about 30°). The increasing unsteadiness of the flow is shown by the increasing scatter of the data.

7.3.4 High-Angle-of-Attack Range

Rotary-balance results of combat aircraft configurations in the high-angle-of-attack range are governed by the forebody flow. For any forebody, an angle of attack exists where a vortex flow is formed: this onset angle of attack depends mainly on forebody fineness ratio. The structure of this vortex flow changes with angle of attack, forebody cross section and detailed shape; one or more vortex pairs may be present. The vortex structure may be symmetric or prone to be bistable and produce a natural asymmetry. All these effects may be influenced by rotation, and small side forces on the forebody can produce large damping or propelling moments around the rotation axis. The presence and position of items such as inlets are usually important only through their indirect effect on the forebody flow, but the wings and tail surfaces may interact directly with the forebody vortices.

The available experience on the dominant geometrical characteristics is still rather limited, as is the knowledge of modifications that may change the actual behavior. A few examples will be given in the following.

Broadly similar configurations (from a general arrangement point of view) may show quite different results. Figures 7-34 to 7-36 show the roll damping of three aircraft designs of the same class (models A, C and D): one of them shows a high damping, one has a moderate damping and the third one shows a propelling behavior. The differences noted are attributed to variations in the fuselage cross-sectional shapes used.

The large contribution from the forebody is shown by Figure 7-37 (model A). The presence of the other aircraft components (wings and empennage) has a minor effect on the overall damped behavior.

Flow asymmetries (at zero rotation) may have profound effects on the results. These may be due either to small model or airflow asymmetries or to the natural bistable behavior of forebody flows, which most configurations show at least in a small angle-of-attack range. Such asymmetries can produce large propelling moments and, moreover, can destroy the effect of rotation rate. Figure 7-38 shows one such case for model E. A very narrow range of large asymmetry is shown from $\alpha = 64°$ to 70°. The rotary-balance results show a progressive increase of damping up to $\alpha = 60°$, and a sharp reduction at $\alpha = 65°$ in the presence of a large flow asymmetry. At higher angles of attack, the value of the damping remains approximately constant while the asymmetry reduces progressively to zero.

The boundary layer state has an important influence on the location of separation on forebodies. Figure 7-39 shows the large effect of transition tripping on the sides of the forebody of model E. The corresponding flow visualizations show the different positions of the turbulent separation versus the laminar separation. This type of effect draws attention to the importance of Reynolds number in this flow regime, and to the need for a proper simulation of the flow state in order that the rotary-balance results may be applicable to the prediction of full-scale aircraft behavior.

7.3.5 Evaluation of Pitch Damping

Within the linear flow regime, information on the pitch damping derivatives C_{L_q} and C_{m_q} can be easily extracted from rotary-balance results under a few simple assumptions, namely:

(a) Aerodynamic coefficients can be represented as the sum of angle of attack, sideslip and rotation rate effects.

(b) There are no interdependencies between longitudinal and lateral-directional effects or, at least, symmetry is maintained, so that lift and pitching moment depend on angle of attack and pitch rate. Possible dependency on sideslip, roll rate, etc. is symmetric.

Under these assumptions, the longitudinal coefficients can be expressed as:

$$C_L = C_L(\alpha) + C_{L_q}(\alpha)qc/2V + C_{L|\beta|}(\alpha)|\beta| + C_{L|p|}(\alpha)|pb/2V|$$

$$C_m = C_m(\alpha) + C_{m_q}(\alpha)qc/2V + C_{m|\beta|}(\alpha)|\beta| + C_{m|p|}(\alpha)|pb/2V|$$

For a model rotating about the wind axis at an angular velocity Ω the angular velocity components with respect to the body axes are:

$$p = \Omega\cos\beta\cos\alpha$$
$$q = \Omega\sin\beta$$
$$r = \Omega\cos\beta\sin\alpha$$

For a test at zero sideslip:

$$C_{L_1} = C_L(\alpha) + C_{L|p|}(\alpha)|pb/2V|$$
$$C_{m_1} = C_m(\alpha) + C_{m|p|}(\alpha)|pb/2V|$$

while a test at sideslip yields:

$$C_{L_2} = C_L(\alpha) + C_{L_q}(\alpha)\Omega c\ \sin\beta/2V + C_{L|\beta|}(\alpha)|\beta| + C_{L|p|}(\alpha)|pb/2V|$$
$$C_{m_2} = C_m(\alpha) + C_{m_q}(\alpha)\Omega c\ \sin\beta/2V + C_{m|\beta|}(\alpha)|\beta| + C_{m|p|}(\alpha)|pb/2V|$$

Thus, the differences between the average slopes of the two tests are

$$d(C_{L_2} - C_{L_1})/d\Omega = d[(C_{L_q}(\alpha)\Omega c\sin\beta/2V + C_{L|\beta|})(\alpha)|\beta|]/d\Omega = C_{L_q}(\alpha)c\sin\beta/2V$$
$$d(C_{m_2} - C_{m_1})/d\Omega = d[(C_{m_q}(\alpha)\Omega c\sin\beta/2V + C_{m|\beta|})(\alpha)|\beta|]/d\Omega = C_{m_q}(\alpha)c\sin\beta/2V$$

since β is constant. Finally,

$$C_{L_q}(\alpha) = (b/c\sin\beta)d(C_{L_2} - C_{L_1})/d(\Omega b/2V)$$
$$C_{m_q}(\alpha) = (b/c\sin\beta)d(C_{m_2} - C_{m_1})/d(\Omega b/2V)$$

An example of test results at sideslip for model C is shown in Figure 7-40. The methodology has proven to be reliable, and, with some care, has even been found to be useful outside the linear flow regime.

7.4 BRITISH AEROSPACE

7.4.0 Introduction

All data discussed in this section were obtained during tests of a research model R38 (Figure 7-41) in the 5.5m low-speed wind tunnel at Warton. The rotary balance is described in Section 3.4.2. The reference geometry of the model is also given in the figure. Tests were made over a range of angle of attack and positive rotation speed, and the effects of the following configuration changes are shown:

(a) wing-body strakes

(b) under-wing fuel tanks

(c) flaps

The data presented in this section are in wind-axes notation.

7.4.1 Effect of Strakes

At low angles of attack, the effect of the wing-body strake on C_l was small, as shown in Figure 7-42(a). However, the strakes did have an effect on C_n, especially at the higher roll rates where the strakes increase both the linearity and gradient of the data. At $\alpha = 25°$ (Figure 7-42(b)), the strakes have a dramatic effect on C_l. Without the strakes, the roll damping is practically zero at all roll rates, whereas with strakes on, C_l increases linearly with $\Omega b/2V$ up to the maximum roll rate tested. At this angle of attack, the strakes cause a slight reduction in C_n at all roll rates. C_{l_Ω} and C_{n_Ω} applicable to $\Omega b/2V < 0.1$ are shown in Figure 7-43. The beneficial effect of the strakes in preventing a loss of roll damping for $15° < \alpha < 25°$ is clearly seen.

7.4.2 Effect of Under-Wing Fuel Tanks

The effects of under-wing fuel tanks are shown in Figure 7-44. At $\alpha = 15°$, for the configuration with flap deflection at 0° and slat deflection at 9°, Figure 7-44(a) shows that the effect of the tanks is to increase the magnitude of C_l at all roll rates tested, but this is not the case at $\alpha = 20°$ with slat at 23° and flap at 20°/12° (Figure 7-44(b)), where the tanks decrease the damping in roll. When the angle of attack was increased to 25° for this same configuration (Figure 7-44(c)), there was no difference, tanks on or off. In this case there is a small increase in the gradient of C_n due to the tanks.

7.4.3 Effect of Flaps

The model was fitted with both inboard and outboard flaps which were set in three combinations: (1) zero deflection inboard and outboard; (2) 20° inboard and 12° outboard; and (3) 41° inboard and 25° outboard. Figure 7-45 shows the effects of flap deflection for $\alpha = 5°$ and $\alpha = 15°$. At an angle of attack of 5°, increasing the flap deflection causes a moderate increase in the magnitude of C_l, but at $\alpha = 15°$ there are substantial losses in roll damping as the flap deflection is increased. Changes in C_n due to the flaps are small.

7.5 RAE-BEDFORD

All data discussed in this section relate to the HIRM 1 and HIRM 2 combat aircraft configurations shown in Figures 7-46 and 7-47, respectively. Tests were made in the 4m × 2.7m Low Speed Wind Tunnel at RAE Bedford and the 2.4m × 1.8m Variable Density Transonic Wind Tunnel at RAE Farnborough. Since the models were rotated about the axis of the wind tunnel all coefficients relate to wind (stability) axes except where stated otherwise. The relations between wind- and body-axes coefficients are as follows:

$$C_{l_w} = C_{l_b} \cos\alpha + C_{n_b} \sin\alpha$$
$$C_{n_w} = C_{n_b} \cos\alpha - C_{l_b} \sin\alpha$$

7.5.1 Effect of Angle of Attack for HIRM1

Variations of the lateral coefficients C_l, C_n and C_y with $\Omega b/2V$ for HIRM 1 are shown in Figures 7-48 to 7-50. At moderate angles of attack, $\alpha = 10°$, 16°, the coefficients vary fairly linearly with rotation rate but as angle of attack is increased to 22° strong nonlinearities are evident, especially in C_l and C_n. As the rate of rotation increases there is a steady increase in differential lift on the wings due to increasing differential angle of attack. Minituft patterns for $\alpha = 16°$, $\Omega b/2V = 0.013$, 0.043 and 0.086 corresponding to 30, 100 and 200 rev/min are shown in Figure 7-51. At 30 rev/min the induced angles of attack at the port and starboard wing tips are small, −0.75° and 0.75°, respectively, and roll damping due to differential lift is small. Figure 7-51(a) shows a virtually symmetric tuft pattern on the wings with attached flow and only small spanwise components. Foreplanes contribute little to damping in roll except insofar as they influence the flow on the wings. A static oil pattern (Figure 7-51(b)), obtained during an earlier test, albeit with a slightly different foreplane setting, shows a pattern very similar to that obtained with tufts at 30 rev/min.

When the roll rate is increased to 100 rev/min, induced angles of attack at the port and starboard tips are −2.5° and 2.5°, respectively, with a proportionate increase in differential lift and rolling moment as shown in Figure 7-48. Flow visualization for 100 rev/min (Figure 7-51(c)) shows marked differences in tuft patterns on port and starboard wings, with evidence of a

vortex on the outer starboard wing and consequent increased suction. At 200 rev/min (Figure 7-51(d)), the induced angles of attack at the port and starboard tips are $-5°$ and $5°$, respectively, giving an increased differential lift due to a strengthened part-span vortex on the starboard wing. The primary separation line of this vortex is along the knuckle of the drooped leading edge. This can be seen more clearly in the static oil flow photograph for $\alpha = 20°$, shown in Figure 7-52(b), where primary reattachment can also be seen. At all three rotation rates the lower-surface pressures would also be expected to contribute to roll damping.

Figure 7-48 shows a marked nonlinearity in the variation of C_l with roll rate at $\alpha = 22°$, especially at low values of $\Omega b/2V$ when the rolling moment is virtually zero. Flow visualization at 30 rev/min (Figure 7-52(a)) indicates flow separation and probably vortex bursting on both wings, since tufts appear blurred and the directions are erratic. At 100 rev/min, Figure 7-52(c) shows that the reduction in angle of attack of the port wing has reestablished an organized vortex near the tip which is creating increased suction on the port wing and contributes a propelling rolling moment instead of a damping rolling moment. The mean angle of attack of the port wing is approximately 20°, so the oil flow pattern in Figure 7-52(b) is comparable. Since the resultant rolling moment is zero, the negative moment indicated by upper-surface flow is presumably offset by a positive moment from lower-wing surface pressures. As rotation speed is increased to 200 rev/min (Figure 7-52(d)) the outboard vortex on the port wing is still visible, indicating that upper surface pressures are continuing to contribute a propelling rolling moment. However, since Figure 7-48 shows that at 200 rev/min the rolling moment is negative, it must be assumed that lower-surface pressures contribute a greater damping moment.

When angle of attack is increased to 30°, Figure 7-48 shows that the variation of rolling moment with rotation rate is again linear but with reduced slope compared with the characteristic for $\alpha = 16°$. As shown by the tuft photographs, Figures 7-53(a-c), the upper-surface flows at all three rotational speeds are complex and relatively insensitive to rotation rate. The net result is a lower damping due to rotation rate.

Effects of angle of attack on the variation of C_n are unremarkable except for a reduction in gradient for low rotation rate at $\alpha = 22°$. However, examination of the body-axis data, not presented here, showed that most of this effect comes from the body-axis rolling moment. The side-force (C_y) characteristics have a positive gradient up to $\alpha = 30°$ but at $\alpha = 40°$ there is a large zero displacement and the gradient has changed sign. The effects of rate of rotation and angle of attack on the longitudinal coefficients C_z and C_m are shown in Figure 7-54. The maximum variations in C_z and C_m are 0.1 and 0.01, respectively, with the greater variations at high angles of attack and high rotation rate.

7.5.2 Effects of Foreplanes

Figures 7-55 and 7-56 show the effect of foreplanes on C_l and C_n for HIRM 1 at $\alpha = 18°$, 20°, 24° and 26°. At $\alpha = 18°$ C_l and C_n vary linearly with rotation rate until $\Omega b/2V \cong 0.1$, when there is some reduction in gradient. The foreplanes give about 20% increase in both C_l and C_n. At $\alpha = 20°$ without foreplanes, the gradient of C_l vs $\Omega b/2V$ is virtually zero at low rotation rate, and there are marked nonlinearities at higher rates. With foreplanes on, however, there is a substantial gradient through the origin with some fall-off at higher rates. It is probable that the foreplane contribution derives mainly from effects on wing lift, rather than the increment due to forces on the actual foreplanes. When the angle of attack is increased to 24°, nonlinearities in C_l increase to the extent that the gradient changes sign for low values of $\Omega b/2V$. The effect is less severe with foreplanes on. At $\alpha = 26°$ there is little variation in C_l for $|\Omega b/2V| < 0.1$, but a sudden increase occurs outside this range. At all angles of attack the variation of C_n with $\Omega b/2V$ is seen to be more linear with foreplanes on.

The effects of foreplanes on HIRM 2 are shown in Figures 7-57 and 7-58 for $\alpha = 22°$ and $\alpha = 50°$, respectively. At $\alpha = 22°$ (Figure 7-57) effects are similar to those on HIRM 1 at a similar angle of attack, but at $\alpha = 50°$, foreplanes off, there are large changes in the body-axis yawing moment with rotation rate (Figure 7-58). It is likely that these large asymmetric changes are caused by 'flipping' of the forebody vortices which is largely suppressed by the presence of the foreplanes.

7.5.3 Effects of Nose Boom

The HIRM 2 configuration was tested with and without a large probe (length = 0.38b) fitted to the nose and the effects are shown in Figures 7-59 and 7-60 for $\alpha = 20°$ and $\alpha = 50°$, respectively. At $\alpha = 20°$, the effects on rolling and yawing moment are small, but at $\alpha = 50°$ the probe has the effect of increasing the linearity and symmetry of the characteristics. This is most probably due to the effect on the forebody flow where the probe prevents or delays the formation of asymmetric nose vortices.

7.5.4 Effects of Fin

Fin contributions to C_y, C_n and C_l for HIRM 1 at $\alpha = 24°$ are shown in Figure 7-61. In general, side force generated by a fin is the sum of contributions due to sidewash over the fin arising from differential lift on the wings and to fin incidence due to rolling. For a positive rate of roll, air flows from port to starboard giving a positive sidewash contribution. At low angles of attack, the contribution from fin incidence is negative, resulting in a small net side-force contribution. However, at high angles of attack, when most of the fin area is below the rotation axis, the contribution from fin incidence is positive and, as shown in Figure 7-61, the total fin contribution is large and positive. As might be expected, a positive fin contribution to C_Y results in a negative increment in C_n and a small negative increment in C_l due to fin displacement below the rotation axis.

7.5.5 Effects of Reynolds Number and Mach Number

Tests to investigate the effects of Reynolds number (Re) and Mach number were made in the 2.4m × 1.2m Pressurized Wind Tunnel at RAE Farnborough. Reynolds number effects on C_l, C_n and C_y for HIRM 2 at $\alpha = 20°$, 50° and 60° are shown

in Figures 7-62 to 7-64. For $\alpha = 60°$, body-axes characteristics are also shown. At a moderate angle of attack, $\alpha = 20°$, there are only small differences in the characteristics for $Rc = 1.35 \times 10^6$ and 3.81×10^6, but at $\alpha = 50°$ and 60° there are significant effects, especially on C_n and C_l. The body-axes data for $\alpha = 60°$ show, however, that the effect of Rc is confined to the body-axis C_n and, although not shown, this is largely the case at $\alpha = 50°$ also. The effect of Rc on body-axis rolling moment is insignificant. This suggests that there is an Rc effect on the flow over the fuselage and fin, reducing the gradient of the yawing-moment characteristic as Rc is increased. Tests were also made in the 4m × 2.7m Wind Tunnel at $Rc = 1.35 \times 10^6$ and results are compared in Figures 7-65 and 7-66 for $\alpha = 20°$ and 60°, respectively. Body-axes results for $\alpha = 60°$ are shown in Figure 7-67. Again, at $\alpha = 20°$ (Figure 7-65) there is little difference between the results, but at $\alpha = 60°$ (Figure 7-66) there are significant differences between results from the two wind tunnels at the same Rc. If the results are plotted in body-axes, as shown in Figure 7-67, it can be seen that the differences originate only from the body-axis yawing moment C_n. Possible reasons for these discrepancies include the differences in downstream rig support structure, test-section sizes and the levels of free-stream turbulence in the wind tunnels. It is felt that the rig support structures are too far downstream to have such a dramatic influence on yawing moment, and it is known that the turbulence level in the 2.4m × 1.8m Wind Tunnel is much greater than in the 4m × 2.7m Tunnel. However, as shown in Section 5.2, a more plausible explanation is the difference in unsteady wall interference in the two wind tunnels.

The effects of a change in Mach number from 0.4 to 0.7 for $\alpha = 0°, 12°$ and 20° are shown in Figures 7-68 to 7-70 for HIRM 1 with zero leading-edge droop. There was a small asymmetry in these zero droop wings due to manufacturing error which will have caused some of the zero displacements in the characteristics. When Mach number is increased from 0.4 to 0.7 the most significant effects are a reduction in the gradient of C_l vs $\Omega b/2V$ at $\alpha = 12°$ and an increase in gradient in C_n vs $\Omega b/2V$ at $\alpha = 20°$. There are also some unexplained discontinuities in C_y vs $\Omega b/2V$ between positive and negative rotations.

7.6 MBB-AIRCRAFT

As a result of international work sharing agreements on recent European programs, only a few tests with the rotary balance of DFVLR have been conducted. Nevertheless, some experimental work has been performed by different investigators on typical configurations of complete aircraft or aircraft components. Thus, representative data for different configurations due to rolling have been obtained through the use of the rotary balance by MBB together with DFVLR. The data are presented in wind axes except where stated otherwise.

7.6.1 Wing Characteristics

Wing shapes of different leading-edge sweep angles and planforms were investigated on a simple rotary rig[9] in order to determine the roll damping characteristics of basic wing configurations. Although the tests emphasized moderate angles of attack, the results presented in Figures 7-71 and 7-72 show the trends of roll damping for wings with low and high sweep at high angles of attack. Figure 7-71 shows the rolling-moment coefficients as a function of dimensionless roll rate for a swept- and an unswept-wing configuration in terms of body axes. Figure 7-72 presents the roll damping derivatives as functions of angle of attack for the wing configurations. The roll damping for a typical delta wing shows a smooth trend with angle of attack, whereas a very abrupt decrease in roll damping is observed for the unswept wing at high angles of attack.

7.6.2 Delta Wing Configuration

The delta wing configuration shown in Figure 7-73 was tested in 1970 by EWR, a forerunner of MBB, on the rotary rig referred to in Chapter 3. Results from measurements of the rolling moment over a range of nondimensional rate of roll are presented for wind axes in Figure 7-73 for the complete model and model components

7.6.3 Variable Sweep Configuration

Data for a fighter model with sweep angles between 25° and 70° have been measured at low speeds using the rotary apparatus at DFVLR. Results for a leading-edge sweep angle of 25° are presented in Figure 7-74. The lateral damping derivatives determined from the rotary data are shown in Figures 7-75 to 7-77. Differences in roll damping at low angles of attack for different sweep angles are obvious although the data are plotted for a constant reference span and area, which affects a direct comparison of the magnitude of the data. For small values of sweep, separated flow on the outer wing reduces the roll damping at high angles of attack. This effect decreases with increasing sweep angle and disappears completely for a sweep angle of 70° where a strong vortical flow field on the wing maintains the damping in roll. The contribution of the tail to side force and yaw damping of the complete configuration for a wing sweep angle of 45° is shown in Figure 7-77. These data are in agreement with results published by Boyden[10] for two configurations with different wing sweep angles as shown in Figure 7-78.

7.7 ONERA-IMFL

The experimental results presented here concern the Alphajet combat aircraft. The scale of the model was 1/12, and the tests were carried out in the vertical wind tunnel of ONERA-IMFL. For the data reduction, the aerodynamic chord c is used as the reference length, and the three moment coefficients are reduced with c ($\Omega^* = \Omega c/V$). The data presented here may be classified in two groups The first group relates to coning motion (rotation about the wind axis). The second group relates to the oscillatory coning motion, where oscillations of α and β are superimposed on a coning motion

7.7.1 Coning Motion Data

The data of this section illustrate the rotation effect with respect to the values of the angle of attack α, sideslip β and the three control surface deflections δ_l, δ_m and δ_n (ailerons, elevator and rudder, respectively). When possible, these effects will be correlated with the free-flight steady spin results. This comparison is particularly interesting and convenient, because such spin motions are steady phenomena at high angles of attack, similar to coning motions on the rotary balance. Furthermore, these spin motions are very well documented, as flight tests and vertical wind-tunnel tests have been carried out on the Alphajet. To illustrate typical results, the measurements of the yawing moment in body axes are presented for several values of $\Omega c/V$ and angles of attack between 40° and 90°, and for three values of sideslip ($\beta = 0°$, $\beta = -15°$ and $\beta = +15°$) as shown in Figures 7-79 to 7-80, 7-81 to 7-82, and 7-83 to 7-84, respectively.

Each case is presented for four control settings on two figures. The values of $\Omega c/V$ correspond approximately to the right and left spin of the Alphajet. The different control setting configurations are numbered 1 to 4, and are:

Number 1: prospin to the right ($\delta_l = -20°$, $\delta_m = 6°$, $\delta_n = -25°$)
Number 2: antispin to the left ($\delta_l = -20°$, $\delta_m = -20°$, $\delta_n = -25°$)
Number 3: stick to the left ($\delta_l = -20°$, $\delta_m = 0°$, $\delta_n = 0°$)
Number 4: neutral ($\delta_l = \delta_m = \delta_n = 0°$)

Control setting configuration number 4 is the basic case. Number 3 shows the effect of the ailerons, which influence the spin equilibrium. Control setting configuration number 2 is the most effective maneuver for recovery from a left spin ($\Omega^* < 0$). Control setting configuration number 1 is the required control setting for a right flat spin. Moreover, the comparison between settings 1 and 2 can show the effect of the elevator. Ailerons and elevator are the two more effective controls at high angles of attack, the efficiency of the rudder being weak.

Figures 7-79 to 7-84 show the results of the yawing moment as a function of angle of attack for two opposite values of Ω^*. It may be observed that the measurements are not perfectly symmetric, but this is well known in the domain of high angles of attack. In these figures, the damping effect of the rotation is clearly in evidence and appears to be very dependent on the values of the control surface deflections, angle of attack and sideslip.

Before discussing the data, it is instructive to consider the spin motions of the Alphajet aircraft. The two main kinds of spin motion are the following:

- A normal spin at $\alpha = 45°$, $\Omega c/V = 0.06$, obtained with the ailerons in the opposite direction to the spin rotation, stick back, and the rudder in the direction of the spin.

- A flat spin at $\alpha = 65°$, $\Omega c/V = 0.075$, obtained with the same lateral control surface position, but with the stick pushed forward.

The values given here for α, $\Omega c/V$ are only average values (in order to give an approximate idea) because the equilibrium conditions in spin are slightly dependent on the values of some parameters like the c.g. location, the inertial moments, the altitude of the spin, etc. During these spins the sideslip is small but not zero. The sign of β is opposite to Ω.

Figure 7-79(a), where the sideslip is null and the control setting is neutral, shows clearly that the rotation effect is quite dependent on the angle of attack. Reductions of the damping can be observed in two regions, at about 45° to 50° and 70° of incidence. These regions seem to be spin equilibrium conditions, particularly the second one. Indeed, a flat spin motion where the tilt angle is small involves a small inertial moment in yaw and consequently a small aerodynamic moment in yaw. The maximum damping effect occurs at about 58° and is observed with the three other control setting configurations. The same effect can be observed in Figure 7-85, where the yawing moment is plotted versus the rotation rate for three different values of α. The damping is significant at $\alpha = 60°$ and remains near zero at $\alpha = 70°$. It may also be observed that the variations of C_n with respect to $\Omega c/V$ are fairly smooth.

The comparison between control-setting configuration numbers 4 and 3 shows that a positive variation of the yawing moment results from the negative aileron deflection, particularly for the values of the angle of attack greater than 60°. So, it may be concluded that movement of the stick to the left induces a positive contribution to C_n. This may be attributed to the fact that, at very high angles of attack, the displacement of the stick (ailerons) in either lateral direction favors spin equilibrium conditions in the opposite direction. In this context "favoring the spin" is only from the yawing-moment point of view. In fact, the spin motion requires equilibrium and stability conditions for all of the six components. Finally, it is noted that the damping effect is not modified by the action of the ailerons.

The comparison between the results for control-setting configuration numbers 3 and 2 clearly shows two main effects: an increase in the damping effect in yaw, and a positive variation of the yawing moment for the curve corresponding to the negative values of the rotation rate. The control displacement has a greater effect in the case of a left rotation.

In global value, the yawing moment becomes largely positive for configuration 2 with Ω^* negative. Control-setting configuration number 2 effectively gives a yawing moment in the direction opposite to the left spin and is antispin to the left

A comparison between the results for control settings number 2 and 1 shows the effect of the elevator (the only difference between 1 and 2) and also the effectiveness of the prospin control setting. A significant reduction of the damping effect is observed from 40° to 80° angle of attack. At 70°, the rotation effect seems to be propelling but its amplitude is small. This characteristic clearly explains the prospin effect (to the right) of this control setting and is very well correlated with flight test

results. Beyond 65° angle of attack, the global yawing moment is positive, even in the case of a right spin ($\Omega c/V$ positive). The differences between configurations 1 and 2 (concerning the elevator setting) indicates the effectiveness of the elevator in the spin equilibrium condition in yaw, and this illustrates the elevator effect on the yawing moment in rotational flow. Indeed, in flight it is necessary to push on the stick to obtain the flat spin when the other controls are prospin.

A comparison between the cases $\beta = 0°$ (Figures 7-79 and 7-80) and the cases $\beta = -15°$ (Figures 7-81 and 7-82) shows that the sideslip has an important influence on yawing moment. A positive value of $\Omega c/V$ produces a negative yawing moment. The comparison between the cases $\beta = -15°$ and $\beta = +15°$ (Figures 7-81 and 7-83) shows that the sideslip effects are almost symmetric up to $\alpha = 80°$.

The effects of the control settings may be summarized as follows : the stick displacement to the left (aileron effect) induces a positive variation of the yawing moment (prospin to the right). The stick pushed forward (elevator effect) promotes the flat and fast spin as mentioned previously in the case with $\beta = 0°$.

7.7.2 Oscillatory Coning Results

The rotary balance presently in service at IMFL has the capability for tilting the angular velocity vector with respect to the free-stream axis. The angle between the velocity vector and the rotational vector is λ, an adjustment degree of freedom of the apparatus. When λ is not equal to zero, the rotary motion induces a sinusoidal oscillatory evolution of α and β, and so the unsteady aerodynamic behavior may be observed on the rotary balance during the motion. The apparatus, the kinematic relations and the data reduction for the oscillatory coning motion are described in Chapter 4.

At low angles of attack, the unsteady aerodynamic characteristics of an aircraft model can be estimated under the assumptions of small disturbance theory. For these conditions, the identification of the dynamic stability parameters like, for instance, the derivatives with respect to rate of change of α and β can give a good estimation of the unsteady behavior. On the other hand, at high angles of attack this hypothesis is not true because the phenomena are nonlinear and time dependent. In this case, a rotary balance with the λ degree of freedom can give some information on this unsteady behavior. As this capability is unique and specific to the IMFL rotary balance, it is of interest to focus attention on some of these results where unsteady phenomena can be observed.

Dynamic stall phenomena can be seen in Figure 7-86, where the lift and the drag variations are presented in wind axes and in Figure 7-87, where the pitching moment and the normal force are plotted in body axes for the same tests. Each test is a periodic test, so the measurement curves are closed loops. On these figures, the tests were performed for the same values of the rotation rate ($\Omega^* = 0.06$), and for the mean or central value of the angle of attack ($\alpha_c = 20°$). Consequently, the values of the angular velocities are identical for all the tests presented. The values of λ are different, so the effect of the amplitude of the oscillation can be observed in these figures. The dashed curves represent the static aerodynamic coefficient values, and these can be compared with the global coefficients to estimate the unsteady contributions to the aerodynamic coefficients Large unsteady effects can immediately be observed, particularly in the case of the high-amplitude test.

Concerning the lift variation, the main characteristics of the phenomena are the following:

- The maximum value of the lift is highly increased
- The stall angle of attack is increased (about 30° instead of about 17° as under stationary conditions)
- An important hysteresis effect is observed.

During the cycle, when α is increasing at low angles of attack, an overshoot of the linear regime occurs and high values of the lift and stall angle of attack are obtained.

After reaching its highest value, the lift is suddenly reduced and the stall is steeper than in the stationary case. Then, when α is decreasing symmetrically, the lift decreases with another slope, and the readjustment to the linear regime does not occur at the stationary value of the stall angle of attack. The lift observed is then smaller than in the stationary case The unsteady contribution is characterized by an important time dependent effect. (The linear regime is found at a value of the angle of attack smaller than the static stall angle.)

Such phenomena have already been described for pitching, plunging or accelerating airfoils by other authors. Flow visualizations and pressure measurements have proved that the dynamic stall was characterized by the shedding and passage over the airfoil upper surface of a vortex-like disturbance inducing a highly nonlinear pressure field. The results presented for the Alphajet model show a similar phenomenon. Of particular interest is to observe it experimentally on a three-dimensional model subjected to an oscillatory coning motion, which constitutes quite a realistic motion at high angles of attack.

Unsteady effects were also found for the other coefficients, and can be observed in Figures 7-86 and 7-87. The drag, pitching moment and normal force show an overshoot over the maximum values obtained in stationary tests and a hysteresis loop.

In Figures 7-88 and 7-89 two effects can be observed: the effect of the oscillation amplitude and the effect of the mean value of the angle of attack. The amplitude effect is nonlinear, and the case $\lambda = 20°$ is considerably more dynamic than the others. The value of the stall angle is quite dependent on λ. The slopes of the lift with respect to α are also very dependent on the amplitude of the oscillation, particularly in the case of the dynamic stall event.

The value of the mean angle of attack also has a large influence on the unsteady aerodynamic coefficients. For instance, in Figure 7-88(a) large differences can be observed between the oscillations about $\alpha_c = 25°$ and $\alpha_c = 50°$. In the first case, the dynamic stall event occurs as previously described because the α variation occurs largely in the attached flow region. At a higher value of α_c, such as 50°, the phenomenon is different because, in this case, the flow is entirely separated over the wing in the whole domain of the α variation. Large unsteady effects exist for all the aerodynamic coefficients.

The importance of the time history of the angle of attack is shown in Figures 7-90 and 7-91 where the coefficients are plotted for two opposite values of the rotation rate Ω^*. During a cycle the values of the angles of attack and sideslip are varying, and a primary question arises as to the unsteady contribution of the sideslip to the results. As shown in Figures 7-90 or 7-91, the loops plotted for two opposite values of the rotation rate are nearly identical. Thus, the results show little effect of the sideslip variation on the measurements. Similar values of the lift, drag and pitching moment are found for opposite values and time histories of sideslip, but for identical time histories of the angle of attack.

Figures 7-92 and 7-93 show the important nonlinear effect of the oscillation frequency on the unsteady behavior. The value of the stall angle in the dynamic tests is dependent on the reduced frequency, and the hysteresis effects are also dependent on these values.

Control settings may also influence the unsteady aerodynamic response as can be seen in Figures 7-94 and 7-95, which present the results for neutral controls and for antispin control settings for a left spin. The effects of the control configuration are not limited to the steady effects, and the unsteady contribution can also be changed when the control surfaces are deflected.

In order to predict high-α dynamic behavior such as departure, recovery, or oscillatory spins, it is necessary to take into account unsteady aerodynamic effects such as the foregoing.

7.8 REFERENCES

1. Clarkson, M. H.; Malcolm, G. N.; and Chapman, G. T.: Experimental Poststall Rotary Aerodynamic Coefficients for Airplane-Like Configurations. AIAA J. of Aircraft, Vol. 13, No. 8, pp 565-570, August 1976.

2. Malcolm, G. N.; and Clarkson, M. H.: Wind-Tunnel Testing with a Rotary-Balance Apparatus to Simulate Aircraft Spin Motions. Proceedings of AIAA 9th Aerodynamics Testing Conferences, June 1976 pp. 143-156

3. Jermey, C.; and Schiff, L. B.: Wind-Tunnel Investigation of the Aerodynamic Characteristics of the Standard Dynamics Model in Coning Motion at Mach 0 6. AIAA Paper 85-1828-CP, August 1985.

4. Malcolm, G. N ; and Schiff, L. B : Recent Developments in Rotary-Balance Testing of Fighter Aircraft Configurations at NASA Ames Research Center. NASA TM 86714, July 1985.

5. Beyers, M. E.; and Moulton, B E : Stability Derivatives Due to Oscillations in Roll for the Standard Dynamics Model at Mach 0.6. Report NAE LTR-UA-64, NRC, Canada, January 1983.

6. Beyers, M. E.; Kapoor, K. B.; and Moulton, B E.: Pitch- and Yaw-Oscillation Experiments on the Standard Dynamics Model at Mach 0 6. Report NAE LTR-UA-76, NRC, Canada, June 1984.

7. Malcolm, G. N.: Rotary-Balance Experiments on a Modern Fighter Aircraft Configuration at High Reynolds Numbers AIAA-85-1829, August 1985

8. Malcolm, G. N.; and Schiff, L. B Recent Developments in Rotary-Balance Testing of Fighter Aircraft Configurations at NASA Ames Research Center. AGARD CP-386, November 1985.

9. Schlottman, F.: Uber die stationaren und instationaren aerodynamischen Beiwerte für Rollbewegung schlanker Flügel/Dissertation/Ruhr Universitat Bochum 1972.

10. Boyden, R. P.: Effects of Leading Edge Vortex Flow on the Roll Damping of Slender Wings. Journal of Aircraft, Vol. 8, No. 7, July 1971.

Table 7-1: Cross-Reference Table For Figures Showing Effects of Different Parameters on Rotary Test Results.

Source of Data	Figure No.	Test Parameters: Ω	α	β	Re	Ma	Component Buildup: General	Fuselage	H Tail	Fin	Wing Parameter: Planform	Sweep	Control Deflection: Fuselage	Flaps	All./Spoil./Rudder	Misc. Components: Nose Boom	Strakes	Wing Fences	Fuel Tanks	Forebody Transition Type	Wind Tunnel	Oscillatory Coning Parameter: ω_n	λ	Ω	Controls	Model Configuration
NASA Langley	7-1 to 7-3	x																								Fighter aircraft
	7-4	x		x																						Fighter aircraft
	7-5	x					x																			Fighter aircraft
	7-6	x															x									Fighter aircraft
	7-7	x						x					x													Fl 'ter aircraft
NASA Ames	7-11 to 7-13	x			x																					Tangent ogive body—Fig. 7-9
	7-15	x		x																						SDM—Fig. 7-14
	7-18 to 7-20	x			x											x										F-15—Fig. 7-17
AerMacchi	7-21		x				x																			Model A-Table 7-2
	7-22	x	x																							Model G-Table 7-2
	7-23	x		x											x											Model G-Table 7-2
	7-24	x																	x							Models B1-Table 7-2
	7-25 to 7-29	x	x																							Models B1,B2,F,G-Table 7-2
	7-30	x																x								Model B2-Table 7-2
	7-31	x		x																						Model C-Table 7-2
	7-32	x													x											Model C-Table 7-2
	7-33 to 7-36	x	x																							Models E,A,C,D-Table 7 2
	7-37	x					x																			Model A-Table 7-2
	7 38	x	x																							Model E-Table 7-2
	7-39	x																		x						Model E-Table 7-2
	7-40	x	x	x																						Model C-Table 7-2
B Ae	7-42	x	x														x									Fig. 7-41
	7-43		x														x									Fig. 7-41
	7-44	x	x																x							Fig. 7-41
	7-45	x	x											x												Fig. 7-41
R.A.E.	7-48 to 7-54	x	x																							HIRM 1 - Fig. 7-46
	7-55 to 7-56	x	x					x																		HIRM 1 - Fig. 7-46
	7-57 to 7-58	x	x					x																		HIRM 2 - Fig. 7-47
	7-59 to 7-60	x	x													x										HIRM 2
	7-61	x	x							x																HIRM 1
	7-62 to 7-64	x	x		x																					HIRM 2
	7-65 to 7-67	x	x																		x					HIRM 2
	7-68 to 7-70	x	x			x																				HIRM 1
DFVLR	7-71 to 7-72	x	x								x															Isolated wings
	7-73		x				x																			Combat aircraft Fig. 7-73
	7-74	x	x																							Fighter aircraft Fig. 7-74
	7-75 to 7-76		x									x														Fighter aircraft Fig. 7-74
	7-77		x						x																	Fighter aircraft Fig. 7-74
	7-78		x								x	x														Configurations, Fig. 7-78
ONERA - IMFL	7-79 to 7-80	x	x												x											Alphajet
	7-81 to 7-84	x	x	x											x											Alphajet
	7-85	x	x																							Alphajet
	7-86 to 7-87																						x			Alphajet
	7-88 to 7-89																					x	x			Alphajet
	7-90 to 7-93																					x		x		Alphajet
	7-94 to 7-95																					x			x	Alphajet

Table 7-2. Geometric Characteristics of Models Tested by AerMacchi

Model designation	Aircraft category	Wing Parameters			
		AR	$\Lambda_{c/4}$	Taper	t/c
A	Subsonic combat aircraft	4.5	20°	.54	9%
B1	Jet trainer	5.34	8°	.58	13%
B2	Jet trainer	4.7	11°	.5	12%
C	Subsonic combat aircraft	3.75	27.5°	5	12%
D	Subsonic combat aircraft	4.6	25°	.41	9.5%
E	High performance canard configured	2.7	39°	.16	5%
F	18-pass commuter	8.2	0°	.59	14%
G	8-pass executive twin turboprop	12.4	~0°	0.4	14%

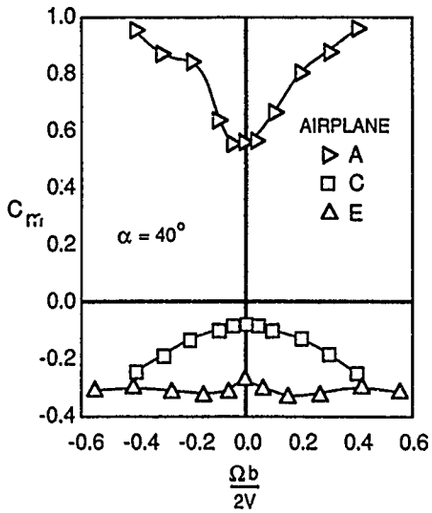

Figure 7-1. Effect of rotation rate on pitching-moment coefficient.

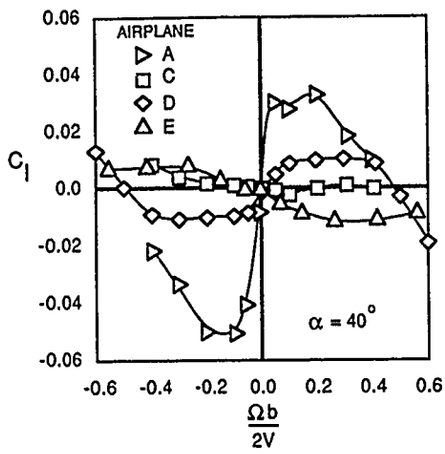

Figure 7-3. Effect of rotation rate on rolling-moment coefficient.

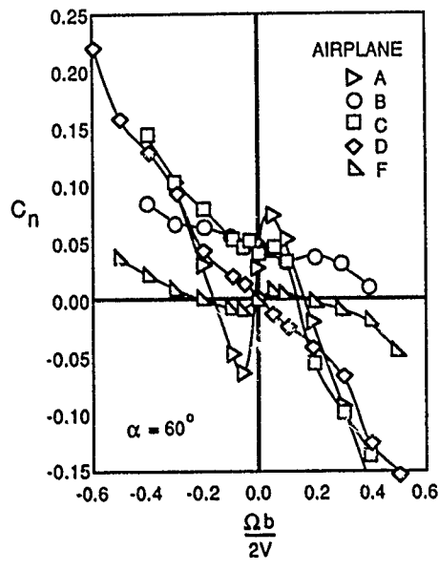

Figure 7-2. Effect of rotation rate on yawing-moment coefficient.

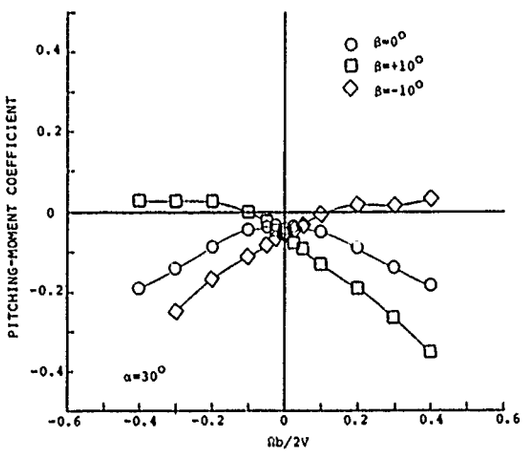

Figure 7-4. Effect of sideslip on rotational pitching-moment coefficient.

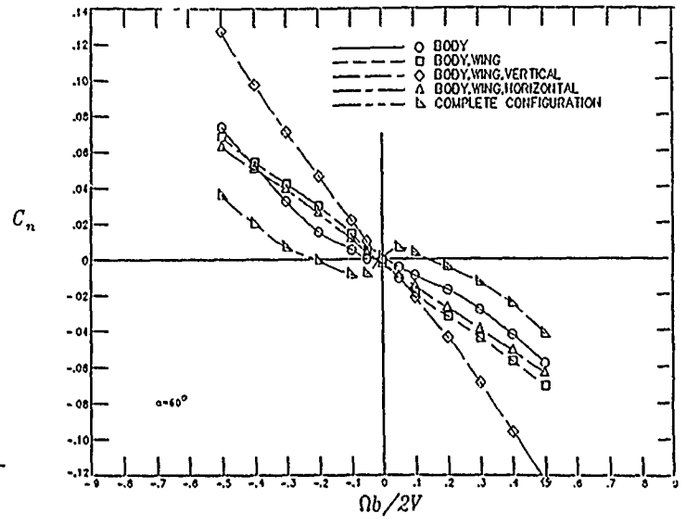

Figure 7-5. Effect of model components on yawing-moment coefficient.

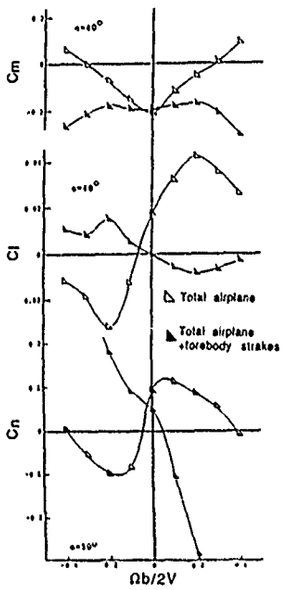

Figure 7-6. Effect of forebody strakes on rotational moments.

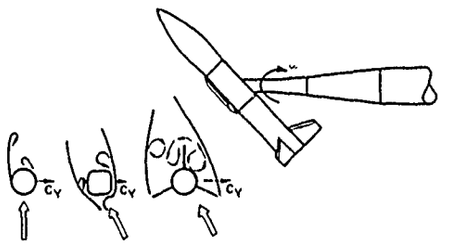

Figure 7-8. Sketch of pro-spin flow mechanisms.

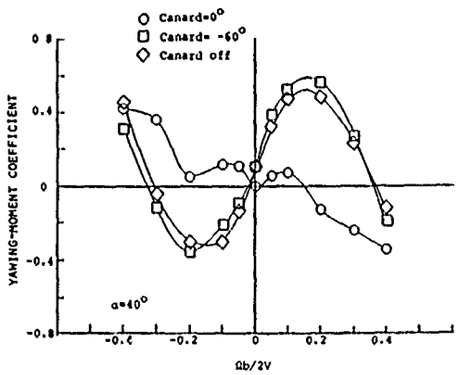

Figure 7-7. Effect of canard deflection on yawing-moment coefficient.

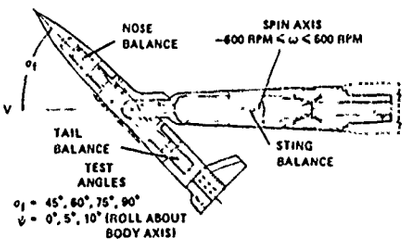

Figure 7-9. Sketch of model and balance combinations

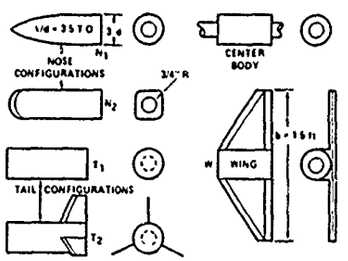

Figure 7-10. Sketch of model components.

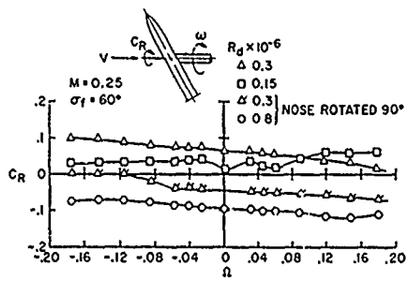

Figure 7-11. Effect of Reynolds number on spinning-moment coefficient for configuration N_1T_1.

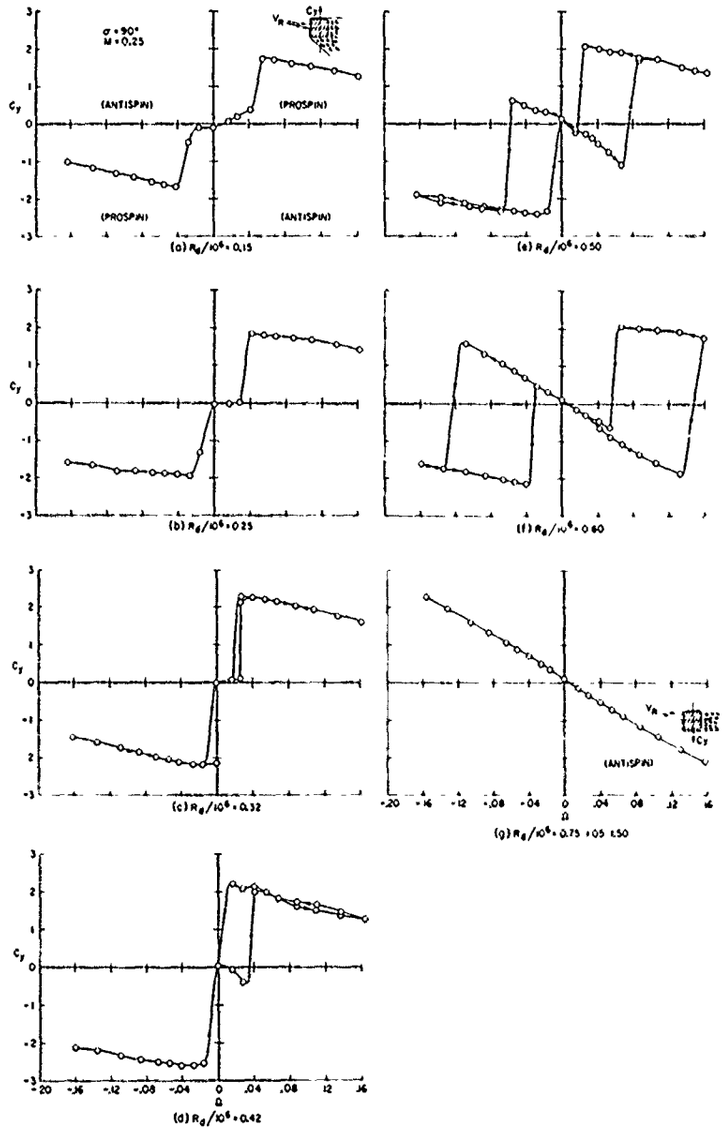

Figure 7-12. Side-force coefficient on the nose section; effect of Reynolds number at $\sigma = 90°$, $M = 0.25$.

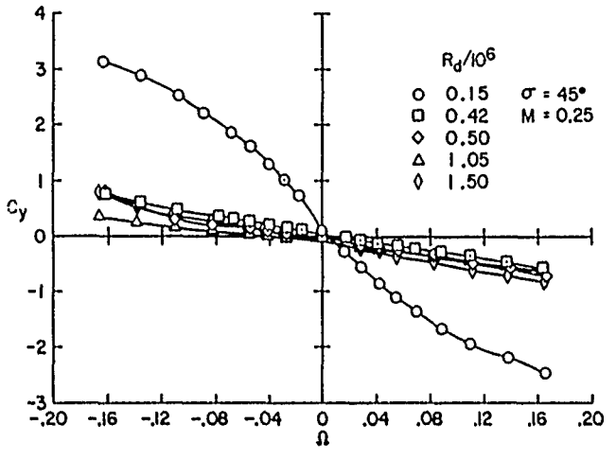

Figure 7-13. Side-force coefficient on the nose section; effect of Reynolds number at $\sigma = 45°$, $M = 0.25$.

Figure 7-14 Standard Dynamics Model on 30° bent sting in 6- by 6-Foot Supersonic Wind Tunnel.

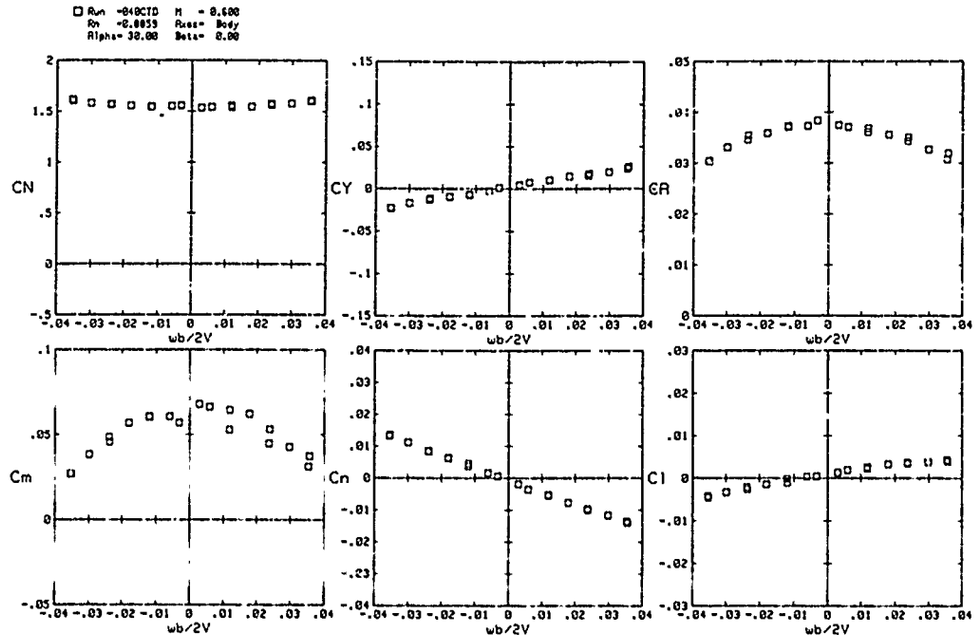

(a) $\beta = 0°$.

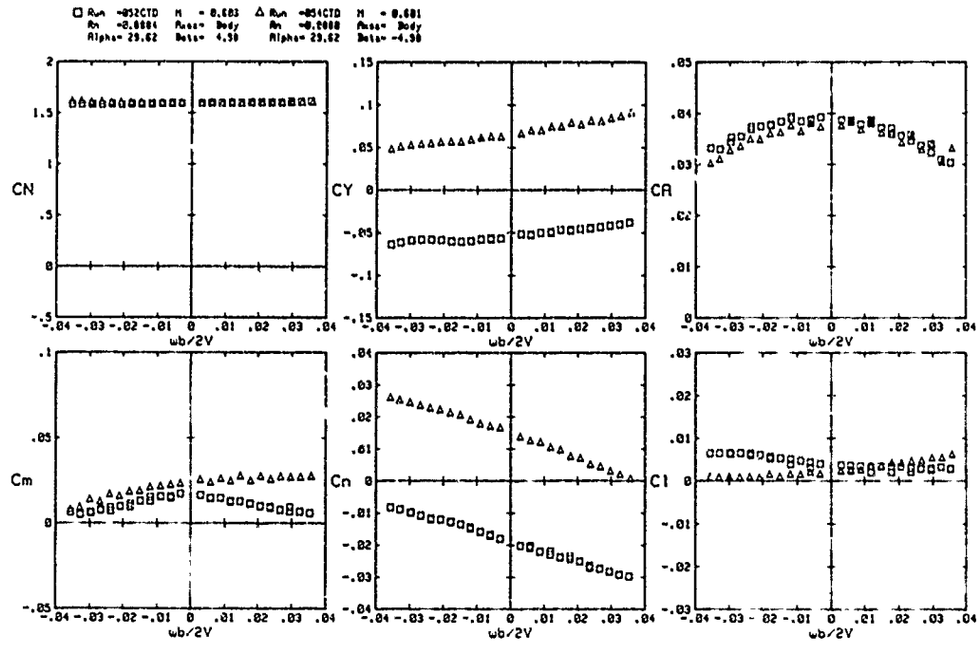

(b) $\beta = \pm 5°$

Figure 7-15 Effect of rotation rate on aerodynamic coefficients for Standard Dynamics Model at $\alpha = 30°$.

Figure 7-16. Model and apparatus in 12-Foot Pressure Wind Tunnel.

Figure 7-17. Model and apparatus on laboratory test stand.

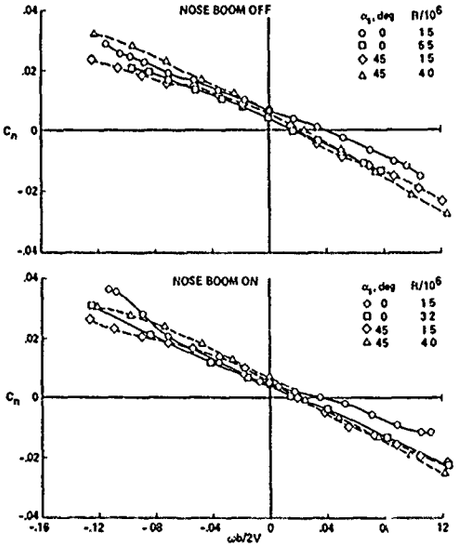

Figure 7-18. Effects of rotation rate and sting angle on the yawing-moment coefficient for the F-15 at $\alpha = 30°$.

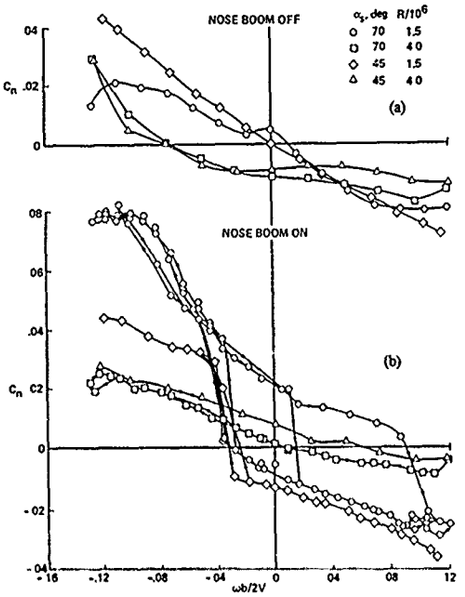

Figure 7-19. Effects of rotation rate and sting angle on the yawing-moment coefficient for the F-15 at $\alpha = 70°$.

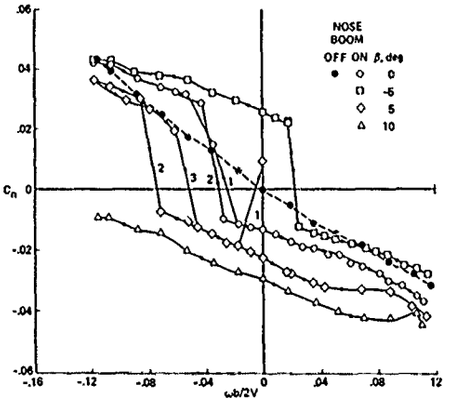

Figure 7-20. Effects of rotation and sideslip angle on the yawing-moment coefficient for the F-15; $\alpha = 70°$, $\alpha_s = 45°$, $R = 1.5$ million.

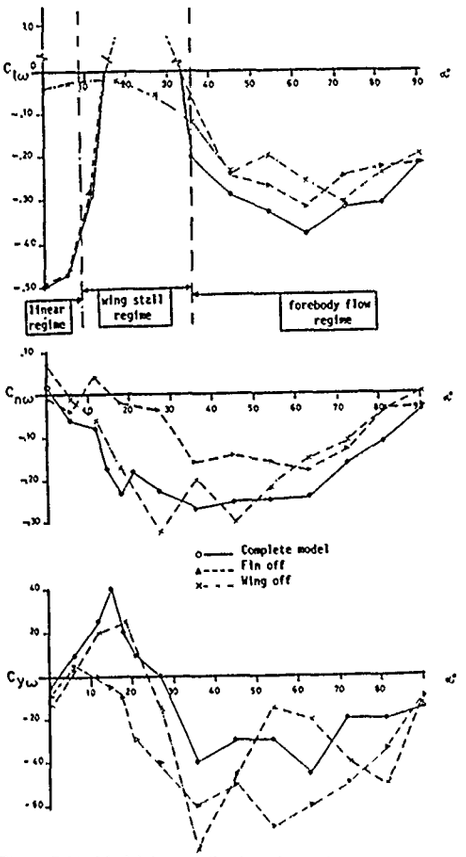

Figure 7-21. Model A: contribution of model components to derivatives at angle of attack

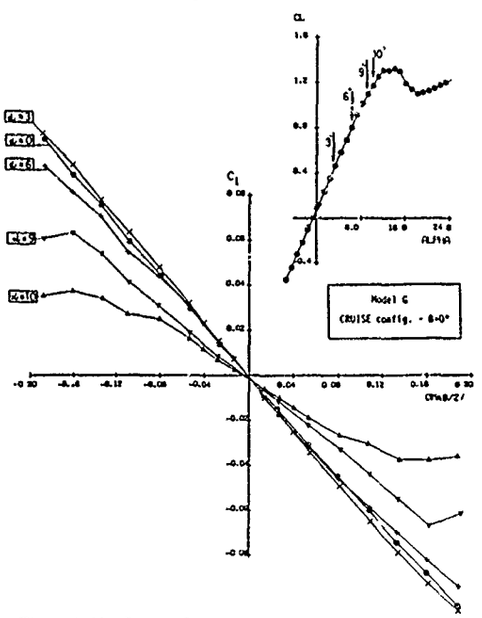

Figure 7-22. Linear flow regime of a high aspect-ratio wing.

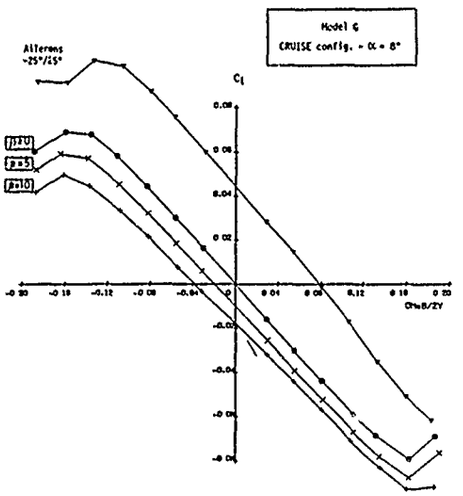

Figure 7-23. Effects of sideslip/ailerons at boundary of linear flow regime.

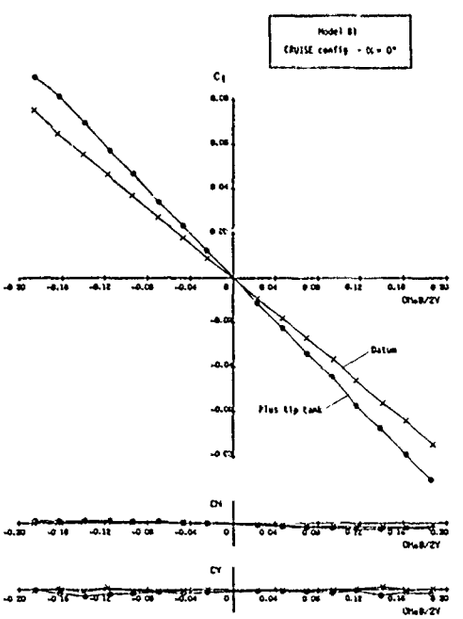

Figure 7-24 Effect of a tip store in the linear flow regime

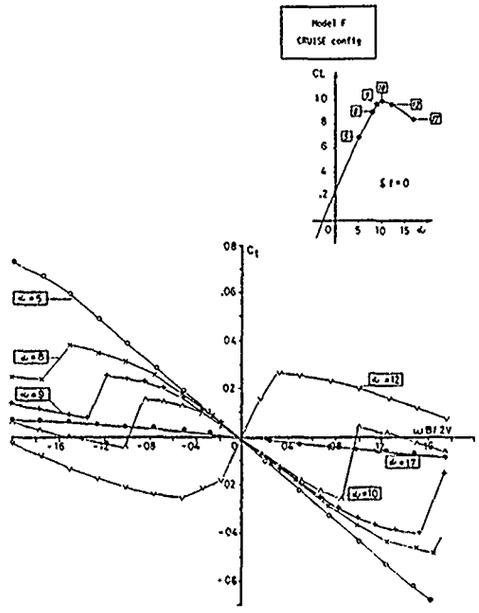

(a) Model F

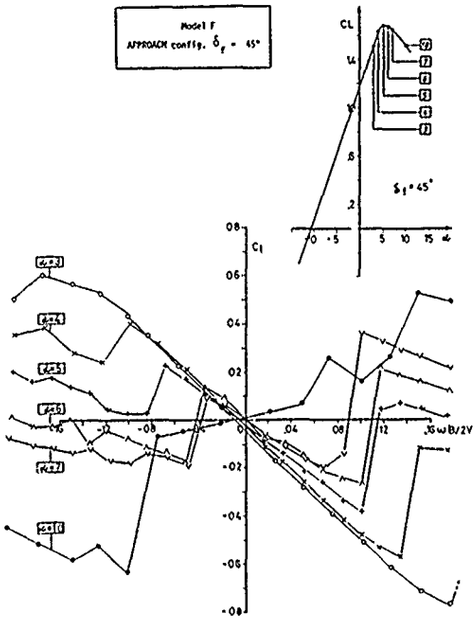

Figure 7-26 Angle-of-attack effects through the stall range high-lift configuration with root stall

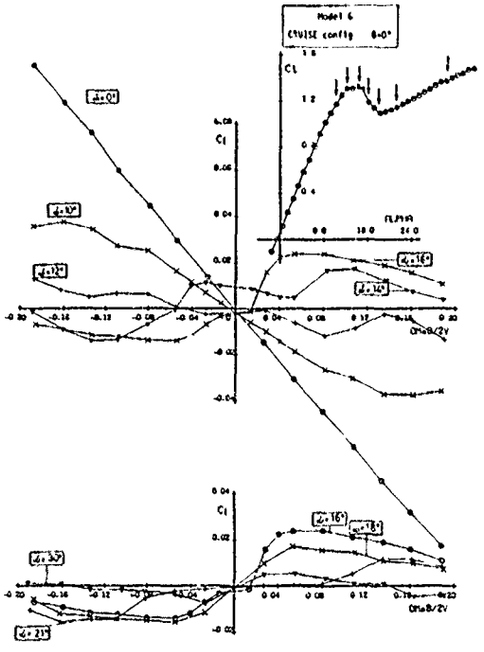

(b) Model G.

Figure 7-25. Angle-of-attack effects through the stall range

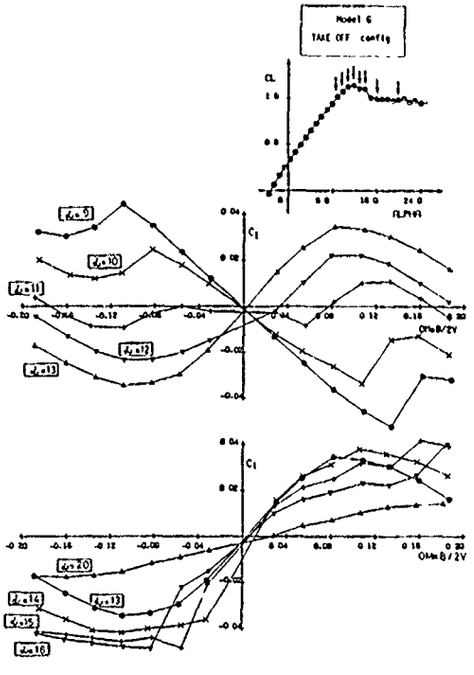

Figure 7-27 Angle-of-attack effects through the stall range. high-lift configuration with outboard stall

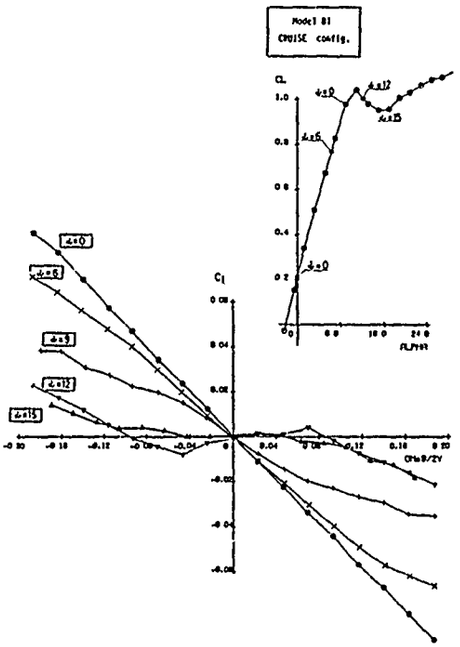

Figure 7-28. Roll damping through stall of a moderate aspect-ratio wing.

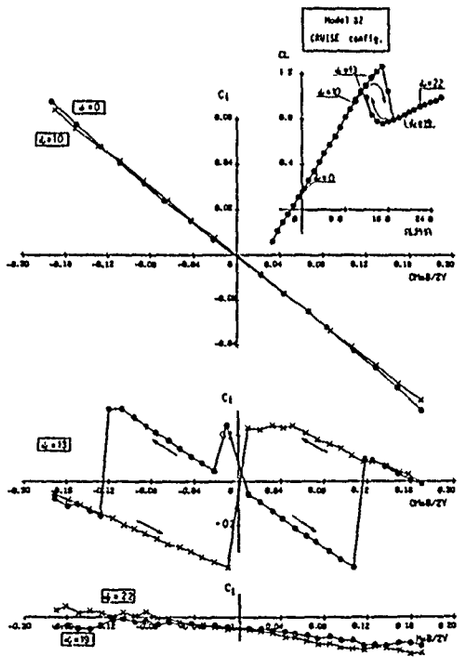

Figure 7-29. Hysteresis effects on a moderate aspect-ratio wing featuring abrupt stall.

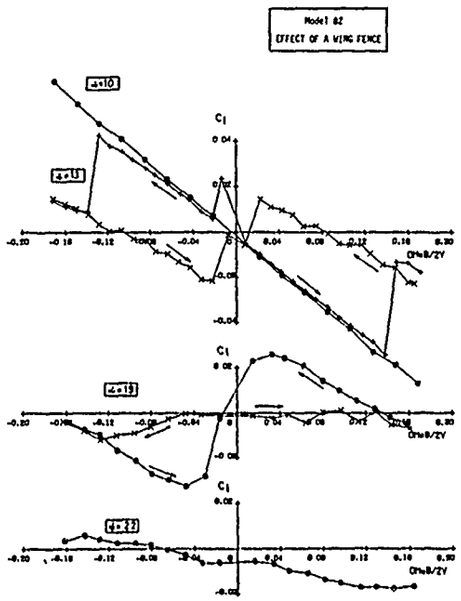

Figure 7-30. Effect of aerodynamic fixes on the wing for reduction of hysteresis.

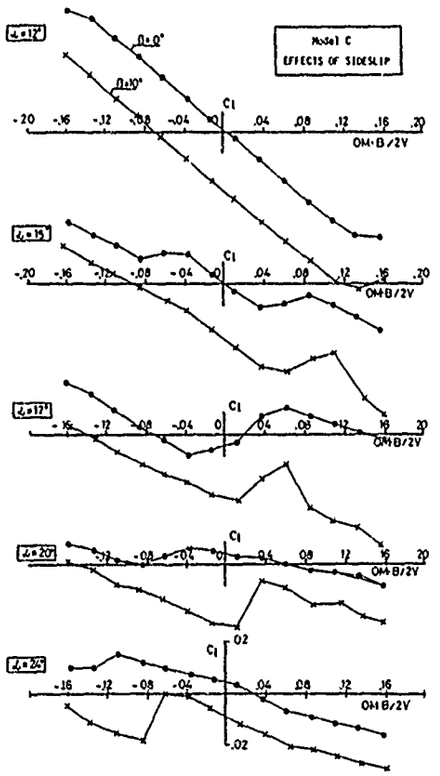

Figure 7-31. Nonlinear effects of sideslip at stall angles of attack.

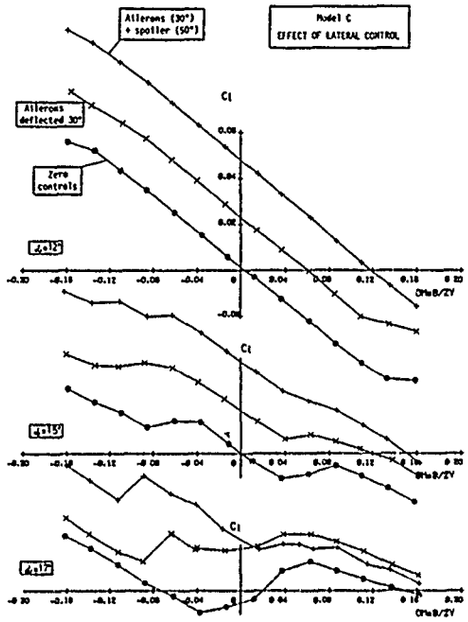

Figure 7-32. Effects of ailerons and spoilers.

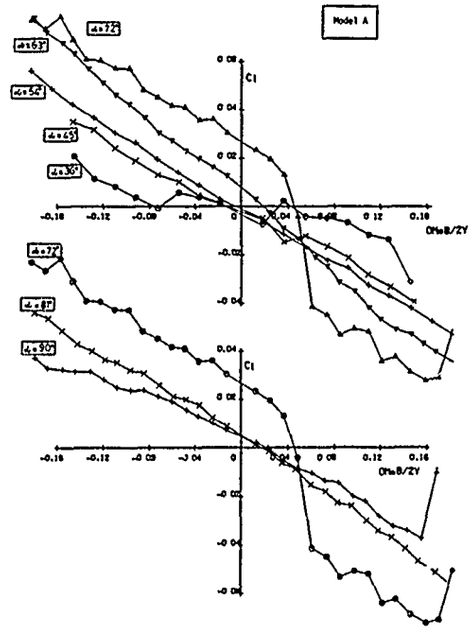

Figure 7-34. Effect of angle of attack in the high-α range - Model A.

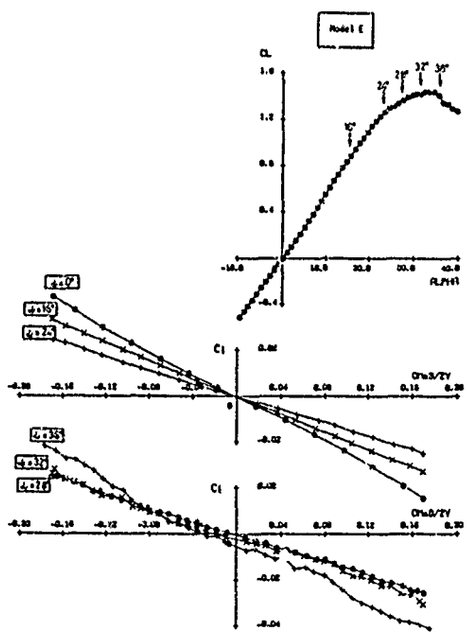

Figure 7-33. Roll damping of a low aspect-ratio configuration with extensive vortex lift.

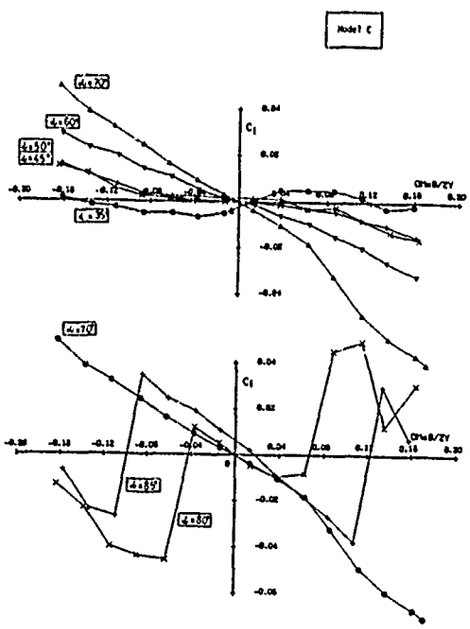

Figure 7-35. Effect of angle of attack in the high-α range - Model C.

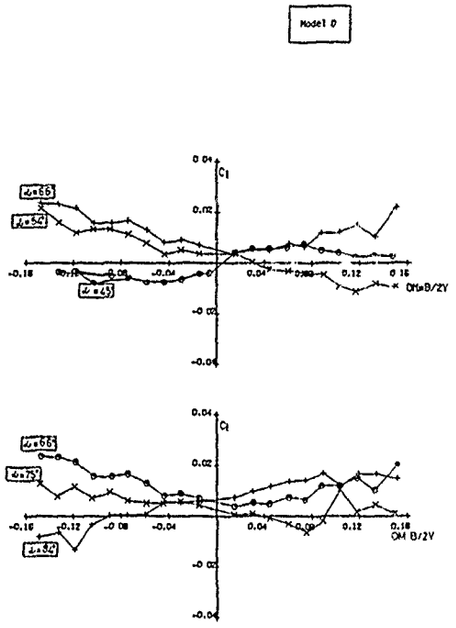

Figure 7-36. Effect of angle of attack in the high-α range - Model D

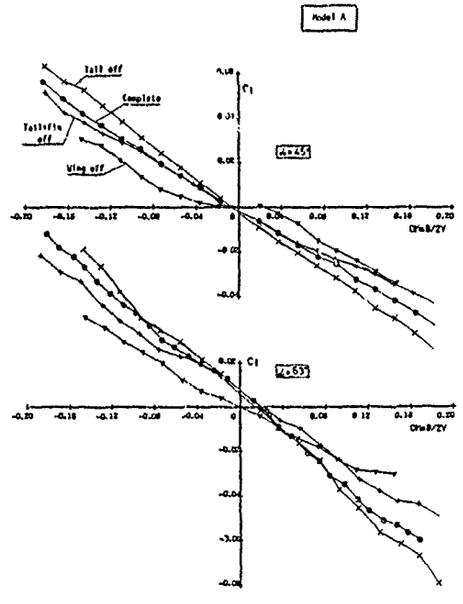

Figure 7-37 An example of model component buildup at high angles of attack.

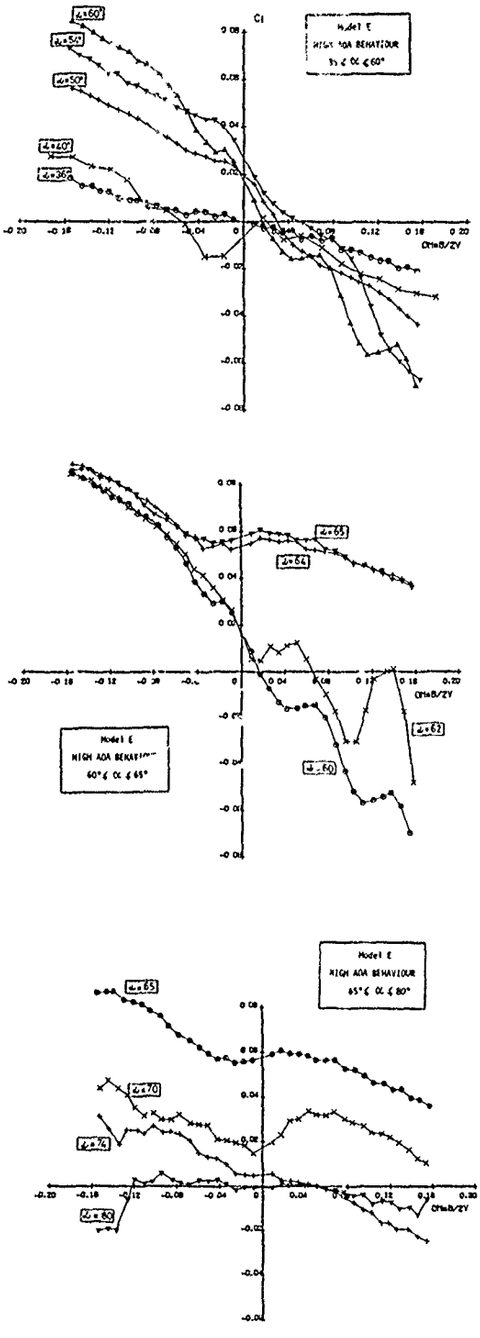

Figure 7-38 Roll damping of a slender configuration at high α

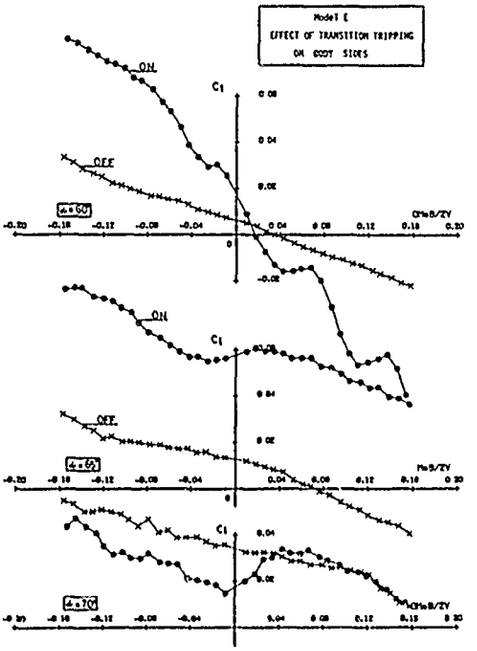

Figure 7-39 Effects of transition tripping on forebody

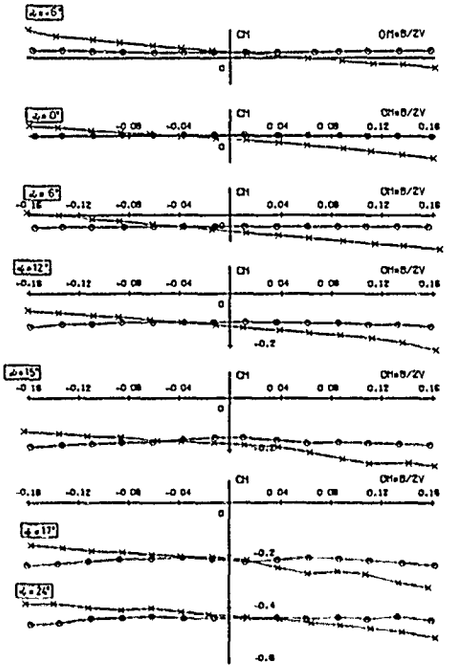

(b) Effect of sideslip on pitching moment

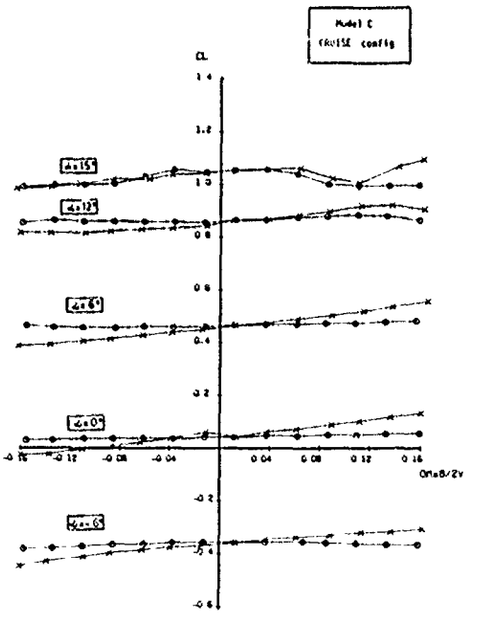

(a) Effect of sideslip on lift coefficient

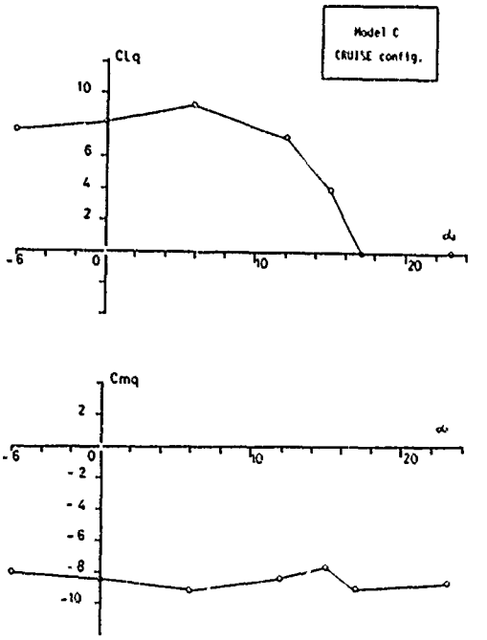

(c) Derivatives due to pitching extracted from rotary-balance data

Figure 7-40 Results for Model C

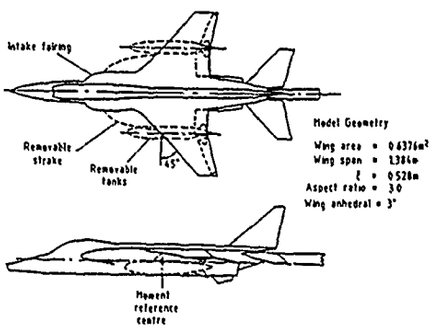

Figure 7-41. General arrangement of model

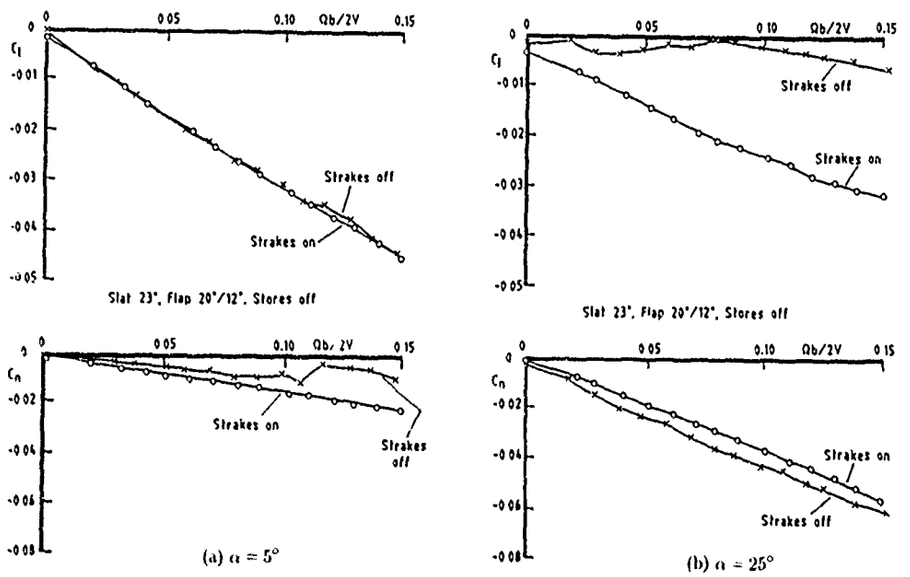

Figure 7-42 Effect of strakes

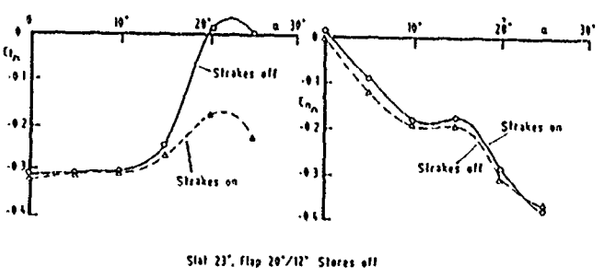

Figure 7-43 Effect of strakes on C_{l_Ω} and C_{n_Ω}

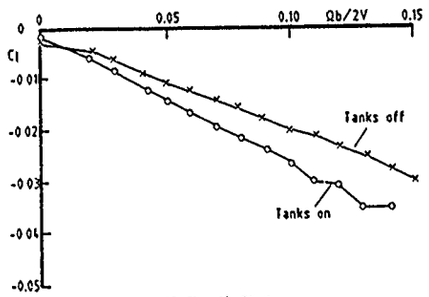

(a) $\alpha = 15°$.

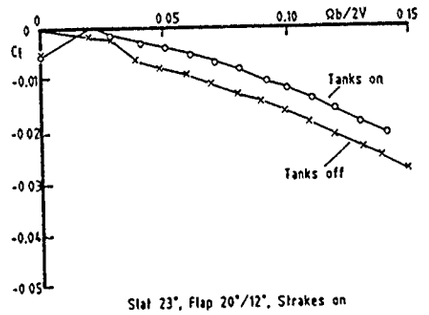

(b) $\alpha = 20°$

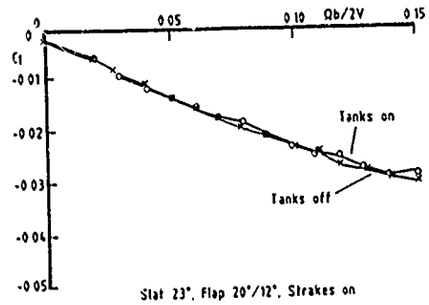

(c) $\alpha = 25°$

Figure 7-44. Effect of 1200ℓ under-wing tanks

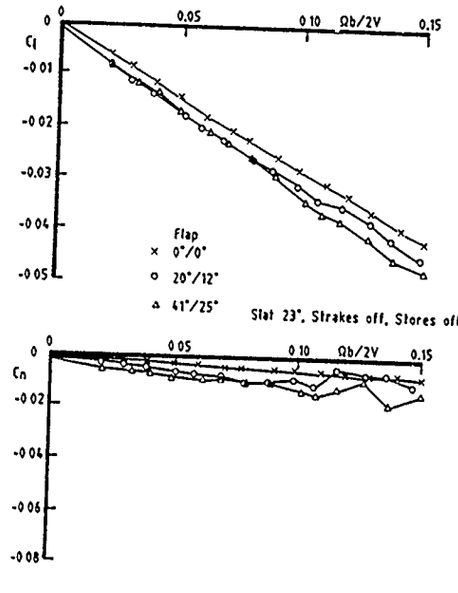

(a) $\alpha = 5°$

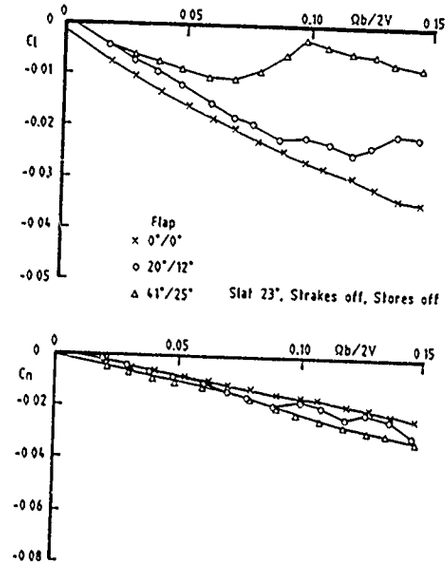

(b) $\alpha = 15°$

Figure 7-45 Effect of flap

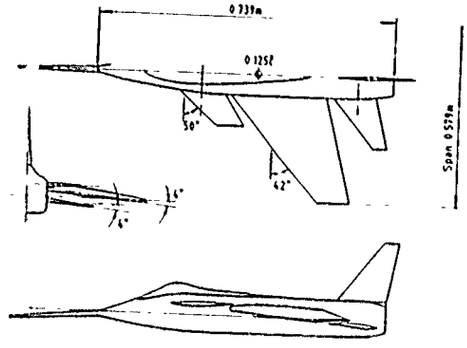

Figure 7-46 General arrangement of HIRM 1

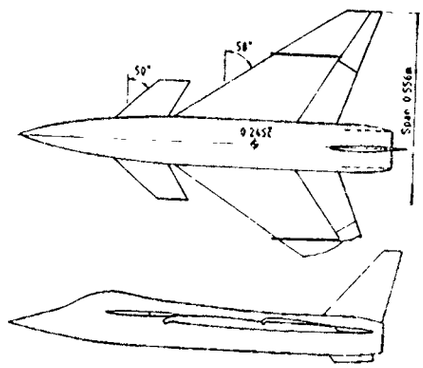

Figure 7-47 General arrangement of HIRM 2

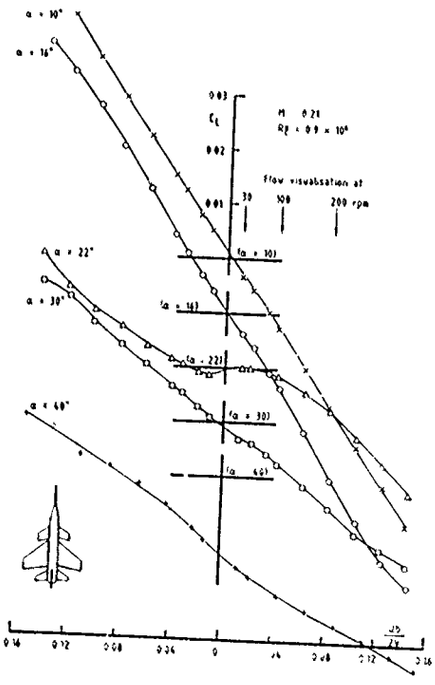

Figure 7-48 Effect of angle of attack on rolling moment, HIRM 1 L.E. droop = 20° $\eta_A = 0°$ $\eta_T = -10°$

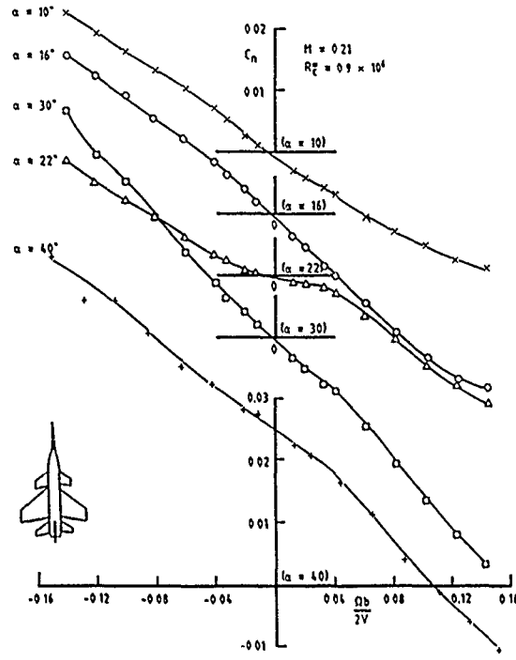

Figure 7-49. Effect of angle of attack on yawing moment; HIRM 1, L.E. droop = 20°, η_c = 0°, η_T = −10°

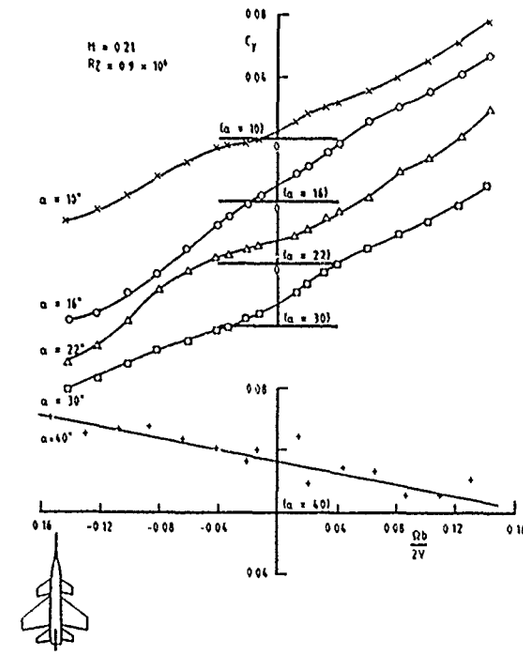

Figure 7-50 Effect of angle of attack on side force, HIRM 1, L.E droop = 20°, η_c = 0°, η_T = −10°

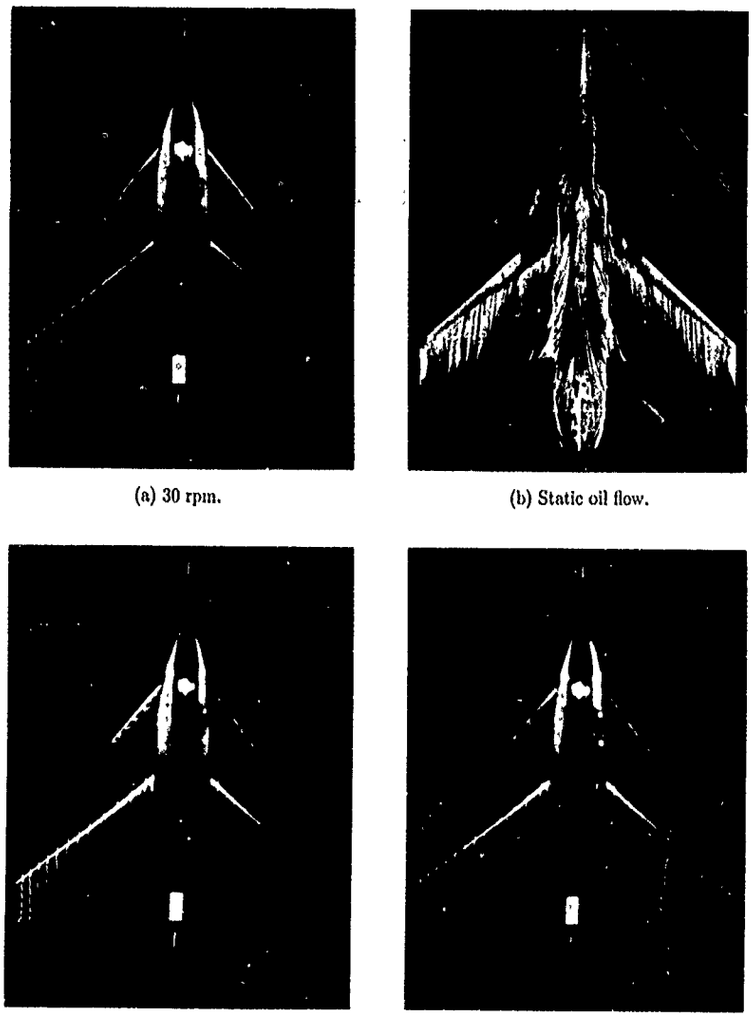

(a) 30 rpm.

(b) Static oil flow.

(c) 100 rpm.

(d) 200 rpm.

Figure 7-51. Flow visualization on HIRM 1. $\alpha = 16°$

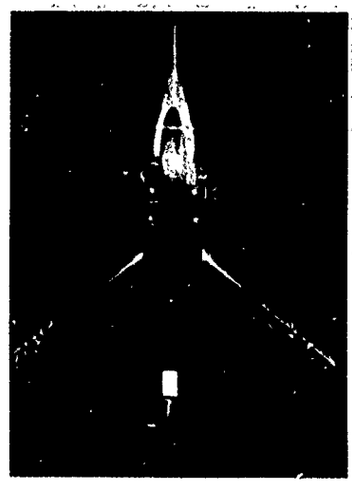

(a) 30 rpm.

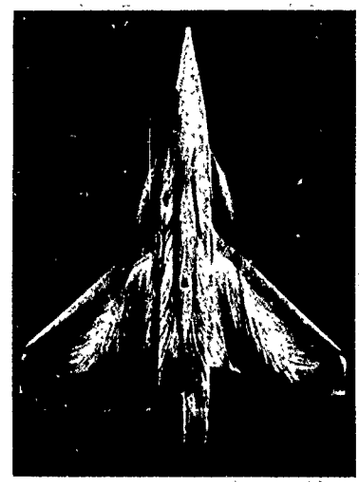

(b) Static oil flow. $\alpha = 20°$.

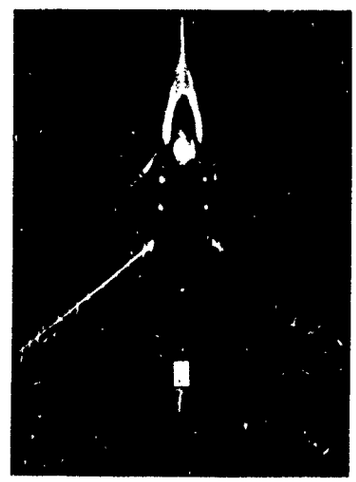

(c) 100 rpm.

(d) 200 rpm

Figure 7-52 Flow visualization on HIRM 1 $\alpha = 22°$

(a) 30 rpm.

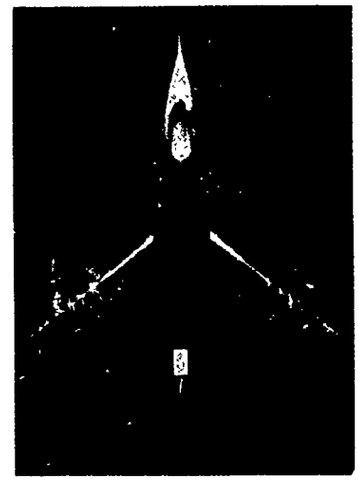

(b) 100 rpm.

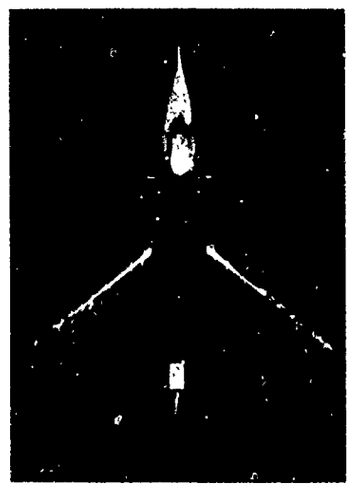

(c) 200 rpm.

Figure 7-53. Flow visualization on HIRM 1. $\alpha = 30°$.

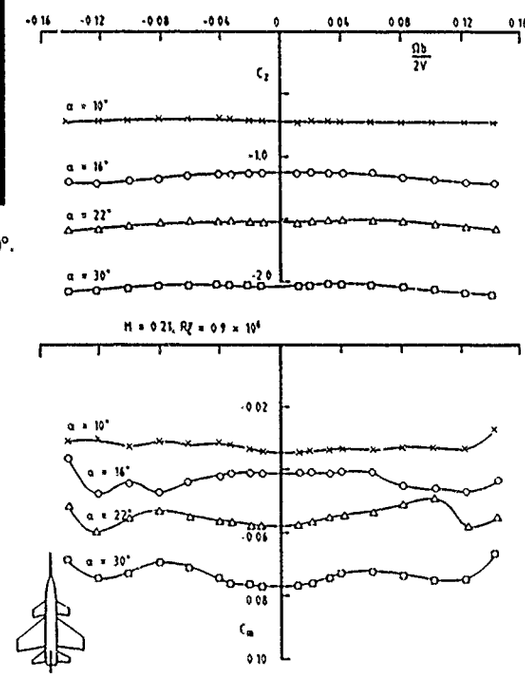

Figure 7-54. Effect of angle of attack on normal force and pitching moment; HIRM 1, L.E. droop = 20°, η_C = 0°, $\eta_T = -10°$

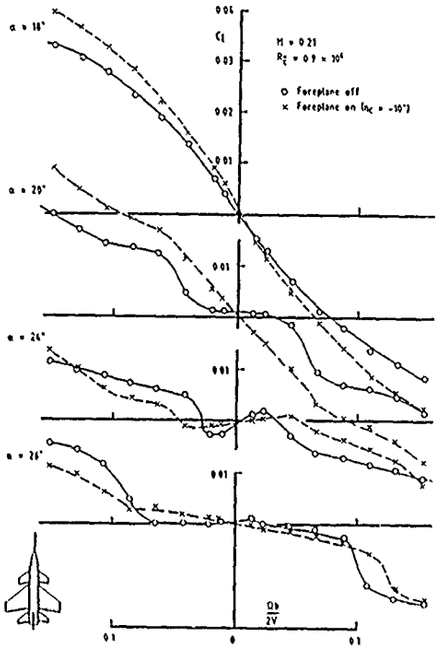

Figure 7-55 Effect of foreplane on C_l, HIRM 1, L E droop = 20°, $\eta_T = -20°$

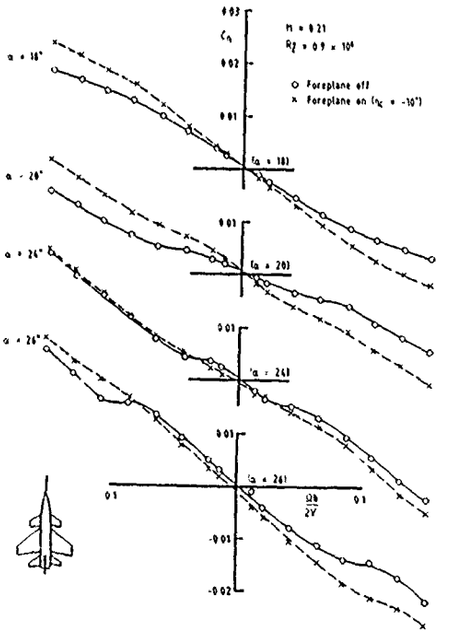

Figure 7-56. Effect of foreplane on C_n, HIRM 1, L E droop = 20°, $\eta_T = -20°$.

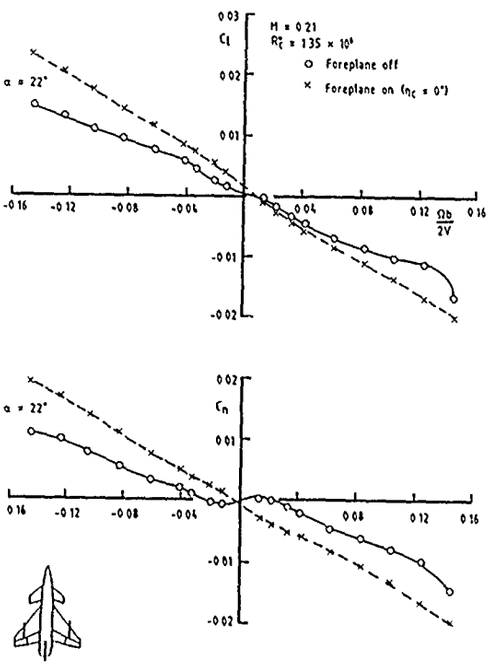

Figure 7-57 Effect of foreplane on rolling and yawing moments, HIRM 2, L.E droop = 12 5°, $\delta_f = 0°$

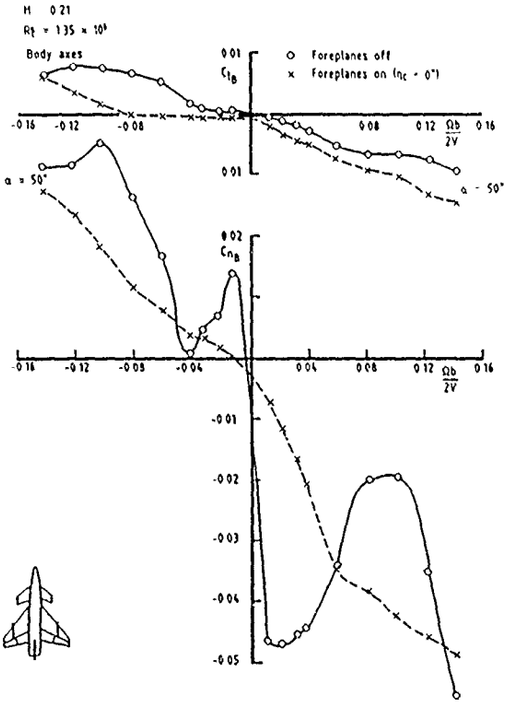

Figure 7-58. Effect of foreplanes on rolling and yawing moments (body axes); HIRM 2, L E droop = 12 5°, $\delta_f = 0°$

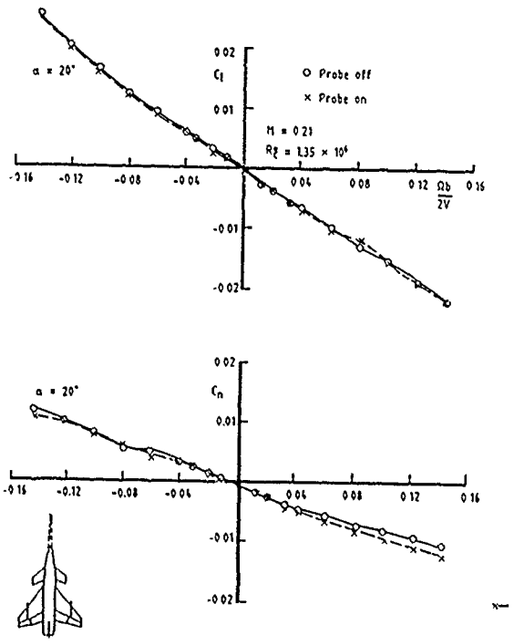

Figure 7-59. Effect of nose probe, HIRM 2, L.E droop = 12.5°, $\eta_c = 0°$, $\delta_f = 0°$, $\alpha = 20°$

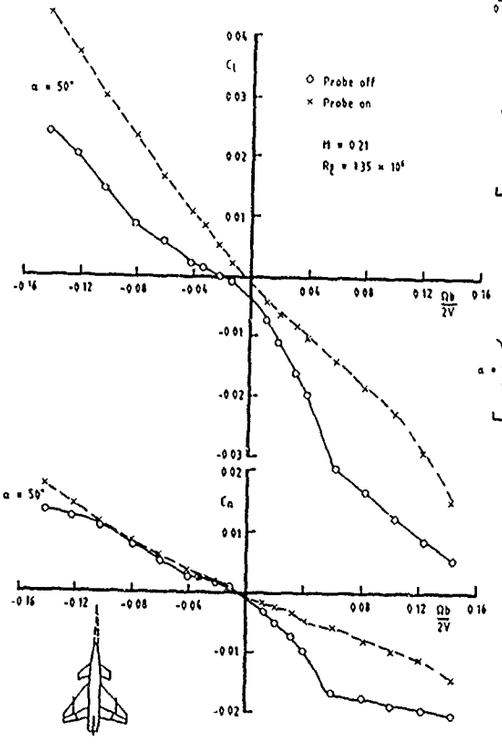

Figure 7-60. Effect of nose probe; HIRM 2, L.E. droop = 12.5°, $\eta_c = 0°$, $\delta_f = 0°$, $\alpha = 50°$.

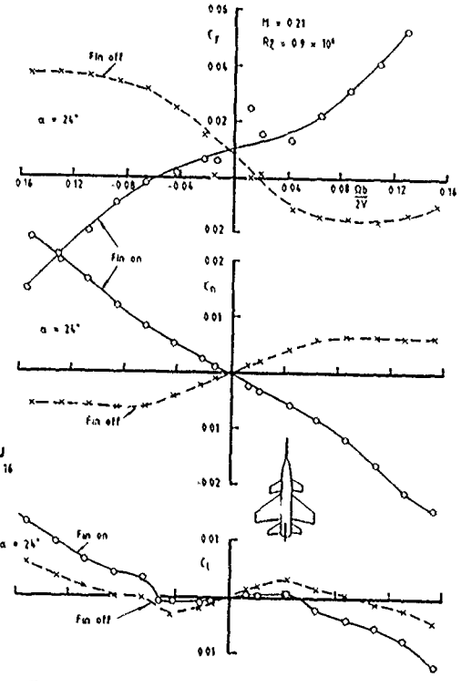

Figure 7-61. Effect of fin on C_Y, C_n and C_l, HIRM 1, L E droop = 20°, $\eta_c = -10°$, $\eta_T = -20°$

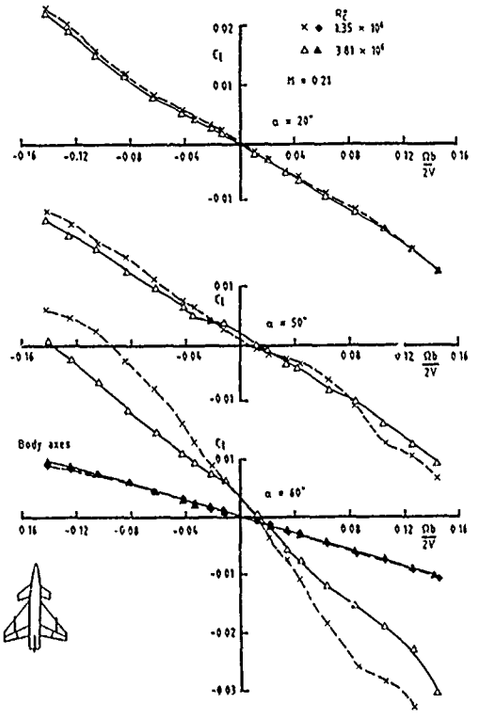

Figure 7-62. Effect of Reynolds number on rolling moment; HIRM 2, L.E. droop = 12.5°, $\eta_c = 0°$, $\delta_f = 0°$

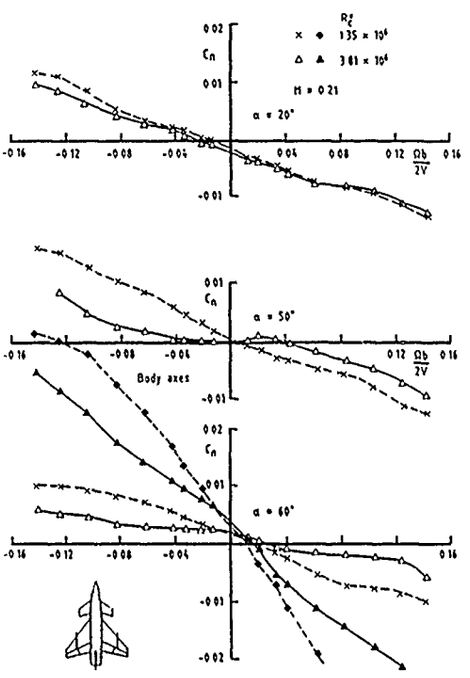

Figure 7-63. Effect of Reynolds number on yawing moment: HIRM 2, L.E. droop = 12.5°, $\eta_c = 0°$, $\delta_f = 0°$.

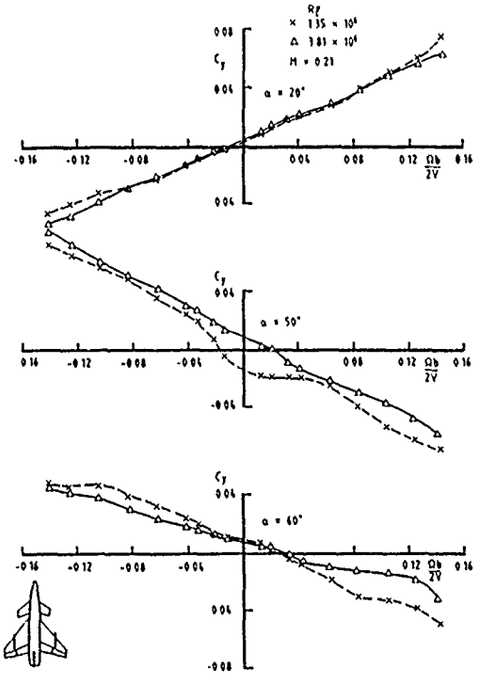

Figure 7-64. Effect of Reynolds number on side force, HIRM 2, L.E. droop = 12.5°, $\eta_c = 0°$, $\delta_f = 0°$.

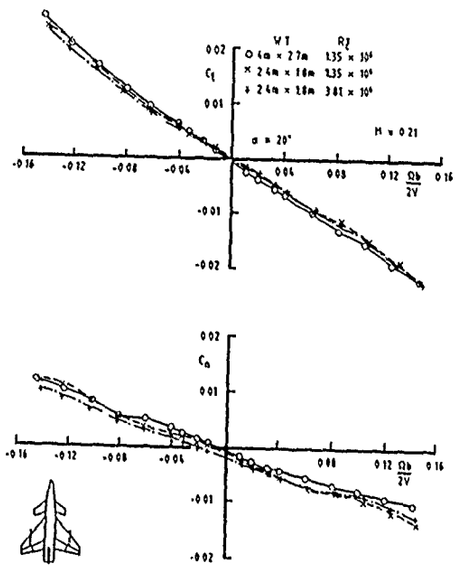

Figure 7-65. Comparison of results from two wind tunnels; HIRM 2, L.E. droop = 12.5°, $\eta_c = 0°$, $\delta_f = 0°, \alpha = 20°$.

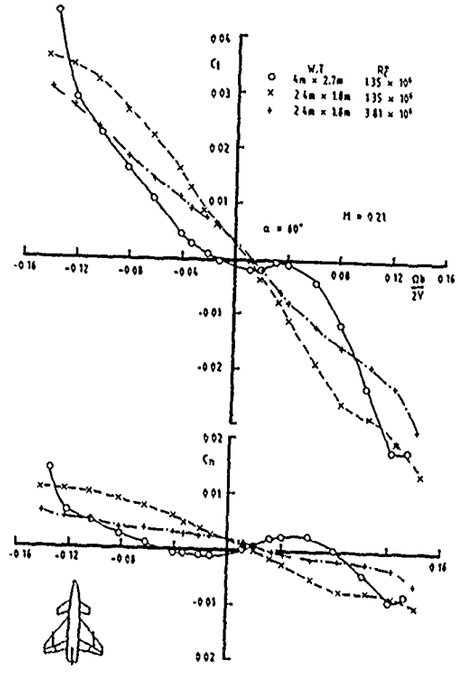

Figure 7-66. Comparison of results from two wind tunnels; HIRM 2, L.E. droop = 12.5°, $\eta_c = 0°$, $\delta_f = 0°, \alpha = 60°$.

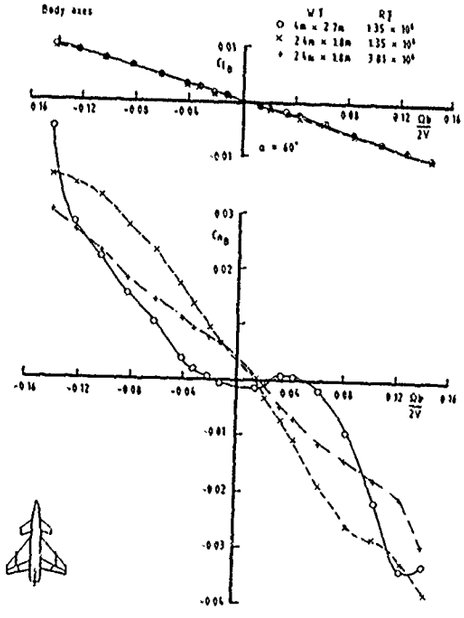

Figure 7-67. Comparison of results from two wind tunnels; HIRM 2, L.E. droop = 12.5°, $\eta_c = 0°$, $\delta_f = 0°$, $\alpha = 60°$, body axes.

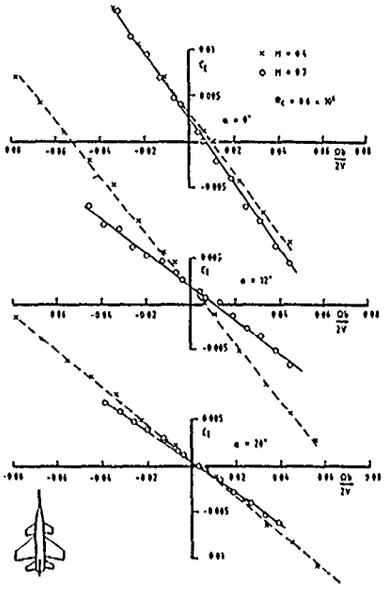

Figure 7-68. Effect of Mach number on rolling moment; HIRM 1, L.E. droop = 0°, $\eta_c = 0°$, $\eta_T = 0°$.

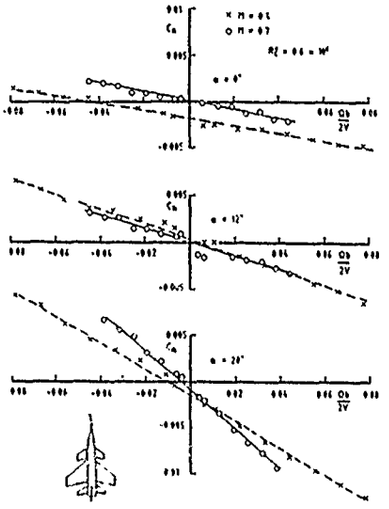

Figure 7-69. Effect of Mach number on yawing moment; HIRM 1, L.E. droop = 0°, $\eta_c = 0°$, $\eta_T = 0°$.

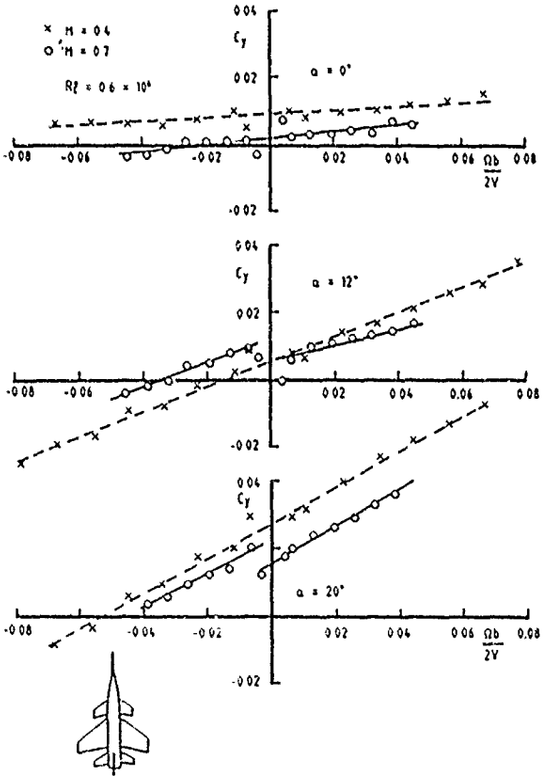

Figure 7-70 Effect of Mach number on side force. HIRM 1, L.E droop = 0° $\eta_c = 0°$, $\eta_T = 0°$

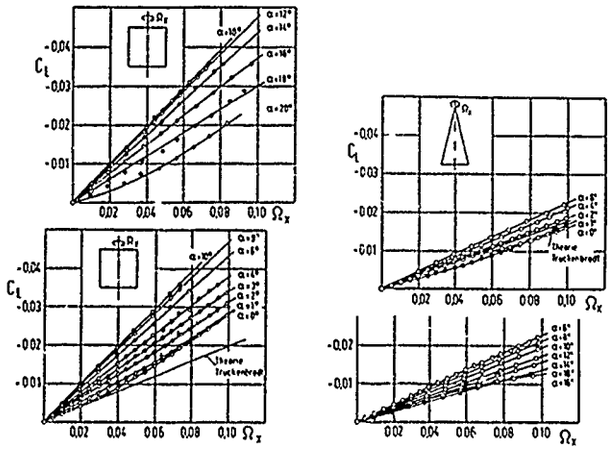

Figue 7-71. Rolling-moment coefficient vs dimensionless rate of rotation for two wings of different planform.

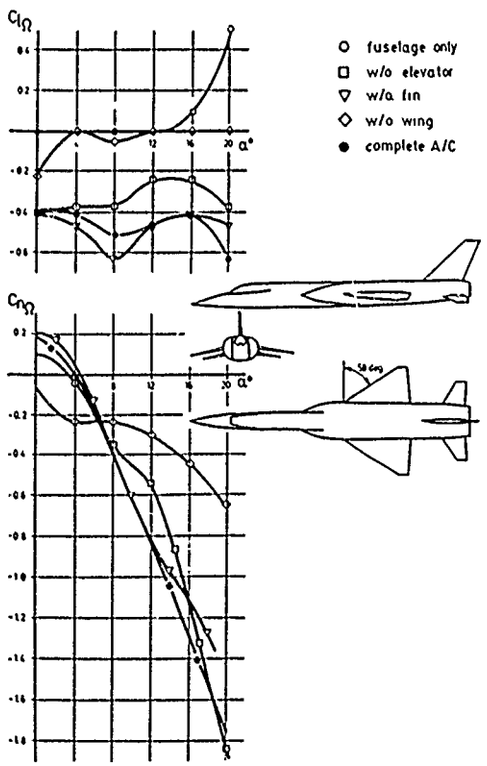

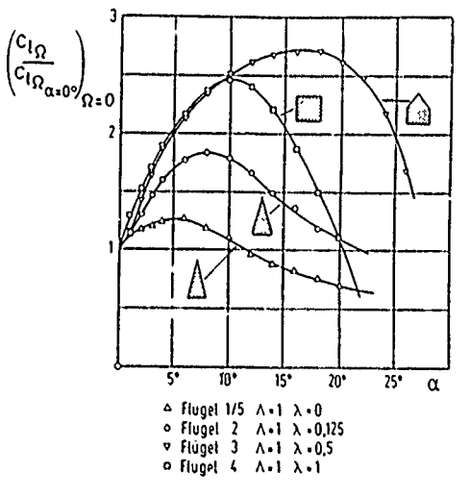

Figure 7-72. Normalized roll-damping derivatives as angle of attack for wings of different planform.

Figure 7-73. Lateral damping derivatives due to rolling, delta wing aircraft.

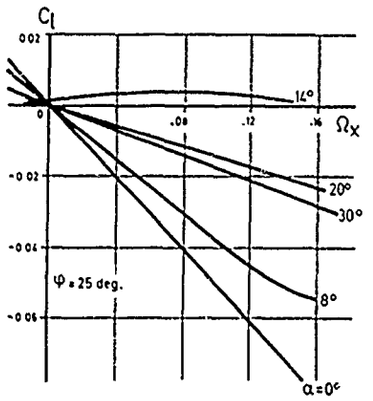

Figure 7-74. Rolling moment vs dimensionless rate of rotation, parameter, angle of attack

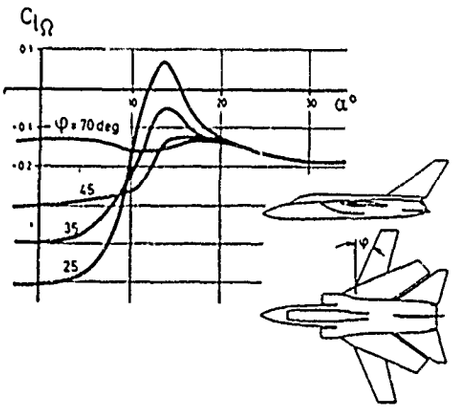

Figure 7-75. Roll damping vs angle of attack, influence of leading-edge sweep angle.

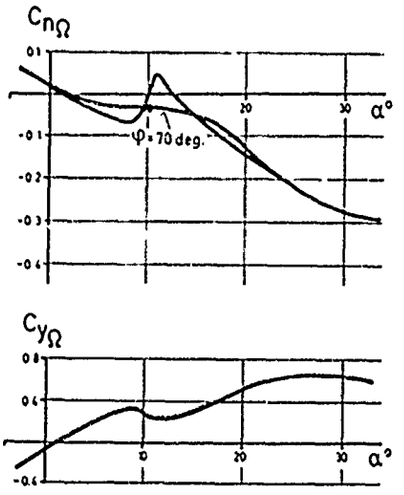

Figure 7-76. Lateral-directional damping derivatives due to rolling.

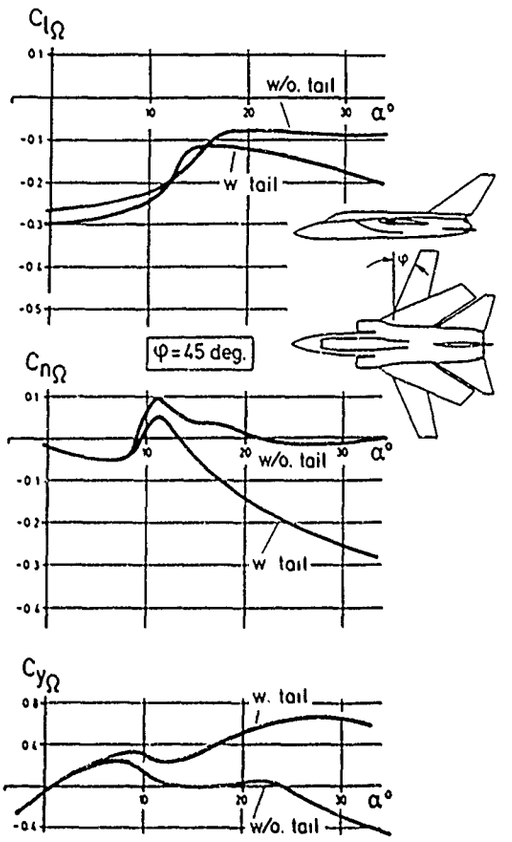

Figure 7-77 Lateral damping derivatives due to rolling, influence of tail (φ = 45°).

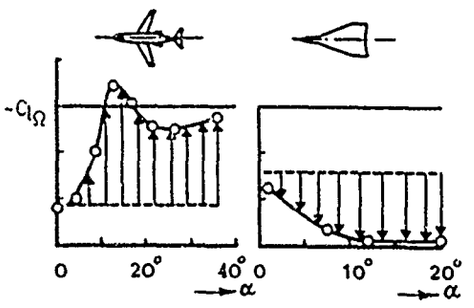

Figure 7-78. Roll damping derivatives for two configurations with different wing sweep angles.

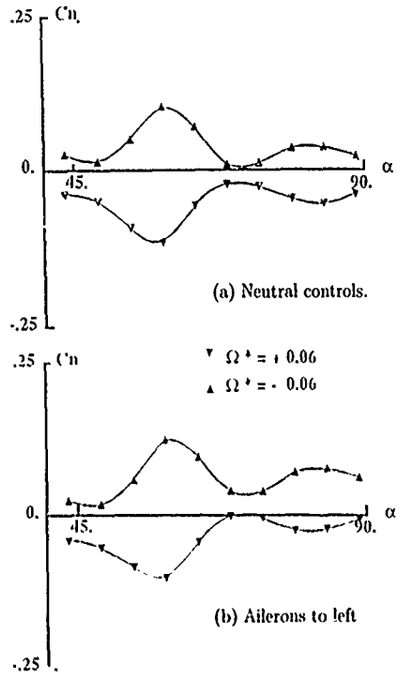

Figure 7-79. Yawing-moment variation with α; $\beta = 0°$

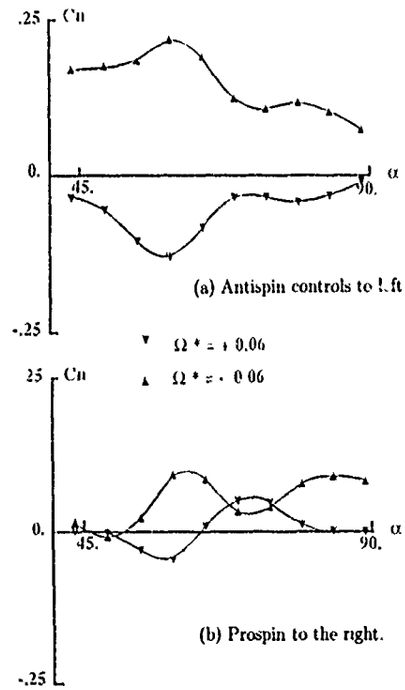

Figure 7-80. Yawing-moment variation with α, $\beta = 0°$

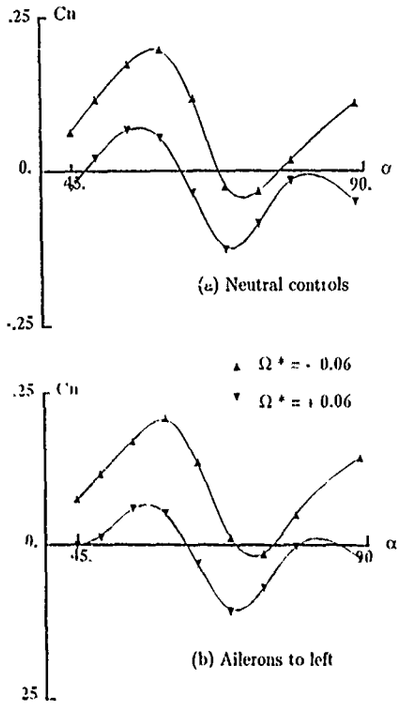

Figure 7-81 Yawing-moment variation with α; $\beta = -15°$

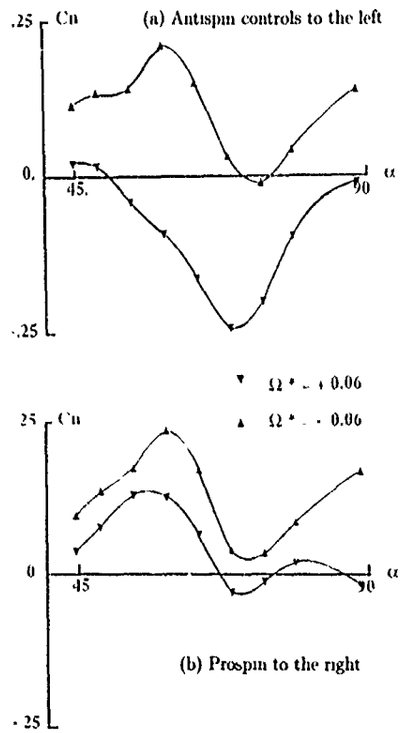

Figure 7-82. Yawing-moment variation with α; $\beta = -15°$

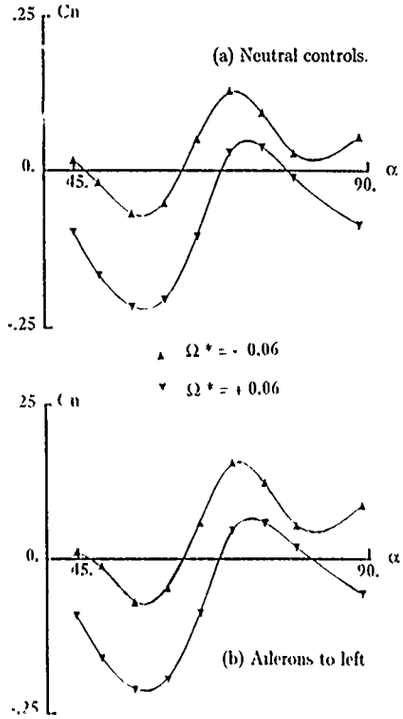

Figure 7-83 Yawing-moment variation with α, $\beta = +15°$

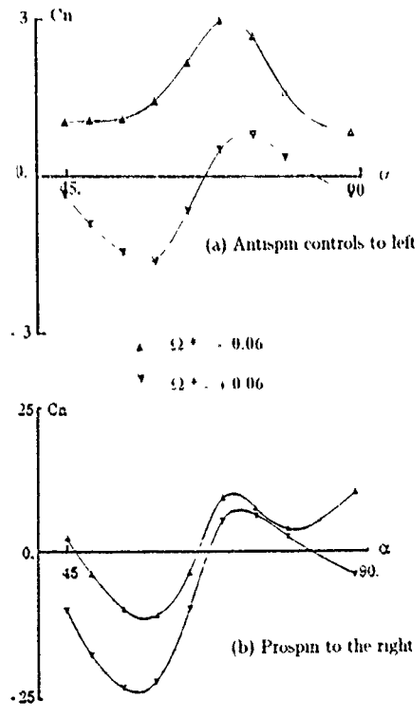

Figure 7-84. Yawing-moment variation with α; $\beta = +15°$

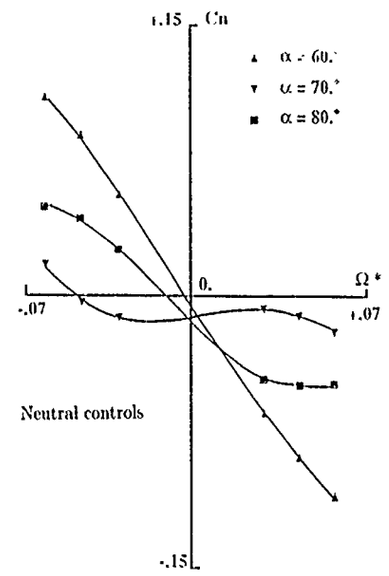

Figure 7-85. Effect of Ω* and angle of attack on yawing moment; $\beta = 0°$

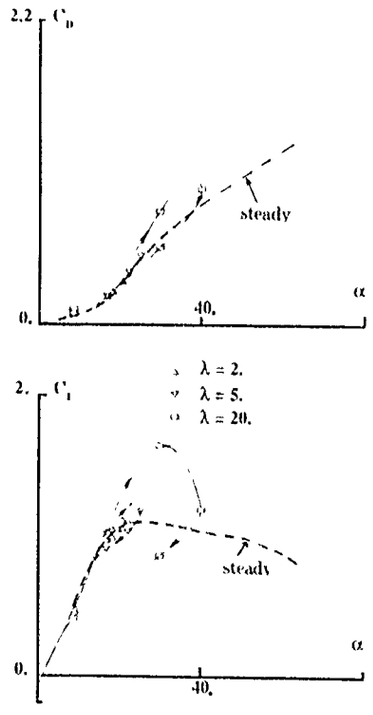

Figure 7-86 Unsteady effects on lift and drag

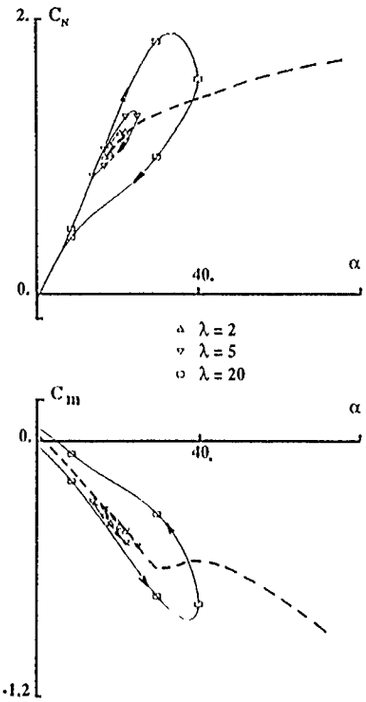

Figure 7-87. Unsteady effects on pitching moment and normal force

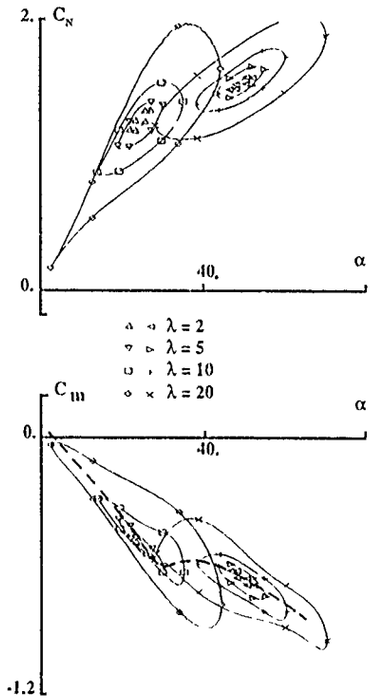

Figure 7-89. Unsteady effects on C_m and C_N for two mean angles; $\alpha_c = 25°$ and $\alpha_c = 50°$

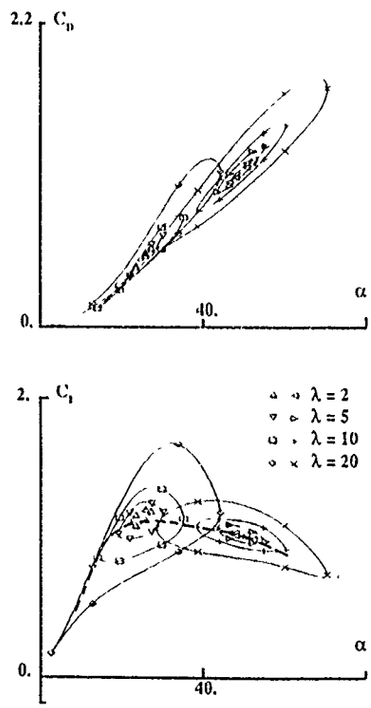

Figure 7-88 Unsteady effects on C_L and C_D for two mean angles· $\alpha_c = 25°$ and $\alpha_c = 50°$.

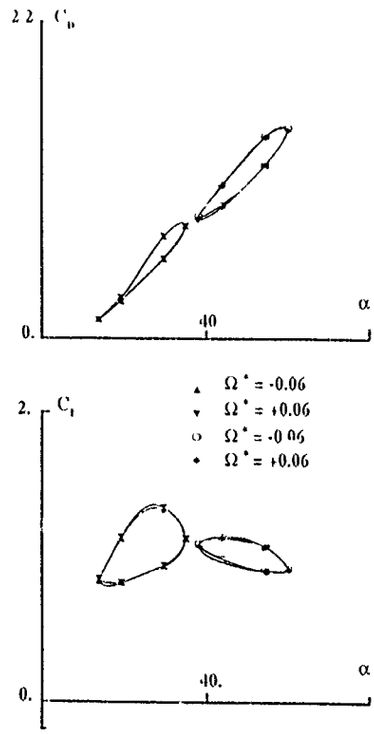

Figure 7-90 Effect of rotation direction on C_L and C_D, $\lambda = 10°$, $\alpha_c = 25°$ and 50°.

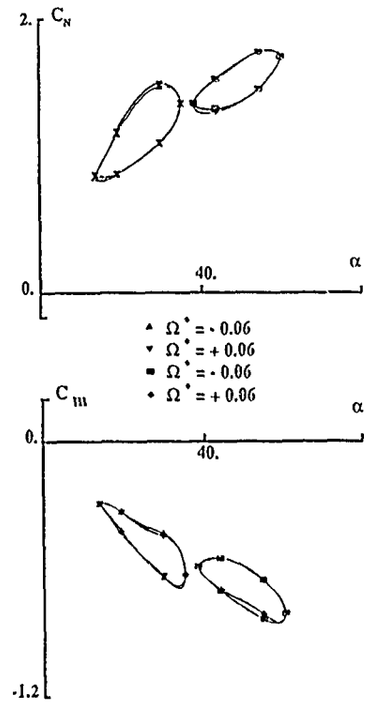

Figure 7-91 Effect of rotation direction on C_m and C_N, $\lambda = 10°$, $\alpha_c = 25°$ and 50°

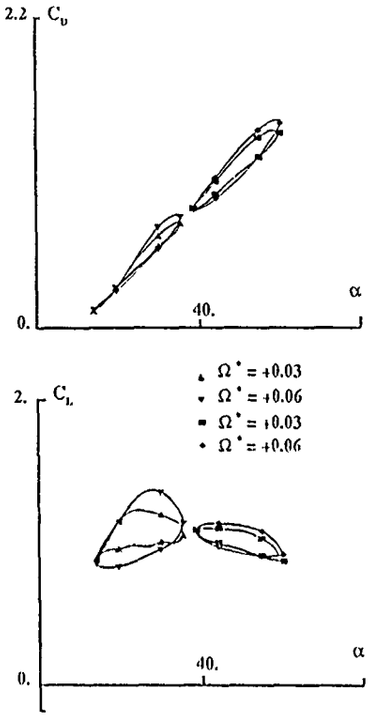

Figure 7-92. Effect of rotation rate on C_L and C_D, $\lambda = 10°$, $\alpha_c = 25°$ and 50°

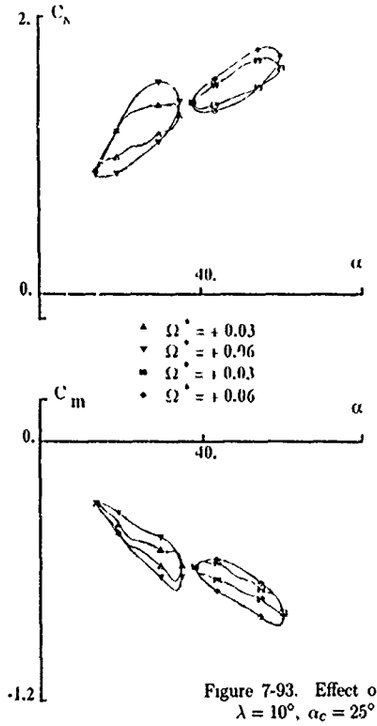

Figure 7-93. Effect of rotation rate on C_m and C_N; $\lambda = 10°$, $\alpha_c = 25°$ and 50°

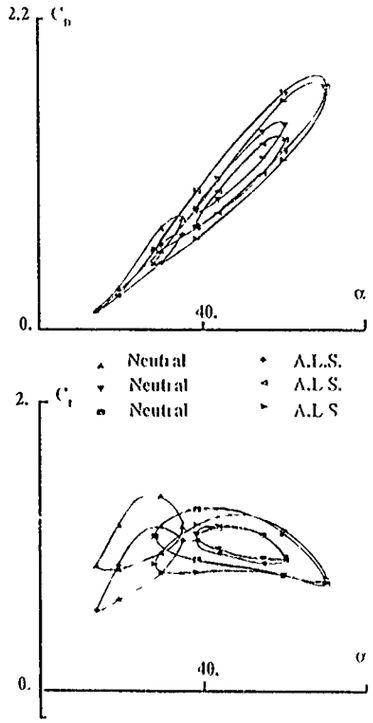

Figure 7-94 Effect of control setting on C_L and C_D, neutral and anti-left-spin positions

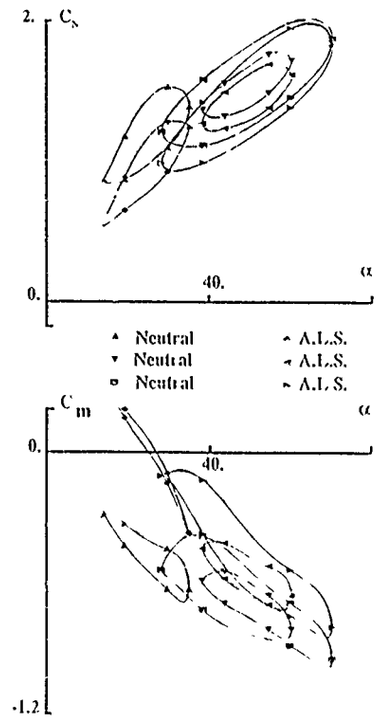

Figure 7-95 Effect of control setting on C_m and C_N, neutral and anti-left-spin positions

CHAPTER 8

FLUID DYNAMICS OF ROTARY FLOWS

8.0 INTRODUCTION

Previous chapters have concentrated on the measurement of forces acting on a rotating model. As in static aerodynamics, there is also a need to study the physics of rotary flows by both experimental and analytical methods. This chapter describes the diagnostic techniques of flow visualization and pressure measurement and analytical prediction methods, including comparison with model test data and extrapolation to full scale conditions. In addition, the importance of viscous flow phenomena in high-α rotary flows is discussed.

8.1 FLOW DIAGNOSTICS

8.1.1 Flow Visualization

As in a static wind-tunnel test, correlation of observations of the flow state on the model with the variation of measured forces is an important aspect of a rotary test. For instance, it may be possible to identify the source of a loss of roll damping and develop a method of rectifying it. Two of the techniques used in static testing, tufts and surface oil flow, are commonly used in rotary testing. Smoke has also been used in certain circumstances. Tufts are particularly suitable for visualizing general flow directions near the surface and identifying areas of separated low-energy flow. This technique has the advantage of instant response to changing conditions and recording of the flow pattern without interruption of the test. Surface oil flow is more suitable for visualizing detailed features such as laminar bubbles, vortex separation and reattachment, and shock waves. There is a possibility that when the ratio of wind speed to total velocity due to rotation is low, centrifugal forces on the oil may cause distortion of the flow at points on the model furthermost from the axis of rotation, but for most practical test cases the distortion is not significant.

At AerMacchi, both tufts and surface oil flow have been used, mainly to study flow phenomena which caused unexpected force variations on a model. Tufts on wing surfaces are observed by a video camera installed on the balance sector rotating with the model. The camera signal is transmitted directly to a TV receiver to avoid electrical noise which may be introduced through slip-rings. When the surface oil flow technique is used the paint is composed of titanium dioxide with oil and a dispersing agent as for static testing. Rotating the model wind-off shows that centrifugal forces do not cause any visible movement of the paint at the usual rotation rates (100 to 150 rpm). Flow patterns are photographed either after stopping the rotation and shutting down the wind tunnel, or by synchronized flash during the test. Examples of the way in which these techniques have been used are as follows:

a. Wool tufts on the upper wing surfaces of one configuration showed the abrupt extensive flow separation, usually near the wing tips, which coincided with severe autorotating moments near the stall

b. Surface-oil-flow patterns correlated with the measured damping effect of small fuselage modifications. The effect of adding two small strakes to the sides of the forebody of a military configuration were studied at very high angles of attack. Figure 8-1 shows the roll damping (about the wind axis) of the two configurations and the corresponding flow visualization is shown in Figures 8-2 to 8-5. The patterns are rather complex, with areas of dead air where the oil does not flow. However, it can be seen that on the basic configuration the flow separates from the highly curved bottom of the fuselage nose The tests showed that this separation could be asymmetrical and induce relatively high asymmetric forces. When the strakes were fitted the separation line was fixed with strong vortices acting on the sides of the canopy and there was symmetrical flow. The strakes were only effective in one position relative to the curved lower fuselage and for an angle-of-attack range of 65° to 85°. Prior to the rotary tests vertical wind tunnel tests with a free model had shown that a flat spin could be damped by the addition of strakes.

Examples of surface flow visualization and flow field visualization at MBB are shown in Figures 8-6 and 8-7. A titanium dioxide and oil mixture was used to show the different flow patterns on a static model (Figure 8-6) and on a model rotating at 200 rpm (Figure 8-7). For the rotating model, the photograph shows a more intense vortex on the downgoing port wing, which is at a higher effective angle of attack. To study interference effects from the rotary rig support structure, MBB built a small-scale, simplified rig for operation in a water tunnel. Colored dye streamlines were used to observe the flow field around the model and rig (Figure 8-8).

On the relatively small models (typically, 0.6 m span) tested on the RAE rotary rig, conventional tufts of 1 mm diameter would, it was felt, cause unacceptable flow interference if applied in the density required to give a flow picture of sufficient detail.

Impressive results have been obtained by Crowder[1] in the U.S. and by Dobney et al.[2] in the 5 m Wind Tunnel at RAE using 'minitufts' These are made from nylon monofilament, 0.04 mm diameter, coated with a fluorescent dye When viewed in ultra violet light their apparent optical diameter is large compared with the actual diameter, which allows them to be easily seen and photographed. These tufts do cause a small interference but for rolling tests the level of interference is considered to be insignificant compared with other limitations on the accuracy of dynamic force measurements. Another possible limitation of the technique for rolling tests is that the centrifugal force on tufts near the wing tips of the model would cause errors in apparent flow direction. However, an approximate calculation indicates that the ratio of aerodynamic force to centrifugal force is in excess of 1,000, so that errors would be negligible.

Although the model is in motion during a rolling test, the tuft pattern should be constant at a steady rotational speed and the requirement is to photograph the tuft pattern at any time during a steady rotation. One possibility is to mount the camera on the rotating element of the rig. However, it was decided that a more elegant and practical method would be to fix the camera to the working section structure and illuminate the tufts with a UV flash. The flash is synchronized with the drive shaft position so that the exposure is made when the wings of the model are normal to the camera lens. Tests[3] were made in the 4 m × 2.7 m (13 ft × 9 ft) Low Speed Wind Tunnel at RAE Bedford at a wind speed of 70 m/s.

A camera and flash units are mounted in the roof of the working section. The flash units are fixed in specially made cut-outs in a roof panel, but the camera position and angle are adjustable to suit the model angle of attack. Exposures are made through a transparent panel in the roof. Using a pair of contacts on an encoder geared to the drive shaft and a specially designed electronic circuit, the flash units can be fired to photograph either the top or bottom of the model or either side of the fin.

The method of attaching tufts is fairly straightforward. After thoroughly cleaning the surface to be tufted, a grid is marked on it. The nylon monofilament is fixed in chordwise lengths, with the ends secured with adhesive tape to the underside of the leading and trailing edges. A hypodermic syringe is then used to apply a small amount of clear cellulose dope at the marked tuft attachment points. When the dope has dried, the nylon is cut with a scalpel upstream of these attachment points. The length of each tuft is about 15 mm. During testing, tufts in some locations tend to break off through fatigue or come unstuck but can easily be replaced individually after each run. Both the camera and flash units are operated remotely from the wind tunnel observation room.

An example of the use of mini-tufts is shown in Figures 8-9(a) to (d). The development of separated flow on the HIRM 1 configuration is shown as angle of attack is increased from 0° to 30°. In each case the rotation speed is 100 rpm, so that the port wing tip is effectively at $\alpha = -2.5°$ and the starboard wing tip at $\alpha = +2.5°$. For $\alpha = 0°$, Figure 8-9(a), the tufts show a symmetrical flow pattern with attached chordwise flow over both wings but at $\alpha = 16°$, Figure 8-9(b), there are differences in the tuft patterns on the port and starboard wings with evidence of a vortex developing on the outer starboard wing due to the increased effective angle of attack. At $\alpha = 22°$, Figure 8-9(c), tufts on the starboard outer wing indicate that the flow is separated and broken down whereas on the port outer wing, at a lower effective angle of attack, the tufts indicate that a strong part-span vortex is established. This would give greater suction on the port wing and tend to decrease roll damping or even result in negative damping. At $\alpha = 30°$, Figure 8-9(d), the tufts show that the flow has broken down on both outboard wings.

When a three-dimensional picture of the flow is required, it may be possible to use smoke or a similar medium for flow visualization. Few tests of this type have been made, but one example, using titanium tetrachloride, is given. This highly volatile and corrosive substance is painted onto a suitably protected model and, in the presence of moist air, produces dense white fumes consisting of titanium dioxide and hydrochloric acid! In low-speed coning tests of a cone-cylinder model, Yoshinaga et al.[4] found through flow visualization that two pairs of asymmetric vortices existed, one forward of the coning axis and one pair aft of it (see sketch in Figure 8-10). In static tests, only three vortices are observed, with the aft one starting roughly at the location of the coning axis. Although the coning motion possibly could aid in the development of a new asymmetric vortex pair aft of the coning axis,[5] as is illustrated in Figure 8-10, flow visualization pictures show that the sting support, in spite of its slenderness, could have had an influence on the asymmetric vortex geometry (Figure 8-11). Two protrusions of the miniature bearings supporting the pitch axle (Figure 8-12) also appear to have had some influence on the flow[4] (Figure 8-13). Further tests are planned to determine what the effects of the very unobtrusive looking support system can have been on the formation of asymmetric vortices and the resulting coning motion.

8.1.2 Pressure Measurement

Measurements of pressure distribution are routinely made in static and, to a lesser extent, in oscillatory wind tunnel tests, but not in rotary tests. One reason for this is the difficulty of implementing such a technique on a rotating model rather than a lack of interest in the data obtained from such tests. Especially when combined with force measurements and flow visualization, a knowledge of the pressure distribution can help in understanding how the wing flow characteristics change with rate of rotation, angle of attack, flap deflection, etc. Wing modifications to avert autorotation, for instance, could then perhaps be more easily accomplished.

An impressive test[6] was made by NACA in 1947, when a set of five large-scale wings (Figure 8-14) were tested in the 40- by 80-Foot Wind Tunnel at Ames. The primary aim of the tests was to study the effects of sweep on roll damping and the wing-sweep angles were 0°, ±30° and ±45° (quarter-chord line). Wing sections were NACA 0015 at the root, changing to NACA 23009 at the tip. Damping in roll C_{l_p} was measured by means of a strain-gauge balance at the hub of the rotating wing and wing surface pressures were measured by manometers at the wing root, connected to 180 orifices located at eight spanwise stations in each pair of wing panels. The effect of wing sweep on the variation of C_{l_p} with α is reproduced in Figure 8-15 for $\lambda = 0°$ and $\lambda = \pm 45°$. Figure 8-15(a) shows that for the forward swept wing ($\lambda = -45°$), C_{l_p} doubles in magnitude as α increases from 0° to 20° before diminishing rapidly to zero at $\alpha = 30°$. For $\lambda = 45°$, Figure 8-15(c), there is only a small increase of C_{l_p} with α and a more gradual fall-off from $\alpha = 15°$. For $\lambda = 0°$, Figure 8-15(b), C_{l_p} is larger at low angles of attack but declines rapidly at $\alpha = 15°$, reaching zero at $\alpha = 20°$. Section lift coefficients were determined from the pressure measurements and plotted against α for each chord station. The plots for $\lambda = -45°$, 0° and 45° reproduced in Figures 8-16(a), (b) and (c), respectively, show the section lift coefficient c_l for the stationary wing as well as for a rotation rate corresponding to $pb/2V = 0.11$ on the upgoing and downgoing sections. Figure 8-16(a) shows that for the outboard sections at high angles of attack the increments in c_l due to rotation are large at $\lambda = -45°$ compared with corresponding data for $\lambda = 0°$ and $\lambda = 45°$, Figures 8-16(b) and (c), respectively. This accounts for the large increase in C_{l_p} at high α for

$\lambda = -45°$. These large increments in outboard section lift are probably due to draining of the boundary layer away from the tips, thereby decreasing tip flow separations and increasing the local $c_{l_{max}}$.

More recently, as part of a study[7] of the effect of component interactions on spin aerodynamics, Bihrle Applied Research at NASA Langley has measured the pressure distributions on the vertical and horizontal tail surfaces and aft fuselage of a trainer airplane configuration during rotary tests in the NASA-Langley Spin Tunnel. A total of 202 pressure ports was installed in a 1/7-scale model (Figure 8-17) and the pressures were measured using a transducer/scanning valve system. Data were obtained at angles of attack of 20°, 40° and 50° over a range of $\Omega b/2V$ of ± 0.5.

It is well known that the relative locations of the vertical and horizontal tails can influence the spin and recovery characteristics of an airplane. The cause of such effects was logically thought to be related to the change of pressures on the vertical tail due to the presence of the horizontal tail, but until the subject tests a systematic set of data was not available for analysis of this effect. Results of the subject tests indicated that with the horizontal tail removed, the trailing side of the vertical tail (left side of the vertical tail in a left spin) experienced a large negative pressure, which produced a damping (anti-spin) moment. With the horizontal tail in place, however, the negative pressure switched to the leading side of the vertical tail, resulting in propelling (pro-spin) moments (Figures 8-18 and 8-19).

8.2 ANALYTICAL PREDICTION TECHNIQUES

The value and efficiency of experimental rotary-balance tests would be significantly increased by the availability of valid computational or semi-empirical methods. At the present time, however, relatively few studies of the accuracy of such approaches have been accomplished due to the complexity of high-alpha unsteady aerodynamics Nevertheless, the development and validation of computational techniques remains an important goal.

The classical approach used for the estimation of rotary effects—particularly for wings—at low angles of attack, involves the application of strip theory and numerical integration of the aerodynamic characteristics of elements of the airplane. At low angles of attack, this approach has proven to be relatively accurate, and it is now used in computer-based design methods. However, for high-angle-of-attack conditions the complexity of separated flows, which involves significant levels of component aerodynamic interference, hysteresis effects, time-dependent behavior and Reynolds-number effects, poses a major obstacle to the valid applications of strip theories and overall progress in the analytical area.

One logical approach to advancing the analytical capability, at least as a first step, is a relatively simple experimental/analytical study of the rotary aerodynamics of isolated airplane components to define the ability of the computations to predict aerodynamic phenomena of interest. An unpublished exploratory project, directed by E. C. Polhamus at NASA Langley, was conducted to evaluate the application of analytical methods to an extension of Polhamus' earlier research on effects of fuselage cross-sectional shape on spinning characteristics.

The investigation consisted of an assessment of strip theory and sectional cross-flow theory when applied to predictions of the spin-damping characteristics of isolated fuselage shapes at an angle of attack of 90°. The study included several key variables, including fuselage cross-sectional shape, rotation rate and Reynolds number. The experimental setup, shown in Figure 8-20, involved isolated fuselage shapes mounted on an internal balance which measured yawing moment in body axes for various free-stream and rotary conditions in the Langley 7- by 10-foot tunnel. The analytical procedure used is depicted in Figure 8-21. The local sectional value of RN and cross-flow angle ϕ were computed for specific free-stream and rotary conditions. A 2-D aerodynamic data bank[8] based on static tests of cross-sectional shapes at combinations of RN and cross-flow angle was then utilized for input data to predict the local sectional aerodynamic characteristics. Finally, the local sectional data were integrated for the entire fuselage, yawing moments were computed, and the results compared with experimental data.

The fuselage shapes tested on the rotary apparatus are shown in Figure 8-22. The cross sections were carefully selected to include shapes known to be sensitive to Reynolds number. Also, the fuselage shapes ranged from simple, constant cross-sectional cylindrical shapes to those more representative of pointed fuselages

Typical 2-D cross-flow data for a circular shape and a square shape with rounded corners are shown in Figure 8-23. The square shape shows that, when subjected to a local flow angle of 10° (as would occur at a typical fuselage station in a spin), the side force generated changes from propelling values at low RN to damping values at higher values of RN. Other cross-sectional aerodynamic characteristics are indicated in Figure 8-24 for a similar range of RN. Additional data are presented in Figure 8-25, which illustrate the nonlinear effects of local flow angle for the rounded-square section, especially at supercritical values of RN These aerodynamic characteristics, and, in particular, their large variations with RN, were felt to present a challenge to the analytical procedure.

Data comparing experimental and analytical results for a constant rounded-square fuselage shape are shown in Figure 8-26. As expected, on the basis of the 2-D shape sensitivity to RN, the fuselage model produced propelling moments for the lower values of $\Omega b/2V$ at $RN = 0.25 \times 10^6$, whereas the model produced damping at $RN = 0.71 \times 10^6$. The analytical predictions indicate trends similar to those observed in the experiments. However, the magnitude of the moment was not accurately predicted, particularly at the lower RN. For certain combinations of cross-sectional shapes, the analytical results were in general agreement with the experimental data, such as in Figure 8-27. On the other hand, for the configuration shown in Figure 8-28 the agreement was very poor, particularly at high RN where the experiment and theory differed completely. Finally, the phenomenon of hysteresis was encountered for certain shapes near the critical cross-flow RN. For example, shown in Figure 8-29 are data obtained at RN values of 0.22×10^6, 0.54×10^6 and 0.44×10^6. The data at the lowest and highest RN were well-behaved and repeatable, however, at $RN = 0.44 \times 10^6$ the model exhibited a large hysteresis effect

which was not fully understood. The results obtained for a simple circular cross-section fuselage with a pointed nose are shown in Figure 8-30, illustrating good agreement between experiment and theory at subcritical and supercritical RN, and the unpredictable hysteresis-prone trends at critical RN.

The conclusions drawn from the Polhamus study were that the strip theory predicted spin damping trends quite well for some of the shapes studied at sub- and supercritical RN, and that the centrifugal effects, hysteresis and 3-dimensional viscous flow effects not included in the theory could account for the lack of agreement between predictions and experiment.

Based on these results, it appears that the technology and understanding required for analytical predictions of rotary data are not in hand The designer should be especially cautious regarding analytical data predictions for complete configurations, which will generally display even more complex phenomena than those mentioned here. It should be emphasized that an aggressive acceleration of the analytical methods is urgently needed to augment the experimental methods now used. Of particular interest is the role that sophisticated CFD methods may play in this effort.

8.3 VISCOUS-FLOW/VEHICLE-MOTION COUPLING

When considering the strong coupling existing between vehicle motion and complex flow phenomena, such as boundary-layer transition and flow separation,[9,10] discussed in Section 5.3, one can understand why there are no purely theoretical methods available for prediction of the unsteady aerodynamic characteristics of advanced aircraft operating at high angles of attack. The only manner in which a realistic prediction of high-alpha aerodynamics presently could be accomplished, short of full-scale flight investigation, is through semi-empirical means, i.e., by using experiment and theory together to provide dynamic simulation through analytic extrapolation from subscale test data to full-scale conditions. This has been accomplished for planar motion of a number of vehicle geometries.[11,12] However, in the case of the high-alpha dynamics of most advanced aircraft the coning motion and associated moving wall effects on flow separation and vortex shedding off a slender forebody[13] greatly complicate the problem of dynamic simulation in experiments and, even more so, the problem of dynamics prediction.

The classical Magnus lift of a rotating circular cylinder represents a well established case of moving wall effects, and the experimental results presented by Swanson[14] will be used as a reference when discussing other types of viscous motion-coupling effects.

8 3.1 Coning Characteristics

At high angles of attack the asymmetric flow separation occurring on a slender body of revolution generates large asymmetric loads[15] which can drive the body in a coning motion[16] (Figure 8-31). The limiting rate is obtained when the driving moment induced by the flow separation asymmetry is balanced by the drag-induced damping moment. The authors[16] revealed that only a slight push was needed to initiate the coning motion in either direction. That is, so-called moving wall effects[13] dominated over the static asymmetry. Superimposing a Reynolds number scale on the velocity scale in Figure 8-31 shows that the initial "spin-up" to 5 rps at $\alpha = 45$ deg occurs for laminar flow conditions. Thus, the laminar Magnus lift results in Reference 14 can be applied, observing that the moving wall effects for the translating cross-section of the coning body (Figure 8-32) are largely the same as for the rotating circular cylinder because the moving wall effects are concentrated into a region near the flow stagnation point, where the boundary layer build-up starts [17]

It has been shown that for a slender, pointed nose the separation asymmetry, determining the characteristics of the shed asymmetric body vortices, is generated on the nose.[15] Consequently, if the moving wall effect on the side force generated by the nose can be predicted, a first step will have been taken towards determining the high-alpha vehicle dynamics, eventually including the downstream vortex-induced effects.

The 2-D Magnus lift characteristics in Reference 14 supply the strip loads for the coning, conical nose. Integrating the strip load contribution to the yawing moment gives the driving moment. It is balanced by the damping moment generated by the drag, with $C_d \approx 1.2$ for laminar flow conditions. The resulting prediction[18] of the coning rate for $\alpha = 45$ deg agrees well with the experimental results[16] (Figure 8-33). The zero offset is caused by the bearing friction present in the test,[16] which was not included in the prediction[18] (as it was not known).

8 3.2 Flat Spin Characteristics

When the coning angle is increased to 90 deg, the direct analogy between the translating cross-section of the coning body and the rotating cross-section, generating Magnus lift, is lost. However, experimental results for a circular cylinder driven in the flat spin mode[19] (Figure 8-34) indicate that similar viscous motion-coupling effects are still present. The critical flow separation asymmetry develops in opposite directions on the two sides of the rotation axis, the direction being determined completely by the spin-induced effects on boundary-layer transition. For the free-to-spin model, the moment generated by the critical separation asymmetry, illustrated in Figure 8-34, drives the circular cylinder up to a flat spin rate $\bar{\Omega}_{FS} = \Omega_{FS} L/2U_\infty$, where it is balanced by the drag-generated damping moment [20] Although the flat spin is initiated by the subcritical/critical separation asymmetry[15] with nonsymmetric spanwise distribution, initially determined by body microasymmetries or flow nonuniformities, the high spin rates ($U_W > U_\infty$ at the cylinder tips in Figure 8-34) cause a change to the critical/supercritical flow separation shown in Figure 8-35(b), before the limiting spin rate is reached.

During the spin-up, the critical separation asymmetry is established momentarily. However, in the free-to-spin case[19] the associated damping effect does not last long enough to have any significant influence before the final separation asymmetry shown in Figure 8-35(b) is established. Here the viscous motion-coupling effect on the retreating side has promoted transition to occur upstream of the separation bubble, wiping it out. On the opposite, advancing side, the effect delays transition, thereby prolonging the existence of the laminar separation bubble. This supercritical/critical separation asymmetry produces the maximum flat spin rate[19] (Figure 8-36). The measured pressure distributions[19] in Figure 8-34, obtained at sections P and Q for close to the maximum flat spin rate, are of this supercritical/critical type,[15] with flow separation occurring at $\Delta\varphi = 100$ and 140 deg, respectively, measured from the flow stagnation point at $\varphi \approx 30$ deg.

The results for the critical flow conditions in Figure 8-30 illustrate the following· The effect of increasing spin rate is to change the crossflow conditions from the critical/critical asymmetry, which gives a yawing moment at $\tilde{\Omega} < 0.5$ that is more damped than at subcritical or supercritical conditions, to the supercritical/critical asymmetry (Figure 8-35(b)), producing a strongly undamping moment at $\tilde{\Omega} > 0.5$. In the free-to-spin case (Figure 8-36), spin-up occurs at critical flow conditions, when a spanwise asymmetric distribution of the streamwise asymmetry is produced by model microasymmetries or nonuniform freestream flow conditions. The experimental data in Figure 8-36 show an almost instantaneous acceleration through the spin rates giving the critical/critical motion-induced asymmetry. That is, contrary to the forced spin case at $\tilde{\Omega} < 0.5$ (Figure 8-30), the critical/critical flow condition never had time to perform its damping action.[13]

Figure 8-30 illustrates another problem, one related to the use of strip theory, which assumes a gradual spanwise progression of the switch between the damping and undamping crossflow asymmetries. A similar assumption is usually made in regard to the stall progression on a helicopter blade. However, it was found in experiments that no such gradual progression occurred. Instead, sudden reattachment or flow separation was established simultaneously over a substantial spanwise extent of the blade.[21] Such a sudden change over a large spanwise extent is also indicated by the discontinuous C_n-change in Figure 8-30, occuring when $\tilde{\Omega}$ exceeds $\tilde{\Omega} \approx 0.5$.

Non-circular cross-sections experience similar motion-coupling effects, as is demonstrated by the measured forebody side force on a square cross-section body with rounded edges in flat spin[22] (Figure 8-37). The angle ϕ_{max} is the maximum, motion-induced, local flow incidence at the nose. As discussed in Reference 23, in a static test of the square cross-section windward-side flow reattachment will not occur until $\alpha > 10°$. This is in sharp contrast to the value $\phi_{max} \approx 1.5°$ in Figure 8-37, illustrating the power of viscous motion-coupling effects to cause early reattachment.

As has been discussed before,[9,13] viscous motion-coupling effects are similar to the effects of Reynolds number and free-stream turbulence, in that they make it difficult to extrapolate to full-scale flight conditions. This is true even when support and wall interference do not complicate the scaling problem (Section 5.3). A prerequisite for any extrapolation is that the dominant flow mechanisms present in the test be fully understood. This, in turn, requires that systematic tests, such as those discussed here, be performed to provide the phenomenological building blocks needed for successful extrapolation to full-scale conditions. This activity should be coordinated with parallel efforts in computational fluid dynamics.

8.3.3 Scaling Considerations

The problem of extrapolating from subscale rotary-rig test data to full-scale vehicle dynamics is difficult by virtue of the strong coupling existing between the vehicle motion and complex flow phenomena, such as boundary-layer transition and flow separation.[9,10] In spite of the progress being made in computational fluid dynamics, no one is presently ready to forecast when numerical simulation of the coupling between boundary-layer transition and vehicle motion will be possible.[24] The prospects for full-scale simulation in ground facility testing are not much better, as the tests need to be performed at the full-scale Reynolds number.[25] Fortunately, there are cases where the viscous flow effects are not significant and the simulation problem disappears. However, at present, the only manner in which a realistic prediction of high-alpha dynamics can be accomplished is through semi-empirical means. Such means have been developed for prediction of the full-scale dynamics of rigid and elastic bodies in planar motion.[11,12] Experiment and theory were used together in the following steps to provide analytic extrapolation to the full-scale vehicle dynamics.

1. Establish analytic relationships between dynamic and static aerodynamic characteristics generated by viscous flow effects.

2. Prove the veracity of the analytic method by predicting dynamic test results using static test data obtained at the same subscale flow conditions.

3. Determine the effect of Reynolds number on static aerodynamic characteristics from subscale test conditions to full-scale flow conditions.

4. Estimate full-scale vehicle dynamics using 1 and 3.

Item 3 is usually undertaken for prediction of the static loads and, if additional tests are needed, they are easy to perform compared to dynamic tests. Thus, analytic extrapolation provides a practical means for prediction of the full-scale vehicle dynamics.

Dynamic stall prediction must rely heavily on experimental data which, as a rule, are obtained at subscale Reynolds numbers. As a consequence, analytic extrapolation is needed for prediction of the full-scale unsteady aerodynamics.[25] For oscillations in pitch of small amplitude and low frequency, $|\dot{\alpha}c/U_\infty| << 1$ and $\tilde{\omega}^2 << 1$, the local linearization concept can be applied even to the nonlinear separated-flow aerodynamics, as long as the characteristics are continuous in nature.[26,27]

The results in Figure 8-38 show that experimental subscale dynamic stall characteristics[28] can be predicted[26] using experimental static data to define the separation-induced effect on the static aerodynamic characteristics. Although flow separation occurs together with boundary layer transition in this case, the analytic relationship between unsteady and steady boundary-layer transition characteristics is of the same form as that between unsteady and steady flow separation characteristics.[10] Thus, Figure 8-38 demonstrates that requirement 2 for analytic extrapolation has been satisfied. In order to satisfy requirement 3 the static test has to be performed at a Reynolds number that is on the same side of the critical value as in full-scale flight, as was amply illustrated in Section 5.3. Thus, in the case of incompressible flow, static tests from subscale to full-scale Reynolds numbers will supply the input needed for analytic extrapolation to full-scale dynamics. However, as the full-scale airfoil stall usually involves locally supersonic regions,[29] compressibility effects must be taken into account.[29–31]

8.3.4 Three-Dimensional Flow Effects

The local linearization concept has also been applied to the case of compressible, three-dimensional flow,[32,33] providing the means for prediction of the highly nonlinear effects on the vehicle dynamics of the Space Shuttle orbiter of shock-induced flow separation and the leading edge separation occurring at higher angles of attack[34] (Figure 8-39). Even the much more complex separation-induced effects on the Space Shuttle launch vehicle[35] could be predicted in this manner.[36] Based upon the agreement shown for the rigid body dynamics (Figure 8-39) the elastic vehicle dynamics of the Space Shuttle launch vehicle could be predicted with the required confidence level.[36]

The effect of three-dimensional pitch-yaw-roll coupling on unsteady flow separation can substantially complicate the mathematical modeling, making the extrapolation from subscale to full-scale vehicle dynamics more difficult than in the planar-motion cases discussed so far. However, by gaining a full understanding of the unsteady viscous flow processes involved, predictive means can, in all probability, be provided also in this case.

Specific three-dimensional flow effects on dynamic stall can be studied for nonplanar motion using the method of oscillatory coning, described in Chapters 4 and 9.2. The typical dynamic-stall-like behavior was observed when the unsteady aerodynamic loads were measured with the coning axis tilted at angles up to 15 deg (see Figure 4-6). Analogous three-dimensional flow separation effects are found on non-slender-wing aircraft in roll oscillations. Since the three-dimensional dynamic stall is the flow mechanism causing wing rock of non-slender wings it is instructive to consider the problems involved in extrapolation from subscale wing rock experiments.

Flight test data for the HIRM 1 aircraft model[37] showed a severe loss of roll damping for $20° < \alpha < 30°$ (Figure 8-40) and, in the case of the X-29A aircraft, the loss was large enough to lead to wing rock[38] (Figure 8-41). In these cases, where the wings do not have highly swept leading edges, it is the negative damping of airfoil plunging oscillations that causes the wing rock.[39] The negative aerodynamic damping measured by Lilva et al[28] for plunging oscillations (Figure 8-42) is caused by the moving wall effect, or the leading-edge-jet effect, as the wall-jet-like effect has been called in the case of dynamic stall of airfoils.[26] The leading-edge-jet effect promotes flow separation, as noted in Section 5.3 (Figure 5-28), and can, therefore, generate the experimentally observed negative damping at stall (Figure 8-42). This is explained in Reference 26.

For a wing at bank angle ϕ the angle of attack is:

$$\alpha = \arctan(\tan \alpha_o \cos \phi) \tag{1}$$

Considering the effect of aspect ratio, the static stall angle in the case of wing rock of an advanced fighter is probably $\alpha_s \approx 20°$ rather than the two-dimensional value $\alpha_s \approx 13°$ in Figure 8-42. This is in agreement with the data trends in Figures 8-40 and 8-41. The straight-wing wing-rock occurs through the following flow processes.[39] When the wing rolls through some disturbance or maneuver, so that α, Eq. (1), decreases towards the static stall angle for the wing, the dynamic stall process described in connection with Figure 8-42 takes place. That is, the negative damping at stall penetration for the plunging airfoil is generated by the moving wall effect near flow stagnation. Since this effect acts in opposite directions on the two wing halves, both contribute to the negative damping in roll[39]. This negative damping is balanced by the positive damping at higher ϕ-values during the oscillation cycle. At the limit cycle amplitude of the wing rock, zero net roll damping is generated.

For the prediction of these wing-rock characteristics, one needs to follow up on the analytic approach presented in Reference 26 for the prediction of the two-dimensional dynamic stall of a plunging wing. This should result in the same type of predictive capability demonstrated for pitching or torsional oscillations[26] (Figure 8-38). However, one must include the three-dimensional flow effects. Even for $\beta = 0$, flow reattachment will not progress gradually inboard from the wing tip for increasing ϕ, but will occur simultaneously over the outboard portion of the span (40% or so), according to experimental results for helicopter blades.[21]

Analytic extrapolation from subscale test data to full-scale vehicle dynamics is possible in many cases of slender-wing wing rock,[39–43] by use of the general method discussed earlier. However, in the case of wing rock generated by forebody vortices, which is by far the most likely type that current and future advanced aircraft will be subject to, more research is needed before the analytic extrapolation capability will be in hand. This wing rock is dominated by moving wall effects, as is evident from the discussion in Section 5-3 (Figure 5-30). The moving wall effect generated by body rotation is responsible for the wing rock observed in wind tunnel tests of a generic aircraft configuration[44] (see Figure 5-30). According to the transitional flow mechanism described in References 45 and 46, this wing rock cannot occur under laminar flow conditions, i.e., at or below half of the actual test Reynolds number,[44,47] $Re = 0.26 \times 10^6$. The test conditions were in the critical range and are likely to have produced the maximum wing rock amplitude. In contrast, at full-scale flow conditions the transitional flow region will be located near the apex of the slender nose and the resulting wing rock amplitude is expected to be smaller.

Thus, in the case of the wing rock of most practical interest there is presently no method available for extrapolation from subscale test results to predict the full-scale vehicle dynamics. Analysis of the flow mechanisms producing this wing rock[45,46] gives an indication of how to proceed to develop a method for prediction of the full-scale flight characteristics. Analogously, such methods could provide the means for predicting full-scale oscillatory spin behavior on the basis of subscale test results. The moving wall effect is the flow mechanism likely to drive both types of oscillatory motions.

8.3.5 Transition Effects

Whether or not reliable extrapolation from subscale test results to full-scale flight conditions will be possible is, to a great extent, determined by the relative importance of transition-induced effects. In general, extrapolation from or across the critical flow regime is not possible. This is especially true for the unsteady aerodynamics, because of the strong coupling existing between boundary layer transition and vehicle motion. There may be occasions where the penalty for breaking this rule is not severe. A possible example could be the high-alpha aerodynamics of an advanced fighter aircraft with a chined or straked forebody. Such cases are, however, exceptions to the general rule.

A laminar test would fail to show the wing rock generated by forebody vortices,[45–47] such as observed in subscale flight and wind-tunnel tests of the X-29A aircraft at $\alpha > 45$ deg[38] (see Figure 5-34). A peculiar situation arises because the static side force measured on a pointed ogive-cylinder at laminar flow conditions is of roughly the same magnitude as that measured in turbulent flow[48] (Figure 8-43). The reason for this is that crossflow separation occurs at $\varphi = 80$ to 90 deg for laminar flow, which is quite close to the values $\varphi = 100$ to 110 deg in fully turbulent flow[15] (Figure 8-44). However, the full-scale aircraft is likely to perform a maneuver of some type when experiencing the forebody flow asymmetry. Consequently, the moving wall effects will play an important role, with those at supercritical flow conditions being potentially up to three times as large as their counterparts at subcritical flow conditions.[14]

The moving wall effects are not only important in regard to the high-alpha flow over slender forebodies, but can also affect the leading edge flow over moderately swept wings, as was illustrated in Figure 5-29. Such motion-coupling effects are likely to have contributed to the differences in the separated flow patterns observed on the two wing halves of the rolling HIRM 1 model (Figure 8-9).

These examples illustrate the importance of acquiring a thorough understanding of the high-alpha fluid mechanics before attempting to extrapolate from subscale test data to full-scale vehicle dynamics.

8.4 EXTRAPOLATION TO FULL-SCALE CONDITIONS

The ability to predict full-scale vehicle characteristics using low Reynolds number wind-tunnel data is always questioned. This concern has prompted investigators, as a matter of course, to determine the applicability of their data through:

- Comparing their data with higher Reynolds number data when available.
- Using their measured data to calculate various aircraft time-history responses for comparison with flight-test results
- In addition, sensitivity and analytical studies are conducted to determine the relative importance of various aerodynamic parameters in determining aircraft flight characteristics, thereby setting the accuracy requirements for the measured parameters.

Based on the experience gained in performing these efforts with many and varied aircraft configurations, the likelihood of a Reynolds number problem with a particular configuration can be anticipated before testing begins, and various experimental and/or analytical procedures can often be adopted to minimize the anticipated Reynolds number problem.

Also, this background permits the dynamicist to judge the level of confidence one can attribute to the predicted flight characteristics, i.e., stall behavior, roll and nose-slice departures, spins, high-alpha maneuvering capability, etc. For instance, as shown in Chapter 11, spin modes for most military configurations can be predicted with low Reynolds number data.

It would be impossible to summarize herein all possible Reynolds number problems that might arise and corresponding analytical and/or experimental procedures to be pursued to alleviate the anticipated problems, but an illustrative example can be given: Consider a configuration with a RN-sensitive wing airfoil for which a steep spin mode is predicted, the stall would occur earlier on the model and, consequently, the full-scale aircraft would be expected to spin at a higher angle of attack than predicted. If high RN data have identified the true stall angle, the low RN C_ℓ vs $\Omega b/2V$ curve can be shifted to this higher stall angle of attack. Provided that the trends in the low-RN characteristics are representative at the higher α and full-scale RN, the approach can yield useful results. However, it should be noted that while this is an accepted procedure it does not have a scientific basis. The nonlinearities in the stall characteristics may be quite different at higher α and full-scale RN for some configurations. In such cases, the assumption that the low-RN characteristic can be shifted to higher α will result in error in the calculated roll departure time history.

Thus, in many situations involving a Reynolds number effect on wing stall characteristics, results can be obtained from which the full-scale spin departure sensitivity and steady spin characteristics can be predicted. In contrast, such an analytical correction should not work for forebody-dominated configurations when the nonlinearities are strongly dependent on transition effects. Only when these effects may be neglected, can the use of laminar flow results be expected to yield representative predictions at full-scale RN. In special circumstances, described in Section 8.3.5 (Figure 8-43), laminar test results can be comparable, in some respects, to the effects in turbulent flow.

More sophisticated methods are needed for satisfactory prediction of high-α maneuvering characteristics of high-performance aircraft. More specifically, there is a need for predicting the transient aerodynamic phenomena prevailing in maneuvers involving large amplitudes and high rates, including the transients leading to the developed spin. To this end, a more complete understanding of the high-α unsteady aerodynamics must be developed.

8.5 REFERENCES

1. Crowder, J. P.: Add Fluorescent Minitufts to the Aerodynamicist's Bag Of Tricks. AIAA Aeronautics and Astronautics November 1980.

2. Dobney, D. G.; Hanson, P.; and Fiddes, S. P.: The 'Minituft' Surface Flow Visualization Method; Experience of Use in the RAE 5 m Pressurized Low Speed Wind Tunnel. RAE Technical Memorandum Aero 2038, April 1985.

3. O'Leary, C. O.; and Drew, W.: Flow Visualization on Rolling Models Using Minitufts, RAE Technical Memorandum Aero 2083, August 1986.

4. Yoshinaga, T.: Private Communication, Jan. 11, 1987.

5. Ericsson, L. E.; and Reding, J. P.: Dynamics of Forebody Flow Separation and Associated Vortices. J. Aircraft, Vol. 22, No. 4, April 1985, pp. 329-335.

6. Hunton, L. W.; and Dew, J. K.: Measurements of the Damping in Roll of Large-Scale Swept-Forward and Swept-Back Wings. NACA RM No. A7D11, July 1947.

7. Bowman, J. S.; Hultberg, R. S.; and Martin, C. A.: Measurements of Pressures on the Tail and Aft Fuselage of an Airplane Model During Rotary Motions at Spin Attitudes. NASA TR 2939, Nov. 1988.

8. Polhamus, E. C.: Effect of Flow Incidence and Reynolds Number on Low-Speed Aerodynamic Characteristics of Several Noncircular Cylinders With Applications to Directional Stability and Spinning. NASA TR R-29, 1959.

9. Ericsson, L. E : Review of Transition Effects on the Problem of Dynamic Simulation. AIAA Paper 88-2004, May 1988.

10. Ericsson, L. E.: Transition Effects on Airfoil Dynamics and the Implication for Subscale Tests. J. Aircraft, Vol. 26, Dec. 1989, pp. 1051-1058.

11. Ericsson, L. E.; and Reding, J. P.: Dynamic Simulation Through Analytic Extrapolation. J. Spacecraft and Rockets, Vol. 9, No. 2, March-April 1982, pp. 160-166.

12. Ericsson, L. E.; and Reding, J. P.: Analytic Extrapolation to Full-Scale Aircraft Dynamics. J. Aircraft, Vol. 21, No. 3, March 1984, pp. 222-224.

13. Ericsson, L. E.: Moving Wall Effects in Unsteady Flow. J. Aircraft, Vol. 25, No. 11, Nov. 1988, pp. 977-990.

14. Swanson, W. M.: Magnus Effect; A Summary of Investigations to Date. J. Basic Eng., Vol. 83, Sept. 1961, pp. 461-470.

15. Ericsson, L. E.; and Reding, J. P.: Asymmetric Vortex Shedding from Bodies of Revolution. Chapter VII, Tactical Missile Aerodynamics, Vol. 104, Progress Astro. and Aero. Series, M. J. Hemsch and J. N. Nielsen, editors, 1986, pp. 243-296.

16. Yoshinaga, T.; Tate, A.; and Inoue, K.: Coning Motion of Slender Bodies at High Angles of Attack in Low Speed Flow. AIAA Paper 81-1899, Aug. 1981.

17. Ericsson, L. E.: Circular Cylinder Response to Karman Vortex Shedding. J. Aircraft, Vol. 25, No. 9, Sept. 1988, pp. 769-775.

18. Ericsson, L. E.: Prediction of Slender Body Coning Characteristics. AIAA Paper 89-2223, Aug. 1989.

19. Kubota, H.; Irai, I., and Matsuaka, M.: Wind Tunnel Investigations for the Flat Spin of Slender Bodies at High Angles of Attack. J. Spacecraft and Rockets, Vol. 20, No. 2, March-April 1983, pp. 108-114.

20. Ericsson, L. E.: Flat Spin of Axisymmetric Bodies in the Critical Flow Region. J. Spacecraft and Rockets, Vol. 24, No. 6, Nov.-Dec. 1987, pp. 532-538.

21 Tarzanin, F. J., Jr.: Prediction of Control Loads Due to Blade Stall. Journal of the American Helicopter Society, Vol. 17, April 1972, pp. 33-46.

22. Malcolm, G. N., and Clarkson, M. H.. Wind Tunnel Testing with a Rotary-Balance Apparatus to Simulate Aircraft Spin Motions. Proceedings of the AIAA 9th Aerodynamic Testing Conference, June 1976, pp. 143-146.

23. Ericsson, L. E.: Aerodynamic Characteristics of Noncircular Bodies in Flat Spin and Coning Motions. J. Aircraft, Vol. 22, No. 5, May 1985, pp. 387-392.

24. Hussaini, M. Y.· Stability, Transition and Turbulence, Supercomputing in Aerospace. NASA CP 2454, March 1987, pp. 211-220.

25. Ericsson, L. E.; and Reding, J. P.: Scaling Problems in Dynamic Tests of Aircraft-Like Configurations. Paper 25, AGARD CP-227, Feb. 1978.

26. Ericsson, L. E.; and Reding, J. P.: Fluid Mechanics of Dynamic Stall, Part I., Unsteady Flow Concepts. J. Fluids and Structures, Vol. 2, 1988, pp. 1–33.

27. Ericsson, L. E.; and Reding, J. P.: Fluid Mechanics of Dynamic Stall, Part II, Prediction of Full Scale Characteristics. J. Fluids and Structures, Vol. 2, No. 2, March 1988, pp. 113–144.

28. Liiva, J.; Davenport, F. J.; Gray, L.; and Walton, I. C.: Two-Dimensional Tests of Airfoils Oscillating Near Stall. TR 68-13A and B, U.S. Army Aviation Materials Labs., Fort Eustis, Virginia, April 1968.

29. Ericsson, L. E.; and Reding, J. P.: Stall Flutter Analysis. J. Aircraft, Vol. 10, No. 1, Jan. 1973, pp. 5–13.

30. Ericsson, L. E.; and Reding, J. P.: Quasi-Steady and Transient Dynamic Stall Characteristics. Paper 25, AGARD CP-204, Sept. 1976.

31. Ericsson, L. E.; and Reding, J. P.: Shock-Induced Dynamic Stall. J. Aircraft, Vol. 21, No. 5, May 1984, pp. 316–321.

32. Ericsson, L. E.; and Reding, J. P.. Effect of Flow Separation Vortices on Aircraft Unsteady Aerodynamics. Paper 24, AGARD CP-235, Sept. 1979.

33. Ericsson, L. E., and Reding, J. P.: Fluid Dynamics of Unsteady Separated Flow, Part II, Lifting Surfaces. Prog. Aerospace Sci., Vol. 24, pp. 249–356, 1987.

34. Boyden, R. P.; and Freeman, D. C., Jr.: Subsonic and Transonic Dynamic Stability Derivatives of a Modified 089B Shuttle Orbiter. NASA TMX-72631, DMS-DR 2107, Dec. 1974.

35 Freeman, D. C., Jr.; Boyden, R. P., and Davenport, E. E.. Subsonic and Transonic Dynamic Stability Characteristics of the Space Shuttle Launch Vehicle. NASA TMX-336, March 1976

36. Reding, J. P., and Ericsson, L. E.. Effects of Flow Separatic ,on Shuttle I ongitudinal Dynamics and Aeroelastic Stability. J. Spacecraft and Rockets, Vol. 14, No. 12, Dec. 1977, pp 711–718.

37. Ross, J. A., Edwards, G. F.; Klein, V.; and Batterson, J. G.: Validation of Aerodynamic Parameters for High Incidence Research Models. J. Aircraft, Vol. 26, No. 7, July 1989, pp. 621–628.

38 Fratello, D. J.; Croom, M. A.; and Nguyen, L. T.. Use of the Updated NASA Langley Radio-Controlled Drop-Model Technique for High-Alpha Studies of the X-29A Configuration Proceedings of AIAA Atmospheric Flight Mechanics Conference, Aug 17-19, 1987, pp. 305-317.

39. Ericsson, L. E.: The Various Sources of Wing Rock. AIAA Paper 88-4370, Aug 1988.

40. Nguyen, L. E.; Yip, L. P.; and Chambers, J. R.. Self Induced Wing Rock of Slender Delta Wings AIAA Paper 81-1883, Aug 1981.

41. Levin, D , and Katz, J.. Dynamic Load Measurements With Delta Wings Undergoing Self-Induced Roll-Oscillations J Aircraft, Vol. 21, Jan. 1984, pp. 30-36.

42. Ericsson, L. E.. The Fluid Mechanics of Slender Wing Rock. J. Aircraft, Vol 21, No 5, May 1984, pp 322-328.

43. Ericsson, L. E Analytic Prediction of the Maximum Amplitude of Slender Wing Rock J. Aircraft, Vol 26, No 1, Jan. 1989 pp. 35–39.

44. Brandon, J. M., and Nguyen, L. T.: Experimental Study of Effects of Forebody Geometry on High Angle of Attack Stability. J. Aircraft, Vol 25, July 1988, pp. 591–597.

45 Ericsson, L. E.: Wing Rock Generated by Forebody Vortices J. Aircraft, Vol 26, No. 2 Feb 1989, pp 110–116.

46. Ericsson, L. E.. Further Analysis of Wing Rock Generated by Forebody Vortices J Aircraft, Vol 26, Dec 1989, pp 1098-1104.

47 Brandon, J. M , Murri, D G. and Nguyen, L T Experimental Study of Effects of Forebody Geometry on High Angle of Attack Static and Dynamic Stability and Control Paper ICAS-86-5 4.1. 1986

48 Lamont, P. J . The Complex Asymmetric Flow Over a 3 4 D Ogive Nose and Cylinder Afterbody at High Angles of Attack AIAA Paper 82-0053, Jan 1982

8.6 NOMENCLATURE

b	wing span
c	cross-sectional chord length, $c = D$ for a circular cylinder
$\bar{c}$	wing reference chord
D	cylinder diameter
d^1	sectional drag: coefficient $c_d = d^1/(\rho_\infty U_\infty^2/2)$
h	cross-sectional height or thickness
L	body length
ℓ'	cross-sectional lift: coefficient $c_\ell = \ell'/(\rho_\infty U_\infty^2/2)c$
ℓ	rolling moment: coefficient $C_\ell = \ell/(\rho_\infty U_\infty^2/2)Sb$
M	Mach number
M_p	pitching moment: coefficient $C_m = M_p/(\rho_\infty U_\infty^2/2)S\bar{c}$
m_p	cross-sectional pitching moment: coefficient $c_m = m_p/(\rho_\infty U_\infty^2/2)c^2$
n	yawing moment: coefficient $C_n = n/(\rho_\infty U_\infty^2/2)Sb$
P	static pressure: coefficient $Cp = (P - P_\infty)/(\rho_\infty U_\infty^2/2)$
p	roll rate
q	pitch rate
Re, RN	Reynolds number $= U_\infty c/\nu_\infty$
S	reference area, body cross-section area or projected wing area
t	time
U_∞, V	freestream horizontal velocity
U_W	wall velocity
Y	sideforce: coefficient $C_Y = Y/(\rho_\infty U_\infty^2/2)S$, c_y = local cross-sectional value
α	angle of attack
ν	kinematic viscosity
ρ	fluid density
ϕ	roll angle, effective crossflow angle (Figure 8-23)
φ	body azimuth (Figure 8-44)
$\Omega, \tilde{\Omega}$	coning and flat-spin rate, $\tilde{\Omega} = \Omega L/2U_\infty$

Subscripts

cr	critical
FS	flat spin
max	maximum
W	wall
2D	two-dimensional
∞	free stream conditions

Differential Symbols

$\dot{\alpha} = \partial\alpha/\partial t$

$C_{m_\alpha} = \partial C_m/\partial\alpha$

$C_{m_{\dot{\alpha}}} = \partial C_m/\partial(\bar{c}\dot{\alpha}/2U_\infty)$: $C_{mq} = \partial C_m/\partial(\bar{c}q/2U_\infty)$

$C_{\ell_p} = \partial C_\ell/\partial(bp/2U_\infty)$

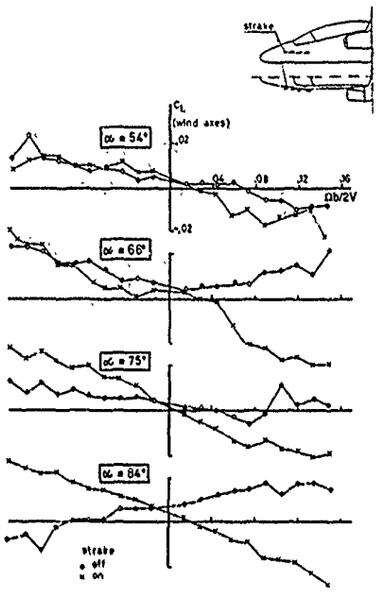

Figure 8-1. Effect of nose strakes on rolling moment.

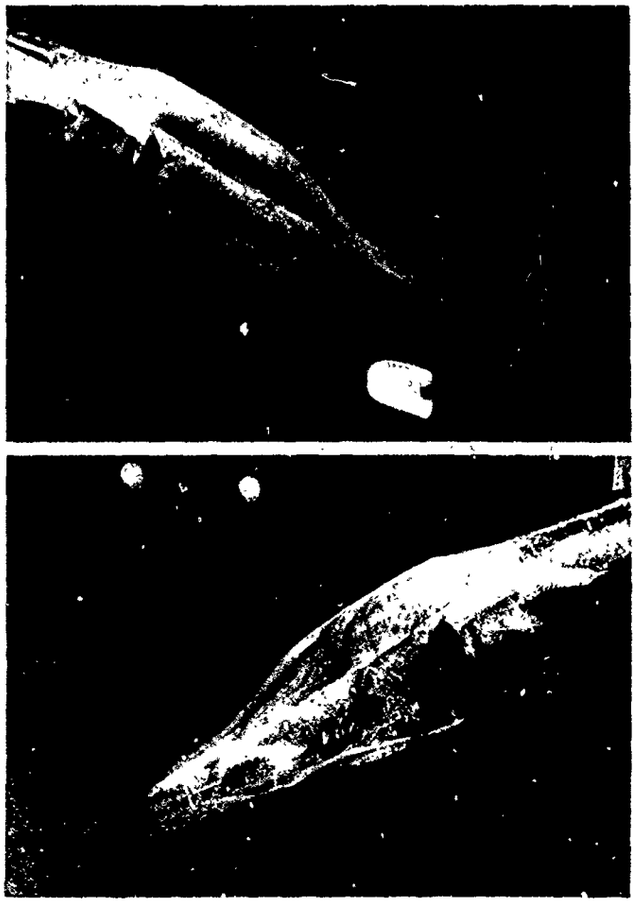

Figure 8-2. Basic configuration. $\alpha = 66°$, RPM = +100, $\frac{\Omega b}{2V} = 0.10$

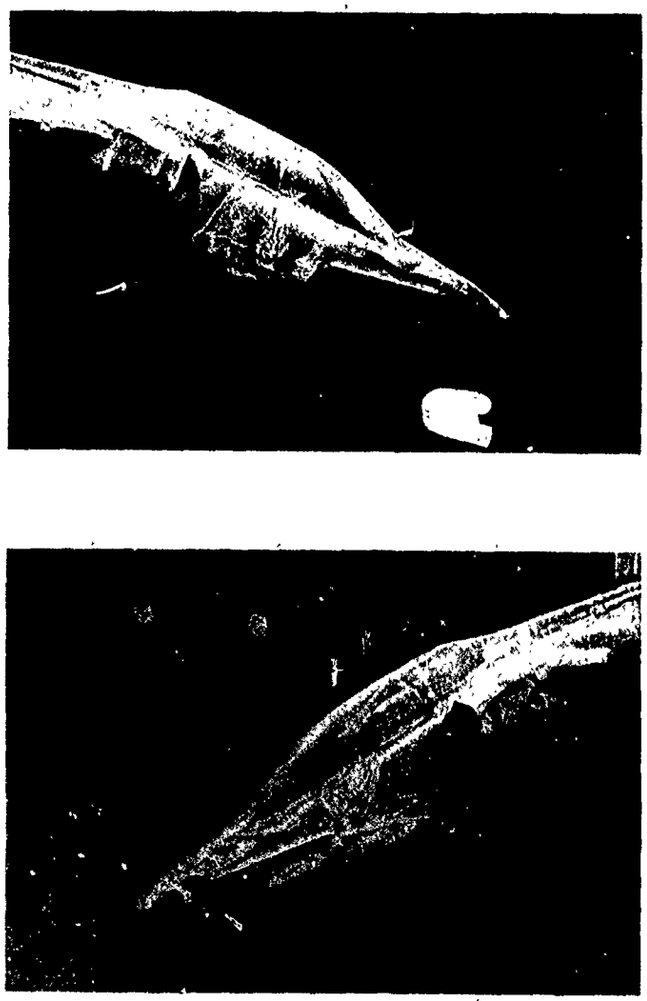

Figure 8-3. Strakes on forebody. $\alpha = 66°$, RPM = +100, $\frac{\Omega b}{2V} = 0.10$.

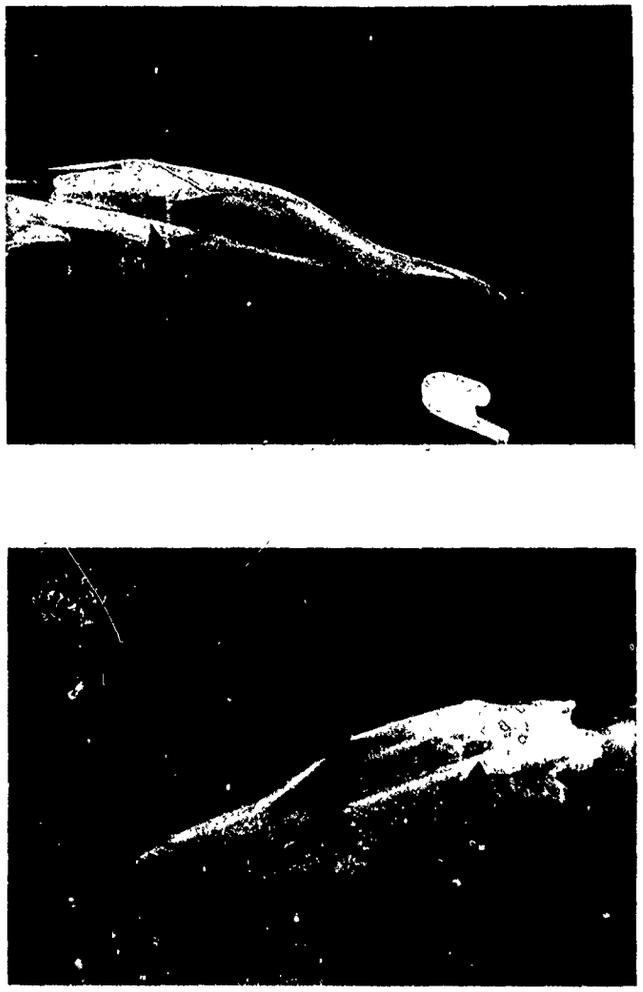

Figure 8-4. Basic configuration. $\alpha = 84°$, RPM $= +100$, $\frac{\Omega b}{2V} = 0.10$.

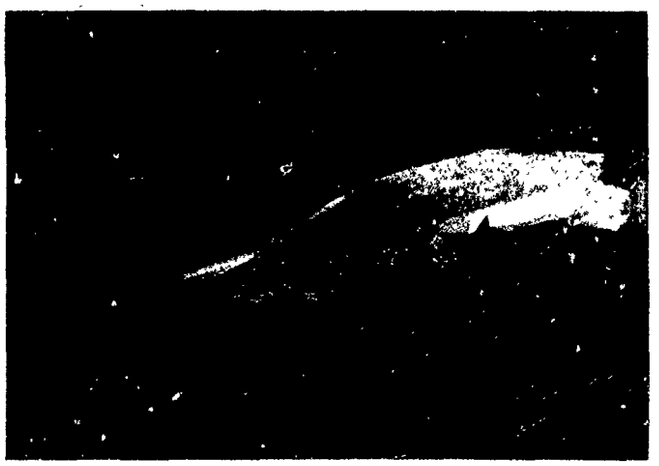

Figure 8-5. Strakes on forebody. $\alpha = 84°$, RPM = +100, $\frac{\Omega b}{2V} = 0.10$.

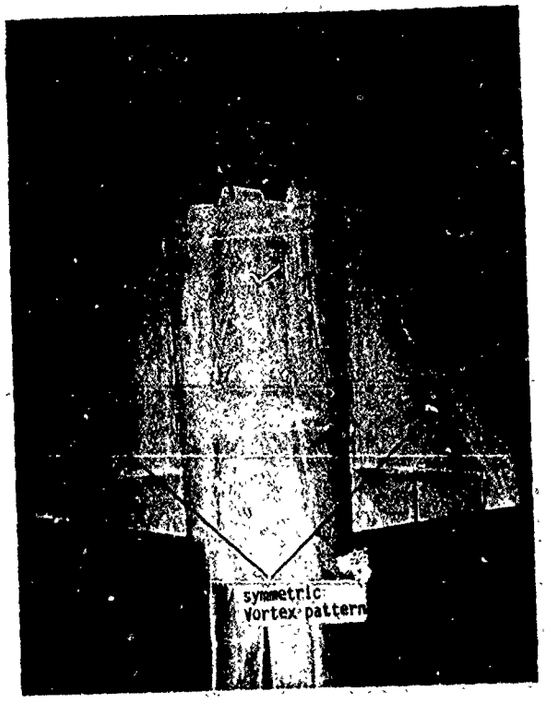

Figure 8-6. Surface flow visualization with oil and titanium dioxide. Rotation speed zero, $\alpha = 12°$, $n = 0$ rpm, $q_\infty = 750$ Pa.

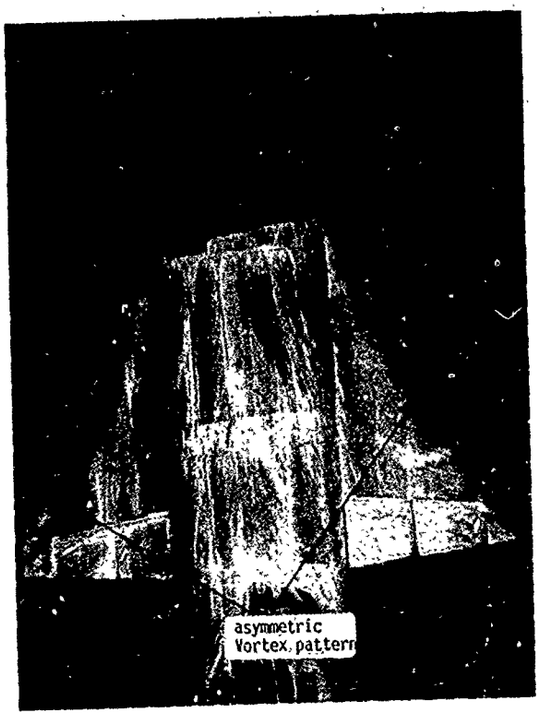

Figure 8-7. Surface flow visualization with oil and titanium dioxide. Rotation speed = −200 rpm, $\alpha = 20°$, $n = 200$ rpm, $q_\infty = 750$ Pa.

Figure 8-8. Flow visualization around a rotating model in the water tunnel.

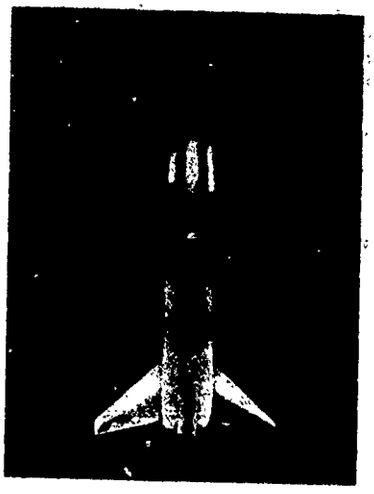

(a) $\alpha = 0°$.

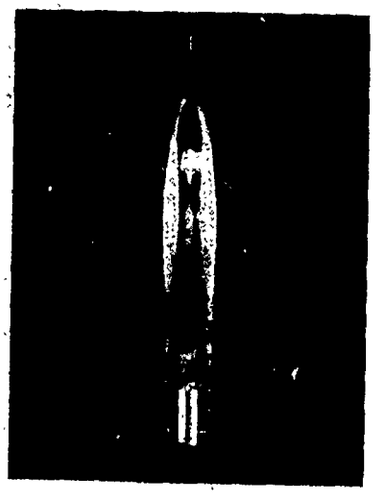

(b) $\alpha = 16°$.

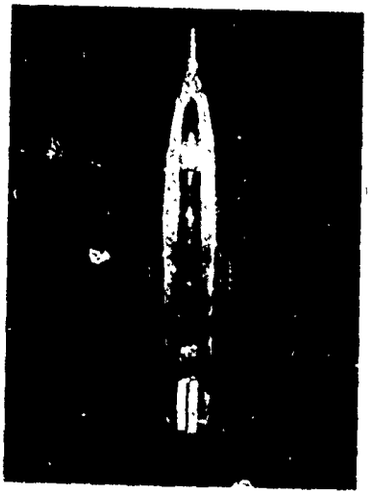

(c) $\alpha = 22°$

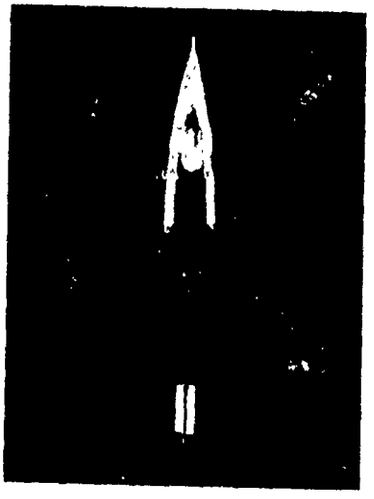

(d) $\alpha = 30°$.

Figure 8-9. Flow visualization with minitufts—HIRM 1, 100 rpm.

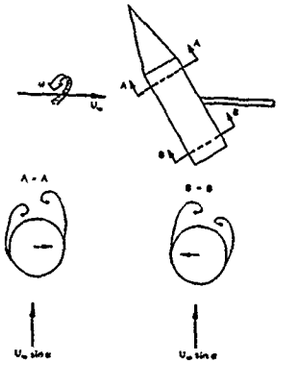

Figure 8-10. Arrangement of vortices on rotating cone-cylinder model.

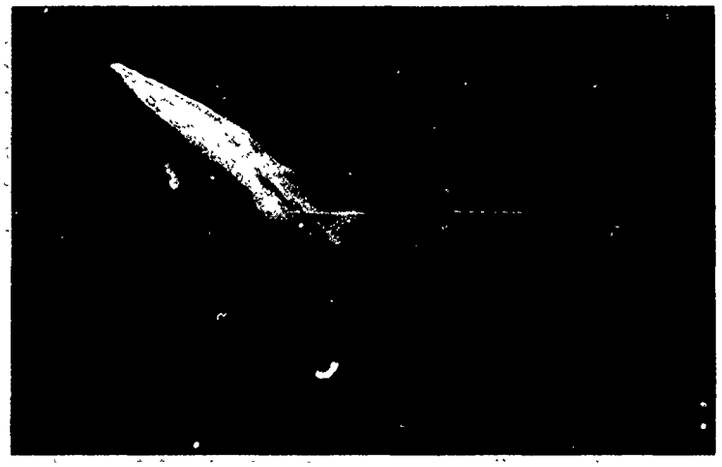

Figure 8-11. Effect of slender support on asymmetric vortices.

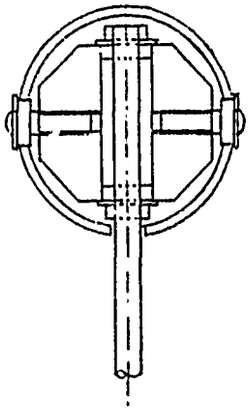

Figure 8-12. Arrangement of support and bearings in rotating cone-cylinder model.

Figure 8-13. Effect of protrusions on flow over rotating model.

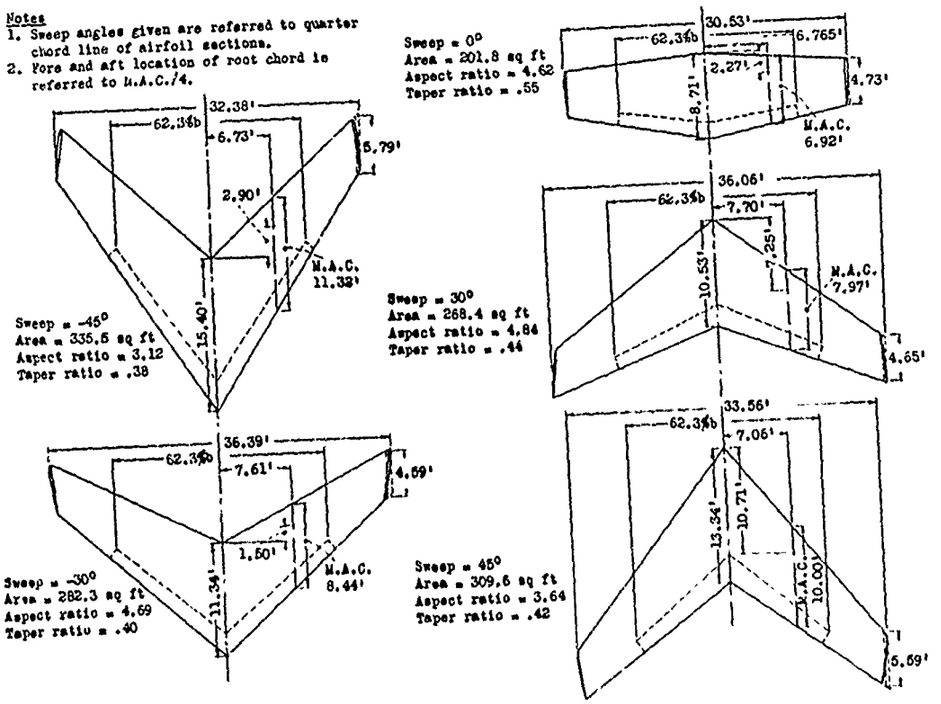

Figure 8-14. Geometric characteristics of the swept wings.

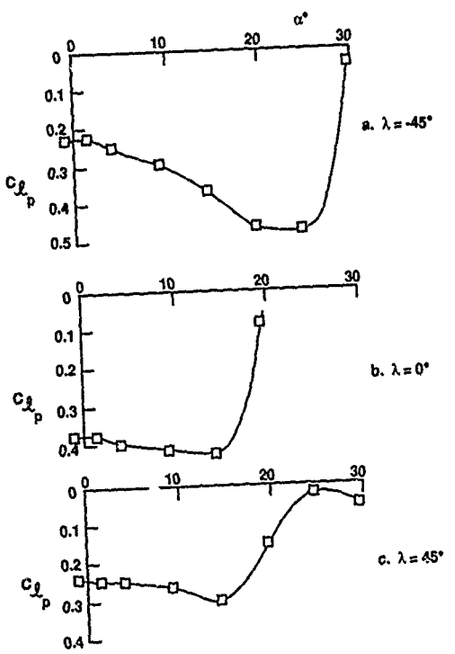

Figure 8-15. Effect of wing sweep on roll damping.

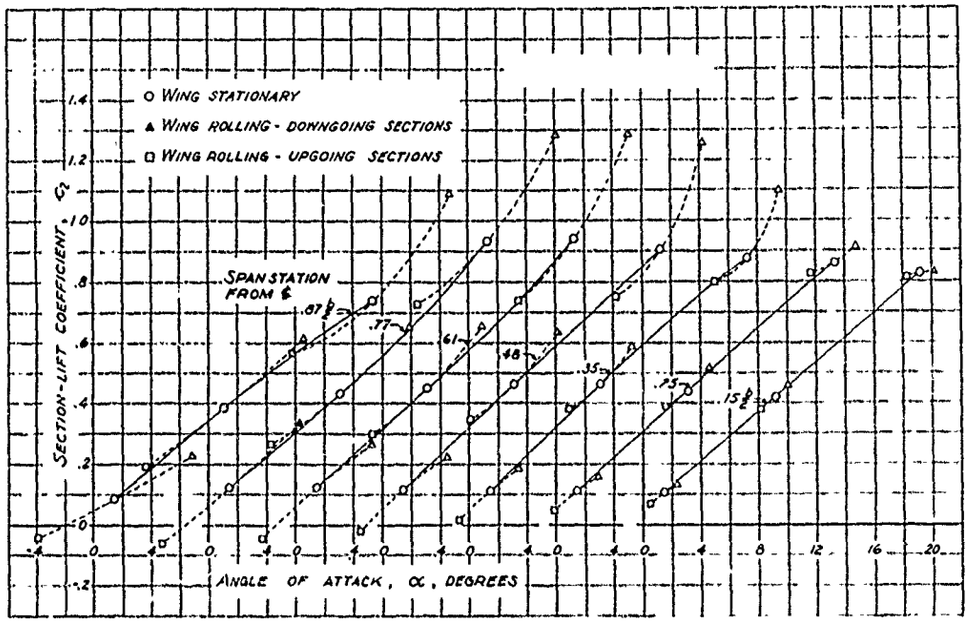

(a) 45° swept-forward wing.

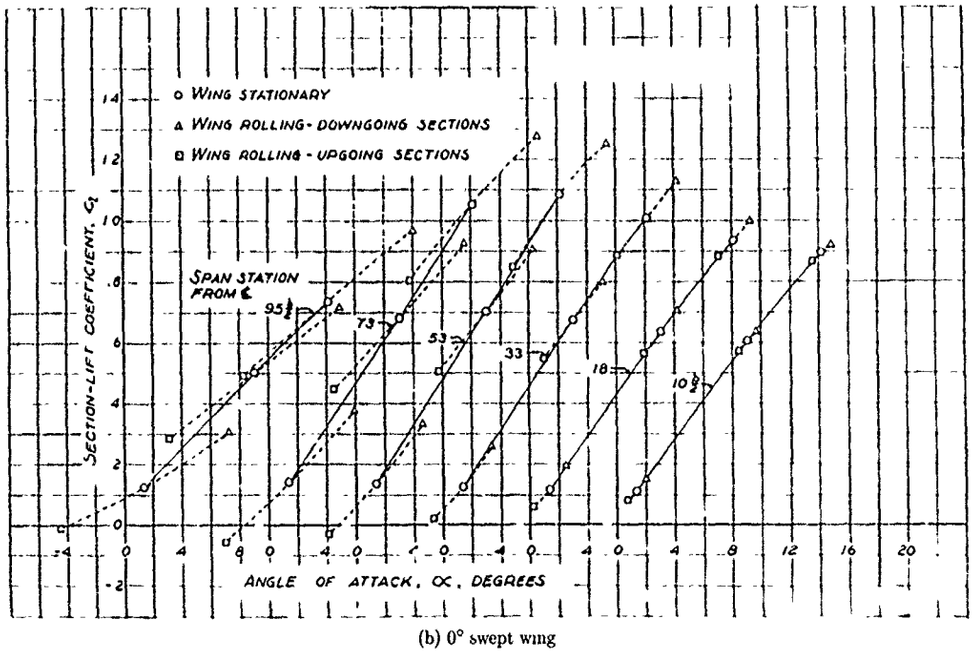

(b) 0° swept wing

Figure 8-16 Variation of section-lift coefficient with angle of attack for the plain wings stationary and in steady roll at $pb/2V = 0.11$.

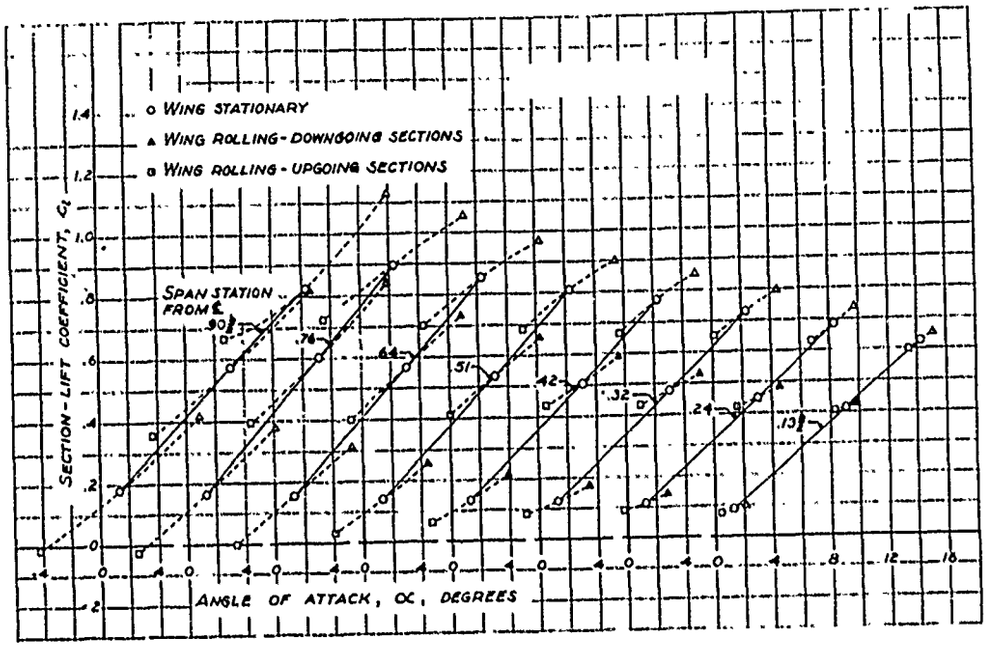

(c) 45° swept-back wing.

Figure 8-16. Concluded.

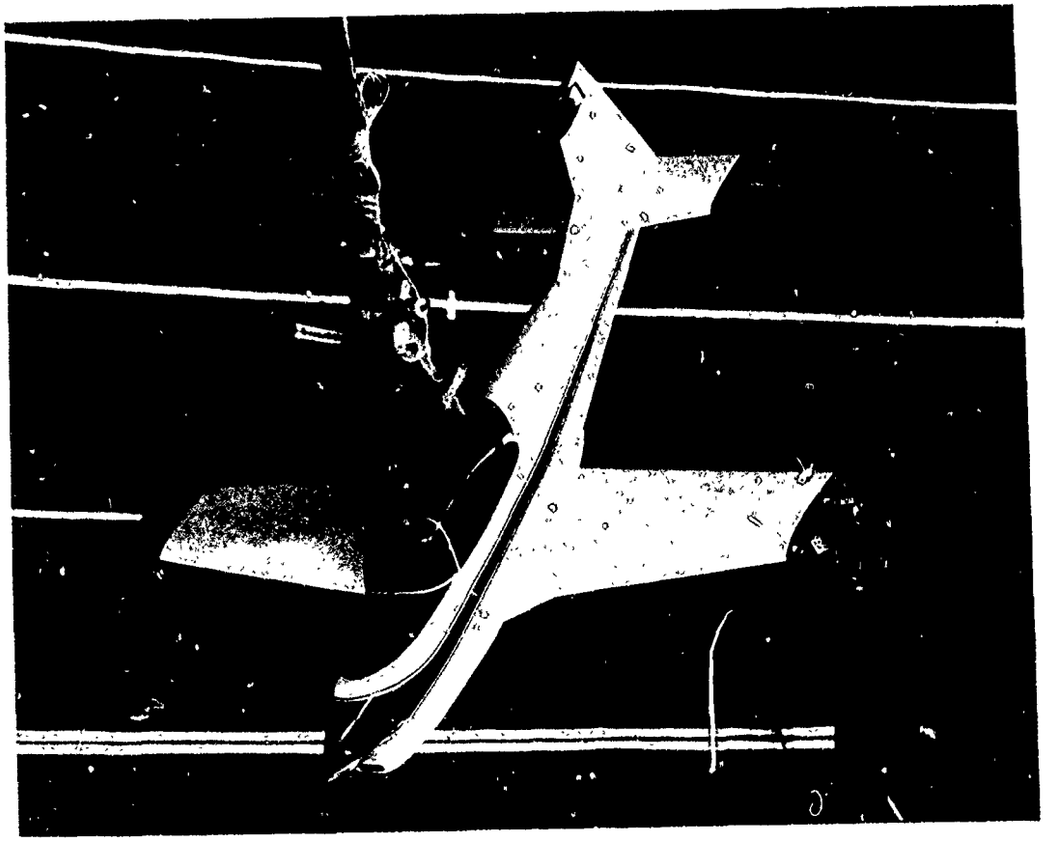

Figure 8-17. Model used in pressure tests.

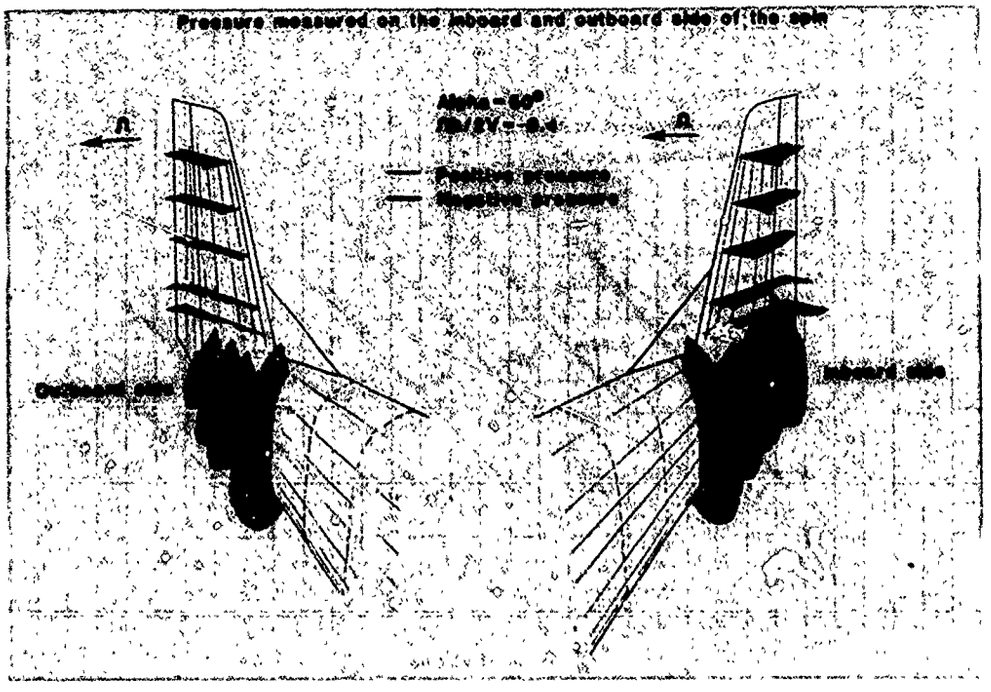

Figure 8-18. Pressure distribution, horizontal tail off.

Figure 8-19. Pressure distribution, horizontal tail on.

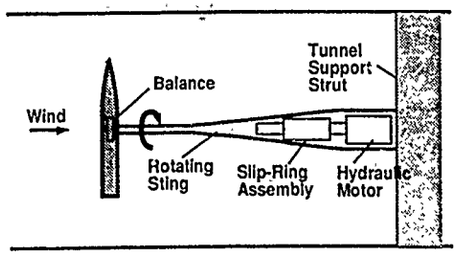

Figure 8-20. Test setup.

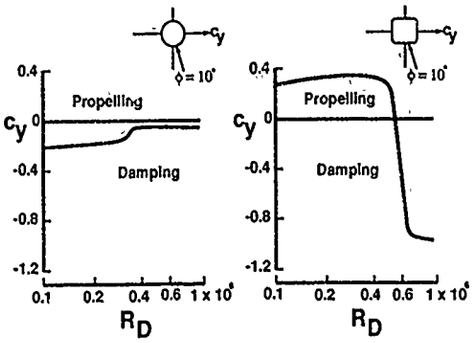

Figure 8-23. Two-dimensional static data for circular and square shapes.

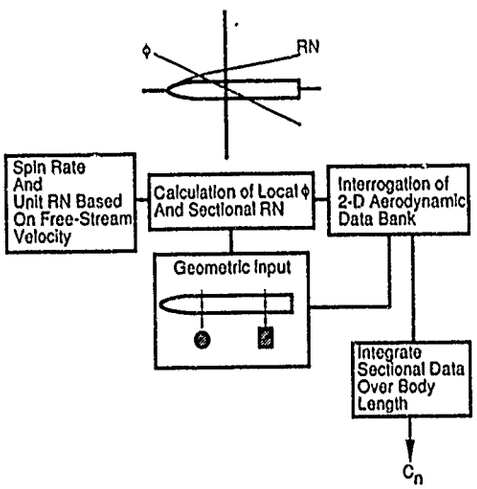

Figure 8-21. Analytical procedure.

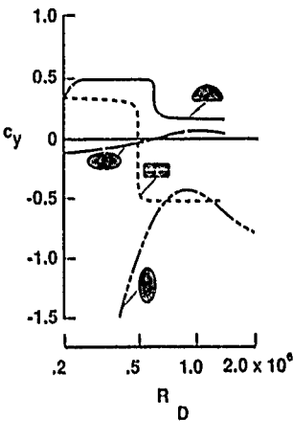

Figure 8-24. Effect of cross-sectional shape.

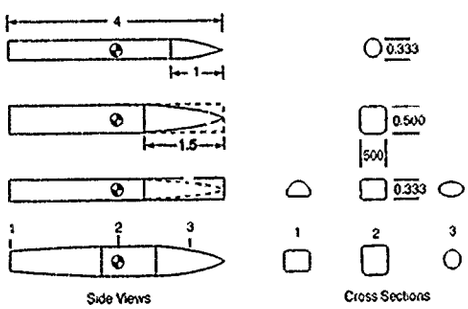

Figure 8-22. Fuselage shapes tested. Dimensions are in feet.

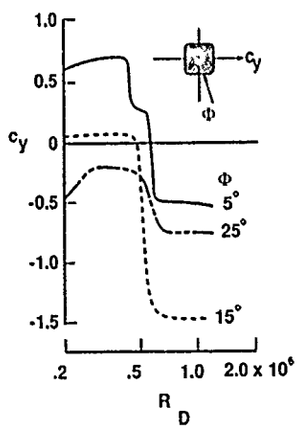

Figure 8-25. Effect of local flow angle.

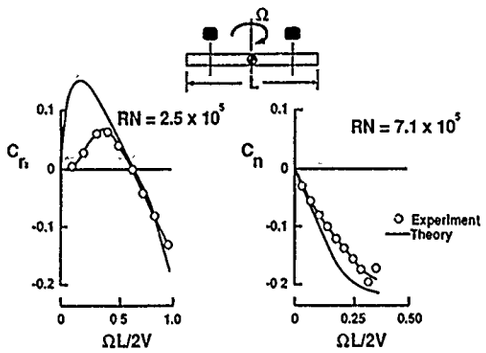

Figure 8-26. Results for rounded-square fuselage model.

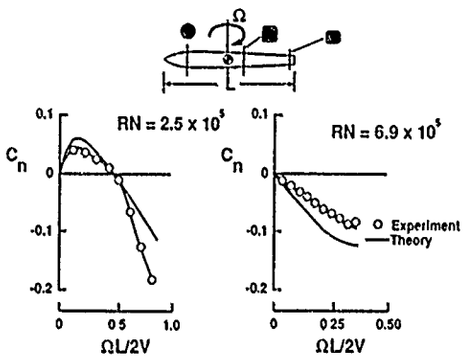

Figure 8-27. Results for model with various cross-sectional shapes.

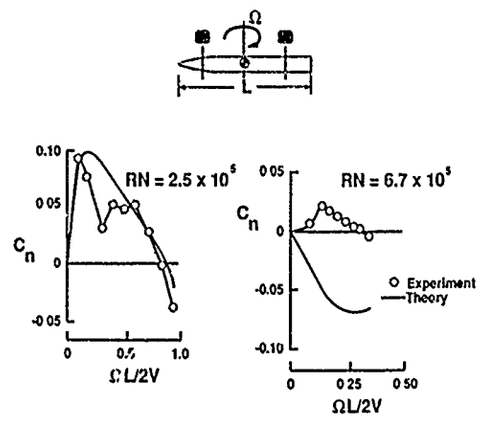

Figure 8-28. Results for rounded-square model with pointed nose.

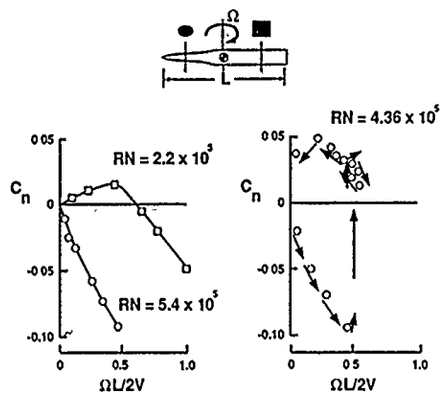

Figure 8-29. Results for model illustrating hysteresis effects.

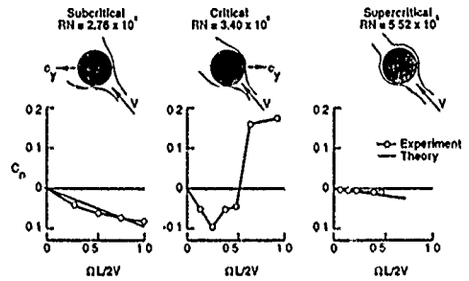

Figure 8-30. Results for circular cross-section model with pointed nose.

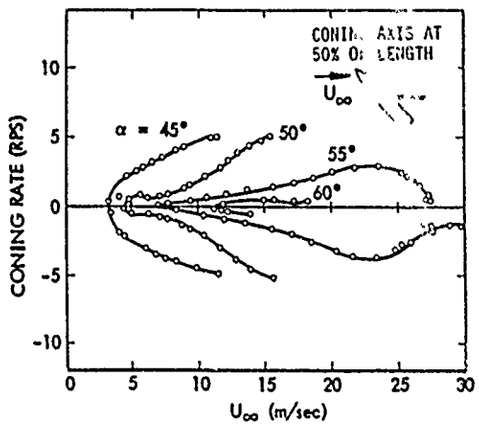

Figure 8-31. Coning motion at high angles of attack.

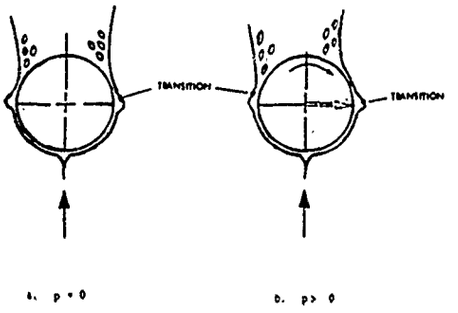

Figure 8-32. Moving wall effects.

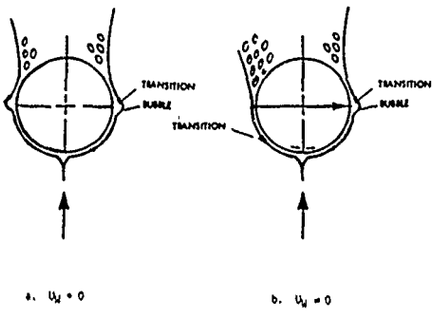

Figure 8-35. Variation of flow state with rotation rate.

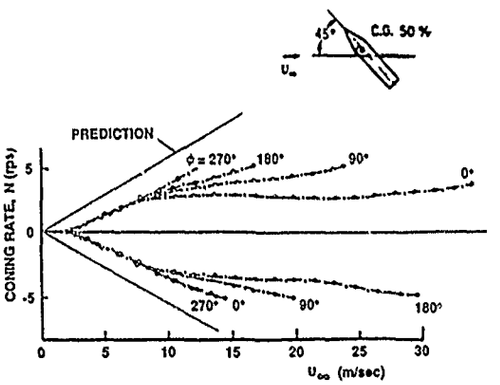

Figure 8-33. Coning rate for $\alpha = 45$ degrees.

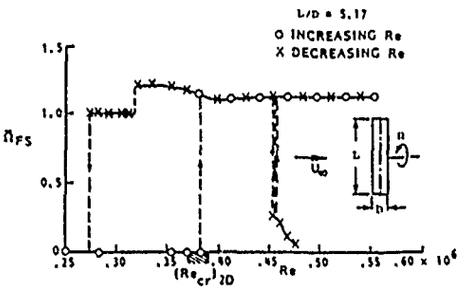

Figure 8-36. Maximum flat-spin rate of a circular cylinder.

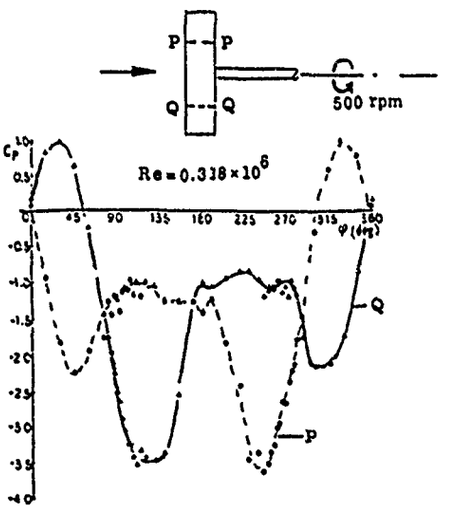

Figure 8-34. Flat spin of circular cylinder.

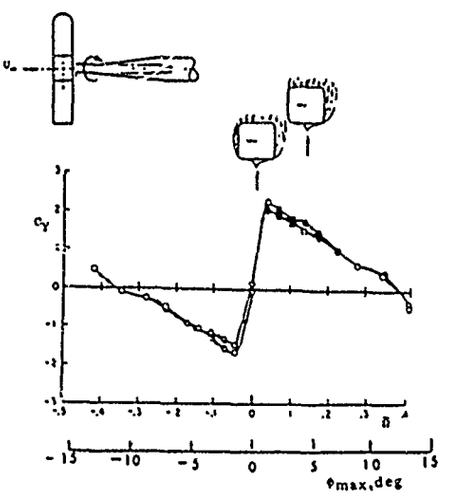

Figure 8-37. Side force measured on forebody in flat spin.

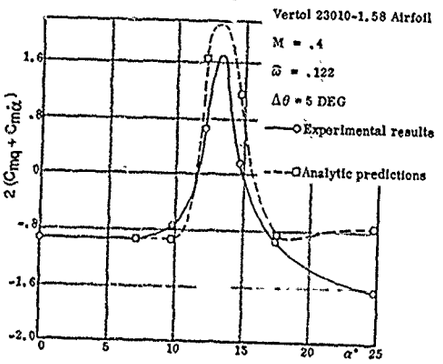

Figure 8-38. Dynamic stall results.

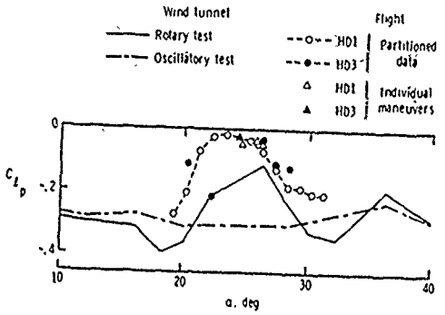

Figure 8-40. Roll damping for HIRM 1 model.

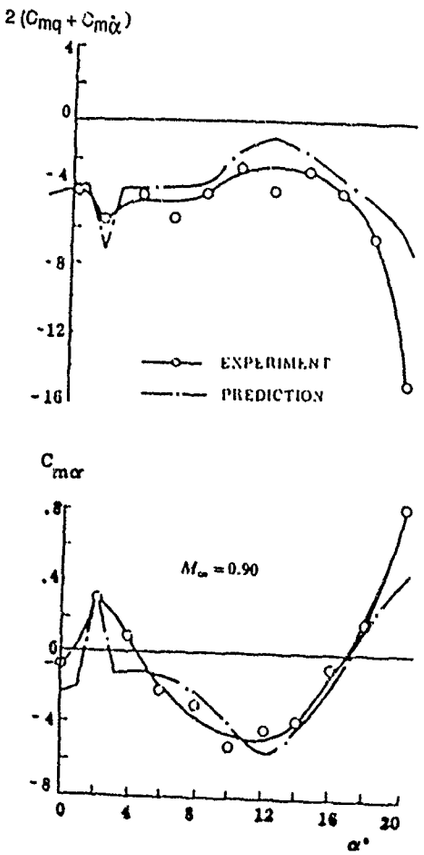

Figure 8-39. Results for the Space Shuttle.

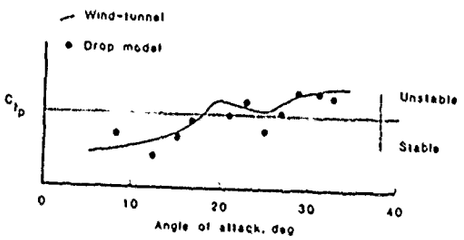

Figure 8-41. Roll damping for X-29A drop model.

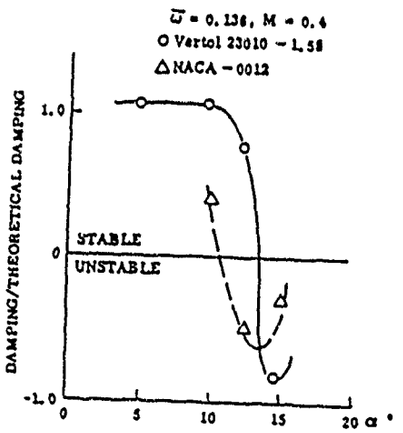

Figure 8-42. Negative damping of plunging airfoil.

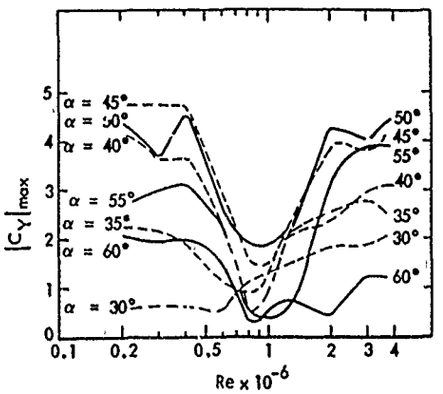

Figure 8-43. Effect of Reynolds number on side-force characteristics.

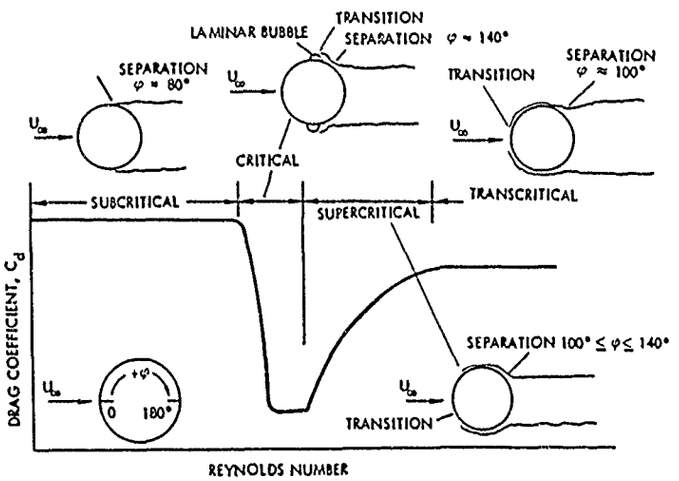

Figure 8-44. Effect of Reynolds number on flow state.

CHAPTER 9

USE OF ROTARY-BALANCE DATA IN THE PREDICTION OF AIRCRAFT DYNAMICS

9.0 INTRODUCTION

The rotary balance commonly measures an aircraft's steady aerodynamic characteristics, both static and rotational. It is the steady rotational moments, measured about the velocity vector at constant angles of attack and sideslip, that are required when computing or analyzing aircraft motions in a developed spin. The rotary-balance data can be used directly, therefore, to predict steady-state spin equilibrium conditions in a simple, straightforward manner employing three moment equations.

If the rotary-balance data are incorporated into a mathematical model, which also includes dynamic derivatives (normally obtained from forced-oscillation tests) in conjunction with large-angle six-degree-of-freedom equations, it is possible to determine if a spin is oscillatory, and investigate the ease or difficulty of entering and recovering from a spin, as well as high-α departures, roll reversal and other post-stall gyration motions and maneuvers.

It should be appreciated that flight dynamicists engaged in predicting high-α aircraft motions use three- and/or six-degree-of-freedom equations in conjunction with rotary-balance data during their studies.[1-25] However, the formulation of the mathematical model representing the aerodynamics and the associated computational technique used can vary considerably among the dynamicists. And, although some procedures may be applicable to a larger class of motions, require a smaller data base, or less solution time, etc., in the final analysis they should yield acceptable predictions of vehicle motions. In this chapter, different organizations have chosen to discuss how they apply rotary-balance data and, in so doing, different approaches are illustrated.

9.1 NASA LANGLEY RESEARCH CENTER

The rotary-balance spin prediction capability[1] identifies all possible steady spin modes for specified airplane inertias, center-of-gravity location, control settings and altitudes. The calculated spin mode sensitivity to these variables can, of course, also be determined. Although large-angle six-degree-of-freedom computations[2] are normally performed when warranted after rotary-balance testing is completed, the following three-degree-of-freedom technique is used to obtain spin predictions at the time of testing.

Analyses[3] as early as the mid-1920s indicate an understanding of the basic equations of motion as applied to the spin. Figure 9-1 illustrates the airplane's orientation and the forces acting upon it in a spin. A steady spin implies that all accelerations are zero along and about the body axes. For practical purposes, therefore, the force equations reduce to the relationships that side force is zero, drag equals weight, and lift is balanced by centrifugal force:

$$mg = 1/2\rho V^2 S C_D \tag{1}$$

$$mR_s\Omega^2 = 1/2\rho V^2 S C_L \tag{2}$$

The three body-axes moment equations reduce to

$$1/2\rho V^2 S b C_l = (I_z - I_y)qr \tag{3}$$

$$1/2\rho V^2 S c C_m = (I_x - I_z)rp \tag{4}$$

$$1/2\rho V^2 S b C_n = (I_y - I_x)pq \tag{5}$$

The angular rates, p, q and r, are clearly a function of the spin rate, Ω. Various authors[4-9] have defined this relationship in different, though generally equivalent, terms depending upon their definition of the airplane's orientation and the order of the axes rotations.

Bamber, Zimmerman and House[10,11] used a notation that is convenient because the axes of rotation are defined in terms of α and β. First, the airplane is considered to be yawed through an angle, $-(\beta + \sigma)$, where σ is the inclination of the flight path from the vertical, defined as

$$\sigma = \tan^{-1} R_s\Omega/V \tag{6}$$

The airplane is then pitched from the vertical by the angle α. This yields the following for the body-axes angular rates:

$$p = \Omega\cos\alpha\cos(\beta + \sigma) \tag{7}$$

$$q = \Omega\sin(\beta + \sigma) \tag{8}$$

$$r = \Omega\sin\alpha\cos(\beta + \sigma) \tag{9}$$

Substituting Equations (7)-(9) into Equations (3)-(5) and solving for the aerodynamic coefficients:

$$C_m = \left(\frac{4}{\rho S c b^2}\right)\left(\frac{\Omega b}{2V}\right)^2 (I_x - I_z)\sin 2\alpha\cos^2(\sigma + \beta) \tag{10}$$

$$C_l = \left(\frac{4}{\rho S b^3}\right)\left(\frac{\Omega b}{2V}\right)^2 (I_z - I_y)\sin\alpha\sin 2(\sigma + \beta) \tag{11}$$

$$C_n = \left(\frac{4}{\rho S b^3}\right)\left(\frac{\Omega b}{2V}\right)^2 (I_y - I_x)\cos\alpha \sin 2(\sigma + \beta) \tag{12}$$

These equations present the necessary requirements for equilibrium of the aerodynamic and inertial terms and must be simultaneously satisfied for a steady spin. Solving Equation (2) for R_s and substituting in Equation (6), σ is redefined in terms of $\Omega b/2V$:

$$\sigma = \tan^{-1}\left(\frac{\rho S b C_L}{4m(\Omega b/2V)}\right) \tag{13}$$

Consequently, the inertial terms (right-hand side of Equations (10)-(12)) are functions of $\Omega b/2V$, β and α, as are the aerodynamic coefficients (left-hand side of equations). Thus, there are three equations to solve for three unknowns, the $\Omega b/2V$, β and α values required for spin equilibrium.

A spin prediction program was generated for the Langley spin tunnel rotary-balance facility based on a 55-year old method of analysis.[10,11] This method sequentially utilizes the pitching-, rolling- and yawing-moment equations to determine the spin equilibrium values of the spin parameters in the following manner.

First, the pitching-moment Equation (10) is satisfied by locating the $\Omega b/2V$ values that result in equal inertial and aerodynamic moments, for each α and β tested. This is demonstrated graphically in Figure 9-2 for zero sideslip angle, where both the aerodynamic pitching-moment coefficient and the inertial term are plotted as functions of $\Omega b/2V$ for constant angles of attack. The locus of intersections of the aerodynamic and inertial curves forms the relationship shown in Figure 9-3 between α and $\Omega b/2V$ for zero β. The computer program repeats this calculation for each sideslip angle tested, yielding a corresponding $\Omega b/2V$ versus α relationship. It is interesting to note that this relationship is only slightly affected by sideslip, since the aerodynamic pitching-moment coefficient is not a strong function of β for most airplanes, nor is the inertial term for any airplane. Consequently, the $\Omega b/2V$ relationship presented in Figure 9-3 for $\beta = 0°$ is shown to be very closely approximated for $\beta = \pm 10°$ values. The pitching-moment equation, Equation (10), is, however, a strong function of $\Omega b/2V$ and α and, therefore, is used to calculate the $\Omega b/2V$ relationship.

The roll equation, on the other hand, is used to determine equilibrium β values because the aerodynamic rolling moment does have a strong functional dependency on β for most airplanes at high α values. Consequently, the inertial value, the right-hand side of the rolling-moment Equation (11), is calculated for the $\Omega b/2V$-relationship values found to satisfy the pitch equation at each of the β values tested. The aerodynamic rolling-moment coefficient is, of course, extracted from the rotary-balance data at these same $\Omega b/2V$, β and α values. From these data, the sideslip angles required to satisfy the rolling-moment equilibrium Equation (11) are determined as a function of angle of attack. This procedure is demonstrated graphically in Figure 9-4, which presents the aerodynamic rolling-moment coefficients and the inertial terms plotted as functions of sideslip angle for several angles of attack. Their intersections yield the required β values for equilibrium of the roll equation at each α. The resulting locus of equilibrium sideslip angles as a function of angle of attack is plotted in Figure 9-5. The equilibrium rotation rate, previously determined as a function of α and β (Figure 9-3) can now be reduced to a function of α alone, as shown in Figure 9-6, by evaluating the $\Omega b/2V$ relationship in Figure 9-3 at the β values satisfying the rolling-moment equation. At this point, the $\Omega b/2V$ (Figure 9-6) and β (Figure 9-5) values that are required to satisfy both the pitch and roll equation at each α tested have been determined. It remains only to use these values in the yawing-moment Equation (12) to find any angles of attack for which the inertial and aerodynamic terms are equal.

The inertial term in the yaw Equation (12) is, therefore, calculated at each angle of attack tested, using the β and $\Omega b/2V$ values from Figure 9-5 and 9-6; the aerodynamic yawing-moment coefficient is, likewise, extracted at these same values. Plots of these inertial and aerodynamic values versus angle of attack are shown in Figure 9-7.

Intersections of the aerodynamic and inertial curves identify angles of attack at which all three moment equations are in equilibrium. Because of the mechanism of the spin, only the intersections where the aerodynamic curve has a negative slope (indicated by squares) can result in spins. This occurs because a longitudinally stable airplane cannot maintain pitch equilibrium at a somewhat higher or lower α than the predicted value without a corresponding increase or decrease in $\Omega b/2V$ (Figure 9-6). At the indicated intersections, however, this $\Omega b/2V$ change is prevented by the presence of restoring lateral-directional moments about the spin axis.

The spin $\Omega b/2V$ and β values are then obtained from Figures 9-6 and 9-5, respectively, at the spin α identified in Figure 9-7. The drag and lift coefficients are then extracted from the rotary-balance data for these equilibrium α, β and $\Omega b/2V$ values. Equations (1) and (2) can then be solved for the descent velocity and spin radius, respectively

9.2 ONERA-IMFL

9.2.1 Introduction

In the high-angle-of-attack flight domain there exist many nonlinear aerodynamic effects which cannot be predicted by computational fluid dynamics. Consequently, many tests and measurements are required to estimate the aerodynamic effects. A mathematical model of the aerodynamic forces and moments that permits the calculation of the aerodynamic effects when the state vector of the aircraft is known, is incorporated with the equations of motion used to simulate the aircraft behavior. In this section the aerodynamic mathematical modeling developed at IMFL to simulate spin motions and to determine spin characteristics of an aircraft (control effects, stability, sensitivity to parameters, etc.) is presented. The application of bifurcation theory to mathematical modeling is then discussed and shown to offer considerable potential for the interpretation and prediction of the nonlinear behavior of aircraft.

9.2.2 Model Structure

Several methods exist to model these aerodynamic effects. Some of them use computational fluid dynamic methods, others consist of linearizing the equations of motion. Taking into account the high level of nonlinearity and the difficulty of calculating the separated flow and the dynamic phenomena, the IMFL developed a more pragmatic approach to model the aircraft aerodynamics over a large flight domain, up to 90° of angle of attack.

This type of approach has the advantage of being directly applicable. It is essentially based on data tables of the type: $C_m = C_m(\alpha, \beta, \delta_m, ql/V)$. In this example the pitching moment is related to the state variables: angle of attack, sideslip, elevator deflection and reduced pitch rate. To obtain the data stored in these tables, tests are carried out in the wind tunnel on the rotary balance for several values of the state variables $(\alpha, \beta \ldots)$. For example, the pitching-moment data are plotted and analyzed with respect to the different state variables and the structure of the pitching moment is modeled; then tables are created. These tables can have several "input" variables. An input variable is chosen by considering its effect on the aerodynamic coefficient.

Instead of using data tables, another method would be to use polynomial approximations of the experimental data. However, with this approach it is necessary to identify the parameters of the polynomial functions and this is quite difficult when the nonlinear effects are important or complex. Furthermore, with the polynomial formulation it is often hard to satisfy the continuity of the aerodynamic coefficients throughout the flight domain.

The tables give the value of the coefficient at each node of the variable set determined from the wind tunnel measurements. For any values of the variable set the aerodynamic model gives an estimated value of the coefficient by means of interpolation functions, using the values at the nodes situated in the neighborhood of the point considered. This kind of aerodynamic modeling has the advantage of being very practical and flexible since the data base can be improved or extended very easily. In the regions where the aerodynamic phenomena are strongly nonlinear the number of nodes of the variable set can be increased so that the nonlinear behavior can be described more completely. Modification of the aerodynamic model to include supplementary data can be accomplished easily, whereas in the case of polynomial formulations new identifications of the parameters would be necessary.

An interesting but delicate aspect of the modeling lies in the analysis of the experimental data. Experience in aerodynamic testing is necessary to recognize the support interference effects and the Reynolds number effects and to try to exclude them from the aerodynamic data base. This problem is particularly difficult because the effects are nonlinear and not predictable before the tests are made.

9.2.3 Importance of Unsteady Effects

The model structure described in Section 9.2.2 is applicable to aerodynamic phenomena that could be nonlinear and complex but not time dependent. When the aircraft motion is unsteady the angles of attack and sideslip are varying quickly. During these unsteady motions, like spin entry for instance, the angle λ between the velocity vector and the rotational vector is important. It is possible to simulate motions on the IMFL rotary balance where unsteady effects can be observed. The analysis of the oscillatory-coning test results contributes to the unsteady aerodynamic modeling (see Chapter 4).

When aircraft motions exhibit large-amplitude variations, the aerodynamic contribution of λ is evidently important. From the spin equilibrium and spin stability points of view, there are two major points of interest associated with the tilt angle capability.

First, the aerodynamic λ effects are important for the calculation of the oscillatory spin. An oscillatory spin can be quite similar to an oscillatory coning motion when the rotation vector is tilted with respect to the velocity vector. This is of interest because oscillatory spins or limit cycles are often encountered with aircraft at high angles of attack.

Second, the stability conditions of the different equilibrium states in the spin can be studied. These equilibrium states can be stable or unstable and, in order to determine the stability characteristics, it is necessary to obtain the aerodynamic responses induced by some elementary disturbance. A disturbance may tilt the rotational vector with respect to the velocity vector (or vice versa) and a small angle λ will be induced. This, in turn, will induce small rate variations of angle of attack and sideslip. Consequently, the knowledge of the λ aerodynamic effects is useful in the determination of the stability characteristics of spins.

9.2.4 Unsteady Modelling

In general, the mathematical modeling of all these unsteady effects will be particularly difficult at high angles of attack, beyond the stall region. Then the aerodynamic responses contain an unsteady part of possibly large amplitude, which cannot be described with simple data tables. The required mathematical model is complex and time dependent; the flight path history (particularly the angle of attack and sideslip time histories) influences the instantaneous values of the aerodynamic effects, and, therefore, cannot be neglected.

At IMFL these unsteady effects have been modeled with transfer functions of the type:

$$C_z(s) = H(s, \alpha, \lambda, \dot{\alpha}), \dot{A}(s)$$

In this expression:

s is the Laplace variable,

$C_z(s)$ is the Laplace transform of the unsteady lift $C_z(t)$,

$\dot{A}(s)$ is the Laplace transform of $\dot{\alpha}l/V$ and

$H(s, \alpha, \lambda, \dot{\alpha})$ is a transfer function relating the motion (or input) to the aerodynamic response (or output).

The coefficients of the transfer function are dependent on the values of α, λ and $\dot{\alpha}$, so this modeling is not linear.

This formulation can describe the aerodynamic response as a function of its time history. The aerodynamic effect is not limited to an instantaneous response but the unsteady lift at $t - \delta t, C_z(t - \delta t)$, may influence $C_z(t)$.

In practice, the model may often be limited to a first order transfer function. Then a gain (or instantaneous contribution) and a time constant (or time lag contribution) characterize the unsteady aerodynamic response. Applied to the oscillatory coning motion test data these parameters have been identified using a least squares method.

9.2.5 Aerodynamic Modelling Procedure

The general modeling procedure used at IMFL is shown in Figure 9-8. The experiments and the modeling must be interactive in this procedure: the construction of the aerodynamic model can modify the test programs. Moreover, the capability of determining a suitable model structure and judicious test programs is highly dependent on the evaluation and analysis of the aerodynamic effects encountered at high angles of attack. This requires a good estimation of the measurement accuracy and reliability, and also requires one to cross-plot the different data using a visualization tool that is well adapted to multidimensional functions. The modeling process allows for the modification of its structure, and further testing, as required when the comparison between the model and the flight test data is not satisfactory.

Applied to the Alphajet data this type of modeling has given fairly good results. These results are presented in Section 11.3, where comparisons are made between IMFL rotary-balance measurements, or modeling, and flight test results.

9.2.6 Bifurcation Analysis

The dynamic system can be described by the state equation

$$\dot{X} = f(X, \delta)$$

where f as a linear function of X and δ has only one equilibrium state ($\dot{X} = 0$) for each value of the control vector δ. However, if f is nonlinear the system can have several equilibrium states for the same value of δ.

In the state space, the set of equilibrium points defines a specific surface called the equilibrium surface. Each equilibrium point corresponds to a zero value of the function f and the stability of this equilibrium depends directly on the eigenvalues of Jf, the Jacobian matrix of f. The set of points, where at least one eigenvalue of Jf has a real part equal to zero, is the set of bifurcation points. The projection of this set into the control space defines a surface called the bifurcation surface. When the system crosses the bifurcation surface, the number of equilibrium possibilities changes and a jump can occur from one branch of the equilibrium surface to another.

One of the purposes of the bifurcation theory is to study the topology of the equilibrium and bifurcation surfaces for the differential system $\dot{X} = f(X, \delta)$. As the flight mechanics equations of an aircraft describe a similar system, it is clear that by using the bifurcation theory, the aircraft behavior may be known and understood, even at high angles of attack where the function f is highly nonlinear.

At ONERA-Chatillon computational methods have been developed by P. Guicheteau to determine the equilibrium surface, the stability characteristics and the bifurcation surfaces of a nonlinear dynamic system.[17] These calculations have been applied to the Alphajet mathematical modeling and, as an example, some results are presented in Figure 9-9. This shows the equilibrium surface in the three-dimensional representation of stick position (elevator and aileron deflections) and angle of attack. Assume that the aircraft is at the equilibrium state as defined by the point A on the equilibrium surface (see Figure 9-9). When the pilot deflects the stick, the equilibrium point moves on this surface.

If the pilot displaces the stick to the left, the aircraft state changes smoothly up to the point B. At this point the surface contains a fold and so, if the pilot moves the stick slightly to the left, the equilibrium state will jump to the point C on the other branch of the surface. The point B is a bifurcation point. The equilibrium state at C corresponds to a spin equilibrium at a high angle of attack.

Reversing from point C to point D, the aircraft state will change in a continuous way. However, the point D is also a bifurcation point. If the pilot displaces the stick slightly to the right then the state will jump to the point A and a spin recovery will be achieved. These characteristics correspond to a hysteresis diagram in the plane (δ_l, α) as shown in Figure 9-10. The main effects of the stick can be observed in Figure 9-9 for the Alphajet aircraft. For instance, the equilibrium surface shows that the stick must be pushed forward to arrive at a flat spin equilibrium state, as described in Sections 7-7 and 11-3.

This type of result is of great interest from a point of view of correlation. It may also be used to predict the aircraft behavior in a complex and nonlinear flight domain or to design optimal control laws designed to move the system from one equilibrium state to another.

9.3 AERMACCHI

9.3.1 Introduction

Investigations of the spinning behavior of aircraft at high angles of attack have been a matter of research at AerMacchi for many years. It was, in fact, considered useful to set up a calculation tool allowing spin behavior to be predicted as early as in the initial design phase. The correlation between the estimated values and the values obtained during flight tests has always been found to be good; the criterion is, therefore, considered adequate for use in predicting the spin behavior of new aircraft.

An accurate program of wind-tunnel tests on static and rotary balances is used to identify the areas of spin equilibrium, to determine the control effectiveness, and to build up a fairly accurate mathematical model for a comprehensive simulation of the aircraft rotation in spin.

9.3.2 Analysis of Wind-Tunnel Tests and Spin Equilibrium

The tests on the rotary balance permit the areas of spin equilibrium to be determined. These are indicated by the moments acting on the aircraft becoming zero simultaneously. It is also emphasized that, in addition to the aerodynamic moments measured in the wind tunnel, the moments due to the aircraft mass and the engine gyroscopic effects must be considered. An example of the procedure followed is shown in Figure 9-11 (Ref. 13). The data refer to the tests performed on a model of the MB-339 jet trainer. Since the tests were made with $\beta = 0°$, the aircraft inertial moments affect the pitching moment only, and the engine gyroscopic moments are small and can be neglected. The calculation procedure used is, in principle, the same as described in Section 9-1. References 12, 13 and 14 give the results of the rotary-balance tests and a few examples of the calculation of the regions of equilibrium for aircraft having very different configurations. This first analysis of the wind-tunnel test results applies to steady spin conditions only, and does not predict the aircraft behavior during spin recovery and entry. However, the experience gained with the aircraft confirms that this analysis is sufficient to locate possible abnormal behavior, to estimate the effectiveness of the controls with fairly good accuracy, and to forecast the most effective spin entry and recovery maneuvers.

Figures 9-12 and 9-13 (from Ref. 14) show the results obtained from the tests performed on a combat aircraft model. The test in Figure 9-12 highlights a condition of spin equilibrium at $\alpha = 45°$, $\Omega b/2V = 0.12$; this condition is obtained with aileron control at full travel. The region of equilibrium can be obtained only when $\Omega b/2V < 0$ (ailerons to full deflection opposite to rotation), and does not exist when $\Omega b/2V > 0$. As shown in Figure 9-13, data taken at $\alpha = 84°$ with neutral controls show that a spin condition is highlighted at $\Omega b/2V = 0.18$.

9.3.3 Mathematical Model and Solution of Six-Degree-of-Freedom Equations

The availability of a very large amount of rotary-balance data and the possibility of expressing the aerodynamic coefficients not only as a function of α and β, but also as a function of $\Omega b/2V$, made it possible to obtain, at an early stage, excellent agreement between the results of the simulation and the aircraft behavior. Phenomena such as stall, wing rock, wing drop, flick roll, departure, spin entry and recovery have been simulated with success.

The computational modeling of aerodynamic coefficients which is presently used at AerMacchi is illustrated in Figure 9-14 and is broadly based on the following criteria:

(a) The aerodynamic coefficients for the steady state ($p = q = r = o$), and zero controls are represented as fully nonlinear functions of α and β. They are obtained from conventional static balance tests up to the maximum angle of attack attainable with such an apparatus, and from rotary-balance data.

(b) The effects of control deflections are assumed to be a function of angle of attack and control deflection, and not of the angular velocities.

(c) The effects of the rotation rate $\Omega b/2V$ on C_l, C_n and C_y are obtained from the rotary balance as nonlinear functions of $\Omega b/2V$, α and β.

(d) The effect of pitch rate is obtained in an average, linearized form as C_{L_q}, C_{m_q}, from rotary-balance data at nonzero sideslip.

(e) The effects of yaw rate and rate of change of α and β are usually not available, and are thus assumed to be zero or estimated on the basis of simple empirical criteria.

The preparation of the aerodynamic data base for the six-degree-of-freedom simulation requires some interpretation of the available wind-tunnel results. It is advisable that the values of the individual derivatives be evaluated prior to simulation, and the equilibrium regions identified directly using the wind-tunnel graphs. The initial evaluation avoids gross mistakes and facilitates correct interpretation of the simulation by mathematical model

A certain amount of adjustment is also required when significant Reynolds number effects exist between wind-tunnel tests and full-scale data in the stall range. In that case, the frequently used procedure is to "shift" the nonlinearities in the data, which appear at stall, by the difference between model and (estimated) full-scale stall angle of attack. While this procedure has yielded useful results for some configurations, it is not scientifically rigorous, and should be applied with caution (see Section 8.4).

As can be noted, many of the coefficients required to build the data base are usually obtained from the static balance tests. These tests are far less costly than those on the rotary balance and can be conveniently used to cross-check and validate the coefficients measured on the rotary balance. In general, the static balance data are used to give the longitudinal and lateral-directional characteristics, while the rotary-balance data are used to supply the damping and control effectiveness characteristics. The rotary-balance tests with β not equal to 0° are used to estimate pitch damping and the effect of β on roll damping.

The α range to be investigated can be from −90° to +90° in the cruise configuration, and smaller in the takeoff and landing configurations (−8° to +30°). The ideal solution would, however, be to test in the entire α range, from 0° to 360°. It would then be possible to obtain a mathematical model which is representative also at extreme angles of attack, and thus to have a valid flight simulation for all aerobatic maneuvers, as well as for spin entry from the vertical attitude.

The tests with varying β can be limited to $\beta < 30°$, while the maximum value of $\Omega b/2V = 0.16$ is more than sufficient in the case of a combat aircraft. Conversely, in the case of a general aviation aircraft, it is advisable to reach a maximum value of $\Omega b/2V = 0.40$.

Examples of typical AerMacchi test programs are given in Table 9-1.

9.3.4 Estimate of the Yaw Damping Derivatives

At present, the values of the yaw damping derivatives are estimated by using the normal low-α computational methods, adjusted to match the data given by the rotary-balance tests at higher α.

9.3.5 Extrapolation to Higher Mach Numbers

The damping characteristics at higher Mach numbers are presently estimated on the basis of transonic static tests. This criterion was adopted because it had been noted that, at low Mach, the autorotation characteristics at stall angles of attack that are measured on the rotary balance could be identified also on the static balance, though less accurately. They appear as rolling moment asymmetries in tests with $\beta = 0°$ and variable α (see Figure 9-15). Therefore, taking the rolling moment asymmetries measured during the high Mach static-balance tests, it is possible to estimate the angle of attack at which autorotation is liable to occur, and the value of the autorotation moment at higher Mach numbers.

9.3.6 Reference Axes

Stability axes are used as the reference axes for the management of the aerodynamic data base. This convention is due to the fact that the most common computational methods of the low-α aerodynamic data permit them to be estimated with respect to these axes. This solution was, therefore, retained also to analyze the results of the rotary-balance tests. Presenting these results in body or wind axes would cause no problems, but preference is given to the stability axes because it is then possible:

- to manage the high-α data using the same reference system as in the case of the low-angle-of-attack data
- to cross-check the measured coefficients with those calculated in the low-α region and so obtain a first validation of the results
- to manage the rotary-balance data in a more direct manner because the rotation imparted to the model during the tests with $\beta = 0°$ is about the stability axes.

9.3.7 Validation of the Mathematical Model

As mentioned in the foregoing, the data obtained on the rotary balance must be validated, and a first cross check can be made using the stability data obtained from the static balance. As far as the damping characteristics at the angles of attack below stall are concerned, another check can be made by comparing the experimental data with those yielded by computation.

The same considerations apply to the preparation of the data base. It is relatively easy to make mistakes in data management, these errors being occasionally difficult to find through simulations of the high-angle-of-attack behavior. In general, it is essential to thoroughly analyze the wind-tunnel test results and have a sound knowledge of the phenomena connected with high-angle-of-attack behavior, before starting to prepare the data base.

Examples of mathematical models used are included in References 15 to 17.

9.4 RAE

9.4.1 Mathematical Modelling for Moderate Angles of Attack for HIRM 1

The data available from rotary rigs are particularly valuable in assessing some of the details of responses of combat aircraft at and near conditions of departure from controlled flight. The applications of the results obtained with the HIRM 1 configuration (Chapter 7.5) is described here, and the simulated responses are compared with results from free-flight experiments in Chapter 11.

The angles of attack under consideration are in the range $20° < \alpha < 35°$, where the flow is separating and reattaching under dynamic conditions on all the lifting surfaces, including the fuselage. The main difficulty encountered in applying the results from rotary rig experiments is obtaining a consistent set of data to account for the forces and moments due to other types of motion, particularly those involving sideslip and yaw rate. As discussed earlier, the forces and moments measured on rotary rigs are necessarily those due to rolling about the wind axis, whereas it is more convenient to use the equations of motion when expressed about geometric body axes. The two main reasons are that the moments and products of inertia remain constant (but vary significantly with angle of attack in wind axes), and that the measurements of linear and angular velocities made in flight must be with respect to geometric body axes. Results for forces and moments due to sideslip are readily available from static wind-tunnel tests, and the usual source of data for yaw rate is oscillatory rig experiments, that is, about body axes. However, for HIRM 1, experiments using a whirling arm to produce steady yawing in wind axes are in progress, and it is hoped to obtain results at moderate angles of attack in the near future. Such data can be combined directly to give moments and angular rates about body axes, using standard equations for axis conversion. In the interim, results from the oscillatory rig have been used to complete the data set.

In order to clarify the form of the equations, the dimensional quantities are used, without the factors needed to give the coefficients; alternatively, the symbols may be considered as denoting the nondimensional form if the normalizing factors are dynamically consistent. Subscripts w and b are used to denote wind (aerodynamic body) and body (that is, geometric) axes, respectively, but to highlight the effects of the transformations on the angular rates, separate symbols are used, with p, r being the rates of roll and yaw respectively about body axes, and Ω, Π being the corresponding rates about wind axes. The form of the rolling moment, L, is discussed in detail, and the yawing moment, N, and side force, Y, have analogous forms. It has to be assumed that the rolling moment due to the various constrained degrees of freedom obtainable in wind tunnels may be added to give the total moment, provided that the linear and angular velocities involved are independent. Thus, the rolling moment in wind axes is assumed to be of the form

$$L_w = L_w(\beta) + L_w(\dot{\beta}) + L_w(\Omega) + L_w(\Pi) + L_w(\delta)$$

where δ denotes the contributions from all of the lateral controls. Each of the components is a function of angle of attack (and of Mach number if that varies during the maneuver). For simulation studies, it is possible to represent each component either by numerical values stored in look-up tables with associated interpolation formula or by algebraic expressions with numerical coefficients specified in the input data. An intermediate form has been used for some of the HIRM studies, the numerical coefficients of the polynomials in β and Ω being stored in look-up tables with the corresponding angle of attack. An example of the polynomial fit obtained at $\alpha = 24°$ for HIRM data is given in Figures 9-16 and 9-17. The first step is to express the motion variables in terms of those referred to body axes:

$$L_w = L_w(\beta) + L_w(\delta) + L_w(p\cos\alpha + r\sin\alpha) + L_w(\dot{\beta}) + L_w(r\sin\alpha - p\cos\alpha)$$

Then the next step of combining this rolling moment with the corresponding yawing moment gives, in principle, the rolling moment about body axes,

$$L_b = L_w\cos\alpha - N_w\sin\alpha$$

The moments due to sideslip and control deflections combine directly to give $L_b(\beta)$ and $L_b(\delta)$, which may be obtained from static wind-tunnel tests. The measurements from the rotary rig experiments may also be included directly, with Ω calculated from the p, r, q given by the equations of motion.

For the effects of rate of yaw and rate of change of sideslip, it is necessary to revert to β and Π as variables, and the assumption has to be made that the moments are linearly dependent on the rates, so that

$$L_w(\dot{\beta}) + L_w(\Pi) = (L_{\dot{\beta}}\dot{\beta} + L_\Pi\Pi)_w$$

The derivatives measured with an oscillatory rig give the combined derivatives in body axes, e.g., $(L_r - L_\beta\cos\alpha)_b$, and the shorthand notation for these oscillatory derivatives is used,

$$L_{\dot{\psi}} = L_r - L_{\dot{\beta}}\cos\alpha \quad \text{and} \quad L_{\dot{\phi}} = L_p + L_{\dot{\beta}}\sin\alpha, \quad \text{etc.}$$

When the set of oscillatory derivatives are converted to wind axes, it is found that the derivatives due to Π and β are combined in the form,

$$(L_\Pi - L_{\dot{\beta}})_w = L_{\dot{\psi}}\cos 2\alpha - N_{\dot{\phi}}\sin 2\alpha - (L_{\dot{\phi}} - N_{\dot{\psi}})\sin\alpha\cos\alpha$$

For maneuvers in which the gravity component is approximately balanced by the aerodynamic side force, the equation of motion gives

$$\begin{aligned}\beta &= -\Pi + (Y/m + g\cos\theta\sin\phi)/V \\ &\approx -\Pi\end{aligned}$$

so that

$$(L_\Pi\Pi - L_{\dot{\beta}}\Pi)_w = (L_\Pi - L_\beta)_w\Pi$$

Thus the combined derivative obtained from the oscillatory derivatives is an approximation to the required contributions, with the corresponding relationship for the yawing moment. When these are converted back to body axes, the rolling moment simplifies to the equation

$$(L_\Pi - L_{\dot\beta})_w \cos\alpha - (N_\Pi - N_{\dot\beta})_w \sin\alpha = L_{\dot\psi}\cos\alpha - L_{\dot\phi}\sin\alpha$$

The final expression for rolling moment about body axes is given by

$$L_b = L_b(\beta) + L_b(\delta) + (L_{\dot\psi}\cos\alpha - L_{\dot\phi}\sin\alpha)(r\cos\alpha - p\sin\alpha) + L_w(p\cos\alpha + r\sin\alpha)\cos\alpha - N_w(p\cos\alpha + r\sin\alpha)\sin\alpha$$

The equation for yawing moment is directly analogous, but that for side force is simpler because only the angular rates need to be converted to body axes.

9.4.2 Example of Mathematical Modeling

The data measured for HIRM 1 have been analyzed, and it was found that cubic polynomials in pb/V gave satisfactory representations of the nonlinear effects. The quadratic term was retained because of the asymmetric dependence on roll rate (for example, Figures 9-16 and 9-17). The linear and cubic coefficients are dominant, the former being close to the local slope taken at $p = 0$ (Figure 9-18), and it is perhaps surprising to find that the variation of the cubic coefficient with angle of attack shows similar characteristics for the three control configurations tested (Figure 9-19).

The effects of the nonlinear contributions have been studied in a Cranfield Institute of Technology PhD thesis (R. Thorne, "Some experimental and theoretical studies in aircraft stability at high angles of attack"). Figure 9-20 shows the growth of the unstable dutch roll oscillation to a limit cycle, the amplitude of which depends on the magnitude of the nonlinear terms.

9.5 NORTHROP CORPORATION

A method of incorporating rotary-balance and forced-oscillation data (including plunging data) in a six-degree-of-freedom (6-DOF) aircraft simulation has been developed by J. Kalviste[18] of the Northrop Corporation, Aircraft Division.

Note that P, Q, R are used interchangeably with p, q, r in this section.

9.5.1 Rotary-Balance Test Data

In a conventional simulation the aerodynamic data for dynamic aircraft motion are defined in terms of dynamic derivatives, C_{l_p}, C_{n_r}, C_{m_q}, etc. These derivatives define aerodynamic data for aircraft rotational motion (p, q, r) about the three body axes. The aircraft total rotational vector is resolved into components about the three axes and the components are used with the derivatives. With the aerodynamic data also defined for rotation about the velocity vector the total rotational vector has to be resolved differently to include the data from the rotary-balance tests.

The basic concept[18] underlying the procedure discussed here is to resolve the total rotation vector into the three components which are closest to the total rotation vector instead of only the three body-axes components. If the rotation vector is close to the velocity vector, for which case rotary-balance data are available, the rotation vector is resolved into three components with one component along the velocity vector. In this way the data are always "interpolated" between known data points.

The procedure for resolving the total rotational vector will be illustrated with some simple vector diagrams. To simplify the diagrams, only the two-dimensional vectors in the aircraft x-z plane will be shown. The general case of a three-dimensional vector diagram will be shown later. Figure 9-21 shows a vector diagram of the total velocity vector (V_T), the total rotational vector (Ω), and body-axes rate components of Ω, (p, r). In this figure, the rotation vector is between the x axis and the velocity vector; therefore, the rotation vector is resolved into a component along the velocity vector (ω) and a component along the x axis (p_{mod}). In Figure 9-22 the rotation vector lies between the velocity vector and the z axis and is resolved into components along these vectors. In both cases the rotation vector is resolved into components along the vectors for which aerodynamic data are available and are closest to the rotation vector. In effect, the aerodynamic data are thereby interpolated between the two data points.

In general, the total rotation vector will be resolved into components along the axes for which aerodynamic data are available. A two-dimensional vector diagram of the aircraft x-z plane is shown in Figure 9-23. The complete $x - z$ plane is divided into six regions by the two body axes and the velocity vector (all extended in the negative direction). The total rotation vector is resolved into two components, depending on which region the rotation vector is in as indicated in Figure 9-23. For the upper right and lower left-hand regions the total rotation vector is resolved into body-axes rate components only, with no component along the velocity vector.

For the general, three-dimensional case, the vectors can be displayed as points on a unit sphere. Figure 9-24 shows a right spherical triangle, which forms one octant of the unit-sphere surface. The vertices of the triangle are the x, y and z axes of the aircraft. The location of the velocity vector is defined by two angles on the unit sphere (α, β). The surface of the unit sphere is divided into three regions by dashed lines. The three components of rate into which the total rotation vector is resolved (a similar triangle exists for the negative direction of the vectors) are indicated for each region. Outside of the triangle the rotation vector is resolved into the three body-axes rates.

9.5.1.1 Computational Procedure

For a general 6-DOF simulation, the total rotation vector is defined in terms of the three body-axes rates (p, q, r). This rotation vector can also be resolved into three components, where one component is along the velocity vector. The choice depends on where the total rotation vector is located relative to the four axes, as illustrated in Figure 9-24. The three components are computed from the following equations:

$$p_{mod} = p - \omega \cos\alpha \cos\beta \tag{1}$$

$$q_{mod} = q - \omega \sin\beta \tag{2}$$

$$r_{mod} = r - \omega \sin\alpha \cos\beta \tag{3}$$

The computational procedure is to compute ω initially from Equation (1) with p_{mod} equal to zero. This value of ω is used with Equations (2) and (3) to compute q_{mod} and r_{mod}. If the computed values of q_{mod} and r_{mod} are smaller in magnitude than, and of the same sign as q and r, respectively, the three rate components are q_{mod}, r_{mod} and ω, with p_{mod} equal to zero. If these conditions are not satisfied, the same procedure is applied to Equation (2), and then to Equation (3). If the tests fail for Equation (2) and also for Equation (3), then the three rate components $(p_{mod}, q_{mod}, r_{mod})$ will be the body-axes rates (p, q, r) with ω equal to zero.

The coefficient buildup for the rotary-balance data and the body-axes derivatives is as follows:

$$C_i = C_i\left(\frac{\omega b}{2V_T}\right) + C_{i_p}\frac{b}{2V_T}p_{mod} + C_{i_q}\frac{\bar{c}}{2V_T}q_{mod} + C_{i_r}\frac{b}{2V_T}r_{mod} \tag{4}$$

where $i = l, m, n, X, Y, Z$. The first term is the nonlinear rotary-balance data function and the other three derivatives are the body-axes dynamic derivatives. One of the four rate components $(p_{mod}, q_{mod}, r_{mod}, \omega)$ will be zero.

The coefficient buildup is illustrated with a simple example. The total rotational rate is held constant at $\Omega = 1.0$ rad/sec while the direction is changed through 360° in the aircraft x-z plane. The body-axes rate components are computed from:

$$p = \Omega \cos\theta \tag{5}$$

$$r = \Omega \sin\theta \tag{6}$$

where θ is the direction of the rotation vector. $\theta = 0°$ is along the $+x$ axis, $\theta = 90°$ is along the $+z$ axis, etc. The modified rate components $(\omega, p_{mod}, r_{mod})$ are computed from Equations (1) and (3) using the procedure described above and the aerodynamic coefficient (C_l) is computed from Equation (4). To simplify the example the rotary-balance data are defined by a linear derivative as follows:

$$C_l\left(\frac{\omega b}{2V_T}\right) = C_{l_\omega}\frac{b}{2V_T}\omega \tag{7}$$

The body-axes components of the total rotation vector are shown in Figure 9-25 as functions of θ. The modified rate components are shown in Figure 9-26 and the coefficient computed from Equation (4) is shown in Figure 9-27. For this example, $C_{l_p} = -0.1$, $C_{l_r} = -0.05$, $\alpha = 30°$ and $C_{l_\omega} = -0.13$. As can be observed from Figure 9-26, only two of the three modified rate components are nonzero as θ varies from 0 to 360°. The aerodynamic coefficient is continuous as a function of θ, equal to the value computed from the dynamic derivatives (C_{l_p}, C_{l_r}) along the x and z axes (indicated by circles), equal to the value computed from the rotary-balance data (C_{l_ω}) along the velocity vector (indicated by squares) and "interpolated" for the values of rate for points between the data points.

In the procedure commonly used for analysis of aircraft spin modes,[1] the aircraft total rotational vector (Ω) is resolved into four components:

$$\omega_{ss} = (p\cos\alpha + r\sin\alpha)\cos\beta + q\sin\beta \tag{8}$$

$$p_{osc} = p - \omega_{ss}\cos\alpha\cos\beta \tag{9}$$

$$q_{osc} = q - \omega_{ss}\sin\beta \tag{10}$$

$$r_{osc} = r - \omega_{ss}\sin\alpha\cos\beta \tag{11}$$

This gives a good approximation of the aerodynamic coefficient when the rotation vector is near the velocity vector but becomes inaccurate farther from the velocity vector. This will be illustrated with the data from the previous example. The three components of the rotation vector are shown in Figure 9-28 and the aerodynamic coefficient is shown in Figure 9-29. The aerodynamic coefficient is equal to the rotary-balance data ($\theta = 30°$ and $\theta = 210°$) but not to the data along the x and z axes. In general, the differences between results from the two procedures can be larger than in this example, since the rotary data are nonlinear functions of the coning rate while the oscillatory data are obtained as linear derivatives.

9.5.2 Forced-Oscillation Test Data

The forced-oscillation tests provide dynamic derivatives for rotations about the three body axes. For $\beta = 0°$ these data are normally defined as follows:

$$C_{i_p} + C_{i_\beta}\sin\alpha_o \quad \text{(for oscillation about the } x \text{ axis)} \tag{12}$$

$$C_{i_q} + C_{i_\alpha} \quad \text{(for oscillation about the } y \text{ axis)} \tag{13}$$

$$C_{i_r} - C_{i_\beta}\cos\alpha_o \quad \text{(for oscillation about the } z \text{ axis)} \tag{14}$$

where $i = l, m, n, X, Y, Z$ and α_o is the nominal angle of attack about which the model is oscillated. These data cannot be used directly in this form in a coefficient buildup since each parameter is the sum of two derivatives. However, the measured parameters can be used directly if the form of the equations is changed.[18] The derivatives in Equations (12) to (14) are due to aircraft rotational motion (p, q, r) and to the $\dot{\alpha}$ and $\dot{\beta}$ produced by aircraft rotation. The motion variables that have not been accounted for are $\dot{\alpha}$ and $\dot{\beta}$ due to aircraft translational motion. Therefore, the coefficient buildup can be changed to include the aircraft rotational variables with the rotational derivatives and the translational motion variables with the acceleration derivatives.

$$C_i = \left(C_{i_p} + C_{i_{\dot{\beta}}} \sin\alpha_o\right) \frac{pb}{2V_T} + \left(C_{i_q} + C_{i_{\dot{\alpha}}}\right) \frac{q\bar{c}}{2V_T} + \left(C_{i_r} - C_{i_{\dot{\beta}}} \cos\alpha_o\right) \frac{rb}{2V_T} + C_{i_{\dot{\alpha}}} \frac{\bar{c}\dot{\alpha}_t}{2V_T} + C_{i_{\dot{\beta}}} \frac{b\dot{\beta}_t}{2V_T} \tag{15}$$

where $\dot{\alpha}_t$ and $\dot{\beta}_t$, due to translation are given by:

$$\dot{\alpha}_t = \dot{\alpha} - q + (p\cos\alpha + r\sin\alpha)\tan\beta \tag{16}$$

$$\dot{\beta}_t = \dot{\beta} - p\sin\alpha + r\cos\alpha \tag{17}$$

9.5.3 Dynamic Coefficient Buildup

The rotary-balance and forced-oscillation data can be combined to obtain the complete coefficient buildup for aircraft dynamic motion:

$$C_i = C_i\left(\frac{\omega b}{2V_T}\right) + \left(C_{i_p} + C_{i_{\dot{\beta}}} \sin\alpha_o\right) \frac{p_{mod}b}{2V_T} + \left(C_{i_q} + C_{i_{\dot{\alpha}}}\right) \frac{q_{mod}\bar{c}}{2V_T} + \left(C_{i_r} - C_{i_{\dot{\beta}}} \cos\alpha_o\right) \frac{r_{mod}b}{2V_T} + C_{i_{\dot{\alpha}}} \frac{\bar{c}\dot{\alpha}_t}{2V_T} + C_{i_{\dot{\beta}}} \frac{b\dot{\beta}_t}{2V_T} \tag{18}$$

The inclusion of the rotary-balance data can make the coefficient buildup asymmetrical about the $x - z$ plane for nonzero sideslip conditions. The coefficient buildup includes the rotary aerodynamic coefficients when the rotation and velocity vectors are on the same side of the $x - z$ plane (Figure 9-24), but excludes these data when the vectors are on opposite sides. This can cause abrupt changes in the interpolated coefficients as the rotation and/or velocity vectors move through the $x - z$ plane. The coefficient buildup can be made continuous by setting $q_{mod} = q$ and resolving (p, r) into $(p_{mod}, r_{mod}, \omega)$, for zero sideslip, using Equations (1) and (3). The approximation made here is that the effect of ω on the pitch rate may be neglected at nonzero sideslip conditions.

9.6 NASA-AMES

The role of the rotary balance in producing a motion in the wind tunnel that can be related to a motion of an aircraft in free flight has been discussed earlier. Besides representing the special case of a steady spin motion, the rotary balance has been considered as an apparatus which produces a motion in the wind tunnel that is one part of a broader application to define a comprehensive aerodynamic mathematical model. Tobak and Schiff,[19–21] for example, have derived mathematical models which represent a general flight motion in terms of characteristic motions, where the coning motion or rotation about the velocity vector is one of the primary motions.

For a general aircraft flight motion described in terms of the aerodynamic axes system, the necessary motion variables can be expressed as: σ, the resultant angle of attack, ψ, the roll angle relative to the plane of σ, and λ, q and r, the aircraft's angular rates. The resulting formulation,[19] valid for slowly varying motions in which the lateral plunging of the aircraft's center of gravity is small, is

$$C_k(t) = C_k[\infty; \delta(t), \psi(t)] + \frac{\dot{\psi}l}{V} C_{k_\psi}[\delta(t), \psi(t)] + \frac{\sigma l}{V} C_{k_\sigma}[\delta(t), \psi(t)] + \frac{\dot{\lambda}l}{V} \frac{1}{\gamma} C_{k_\phi}[\infty, \delta(t), \psi(t)]; \quad k = \begin{Bmatrix} X, & Y, & Z \\ l, & m, & n \end{Bmatrix} \tag{1}$$

where $\delta = \sin\sigma$. Each term in Equation (1) is identified with a characteristic motion from which it can be evaluated. Thus, the term $C_k(\infty; \delta(t), \psi(t))$ is the coefficient that would be measured in a steady planar motion with the resultant angle of attack σ and roll angle ψ held fixed. The term C_{k_ψ} is a coefficient due to roll oscillations that would be measured for small oscillations in ψ about $\psi = \text{const}$ with σ held fixed. Similarly, C_{k_σ} is a coefficient due to pitch oscillations that would be measured for small planar oscillations in σ about $\sigma = \text{const.}$, with ψ held fixed. The term C_{k_ϕ} is the rate of change with coning rate $\dot{\phi}l/V$, evaluated at $\dot{\phi} = 0$, of the coefficient that would be measured in a steady coning motion, $\sigma = \text{const.}$, $\psi = \text{const.}$, $\dot{\phi} = \text{const}$. These four characteristic motions are illustrated schematically in Figure 9-30. It is important to note that the formulation requires determination of the usually ignored cross-coupling coefficients, such as the rolling moment

due to pitch oscillations, as well as the direct dynamic coefficients. Note also that Equation (1) and Figure 9-30 define a complete set of characteristic motions for the case of small plunging. In the aerodynamic axes system, there is no need for a characteristic motion involving oscillations in yaw. The aerodynamic contributions due to yaw are contained within the coning motion.

A mathematical model equivalent to Equation (1) can be developed for aircraft motions described in terms of a body-fixed axes system. In the body-fixed axes the variables describing a motion are $\hat{\alpha}$ and $\hat{\beta}$, the angle of attack and angle of sideslip parameters, and p_B, q_B and r_B, the aircraft's angular rates. The resulting formulation, valid for small plunging, is

$$\begin{aligned}\hat{C}_k(\dot{t}) = \hat{C}_k(\infty;\hat{\alpha},\hat{\beta}) &+ \frac{1}{\gamma}\frac{\dot{\hat{\alpha}}l}{V}\left[\hat{C}_{k_{q_b}}(\infty;\hat{\alpha},\hat{\beta}) + \gamma\hat{C}_{k_{\dot{\hat{\alpha}}}}(\hat{\alpha},\hat{\beta})\right] \\ &- \frac{1}{\gamma}\frac{\dot{\hat{\beta}}l}{V}\left[\hat{C}_{k_{r_b}}(\infty;\hat{\alpha},\hat{\beta}) - \gamma\hat{C}_{k_{\dot{\hat{\beta}}}}(\hat{\alpha},\hat{\beta})\right] \\ &+ \frac{1}{\gamma}\frac{p_b l}{V}\hat{C}_{k_{\dot{\phi}}}(\infty;\hat{\alpha},\hat{\beta});\quad k = \begin{Bmatrix} X, & Y, & Z \\ l, & m, & n \end{Bmatrix}\end{aligned} \tag{2}$$

In the body-fixed axes the characteristic motions are: (1) steady planar motion at fixed angles of attack and sideslip, (2) small-amplitude planar oscillations in $\hat{\alpha}$ about fixed $\hat{\alpha}$, with $\hat{\beta}$ held fixed, (3) small-amplitude planar oscillations in $\hat{\beta}$ about fixed $\hat{\beta}$ with $\hat{\alpha}$ held fixed, and (4) steady coning motion with $\hat{\alpha}$ and $\hat{\beta}$ held fixed. The characteristic motions called for in the body-axes system are illustrated schematically in Figure 9-31. Here, too, measurements of the aerodynamic reactions to the oscillatory motions must include an evaluation of the cross-coupling contributions. In the body-fixed axes system there is no need for a characteristic motion involving roll oscillations, as the aerodynamic contributions due to roll oscillations are contained within the coning motion. A relation linking the aerodynamic reactions to the oscillatory motions in both axes systems and the contributions due to coning motion is found in Reference 21.

The mathematical model was extended in Reference 20 to accommodate a nonlinear variation of the aerodynamic forces and moments with coning rate. The modification makes the model more consistent with wind-tunnel experimental measurements made on aircraft models in coning motion. Three characteristic motions are called for by the formulation in the aerodynamic axes, as shown schematically in Figure 9-32. They are: steady coning motion, small-amplitude pitch oscillations in the presence of coning, and small-amplitude roll oscillations in the presence of coning. The corresponding motions in the body-fixed axes (Figure 9-33) are steady coning motion and small-amplitude pitch and yaw oscillations superimposed on the coning motion.

9.7 NAE

An analysis and extension of the Tobak-Schiff mathematical model[19] described in Section 9.6 was recently undertaken by Beyers.[22] The following formulation in body axes of the aerodynamic mathematical model was derived on the assumption of linear dependence on the motion rates, in terms of the conventional, α, β, V system of coordinates

$$\begin{aligned}\hat{C}_k(t) = \hat{C}_k(\infty;\alpha,\beta) &+ \frac{1}{\gamma}\frac{p_B l}{V}\hat{C}_{k_{\dot{\phi}}}(\infty;\alpha,\beta) \\ &+ \frac{l}{V}(\dot{\alpha} - \dot{\beta}\tan\alpha\tan\beta)\hat{C}^*_{kq_B}(\alpha,\beta) \\ &- \frac{1}{\cos\alpha}\frac{\dot{\beta}l}{V}\hat{C}^*_{kr_B}(\alpha,\beta);\quad k = \begin{Bmatrix} X, & Y, & Z \\ l, & m, & n \end{Bmatrix}\end{aligned} \tag{1}$$

where $\gamma = \cos\alpha\cos\beta$.

Equation (1) is, exactly, the counterpart of the formulation in parametric notation, Equation (9.6-2). The definitions of the composite derivatives are

$$\left.\begin{aligned}\hat{C}^*_{iq_B} &= \hat{C}_{iq_B} + \hat{C}_{i\dot{\alpha}} \\ \hat{C}^*_{ir_B} &= \hat{C}_{ir_B} - \hat{C}_{i_{\dot{\beta}}}\cos\alpha - \hat{C}_{i_{\dot{\alpha}}}\sin\alpha\tan\beta \\ \hat{C}^*_{ip_B} &= \hat{C}_{ip_B} + \hat{C}_{i_{\dot{\beta}}}\sin\alpha - \hat{C}_{i_{\dot{\alpha}}}\cos\alpha\tan\beta\end{aligned}\right\} \quad i = \begin{Bmatrix} X, & Y, & Z \\ l, & m, & n \end{Bmatrix} \tag{2}$$

The identity derived by Tobak and Schiff,[19] linking the reactions in the two axes systems, may then be written in the form

$$\begin{aligned}\hat{C}_{n_\phi}\cos\psi + \hat{C}_{m_\phi}\sin\psi - \gamma\left(\hat{C}^*_{np_B}\cos\psi + \hat{C}^*_{mp_B}\sin\psi\right) \\ = \delta\left(\hat{C}^*_{nr_B} + \hat{C}^*_{mq_B} - C_{m_\alpha}\right)\end{aligned} \tag{3}$$

where ψ is the bank angle. The detailed derivation of these equations is given in Reference 22.

Equations (1) and (3) are applicable at arbitrary angles of attack and sideslip and are expressed in terms of oscillatory derivatives appearing exclusively in the combinations defined in Equation (2), i.e., in the form measured in conventional oscillatory experiments. The steady and unsteady rotary terms are grouped on the left-hand side of Equation (3) and

the planar oscillatory derivatives on the right. When ψ takes on appreciable values, the cross-coupling terms containing $\hat{C}_{m_{\dot{\psi}}}$, $\hat{C}^*_{mpB}$ become significant, while the effects of the cross derivatives, $\hat{C}_{n_{\dot{\psi}}}$ and $\hat{C}^*_{npB}$, diminish.

An experimental validation of the nonplanar mathematical model is currently being pursued. The data base available on the Standard Dynamics Model[23,24] (see Figure 3-21) at Mach 0.6, over the range $0 \leq \alpha \leq 30°$, with $\beta = 0, \pm 5°$, contains all of the derivatives required in a rigorous correlation based on Equation (3). The results of a correlation of the rotary and oscillatory derivatives at $\beta = 0$ are discussed in Section 10.2. It is expected that the aerodynamic model can be evaluated over a range of test conditions for which the dependence on the motion rates is linear. This would at once demonstrate the validity of the basic premise underlying the Tobak-Schiff model and the integrity of the combined rotary/oscillatory data base.

The formulation of a nonplanar model applicable when the lateral acceleration is not small was undertaken.[25] Partitioning the equations of motion as suggested by Kalviste,[18] the contributions to the angular rates due to rotation and translation can be separated. Then, following the procedure introduced by Tobak and Schiff, the force and moment system was derived in the form

$$\begin{aligned}\hat{C}_k(t) = \hat{C}_k(\infty;\alpha,\beta) &+ \frac{1}{\gamma}\frac{p_B\ell}{V}\hat{C}_{k\dot{\phi}}(\infty;\alpha,\beta) \\ &+ (\dot{\alpha}_R - \dot{\beta}_R \tan\alpha\tan\beta)\frac{\ell}{V}\hat{C}^*_{kq_B}(\alpha,\beta) - \frac{1}{\cos\alpha}\frac{\dot{\beta}_R\ell}{V}\hat{C}^*_{kr_B}(\alpha,\beta) \\ &+ \frac{\dot{\alpha}_T\ell}{V}\hat{C}_{k\dot{\alpha}_T}(\alpha,\beta) + \frac{\dot{\beta}_T\ell}{V}\hat{C}_{k\dot{\beta}_T}(\alpha,\beta); \\ & k = X, Y, Z, \ell, m, n \end{aligned} \tag{4}$$

where $\dot{\alpha}_T$ and $\dot{\beta}_T$ are the angular rates due to translation and $\dot{\alpha}_R$ and $\dot{\beta}_R$ those due to fixed-axis rotation. The first four terms on the right hand side are the same as in Equation (1) and the last two correspond to the translational characteristic motions. The derivatives $\hat{C}_{k\dot{\alpha}_T}$ and $\hat{C}_{k\dot{\beta}_T}$ are determined in pure translational acceleration tests and are, in general, different from their rotational counterparts (Equation (2)).

A further modification of the mathematical model, discussed in Section 6.2, could extend its applicability under nonlinear motion conditions. In this formulation,[25] the oscillatory characteristic motions are replaced by directional characteristic motion vectors (see Figure 6-17) and the oscillatory derivatives, by directional rate-dependent parameters.

9.8 REFERENCES

1. Bihrle, W., Jr.; and Barnhart, B.: Spin Prediction Techniques. Journal of Aircraft, Vol. 20, Feb. 1983, pp. 97–101.

2. Bihrle, W., Jr.: Prediction of High-Alpha Flight Characteristics Utilizing Rotary Balance Data. 13th ICAS Congress/AIAA Aircraft System and Technology Conference Proceedings, August 1981.

3. Gates, S. B.; and Bryant, L. W.: The Spinning of Aeroplanes. R&M 1001, British A.R.C., 1926.

4. Bamber, M. J.; and Zimmerman, C. H.: The Aerodynamic Forces and Moments Exerted off a Spinning Model of the "NY-1" Airplane as Measured by the Spinning Balance. NACA TR 456, 1933.

5. Babister, A. W.: Aircraft Stability and Control. Pergamon Press, New York, 1961.

6. Crow, J. H.: An Elementary Study of the Spin. Aircraft Engineering, Vol. XI, Feb. 1939, pp. 39–43; March 1939, pp. 111–114; April 1939, pp. 158–160; May 1939, pp. 203-208; July 1939, pp. 273-278.

7. Bazzocchi, E.: Etude Analytique de la Vrille en Utilisant des Donnès a la Soufflerie Horizontale et Methode d'Essai des Modèles a l'Air Libre. Proceeding of the Second European Aeronautical Congress, Scheveningen, The Netherlands, 1956, pp. 5.1.-5.43.

8. Tischler, M. B.; and Barlow, J. B.: Application of the Equilibrium Spin Technique to a Typical Low-Wing General Aviation Design. AIAA Paper 79-1625, Aug. 1979.

9. McCormick, B. W.: Equilibrium Spinning of a Typical Single-Engine Low-Wing Light Aircraft. Journal of Aircraft, Vol. 18, March 1981, pp. 192–199.

10. Bamber, M. J.; and Zimmerman, C. H.: Spinning Characteristics of Wings, I.- Rectangular Clark Y Monoplane Wing. NACA TR 519, 1935.

11. Bamber, M. J.; and House, R. O.: Spinning Characteristics of the XN-2Y-1 Airplane. NACA TR 607, 1937.

12. Bazzocchi, E.: Use of Rotary Balance Data for the Study of Spin. Lecture held by Dr. Ermanno Bazzocchi, Italy, at China Defense Science and Technology Information Center, Beijing, April 1988.

13. Valtorta, E.: MB-339, Analysis of Rotary Balance Wind Tunnel Tests and Investigation of the Areas of Equilibrium in Spin. Aermacchi Report 340-39X-13, 1979.

14. Valtorta, E.: Spin Behavior of a Combat Plane Estimated From Fixed and Rotary Balance Wind Tunnel Testing. Aermacchi Report 340-099-22, 1979.

15. Bazzocchi, E.: Stall Behavior and Spin Estimation Method by Use of Rotating Balance Measurement. AGARD CP-99, 1975.

16. Valtorta, E.: MB-339, Erect Spin Behavior. Aermacchi Report 340-39X-15, 1979.

17. Guicheteau, P.: Bifurcation Theory Applied to the Study of Control Losses on Combat Aircraft. Recherche Aerospatiale, No. 1982-2, March 1982, pp. 61–73.

18. Kalviste, J.: Use of Rotary Balance and Forced Oscillation Test Data in a Six-Degree-of-Freedom Simulation. AIAA 82-1364, Aug. 1982.

19. Tobak, M.; and Schiff, L. B.: Generalized Formulation of Nonlinear Pitch-Yaw-Roll Coupling: Part I - Nonaxisymmetric Bodies. AIAA Journal, Vol. 13, No. 3, March 1975, pp. 323–326.

20. Tobak, M.; and Schiff, L. B.: Generalized Formulation of Nonlinear Pitch-Yaw-Roll Coupling: Part 2 - Nonlinear Coning-Rate Dependence. AIAA Journal, Vol. 13, No. 3, March 1975, pp. 327–332.

21. Tobak, M.; and Schiff, L. B.: On the Formulation of the Aerodynamic Characteristics in Aircraft Dynamics. NASA TR R-456, Jan 1976.

22. Beyers, M. E.: A New Look at the Tobak-Schiff Model of Nonplanar Aircraft Dynamics. NRC, NAE LTR-UA-101, Ottawa, Dec. 1989.

23. Beyers, M. E.; and Szyszkowicz, M.: Stability Derivatives of the Standard Dynamics Model at Mach 0.6. To appear as NAE publication.

24. Jermey, C.; and Schiff, L. B.: Wind-Tunnel Investigation of the Aerodynamic Characteristics of the Standard Dynamics Model in Coning Motion at Mach 0.6 AIAA-85-1828-CP, Aug. 1985.

25. Beyers, M. E.: Nonplanar Formulation of Maneuvering Aircraft Dynamics. To be published as NAE report.

Table 9-1. Example of Typical AerMacchi Test Program.

Group	Balance Type	α Dvg	β Deg	Model & Flight Controls	Measured Coefficients	No. of Tests Required and Comments
1A	Static	Trav.	0	Basic controls at neutral	C_m, C_L, C_D and asymmetries in C_l, C_n, C_y	1 test in each configuration. These tests give a general indication of the aircraft longitudinal behavior and highlight the critical areas.
1B	"	"	0	Partial controls at neutral	As 1A	1 test in each configuration. The effect of the horizontal tail is usually the only data evaluated These tests permit the effects of the different components to be evaluated.
2	"	"	$\neq 0$	Basic controls at neutral	$C_{n_\beta}, C_{l_\beta}, C_{y_\beta}$ and effect of β on C_m, C_L, C_D	2 tests in each configuration, with two different values of β. One test only at $\beta = 10°$ is sufficient, provided the tests detailed in point 4 are carried out correctly
3	"	"	0	Basic controls at full deflection	Control effectiveness	1 test in each configuration on each flight control and some additional tests with concurrently deflected controls if interference on the aerodynamic effects is suspected.
4	"	Fixed	Trav.	Basic controls at neutral	Coefficients as a function of α, β	1 series of tests for each configuration. The investigation is to be performed with AOA increments of 2-3 deg in the stall region and where marked nonlinearities occur. Tests every 5 deg AOA can be sufficient in the other regions.
5A	Rotary	"	0	Basic controls at neutral	Coefficients as a function of α, Ω, and C_m, C_L, C_D to be compared with A	As in 4.
5B	"	"	0	Partial controls at neutral	As in 5A	1 series of tests in each configuration, performing the measurements every 5+10 deg AOA. These tests permit the effects of the different model components to be evaluated, and supply the data required to estimate other coefficients (yaw damping)
6	"	"	$\neq 0$	Basic controls at neutral	C_{m_q}, C_{l_q} effect of β on damping and cross-check of lateral-directional stability with the results to point 2	1 series of tests in each configuration, obtaining the data at least every 10 deg AOA in the whole envelope and every 2-5 deg AOA in the areas found to be critical
7	"	"	0	Basic controls at full deflection	Control effectiveness as a difference with respect to test 5A, to be compared with the results to point 3, and possible effect of controls on damping	1 series of tests as in 3

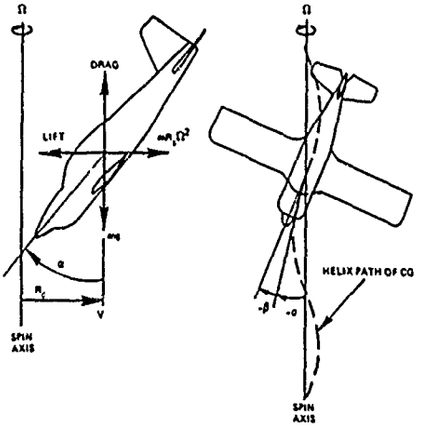

Figure 9-1. Illustration of an airplane in a steady spin.

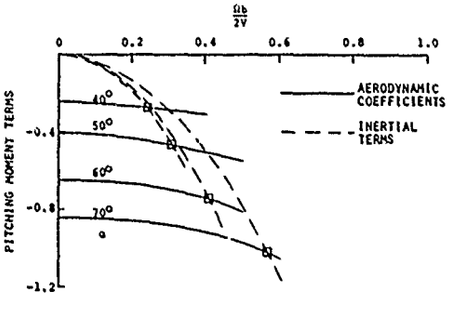

Figure 9-2. Pitching-moment coefficients and inertial pitch terms vs $\Omega b/2V$ for selected αs and zero β.

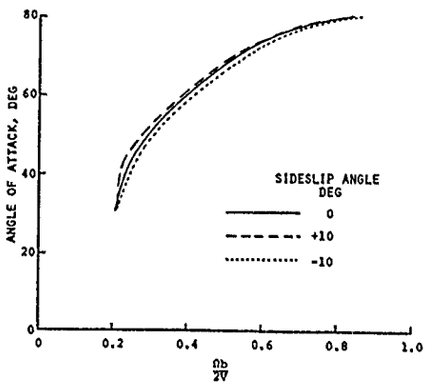

Figure 9-3. Locus of α vs $\Omega b/2V$ resulting in pitch equilibrium for constant β values.

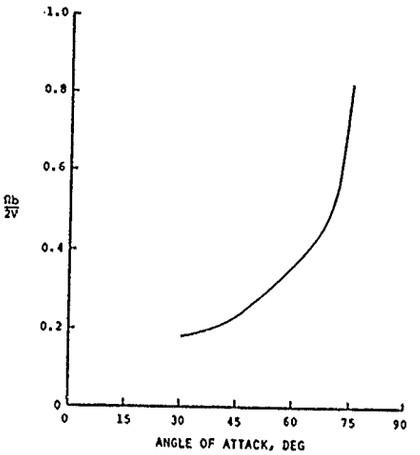

Figure 9-6. $\Omega b/2V$ values required for pitch and roll equilibrium vs α.

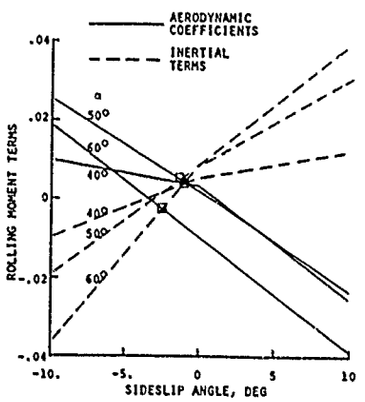

Figure 9-4. Rolling-moment coefficients and inertial roll terms vs β for selected αs.

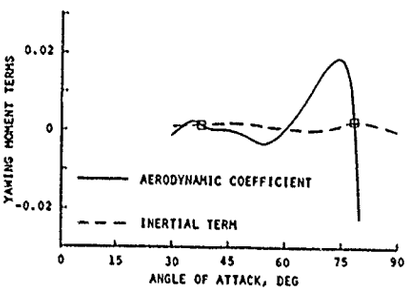

Figure 9-7. Yawing-moment coefficient and inertial yaw term vs α curves identifying spin equilibrium αs.

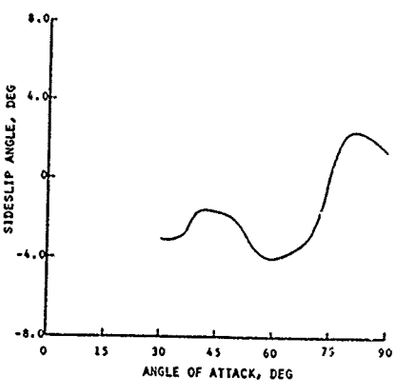

Figure 9-5. Sideslip angles required for pitch and roll equilibrium vs α.

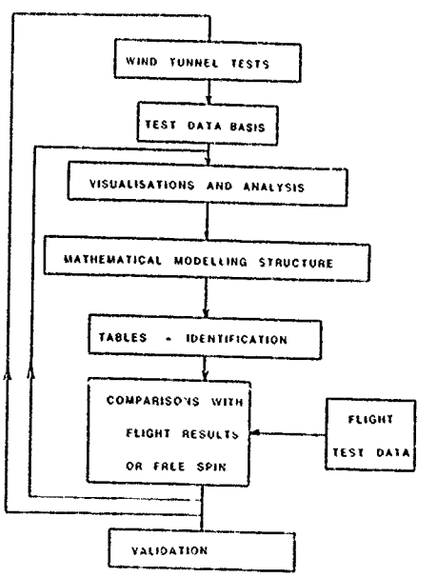

Figure 9-8 Modeling process used at ONERA-IMFL.

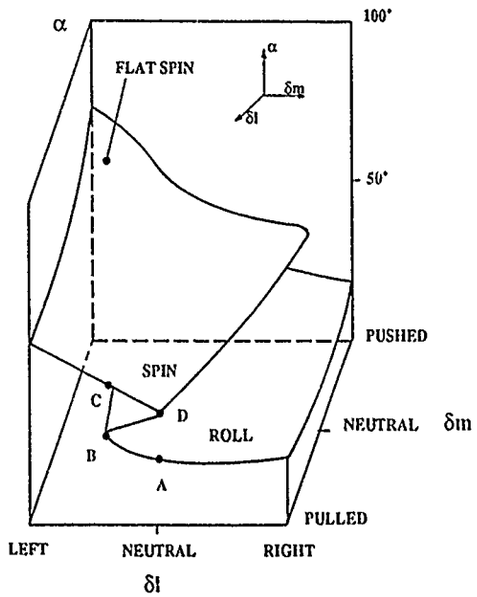

Figure 9-9. Equilibrium surface.

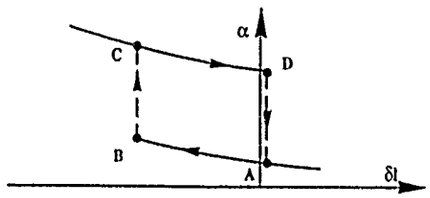

Figure 9-10. Hysteresis effect diagram for equilibrium states.

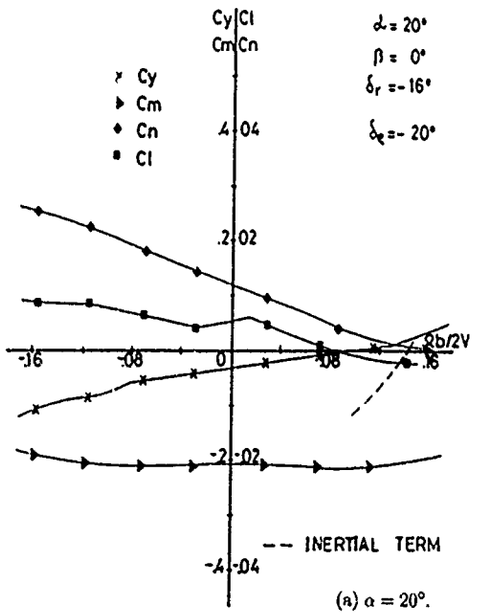

(a) $\alpha = 20°$.

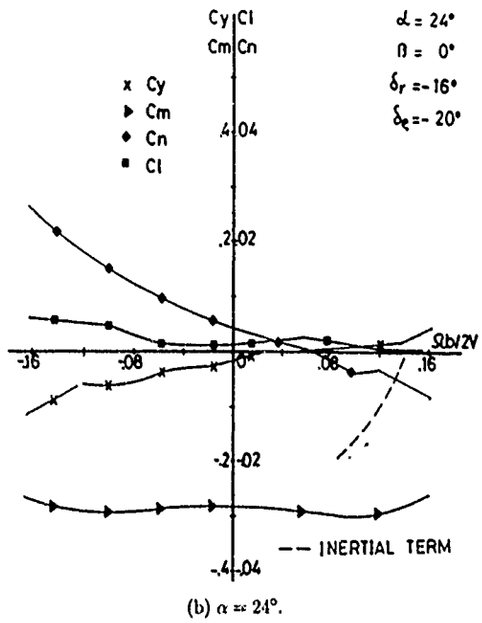

(b) $\alpha = 24°$.

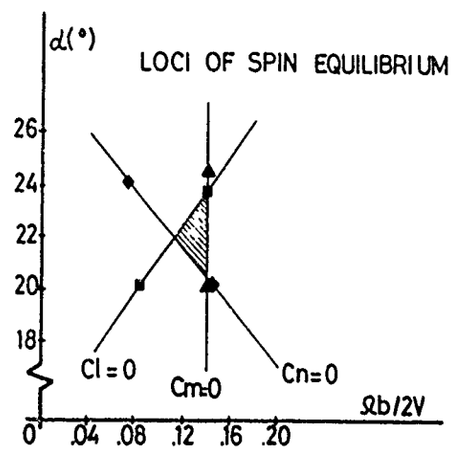

(c) Loci of equilibrium conditions.

Figure 9-11. Spin equilibrium procedure.

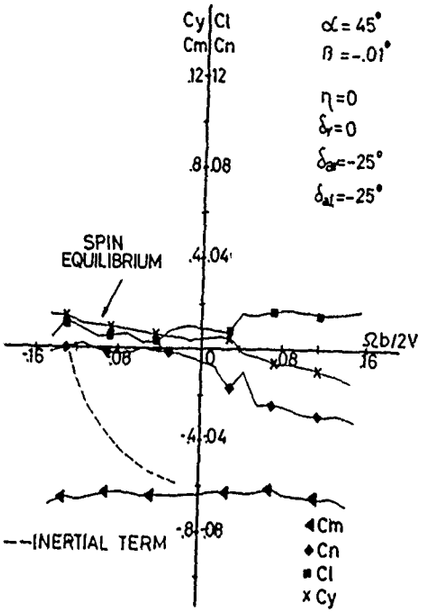

Figure 9-12. Spin equilibrium at $\alpha = 45°$.

$$C_D = C_D(\alpha,\beta) + C_{D\delta e}(\alpha)\delta_e$$

$$Cy = Cy(\alpha,\beta) + Cy_{\delta e}(\alpha)\,\delta_e + Cy_{\delta a}(\alpha)\,\delta a + Cy_{\delta r}(\alpha)\,\delta_r + \delta C_{y\frac{pb}{2V}}\left(\alpha,\frac{pb}{2V},\beta\right) + Cy_r(\alpha)\,\frac{rb}{2V}$$

$$C_L = C_L(\alpha,\beta) + C_{L\delta e}(\alpha)\,\delta_e + C_{Lq}\,\frac{qc}{2V}$$

$$C_l = C_l(\alpha,\beta) + C_{l\delta e}(\alpha)\,\delta_e + C_{l\delta a}(\alpha)\,\delta a + C_{l\delta r}(\alpha)\,\delta_r + \delta C_{l\frac{pb}{2V}}\left(\alpha,\frac{pb}{2V},\beta\right) + C_{lr}(\alpha)\,\frac{rb}{2V}$$

$$C_m = C_m(\alpha,\beta) + C_{m\delta e}\cdot\delta_e + C_{mq}(\alpha)\,\frac{qc}{2V}$$

$$C_n = C_n(\alpha,\beta) + C_{n\delta e}(\alpha)\,\delta_e + C_{n\delta a}(\alpha)\,\delta a + C_{n\delta r}(\alpha)\,\delta_r + \delta C_{n\frac{pb}{2V}}\left(\alpha,\frac{pb}{2V},\beta\right) + C_{nr}(\alpha)\,\frac{rb}{2V}$$

Figure 9-14. Mathematical model used by AerMacchi

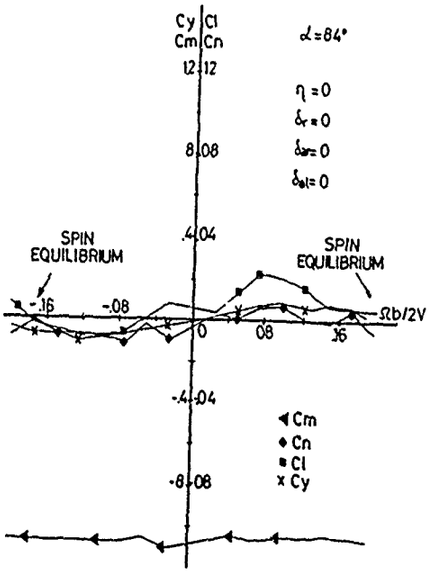

Figure 9-13. Spin equilibrium at $\alpha = 84°$.

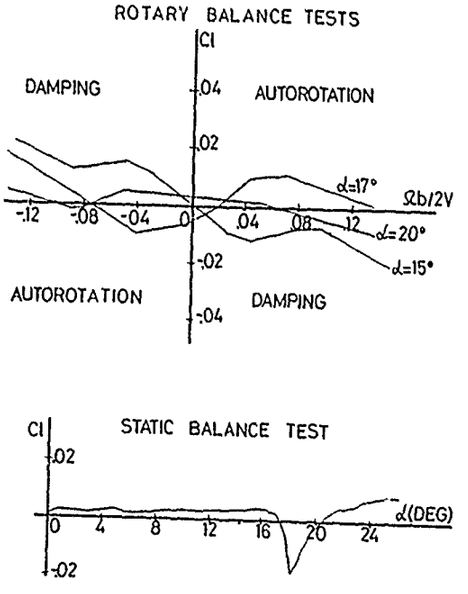

Figure 9-15. Rolling-moment correlation of static and rotary-balance tests.

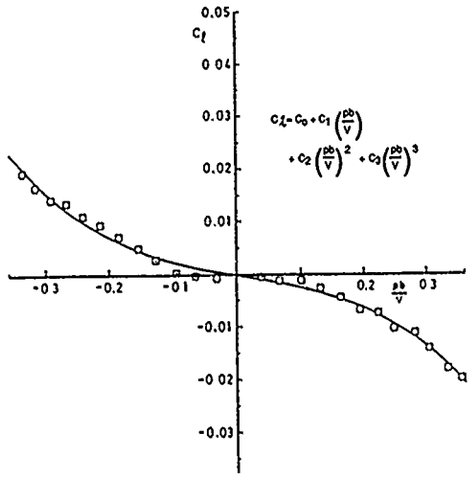

Figure 9-16. Cubic regression on rotary rolling-moment data, $\alpha = 24°$.

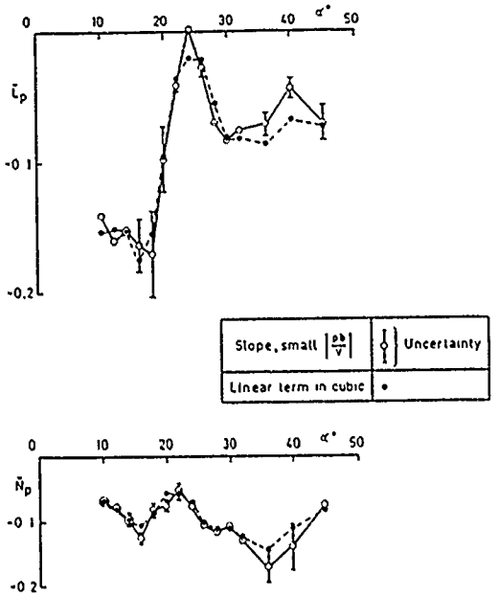

Figure 9-18. Comparison of "derivatives" due to steady rolling.

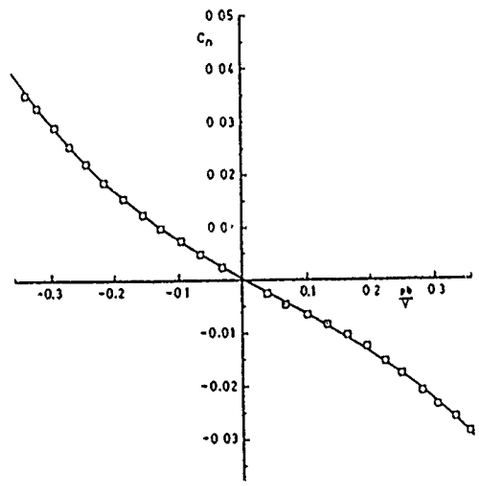

Figure 9-17. Cubic regression on rotary yawing-moment data, $\alpha = 24°$.

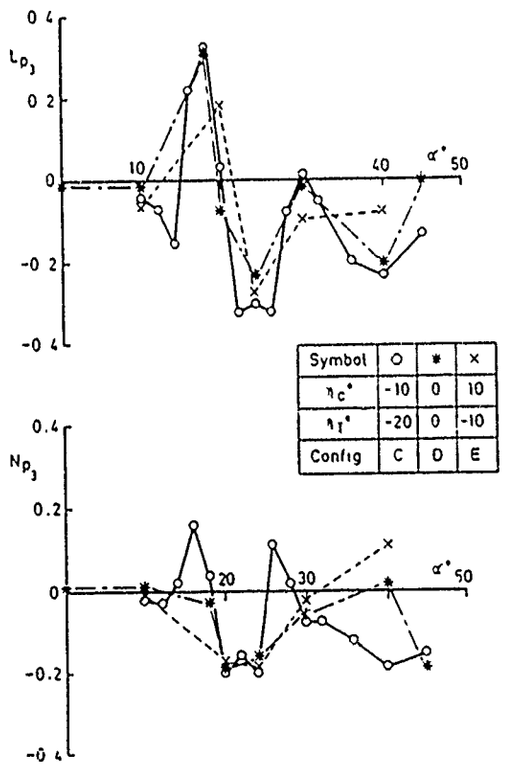

Figure 9-19. Cubic contribution to moments due to steady rolling.

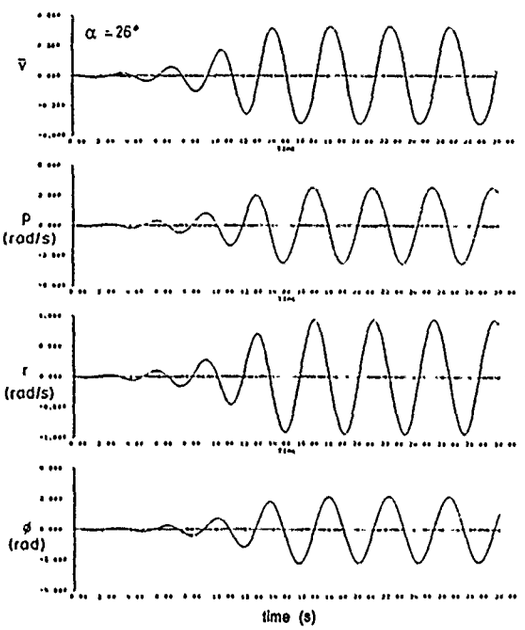

Figure 9-20. Body-axes simulation with nonlinearities in roll rate.

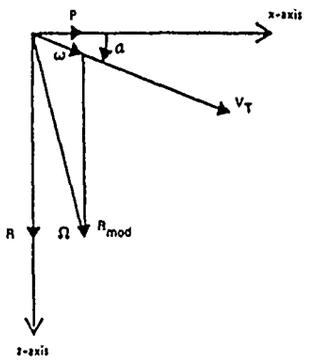

Figure 9-22. Rotation vector resolved into r_{mod} and ω components.

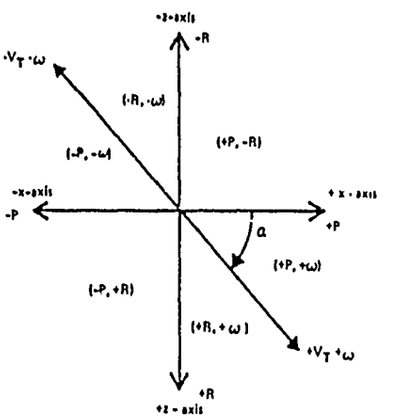

Figure 9-23 The two components of rotation vector for the six regions on the X-Z plane.

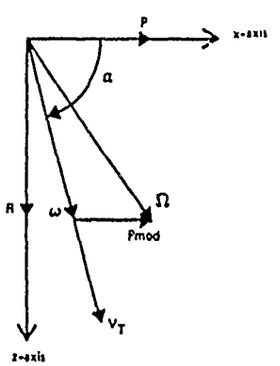

Figure 9-21. Rotation vector resolved into p_{mod} and ω components.

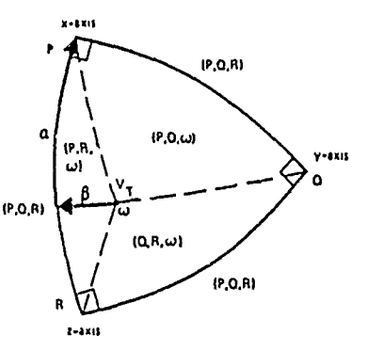

Figure 9-24. Three components of rotation vector, general case.

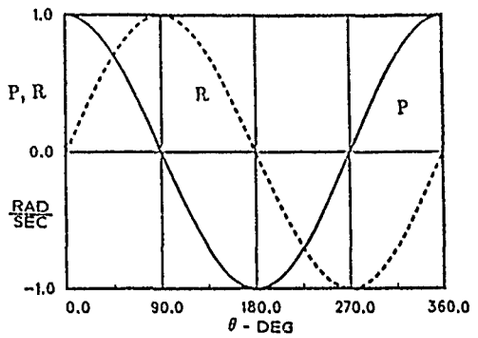

Figure 9-25. Body-axes components of total rotation vector.

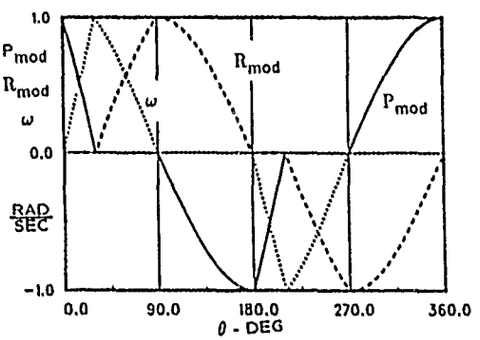

Figure 9-26. Rotation vector resolved into two components.

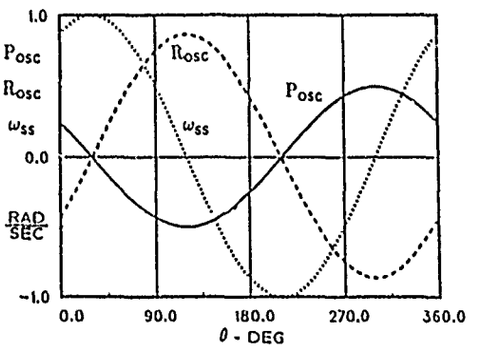

Figure 9-28. Rotation vector resolved into three components.

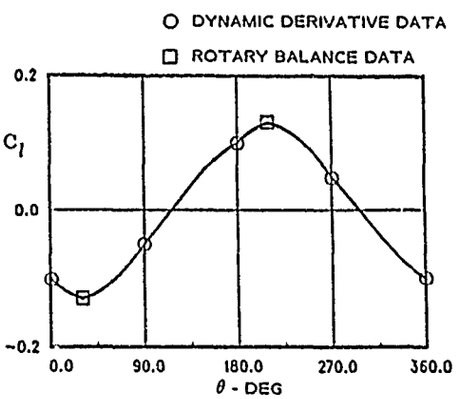

Figure 9-27. Dynamic coefficient for two-component interpolation.

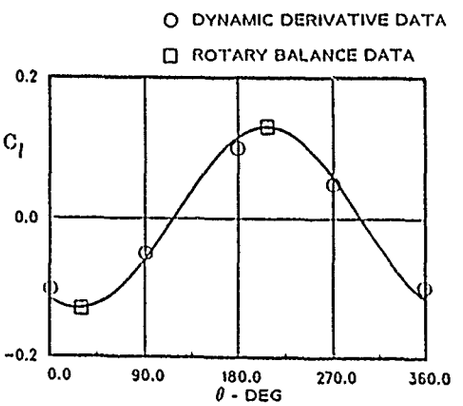

Figure 9-29 Dynamic coefficient for three-component expansion.

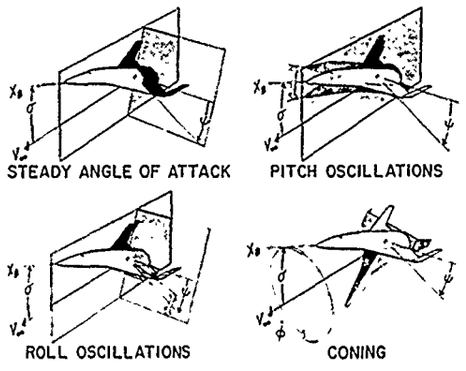

Figure 9-30. Characteristic motions in the aerodynamic axes system with linear dependence on the angular rates.

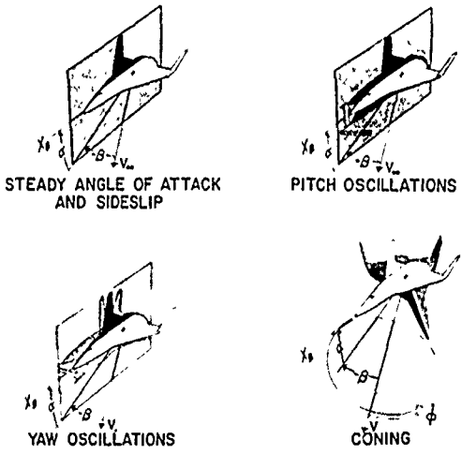

Figure 9-31. Characteristic motions in the body-axes system with linear dependence on the angular rates.

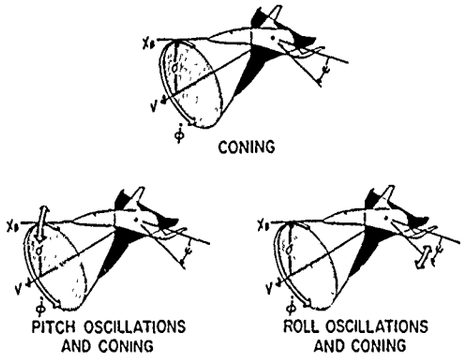

Figure 9-32. Characteristic motions in the aerodynamic axes system with nonlinear coning-rate dependence.

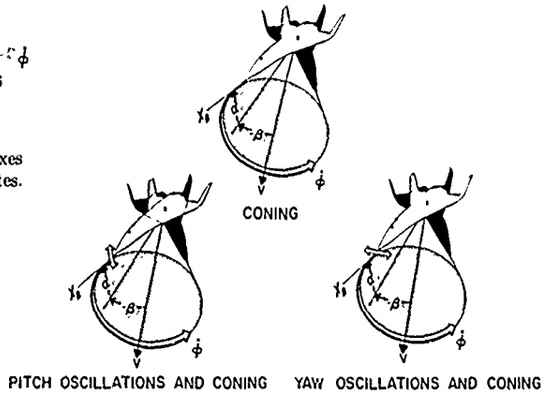

Figure 9-33. Characteristic motions in the body-axes system with nonlinear coning-rate dependence.

CHAPTER 10

RELATION BETWEEN ROTARY AND OSCILLATORY TEST RESULTS

10.0 INTRODUCTION

Before discussing the relation between results from oscillatory and rotary tests it is useful to consider briefly the background and reasons for these different types of test and the application of the data obtained.

The fundamental problem confronting workers in the field of flight dynamics is the correct representation of the relationship between the aerodynamic reactions and the motion variables in the equations of motion of an aircraft. The formulation of an adequate mathematical model is essential. For flight at low angles of attack, adequate prediction of aircraft motion characteristics is often possible using linearized small perturbation equations with aerodynamic transfer functions or derivatives, which are constant and can usually be estimated with sufficient accuracy. When the motion involves large excursions in any of the state variables some derivatives may vary appreciably and the terms involving them become non-linear. It is then necessary to consider derivatives as functions of those variables and use the appropriate local values of the function for each equilibrium condition. The derivatives invariably have to be measured over a range of one or more of the displacement variables. A number of techniques may be employed, including oscillatory and rotary testing. However, careful consideration should be given to the applicability of test data when constructing a mathematical model since the flow mechanism and hence the forces and moments are not completely determined by the current values of the state variables but depend to a greater or lesser extent on the past history.

Several proposals, including those of Tobak and Schiff,[1] Thomas and Edwards[2] and Beyers,[3] have been made concerning the types of wind-tunnel test, usually combining oscillatory and rotary motion, most likely to produce the data required for calculation of a range of flight motions including large excursion motions such as high-angle-of-attack departure and spin entry. However, the practical difficulties of carrying out such tests and extracting meaningful data have meant that the only wind-tunnel dynamic test data generally available are from separate oscillatory and rotary tests, where the model motion does not exactly simulate the relevant flight motion.

In a conventional rotary (coning) test the axis of rotation is parallel to the wind-tunnel axis. Aerodynamic loads on the model due to steady coning motion are measured by a strain-gauge balance which is aligned along the model body axis. These loads can be converted to wind axes in the normal manner to give a consistent set of data. When plotted against reduced rotation rate, wind axes derivatives may be obtained from the gradients. In an oscillatory test the model usually oscillates about body axes and the data, in the form of derivatives, may be converted to wind axes if a complete set of derivatives has been measured. However, since the motion is not of constant rate the flow is constantly changing and under certain conditions the measurements may be a function of the history of the flow. At low angles of attack and sideslip, where there is attached flow over virtually all surfaces of the model, it is possible that there will be agreement between derivatives obtained from rotary test data and derivatives from oscillatory tests. However, when the angle of attack is increased flow separation and lag effects may have a strong influence and results may then be significantly different.

It is fairly obvious that for calculations concerning the developed spin, data from rotary-balance tests are appropriate but there is less certainty about which data are appropriate to other flight regimes, such as low-to-high angle-of-attack oscillatory modes and gust response and high angle-of-attack departure.

Classical mathematical models, including those constructed by NASA and RAE require data from small amplitude oscillation tests in pitch, roll and yaw, but where large amplitude responses are likely, e.g., in the departure and post stall regimes, rotary rig data are also incorporated.[4]

Although reasonable correlation has been obtained between flight and simulated responses using these mathematical models, invariably some of the wind-tunnel data have to be modified to some degree.[4] More information is required to determine whether there are significant differences between oscillatory and rotary data and how these differences are affected by configuration and changes in the state variables such as angle of attack and sideslip. In a limited number of cases the same configuration has been tested on both oscillatory and rotary rigs and results are discussed in the following sections: first by direct comparison and secondly by correlation based on a mathematical model.

10.1 DIRECT COMPARISONS OF ROTARY AND OSCILLATORY TEST RESULTS

10.1.1 HIRM 1 and HIRM 2

Both HIRM 1 and HIRM 2 have been tested on the rotary and oscillatory rigs at RAE Bedford. The models tested on the rotary rig are half the scale of the oscillatory rig models. Results obtained from oscillatory rig tests are the body-axes derivatives,[5] $C_{l_p} + C_{l_{\dot\beta}} \sin\alpha, C_{n_p} + C_{n_{\dot\beta}} \sin\alpha$ and $C_{y_p} + C_{y_{\dot\beta}} \sin\alpha$, which are converted to wind-axes derivatives $C_{l_\Omega}, C_{n_\Omega}$ and C_{y_Ω} respectively. For the rotary tests, gradients of the characteristics C_l, C_n and C_y vs $\Omega b/2V$ are measured near the origin since the reduced roll rate for oscillatory tests was in the range $\Omega b/2V = \pm 0.05$. At higher angles of attack, some of the characteristics are nonlinear over this range of rotation rate and the measured gradients can then only be mean values.

Results for HIRM 1 are compared in Figures 10-1, 10-2 and 10-3 for three model configurations:

a. complete configuration,

b. fin off and

c. foreplane and tailplane off.

Figure 10-1 shows that for all three configurations there is fairly close agreement in the measurements of damping in roll C_{ℓ_Ω} for angles of attack less than 20°. However, where the rotary results show a sudden loss of damping for angles of attack between 20° and 25°, the oscillatory results show a more gradual loss over a larger range of angle of attack. The variation of C_{ℓ_Ω} with α is broadly similar for configurations a and b; since the fin contributes only a small part to the overall damping, but with foreplane and tailplane off, configuration c, C_{ℓ_Ω} from rotary test data is strongly positive at $\alpha = 24°$, indicating that the foreplane acts to alleviate the loss in roll damping. For configuration c oscillatory tests were unfortunately not made for $20° \leq \alpha \leq 30°$, but again, there is good agreement only for $\alpha \leq 20°$. Figures 10-2 and 10-3 show that for C_{n_Ω} and C_{y_Ω} there is fair agreement between rotary and oscillatory results for all configurations although there is considerable scatter in the oscillatory measurements of C_{y_Ω}. There is a significant negative contribution to C_{n_Ω} from the fin since, as angle of attack increases, the fin displacement from the axis of rotation increases in the positive z direction so that a positive rate of roll results in the positive side force and negative yawing moment contribution due to the fin. This trend is apparent for both rotary and oscillatory results.

Results for one configuration of HIRM 2 are shown in Figure 10-4. Two sets of rotary test data are presented from two series of tests. Measurements of C_{y_Ω} are not available for the first series owing to excessive electrical noise on the side-force channel of the balance during the test. Results from the two series of rotary tests are in quite close agreement but there is considerable scatter in the oscillatory rig measurements of C_{y_Ω}.

From tests on HIRM 1 and HIRM 2 it would appear that the differences between oscillatory and rotary results depend on configuration and angle of attack. For the moderately swept wing of HIRM 1 only the results for C_{ℓ_Ω} are significantly different at the higher angles of attack but for the more highly swept wing of HIRM 2 the differences are smaller.

10.1.2 YF-17 Airplane at Spin Angles of Attack

The coefficient C_{n_Ω} from forced oscillation tests is shown in Figure 10-5 as a gradient on plots of C_n vs $\Omega b/2V$ from rotary-balance tests. At $\alpha = 50°$ and 55° the rotary data show strong nonlinearities near the origin but at $\alpha = 80°$ and 85° the data are relatively linear. There is good agreement with C_{n_Ω} from forced oscillation tests except at $\alpha = 55°$ where the gradient of the rotary data is virtually zero near the origin, whereas the forced oscillation coefficient is strongly positive.

10.1.3 Comments on Direct Comparisons of Rotary and Oscillatory Test Results

It is shown that while there is reasonably good agreement between rotary and oscillatory tests results at low and moderate angles of attack where the flow over the model is mainly attached, at higher angles of attack, where there are significant flow separations, there are differences in one or more of the coefficients. Under these conditions, time history of the motion is likely to have an over-riding influence on the measurements. For HIRM 1, which has a wing of moderate sweep, the greatest differences are apparent in C_{ℓ_Ω} for $\alpha > 20°$ when the flow has started to separate from the wings. This model has a relatively short forebody and up to $\alpha = 40°$ there is broad agreement between rotary and oscillatory results for C_{n_Ω}. The HIRM 2 configuration has the same forebody as HIRM 1 but the wing leading edge is more highly swept. Thus, the flow separations are more progressive, in the form of vortices from the leading edge, and may explain why there is better agreement between the two sets of data for this model. The difference in gradient of C_n vs $\Omega b/2V$ between rotary and oscillatory data for the YF-17 at $\alpha = 55°$ is probably due to flow lag effects which are only present under oscillatory conditions. It is likely that the time history of the motion has a significant influence at certain critical angles of attack.

In general, it is probable that oscillatory and rotary data will be in agreement at low and moderate angles of attack, before there is significant flow breakdown, but at high angles of attack, depending on the configuration, there are likely to be significant differences due to time history and lag effects on wing and forebody flow separations.

10.2 CORRELATIONS BASED ON MATHEMATICAL MODEL

In utilizing an aerodynamic data base to predict dynamic behavior of aircraft in flight, two important questions arise in addition to the scaling problem (Section 8.3). These questions relate to the consistency of the aerodynamic data obtained from more than one apparatus/facility and to the validity of the mathematical model used, and require some form of comparison for their assessment.

Although, as shown in the preceding section, there are instances where reasonable agreement can be obtained when comparing rotary and oscillatory derivatives directly, there is no theoretical basis for doing so. Strictly speaking, these derivatives can be compared directly only in degenerative cases (e.g., $\alpha \to 0°$, $\beta \to 0°$, or for axisymmetrical bodies at low α), where the equivalence of the reactions in the respective motions is predicted by potential flow theory. However, at angles of attack below stall, the consistency check can be made indirectly, through the implementation of an aerodynamic force model that establishes a relationship between the respective derivatives. At higher α, the unsteady flow fields associated

with rotary and oscillatory motions are fundamentally different and the model may become invalid, ruling out the possibility of a consistency check.

One such opportunity for performing the consistency check is introduced by the Tobak-Schiff mathematical model, applicable to arbitrary maneuvers within the restrictions of linear dependence on the angular rates and near-rectilinear motion[6] (see Section 9.6). An identity was derived,[6] linking the formulations in the aerodynamic and body-axes systems. Expressing the rolling derivatives in terms of fixed-axis oscillatory derivatives, the identity is obtained in a convenient form[7] (see Equation (9.7-(3))), which equates the combination of steady and unsteady rotational derivatives to a combination of the planar damping derivatives. At zero sideslip, Equation (9.7-(3)) reduces to

$$\left(C_{n_{\dot{\beta}}} - \gamma \bar{C}_{n_p}\right)/\delta = \bar{C}_{n_r} \tag{1}$$

where the derivatives are referred to body axes.

With the objective of rotary-oscillatory data correlation in mind, an experimental approach is being pursued to validate this identity. In the interests of generality, dynamic data sets obtained on the Standard Dynamics Model[8,9] (SDM) (see Figures 3-21 and 7-14), a generic fighter aircraft configuration,[10] as well as on a body of revolution[11,12] are being considered.

10.2.1 Body of Revolution

Applied to a body of revolution, $\bar{C}_{n_p} \simeq 0$, so that Equation (1) predicts the equivalence of the aerodynamic reactions in the coning and yaw-oscillation characteristic motions. This is illustrated in Figure 5-18. The yaw-damping[11] and coning-rate derivatives[12] were measured on a 10-degree cone at $M_\infty = 2.0$ in two different wind tunnels. The results of the correlation of these data appear in Figure 10-6.

Because of the need to fix transition at low α in the oscillatory experiment,[11] the results for $\alpha \leq 20°$ were obtained with boundary-layer trip. The agreement between $C_{n_{\dot{\beta}}}$ and the term $\delta \bar{C}_{n_r}$ is generally good, at least up to $\alpha = 30°$ ($\delta = 0.5$). These results, therefore, demonstrate the equivalence of the yaw-damping and coning-rate derivative terms for a body of revolution at high α ($\alpha \leq 30°$), thereby corroborating this aspect of the Tobak-Schiff model.[6]

On the other hand, the expected difference between the yaw and pitch damping of the 10-degree cone at $\alpha > 0°$ had been found to increase with α.[11] Similarly, the divergence of the $\bar{C}_{n_r}$ and $C_{n_{\dot{\beta}}}$ data sets from the theoretical linear pitch damping[13] (Fig. 10-6) increases at $\alpha > \alpha_{av}$ ($\alpha_{av} \simeq 20°$) as the nonlinearity due to unsteady flow separation grows, although the vortex asymmetry is small at $M_\infty = 2.0$.

10.2.2 Standard Dynamics Model

The SDM oscillatory derivatives were determined at NAE[8] at $M_\infty = 0.6$, and α up to 40°, for $\beta = 0°$ and 5°. The same model was then tested at NASA Ames at α up to 30° to obtain the rotary derivatives[9] (Section 7.2). All four experiments, involving oscillations in yaw roll and in pitch, about both aerodynamic and body pitch axes,[8] as well as coning,[9] were carefully controlled to achiev a high degree of consistency. A preliminary correlation based upon Equation (9.7-(3)) suggests that satisfactory agreement between the rotary and oscillatory terms can be obtained at both angles of sideslip; the analysis covered the range $0° \leq \alpha \leq 30°$. The $\beta = 0°$ results are presented here.

The experimental data used to evaluate Equation (1) were interpolated at α intervals of 2.5°, using cubic splines. The results derived from the interpolated data are plotted in Figures 10-7 and 10-8, with connecting curves also generated by cubic splines. The left hand side of Equation (1) was evaluated for $\bar{C}_{n_p}$ at two oscillation frequencies, $\bar{\omega}_b = 0.17$ and 0.10, but the associated differences are not significant except near $\alpha = 30°$. Within the average uncertainty due to measurement and interpolation errors (but excluding that due to aerodynamic interference), denoted by the error bars, the rotary and oscillatory terms are in good agreement at α up to about 18°, the static stall angle for this configuration [8](Fig. 10-7).

At post-stall angles of attack the trends in the rotary and oscillatory terms diverge. This appears to be the result of nonlinear frequency dependence of the rotational derivatives caused by effects of motion coupling with the unsteady flow separation, and is qualitatively consistent with the observations of Section 10.1, as before, time history effects become significant at high α.

The effect of oscillation frequency was further investigated by evaluating Equation (1) at $\bar{\omega}_b = 0.05$, using data obtained at DFVLR in Germany[14] together with the NASA coning data.[9] These data are compared in Figure 10-8 with the NAE/NASA set at $\bar{\omega}_b = 0.12$ and 0.17.[8] Neglecting smaller differences present, for the most part within the uncertainty, the basic trends in the two sets of curves are quite similar.

The generally satisfactory agreement between the rotary and oscillatory terms at low α ($\alpha < 18°$) and $\beta = 0°$, and the encouraging degree of consistency obtained in the interfacility correlation (Fig. 10-8), constitute a partial validation of the Tobak-Schiff mathematical model[6] and demonstrate the integrity of the combined data base. The preliminary correlation of the full identity (Eq. (9.7-(3))), using the complete set of damping derivatives at $\beta = 5°$, has also demonstrated good agreement but final results are not yet available.

The conclusion which may tentatively be drawn from the results obtained thus far is that, although the rotary and oscillatory derivatives cannot be equated directly, these physical quantities are entirely consistent within the framework and restrictions of the Tobak-Schiff mathematical model.[6]

10.3 REFERENCES

1. Tobak, M.; and Schiff, L. B.: A Non Linear Aerodynamic Moment Formulation and Its Implications for Dynamic Stability Testing. AIAA Paper 71-275, 1971.

2. Thomas, H. H. B. M.; and Edwards, G.: Mathematical Models of Aircraft Dynamics for Extreme Flight Conditions (Theory and Experiment). AGARD-CP-235, Paper 27, 1978.

3. Beyers, M. E.: Aerodynamic Simulation of Multi-Degree-of-Freedom Aircraft Motion. International Congress on Instrumentation in Aerospace Simulation Facilities. September/October 1981.

4. Ross, A. Jean; and Edwards, Geraldine F.: Correlation of Predicted and Free-Flight Responses Near Departure Conditions of a High Incidence Research Model. AGARD-CP-386, Paper 31, 1985.

5. Gainer, T. G.; and Hoffman, S.: Summary of Transformation Equations and Equations of Motion Used in Free-Flight and Wind-Tunnel Data Reduction and Analysis. NASA SP-3070, 1972.

6. Tobak, M.; and Schiff, L. B.: Aerodynamic Mathematical Modeling—Basic Concepts. AGARD-LS-114, No. 1, March 1981.

7. Beyers, M. E.: A New Look at the Tobak-Schiff Model of Nonplanar Aircraft Dynamics. NRC, NAE LTR-UA-101, December 1989.

8. Beyers, M. E.; and Szyszkowicz, M.: Stability Derivatives of the Standard Dynamics Model at Mach 0.6, to appear as NAE publication.

9. Jermey, C.; and Schiff, L. B.: Wind-Tunnel Investigation of the Aerodynamic Characteristics of the Standard Dynamics Model in Coning Motion at Mach 0.6. AIAA-85-1828-CP, August 1985.

10. Beyers, M. E.: Subsonic Roll Oscillation Experiments on the Standard Dynamics Model. AIAA Paper 83-2134, Aug. 1983.

11. Beyers, M. E.; and Kapoor, K. B.: Dynamic Derivatives Due to Oscillation in Yaw for a 10-Degree Cone at Mach 2.0 NRC, NAE LTR-UA-71, Ottawa, Aug. 1983.

12. Schiff, L. B.; and Tobak, M.: Results from a New Wind-Tunnel Apparatus for Studying Coning and Spinning Motions of Bodies of Revolution. AIAA J., Vol. 8, Nov. 1970, pp. 1953-1957.

13. Tobak, M.; and Wehrend, W. R.: Stability Derivatives of Cones at Supersonic Speeds. NACA TN 3788, 1956.

14. Schmidt, E.: Standard Dynamics Model Experiments with the DFVLR/AVA Transonic Derivative Balance. AGARD-CP-386, No. 21, Nov. 1985.

10.4 NOMENCLATURE

b	wingspan
$\bar{c}$	mean aerodynamic chord
C_{ik}	dynamic derivative with respect to reduced-rate parameter $\frac{\partial C_i}{\partial\left(\frac{k\ell}{2V_\infty}\right)}$; $i = \ell, m, n, y$; $k = p, r, \dot{\beta}, \dot{\phi}, \Omega$ ($\ell = b$ or d)
C_ℓ	rolling-moment coefficient, $L/(q_\infty S\ell)$, $\ell = b$ or d
C_m	pitching-moment coefficient, $M/(q_\infty S\ell)$, $\ell = c$ or d
C_n	yawing-moment coefficient, $N/(q_\infty S\ell)$, $\ell = b$ or d
C_y	side-force coefficient, $Y/(q_\infty S)$
d	base diameter
L, M, N	rolling, pitching and yawing moments
M_∞	freestream Mach number
p, q, r	body-axes angular velocities
q_∞	freestream dynamic pressure
Re_ℓ	freestream Reynolds number based on b
S	reference area
V_∞	freestream velocity
α, β	angles of attack and sideslip
α_{av}	angle for onset of asymmetrical vortex shedding
γ	$= \cos\sigma$
δ	$= \sin\sigma$
σ	total angle of attack
$\dot{\phi}, \Omega$	coning rate
$\bar{\omega}$	reduced coning-rate parameter, $\dot{\phi}\ell/(2V_\infty)$
$\bar{\omega}_b$	reduced circular frequency, $\omega b/(2V_\infty)$

Superscripts

$(\dot{\cdot})$	differentiation with respect to time
$(\bar{\ })$	composite fixed-axis derivative (body axes)

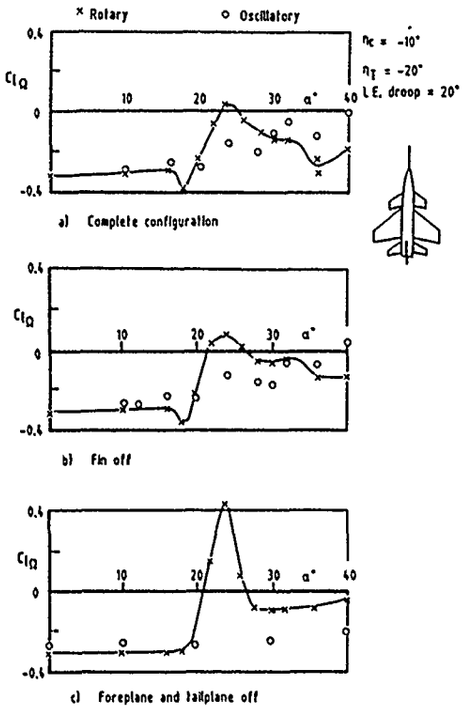

Figure 10-1. Comparison of rotary and oscillatory derivatives for HIRM 1—C_{l_Ω}.

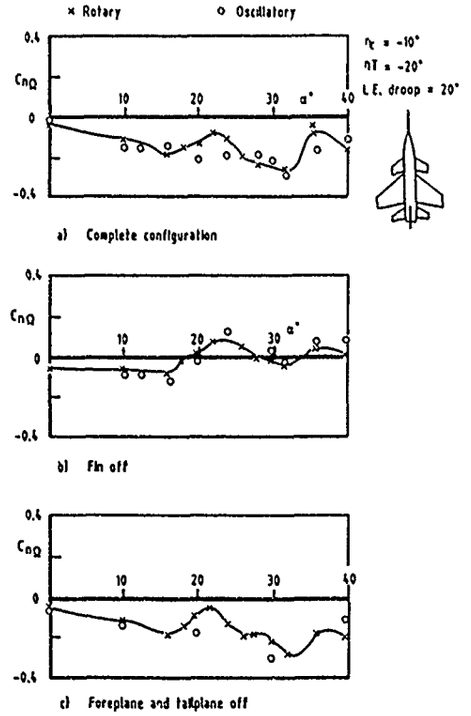

Figure 10-2. Comparison of rotary and oscillatory derivatives for HIRM 1—C_{n_Ω}

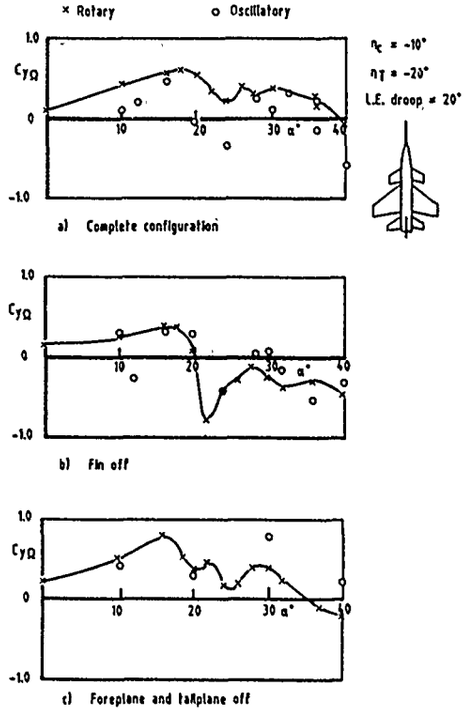

Figure 10-3. Comparison of rotary and oscillatory derivatives for HIRM 1- $-C_{y_\Omega}$.

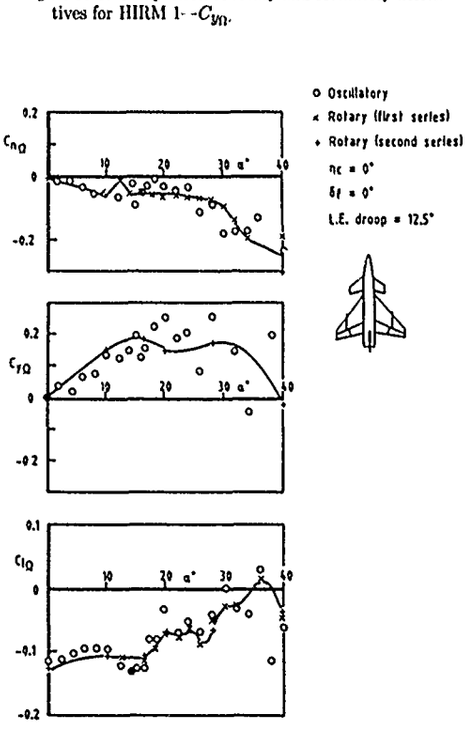

Figure 10-4. Comparison of rotary and oscillatory derivatives for HIRM 2.

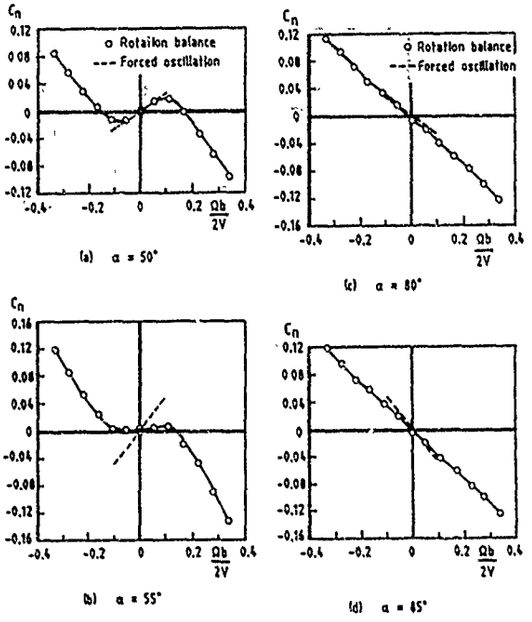

Figure 10-5. Comparison of rotary and oscillatory data for the YF-17.

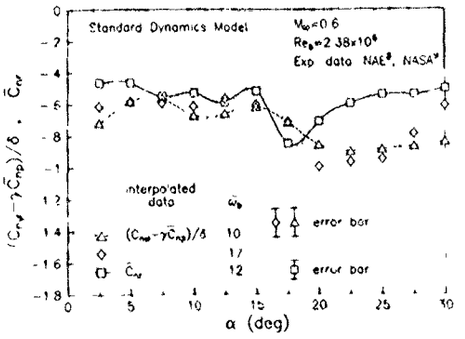

Figure 10-7 Comparison of rotary and oscillatory terms at zero sideslip.

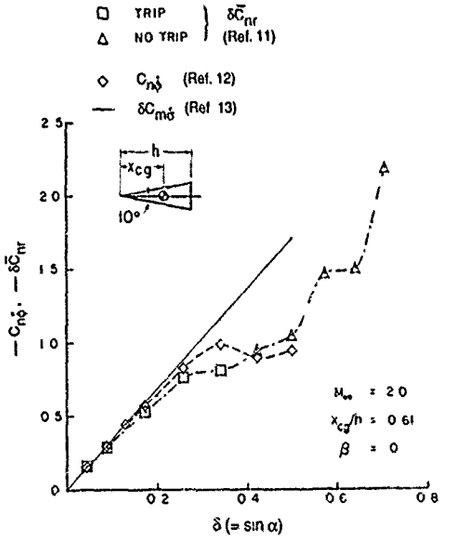

Figure 10-6. Comparison of yaw-damping and coning-rate derivatives.

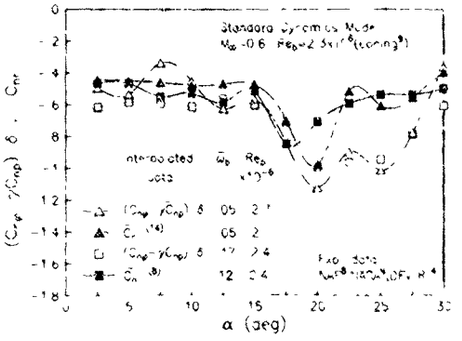

Figure 10-8 Comparison of rotary and oscillatory terms— interfacility/reduced-frequency effects.

CHAPTER 11

CORRELATION WITH FLIGHT TESTS

11.0 INTRODUCTION

The final objective in a rotary-balance testing programme is the prediction and analysis of aircraft behavior at high angles of attack and spin conditions. Thus, the comparison of predictions with flight results allows the ultimate assessment of the validity of the approach in its experimental and analytical aspects. On the experimental side, wind-tunnel results are affected by the various sources of error, such as Reynolds number effects, model fidelity and support and wall interference, which have been covered in previous chapters. On the analytical side, the assumptions made in modeling the phenomena of interest play a role which is at least as important.

Three types of flight tests can be used for this kind of validation:

- Free-flight tests of dynamically scaled models in a vertical wind tunnel, which allow simulation of developed spin conditions and spin recovery maneuvers.

- Free-flight tests of powered or unpowered, scaled and remotely controlled flying models; in this case, high-angle-of-attack flying qualities, departure characteristics, spin entry and recovery can be simulated. Models may be dynamically scaled when the behavior of an aircraft design is to be simulated, or not scaled when the only purpose is validation of a prediction technique or extraction of aerodynamic data.

- Flight tests of full-scale aircraft, which, of course, are the final aim of the investigation.

Different kinds of data may also be extracted from the tests for comparison with predictions. In an attempt to classify the options the following can be listed:

- Overall characteristics of the spin, in terms of quantitative features like mean attitude, time per turn and descent speed and qualitative features like steady or oscillatory character, flat or steep attitude, etc. The effect of controls on spin features and time/number of turns required for recovery are also of importance. Even though this kind of information is the most directly useful in aircraft design, it is also evident that any comparison of such global values does not allow one to break down the final result into its components and evaluate the different contributions of experimental data and aerodynamic modeling to the final results.

- Aerodynamic coefficients, which may be analyzed both as time histories of aerodynamic forces, or as aerodynamic derivatives obtained by parameter identification techniques on the basis of a predefined aerodynamic modeling scheme.

- Time histories of flight parameters like angle of attack and sideslip, accelerations, angular velocities, etc., thus allowing a more detailed analysis as compared to the simple average values considered above.

In order to obtain precise and reliable data from flight tests at high angles of attack, considerable care is required. A specialized instrumentation system has to be installed in the aircraft or flying model. As the spin tests are very dynamic, the main difficulty encountered will be to determine the airflow velocity components accurately. Accurate determination of the aircraft trajectory and angular velocities and precise evaluation of the airspeed components, the aircraft attitudes and the aerodynamic forces and moments are required.

Consequently, the following characteristics of the instrumentation system are of great importance:

- A large bandwidth of the sensors.

- A high level of redundancy to identify the sensor characteristics and to validate each part of the instrumentation system under extreme flight conditions.

- A high degree of precision in the sensors. For example, in order to determine the aerodynamic coefficients, accurate values of the relative airflow (ρ, V) data and of the inertial characteristics are required.

As a matter of fact, concerning the flight test data, the main difficulty is to obtain accurate estimates of the values of the trajectory parameters and of the aerodynamic coefficients. The usefulness of flight test data in experimental validation would vanish if the accuracy level were not sufficiently high as to provide a good reference for the rotary-balance results.

The purpose of the present chapter is to give an overview of the correlation techniques used by the various organizations and to show a selected set of comparisons between predictions and results in an attempt to highlight the available experience

Unfortunately, due to the relatively low interest in a deeper understanding of high angle-of-attack behavior during the 60 s and 70 s, only a limited number of basic research programs exist, while most of the information and experience pertains to specific military aircraft and is normally not available to the scientific community due to industrial or military classification Only recently have a number of fundamental research programs been undertaken in different countries (High Incidence

Research Models at RAE, Light Airplane Spin Resistance and High-Angle-Of-Attack Technology programs at NASA, and research at ONERA-IMFL), which are now greatly improving the knowledge in the field.

11.1 NASA LANGLEY RESEARCH CENTER

Over 60 general aviation and military aircraft have been tested on the Langley spin tunnel rotary-balance over the past 8 years. For most of these designs, dynamically scaled free-spinning model tests results and, to a much lesser extent, full-scale results were available. A comparison of predicted versus experimentally determined spins is presented in Tables 11-1 and 11-2 for some representative military and general aviation configurations, respectively. The predicted steady spin characteristics (angle of attack and time per turn) were obtained from rotary-balance tests by the on-line steady equilibrium spin technique described in Chapter 9.1 and Reference 1. No smoothing, shifting, etc. of these data were performed.

A computational method can be validated by demonstrating acceptable correlation between predicted and experimentally determined results. In this instance, however, both the method for computing steady-state spin equilibrium conditions and the use of low Reynolds number rotary-balance data must be justified. Consequently, low Reynolds number free-spinning dynamically scaled model results obtained in the spin tunnel are compared with the predicted values to verify the computational method; whereas full-scale airplane results are reviewed to identify possible Reynolds number related difficulties.

The correlation obtained between predicted steady spin and spin model results is considered excellent and indicates the sufficiency of the computational method. As shown, no spins were obtained that had not been predicted. For each predicted spin mode, three possibilities exist in flight: a steady spin will be realized, the spin will be oscillatory about the steady spin values, or non-existent. The latter two conditions reflect the underlying spin mode's level of instability. Obviously, to identify the oscillatory nature (stability) of a spin, large-angle six-degree-of-freedom computations must be performed, which is not practical during the rotary-balance test phase.

The correlation obtained between full-scale flight results and predicted steady spins is also considered excellent for the military configurations presented in Table 11-1. Unfortunately, not many documented spins performed with current state-of-the-art instrumentation are presently available for correlation.

As shown in Table 11-2, the level of agreement between predicted and full-scale flight results for general aviation configurations, while still considered good, has on occasion been somewhat lower than that obtained for military configurations. Instances are also shown in which predicted spin modes are experienced by the spin model but not demonstrated by the full-scale airplane. This does not necessarily infer that these spin modes do not exist, as it is possible that the airplane was not able to generate the required equilibrium conditions. Since the wing characteristics are largely responsible for steep and moderately steep spins, the use of low Reynolds number data may adversely affect the accuracy of such predicted spin modes. For instance, the model A flight-test spin angle of attack was more closely predicted when the model wing leading-edge radius was increased. This change in wing geometry tends to compensate for the suspected effects of Reynolds number.

The level of agreement between predicted and full-scale flight results would indicate that use of low Reynolds number rotary-balance data is sufficient for calculating steady spin modes for military configurations and for general aviation configurations not having steep spins with Reynolds number sensitive airfoil-wing characteristics.

11.2 AERMACCHI

Many of the aircraft designs that have been tested on the AerMacchi rotary balance have developed into production aircraft, so that flight test information is available for a few of them. For a few others, vertical spin tunnel tests are available. Unfortunately, data are often restricted by military or commercial classification, and systematic correlations are rare. For these reasons, only a limited selection of results can be presented. Model designations used in the following discussion are the same as those presented in Table 7-1 of Section 7.3.

(a) Aircraft "B1" spin characteristics[2,3]

The full-scale aircraft B1 spin is characterized by:

- An average angle of attack of 23°.
- A time per turn of 2-2.5 sec.
- A spin parameter $\Omega b/2V = 0.13$.
- Pro-spin controls are: rudder with, elevator up, zero ailerons.
- Most effective spin recovery maneuver is rudder against and elevator to zero.

Figure 11-1 shows the loci of the equilibrium conditions from rotary-balance tests with pro-spin controls. Spin equilibrium is identified at $\alpha = 23°$, $\Omega b/2V = 0.14$, $\beta = +2°$. The wind-tunnel results (Figure 11-2) for $\alpha = 23°$ and $\beta = 0$ show both the equilibrium condition (positive Ω) and the large damping force which is available when the rudder is deflected against (negative Ω). For the same aircraft a number of 6-DOF simulations have also been computed and compared with time histories from flight tests. Figure 11.3 shows an example of such correlation, obtained with a mathematical model based on fixed- and rotary-balance data as described in Section 9.3.

(b) Aircraft "C" spin characteristics

Vertical spin tunnel test results are available for this configuration. The following comparison of the equilibrium spin modes from the two sources can be made.[13]

Flight Tests	Spin Tests
$\alpha = 32°$, 3.2 sec/turn	
$\alpha = 62°$, 2.4 sec/turn	$\alpha = 55°$-$60°$, 2.5-3.4 sec/turn
$\alpha = 76°$, 1.8 sec/turn	$\alpha = 70°$-$80°$, 1.4 sec/turn

Pro-spin controls are: elevator-up, aileron against and rudder with, even though some of the spin modes can be found with other control combinations. The spin tests showed an oscillatory spin regime at α near 55°-60° and a rapid flat-spin regime near 70°-80°. The equilibrium spin technique agrees with these data but also shows a further equilibrium condition at approximately 30° angle of attack.

The corresponding equilibrium plots and some aerodynamic data from the rotary balance are shown in Figures 11-4 to 11-6. Real-time simulations based on the same data confirmed these results, and also showed a great resistance of the aircraft to reaching higher angles of attack. This would mean that the two spin modes at $\alpha = 62°$ and 76° cannot be obtained in a real flight situation. Preliminary information from flight tests of the aircraft have confirmed the presence of the $\alpha = 30°$ spin mode and resistance to entering other types of spins.

Mathematical modeling of aerodynamic forces by taking into account the nonlinear effects shown by rotary-balance data as a function of Ω was shown to be useful also for the simulation of maneuvers other than equilibrium spin. Figure 11-7 shows time histories of the aircraft stall which is accompanied by a moderate wing-rock: the comparison of flight test data with a simulation shows good agreement from both qualitative and quantitative points of view.

(c) Aircraft "D" spin characteristics

Vertical spin tunnel tests of aircraft "D" showed two spin modes:

- A flat and rapid spin with $\alpha = 80°$, time per turn 2-2.5 sec, descent speed of 60 m/sec.
- An oscillatory flat spin with average characteristics similar to the above , but with oscillations of $\pm 10°$ in angle of attack and $\pm 20°$ in bank angle. This spin mode could develop into divergent oscillations.

Rotary balance tests showed autorotation characteristics at $\alpha = 84°$ (Figure 11-8), with a well-defined spin equilibrium condition, and a broad range of angles of attack with definitive zero damping values. The effectiveness of forebody modifications on the flat spin mode were also well correlated between the two tests.

11.3 ONERA-IMFL

Several methods of comparing wind-tunnel data with flight exist:

(a) direct comparison of the aerodynamic coefficients

(b) comparison of the aircraft responses in flight and in simulation

(c) assessment of the aircraft behavior by an analysis of the equilibrium and bifurcation surfaces (Section 9.2.6)

The first two methods will now be discussed.

11.3.1 Comparisons of Aerodynamic Coefficients

At IMFL comparisons have been carried out using the results obtained on a jet trainer aircraft. The mathematical modeling process was applied in order to define a mathematical model as described in Section 9.2. This model structure separates the steady and unsteady effects. The former are defined by data tables and the latter represented by transfer functions, their coefficients depending on the values of α, λ and $\dot{\alpha}$.

A comparison between the coefficients predicted by the model and those obtained from flight tests is useful because it allows one to evaluate and validate the features introduced in the model structure. The large unsteady effects noticed during oscillatory coning tests at high angles of attack (see Section 7.7) are examples of the effects modeled. These aerodynamic phenomena were measured using the λ degree of freedom of the IMFL rotary balance, where λ is the angle between the velocity vector and the rotational vector (see Chapter 4).

This kinematic parameter can be calculated when the flight trajectory has been evaluated. Figures 11-9 to 11-11 show the flight trajectory in the planes of (α,β), (α,Ω^*) and (α,λ), respectively. The aircraft state during a spin is shown. The equilibrium spin state is at approximately $\alpha = 43°$, $\Omega^* = 3.2°$ and $\lambda = 2°$. However, during the entry and recovery phases the aircraft equilibrium is changing and the angle λ may attain very high values. Consequently, the angles of attack (Figure 11-12) and sideslip vary rapidly, and the unsteady aerodynamic contributions may be important.

Indeed, these unsteady effects have been noticed in the variation of the normal force (Figure 11-13) calculated during this flight. During the spin entry phase, the normal force exhibits very large variations and the maximum value attained is much larger than it would be under steady conditions.

Once the aircraft trajectory has been determined, it is possible to calculate the value of the normal force in flight as given by the mathematical model. Figure 11-14 shows this coefficient plotted for the case of the steady mathematical model (not taking into account the aerodynamic λ effect). It is clear that the normal force is not well estimated, since the amplitude of the oscillation is not as large as in the previous figure. On the other hand, a mathematical model taking into account the unsteady behavior such as that outlined in Section 9.2 gives better results (see Figure 11-15). The spin entry phase as described by the two modeling cases discussed here is presented in Figures 11-16 and 11-17. The normal force calculated from the flight recordings is also plotted in these figures.

It can be seen that the amplitude and phase variations are much better represented by the unsteady modeling (Figure 11-17) even if some differences remain when comparing to the flight test data. Furthermore, the accuracy of the flight test results is not perfect and a part of the discrepancies can certainly be attributed to the trajectory estimation. This example illustrates the flight test—wind-tunnel correlation and shows:

- The value of comparing the aerodynamic coefficient variation in flight with the mathematical modeling for validation purposes.
- The relative importance of the unsteady aerodynamics contributions at high angles of attack.
- The value of the oscillatory coning motion tests carried out with the λ degree of freedom on the rotary balance.

This type of comparison can be defined as "a direct aerodynamics approach." A comparison with the flight mechanics results is now presented.

11.3.2 Flight Evolutions and Simulations

Another method of comparing flight test and rotary-balance data involves performing numerical simulations of specific maneuvers. By integrating the flight mechanics equations of motion, the simulation results can be compared with the flight maneuvers. Obviously, the motion calculations require not only an accurate knowledge of the mass and inertial characteristics of the aircraft, but also a good model of the aerodynamics for a large flight domain.

This type of comparison offers great flexibility. Different simulations can be made by varying the values of certain parameters such as the center-of-gravity location, mass, moment of inertia or the initial conditions. In this way the effects of these parameters can be estimated. Furthermore, the control surface effects are easily estimated and can be compared with the flight test results. As the effects of the control surface deflections with respect to the spin equilibrium can be determined, the simulation process is not only a correlation method but could also become a convenient prediction method for aircraft behavior at high angles of attack, once the modeling has been validated. Simulations allow comparisons of the parametric effects and the equilibrium states but are not limited to these points only.

Another point of interest lies in the fact that the transient phases can be calculated and the dynamic characteristics such as oscillatory modes, frequencies, damping and time constants can be determined. Figures 11-18 and 11-19 present results of two simulations involving the Alphajet aircraft. The following parameters are plotted as functions of reduced time $T^* = \frac{VT}{c}$.

- α, β angles of attack and sideslip
- p, q, r components of the rotational vector
- θ, ϕ, V the pitch and roll angles, and the airspeed
- $\delta_l, \delta_m, \delta_n$ the control surface deflections: ailerons, elevator and rudder, respectively

These results apply to the following maneuvers at high angles of attack. (a) A spin entry to the left obtained from low incidence flight after the following control surface deflection sequence. full rudder to the left, stick back and ailerons to the right (7°). The spin equilibrium is obtained at about 42° angle of attack and 5° sideslip (Figure 11-18). (b) A fast and flat spin obtained with ailerons completely to the right and stick pushed forward (Figure 11-19). (c) A recovery from the fast and flat spin to the left obtained with controls at neutral positions (Figure 11-19).

These simulations are satisfactory and contribute to the validation of the mathematical model by comparing the equilibrium states, the control surface effects and the different dynamic characteristics of the motions. Finally, another aspect of the simulations is the possibility to carry out comparisons with the spin tests in a vertical wind tunnel. The spin equilibrium control positions and the effects of different parameters can be compared, at least in a qualitative way.

11.4 RAE

11.4.1 The RAE HIRM Program

In 1982 the RAE initiated a program of research on the flight dynamics of departure using a High-Incidence Research Model (HIRM). The main objective of the program[4] was "The widening of understanding of the flight dynamics phenomena of aircraft at high angles of attack." Both wind-tunnel and free-flight drop tests were employed in order to gather experimental data for the development and validation of the mathematical modeling process. The wind-tunnel measurements included static, oscillatory and rotary tests using models of various sizes.

In the following discussion, results are presented for drop tests[5–11] performed under a collaborative agreement between RAE and NASA. After a short description of the model and flight data analysis techniques, some selected results are used to show the correlation of aerodynamic derivatives between flight and wind-tunnel data and of predicted and measured time histories.

11.4.2 Flight Tests and Data Analysis Techniques

The HIRM is a three-surface unpowered model with an advanced transonic swept wing, an all-moving canard and stabilator, and an oversized vertical tail with rudder. The wing has no moving control surfaces. Roll control is provided by differential canard and stabilator deflection. The general arrangement of the model is shown in Figure 11-20. The model is fully instrumented with the transducer signals telemetered to a ground station. A nose boom carrying angle-of-attack and sideslip vanes, and a pitot-static probe have been included. Flight maneuvers are preprogrammed into the system and executed by a timer after the model is released from a carrier helicopter.

The model was flight tested at NASA Dryden Flight Research Facility, Edwards, California. During those tests the model was towed by helicopter to 3,000–4,000 meters above the impact range and released at a speed of approximately 150 km/hour. At the time of release a timer began a preprogrammed test sequence which activated a series of switches, thus positioning the model's flight control surfaces. The duration of the flights varied between 80 and 160 sec. At a predetermined time, or at a given height above ground, three parachutes were deployed to recover the model. The landing was cushioned by low pressure air bags which were deployed from a door beneath the fuselage.

The motion of the HIRM was initially excited by the model's release from the helicopter cable and then by the activation of control surfaces. For each test run, either a doublet in differential tail or canard, or a simple rudder pulse was used. In some maneuvers a step deflection of symmetric tail was added. The various trim conditions were established by the canard setting at either 0° or −10° and by the tailplane setting between −14° to −20°. Most of the responses were within the α-range of 20° to 40°, though in three maneuvers α reached 60°.

The measured data from five flights with 26 maneuvers were obtained as time histories of control and response variables sampled at 0.012 sec intervals. The two flights with $\delta_c = -10°$ and $\delta_h = -18°$ are designated as HD1 and HD3, the remaining three flights with $\delta_c = 0°$ and $\delta_h = -15°$ as HD2, HD4 and HD6. When appropriate, the measured data were corrected for the c.g. offset and airflow effect.

In addition to analyzing almost all of the 26 individual maneuvers, the data from each flight were joined together into one set of data. The resulting ensemble was then partitioned into subsets according to the value of α. For these new subsets of data, the aerodynamic coefficients were modeled mostly on one degree subspaces of the original α-space.

11.4.3 Results and Discussion

Because of the experimental design and type of motion displayed by the model, the main emphasis in the flight data analysis was constrained to the lateral aerodynamic equations and the corresponding parameters in these equations. Some of the important lateral parameters are presented to show their variation with α and δ_c and closeness to the wind-tunnel test results. Three maneuvers in flight HD1 and one in HD3 consisted mostly of lightly-damped large amplitude oscillations. The remaining three maneuvers in HD3 flight exhibited large excursions in α with some lateral coupling. The stepwise regression procedures demonstrated that for the oscillatory maneuvers, analyzed as partitioned data, models with linear parameters were adequate for all three lateral coefficients C_Y, C_n and C_l. From the analysis of the individual maneuvers, the technique also selected nonlinear terms $\beta\alpha$ and $p\alpha$ into the model equations for the coefficients C_n.

In Figure 11-21 the damping derivative C_{l_p} and cross-derivative C_{n_p} from flight testing are compared with the results from the oscillatory and rotary wind-tunnel tests. The rotary data predicted a decrease in damping for $20° < \alpha < 28°$; whereas, the oscillatory tests show no deterioration in this region. The flight data indicate even less damping in roll than the rotary test. The flight results are in agreement with the observed responses of the drop model, which showed very little damping or no damping at all. The reason for the discrepancy between the oscillatory data and flight results can be due to the different amplitude of oscillations in the wind tunnel (±5°) and in flight (around ±35°). The comparison of C_{n_p} parameters from various tests shows a similar pattern to that of C_{l_p}. No nonzero estimates of C_{n_p} could be obtained from the partitioned data for $19° < \alpha < 23°$.

The effect of different canard settings is shown in Figure 11-21 and in the lower part of Figure 11-22, which contain the damping parameters C_{l_p} from flight and wind-tunnel testing. The rotary test results agree with flight data for $22° < \alpha < 27°$ For the region between 27° to 35° the flight data still indicate low damping in roll, which is not confirmed by wind-tunnel measurements. The comparison of flight results in Figures 11-21 ($\delta_c = -10°$) and 11-22 ($\delta_c = 0°$) indicates strong effect of canard setting on damping in roll.

The final set of flight-derived aerodynamic parameters was obtained by averaging and fairing the various estimates for each configuration tested. The first step in the verification of these parameters was the already mentioned comparison with wind-tunnel results. The next step in the verification was made by checking the prediction capabilities of the equations modeled. This test included the simulation of maneuvers in terms of response variable time histories and time histories of the aerodynamic force and moment coefficients. In Figure 11-23, the computed and measured time histories of lateral motion variables from one maneuver in flight HD1 are given. Only three-degree-of-freedom simulation was used, with the longitudinal motion variables computed from measured data. Figure 11-23 is completed by the measured time history of the angle of attack. In Figure 11-24, the measured and predicted time histories of lateral aerodynamic coefficients from the same maneuver are compared. From both figures, it is apparent that the current model can predict the motion of the HIRM

within the α-range of 18° and 30° reasonably well. Some deficiencies of the model, however, still remain. The change in the frequency around $\alpha \approx 23°$ is not accurately predicted, and the amplitude of computed variables are, in general, greater than those measured. For further improvement of the mathematical model, the analysis of additional flight data would be necessary.

11.5 REFERENCES

1. Bihrle, W.; and Barnhart, B.: Spin Prediction Techniques. J. of Aircraft, Vol. 20, No. 2, Feb. 1983, pp. 97–101.

2. Valtorta, E.: Analisi delle prove in galleria con bilancia rotante e ricerca delle zone di equilibrio in vite - Macchi report 340-39x-13, 1979.

3. Bazzocchi, E.: Use of Rotary Balance Data for the Study of Spin. Lecture held at China Defense Science and Technology Information Center, 1988.

4. Moss, G. F.; Ross, A. Jean; and Butler, G. F.: A Programme of Work on the Flight Dynamics of Departure Using a High Incidence Research Model (HIRM). RAE Unpublished Report, July 1982.

5. Ross, A. Jean; and Edwards, Geraldine F.: Correlation of Predicted and Free-Flight Responses Near Departure Conditions of a High Incidence Research Model. Paper 31, AGARD CP 386, May 1985.

6. Klein, Vladislav; and Batterson, James G.: Determination of Airplane Model Structure from Flight Data Using Splines and Stepwise Regression. NASA TP-2126, 1983.

7. Ross, A. Jean; and Reid, G. E. A.: The Development of Mathematical Models for a High Incidence Research Model (HIRM) Part 1. Analysis of Static Aerodynamic Data. RAE Technical Report 83037, 1983.

8. Ross, A. Jean; and Reid, G. E. A.: The Development of Mathematical Models for a High Incidence Research Model (HIRM) Part 2. Analysis of Dynamic Test Data. RAE Technical Report 84072, 1984.

9. Allen, R. J.; and Booker, D.: Large-Scale Rolling Rig Tests on the RAE Model 2130 (HIRM 2) in the BAe Warton 5.5m Low-Speed Wind Tunnel. BAe Report AXR103, 1982.

10. O'Leary, C. O.: Dynamic Tests on a High Incidence Research Model (HIRM) in a Low-Speed Wind Tunnel. RAE Technical Report 84111, 1984.

11. Klein, Vladislav; Batterson, James G.; and Murphy, Patrick C.: Determination of Airplane Model Structure from Flight Data Using Modified Stepwise Regression. NASA TP-1916, 1981.

12. Bach, Ralph E., Jr.: A Variational Technique for Smoothing Flight-Test and Accident Data. AIAA Paper 80-1601, 1980.

13. Bava, R.: Confronto tra la vite simulata e la vite sperimentata nelle galleria verticale di Lille. AERITALIA Report 06/NT/T823/87325.

TABLE 11-1

COMPARISON OF CALCULATED[a] AND EXPERIMENTAL
SPIN MODES FOR MILITARY CONFIGURATIONS

MODEL	CONTROLS	SOURCE	SPIN MODE	
			α	Sec/turn
A	Neutral	Spin Tunnel	83	2.3
		Calculated	81	2.5
	Recovery	Flight Test	78	3.8
		Calculated	78	3.7
B	Pro-Spin	Spin Tunnel	83	2.2
		Calculated	81	1.9
	Neutral	Spin Tunnel	66	8.0
		Calculated	66	8.5
C	Pro-Spin	Flight Test	85	2.5
		Spin Tunnel	83	2.5
		Calculated	83	2.5
	Neutral	Flight Test	70[b]	5.1
		Spin Tunnel	70[b]	5.3
		Calculated	69	5.2
D	Pro-Spin	Flight Test	75	3.0
		Spin Tunnel	80	2.5
		Calculated	80	2.7
	w/Tanks			
	Pro-Spin	Spin Tunnel	84	2.1
		Calculated	81	2.3
E	Pro-Spin	Flight Test	Flat	2.2
	($\delta_d = 7°$)	Spin Tunnel	86	2.1
		Calculated	85	1.9
	Pro-Spin	Spin Tunnel	86	1.7
	($\delta_d = 12°$)	Calculated	88	1.7
	Stick-Aft	Spin Tunnel	67	6.2
	($\delta_d = \delta_r = 0°$)	Calculated	64	5.7
F	Pro-Spin	Flight Test	53	3.9
	w/Tanks	Spin Tunnel	54	3.8
		Calculated	50	3.8
	Pro-Spin	Spin Tunnel	48	3.9
	w/Stores	Calculated	47	3.9
	Recovery	Flight Test	43	5.5
		Calculated	41	5.0
G	Pro-Spin	Spin Tunnel	49	3.0
	($\delta_a = 0°$)	Calculated	50	3.3
	Pro-Spin	Spin Tunnel	56	2.9
	(δ_a against)	Calculated	58	3.0
H	Pro-Spin	Flight Test	35	3.57
		Calculated	37	3.70
	Rudder Alone	Flight Test	25	2.80
		Calculated	26	2.36
I	Pro-Spin	Spin Tunnel	60	3.2
		Calculated	60	3.1
	Rudder & Elevator	Spin Tunnel	49	2.9
		Calculated	46	3.3
J	Neutral	Spin Tunnel	82	2.6
		Calculated	81	2.4
	Stick Aft	Spin Tunnel		NO SPIN
		Calculated		NO SPIN

[a]Using simple steady-state spin analysis technique with on-line wind-tunnel data.

[b]Oscillatory spin average values

TABLE 11-2

COMPARISON OF CALCULATED[a] AND EXPERIMENTAL
SPIN MODES FOR GENERAL AVIATION CONFIGURATIONS

MODEL	CONTROLS	SOURCE	SPIN MODE	
			α	Sec/turn
A	Pro-Spin	Flight Test	43	2.7
		Spin Tunnel	30	2.3
		Calculated	29	2.8
		Spin Tunnel (Modified Wing Leading-Edge)	47	2.9
		Calculated (Modified Wing Leading-Edge)	48	2.9
B	Pro-Spin	Flight Test	39	2.3
		Spin Tunnel[c]	38	2.5
			77	1.1
		Predicted[c]	38	2.2
			77	1.2
	Neutral	Flight Test[b]	54	1.7
		Predicted[c]	36	1.7
			55	1.7
			79	1.0
		Spin Tunnel[b]	42	1.5
			78	1.0
		Predicted[c]	35	1.5
			77	1.0
C	Pro-Spin	Flight Test	20	1.8
		Spin Tunnel	22	2.0
		Predicted	18	1.3
D	Pro-Spin	Flight Test	29	2.2
		Predicted	23	1.7
E	Pro-Spin	Flight Test	44	2.8
		Spin Tunnel	30	2.3
		Predicted	33	2.6

[a]Using simple steady-state spin analysis technique with on-line wind-tunnel data.

[b]Different inertia distribution for flight and spin model.

[c]Multiple spin modes.

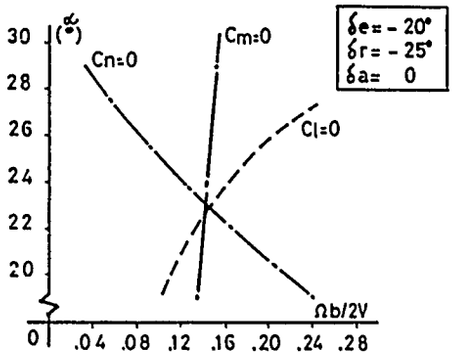

Figure 11-1. Aircraft "B1": loci of spin equilibrium conditions.

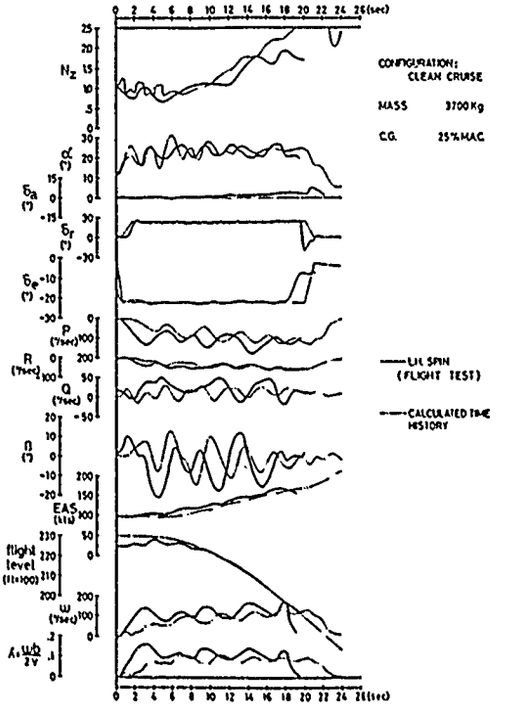

Figure 11-3. Aircraft "B1": comparison between flight test and computed time history.

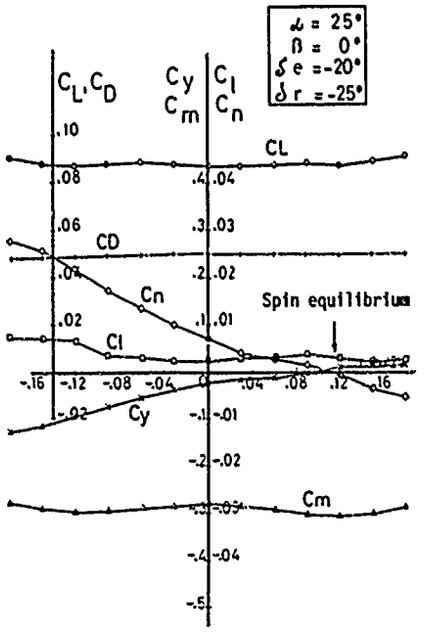

Figure 11-2. Aircraft "B1": rotary-balance data at near spin equilibrium conditions.

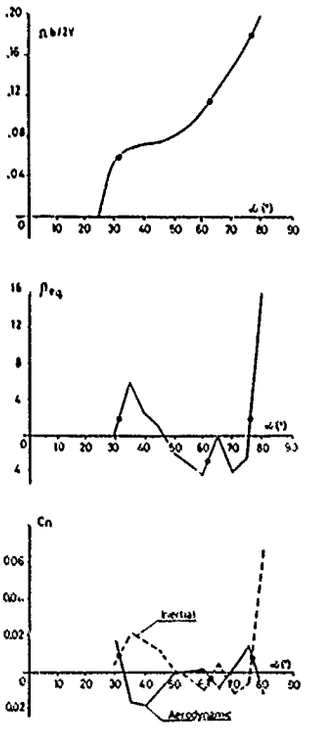

Figure 11-4. Aircraft "C". spin equilibrium conditions from rotary-balance data.

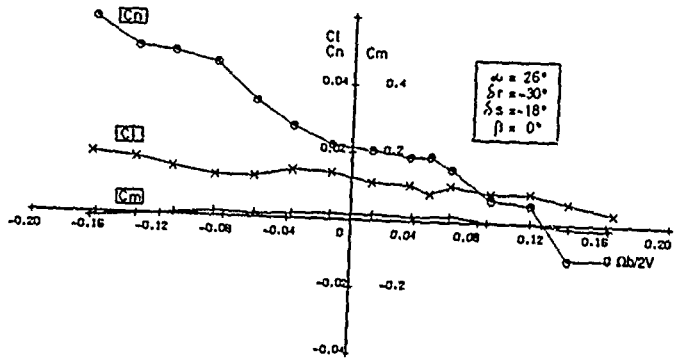

Figure 11-5. Aircraft "C" rotary-balance data approximately at the steep spin attitude.

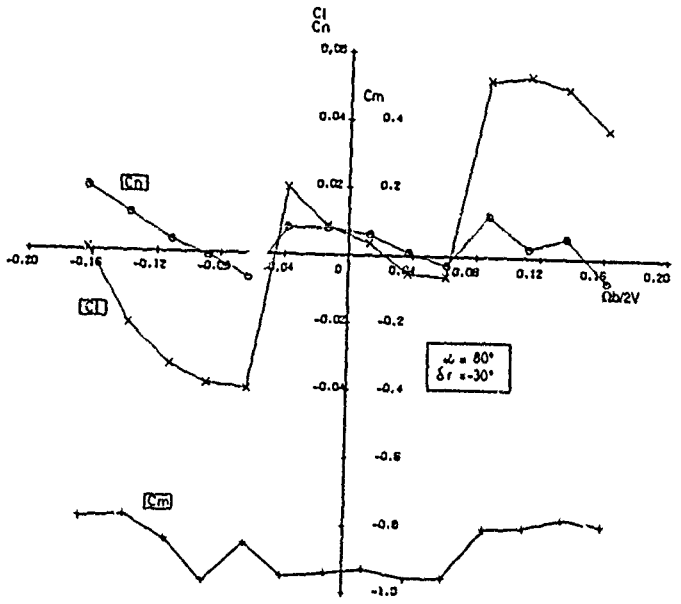

Figure 11-6. Aircraft "C": rotary-balance data at the flat spin attitude

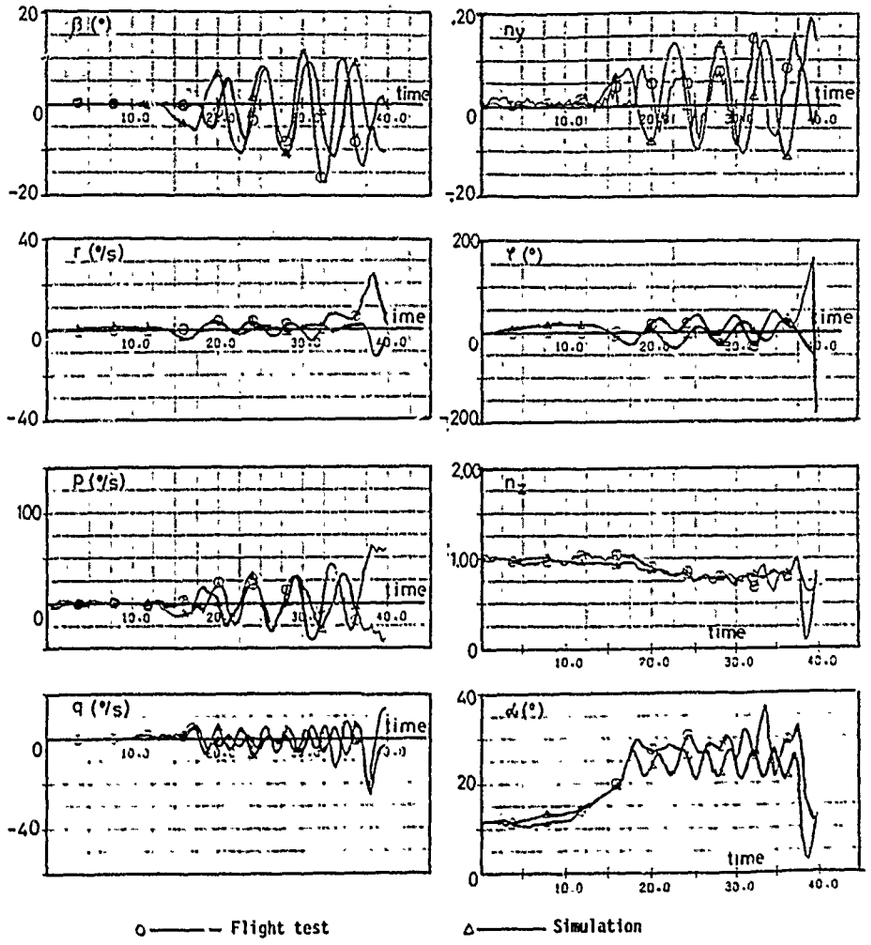

Figure 11-7 Aircraft "C": comparison of simulation and flight test for wing rock produced by a stall maneuver.

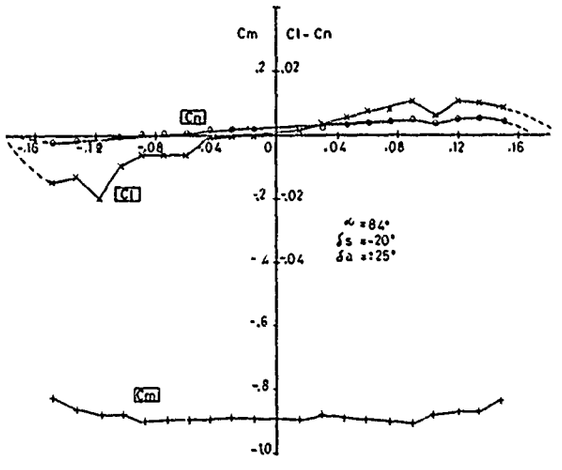

Figure 11-8. Aircraft "D": rotary-balance data at flat spin attitude.

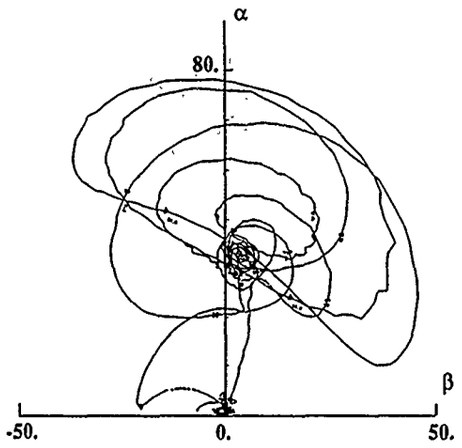

Figure 11-9. Spin test result: flight trajectory in the (β, α) plane.

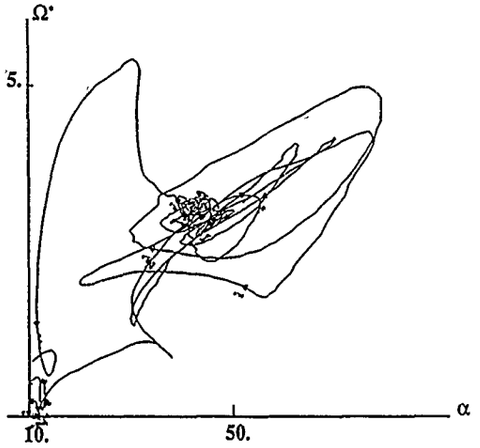

Figure 11-10. Spin test result: flight trajectory in the (α, Ω^*) plane.

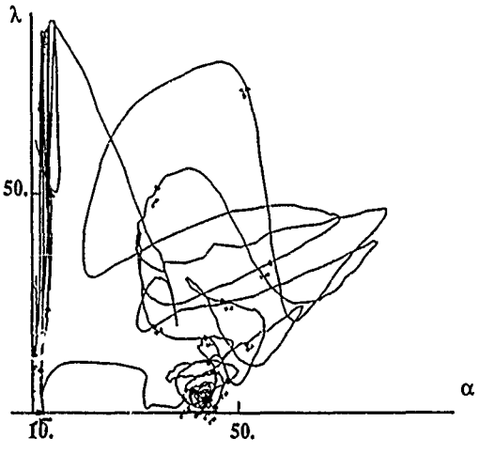

Figure 11-11. Spin test result: flight trajectory in the (α, λ) plane.

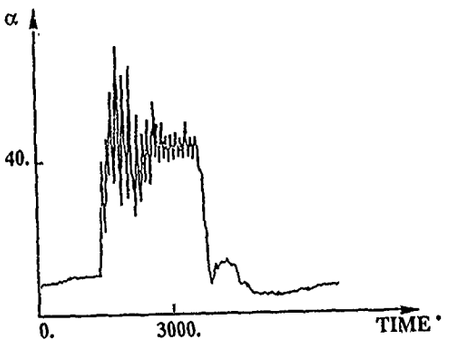

Figure 11-12. Flight spin test result: angle-of-attack time history.

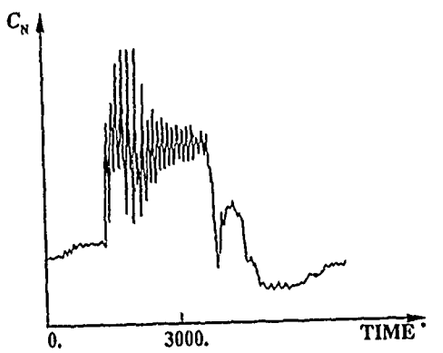

Figure 11-13. Flight spin test result: normal-force time history.

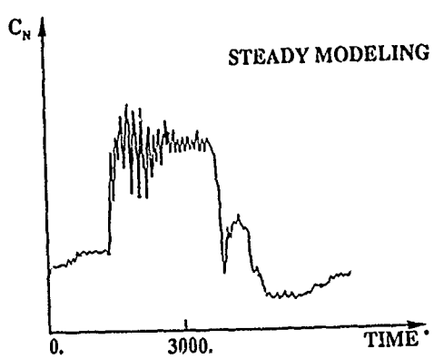

Figure 11-14. Normal force as given by steady modeling (and using the flight trajectory estimation).

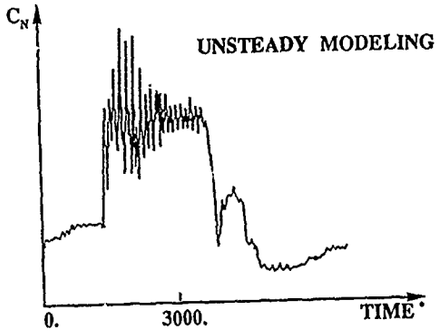

Figure 11-15. Normal force as given by unsteady modeling.

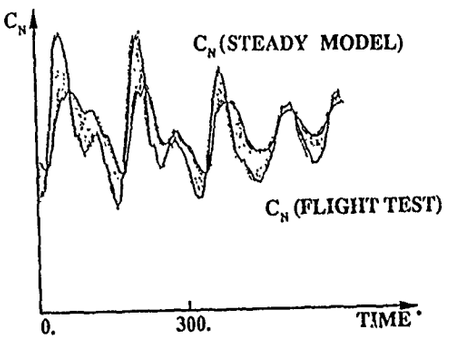

Figure 11-16. Correlation of flight test spin and steady modeling.

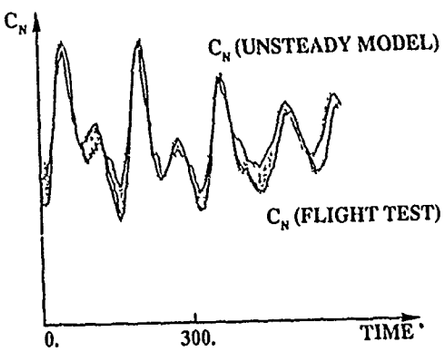

Figure 11-17. Correlation of flight test spin and mathematical modeling with λ effect (unsteady).

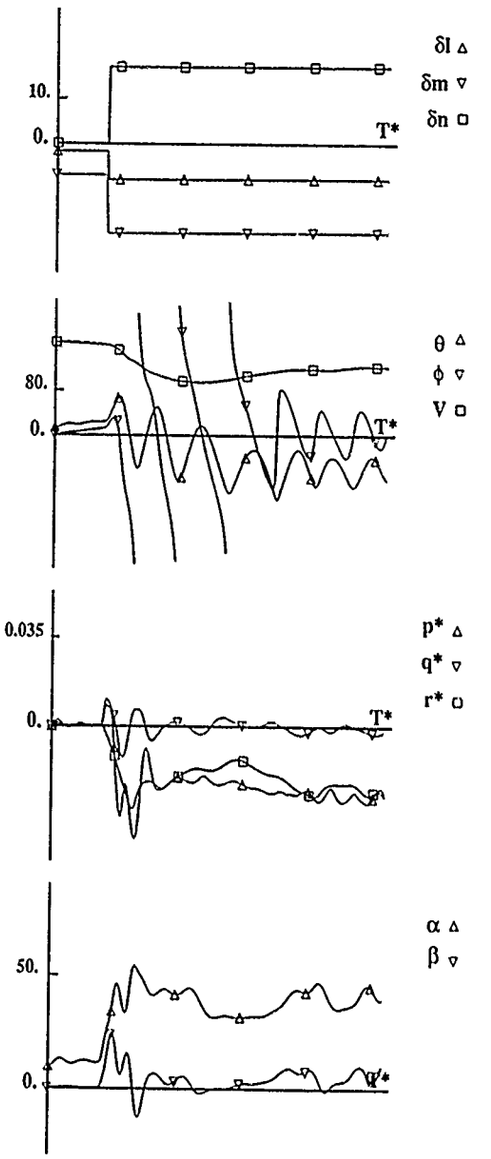

Figure 11-18. Simulated spin entry to the left.

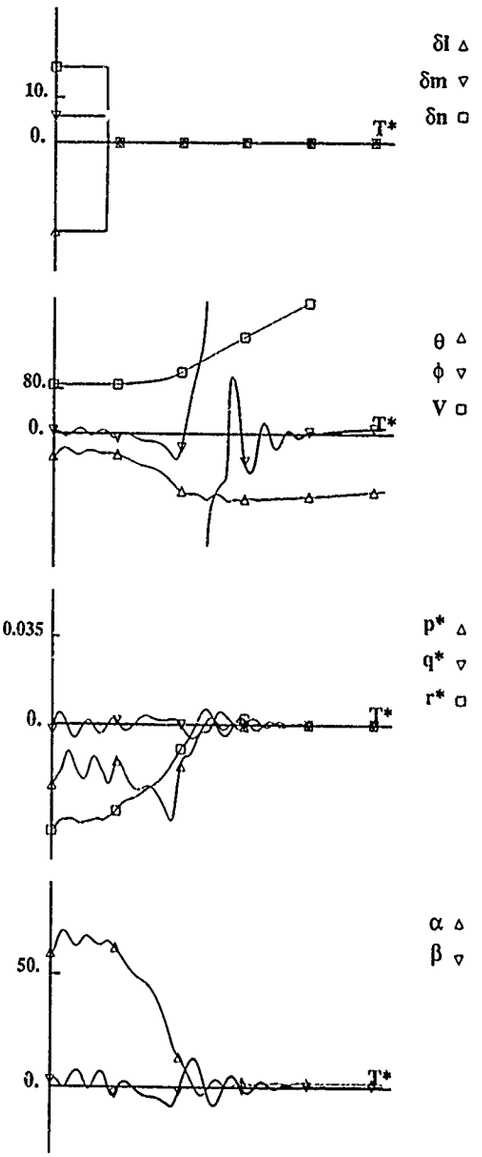

Figure 11-19 Simulated recovery from a fast and flat spin to the left

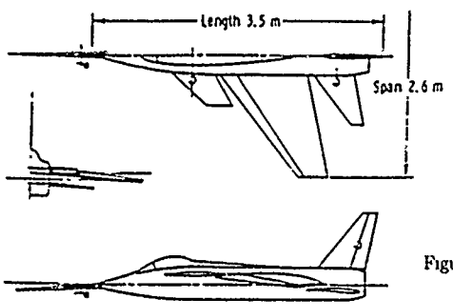

Figure 11-20. Three-view drawing of test model

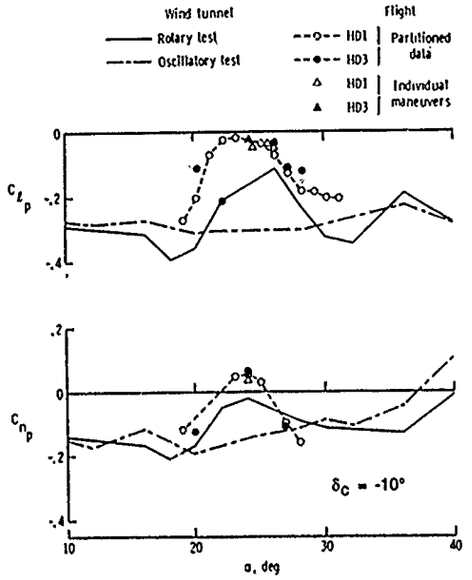

Figure 11-21. Comparison of oscillatory roll-rate parameters estimated from flight data and wind-tunnel measurement.

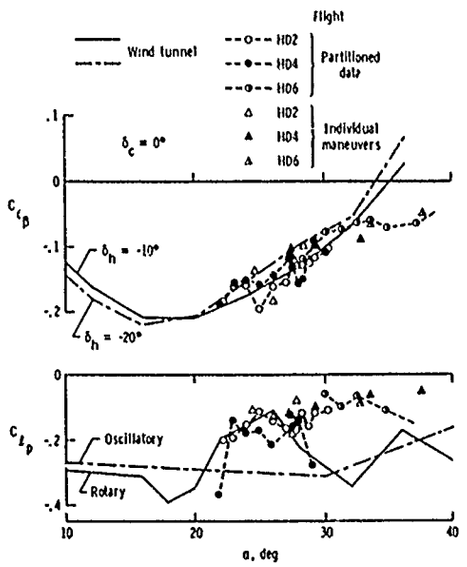

Figure 11-22. Comparison of sideslip and oscillatory roll-rate parameters estimated from flight data and wind-tunnel measurement.

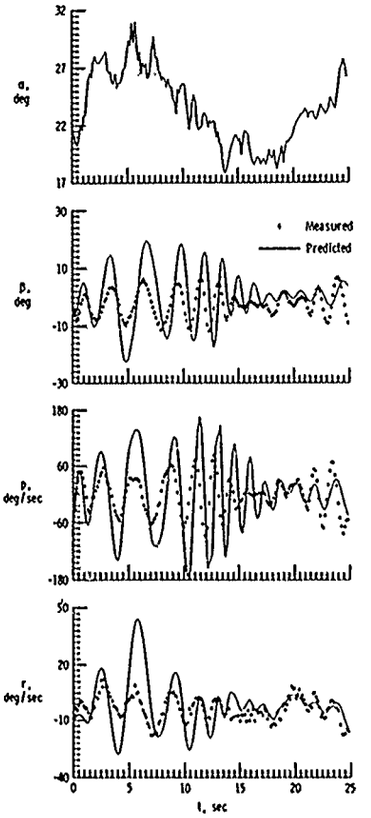

Figure 11-23. Comparison of measured lateral response time histories with those computed from mathematical model of HIRM.

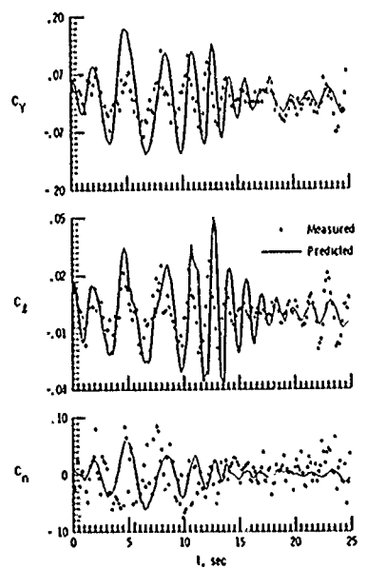

Figure 11-24. Comparison of measured lateral-directional aerodynamic coefficients with those computed from mathematical model of HIRM.

CHAPTER 12

PROPOSAL FOR COOPERATIVE AGARD RESEARCH PROGRAM

12.0 FUTURE CHALLENGES

Rotary balances, as we know them today, were first proposed by Gates and Bryant[1] in 1926 and first put to use in the US[2] in 1933 and in the UK[3] in 1934. In the 55 years or so of their existence the rotary-balance techniques have been used to obtain a large amount of experimental data which were applied in the equations of motion to predict spin characteristics of aircraft. In most cases these predictions were quite successful, that is, the observed spin behavior was close to the predicted one. Thus, on the whole, the rotary-balance data appear to be reliable and their quality acceptable for the purpose for which they were initially intended.

More recently, however, developments have taken place which have put a new emphasis on obtaining rotary-balance data and which have identified a new important area for their application. These developments were triggered by our recent interest in highly agile fighter aircraft, which are being designed not only to fly at high angles of attack but also to perform rapid large-amplitude angular motions, resulting in highly nonlinear and unsteady aerodynamic flows. The best way to experimentally study such rapid rotational maneuvers at high angles of attack is through the use of rotary balances. However, in addition to obtaining aerodynamic coefficients in the presence of rotary motion, the new application will also require studies of the flow fields involved, flow visualization experiments, pressure measurements and determination of static and dynamic derivatives. Furthermore, the new requirements may include studies of very complex and unorthodox configurations, extension of the speed range to high subsonic speeds, and consideration of various perturbations of the basic rotary motion.

It is likely that some of these expanded applications of rotary-balance techniques may require a refinement of the accuracy with which the data are obtained. This applies to better definition and resolution of the results obtained with our present data acquisition and reduction methods (including both instrumentation and software) as well as to a better understanding of the various aerodynamic interference effects that may be present in the results.

It is suggested that at least some of the new applications and problem areas mentioned above be investigated under an AGARD FDP cooperative program, with the participation of organizations represented on the present Working Group.

12.1 PROPOSED COOPERATIVE RESEARCH

More work is obviously needed in several areas covered by the present report. Some of these have already been discussed in the previous chapters and some follow the remarks in Section 12.0 above. Capabilities to perform the study required exist in more than one NATO country, and in such cases the possibility of carrying out the work jointly, under auspices of an AGARD cooperative program, would probably represent the most efficient approach. The proposed program can be roughly described in terms of the following subprograms.

12.1.1 Accuracy of Rotary-Balance Experiments

As discussed at some length in Chapter 5, the data obtained from wind-tunnel experiments using rotary balances may, under some circumstances, contain considerable errors due to the effects of (a) aerodynamic support interference, (b) wind-tunnel wall interference and (c) the interaction of these two effects in the presence of unsteady flows Occasionally, the data may also be affected by inaccuracy in (1) wind-tunnel flow quality, (2) model geometry, (3) data acquisition and calibration technique, etc. Although, as pointed out in Section 12.0, the accuracy of rotary-balance data was adequate in the past, in cases involving spin predictions at low speeds, the situation may be different for applications involving rapid maneuvers, higher speeds or unorthodox configurations, which will be of interest in the future. Thus, the accuracy of rotary-balance experiments has to be investigated in order to assess the situation and possibly suggest remedies in the form of modifications of the experimental techniques or corrections to data.

The availability of several rotary balances in the various NATO countries provides AGARD with a unique opportunity to examine systematically some of the above concerns by conducting a carefully designed series of experiments, in which:

(a) the same model is tested on different rotary balances, each in its own wind tunnel;

(b) the same model is tested on the same rotary balance in different wind tunnels; and

(c) the same model is tested on a particular rotary-balance/wind-tunnel combination, in an open and a closed test section, in a slotted-wall facility and/or with the wind-tunnel walls lined with sound-absorbing material.

Some of the models that could be considered for such a series of experiments include a model of an F-4 aircraft (with a modified nose), a model of a preliminary configuration of the French ACF or the Standard Dynamics Model. Some of these models already exist in a scale which would be compatible with several available rotary balances and wind tunnels.

At least two of the rotary balances discussed in Chapter 3 (at BAe, RAE and possibly DFVLR) have been used or can be used in more than one wind tunnel.

At least two of the participating organizations (DFVLR and AerMacchi) have the capability to change or vary the wall geometry from an open to a closed test section; this includes, in the case of DFVLR, the possibility of using slotted walls.

The value of the experiments could, in some cases, be further increased by studying the effect of dummy parts of a support system, by examining the effects of higher speeds (where possible), and by including measurements of the unsteady wall pressures to help assess possible upstream effects of fluctuating wake blockage. Even so, and particularly in the case of unsteady experiments, it may be difficult to separate aerodynamic effects due to tunnel-wall interference and support interference; additional experiments, perhaps involving some of the concepts discussed in Chapter 6, may be needed to fully resolve the problem.

The most pressing need, however, is to assess the magnitude of the possible overall inaccuracy of the rotary-balance data. This can be done most efficiently by a series of experiments, preferably on two geometrically widely different models, using several rotary-balance/wind-tunnel combinations as per (a) above. The limited results available confirm that these possible inaccuracies can indeed be considerable (see Section 5.1 and 5.2), and, therefore, there is a need to continue the experiments as per (b) and (c) above, in order to identify the causes of the observed differences in more detail.

No conclusive comparison of rotary-balance data obtained in two different facilities has ever been documented. One set of data that could be so compared is shown in Figures 12-1 and 12-2. The data were obtained on two models representing the same aircraft but built to somewhat different geometrical specifications and the Reynolds number of the two tests was not the same. Another such comparison was discussed in Section 7.5.5 and shown in Figures 7-65 to 7-67. Although the results were nearly the same at $\alpha = 20°$, significant differences were observed at $\alpha = 60°$ between tests in two facilities of different size. It seems likely that the discrepancies were caused by differences in the unsteady wall interference in the two facilities (see Section 5.2). However, although the model, the rotary balance and the test Reynolds number were all the same, there were differences in the geometry of the rig support structure and in the levels of free-stream turbulence in the two wind tunnels. Thus the interpretation is not conclusive and a set of carefully planned and executed experiments which are specifically intended to clarify possible inaccuracies is still needed.

12.1.2 Prediction of Rotary Aerodynamics

As discussed in detail in Chapter 8, the complexity of unsteady flows associated with high-angle-of-attack angular maneuvers prevents the immediate development of reliable analytical or computational methods for prediction of rotary flows. In order to render such developments possible in the future there is a need to:

(a) substantially increase our understanding of the physics of rotary flows;

(b) provide systematic high-quality wind-tunnel data to be used for validation of future analytical or computational methods; and

(c) obtain reliable "bench mark" aerodynamic data in flight to address the problem of extrapolation of wind-tunnel data to full-scale conditions.

Objectives (a) and (b) can be attained by performing a carefully controlled set of rotary balance tests on (1) a schematic configuration, such as the Standard Dynamics Model, and (2) a model of an actual fighter aircraft. The tests should include as many flow diagnostic elements as possible, such as flow visualization and pressure measurements on critical parts of the models. In order to gain a good insight into the detailed flow phenomena the tests should also include some experiments with a successive build-up of model components.

Since the amount of work required is rather substantial, probably no single organization could undertake such a project in its entirety. By dividing the total effort among several NATO rotary-balance centers, the individual effort required would become manageable.

Objective (c) requires resources outside the NATO rotary-balance community but still accessible to several of the participating organizations and countries. Obtaining aerodynamic data in full-scale flight maneuvers and comparing them with wind-tunnel results obtained under (b) would provide validation of methods used for predicting Reynolds number effects

12.1.3 Simulation and Analysis of Complex Motions

As indicated in Chapter 10, the only wind-tunnel dynamic test data generally available are from separate rotary and oscillatory experiments, where the rotary data are in the form of aerodynamic coefficients obtained for various spin rates and the oscillatory data are given as static and dynamic derivatives. Such an aerodynamic input is usually adequate for predicting fully developed spin, but becomes questionable when trying to predict more complex motions, especially those involving large excursions and high rates such as are representative of high-angle-of-attack maneuvers, flight in the post-stall regime, departure and spin entry. For such more complex situations, experimental simulation of a combination of the rotary and oscillatory motions is needed. If the oscillatory component of such a combined motion is small the results may be presented as static and dynamic stability derivatives in the presence of rotation. If the oscillatory component is large, some nonlinear methods of representation, such as proposed by Hanff,[4] may have to be utilized.

Needless to say, any simulation of such complex motions in a wind tunnel meets with considerable practical difficulties and, therefore, has only recently been explored. Several conceptual methods of combining the rotary and oscillatory motions or of producing oscillatory perturbations of a steady rotary motion have already been examined in this report, namely:

(a) oscillatory coning, such as already in use at ONERA-IMFL (described in Chapter 4);

(b) orbital fixed-plane motion, as studied at NAE (described in Chapter 6.1);

(c) orbital-platform epicyclic coning (OPLEC), as proposed by NAE (described in Chapter 6.2);

(d) magnetic suspension, as examined at NASA Langley (described in Chapter 6.3); and

(e) oscillatory motion in a rotating-flow test section, as already initiated by NASA Langley.

With several conceptual methods being considered or being actively developed at three of the participating organizations, there is a unique opportunity to coordinate the efforts in order to evaluate the emerging results and assess the comparative advantages and disadvantages of each method. Of particular interest here is the effect of superposing rotary flows on the oscillatory derivatives measured, as well as the adaptability of each method to simulate actual flight maneuvers and, consequently, the importance of obtaining the most representative aerodynamic input to be used with appropriate mathematical models to predict such maneuvers.

12.1.4 Optimization of Flight Mechanics Predictions

As pointed out in Chapter 9, although flight dynamicists commonly use three- or six-degree-of-freedom equations to predict high-alpha aircraft motions, the actual formulation of the aerodynamic mathematical model and the associated computational technique used can vary considerably among the various NATO organizations. Also, the accuracy of the flight dynamics prediction (as compared to spin tunnel or flight) can be strongly dependent on the assumptions made and the type and quality of the aerodynamic input used. The availability of high-quality rotary data, such as would be obtained as the result of subprograms discussed in Sections 12.1.1, 12.1.2 and 12.1.3, coupled with the existence of several mathematical models and procedures in the various NATO countries, would afford a unique opportunity to assess the adequacy of the different approaches for a few typical maneuvers and to optimize the data base required and the computational technique used. This could be achieved by:

(a) inserting existing data and, when available, high-quality data obtained in the three subprograms previously discussed in the mathematical models used by various organizations and comparing the resulting predictions of a few typical maneuvers;

(b) comparing the predictions so obtained with the results of spin-tunnel or flight tests, in order to validate the mathematical models;

(c) comparing, for validated models and predictions, the time and cost of obtaining the solutions, in order to optimize the procedures; and

(d) assessing the sensitivity of predictions to systematic variations in the aerodynamic data base in order to establish realistic accuracy requirements for determining these data experimentally.

It is believed that the cooperative program suggested here would:

(1) make good use of the unique opportunities offered by AGARD;

(2) result in a much better definition of the requirements for experimental and modeling techniques than that presently available; and

(3) result, in the long run, in better aircraft dynamics prediction capabilities or less expensive and faster predictions, or both.

12.2 REFERENCES

1. Gates, S. B.; and Bryant, L. W.: The Spinning of Aeroplanes British ARC R&M 1001, 1926

2. Bamber, M. J. ; and Zimmerman, C. H.: The Aerodynamic Forces and Moments Exerted on a Spinning Model of the NY-1 Airplane as Measured by the Spinning Balance. NACA TR 456, February 1933

3. Allwork, P. H.: A Continuous Rotation Balance for the Measurement of Yawing and Rolling Moments in a Completely Represented Spin. British ARC R&M 1579, 1934.

4. Hanff, E. S.: Dynamic Nonlinear Airloads—Representation and Measurement. AGARD CP-386, Paper 27, 1985.

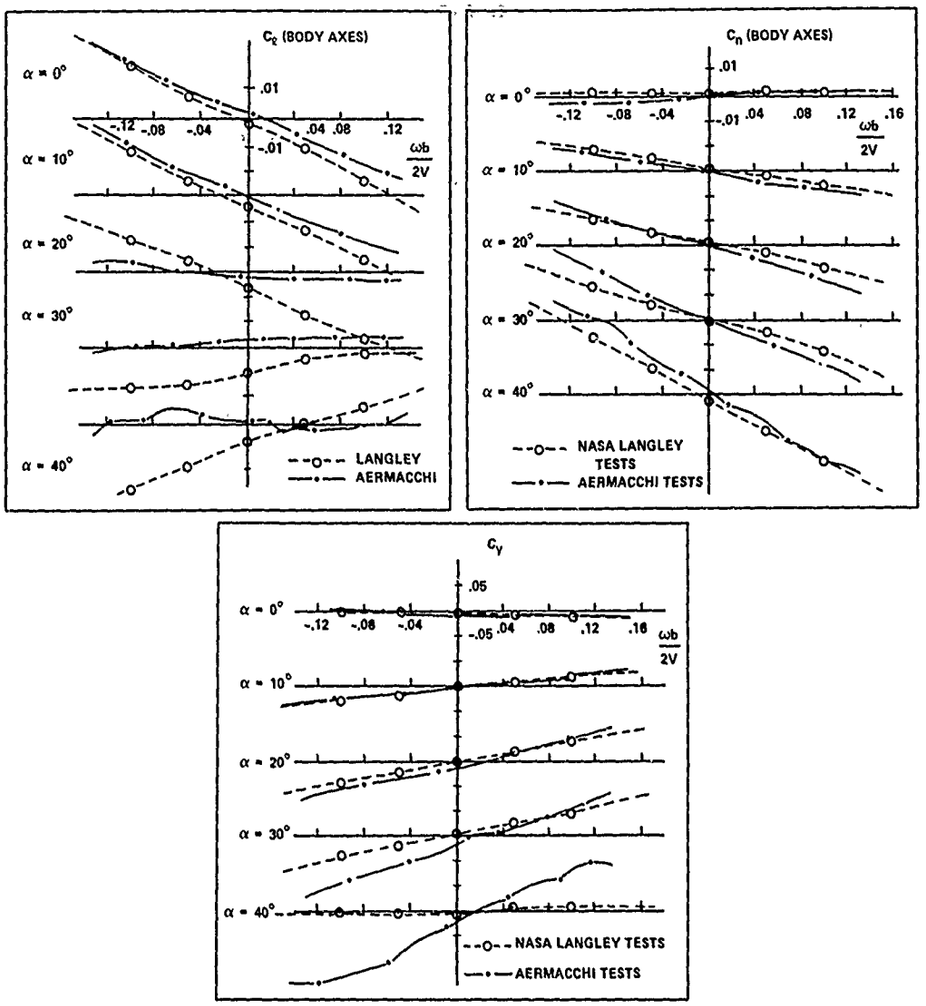

Figure 12-1. Lateral-directional aerodynamic coefficients as functions of the spin parameter.

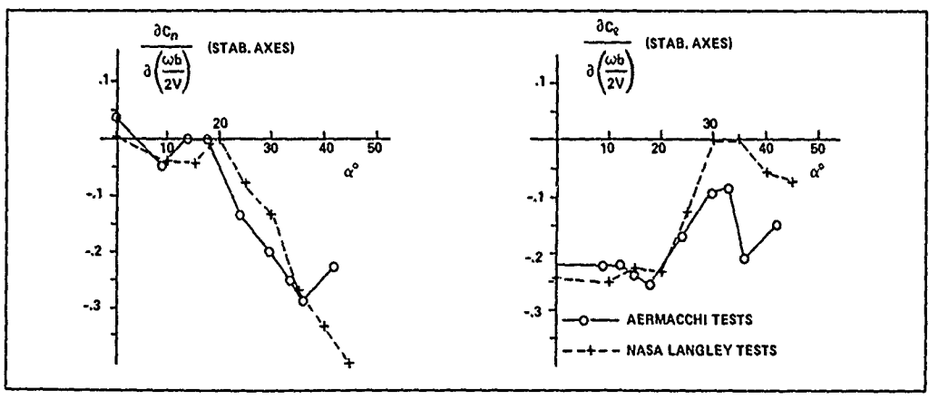

Figure 12-2. Lateral-directional moment derivatives as functions of angle of attack.

CHAPTER 13

SUMMARY AND RECOMMENDATIONS

This report constitutes the first comprehensive text on rotary-balance techniques and their application to aircraft dynamics predictions. Part I on Experimental Techniques contains information on the history, development and general nature of the test techniques, details about the rotary apparatuses used in various countries, descriptions of the present and future advanced versions of the rotary-balance techniques and, finally, an assessment of the aerodynamic interference effects and viscous-flow considerations that are applicable to this type of experiment. Part II on Test Results and Applications begins with a presentation of a comprehensive set of examples of rotary data, illustrating significant trends and effects of both configuration variables and test conditions, and is followed by a discussion of the fluid dynamics of rotary flows, a review of the mathematical models and procedures employed in various countries in the prediction of flight dynamic behavior of aircraft and, finally, correlations with oscillatory test data and with sub-scale and full-scale flight tests. The report concludes with a chapter in which some of the more important remaining problems are identified and in which research activities required to study and hopefully resolve these problems are proposed, possibly as an AGARD cooperative program. The report also contains a selected, annotated bibliography of the pertinent reports and publications.

It is expected that the report will be useful not only to the present and future practitioners of rotary-balance techniques but also to a large number of scientists and engineers involved in aircraft design and, in particular, in the prediction of aircraft dynamic behavior. As is strongly emphasized in the report, the latter should involve not only dynamic behavior during incipient and fully-developed spin, but also during rapid high-angle-of-attack maneuvers that are characteristic of present and future fighter aircraft. In addition, the significant amount of rotary-balance data compiled should provide a valuable input for validating future CFD codes that no doubt will be developed for prediction of flow fields and aerodynamic reactions on aircraft performing rotary motions.

Some of the areas identified in the report which will require further attention include:

(1) Accuracy of Rotary-Balance Experiments, including the effect of aerodynamic interference.

(2) Prediction of Rotary Aerodynamics, including the interpretation of sub-scale results in terms of full-scale conditions.

(3) Simulation and Analysis of Complex Motions, as part of the required expansion of the available mathematical models to more realistic scenarios.

(4) Optimization of Flight Mechanics Predictions, including validation of mathematical models and sensitivity studies for determination of realistic accuracy requirements for experimental data.

The Working Group strongly recommends setting up of an AGARD FDP Cooperative Research Program on "Rotary Experiments for Maneuvering Aircraft Dynamics," to address the above problem areas as outlined in more detail in Chapter 12 of the report.

The ever-increasing demands on aircraft maneuverability, coupled with the advent of more and more complex and unorthodox configurations, have greatly emphasized the need to have access to a high-quality, dependable aerodynamic data base for better prediction of aircraft behavior during intended or undesired rotary motions. At the present time, this data base can only be obtained through experimental means. The appreciation of the importance of this requirement is steadily growing, as witnessed by the considerable developments in this field that have occurred during the short period (3 years) of the existence of the Working Group. It is imperative that this momentum be maintained and that the necessary efforts be undertaken to clarify and resolve some of the remaining problems in measuring aerodynamic data for aircraft performing rotary motions, and in making use of such data in predicting aircraft dynamic behavior.

CHAPTER 14

BIBLIOGRAPHY

ROTARY BALANCES - A SELECTED, ANNOTATED BIBLIOGRAPHY

This Bibliography with abstracts is reproduced with the permission of NASA from their Technical Memorandum 4105.

BIBLIOGRAPHY

1 *Glauert, H.: **The Investigation of the Spin of an Aeroplane.** British ARC R&M 618, June 1919, 45 pp.

Langley Research Center library number 1104.3
35

This paper discusses the characteristics of a spin. It describes the first scientific experiments on the behavior of an airplane in a spin which were carried out in 1916. It discusses some laboratory experiments, later carried out at the National Physical Laboratory, and analyzes the results. It presents dangers involved in spinning, stresses on the wing structure, and causes of accidents during spinning. The paper discusses the mathematical theory and the need for steady-state rotational flow aerodynamics for spin analysis. The author attempts to calculate data theoretically using strip theory. Two appendices are: "Major F. W. Goodden's Report on the Spinning of an 'F' Aeroplane," and "Experiments Using a Twisted Aerofoil."

*National Physical Laboratory, Teddington, UK

2 *Relf, E. F.; and *Lavender, T.: **A Continuous Rotation Balance for the Measurement of L_p at Small Rates of Roll.** British ARC R&M 828, (Ae. 79) Aug. 1922, 4 pp. (1 folding diagram).

Langley Research Center library number 5341.2
NPL/6

This report describes an apparatus to measure the variation of rolling moment with angular velocity of roll when the latter quantity is small. It does this either for a complete model aeroplane or for wings alone. The R.A.E. has recently constructed a similar apparatus, but this was not intended for use at very low rotational speeds. It is not suitable for that purpose because the measurement of rolling moment includes the friction of the supporting bearings. The present apparatus substitutes a two-point support for the ball bearings of the R.A.E. design. Also, the gear-ratio between motor and model is much greater, to secure steady rotation at a very low speed. The paper includes drawings of the apparatus and the procedure for using it.

*National Physical Laboratory, Teddington, UK

3 *Lavender, T.: **A Continuous Rotation Balance for the Measurement of Pitching and Yawing Moments Due to Angular Velocity of Roll (M_p and N_p).** British ARC R&M 936, (Ae. 157), Feb. 1925, 3 pp. (2 figs.)

Langley Research Center library number 5341.2
NPL/10

R. & M. 828 (see entry 2) gives a description of a continuous rotation balance for the measurement of L_p at small rates of roll. We have modified this apparatus to allow a continuous rotation of the model about an axis parallel to the wind, while permitting a small angular oscillation about a second axis at right angles to the wind. We can arrange this second axis either as a *pitch* or a *yaw* axis. As in the L_p apparatus, the small electric motor through a suitable reduction gear (in this case a double spur gear, substituted for the worm) drives the hollow shaft mounted on ball bearings. We suspend the whole assembly from the roof of the wind tunnel by wires. The apparatus itself is supported on hardened steel points and cups.

*National Physical Laboratory, Teddington, UK

4 *Gates, S. B.; and **Bryant, L. W.: **The Spinning of Aeroplanes.** British ARC R&M 1001, (Ae. 242), 1926, 128 pp.

Langley Research Center library number 1104.3
18

Note: For another form of this report see Royal Aeronautical Society Journal, July 1927, pp. 619-688.

This report is a comprehensive survey of recent work in England on the subject of spinning. The problem is extraordinarily complex, and a complete solution can only follow the production of much more experimental data than is available. Nevertheless, we have made much solid progress in fundamental parts of the subject with the comparatively rudimentary material at our disposal. The geometry and the mechanics of the steady spin are now understood in general outline. It is our intent to put on record this knowledge, the evidence on which it rests, and speculations regarding the character of the accelerated motions of entry to, and recovery from, the steady spin. We have recently planned an elaborate experimental programme involving a radical change in wind-tunnel technique, but we cannot expect this to bear fruit for a long time. Now seems to be a favourable moment for taking stock of the progress already made. The paper notes we must replace the rotation balances in wind tunnels by a more effective apparatus.

*Royal Aircraft Establishment, Bedford, UK
**National Physical Laboratory, Teddington, UK

5 *Irving, H. B.; and *Batson, A. S.: **Further Experiments on a Model of the "Bantam" Aeroplane With Special Reference to the "Flat Spin."** British ARC R&M 1107, (Ae. 284), June 1927, 37 pp.

Langley Research Center library number 1104.3
BAT Bantam/2

We have extended the incidence range of previous experiments from about 40° to nearly 90° and made measurements of the three moments due to rolling about the wind axis through the center of gravity of the aeroplane. We have studied the contribution of the tail to these moments in some detail. We have measured the effect of rolling on drag for the complete model and for body with tail. The paper includes an appendix entitled "Notes on Measurement of Yawing and Pitching Moments Due to Rolling."

*National Physical Laboratory, Teddington, UK

6 *Irving, H. B.; and *Batson, A. S.: **Experiments on a Model of a Single Seater Fighter Airplane in Connection With Spinning.** British ARC R&M 1184, (Ae. 347), May 1928, 19 pp.

Langley Research Center library number 1105 62
1

This paper describes the behaviour of the tail unit in a spin at a very large angle of incidence. We measured the pitching moments on a model of a single seat fighter which had experienced difficulty in recovering from a spin. We made the measurements at the request of the Design Sub-Committee, first with the normal body and tail, then with lengthened body. We made the tests on the rolling balance in the usual manner. We confined our measurements to rolling moments in view of the considerable difficulty previously experienced in obtaining reliable measurements of yawing moments on the Bantam model. In general, the results show the moments due to fin and rudder, largely shielded as they are by the tailplane, are liable to show wide variations of uncertain sign, even though we may expect the change in flow of the air approaching the tail to be slight.

*National Physical Laboratory, Teddington, UK

7 *Harris, T. A.: **The 7 by 10 Foot Wind Tunnel of the National Advisory Committee for Aeronautics.** NACA TR 412, 1931, 7 pp.

Langley Research Center library number 5341
NACA
7' x 10'/1

This report describes the 7 by 10 foot wind tunnel and associated apparatus of the National Advisory Committee for Aeronautics. Included are calibration test results and typical data from both static force tests and autorotation tests made in the tunnel. The tunnel has a 6-component indicating balance, on which we measure, directly and independently, the forces and moments. We make all tests at the same dynamic pressure on models having the same area and aspect ratio. This way we obtain the results in coefficient form and require very little time to reduce the test data. We can also use the balance for making stable autorotation tests or for measuring the rolling moment due to roll. In such cases we replace the force-test model support with one designed for rotation tests.

*Langley Memorial Aeronautical Laboratory, NACA (became NASA), Langley Field, Va., USA

8 *Knight, M.; and *Wenzinger, C. J.: **Rolling Moments Due to Rolling and Yaw for Four Wing Models in Rotation.** NACA TR 379, 1931, 24 pp.

This report presents results of autorotation and torque tests on four wing systems at various rates of roll and at several βs. The test covered an α range up to 90° and βs of 0°, 5°, 10°, and 20°. We made tests in the 5-foot, closed-throat atmospheric wind tunnel of the National Advisory Committee for Aeronautics. The object of the tests was primarily to determine the effect of β on the rolling moments of the rotating wings up to large αs. We found at αs above maximum lift the rolling moments on the wings due to yaw (or side slip) from 5° to 20° were roughly the same as those due to rolling. There was a wide variation in the rolling moment due to yaw angle with both α and with pb/2V. The rates and ranges of stable autorotation for the monoplane models were considerably increased by yaw, where, for an unstaggered biplane, they were little affected. The immediate cause of the rolling moment due to yaw is apparently the building up of large loads on the forward wing tip and the reduction of loads on the rearward wing tip. The rolling moments were measured on a small electric dynamometer designed especially for the purpose.

*Langley Memorial Aeronautical Laboratory, NACA (became NASA), Langley Field, Va., USA

9 *Bamber, M. J.; and *Zimmerman, C. H.: **The Aerodynamic Forces and Moments Exerted on a Spinning Model of the NY-1 Airplane as Measured by the Spinning Balance.** NACA TR 456, Feb. 1933, 12 pp.

NACA TR 456

The tests were made on the spinning balance developed for use in the 5-foot vertical wind tunnel of the NACA. The wind tunnel is of the open-jet type. This spinning balance has 6-components from which we obtain wind-tunnel data for any of a wide range of spinning conditions. We made the present series of tests to study the effects of changes in Reynolds Number, attitude, and elevator and rudder settings on the aerodynamic forces and moments on a model when spinning. We used a model of the NY-1 airplane to compare the tunnel data with data obtained from full-scale spins of the airplane. We conclude this spinning balance is a practical and economical method of obtaining valuable data on the aerodynamic forces and moments given by a spinning model and its component parts.

*Langley Memorial Aeronautical Laboratory, NACA, Langley Field, Va., USA

10 *Allwork, P. H.: **A Continuous Rotation Balance for the Measurement of Yawing and Rolling Moments in a Completely Represented Spin.** British ARC R&M 1579, 1934, 6 pp. and illustrations and with an appendix on the Experience Gained in the Use of the Apparatus by H. B. Irving and A. S. Batson.

Langley Research Center library number 5141.2
NPL/11

This paper describes a balance installed in the British NPL 7-ft wind tunnel. We designed the balance to measure yawing moments about an aeroplane body axis due to continuous rotation about the axis. The radius of spin is variable from zero to 12 inches. The maximum rate of spin is three revolutions per second. We can set the model at any presentation to the wind within limits. We propose the apparatus be further developed to measure pitching and rolling moments about body axes, and also total drag.

*National Physical Laboratory, Teddington, UK

11 *Bennett, C. V.; and *Johnson, J. L., Jr.: **Experimental Determination of the Damping in Roll and Aileron Rolling Effectiveness of Three Wings Having 2°, 42°, and 62° Sweepback.** NACA TN-1278, May 1947, 19 pp.

NACA TN-1278

The damping tests and aileron-rolling-effectiveness tests were made in the Langley 15-foot free-spinning tunnel on a special stand which was free in roll about the wind axis. The paper includes a photograph of the stand as set up for rotation tests. It also includes a sketch of the stand as set up to measure rolling moments with a calibrated torque rod. We obtained the damping in roll of the wings from steady-rotation tests on the roll stand and static rolling-moment tests. We obtained the stand and wing rotation by deflecting the vane. In steady rotation, we assumed the forcing moment to be equal to the damping moment and of opposite sign.

*Langley Memorial Aeronautical Laboratory, NACA, Langley Field, Va., USA

12 *MacLachlan, R., and *Letko, W.: **Correlation of Two Experimental Methods of Determining the Rolling Characteristics of Unswept Wings.** NACA TN-1309, May 1947, 9 pp. (diagrs, photos, curves)

Langley Research Center library number 1115.5
624

We must have accurate values of the dynamic lateral-stability derivatives of the airplane to predict either its dynamic stability or its motions resulting from movement of the lateral controls. Included in the present study are two methods by which we may measure the derivatives resulting from roll. The first of these methods, used in the past by NACA, provides for forced rotation of the model in a straight air stream. The second method provides for rotation of the air stream (rolling flow) with the model fixed. A tapered wing and two geometrically similar rectangular wings were measured both in rolling flow with the wing stationary and in straight flow with forced rotation of the wing to obtain a correlation between the two methods and to determine the rolling characteristics of the wings. For unswept wings the rolling characteristics (the rate of change of rolling-moment coefficient and the rate of change of aileron hinge-moment coefficient with rolling velocity) obtained by rotation of the air agreed with those obtained by forced rotation of the wing. Calculated values of the rolling characteristics of the three wings checked closely with the experimental values.

*Langley Memorial Aeronautical Laboratory, NACA, Langley Field, Va., USA

13 *Ribner, H. S.: **The Stability Derivatives of Low-Aspect-Ratio Triangular Wings at Subsonic and Supersonic Speeds.** NACA TN 1423, 1947, 34 pp.

NACA TN 1423

This paper treats low-aspect-ratio wings having triangular plan forms by assuming the flow potentials in planes at right angles to the long axis of the airfoils are similar to the corresponding two-dimensional potentials. We obtain pressure distributions caused by downward acceleration, pitching, rolling, sideslipping, and yawing for wings with and without dihedral. We expect the stability derivatives calculated from these distributions to apply at both subsonic and supersonic speeds, except for the transonic region, up to a limiting speed at which the triangle is no longer narrow compared with the Mach cone from its vertex.

*Langley Memorial Aeronautical Laboratory, NACA, Langley Field, Va., USA

14 *Ribner, H. S.; and *Malvestuto, F. S., Jr.: **Stability Derivatives of Triangular Wings at Supersonic Speeds.** Rep. No. 908 1948, 9 pp.

This paper extends the analysis given in NACA TN No. 1423, to apply to triangular wings having large vertex angles and traveling at supersonic speeds. The lift, rolling moment due to sideslip, and damping in roll and pitch for this case are treated elsewhere using the theory of small disturbances. We use the surface potentials for cand rolling taken therefrom to obtain the several side-force and yawing-moment derivatives that depend on leading-edge suction, and a tentative value for the rolling moment due to yawing. We obtain the lift and moment due to downward acceleration using an unpublished unsteady-flow solution. All known stability derivatives of the triangular wing at supersonic speeds, regardless of source, are summarized and presented with respect to both body axes and stability axes. The results apply only to Mach numbers for which the triangular wing lies within the Mach

cone from its vertex. The spanwise variation of Mach number in the case of yawing is regulated, although the effect must be of importance.

*Langley Memorial Aeronautical Laboratory, NACA, Langley Field, Va., USA

15 *Polhamus, E. C.: **A Simple Method of Estimating the Subsonic Lift and Damping in Roll of Sweptback Wings.** NACA Tech. Note 1862, Apr. 1949, 20 pp.

NACA TN-1862

A method of modifying existing correction factors of lifting-surface theory to account approximately for the effects of sweep has been derived. We have applied these factors to existing lifting-line theories for the lift and damping in roll of swept wings. Despite the simplicity of the resulting formulas the agreement with experimental data for low speeds is very good. We express the equation for lift entirely in terms of the geometric characteristics of the wing and the section-lift-curve slope. This eliminates the necessity for any charts. The equation for the damping in roll, however, requires a chart to determine the effective lateral center of pressure for rolling moment due to rolling. If we use the Glauert-Prandtl transformation, we can apply the formulas obtained to swept wings at subsonic speeds below the critical speed.

*Langley Memorial Aeronautical Laboratory, NACA, Langley Air Force Base, Va., USA

15A *Kuhn, Richard E.; and Wiggins, James W.: **Wind-Tunnel Investigation to Determine the Aerodynamic Characteristics in Steady Roll of a Model at High Subsonic Speeds.** NACA RM L52K24, Jan. 1953, 39 pp.

This paper presents data taken during steady-roll tests of a complete swept-wing model and its component parts. It also describes the forced-roll sting-support system. The model was rotated about the x-stability axis. The angle of attack was changed by using offset sting adapters. The model was driven by a constant-displacement reversible hydraulic motor, located inside the main sting body. The motor was driven by a variable-displacement hydraulic pump driven by a constant-speed electric motor. Speed of rotation was varied by controlling the fluid displacement of the pump. The direction of rotation was changed by reversing the flow through an arrangement of electrically controlled solenoid valves in the hydraulic system. The forces and moments, measured by an electrical strain-gage balance inside the model, were transmitted to the recording devices through brushes and slip rings.

16 *Billion, E.: **Elementary Model for the Study of Dynamic Stability.** Presented at the AGARD Wind Tunnel and Model Testing Panel meeting, Paris, Nov. 2-6, 1954, 19 pp., in French. (English translation attached)

Langley Research Center library number N-34313

This paper describes the model and gives a report of the experiment. It also gives a brief description of the stability balance and the calculation of the damping-in-roll coefficient C_p by electrical analogy.

*ONERA/CERT, BP 4025, 31055 Toulouse Cedex, France

17 *Johnson, J. L., Jr.: **Low-Speed Measurements of Rolling and Yawing Stability Derivatives of a 60° Delta-Wing Model.** NACA RM L54G27, Dec. 1954, 17 pp.

NACA RM L54G27

This paper contains results of a study in the Langley free-flight tunnel to determine the low-speed rolling and yawing stability derivatives of a 60° delta-wing model from 0° to 30° α. The derivatives were measured by the free-to-damp oscillation technique and by the steady-roll technique.

*Langley Memorial Aeronautical Laboratory, NACA, Langley Field, Va., USA

18 *Kolb, A. W.; and *Little, F. W.: **A Rotary Balance System for Model Spin Investigations in Wind Tunnels.** Wright Air Development Center TN 59-316, Sept. 1959, 16 pp.

Langley Research Center library number N-78446

We developed a rotary balance to advance the testing techniques used in model spin investigations. The balance is capable of measuring forces and moments on spinning or tumbling models. The force measuring system has an accuracy comparable to a static balance system. The hydraulic balance drive system has excellent speed regulation and small physical size with high torque output. This paper discusses in detail the balance, its capabilities, calibration procedures, and test performances.

*Wright Air Development Center, Wright Field, Ohio, USA

19 *DeMeritte, F. J.: **The Correlation of Range and Wind-Tunnel Dynamic Stability Measurements.** NAVORD Rep. 6765, Aerodynamics Research Rep. 78, Dec. 7, 1959, 19 pp.

Langley Research Center library number N-86322

This paper describes techniques used to measure pitch damping, roll damping, and Magnus forces and moments in wind tunnels. It compares wind-tunnel data with ballistic range results. The comparison of the measurements made in the wind tunnel and firing ranges shows the data are in good agreement.

*Naval Ordnance Lab., Silver Springs, MD, USA

20 *Heyser, A.: **Aerodynamic Measurement Technique, a report on the third meeting of subcommittee (aerodynamische messtechnik bericht uber die 3.sitzung des unterausschusses.)** Rep. # WGLR-8/1963, 1963, 153 pp., in German.

N64-21695#

This report contains a section by E. Klinke** which describes the measurement apparatus of multi-component installable rotary balances. A study is made of the rotating behavior of a model rotating about its center of gravity. The report also describes model rotation about the stream axis, X_s, of the wind tunnel at different rotation angular velocities, ω, and for variable stagnation pressure, q.

*Wissenschaftliche Gesellschaft fuer Luft- und Raumfahrt, Cologne, West Germany
**Entwicklungsring Sued, Munich, West Germany

21 *Judd, M.; and *Goodyer, M. J.: **Some Factors in the Design of Magnetic Suspension Systems for Dynamic Testing.** Presented at the ARL Magnetic Wind Tunnel Model Suspension and Balance Symposium, held at Wright-Patterson Air Force Base, Ohio, Apr. 13-14, 1966. In: Dayton Univ. Summary, ARL-66-0135, (N67-13593), July 1966, pp. 349-385.

N67-13593

This paper discusses some general characteristics, difficulties and limitations of dynamic testing with magnetically suspended models together with possible improvements. It draws parallels between mechanical and magnetic support test techniques. It emphasizes the problem of large acceleration loads. It suggests large reductions of power requirements are possible by making the model so its outside inflexible shape is spring connected with an inner magnetic mass. The mass-spring-mass system is tuned for a desired natural frequency. The paper discusses the effect on the overall feedback characteristics and some practical considerations.

*The University, Southampton S09 5NH, Hampshire, UK

22 *Scherer, M.; and *Aguesse, M-O.: **Etude Analytique de la Vrille. (Analytical Study of the Spin.)** Presented at the AGARD Flight Mechanics Panel Specialists' Meeting held at Churchill College, Cambridge, England, Sept. 20-23, 1966. In: AGARD CP-17, Stability and Control, Part I, (N68-17439), pp. 127-159, in French.

N68-17445#

Results from the first phase of an analytical study to find a method for calculating spin agree with measurements made on a model in free spin in a vertical wind tunnel. We consider the proposed method applicable for calculations with measurements made during the flight of actual

aircraft. We present calculations for the spin of a small delta aircraft model. We eliminated the uncertainties associated with scale effect and inertia constants in these studies in a horizontal wind tunnel. Two configurations were studied; one of spin stabilization and the other of escaping spin. This paper gives details of analytical results, calculations, and applications, including analytical measurements in forced rotation.

*ONERA, BP 72, 92322 Châtillon Cedex, France

23 *Wykes, J. H.; and *Casteel, G. R.: **Comparison of Computer and Flight Test Results for a Spinning Airplane.** Presented at the AGARD Flight Mechanics Panel Specialists' Meeting held at Churchill College, Cambridge, England, Sept. 20-23, 1966. In: AGARD CP-17, Stability and Control, Part I, (N68-17439), pp. 101-125.

N68-17444#

This paper reports a study designed to analytically determine the complete spinning characteristics (spin entry, steady spin, and recovery) of an airplane. We based the study on the assumption we can describe a spinning airplane in the same manner as a rolling airplane. To determine the validity of this assumption, the following were pursued: (1) We analyzed existing flight test data obtained during spin demonstrations of the F-100D to obtain data on the mechanics of spin. (2) We made a low speed wind tunnel test of the F-100D through spin os and sideslip to obtain static aerodynamic stability and control data. (3) We developed a technique for using static aerodynamic data to obtain the rotary derivatives. Using results from the above studies, we made a series of spin calculations using digital computer methods. We compared results of these calculations with flight test data. Results show we can calculate the spin characteristics of an airplane, from incipient spin through recovery phases, using static aerodynamic wind tunnel data and estimated rotary derivatives based on these static test data. The proposed method of calculation enables the systematic study of the effects of several important variables influencing aircraft spin response and, in doing so, serves to prevent expensive redesign in later phases.

*North American Aviation, Inc., Los Angeles, CA, USA

24 *Schueler, C. J.; *Ward, L. K.; and *Hodapp, A. E., Jr.: **Techniques for Measurement of Dynamic Stability Derivatives in Ground Test Facilities.** AGARDograph 121, Oct. 1967, 209 pp., 432 refs.

N68-23768

This paper describes some of the techniques in current use for measuring dynamic stability derivatives in wind tunnels. It emphasizes the important characteristics of balance system design, data reduction methods, instrumentation and typical balance systems. It treats the use of gas bearings for dynamic stability and roll damping. It describes a three-degree-of-freedom balance system employing a spherical gas bearing.

*ARO, Inc., Arnold Air Force Station, Tullahoma, TN 37389, USA

25 *Judd, M.: **The Magnetic Suspension System as a Wind Tunnel Dynamic Balance.** Presented at the 3rd International Congress on Instrumentation in Aerospace Simulation Facilities, Polytechnic Institute of Brooklyn, Farmingdale, New York, May 5-8, 1969. In: ICIASF '69 Record, (A69-35714), pp. 198-206.

TK 7882.M4 I5, 1969, pp. 198-206 A69-35738#

This paper outlines the principles of design and operation of a magnetic suspension system together with the features and problems associated with its use as a dynamic balance. It describes the technique developed to improve resolution of measurement. It presents results for delta wing models chosen because of the availability for comparison of other theoretical and experimental data. We did the work using equipment developed in the University of Southampton.

*Massachusetts Institute of Technology, Cambridge, MA 02139, USA

26 *Schiff, L. B.; and *Tobak, M.: **Results From a New Wind-Tunnel Apparatus for Studying Coning and Spinning Motions of Bodies of Revolution.** AIAA Journal, vol. 8, Nov. 1970, pp. 1953-1957.

A71-10930#

This paper describes a rig which gives either separate or combined coning and spinning motions to a body of revolution in a wind tunnel. It uses a six-component strain gage balance to measure the aerodynamic forces and moments. Tests with a slender cone in coning motion show at small α the side-force and side-moment coefficients normalized by the coning rate are linear functions of α. The slopes are in excellent agreement with the damping-in-pitch coefficients $C_{N_q} + C_{N_{\dot{\alpha}}}$ and $C_{m_q} + C_{m_{\dot{\alpha}}}$. This agreement is predicted by linearized theory. It indicates at small α we can measure the dynamic damping-in-pitch coefficients of a body of revolution as the steady side force and moment coefficients of the body undergoing coning motion. For larger α, where vortices appear on the leeside of the body, the normalized side force and moment coefficients become nonlinear functions of α. Photographs of the vortices show them displaced from the α plane by coning motion. This asymmetric displacement of the vortices persists over the length of the body, making them a possible source of nonlinear side moment.

*NASA Ames Research Center, Moffett Field, CA 94035, USA

27 *Orlik-Rückemann, K. J.: **Dynamic Stability Testing of Aircraft--Needs Versus Capabilities.** Presented at the 5th International Congress on Instrumentation in Aerospace Simulation Facilities, Pasadena, Calif., Sept. 10-12, 1973. In: ICIASF '73 Record, pp. 8-23.

A74-26477

Note: For recent forms of this paper and an abstract see nos. 29 and 32.

*National Aeronautical Establishment, National Research Council, Ottawa, ON K1A OR6, Canada
Contract: NAS2-7279

28 *Covert, E. E.; *Finston, M.; *Vlajinac, M.; and *Stephens, T.: **Magnetic Balance and Suspension Systems for Use with Wind Tunnels.** In Progress in Aerospace Sciences, vol. 14. Oxford and New York, Pergamon Press, 1973, (A74-12203), pp. 27-107.

A74-12204

This paper describes the principles of operation and the design of magnetic balance and suspension systems used to provide interference-free support of models in wind-tunnel tests. We apply the term *balance* to cases where we use the suspension for direct measurement, e.g., we balance unknown aerodynamic forces and torques by (1) known gravitational and inertial forces and torques and (2) magnetic forces and torques given in terms of electric currents. This paper discusses elementary magnetic concepts, generation of forces and torques, system analysis procedures, magnetic field configurations, materials, power supplies, cooling techniques, control systems, and scaling laws.

*Massachusetts Institute of Technology, Cambridge, MA 02139, USA

29 *Orlik-Rückemann, K. J.: **Survey of Needs and Capabilities for Wind Tunnel Testing of Dynamic Stability of Aircraft at High Angles of Attack.** NASA CR-114583, 1973, 128 pp.

N73-22201#

Note: For a later version of this report see no. 32.

This paper gives the results of a survey of future requirements for dynamic stability information for such aerospace vehicles as the Space Shuttle and advanced high performance military aircraft. High α and high-Reynolds number conditions are emphasized. The author reviews the wind-tunnel capabilities in North America for measuring dynamic stability derivatives. He reports an almost total lack of capabilities to satisfy these requirements. He makes recommendations about equipment that should be built to remedy this situation. He describes some of the more advanced existing capabilities, which we use to at least partly satisfy immediate demands.

*National Aeronautical Establishment, National Research Council, Ottawa, ON K1A OR6, Canada
Contract: NAS2-7279

30 *Marchman, J. F., III; *Lutze, F. H., Jr.; and *Cliff, E. M.: **A Facility for the Measurement of Individual Rotary Motion Aerodynamic Stability Derivatives.** Presented at the 6th International Congress on Instrumentation in Aerospace Simulation Facilities, Ottawa, Canada, Sept. 22-24, 1975. In: ICIASF '75 Record (A76-22728), N.Y., Institute of Electrical and Electronics Engineers, Inc., 1975, pp. 169-174.

TK7882.M415 A76-22745

This paper describes a unique wind tunnel, the Stability Wind Tunnel, in the Aerospace and Ocean Engineering Department at Virginia Polytechnic Institute and State University. It can generate curved or rolling flow giving a means to measure pure rotary aerodynamic derivatives. The paper describes the means for providing this capability as well as the modifications made to allow sting mounting of a model with large α and β range. It describes methods of tunnel calibration, testing and data reduction and presents some results of a recent test.

*Virginia Polytechnic Institute and State University, Blacksburg, VA 24061, USA

31 *Bazzocchi, E.: **Stall Behavior and Spin Estimation Method by Use of Rotary Balance Measurements.** Presented at the AGARD Flight Mechanics Panel Specialists' Meeting on Stall/Spin Problems of Military Aircraft held at the von Karman Institute, Brussels, Nov. 18-22, 1975. In: AGARD CP-199 (N76-29245#), pp. 8-1 through 8-16.

N76-29253#

This paper describes wind tunnel studies of stall behavior, evaluation of lateral control devices, measurement of the aerodynamic coefficients to determine lateral-directional stability and the analytical study of spin. This research required the development of special test equipment, measurement methods, and calibration systems. The paper describes the test equipment, its use, and some of the results obtained.

*Aeronautica Macchi S.p.A., Varese, Italy

32 *Orlik-Rückemann, K. J.: **Dynamic Stability Testing of Aircraft--Needs Versus Capabilities.** In: Progress in Aerospace Sciences, TL500.P7, 1975, vol. 16, no. 4, pp. 431-447.

AD-773160 N74-19526#

Note: For an earlier form of this report see no. 29.

This paper presents highlights of a recent survey of the future needs for dynamic stability information for aerospace vehicles such as the Space Shuttle and advanced high-performance military aircraft. The author explains the importance of obtaining this information for high-α high-Reynolds-number flight conditions. A review of the wind-tunnel capabilities in North America for measuring dynamic stability derivatives reveals an almost total lack of such capabilities for Mach numbers above 0.1 at αs higher than 25°. In addition, capabilities to determine certain new cross-coupling derivatives and to obtain information on effects of the coning motion are almost completely lacking. The author makes recommendations regarding equipment needed to remedy this situation. He describes some of the more advanced existing facilities which we can use to satisfy, at least partly, the immediate needs.

*National Aeronautical Establishment, National Research Council, Ottawa, ON K1A OR6, Canada

33 *Finck, H. D.; and *Sachs, G.: **Investigations of the Dynamical Behavior of an Airplane Uadergoing Rolling Motion.** Untersuchung der Flugdynamik beim Rollen. Institut für Flugtechnik, Darmstadt/IFD Nr. 8/76. DCAF E002631, Apr. 5, 1976, 58 pp., in German.

N77-31177#

We studied the dynamics of a highly maneuverable subsonic aircraft during multiple roll around the length axis with a 6 degree of freedom computer program. We accounted for the nonlinear dependencies on the aerodynamic forces and moments. We show the effect of the dynamic derivation of lateral motion on the overall motion. We represent the relationship between the position of the overall rotation vector and the velocity vector.

*Technische Hochschule, Darmstadt, West Germany

34 *Malcolm, G. N.; and **Clarkson, M. H.: **Wind-tunnel Testing With a Rotary-Balance Apparatus to Simulate Aircraft Spin Motions.** Presented at the AIAA 5th Aerodynamic Testing Conference, Arlington, Tex., June 7-9, 1976. In: Technical Proceedings, pp. 143-156. A76-38642#

Tests were made in the Ames 12-Foot Pressure Wind Tunnel on a simple airplane-like model using a rotary-balance rig to simulate a steady spin motion at high α. Tests were at Mach numbers of 0.1 and 0.25 over a wide Reynolds number range with α varying from 45 to 90 deg. During previous tests of the same research model, some difficulties were experienced with measurement accuracy in the low-to-medium range of Reynolds number because of limitations in the sensitivity of the force balances. For the present tests, we built special balances to provide accurate measurements of the nose and tail contributions to spin motions. We also made improvements to the overall test rig. This paper describes the results of this test, including some interesting hysteresis effects with spin rate. We discuss some of the problems associated with rotary-balance tests at high Reynolds numbers. We also describe briefly a new large-scale rotary rig now nearing completion for use in the Ames 12-Foot and 11- by 11-Foot Wind Tunnels.

*NASA Ames Research Center, Moffett Field, CA 94035, USA
**Florida University, Gainesville, FL 32611, USA

35 *Craig, A.: **Development of Capabilities for Stall/Spin Research. Final Rep., 1 June 1975 - 20 June 1976.** NACA CR-148, 287, June 20, 1976, 42 pp.

N76-26221#

Apparatus and techniques were developed for measuring in a low-speed wind tunnel the static and dynamic (rotary balance) aerodynamic data pertinent to spin behavior of a general aviation aircraft. The main results were: (1) collection of static force and moment data for several airplane configurations at αs from 0 to 90 degrees and βs from 0 to 40 degrees; and (2) discovery of difficulties, shortcomings, and unsuitability of some aspects of the rotary balance mount. These were identified for avoidance in a design for a new mount.

*Wichita State University, Wichita, KS 67208, USA
Contract NSG-1189

36 *Chambers, J. R.; *Bowman, J. S., Jr.; and **Malcolm, G. N.: **Stall/Spin Test Techniques Used by NASA.** June 1976.

N76-29258

This paper reports unique test techniques and facilities used to predict the stall/spin characteristics of highly maneuverable military aircraft. Three of the more important test techniques are: (1) flight tests of dynamically scaled models; (2) rotary balance tests; and (3) piloted simulator studies. Recent experience has shown extension of piloted simulation techniques to high α gives insight in to the spin susceptibility of fighter configurations during representative air combat maneuvers. In addition, use of the technique is an effective way to develop and evaluate automatic spin prevention concepts.

*NASA Langley Research Center, Hampton, VA 23665-5225, USA
**NASA Ames Research Center, Moffett Field, CA 94035, USA

37 *Burk, S. M., Jr.; and *Bowman, J. S., Jr.; and *White, W. L.: **Spin-Tunnel Investigation of the Spinning Characteristics of Typical Single-Engine General Aviation Airplane Designs. I - Low-Wing Model A: Effects of Tail Configurations.** NASA TP-1009, Sept. 1977, 92 pp.

N77-33111#

Tests were made on a 1/11-scale model of a research airplane in the Langley Spin Tunnel. The model represents a typical low-wing,

single-engine, light-weight general aviation airplane. We made the test to determine the effects of tail design on spin and recovery characteristics and to evaluate a tail design criterion for satisfactory spin recovery for light airplanes. We also determined the effects of other geometric design features on the spin and recovery characteristics. The results of the test show we cannot use the existing tail design criterion for light airplanes, which uses the tail damping power factor (TDPF) as a parameter, to predict spin-recovery characteristics.

*NASA Langley Research Center, Hampton, VA 23665-5225, USA

38 *Malcolm, G. N.: **New Rotation-Balance Apparatus for Measuring Airplane Spin Aerodynamics in the Wind Tunnel.** Presented at the AIAA 10th Aerodynamic Testing Conference, San Diego, Calif., Apr. 19-21, 1978. In: Technical Papers (A78-32326), pp. 495-502.

AIAA Paper 78-835 A78-32386#

Note: For a later form of this paper see no. 46.

An advanced rotary-balance rig was developed for the Ames 12-ft Pressure Wind Tunnel. Its purpose is to study the effects of spin rate, α and β, and, particularly, Reynolds number on the aerodynamics of fighter and general aviation aircraft in a steady spin. αs to 100° and βs to 30° are possible with spin rates to 42 rad/s (400 rpm) and Reynolds numbers to 30 million/ m on fighter models with wing spans typically 0.7 m. This paper gives a complete description of the new rotary-balance rig, the sting/balance/model assembly, and the operational capabilities.

*NASA Ames Research Center, Moffett Field, CA 94035, USA

39 *Orlik-Rückemann, K. J.: **Techniques for Dynamic Stability Testing in Wind Tunnels.** Presented at the AGARD Fluid Dynamic Panel Symposium, Dynamic Stability Parameters, held in Athens, Greece, May 22-24, 1978. In: AGARD-CP-235, (N79-15061#), Nov. 1978, pp. 1-1 through 1-24, 48 refs.

N79-15062#

This paper gives a systematic review of the methods and techniques used for wind-tunnel measurements of the dynamic stability parameters (derivatives) of an aircraft. It illustrates the review with many examples of experimental equipment available in aerospace laboratories in Canada, France, the United Kingdom, the United States, and West Germany.

*National Aeronautical Establishment, National Research Council, Ottawa, ON K1A OR6, Canada

40 *Malcolm, G. N.; and *Davis, S. S.: **New NASA-Ames Wind Tunnel Techniques for Studying Airplane Spin and Two-Dimensional Unsteady Aerodynamics.** Presented at the AGARD Fluid Dynamics Panel Symposium, Dynamic Stability Parameters, held in Athens, Greece, May 22-24, 1978. In: AGARD-CP-235, (N79-15061#), Nov. 1978, pp. 3-1 through 3-12, 6 refs.

N79-15064#

Two new wind tunnel test rigs were developed at NASA-Ames Research Center. The first is a rotary-balance rig for the Ames 12-Foot Pressure Tunnel to study the effects of Reynolds number, spin rate, and α on the aerodynamics of fighter and general aviation aircraft in a steady spin motion. The second rig provides capability for oscillating a large two dimensional wing (0.5 m chord, 1.35 m span) instrumented with steady and unsteady pressure transducers in the Ames 11 x 11 ft. Transonic Wind Tunnel. This paper gives a complete description of the rigs, their capabilities, and some typical wind tunnel results.

*NASA Ames Research Center, Moffett Field, CA 94035, USA

41 *Matthews, A. W.: **Experimental Determination of Dynamic Derivatives Due to Roll at British Aerospace, Warton Division.** Presented at the AGARD Fluid Dynamics Panel Symposium, Dynamic Stability Parameters, held in Athens, Greece, May 22-24, 1978. In: AGARD-CP-235, (N79-15061#), Nov. 1978, pp. 4-1 through 4-16, 9 refs.

N79-15065#

Two rigs for the determination of dynamic derivatives due to roll are under development at British Aerospace, Warton Division. They use the principle of continuously rolling a model in a wind-tunnel about an axis parallel to the wind. They cover a test envelope up to M = 0.95, R = 46 million/m, α = 90°, pb/2V = 0.25. We have already used one to measure derivatives on complete models at low Mach number and Reynolds number. The second, designed for operation at high subsonic Mach numbers and high Reynolds numbers, is undergoing calibration and commissioning before tunnel installation. This paper describes the general features of the rigs themselves, together with the instrumentation and control systems. It also describes the problems met during design, manufacture, calibration, commissioning and testing, together with their solutions. It presents data from complete models and compares it with data compiled for similar configurations from flight testing and other wind-tunnel sources. The comparison shows we can obtain repeatability of data approaching that achievable in steady-state, six-component testing.

*British Aerospace (Aircraft Group) Warton Division, Warton Aerodrome, Preston, PR4 1AX, Lancashire, UK

42 *Hafer, X.: **Wind Tunnel Testing of Dynamic Derivatives in W.-Germany.** Presented at the AGARD Fluid Dynamics Panel Symposium, Dynamic Stability Parameters, held in Athens, Greece, May 22-24, 1978. In: AGARD-CP-235, (N79-15061#), Nov. 1978, pp. 5-1 through 5-12, 33 refs.

N79-15066#

This paper gives a survey of the activities of the German national working group developing dynamic wind tunnel test installations. Sponsored by the Ministry of Research and Technology, the group planned to develop four different test rigs. So far, they have completed three test rigs. The rigs are now available for routine use, which has been confirmed by many successful tests. Each rig meets very specific test requirements. The paper discusses these requirements in detail. It also gives results of a comparison of tests with the same model mounted on different test rigs in different wind tunnels. It compares the data with some flight test results of the corresponding original plane. Finally, it gives some results of linearized flight dynamic studies to demonstrate the influence of the several dynamic derivatives on the longitudinal and lateral aircraft dynamics. This paper has an excellent reference section.

*Technical University Darmstadt, Petersenstraße 30, 6100 Darmstadt, West Germany

43 *von der Decken, J.; *Schmidt, E.; and **Schulze, B: **On the Test Procedures of the Derivative Balances Used in West Germany.** Presented at the AGARD Fluid Dynamics Panel Symposium, Dynamic Stability Parameters, held in Athens, Greece, May 22-24, 1978. In: AGARD-CP-235, (N79-15061#), Nov. 1978, pp. 6-1 through 6-17, 17 refs.

N79-15045#

The low-speed wind tunnels in West-Germany use three different rigs to measure dynamic stability derivatives on rigid models of aeroplanes and missiles: (1) a mobile oscillatory rig with rigid mechanical drive; (2) a multi-degree-of-freedom forced-oscillation rig with electrodynamic excitation; and, (3) a steady-state forced-roll rig with hydraulic motor drive. This paper gives a short description of the measuring technique and the appropriate derivative evaluation method used with each rig.

*DFVLR, Flughafen, D-3300 Braunschweig, West Germany
**Messerschmitt-Boelkow-Blohm GmbH, Munich, West Germany

44 *Orlik-Rückemann, K. J., Editor: **Dynamic Stability Parameters.** Papers presented and discussions held at the Fluid Dynamics Panel Symposium held in Athens, Greece, May 22-24, 1978. AGARD-CP-235, published Nov. 1978, 636 pp.

ISBN 92-835-0222-X N79-15061#

Note: Included and placed immediately before this total compilation are five separate conference papers pertaining to rotary balances.

Discussed are the specific needs for dynamic stability information of

aerospace vehicles, the form in which it should be presented, and the various means of obtaining it. Includes reports on new developments in wind-tunnel, flight test, and analytical techniques; motion analysis and non-linear formulations; and sensitivity and simulator studies. Specialists discussed a broad range of approaches to the determination of dynamic stability parameters.

*National Aeronautical Establishment, National Research Council, Ottawa, ON K1A OR6, Canada

45 *Thor, W. A.: **An Investigation of the Rolling Stability Derivatives of a T-Tail Fighter Configuration at High Angles of Attack.** Society of Flight Test Engineers, Journal, vol. 1, Jan. 1979, pp. 21-25.

A79-50165

We used a wind tunnel model to study the F-104 high-load-factor stability problem. As we increase α near the stall for the model with a clean wing, roll damping drops off abruptly and yaw due to roll increases negatively (adverse yaw). This characteristics is more pronounced with the wing in the high-lift configuration of 12° leading-edge flap and 13° trailing-edge flap. This is due to the slope of the lift-curve decreasing at an earlier α for the flapped wing. Wing fences, slats, and strakes have a favorable effect on the roll damping and adverse yaw. We consider these to be the simplest and most effective aerodynamic modification to increase roll damping at high αs without degrading the longitudinal characteristics. Wing tip end plates decrease the roll damping at αs below stall.

*Wright-Patterson AFB, Dayton, OH 45433, USA

46 *Malcolm, G. N.: **New Rotation-Balance Apparatus for Measuring Airplane Spin Aerodynamics in the Wind Tunnel.** Journal of Aircraft, vol. 16, no. 4, Apr. 1979, pp. 264-268.

A78-32386

Note: For an earlier form and an abstract see no. 38.

*NASA Ames Research Center, Moffett Field, CA 94035, USA

47 *Tischler, M. B.; and *Barlow, J. B.: **Application of the Equilibrium Spin Technique to a Typical Low-Wing General Aviation Design.** Presented at the AIAA Atmospheric Flight Mechanics Conference for Future Space Systems, Boulder, Colo., Aug. 6-8, 1979. In: Technical Papers (A79-45302), 1979, pp. 32-42.

AIAA Paper 79-1625 A79-45307#

This paper gives a graphical implementation of the equilibrium technique for obtaining spin modes from rotary balance data. Using this technique, we computed spin modes for the NASA Low-Wing General Aviation Aircraft. The computed αs are within 10° of the NASA spin tunnel results. The method also gives information on the dynamic nature of spin modes. This technique provides a great deal of information on spin modes and recovery, using data from a single experimental installation. You can use this technique in the preliminary design phase to provide basic information on aircraft spin and recovery characteristics. This paper discusses results, advantages, and limitations of using this technique.

*Maryland Univ., College Park, MD 20740, USA

Research supported by the Minta Martin Fund for Aeronautical Research

48 *Vanmansart, M.; and *Tristrant, D.: **New Directions in Spin Research.** Presented at the Association Aeronautique et Astronautique de France 16th Colloque d'Aerodynamique Appliquee, Lille, France, AAAF Paper NT 80-12, Nov. 13-15, 1979, 27 pp, in French.

A80-36843#

This paper describes studies recently undertaken or planned at IMF Lille in the field of aircraft spin research. Efforts include better use of telemetered data for comparison of flight and wind tunnel tests. They also include spin animation, and the development of spin testing methods based on free spin model instrumentation. Finally, they include spin initiation in the laboratory and studies using a rotary balance, the study of statistical correlations between aircraft configurations and spin characteristics, and analytical modeling for spin prediction. Spin research has developed considerably in the past three years. This is due to improvements in equipment, the comparison of flight test and vertical wind tunnel data, and the development of new tests specifically adapted to spin studies. All of this allows us to make progress in the understanding of spin phenomena.

*Institute of Fluid Mechanics of Lille, France

49 *Verbrugge, R.: **The IMF Lille Rotation Balance and Associated Experimental Techniques.** Balance rotative de l' IMF, Lille et techniques experimentales associees. Lille no. 79/63, 1979. AAAF paper NT 80-13, Nov. 1979, 50 pp., in French.

A80-36844#

We have developed a rotation balance for wind tunnel simulation of aerodynamic processes at high α. In particular, the balance allows the study of control loss during flight at high α and stall/spin conditions. This paper discusses the performance of the balance in relation to geometrical and kinematic characteristics, mechanical and structural properties, aerodynamic aspects, and data acquisition and processing considerations. We developed the balance as a simulation tool in support of analytical studies of large-amplitude aerodynamic processes involving continuous spin.

*Institute de Mecanique des Fluides de Lille, 5 Blvd. Paul Painlevé, 59000 Lille, France

50 *Lutze, F. H., Jr.: **Experimental Determination of Pure Rotary Stability Derivatives Using a Curved and Rolling Flow Wind Tunnel.** Presented at the AIAA 18th Aerospace Sciences Meeting, Pasadena, Calif., Jan. 14-16, 1980, 8 pp.

AIAA Paper 80-0309 A80-18308#

This paper describes the technique of using a curved and rolling flow wind tunnel to extract pure rotary stability derivatives. It describes the curved flow and the rolling flow test sections of the Virginia Tech Stability Wind Tunnel. It includes methods for obtaining the proper velocity profiles and correcting the data acquired. It presents results from tests of current fighter configurations. It gives particular attention to comparing pure rotary derivatives with combined rotary and unsteady derivatives obtained by standard oscillation tests. It also examines the effect of curved and rolling flow on lateral static stability derivatives.

*Virginia Polytechnic Institute and State University, Blacksburg, VA 24061, USA

Contract NAS1-13175-16

51 *Bihrle, W., Jr.; and **Bowman, J. S., Jr.: **Influence of Wing, Fuselage, and Tail Design on Rotational Flow Aerodynamics Beyond Maximum Lift.** Presented at the AIAA 11th Aerodynamic Testing Conference, Colorado Springs, Colo., March 18-20, 1980. In: Technical Papers (A80-26929), 1980, pp. 237-246. Also: Journal of Aircraft, vol. 18, Nov. 1981, pp. 920-925, 16 refs.

AIAA 80-0455 A80-26955#

Note: For a later version of this paper and an abstract see no. 67.

*Bihrle Applied Research, Inc., Jericho, NY 11753, USA
**NASA Langley Research Center, Hampton, VA 23665-5225, USA

52 *Bihrle, W., Jr.; and *Barnhart, B.: **Spin Prediction Techniques.** Presented at the AIAA Atmospheric Flight Mechanics Conference, Danvers Mass., Aug. 11-13, 1980. In: Technical Papers (A80-45855) pp. 76-82. Also: Journal of Aircraft, vol. 20, no. 2, Feb. 1983, pp. 97-101.

AIAA Paper 80-1564 N80-45863#

The NASA Langley Research Center is responsible for advancing the state-of-the-art of stall/spin technology. This includes developing and confirming experimental and analytical techniques for predicting stall/spin characteristics. As a part of this effort, two and a half years ago we developed a rotary balance rig at the Langley spin tunnel. Its

purpose is to identify rapidly an airplane's aerodynamic characteristics in rotational flow. On-line rotary balance data plots and on-line predicted steady spin modes permit the designer to develop, on site, a configuration highly resistant to spins. Or, for airplanes intended for acrobatic maneuvers or training, one with good spin characteristics, that is, no spin equilibrium conditions possible with lateral-directional controls neutral. The rotary balance data are also used to compute time histories of the incipient, developed, and recovery phases of a spin. This paper discusses these spin analysis techniques and their correlation with spin-tunnel model and full-scale flight results.

*Bihrle Applied Research, Inc., Jericho, NY 11753, USA
Contracts: NAS1-14849 and NAS1-16205

53 *Orlik-Rückemann, K. J.; and *Hanff, E. S.: **Dynamic Stability Parameters at High Angles of Attack.** Presented at the 12th International Council of the Aeronautical Sciences, Congress, Munich, West Germany, Oct. 12-17, 1980. In: ICAS Proceedings, (A81-11601), AIAA, Inc., 1980, pp. 265-277.

TL 505.A24 1980 A81-11624
pp. 265-277

This paper presents a review of some of the fluid dynamics phenomena associated with oscillatory flight at high αs. It gives emphasis to asymmetric shedding of forebody vortices, asymmetric breakdown of leading edge vortices, the oscillatory motion of such vortices, and the time lag between the vortex motion and the causative motion of the aircraft. These phenomena cause a number of important effects on the dynamic stability parameters at high α. These include strong non-linearities with α, significant static and dynamic aerodynamic cross coupling, large time-dependent effects, and a strong configuration dependence. The paper briefly describes new wind tunnel testing techniques to determine all the required direct, cross, and cross-coupling moment derivatives due to oscillation in pitch, yaw, and roll as well as in vertical and lateral translation.

*National Aeronautical Establishment, National Research Council, Ottawa, ON K1A OR6, Canada

54 *Otto, H.: **Roll and Spin Measurements in the Low Speed Wind Tunnel at Braunschweig.** (Roll- und Trudelmessungen im Niedergeschwindigkeits-Windkanal in Braunschweig). DFVLR-Nachrichten, Nov. 1980, pp. 16-18, in German.

A81-15704

This paper examines the measurements of aerodynamic forces and moments on aircraft models undergoing roll and spin movements in wind tunnels. The model carries out a uniform rotary motion on an axis in the direction of the wind. It has a rolling motion when the axis of rotation serves as the reference point of the model. A spin movement occurs when the reference point lies away from the axis of rotation. The assembly has the advantage that we can change the angle of pitch between the model and the axis of rotation by remote control without bringing it to a standstill.

*DFVLR, Hauptabteilung Niedergeschwindigkeits-Windkanäle, Braunschweig, West Germany

55 *Patton, J. M., Jr.: **A Status Report on NASA General Aviation Stall/Spin Flight Testing.** In: Society of Experimental Test Pilots, Technical Review, vol. 15, no. 1, (N80-33337), 1980, pp. 36-49.

N80-33340 or A81-19471

The NASA Langley Research Center has started a comprehensive program involving spin tunnel, static and rotary balance wind tunnel, full-scale wind tunnel, free flight radio control model, flight simulation, and full-scale testing. Work includes aerodynamic definition of various configurations at high αs, testing of stall and spin prevention concepts, definition of spin and spin recovery characteristics and development of test techniques and emergency spin recovery systems. This paper presents some results for the first aircraft (low-wing, single-engine) in the program, in the areas of tail design, wing leading edge design, mass distribution, center of gravity location, and small airframe changes. It also gives associated pilot observations. The paper discusses the design philosophy of the spin recovery parachute system in addition to test techniques.

*NASA Langley Research Center, Hampton, VA 23665-5225, USA

56 *Beyers, M. E.: **A New Concept for Dynamic Stability Testing.** Presented at the AIAA 19th Aerospace Sciences Meeting, St. Louis, Mo., Jan. 12-15, 1981, pp. 5-14. NAE LTR-UA-53, Sept. 1980. Also, Journal of Aircraft, vol. 20, no. 1, Jan. 1983, pp. 5-14.

AIAA Paper 81-0158 A81-20638#

This paper introduces an approach to dynamic stability testing based on the concept of orbital fixed-plane motion. A rig is conceived which forces an aircraft model in an orbital path while constrained to the fixed-plane reference system. The paper gives an exposition of the concept and shows the potential advantages in captive model testing and applications in flight mechanics. Using a single apparatus, it is possible to 1) determine a complete set of first-order dynamic stability derivatives, 2) vary the relationships between the associated motion parameters, and 3) simulate modes of aircraft motion. A validation scheme, which exploits the considerable flexibility of the method, makes it easier to extend the dynamic data to actual flight conditions.

*National Aeronautical Establishment, National Research Council, Ottawa, ON K1A OR6, Canada

57 *McCormick, B. W.: **The Prediction of Normal Force and Rolling Moment Coefficients for a Spinning Wing.** NASA CR-165680, Feb. 1981, 22 pp.

N81-20068#

We used nonlinear airfoil section data for αs from 0° to 180° in a small computer code to integrate numerically the section normal force coefficients along the span as a function of the local velocity and α resulting from the combined spinning and descending motion. We developed a correction to account for the radial pressure gradient in the separated, rotating flow region above the wing. We needed this correction to obtain agreement, both in form and magnitude, with rotary balance test data.

*Pennsylvania State Univ., University Park, PA 16802, USA
NASA Order L-13435-8

58 *Orlik-Rückemann, K. J.: **Review of Techniques for Determination of Dynamic Stability Parameters in Wind Tunnels.** Presented at the NATO/ AGARD Lecture Series on Dynamic Stability Parameters, Moffett Field, Calif., Mar. 2-5, 1981, and Rhode-Saint-Genèse, Belgium, Mar. 16-19, 1981. In: AGARD-LS-114, (N81-31105), May 1981, pp. 3-1 through 3-28, 60 refs.

N81-31108#

This paper discusses the basic principles of various methods of wind tunnel testing and the practical aspects of various techniques. It illustrates these methods by examples, descriptions, and sketches of existing apparatuses. It reviews methods of measuring dynamic derivatives. It also considers the measurement of reaction and of motion, rotary and half model techniques, derivatives due to translational acceleration and pure rotation, free model techniques, and control surface oscillation techniques.

*National Aeronautical Establishment, National Research Council, Ottawa, ON K1A OR6, Canada

59 *Malcolm, G. N.: **Rotary and Magnus Balances** Presented at the NATO/AGARD Lecture Series on Dynam.. Stability Parameters, Moffett Field, Calif., Mar. 2-5, 1981. In: AGARD-LS-114, May 1981, (N81-31105), pp. 6-1 through 6-26, 43 refs.

N81-31111#

This paper describes two wind tunnel techniques for determining part of the aerodynamic information required to describe the dynamic behavior of vehicles in flight. We measure forces and moments three ways: with a rotary-balance in coning motion, a Magnus balance in coning motion, and a Magnus balance in a high-speed spinning motion. Coning motion is important to both aircraft and missiles, and spinning is important for spin stabilized missiles. This paper describes basic principles of both techniques and gives examples of each type of apparatus. This paper

also discusses typical experimental results.

*NASA Ames Research Center, Moffett Field, CA 94035, USA

60 *Chambers, J. R.; *Grafton, S. B.; and **Lutze, F. H.: **Curved-Flow, Rolling-Flow, and Oscillatory Pure-Yawing Wind-Tunnel Test Methods for Determination of Dynamic Stability Derivatives.** Presented at the NATO/AGARD Lecture Series on Dynamic Stability Parameters, Moffett Field, Calif., Mar. 2-5, 1981, and Rhode-Saint-Genèse, Belgium, Mar. 16-19, 1981. In AGARD-LS-114, May 1981, (N81-31105), pp. 7-1 through 7-14, 7 refs.

A81-26933# or N81-31112#

This paper describes the test capabilities of the Stability Wind Tunnel of the Virginia Polytechnic Institute and State University. It gives calibrations for both curved and rolling flow techniques. It describes oscillatory snaking tests to determine pure yawing derivatives. It gives typical aerodynamic data for a current fighter configuration using the curved and rolling flow techniques. It discusses the application of dynamic derivatives obtained in such tests to the analysis of airplane motions in general, and to high α flight conditions in particular.

*NASA Langley Research Center, Hampton, VA 23665-5225, USA
**Virginia Polytechnic Inst. and State Univ., Blacksburg, VA 24061, USA

61 *Orlik-Rückemann, K. J., Editor: **Dynamic Stability Parameters,** AGARD Lecture Series held at Moffett Field, Calif., Mar. 2-5, 1981 and Rhode-Saint-Genèse, Belgium, Mar. 16-19, 1981. AGARD-LS-114, May 1981, 389 pp.
ISBN-92-835-1385-1 N81-31105#

This Lecture Series reviews the impact of high α aerodynamics on dynamic stability characteristics of aerospace vehicles. It surveys analytical, wind tunnel, and flight test techniques. Three papers from this symposium are especially pertinent to the subject of rotary balances. They are included separately as numbers 58, 59, and 60 in this bibliography.

*National Aeronautical Establishment, National Research Council, Ottawa, ON K1A OR6, Canada
Sponsored in part by the von Karman Inst. for Fluid Dynamics

62 *McCormick, B. W.: **Equilibrium Spinning of a Typical Single-Engine Low-Wing Light Aircraft.** Journal of Aircraft, vol. 18, Mar. 1981, pp. 192-199.

A81-31598#

This paper presents a study of rotary balance data, spin tunnel model, radio-controlled model, and full-scale flight results relating to the spinning of light aircraft. It also gives a method for predicting steady spin modes using rotary balance data. It discusses differences in spin characteristics of various wing, tail, and fuselage modifications as well as scale effects. The author concludes the yawing moment coefficient primarily governs an equilibrium flat spin.

*Pennsylvania State Univ., University Park, PA 16802, USA

63 *Schulze, B.: **Development and Trial of a Rotary Balance for the 3 m Low Speed Wind Tunnels in the Federal Republic of Germany: Final Report, Dec. 1979.** DCAF E002631, Rep. no. BMFT-FB-W-81-022, July 1981, 70 pp., in Germar.

ISSN-0170-1339 N82-15083#

Note: For an English version see the following citation.

We developed a rotary balance to determine aerodynamic damping due to rolling using a stationary measuring procedure. Due to the uniform rotation around the wind tunnel axis, we avoid vortex relaxation effects that might result from oscillatory balances. This paper describes the layout, instrumentation, and data processing. Results obtained during different wind tunnel tests with a calibration model correlate well with existing reference data and flight data. We can measure dynamic stability derivatives due to rolling for αs up to 90° and for extreme angles of inclination.

*Messerschmitt-Boelkow-Blohm GmbH, Postfach 80 11 09, D-8000 Munchen 80, West Germany

64 *Schulze, B.: **Development and Trial of a Rotary Balance for the 3m-Low Speed Wind Tunnels of West-Germany.** Presented at the International Congress on Instrumentation in Aerospace Simulation Facilities, Dayton, Ohio, Sept. 30-Oct. 2, 1981, 11 pp.

A83-11082

Note: This paper is not in the ICIASF '81 Record.
For the original German report, see the previous citation.

We have developed a rotary balance for 3 meter low-speed wind tunnels. It allows us to determine dynamic stability derivatives in the wind tunnel on continuously rotating aircraft models. This paper gives principal design aspects of the mechanical set-up and describes the measuring system. Test results from a calibration model on the rotary balance show a good correlation with existing reference data.

*Messerschmitt-Boelkow-Blohm GmbH, Postfach 80 11 09, D-8000, Munchen 80, West Germany

65 *Beyers, M. E.: **Aerodynamic Simulation of Multi-Degree-of-Freedom Aircraft Motion.** Presented at the International Congress on Instrumentation in Aerospace Simulation Facilities, Dayton, Ohio, Sept. 30-Oct. 2, 1981, 10 pp.

Note: This paper is not in the ICIASF '81 Record.

This paper reviews the rationale underlying simulations of high α aircraft motion using constrained as well as free model motions. It discusses concepts for generating several different modes of motion in a wind tunnel, including pitching and heaving, spinning, and wing rock. The methods use the NAE Orbital Apparatus, now being developed, in addition to existing free-flight test facilities. The Orbital Apparatus provides the unique opportunity of simulating aircraft motion on the same rig used to obtain a complete set of dynamic derivatives for the aircraft. We demonstrate its principles of operation using a conceptual apparatus. The exploitation of its capabilities could significantly contribute to the rational implementation of the existing mathematical model and the accuracy of the resulting computational flight simulations.

*National Aeronautical Establishment, National Research Council, Ottawa, ON K1A OR6, Canada

66 *Krag, B.: **Dynamic Simulation in Wind Tunnels.** Presented at the ICIASF '81, International Congress on Instrumentation in Aerospace Simulation Facilities, Dayton, Ohio, Sept. 30, 1981. In: ICIASF '81 Record (A83-11051), pp. 271-282.

A83-11079

The Installation for Dynamic Simulation is a new wind tunnel facility which uses remotely controlled models with a special model suspension rig. This facility allows the study of both rigid body motion and elastic deformations, thus combining flight mechanic and aeroelastic testing. The model is usually of a specific aircraft and is fully instrumented. Computerized model command and control and data processing of measurements are features of the facility. Uses of the facility include the identification of dynamic flight mechanics derivatives, basic research into active control systems technology, and the development of a general aviation aircraft ride smoothing system. This paper also describes the development and testing of four different gust generators used in the simulation of realistic flight environment.

*DFVLR, Institute for Fluid Mechanics, D-3300 Brunswick, West Germany

67 *Bihrle, W., Jr.; and **Bowman, J. S., Jr.: **Influence of Wing, Fuselage, and Tail Design on Rotational Flow Aerodynamics Beyond Maximum Lift.** Journal of Aircraft, vol. 18, Nov. 1981, pp. 920-925.

Note: For an earlier version of this paper see no. 51.

The NASA Langley Research Center has started a broad general aviation stall/spin research program. Researchers at Langley developed

a rotary balance system, located in the spin tunnel, to support this effort. This system makes it possible to identify airplane aerodynamic characteristics in a rotational flow environment, and thereby permits prediction of spins. This paper presents a brief description of the experimental setup, testing technique, and five model test programs. It also gives an overview of the rotary balance results and their correlation with spin tunnel free-spinning model results. We show, for example, a pronounced configuration sensitive nonlinear dependency of the aerodynamic moments on rotational rate. We show fuselage shape, horizontal tail, and, in some instances, wing location to appreciably influence the yawing moment characteristics above $\alpha = 45°$.

*Bihrle Applied Research, Inc., Jericho, NY 11753, USA
**NASA Langley Research Center, Hampton, VA 23665-5225, USA

68 *Beyers, M. E.: **Direct Free-Flight Analysis of Aircraft Dynamics at High Angles of Attack.** In: Aeronautical Society of South Africa and South African Institute of Aeronautical Engineers, Journal, vol. 2, no. 1, 1981, pp. 17-28, 26 refs.

A82-15596

This paper examines concepts for the analysis of high-maneuverability aircraft dynamics from gross flight-dynamic effects observed in wind-tunnel free-flight experiments. It reviews experimental and analytical techniques developed to study the generic non-oscillatory free-flight motion of flight vehicles trimmed at significant α. It demonstrates the feasibility of aircraft model free-flight tests from simulations. Trajectory validation schemes are proposed for the corroboration of free-flight and captive model dynamic data. Finally, the paper examines the rationale underlying the use of data gathered in captive- and free-model dynamic stability tests of high-performance aircraft in the context of design objectives of high maneuverability and good flying qualities.

*South African Council for Scientific and Industrial Research, National Institute for Aeronautical and Systems Technology, Pretoria, Republic of South Africa

69 *Ericsson, L. E.; and *Reding, J. P.: **Review of Support Interference in Dynamic Tests.** Presented at the AIAA 12th Aerodynamic Testing Conference, Williamsburg, Va., March 22-24, 1982. In: Technical Papers (A82-24651), 1982, pp. 166-190, 79 refs. Also: AIAA Journal, vol. 21, Dec. 1983, pp. 1652-1666.

AIAA Paper 82-0594 A82-24668#

A review of information on support interference shows support interference effects are much more severe in dynamic than in static tests. Furthermore, support interference is aggravated greatly by a boat-tail or dome shaped base, even by modest base shoulder roundness, from what it is for a flat-based model. The general conclusion is we should not use asymmetric stings or sting-strut combinations. For slender bodies at low αs a transverse rod comes close to letting us measure the true dynamically destabilizing effect of a bulbous base. However, even a very slender sting distorts the near wake effect and gives an unconservatively high measure of the dynamic stability. At intermediate and high αs the sting support is superior to other support methods: the transverse rod or the strut mounting. Often, half-model testing lets us avoid most of the support interference effects. Sometimes, as for a short blunt body such as the Viking configuration, the best approach is to allow sting plunging, using a very slender sting.

*Lockheed Missiles & Space Co., Inc., Sunnyvale, CA 94086, USA

70 *Orlik-Rückemann, K. J.: **Aerodynamic Aspects of Aircraft Dynamics at High Angles of Attack.** Presented at the AIAA 9th Atmospheric Flight Mechanics Conference, San Diego, Calif., Aug. 9-11, 1982, 15 pp. Also: Journal of Aircraft, vol. 20, no. 9, Sept. 1983, pp. 737-752, 46 refs.

AIAA Paper 82-1363 A82-39836#

Note: This paper is updated in AGARD Rep. 740, Oct. 1987. (See no. 94)

This paper reviews some of the fluid dynamics phenomena associated with the oscillatory flight at high αs. It places particular emphasis on asymmetric shedding of forebody vortices, asymmetric breakdown of leading edge vortices, the oscillatory motion of such vortices, and the time lag between the motion of the vortices and the aircraft. These phenomena cause a number of important effects on the dynamic stability parameters at high αs. These include strong nonlinearities with α, significant static and dynamic aerodynamic cross-coupling, large time-dependent and hysteresis effects, and a strong configuration dependence. The paper emphasizes the need to consider all the aerodynamic reactions in their vectorial form. It discusses the importance of the above mentioned effects on our prediction capabilities of aircraft behavior at α. The author advocates the development of adequate mathematical models and describes the requirements for advanced wind tunnel techniques for performing the necessary oscillatory experiments.

*National Aeronautical Establishment, National Research Council, Ottawa, ON K1A OR6, Canada

71 *Kalviste, J.: **Use of Rotary Balance and Forced Oscillation Test Data in a Six Degrees of Freedom Simulation.** Presented at the AIAA 9th Atmospheric Flight Mechanics Conference, San Diego, Calif., Aug. 9-11, 1982, 11 pp.

AIAA Paper 82-1364 A82-39129#

This paper presents new analysis techniques that will blend the data from rotary balance tests, forced oscillation tests, and computed dynamic derivatives for a nonlinear 6 degree-of-freedom simulation. It uses a component of the rotation vector about the velocity vector with the rotary balance test data. It uses the other components of the rotation vector with the forced oscillation test data and computed derivatives. The technique resolves the problem of separating the pure rotational and acceleration terms of the forced oscillation test data. The author makes recommendations about the data reduction procedure for forced oscillation testing to make the results more usable for aircraft motion simulation.

*Northrop Corporation, 3901 West Broadway, Hawthorne, CA 90250, USA

72 *Bihrle, W., Jr.: **Prediction of High Alpha Flight Characteristics Utilizing Rotary Balance Data.** Presented at the 13th ICAS Congress, and the AIAA Aircraft Systems and Technology Conference, Seattle, Wash., Aug. 22-27, 1982. In: Proceedings, vol. 1, (A82-40876), AIAA, 1982, pp. 761-768.

A82-40953#

The author uses rotational flow aerodynamic data, as measured on a rotary balance at low Reynolds number, to predict steady spin modes and post-stall motions. The excellent agreement obtained between predicted and full-scale flight results show low Reynolds number rotary balance data is sufficient for calculating steady-spin modes for military and general aviation configurations not having large wing leading-edge radii. The author discusses considerations in the use of low Reynolds number data to steady-state spin analysis, as well as large angle, six degree-of-freedom high α studies. The author also illustrates the procedure for developing a configuration highly resistant to spins.

*Bihrle Applied Research, Inc., Jericho, NY 11753, USA

73 *Beyers, M. E.: **A New Concept for Aircraft Dynamic Stability Testing.** Journal of Aircraft, vol. 20, no. 1, Jan. 1983, pp. 5-14.

A83-15310

Note: For an earlier form of this report and an abstract see no. 56.

*National Aeronautical Establishment, National Research Council, Ottawa, ON K1A OR6, Canada

74 *Bihrle, W., Jr.; and *Barnhart, B.: **Spin Prediction Techniques.** Journal of Aircraft, vol. 20, Feb. 1983, pp. 97-101.

A83-18401#

Note: For an earlier form of this paper see no. 52.

Researchers developed a rotary balance rig located in the Langley spin tunnel to identify rapidly an airplane's aerodynamic characteristics in a

rotational flow environment. The generation of on-line rotary balance data plots and predicted steady spin modes concurrent with data acquisition permit the designer to develop, on site, a configuration highly resistant to spins, or one exhibiting desirable spin characteristics if it is to be used for aerobatics or training. The rotary balance data are also used to compute time histories of the incipient, developed, and recovery phases of a spin. This paper discusses these spin analysis techniques, i.e., evaluation of rotary balance data, predicted steady spin equilibrium, and large angle, six-degree-of-freedom time history calculations.

*Bihrle Applied Research, Inc., Jericho, NY 11753, USA
Contracts: NAS1-14849 and NAS1-16205

75 *Ericsson, L. E.; and *Reding, J. P.: **Dynamics of Forebody Flow Separation and Associated Vortices.** Presented at the AIAA Atmospheric Flight Mechanics Conference, Gatlinburg, Tenn., Aug. 15-17, 1983, 12 pp., 26 refs. Also: Journal of Aircraft, vol. 22, no. 4, Apr. 1985, pp. 329-335.

AIAA Paper 83-2118 A83-41943#

We know there is a strong coupling between body motion and boundary layer separation with attendant vortex shedding. This paper studies this coupling for the particular case of a missile or an aircraft fuselage at very high αs. We can explain the unusual results obtained in recent tests by considering the so-called "moving-wall effect" on boundary layer transition and/or separation.

*Lockheed Missiles & Space Company, Inc., Sunnyvale, CA 94086, USA

76 *Orlik-Rückemann, K. J.; *Hanff, E. S.; and *Beyers, M. E.: **Recent Developments and Future Directions in Dynamic Stability Research at NAE, Ottawa.** Presented at the Fluid Dynamics Panel Symposium, Cesme, Turkey, Sept. 26-29, 1983. In: AGARD-CP-348, (N84-23564), Wind Tunnels and Testing Techniques, Feb. 1984, pp. 17-1 through 17-6, 14 refs.

N84-23582#

This paper gives a review of recent developments in dynamic stability research in the Unsteady Aerodynamics Laboratory of the NAE. The developments include design and construction of several new oscillatory rigs, conceptual studies of some additional rigs and thoughts about the future direction of the activities in this field. It briefly describes a method to account for sting oscillation effects on direct derivatives measured in a pitch oscillation experiment. It discusses some representative oscillatory results recently obtained on the so called Standard Dynamics Model.

*National Aeronautical Establishment, National Research Council, Ottawa, ON K1A OR6, Canada

77 *Marazzi, R.; *Malara, D.; *Lucchesini, M.; *Comoretto, S.; and *Pacori, F.: **Use of a Small Scale Wind Tunnel and Model Shop at Aeronautica Macchi as an Industrial Tool.** Presented at the Fluid Dynamics Panel Symposium, Cesme, Turkey, Sept. 26-29, 1983. In: AGARD-CP-348, (N84-23564), Wind Tunnels and Testing Techniques, Feb. 1984, pp. 20-1 through 20-15, 10 refs.

N84-23585#

The paper describes some facilities and capabilities available at the Aerodynamic Test Department of Aeronautica Macchi. Special testing techniques allow us to use a small scale wind tunnel to obtain useful data for the development of aircraft configurations. Model work-shop capabilities permit the manufacture of specialized wind tunnel models for detailed analysis of problem areas. The paper describes the updating of a rotary balance rig to measure dynamic derivatives due to roll in the full range of model attitudes. It includes an assessment of Reynolds number effects on high lift devices of modern design. Finally, it describes the design and manufacture of an afterbody model and the manufacture and testing of flutter models.

*Aermacchi SpA, Varese, Italy

78 *Orlik-Rückemann, K. J.: **Aerodynamic Aspects of Aircraft Dynamics at High Angles of Attack.** Journal of Aircraft, vol. 20, no. 9, Sept. 1983, pp. 737-752.

A83-43964#

Note: For an earlier form of this paper and an abstract see no. 70.

*National Aeronautical Establishment, National Research Council, Ottawa, ON K1A OR6, Canada

79 *Ericsson, L. E.; and *Reding, J. P.: **Review of Support Interference in Dynamic Tests.** AIAA Journal, vol. 21, Dec. 1983, pp. 1652-1666, 81 refs.

ISSN 0001-1452 A84-13572

Note: For an earlier version and an abstract see no. 69.

*Lockheed Missiles & Space Co., Inc., Sunnyvale, CA 94068, USA

80 *Larson, M. S.: **The Effect of Constant Versus Oscillatory Rates on Dynamic Stability Derivatives.** Air Force Inst. of Tech., M.S. Thesis, AFIT/GAE/ENY/83D-11, Dec. 1983, 101 pp.

AD-A136913 N84-19293#

The purpose of this thesis was to determine if there are phenomenological differences between dynamic derivations calculated from F-15A rotary balance data and data from other sources. To do this, two additional sets of F-15A stability derivative data were obtained: (1) design phase, and (2) production phase. The lateral dynamic derivatives were then compared through derivatives of the lateral moments with respect to the rotation rate about the velocity vector (wind vector). The author concluded differences exist between the data sets, but the dominant characteristics were the same for all of the data sets. The differences in the data were not indicative of basic (phenomenological) differences in the data itself. Therefore, the contention that oscillatory rates affect determination of the dynamic derivations was not substantiated by this study.

*Wright-Patterson AFB, Dayton, OH 45433, USA

81 *McCormick, B. W.; **Zilliac, G. G.; and ***Ballin, M. G.: **Wind Tunnel Testing and Analysis Relating to the Spinning of Light Aircraft.** Presented at the AIAA 22nd Aerospace Sciences Meeting, Reno, Nev., Jan. 9-12, 1984, 13 pp.

AIAA Paper 84-0558 A84-18163#

Included is a summary of two studies related to the spinning of light aircraft. We made the first study to demonstrate we can obtain the aerodynamic forces and moments acting on the tail of a spinning aircraft from static wind-tunnel tests. The second was an analytical study of spinning using a high α aerodynamic model derived from a static wind-tunnel data base. We show the validity of the aerodynamic model by comparisons with rotary-balance and forced-oscillation data. The results of a six-degree-of-freedom analysis show we have properly modeled the dynamics and aerodynamics of the steep- and flat-spin modes of a modified Yankee airplane.

*Pennsylvania State University, University Park, PA 16802, USA
**NASA Ames Research Center, Moffett Field, CA 94035, USA
***Rockwell International Corp., Downey, CA 90241, USA

82 *Beyers, M. E.: **Characteristic Motions for Simulation of Post-Stall Maneuvers and Flight Instabilities.** In: Aeronautical Society of South Africa and South African Institute of Aeronautical Engineers, Journal, vol. 5, no. 1, 1984, pp. 20-34.

ISSN 0250-3786 A85-21679

This paper proposes an approach to the problems of experimentally determining the aerodynamic characteristics of aircraft maneuvering in the nonlinear, post-stall flight regime. It recognizes the importance of correctly representing the motion characteristics in unsteady aerodynamic measurements under these conditions. It indicates different approaches depending on whether the flight is oscillatory or nonoscillatory (aperiodic) and nonplanar or near-planar. The paper discusses the requirements for captive-model tests designed to yield the

instantaneous dynamic-load histories of ramp-shaped intermittent motions and nonplanar oscillatory motions. The paper introduces the principle or "orbital epicyclic motion" and gives an analysis of its potential for high-α nonplanar oscillatory tests. In the simulation of complex, nonplanar maneuvers, it suggests an approach based on complementing the captive-model tests with wind tunnel free-flight studies of models trimmed at high α.

*National Aeronautical Establishment, National Research Council, Ottawa, ON K1A OR6, Canada

83 *Poppen, W. A., Jr.: **A Method for Estimating the Rolling Moment Due to Spin Rate for Arbitrary Planform Wings.** NASA TM-86365, Jan. 1985, 23 pp.

N85-18990#

The use of aerodynamic theory for estimating the force and moments acting on spinning airplanes is of interest. For example, researchers have used strip theory to estimate the aerodynamic characteristics as a function of spin rate for wing-dominated configurations for αs up to 90°. This paper extends this work, previously limited to constant chord wings, to wings consisting of tapered segments. Comparison of the analytical predictions with rotary balance wind tunnel data shows large discrepancies remain, particularly for αs greater than 40°.

*NASA Langley Research Center, Hampton, VA 23665-5225, USA

84 *Ericsson, L. E.; and *Reding, J. P.: **Dynamics of Forebody Flow Separation and Associated Vortices.** Journal of Aircraft, vol. 22, no. 4, Apr. 1985, pp. 329-335.

ISSN 0021-8669 A85-29262#

Note: For an earlier version of this paper and an abstract see no. 75.

*Lockheed Missiles & Space Company, Inc., Sunnyvale, CA 94086, USA

85 *Malcolm, G. N.; and *Schiff, L. B.: **Recent Developments in Rotary-Balance Testing of Fighter Aircraft Configurations at NASA Ames Research Center.** Presented at the symposium on Unsteady Aerodynamics--Fundamentals and Application to Aircraft Dynamics held in Göttingen, West Germany, May 6-9, 1985. In: AGARD-CP-386 (N86-27224#), Nov. 1985, pp. 18-1 through 18-25.

N86-27242#

Note: For another form of this paper and an abstract see no. 91.

*NASA Ames Research Center, Moffett Field, CA 94035, USA

86 *O'Leary, C. O.; and *Rowthorn, E. N.: **New Rotary Rig at RAE and Experiments on HIRM.** Presented at the symposium on Unsteady Aerodynamics--Fundamentals and Applications to Aircraft Dynamics held in Göttingen, West Germany, May 6-9, 1985. In: AGARD-CP-386 (N86-27224#), Nov. 1985, pp. 19-1 through 19-14. Also: Aeronautical Journal, (ISSN 000-1-9240), vol. 90, Dec. 1986, pp. 399-409.

N86-27243#

Note: For another form of this report see no. 97.

Researchers at the Royal Aircraft Establishment, Bedford, have commissioned a rig to measure the forces and moments due to continuous rate of roll. Tests were made on a High Incidence Research Model (HIRM) in two wind tunnels at M = 0.2, 0.4, and 0.7. We can test models up to α = 40° at rotational speeds up to 350 rpm. Tests on HIRM included a study of configuration and Reynolds number effects. We compare results with similar data from another rolling rig and from small-amplitude oscillatory tests.

*Royal Aircraft Establishment, Bedford, MK41 6AE, UK

87 *Jansson, T.; and *Torngren, L.: **New Dynamic Testing Techniques and Related Results at FFA.** Presented at the symposium on Unsteady Aerodynamics--Fundamentals and Applications to Aircraft Dynamics held in Göttingen, West Germany, May 6-9, 1985. In: AGARD-CP-386 (N86-27224#), Nov. 1985, pp. 20-1 through 20-14.

N86-27244#

In recent years we have seen an emphasis on the extraction of dynamic derivatives from wind tunnel testing. This is apparent from the number of different rigs developed and in use, both in the subsonic and transonic wind tunnels. This paper briefly describes the different rigs, testing procedures and data handling. It presents a wide survey of the different rigs used for dynamic derivative testing and the corresponding testing capability.

*The Aeronautical Institute of Sweden (FAA)
S-161 11 Bromma, Sweden

88 *Tristrant, D.; and *Renier, O.: **Recents Developements des Techniques de Simulation Dynamique Appliquees a l'Identification des Parametres de Stabilite.** Presented at the symposium on Unsteady Aerodynamics--Fundamentals and Applications to Aircraft Dynamics held in Göttingen, West Germany, May 6-9, 1985. In: AGARD-CP-386 (N86-27225#), Nov. 1985, pp. 22-1 through 22-14.

N86-27246#

In the context of aircraft dynamic behavior prediction, this paper describes experimental and analytical methods to identify mathematical linear modeling parameters using a test rig at the Institut de Mecanique des Fluides de Lille. We describe the rig characteristics, the experimental procedures, the identification methods, and results from different aircraft models. Emphasis is put on the interest of a specific λ degree of freedom angle formed by the rotational vector and velocity vector. Effectively, we show that rotational tests with a non zero value of λ offer interesting possibilities for identification and allow the estimation of linear model parameters in the case of a quasi-linear path. We obtained a different degree of freedom called *gyration radius* by fixing a special mechanism onto the test rig. By carrying out a carefully selected test program, this degree of freedom allows us to identify the whole set of stability parameters, given the structure of the linear mathematical model. Finally, dynamic measures obtained during oscillatory coning using a complete aircraft model produced in evidence the large amplitude of unsteady aerodynamic phenomena at high α, which we can not ignore if we seek prediction of post stall evolutions.

*ONERA-IMFL, 5 boulevard Paul Painlevé 5900 Lille, France

89 *Orlik-Rückemann, K. J., Editor: **Unsteady Aerodynamics - Fundamentals and Applications to Aircraft Dynamics.** Fluid Dynamics and Flight Mechanics Panel Symposium held in Göttingen, West Germany, May 6-9, 1985. AGARD-CP-386, Nov. 1985, 620 pp., in English and French.

AD-A165045 N86-27224#
ISBN-92-835-0382-1

Note: See nos. 87 and 88 for some relevant papers presented at this symposium. There is a Technical Evaluation Report on this symposium, AGARD-AR-222 (N86-27182#), Jan. 1986.

This paper examines recent advances experimental and computational methods for predicting nonlinear flow phenomena in unsteady aerodynamics and stability parameters required to describe adequately the dynamic behavior of aircraft. It gives special emphasis to high α. Topics addressed include: unsteady boundary layers; unsteady separation and stall; buffeting; unsteady airloads; wind tunnel and flight test techniques, with emphasis on the measurement of nonlinearities, aerodynamic cross-coupling, hysteresis, and time dependent effects; mathematical modeling; bifurcation theory; prediction of wing rock; and advanced control systems.

*National Aeronautical Establishment, National Research Council, Ottawa, ON K1A OR6, Canada

90 *Demeis, R.: **Taming the Deadly Spin.** Aerospace America, vol. 23, June 1985, pp. 74-77.

ISSN 0740-722X A85-36148#

Research into techniques and aircraft components which avoid stall and

spin and/or enhance recovery began in the 1930s. Devices which delayed stall frequently accelerated the transition when it did occur. Military aircraft received the most spin wind tunnel research from the 1940s to the 1970s, when NASA began looking at light aircraft in spin. Researchers have measured forces and moments on spinning aircraft using a rotary balance. Wind tunnel tests have examined the spin aerodynamics of fuselages, airfoils, tail surfaces, strakes, and fins. Stops and warning devices have been devised to keep the nose down. Studies are now focusing on the wing leading edge because it is the initiator and center of the stall conditions. Outboard drooping wings inhibit the spread of the stall vortices across the wing. Researchers have extended this method to a discontinuous outboard droop which is being used on the British Firecracker trainer.

*Engineering Editor of "Aerospace America", 1633 Broadway, New York, NY 10019, USA

91 *Malcolm, G. N.; and *Schiff, L. B.: **Recent Developments in Rotary-Balance Testing of Fighter Aircraft Configurations at NASA Ames Research Center.** NASA TM-86714, July 1985, 28 pp.

N85-32090#

Note: For an earlier form of this report see no. 85.

Two rotary balance rigs were developed for testing airplane models in a coning motion. A large rig was developed for use in the 12-Foot Pressure Wind Tunnel primarily to permit testing at high Reynolds numbers. This rig was recently used to study the aerodynamics of 0.05-scale model of the F-15 fighter aircraft. Effects of Reynolds number, spin rate parameter, model attitude, presence of a nose boom, and model/sting mounting angle were studied. A smaller rig, which studies the aerodynamics of bodies of revolution in a coning motion, was used in the 6-by-6 foot Supersonic Wind Tunnel to study the aerodynamic behavior of a simple representation of a modern fighter, the Standard Dynamic Model (SDM). Effects of spin rate parameter and model attitude were studied. This paper gives a description of the two rigs and discusses some of the results obtained in the respective test.

*NASA Ames Research Center, Moffett Field, CA 94035, USA

92 *Malcolm, G. N.: **Rotary-Balance Experiments on a Modern Fighter Aircraft Configuration at High Reynolds Numbers.** Presented at the AIAA 12th Atmospheric Flight Mechanics Conference, Snowmass, Colo., Aug. 19-21, 1985. In Technical Papers (A85-43826), 1985, pp. 462-482.

AIAA Paper 85-1829 A85-43870#

NASA Ames Research Center's research program to study high-angle-of-attack aerodynamic phenomena associated with high-performance aircraft includes the development and use of rotary balance rigs for wind tunnel tests of airplane models in a coning motion. A large scale rig, developed for testing models at high Reynolds numbers in the Ames 12-Foot Pressure Wind Tunnel, was recently tested with a 0.05-scale F-15 fighter model. Measurements were made at low subsonic Mach numbers and chord Reynolds numbers of 1 to 5.5 million, with angles of attack from 0 to 90 deg and sideslip angles from -15 to +15 deg. Effects of Reynolds number, spin-rate parameter, model attitude, presence of a nose boom, and model/sting mounting angle were studied.

*NASA Ames Research Center, Moffett Field, CA 94035, USA

93 *Ericsson, L. E.: **Reflections Regarding Recent Rotary Rig Results.** Presented at the AIAA 24th Aerospace Sciences Meeting, Reno, Nev., Jan. 6-9, 1986, 8 pp., 16 refs. Also: Journal of Aircraft, vol. 24, no. 1, Jan. 1987, pp. 25-30.

AIAA Paper 86-0123 A86-19703#

This paper examines recent rotary rig experiments to evaluate how well they simulate dynamic conditions existing in full scale flight. Most rig designs are prone to cause significant interference with the vortex wake shed from an advanced aircraft at high αs. The coupling existing between vehicle motion and boundary layer transition in the critical Reynolds number range, can aggravate the support interference problem. This coupling is unlikely to have been simulated in most wind tunnel tests.

*Lockheed Missiles & Space Company, Inc., Sunnyvale, CA 94086, USA

94 *Orlik-Rückemann, K. J.: **Aircraft Dynamics: Aerodynamic Aspects and Wind Tunnel Techniques.** Presented at the Special Course on Fundamentals of Fighter Aircraft Design sponsored by AGARD Fluid Dynamics Panel and the von Karman Institute, Feb. 17-28, 1986. In: AGARD Rep. 740, Oct. 1987, (N88-13315), pp. 5-1 through 5-16.

N88-13320#

Note: For earlier forms of this paper see nos. 70 and 78.

The dynamic behavior of modern fighter aircraft depends more and more on unsteady aerodynamics. Until recently, the designer concentrated on classical problems such as aeroelasticity and flutter. Dynamic stability parameters were most often determined by low α calculation methods, without much recourse to experiment. The results obtained from the few dynamic experiments were used to confirm the absence of problems rather than as design parameters. New requirements for fighter aircraft performance include the ability to fly at high α in the presence of extensive regions of separated or vortical flows, relaxed static stability, greatly increased agility, and an interest in unorthodox geometries such as closely-coupled-canard or tail-first configurations. The time lags and unsteady phenomena associated with flow fields, resulting from rapid maneuvers and large amplitude motions, significantly affect the dynamic behavior of modern fighter aircraft and become as important for aircraft design as the classical static performance criteria. A review is made of the various aerodynamic aspects affecting aircraft dynamic behavior, followed by a survey of the most pertinent experimental techniques.

*Unsteady Aerodynamics Laboratory, National Research Council of Canada, Ottawa, Ontario, K1A 0R6, Canada

95 *Ericsson, L. E.; and *Reding, J. P.: **Dynamic Support Interference in High Alpha Testing.** Presented at the AIAA 14th Aerodynamic Testing Conference (A86-24726), West Palm Beach, Fla., Mar. 5-7, 1986, pp. 203-214, 32 refs.

AIAA Paper 86-0760 A86-24746#

This paper analyzes support interference effects on aerodynamic test results of aircraft models at high αs. Single degree of freedom oscillatory tests in pitch or yaw are subject to the same type of support interference through the near wake recirculatory region as experienced by slender bodies of revolution. Thus, we can correct the measurements for support interference using the same methodology. The support interference associated with rotary rigs used in coning experiments is of a different type. It is stationary in nature rather than unsteady, with the coning motion inducing a displacement of the vortex wake similar to that caused by sideslip in a static test. Making static tests at varying incidence and sideslip angles with two alternate supports can provide the information needed to correct coning experiments for support interference.

*Lockheed Missiles & Space Company, Inc., Sunnyvale, CA 94086, USA

96 *O'Leary, C. O.; and *Drew, W.: **Flow Visualization on Rolling Models Using Minitufts.** RAE TM Aero 2083, Aug. 1986, 20 pp., 4 refs.

Note: For another form of this report see no. 100.

Minitufts are increasingly used for flow visualization on static wind tunnel models. This is because we can apply them in larger numbers for increased detail and with less interference compared with conventional tufts. This Memorandum describes an extension of their use to continuously rotating models where the heavier conventional tufts are inadequate. We describe tests on two combat aircraft models in the 4m x 2.7m Low Speed Wind Tunnel. We explain measured variations of rolling moment with the aid of the minituft photographs. We include drawings and description of the RAE rotating rig.

*Royal Aircraft Establishment, Bedford MK41 6AE, UK

97 *O'Leary, C. O.; and *Rowthorn, E. N.: **New Rotary Rig at RAE and Experiments on HIRM.** Aeronautical Journal, vol. 90, Dec. 1986, pp. 399-409.

ISSN 0001-9240 A87-29264
Note: For an earlier form of this paper and abstract see no. 86.

*Royal Aeronautical Establishment, Bedford MK41 6AE, UK

98 *Ericsson, L. E.: **Reflections Regarding Recent Rotary Rig Results.** Journal of Aircraft, vol. 24, no. 1, Jan. 1987, pp. 25-30, 20 refs.

ISSN 0021-8669 A87-28070#

Note: For an earlier version of this report and an abstract see no. 93.

*Lockheed Missiles & Space Company, Inc., Sunnyvale, CA 94086, USA

99 *Kausche, G.: **Dynamic Wind Tunnel Balances in the DFVLR subsonic wind tunnel in Braunschweig (Dynamische Windkanalwaagen am Niedergeschwindigkeits-Windkanal der DFVLR in Braunschweig).** In: Zeitschrift für Flugwissenschaften und Weltraumforschung, vol. 11, May-June 1987, pp. 185-187, 7 refs., in German.

ISSN 0342-068X A88-12488

This paper briefly describes two dynamic balances for measuring dynamic derivatives in wind tunnels of the DFVLR subsonic wind tunnel in Braunschweig, the Mobile Oscillatory Derivative Balance (MODB) and the Rotary Derivative Balance (RDB). Information is presented on the measurement methods used, recent improvements and operations, and the attainable results. It is shown that the MODB, due to its mobility, has a higher productivity than the RDB.

*DFVLR, Institute für Flugmechanik, Braunschweig, West Germany

100 *O'Leary, C. D.; and *Drew, W.: **Flow Visualisation on Rolling Models Using Minitufts.** Aeronautical Journal, vol. 91, June-July 1987, pp. 269-274.

ISSN 0001-9240 A87-50587

Note: For an earlier form of this paper and an abstract see no. 96.

*Royal Aeronautical Establishment, Bedford MK41 6AE, UK

101 *Beyers, M. E.; and *Huang, X. Z.: **The Orbital-Platform Concept for Nonplanar Dynamic Testing.** Aeronautical Note NAE-AN-52, NRC No. 29133, May 1988, 40 pp.

A new concept is introduced for large-amplitude testing at high incidence. The dynamic test apparatus is characterized by an annular, orbital platform on which the model support and secondary drive mechanisms are mounted. The device can be used as a rotary apparatus, while arbitrary epicyclic motions (including fixed-plane, orbital modes) and oscillatory motions superimposed on the coning mode may be generated. The system is inherently very rigid and vibration levels can be kept very low. Aerodynamic interference is also very low as there is no need for bulky support hardware and the test section is circular. Accordingly, the system may be used to assess levels of support interference in conventional rotary tests

*Unsteady Aerodynamics Laboratory, National Research Council of Canada, Ottawa, Ontario, K1A OR6, Canada

AUTHOR INDEX

SUBJECT INDEX

Note: The following index, although in no way complete, may be useful by giving an indication of where some material on definite subject areas may be found. Surveys and summaries are not indexed in depth.

SOURCE INDEX

REPORT DOCUMENTATION PAGE

1. Recipient's Reference	2. Originator's Reference	3. Further Reference	4. Security Classification of Document
	AGARD-AR-265	ISBN 92-835-0577-2	UNCLASSIFIED

5. Originator Advisory Group for Aerospace Research and Development
North Atlantic Treaty Organization
7 rue Ancelle, 92200 Neuilly sur Seine, France

6. Title ROTARY-BALANCE TESTING FOR AIRCRAFT DYNAMICS

7. Presented at

8. Author(s)/Editor(s)	9. Date
Various	December 1990
10. Author's/Editor's Address	**11. Pages**
Various	264

12. Distribution Statement This document is distributed in accordance with AGARD policies and regulations, which are outlined on the Outside Back Covers of all AGARD publications.

13. Keywords/Descriptors

Fighter aircraft
Mathematical models
Dynamics
Aerodynamic loads
Wind tunnel tests
Rotation
Test procedures

14. Abstract

The results of a study on rotary-balance testing for aircraft dynamics are presented. The study — conducted by Working Group 11 of the AGARD Fluid Dynamics Panel —examined both the experimental techniques used to obtain rotary-flow aerodynamic data and the procedures involved in using this type of data in the mathematical modeling of the dynamic behavior of a maneuvering fighter aircraft. A special effort was made to summarize experiences involving correlation of dynamic behavior predictions with the observed motions of free-flight models and aircraft in flight. Specific hardware and problems encountered in rotary-balance experiments were addressed for experimental facilities in several countries and advanced applications were noted. The participants in WG11 represented Canada, France, Germany, Italy, the United Kingdom, and the United States.

AGARD Advisory Report No.265 Advisory Group for Aerospace Research and Development, NATO ROTARY-BALANCE TESTING FOR AIRCRAFT DYNAMICS Published December 1990 264 pages The results of a study on rotary-balance testing for aircraft dynamics are presented. The study — conducted by Working Group 11 of the AGARD Fluid Dynamics Panel — examined both the experimental techniques used to obtain rotary-flow aerodynamic data and the procedures involved in using this type of data in the mathematical modeling of the dynamic behavior of a maneuvering fighter aircraft. A special effort was made to summarize P.T.O.	AGARD-AR-265 Fighter aircraft Mathematical models Dynamics Aerodynamic loads Wind tunnel tests Rotation Test procedures	AGARD Advisory Report No.265 Advisory Group for Aerospace Research and Development, NATO ROTARY-BALANCE TESTING FOR AIRCRAFT DYNAMICS Published December 1990 264 pages The results of a study on rotary-balance testing for aircraft dynamics are presented. The study — conducted by Working Group 11 of the AGARD Fluid Dynamics Panel — examined both the experimental techniques used to obtain rotary-flow aerodynamic data and the procedures involved in using this type of data in the mathematical modeling of the dynamic behavior of a maneuvering fighter aircraft. A special effort was made to summarize P.T.O.	AGARD-AR-265 Fighter aircraft Mathematical models Dynamics Aerodynamic loads Wind tunnel tests Rotation Test procedures
AGARD Advisory Report No.265 Advisory Group for Aer[illegible]e Research and Development, NATO ROTARY-BALANCE TESTING FOR AIRCRAFT DYNAMICS Published December 1990 264 pages The results of a study on rotary-balance testing for aircraft dynamics are presented. The study — conducted by Working Group 11 of the AGARD Fluid Dynamics Panel — examined both the experimental techniques used to obtain rotary-flow aerodynamic data and the procedures involved in using this type of data in the mathematical modeling of the dynamic behavior of a maneuvering fighter aircraft. A special effort was made to summarize P.T.O.	AGARD-AR-265 Fighter aircraft Mathematical models Dynamics Aerodynamic loads Wind tunnel tests Rotation Test procedures	AGARD Advisory Report No.265 Advisory Group for Aerospace Research and Development, NATO ROTARY-BALANCE TESTING FOR AIRCRAFT DYNAMICS Published December 1990 264 pages The results of a study on rotary-balance testing for aircraft dynamics are presented. The study — conducted by Working Group 11 of the AGARD Fluid Dynamics Panel — examined both the experimental techniques used to obtain rotary-flow aerodynamic data and the procedures involved in using this type of data in the mathematical modeling of the dynamic behavior of a maneuvering fighter aircraft. A special effort was made to summarize P.T.O.	AGARD AR-265 Fighter aircraft Mathematical models Dynamics Aerodynamic loads Wind tunnel tests Rotation Test procedures

experiences involving correlation of dynamic behavior predictions with the observed motions of free-flight models and aircraft in flight. Specific hardware and problems encountered in rotary-balance experiments were addressed for experimental facilities in several countries and advanced applications were noted. The participants in WG11 represented Canada, France, Germany, Italy, the United Kingdom, and the United States. ISBN 92-835-0597-2	experiences involving correlation of dynamic behavior predictions with the observed motions of free-flight models and aircraft in flight. Specific hardware and problems encountered in rotary-balance experiments were addressed for experimental facilities in several countries and advanced applications were noted. The participants in WG11 represented Canada, France, Germany, Italy, the United Kingdom, and the United States. ISBN 92-835-0597-2
experiences involving correlation of dynamic behavior predictions with the observed motions of free-flight models and aircraft in flight. Specific hardware and problems encountered in rotary-balance experiments were addressed for experimental facilities in several countries and advanced applications were noted. The participants in WG11 represented Canada, France, Germany, Italy, the United Kingdom, and the United States. ISBN 92-835-0597-2	experiences involving correlation of dynamic behavior predictions with the observed motions of free-flight models and aircraft in flight. Specific hardware and problems encountered in rotary-balance experiments were addressed for experimental facilities in several countries and advanced applications were noted. The participants in WG11 represented Canada, France, Germany, Italy, the United Kingdom, and the United States. ISBN 92-835-0597-2

AGARD
NATO OTAN
7 RUE ANCELLE · 92200 NEUILLY-SUR-SEINE
FRANCE
Téléphone (1)47.38.57.00 · Télex 610 176
Télécopie (1)47.38.57.99

DIFFUSION DES PUBLICATIONS
AGARD NON CLASSIFIEES

L'AGARD ne détient pas de stocks de ses publications, dans un but de distribution générale à l'adresse ci-dessus. La diffusion initiale des publications de l'AGARD est effectuée auprès des pays membres de cette organisation par l'intermédiaire des Centres Nationaux de Distribution suivants. A l'exception des Etats-Unis, ces centres disposent parfois d'exemplaires additionnels; dans les cas contraire, on peut se procurer ces exemplaires sous forme de microfiches ou de microcopies auprès des Agences de Vente dont la liste suite.

CENTRES DE DIFFUSION NATIONAUX

ALLEMAGNE
Fachinformationszentrum,
Karlsruhe
D-7514 Eggenstein-Leopoldshafen 2

BELGIQUE
Coordonnateur AGARD-VSL
Etat-Major de la Force Aérienne
Quartier Reine Elisabeth
Rue d'Evere, 1140 Bruxelles

CANADA
Directeur du Service des Renseignements Scientifiques
Ministère de la Défense Nationale
Ottawa, Ontario K1A 0K2

DANEMARK
Danish Defence Research Board
Ved Idraetsparken 4
2100 Copenhagen Ø

ESPAGNE
INTA (AGARD Publications)
Pintor Rosales 34
28008 Madrid

ETATS-UNIS
National Aeronautics and Space Administration
Langley Research Center
M/S 180
Hampton, Virginia 23665

FRANCE
O.N.E.R.A. (Direction)
29, Avenue de la Division Leclerc
92320, Châtillon sous Bagneux

GRECE
Hellenic Air Force
Air War College
Scientific and Technical Library
Dekelia Air Force Base
Dekelia, Athens TGA 1010

ISLANDE
Director of Aviation
c/o Flugrad
Reykjavik

ITALIE
Aeronautica Militaire
Ufficio del Delegato Nazionale all'AGARD
3 Piazzale Adenauer
00144 Roma EUR

LUXEMBOURG
Voir Belgique

NORVEGE
Norwegian Defence Research Establishment
Attn: Biblioteket
P.O. Box 25
N-2007 Kjeller

PAYS-BAS
Netherlands Delegation to AGARD
National Aerospace Laboratory NLR
Kluyverweg 1
2629 HS Delft

PORTUGAL
Portuguese National Coordinator to AGARD
Gabinete de Estudos e Programas
CLAFA
Base de Alfragide
Alfragide
2700 Amadora

ROYAUME UNI
Defence Research Information Centre
Kentigern House
65 Brown Street
Glasgow G2 8EX

TURQUIE
Milli Savunma Başkanlığı (MSB)
ARGE Daire Başkanlığı (ARGE)
Ankara

LE CENTRE NATIONAL DE DISTRIBUTION DES ETATS-UNIS (NASA) NE DETIENT PAS DE STOCKS DES PUBLICATIONS AGARD ET LES DEMANDES D'EXEMPLAIRES DOIVENT ETRE ADRESSEES DIRECTEMENT AU SERVICE NATIONAL TECHNIQUE DE L'INFORMATION (NTIS) DONT L'ADRESSE SUIT.

AGENCES DE VENTE

National Technical Information Service
(NTIS)
5285 Port Royal Road
Springfield, Virginia 22161
Etats-Unis

ESA/Information Retrieval Service
European Space Agency
10, rue Mario Nikis
75015 Paris
France

The British Library
Document Supply Division
Boston Spa, Wetherby
West Yorkshire LS23 7BQ
Royaume Uni

Les demandes de microfiches ou de photocopies de documents AGARD (y compris les demandes faites auprès du NTIS) doivent comporter la dénomination AGARD, ainsi que le numéro de série de l'AGARD (par exemple AGARD-AG-315). Des informations analogues, telles que le titre et la date de publication sont souhaitables. Veuiller noter qu'il y a lieu de spécifier AGARD-R-nnn et AGARD-AR-nnn lors de la commande de rapports AGARD et des rapports consultatifs AGARD respectivement. Des références bibliographiques complètes ainsi que des résumés des publications AGARD figurent dans les journaux suivants:

Scientifique and Technical Aerospace Reports (STAR)
publié par la NASA Scientific and Technical
Information Division
NASA Headquarters (NTT)
Washington D.C. 20546
Etats-Unis

Government Reports Announcements and Index (GRA&I)
publié par le National Technical Information Service
Springfield
Virginia 22161
Etats-Unis

(accessible également en mode interactif dans la base de données bibliographiques en ligne du NTIS, et sur CD-ROM)

Imprimé par Specialised Printing Services Limited
40 Chigwell Lane, Loughton, Essex IG10 3TZ

AGARD
NATO OTAN
7 RUE ANCELLE · 92200 NEUILLY-SUR-SEINE
FRANCE
Telephone (1)47.38.57.00 · Telex 610 176
Telefax (1)47.38.57.99

DISTRIBUTION OF UNCLASSIFIED AGARD PUBLICATIONS

AGARD does NOT hold stocks of AGARD publications at the above address for general distribution. Initial distribution of AGARD publications is made to AGARD Member Nations through the following National Distribution Centres. Further copies are sometimes available from these Centres (except in the United States), but if not may be purchased in Microfiche or Photocopy form from the Sales Agencies listed below.

NATIONAL DISTRIBUTION CENTRES

BELGIUM
Coordonnateur AGARD — VSL
Etat-Major de la Force Aérienne
Quartier Reine Elisabeth
Rue d'Evere, 1140 Bruxelles

CANADA
Director Scientific Information Services
Dept of National Defence
Ottawa, Ontario K1A 0K2

DENMARK
Danish Defence Research Board
Ved Idraetsparken 4
2100 Copenhagen Ø

FRANCE
O.N.E.R.A. (Direction)
29 Avenue de la Division Leclerc
92320 Châtillon

GERMANY
Fachinformationszentrum
Karlsruhe
D-7514 Eggenstein-Leopoldshafen 2

GREECE
Hellenic Air Force
Air War College
Scientific and Technical Library
Dekelia Air Force Base
Dekelia, Athens TGA 1010

ICELAND
Director of Aviation
c/o Flugrad
Reykjavik

ITALY
Aeronautica Militare
Ufficio del Delegato Nazionale all'AGARD
3 Piazzale Adenauer
00144 Roma/EUR

LUXEMBOURG
See Belgium

NETHERLANDS
Netherlands Delegation to AGARD
National Aerospace Laboratory, NLR
Kluyverweg 1
2629 HS Delft

NORWAY
Norwegian Defence Research Establishment
Attn: Biblioteket
P.O. Box 25
N-2007 Kjeller

PORTUGAL
Portuguese National Coordinator to AGARD
Gabinete de Estudos e Programas
CLAFA
Base de Alfragide
Alfragide
2700 Amadora

SPAIN
INTA (AGARD Publications)
Pintor Rosales 34
28008 Madrid

TURKEY
Millî Savunma Başkanlığı (MSB)
ARGE Daire Başkanlığı (ARGE)
Ankara

UNITED KINGDOM
Defence Research Information Centre
Kentigern House
65 Brown Street
Glasgow G2 8EX

UNITED STATES
National Aeronautics and Space Administration (NASA)
Langley Research Center
M/S 180
Hampton, Virginia 23665

THE UNITED STATES NATIONAL DISTRIBUTION CENTRE (NASA) DOES NOT HOLD STOCKS OF AGARD PUBLICATIONS, AND APPLICATIONS FOR COPIES SHOULD BE MADE DIRECT TO THE NATIONAL TECHNICAL INFORMATION SERVICE (NTIS) AT THE ADDRESS BELOW.

SALES AGENCIES

National Technical
Information Service (NTIS)
5285 Port Royal Road
Springfield, Virginia 22161
United States

ESA/Information Retrieval Service
European Space Agency
10, rue Mario Nikis
75015 Paris
France

The British Library
Document Supply Centre
Boston Spa, Wetherby
West Yorkshire LS23 7BQ
United Kingdom

Requests for microfiches or photocopies of AGARD documents (including requests to NTIS) should include the word 'AGARD' and the AGARD serial number (for example AGARD-AG-315). Collateral information such as title and publication date is desirable. Note that AGARD Reports and Advisory Reports should be specified as AGARD-R-nnn and AGARD-AR-nnn, respectively. Full bibliographical references and abstracts of AGARD publications are given in the following journals:

Scientific and Technical Aerospace Reports (STAR)
published by NASA Scientific and Technical
Information Division
NASA Headquarters (NTT)
Washington D.C. 20546
United States

Government Reports Announcements and Index (GRA&I)
published by the National Technical Information Service
Springfield
Virginia 22161
United States
(also available online in the NTIS Bibliographic
Database or on CD-ROM)

Printed by Specialised Printing Services Limited
40 Chigwell Lane, Loughton, Essex IG10 3TZ

ISBN 92-835-0597-2